

# Numerical modelling of the effects of biofouling on ship resistance and propulsion characteristics

---

Farkas, Andrea

Doctoral thesis / Disertacija

2021

*Degree Grantor / Ustanova koja je dodijelila akademski / stručni stupanj:* **University of Zagreb, Faculty of Mechanical Engineering and Naval Architecture / Sveučilište u Zagrebu, Fakultet strojarstva i brodogradnje**

*Permanent link / Trajna poveznica:* <https://urn.nsk.hr/urn:nbn:hr:235:402773>

*Rights / Prava:* [In copyright](#)/[Zaštićeno autorskim pravom.](#)

*Download date / Datum preuzimanja:* **2024-07-10**

*Repository / Repozitorij:*

[Repository of Faculty of Mechanical Engineering and Naval Architecture University of Zagreb](#)





University of Zagreb  
Faculty of Mechanical Engineering and Naval Architecture

Andrea Farkas

**Numerical modelling of the effects of biofouling on  
ship resistance and propulsion characteristics**

DOCTORAL THESIS

Zagreb, 2021





Sveučilište u Zagrebu  
Fakultet strojarstva i brodogradnje

Andrea Farkas

**Numeričko modeliranje utjecaja obraštanja na  
značajke otpora i propulzije broda**

DOKTORSKI RAD

Zagreb, 2021



## BIBLIOGRAPHY DATA

UDC: 629.5.015.2:629.5.016.7

Keywords: biofouling; ship hydrodynamics; Computational Fluid Dynamics; Reynolds Averaged Navier-Stokes; roughness function; performance prediction method

Scientific area: Technical sciences

Scientific field: Naval architecture

Institution: University of Zagreb, Faculty of Mechanical Engineering and Naval Architecture

Supervisor: PhD Nastia Degiuli, full professor

Number of pages: 270

Number of figures: 137

Number of tables: 95

Number of references: 262

Date of examination: 4<sup>th</sup> March 2021

Committee for the evaluation: PhD Željko Tuković, full professor  
PhD Roko Dejhalla, full professor  
PhD Yigit Kemal Demirel, Senior Lecturer

Archive: University of Zagreb, Faculty of Mechanical Engineering and Naval Architecture

## Acknowledgements

I would like to express my most sincere gratitude to my supervisor, professor Nastia Degiuli, who has been wonderful mentor to me, who provided me with an opportunity to study for a PhD and encouraged me during this whole period. I appreciate that she was always helpful and willing to set aside her own time to discuss my questions and ideas. Also, I wish to thank her for all of the supportive comments and conversations regarding my PhD research, which, along with her very detailed reading of my work really improved my thesis. Her advices regarding my research and teaching activities, as well as with career in general have been precious. I am also thankful to her, along with professor Kalman Žiha, for introducing me to the world of scientific publishing through my engagement in journal Brodogradnja. Professor Žiha taught me a lot about scientific publishing through our work and interesting conversations. Also, I would like to express my deepest gratefulness to my colleague Ivana Martić for showing me what it means to have a colleague who is always very helpful and available for observations regarding my reflections, ideas and hypotheses related to my research. She was also there to help regarding all tasks and activities related to my PhD study. Besides that, she was also a good friend and along with professors Degiuli and Žiha helped to make my time during PhD more enjoyable.

Furthermore, I wish to express my honest appreciation to PhD Yigit Kemal Demirel for hosting me twice at the University of Strathclyde, providing me with a warm welcome, sharing advices and discussing topics related to biofouling. Also, his effort invested in reading my PhD thesis and providing me with specific comments and feedback was helpful and meaningful. I wish to express my gratitude to his colleague PhD Soonseok Song for his availability to show me Kelvin Hydrodynamics Laboratory and turbulent channel flow facility, as well as for exchanging knowledge during my stay at the University of Strathclyde and through online meetings as well. Scientific collaboration with both of them has improved my PhD thesis. I wish to express my thankfulness to the University of Zagreb and AMAC UK for giving me an opportunity to visit this prestigious University in UK. Also, I wish to thank The society of university teachers, scholars and other scientists – Zagreb and Faculty of Mechanical Engineering and Naval Architecture for awards that I received related to my research. These awards have given me additional motivation towards my further research activities.

I would like to thank professor Željko Tuković for his effort regarding reading my PhD thesis, for giving suggestions and for his availability to discuss and provide help regarding all of my questions related to my studies and research. I would also like to express my gratitude to professor Roko Dejhalla for reading my PhD thesis and for his comments related to it. Also, I am grateful for all discussions regarding ship hydrodynamics, especially in the early stages of my PhD study.

I am grateful to professor Michael Schultz who shared his experimental results regarding biofilm. Also, I am very grateful to professor Milovan Perić, for his support, advices, comments and sharing a knowledge regarding CFD. I wish to express my gratitude to my colleagues Josip, Deni and Antonio for our discussions related to problems in naval architecture. Also, I would like to express my gratefulness to Ivica who, besides having been a work colleague, kept me company during our meetings, at conferences, in café bars and on the football field.

Furthermore, many thanks go to all of my friends, especially Bože, Ivan, Marko and Nikola for their support, encouragements and for being interested in my PhD study. Our times spent

together in Zagreb, Split as in all other places really made these years even more enjoyable. I would like to express my most special gratitude to my family, my father Andrea, my mother Ljiljana, my brother Antonio and my sister Katarina for believing in me and supporting me all the time. Their prayers and encouragements helped me and empowered me.

Finally, words cannot express how grateful I am to my better half Mirna for her understanding and support during my PhD thesis. Thank you for always hearing me out, believing in me, encouraging me, and also for many delicious meals you have prepared, all of which made these times even better. Finally, thank you for bringing joy to my life. Without you, I would not be able to achieve this.



## Statement of Originality

I hereby declare that to the best of my knowledge, the content of this thesis is my own work. This thesis has not been submitted for any degree or other purposes. I certify that the intellectual content of this thesis is the product of my own work and that all the assistance received in preparing this thesis and sources have been acknowledged.

Andrea Farkas

A handwritten signature in blue ink that reads "Farkas". The signature is written in a cursive style and is contained within a light blue rectangular box.

## Abstract

The effect of biofouling on the hydrodynamic characteristics of ship resistance and propulsion in calm water is very important from both an economic and environmental point of view. Hydrodynamic performance of a ship is disrupted because of the presence of biofouling organisms, which results in increased fuel consumption, ship speed reduction and increased emission of harmful gases. Presently, there is no comprehensive procedure, which could reliably predict the effect of biofouling on the ship hydrodynamic characteristics. Consequently, International Towing Tank Conference (ITTC) has advised scientists to present new formulae or methods based on the experimental data to determine the effect of biofouling on the ship resistance and propulsion characteristics.

Since biofouling depends on many parameters and it is very difficult to predict how long will antifouling coatings prevent fouling of a ship, the proposed research is focused on the effects of predetermined surface conditions on the ship hydrodynamic characteristics. Biofouling can be classified into the soft, hard and composite fouling. In this thesis the effects of biofilm and hard fouling on ship resistance, propeller open water and ship self-propulsion characteristics are investigated.

Within the proposed research commercial software package is used. The mathematical model is based on the averaged continuity equation and Reynolds Averaged Navier-Stokes (RANS) equations. Governing equations are discretised utilizing Finite Volume Method (FVM). After the analysis of several turbulence models for the closure of set of equations and their influence on the obtained ship hydrodynamic characteristics has been performed,  $k - \omega$  Shear Stress Transport turbulence model is selected as a compromise between accuracy and computational time. Volume of Fluid method is utilized for tracking and locating the free surface. The effects of biofouling are modelled through the implementation of roughness function model within the wall function of Computational Fluid Dynamics (CFD) solver. The research is based on the wall similarity hypothesis which claims that roughness effects are limited to inner layer of turbulent boundary layer.

The validity of numerical procedure is examined through verification and validation of the obtained results. The validation of the obtained numerical results for the smooth surface condition is carried out by comparison with the extrapolated towing tank results and other numerical studies available in the literature. The validation of numerical drag characterization study is performed by comparison of the obtained numerical results and experimental ones. Also, the obtained numerical results in terms of the increase in frictional resistance for a flat plate having the same length as a ship are compared with the ones obtained using the Granville similarity law scaling method. Thereafter, the applicability of the proposed CFD approach is demonstrated on the example of three full-scale merchant ships.

Also, the newly proposed performance prediction method for fouled surfaces is presented, which can account for fouling effects on the ship performance. The applicability of this method is demonstrated for fouling conditions with lower fouling rates. Thus, a robust and rapid assessment of the effects of biofouling on the ship hydrodynamic characteristics in calm water is enabled.

**Keywords:** biofouling; ship hydrodynamics; Computational Fluid Dynamics; Reynolds Averaged Navier-Stokes; roughness function; performance prediction method

# Prošireni sažetak

## Uvod

Obraštanje je nakupljanje mikroorganizama, biljaka, algi ili životinja na površinama koje su u kontaktu s vodom te predstavlja rastući problem s ekonomskog, ali i ekološkog stajališta. Iako je obraštanje prisutno u mnogim različitim područjima, pomorska industrija je najviše pogođena prisutnošću i rastom organizama. Prisutnost raznih organizama na trupu broda uzrokuje povećanje hrapavosti trupa broda. Zbog toga se otpor trenja povećava, što uzrokuje povećanje potrošnje goriva, smanjene brzine broda i povećanje opterećenja motora. Pokazano je kako su svi troškovi vezani uz razvoj, nabavu i primjenu, kao i relativno skupo tehničko ili plansko rješenje za antivegetativnu zaštitu brodova, ekonomski opravdani ukoliko i u maloj mjeri poboljšavaju stanje obraštenog trupa. Još jedan problem vezan uz obraštanje trupa broda je rasprostiranje biljnih i životinjskih vrsta svjetskim morima i posljedični poremećaj i promjena postojećih bio sustava. Energetska učinkovitost broda, koja se može razmatrati kroz potrošnju goriva po satu, brzinu i nosivost broda, ovisi o otporu broda, stupnju djelovanja propulzije, interakciji trupa broda i brodskog vijka, specifičnoj potrošnji goriva motora itd. Iako je u procesu osnivanja broda jedan od glavnih zadataka postizanje određene brzine tijekom pokusne plovidbe na određenom gazu uz određenu potrošnju goriva, jednako je tako važno točno predvidjeti brzinu broda i potrošnju goriva u uvjetima službe, što u velikoj mjeri ovisi o obraštanju. Važnost određivanja utjecaja obraštanja na hidrodinamičke značajke broda u mirnoj vodi jednako je važna kao i povećanje energetske učinkovitosti postojećih brodova kroz primjenu novih antivegetativnih premaza, budući da može ukazati na važnost čišćenja trupa broda i brodskog vijka. Naime, iako postoje razne mjere za povećanje energetske učinkovitosti brodova, brodovlasnici ili operateri broda oklijevaju s njihovom primjenom zbog nedostataka pouzdanih informacija vezanih uz potencijalne uštede prilikom primjene pojedine mjere. Točan proračun povrata investicije za brodovlasnike ili operatere broda je nužan prilikom odlučivanja o implementaciji pojedine mjere. Optimizacija čišćenja trupa broda i brodskog vijka jedna je od mjera za poboljšavanje energetske učinkovitosti brodova nad kojom brodovlasnik ili operater broda ima veliki utjecaj. Točna procjena utjecaja obraštanja na hidrodinamičke značajke broda, a time i utjecaja čišćenja na iste omogućuje procjenu ekonomskog aspekta ove mjere, što omogućuje točniju procjenu povrata investicije. Trenutno, ne postoji sveobuhvatna procedura pomoću koje bi se mogao pouzdano predvidjeti utjecaj obraštanja na hidrodinamičke značajke broda u službi. Iz tog razloga je International Towing Tank Conference (ITTC) izdao preporuke istraživačima da predlože nove izraze ili metode temeljene na eksperimentalnim podacima za predviđanje utjecaja obraštanja.

## Metodologija

Glavni cilj ovog doktorskog rada je razvoj numeričkog postupka temeljenog na računalnoj dinamici fluida (RDF), koji može simulirati utjecaj obraštanja na strujanje oko oplakane površine obraslog trupa broda i brodskog vijka. Primjenom ovoga modela moguće je odrediti utjecaj obraštanja na hidrodinamičke značajke otpora i propulzije u mirnoj vodi.

Model se temelji na hipotezi o sličnosti zida (eng. *wall similarity hypothesis*), odnosno na hipotezi da je utjecaj hrapavosti ograničen na unutarnji sloj turbulentnog graničnog sloja. Tako je ponašanje pojedine hrapave površine moguće opisati funkcijom hrapavosti, koja ustvari predstavlja pomak profila srednje brzine u logaritamskom području prema dolje. Kako ne postoji funkcija hrapavosti koja bi mogla opisati svaki pojedini tip hrapavosti, potrebno je izraditi studiju karakterizacije otpora (eng. *drag characterization study*) određenih tipova hrapavosti i na taj način odrediti tip funkcije i skalu hrapavosti, koja se koristi u definiciji Reynoldsovog broja hrapavosti. Za potrebe razvoja modela temeljenog na RDF-u, koji može simulirati utjecaj obraštanja, potrebno je odrediti model funkcije hrapavosti, odnosno ovisnost funkcije hrapavosti o Reynoldsovom broju hrapavosti. U ovome radu, temeljem studija karakterizacije otpora dostupnih u literaturi za dva tipa obraštanja, tj. biofilm i tvrdi obraštaj, predloženi su modeli funkcije hrapavosti za ova dva tipa obraštanja. Ovi modeli implementirani su u zidnu funkciju RDF rješavača te je time omogućeno određivanje utjecaja ovih tipova obraštanja na hidrodinamičke značajke proizvoljnog tijela. Budući da obraštanje ovisi o mnogim parametrima te da još uvijek nije moguće predvidjeti koliko dugo će antivegetativni premazi sprječavati obraštanje, ovo istraživanje je provedeno za unaprijed određena stanja obraštanja biofilmom i tvrdim obraštanjem.

Razvijeni RDF model temelji se na Reynoldsovim osrednjenim Navier-Stokesovim jednadžbama (eng. *Reynolds Averaged Navier-Stokes*, RANS), koje su diskretizirane primjenom metode konačnih volumena. Provedena je detaljna analiza utjecaja odabira modela turbulencije na dobivene hidrodinamičke značajke broda te je pokazano kako  $k-\omega$  Shear Stress Transport model turbulencije predstavlja najbolji kompromis između točnosti i proračunskog vremena za zatvaranje sustava RANS jednadžbi i osrednjene jednadžbe kontinuiteta. Za praćenje i određivanje položaja slobodne površine primijenjena je metoda udjela fluida u volumenu. Numeričke simulacije pokusa slobodne vožnje vijka provedene su primjenom metode višestrukih referentnih koordinatnih sustava, dok je utjecaj broskog vijka u numeričkim simulacijama pokusa vlastitog pogona modeliran pomoću metode virtualnog diska.

Ukupni otpor broda određen je numeričkim simulacijama temeljenim na viskoznom strujanju oko trupa broda, koje uključuju utjecaj slobodne površine (eng. *Free Surface Simulation*, FSS). Viskozni otpor određen je primjenom numeričkih simulacija s udvojenim modelom (eng. *Double Body Simulation*, DBS), koje ne uzimaju u obzir utjecaj slobodne površine. U DBS simulacijama simulira se strujanje oko duboko uronjenog udvojenog modela broda ili broda te je tako dobiveni ukupni otpor jednak viskoznom otporu. U DBS simulacijama otpor trenja određuje se integracijom tangencijalnih naprezanja po oplakanoj površini, dok se viskozni otpor tlaka određuje integracijom tlaka po oplakanoj površini. Otpor valova određuje se oduzimanjem ukupnog otpora dobivenog u FSS i viskoznog otpora u DBS simulacijama. Tako je omogućeno istraživanje utjecaja različitih stanja površine na pojedine komponente ukupnog otpora. Važan parametar za ukupni stupanj djelovanja propulzije predstavlja sustrujanje, koje se može podijeliti na efektivno i nominalno sustrujanje. Utjecaj stanja površine trupa broda na nominalno sustrujanje do danas je gotovo u potpunosti neistražen, zbog nemogućnosti mjerenja nominalnog sustrujanja na brodu u naravi. U okviru predloženog istraživanja nominalno sustrujanje broda u naravi određeno je prema proceduri opisanoj u ITTC preporukama, a utjecaj obraštanja na nominalno sustrujanje primjenom predloženih modela funkcija hrapavosti i određene skale hrapavosti te usporedbom s nominalnim sustrujanjem glatkog trupa broda. Utjecaj obraštanja na hidrodinamičke značajke slobodne vožnje vijka određen je primjenom

predloženih modela funkcija hrapavosti i određene skale hrapavosti u numeričkim simulacijama pokusa slobodne vožnje vijka te usporedbom s hidrodinamičkim značajkama slobodne vožnje glatkog vijka. Utjecaj obraštanja trupa broda i brodskog vijka na propulzijske značajke istražen je numeričkim simulacijama pokusa vlastitog pogona obraslog i glatkog broda te analizom rezultata, koristeći rezultate pokusa otpora i rezultate pokusa slobodne vožnje brodskog vijka. Konačno, primjenom numeričkog postupka moguće je odrediti utjecaj obraštanja na radnu točku brodskog vijka, definiranu brzinom, snagom predanom vijku te brzinom vrtnje vijka.

Premda procjena utjecaja obraštanja na hidrodinamičke značajke otpora i propulzije primjenom razvijenog numeričkog postupka omogućuje detaljan uvid u strujanje oko obraslog broda, primjena ovog postupka može biti složena za neiskusne korisnike RDF-a. Također, kako se RDF analiza sastoji od pripreme numeričkih simulacija, proračuna i analize dobivenih rezultata vrijeme trajanja proračuna je relativno dugo. U okviru optimizacije rasporeda čišćenja trupa broda i brodskog vijka bilo bi od velike koristi predložiti metodu, koja bi omogućila brzu procjenu utjecaja obraštanja na hidrodinamičke značajke otpora i propulzije. Štoviše, ITTC je izdao preporuke istraživačima da modificiraju trenutne poluempirijske izraze za koeficijent otpora i uzgona profila, a koji bi uzeo u obzir utjecaj obraštanja. U ovom radu, predložena je nova metoda za procjenu utjecaja obraštanja na hidrodinamičke značajke otpora i propulzije broda. Svrha ove metode je brza procjena utjecaja obraštanja na hidrodinamičke značajke broda. Štoviše, ova metoda omogućuje preciznije predviđanje negativnih učinaka obraštanja od onih dobivenih primjenom Granvilleove metode zakona sličnosti, kojom je moguće odrediti samo porast ukupnog otpora obraslog broda. Konačno, ovom metodom je moguće odrediti zaseban utjecaj obraštanja trupa broda i brodskoga vijka na ukupne hidrodinamičke značajke broda.

## Verifikacija i validacija

Za potvrdu točnosti i vjerodostojnosti numeričkog postupka, potrebno je provesti opsežan postupak verifikacije i validacije dobivenih rezultata. Postupak verifikacije i procjene numeričke nesigurnosti u određivanju hidrodinamičkih značajki proveden je metodom indeksa konvergencije mreže (eng. *Grid Convergence Index*, GCI). Validacija dobivenih numeričkih rezultata za glatki brod i brodski vijak u naravi provedena je usporedbom s ekstrapoliranim rezultatima ispitivanja u bazenu, kao i s rezultatima dostupnih numeričkih istraživanja. Postupak validacije numeričkog postupka proveden je usporedbom dobivenih numeričkih rezultata s eksperimentalnim rezultatima studija karakterizacije otpora dostupnim u literaturi. Nadalje, dobiveni porasti koeficijenta otpora trenja primjenom predloženog numeričkog postupka uspoređeni su s porastima koeficijenta otpora trenja dobivenih primjenom Granvilleove metode zakona sličnosti. Promjene značajki otpora i propulzije broda dobivene primjenom novo predložene metode za procjenu utjecaja obraštanja uspoređene su s dobivenim rezultatima predloženog numeričkog postupka.

## Znanstveni doprinos

Ovaj rad je rezultirao predloženim numeričkim postupkom modeliranja obraštanja, kao i novo predloženom metodom predviđanja značajki, koji se mogu primijeniti za procjenu utjecaja

obraštanja na hidrodinamičke značajke otpora i propulzije broda u mirnoj vodi. To uključuje određivanje utjecaja obraštanja trupa broda i broskog vijka na ukupni otpor, otpor trenja, otpor viskoznog tlaka i otpor valova, kao i na strujanje oko trupa broda i broskog vijka. Nadalje, omogućeno je određivanje utjecaja obraštanja na značajke slobodne vožnje broskog vijka, koeficijent upijanja, nominalno i efektivno sustrujanje, koeficijent napredovanja za točku vlastitoga pogona, stupanj djelovanja u slobodnoj vožnji, koeficijent prijelaza te kvazi propulzivni koeficijent. Uz to omogućeno je određivanje radne točke broskog vijka, kao i energetske učinkovitosti broda za različita stanja obraštanja trupa broda i broskog vijka. Procjena ovih utjecaja može se koristiti u alatima za optimizaciju rasporeda čišćenja trupa broda i broskog vijka, gdje je predviđanje optimalnog vremena čišćenja od presudne važnosti. Dobiveni rezultati ukazuju na važnost čišćenja trupa broda i broskog vijka. Glavni znanstveni doprinosi sastoje se od predloženih modela funkcija hrapavosti za određivanje otpora trenja površina prekrivenih biofilmom te njihova implementacija u programski paket za RDF, određivanje utjecaja biofilma na značajke otpora i nominalnog sustrujanja broda, značajke slobodne vožnje broskog vijka i propulzijske značajke broda. Daljnji znanstveni doprinos je implementacija modela funkcije hrapavosti za određivanje otpora trenja površina prekrivenih tvrdim obraštanjem, određivanje utjecaja tvrdog obraštanja na značajke otpora i nominalnog sustrujanja broda, značajke slobodne vožnje broskog vijka i propulzijske značajke broda. Konačno, znanstveni doprinos predstavlja novo predložena metoda za brzu procjenu utjecaja obraštanja na značajke otpora i propulzije broda.

**Ključne riječi:** obraštanje; brodska hidrodinamika; računalna dinamika fluida; Reynoldsove osrednjene Navier-Stokesove jednadžbe; funkcija hrapavosti; metoda predviđanja značajki

## Content

List of Figures .....	12
List of Tables.....	18
Nomenclature .....	21
Abbreviations .....	31
1. Introduction .....	1
1.1. General overview .....	1
1.2. Biofouling.....	4
1.3. The research problem definition .....	9
1.4. The research .....	12
1.4.1. Motivations behind this research.....	12
1.4.2. Research objectives and hypothesis .....	13
1.4.3. Scientific contribution of the research .....	15
1.5. Structure of the Thesis.....	17
2. Critical review – Roughness effects on the flow.....	18
2.1. Flow around immersed bodies .....	18
2.2. Effects of surface roughness. Roughness functions.....	21
2.2.1. Wall roughness .....	21
2.2.2. Roughness functions .....	23
2.3. Effects of surface roughness on the ship resistance and propulsion characteristics .....	32
2.3.1. Ship resistance and propulsion characteristics .....	32
2.3.2. The influence of surface roughness on ship resistance and propulsion characteristics – PPM perspective.....	37
2.3.3. Granville similarity law scaling method .....	42
2.3.4. The influence of surface roughness on ship resistance and propulsion characteristics – CFD perspective .....	44
3. Methodology .....	49
3.1. Approach .....	49
3.2. Numerical modelling.....	51
3.2.1. Governing equations .....	51
3.2.2. Finite Volume method.....	53
3.2.3. Volume of fluid method .....	55
3.2.4. Moving reference frame method .....	56
3.2.5. Body force method .....	57

3.2.6. Verification and validation studies.....	59
4. Development and validation of roughness function models for biofouling.....	62
4.1. Roughness function model for biofilm.....	62
4.1.1. Biofilm .....	62
4.1.2. Experiments in TCF .....	63
4.1.3. Roughness length scale and roughness functions for biofilm .....	66
4.1.4. CFD model for simulation of biofilm effects on the flow around biofilm covered surface – validation .....	72
4.2. Roughness function model for hard fouling.....	81
4.2.1. Hard fouling .....	81
4.2.2. Experiments in towing tank.....	82
4.2.3. Roughness length scale and roughness function for hard fouling.....	83
4.2.4. CFD model for simulation of hard fouling effects on the flow around surface covered with hard fouling – validation .....	86
5. The impact of biofouling on the ship performance .....	92
5.1. Case study – the investigated ships and fouling conditions .....	92
5.2. The impact of biofouling on the frictional resistance of the flat plate having the same length as a ship .....	97
5.2.1. Numerical modelling and verification study .....	97
5.2.2. The validation study and comparison with Granville similarity law scaling method .....	101
5.3. The impact of biofouling on the resistance characteristics and nominal wake .....	106
5.3.1. Numerical modelling and verification study .....	107
5.3.2. The validation study .....	124
5.3.3. Results of the analysis of the impact of biofouling on the resistance characteristics and nominal wake.....	127
5.3.4. The impact of biofouling on the flow around the ship hull.....	139
5.4. The impact of biofouling on the open water characteristics .....	158
5.4.1. Numerical modelling and verification study .....	158
5.4.2. The validation study .....	162
5.4.3. Results of the analysis of the impact of biofouling on the open water characteristics .....	164
5.4.4. The impact of biofouling on the flow around the fouled propeller .....	168
5.5. The impact of biofouling on the propulsion characteristics .....	173
5.5.1. The numerical modelling and verification study.....	173
5.5.2. The validation study .....	182



5.5.3. Results of the analysis of the impact of biofouling on the propulsion characteristics .....	184
5.5.4. The impact of biofouling on the flow around the fouled ship hull in the self-propulsion test .....	196
6. The performance prediction method for fouled surfaces .....	206
6.1. The newly proposed performance prediction method for fouled surfaces.....	206
6.2. The impact of biofouling on the ship performance obtained using the newly proposed PPM.....	212
6.2.1. The impact of biofouling on the ship performance obtained using the newly proposed PPM and towing tank measurements as an input data.....	212
6.2.2. The impact of biofouling on the ship performance obtained using the newly proposed PPM and full-scale CFD results as an input data .....	218
6.3. Discussion regarding the newly proposed PPM for fouled surfaces.....	231
7. Conclusions .....	235
7.1. Plans for future research.....	239
References .....	241
A Appendix .....	256
The influence of the applied turbulence model on the numerically obtained hydrodynamic characteristics .....	256
Curriculum vitae.....	270

## List of Figures

Figure 1.1 CO <sub>2</sub> emission reduction potential [5].....	2
Figure 1.2 Fouling rating scale for soft fouling [40].....	7
Figure 1.3 Fouling rating scale for hard and composite fouling [40] .....	8
Figure 2.1 The development of TBL over the flat plate.....	18
Figure 2.2 Law of the wall, adapted from [79] .....	19
Figure 2.3 TBL shear stress profile, adapted from [82].....	20
Figure 2.4 Velocity defect for smooth and rough walls, adapted from [94].....	23
Figure 2.5 The roughness effect on the law of the wall (adapted from [107]).....	24
Figure 2.6 Constant $B$ in terms of $k^+$ for Nikuradse sand roughness (adapted from [77])....	27
Figure 2.7 $\Delta U^+$ of Nikuradse and Colebrook .....	28
Figure 2.8 TCF facility at the United States Naval Academy (adapted from [147]) .....	31
Figure 2.9 Granville similarity law scaling procedure .....	42
Figure 3.1 The flow chart representing methodology of this study .....	50
Figure 4.1 SEM top-view (left) and cross sections (right) of the specimens covered with biofilm after 4.5 month of immersion (adapted from [134]) .....	62
Figure 4.2 The sketch of TCF (adapted from [104]).....	65
Figure 4.3 The experimentally obtained $C_f$ for fouled flat plates after 3 months (upper) and 6 months (lower) of exposure [133].....	67
Figure 4.4 The comparison between the proposed $\Delta U^+$ model and experimentally [133] obtained $\Delta U^+$ values for %SC>25% (adapted from [104]) .....	69
Figure 4.5 The plot of $\Delta U^+$ versus $k^+$ for surfaces with %SC < 25% (adapted from [104]).	70
Figure 4.6 The comparison between the proposed $\Delta U^+$ model and experimentally [133] obtained $\Delta U^+$ values for 10% < %SC < 25% (adapted from [104]).....	71
Figure 4.7 The comparison between the proposed $\Delta U^+$ model and experimentally [133] obtained $\Delta U^+$ values for %SC < 10% (adapted from [104]).....	72
Figure 4.8 The applied boundary conditions in CFD simulations of TCF.....	73
Figure 4.9 The cross section of the fine mesh used in CFD simulations of TCF (adapted from [104]).....	73
Figure 4.10 The obtained $y^+$ distribution at B3 plate in TCF at $Rn_m = 107527$ .....	73
Figure 4.11 The obtained $u_r$ (upper) and $k^+$ (lower) distributions for plate A3 at $\bar{U} = 4$ m/s .....	79
Figure 4.12 The comparison between $k_{CFD}^+$ and $k_{EXP}^+$ for plates that were exposed for 3 months (adapted from [104]) .....	80
Figure 4.13 The comparison between $k_{CFD}^+$ and $k_{EXP}^+$ for plates that were exposed for 6 months (adapted from [104]) .....	80
Figure 4.14 The experimentally obtained $C_f$ for fouled plates [123].....	84
Figure 4.15 The plot of $\Delta U^+$ versus $k^+$ for fouled plates adapted from [123].....	85
Figure 4.16 The definition of computational domain boundaries (left) and applied boundary conditions (right) in CFD simulations.....	87

Figure 4.17 The profile view cross section of the volume mesh (upper left), refinement around plate leading edge (upper right) and top view cross section of the volume mesh (lower).....	88
Figure 4.18 The obtained $y^+$ distribution at S plate in CFD simulations of towing tank tests at $Rn = 2.8 \cdot 10^6$ .....	89
Figure 5.1 Bottom-up $CO_2$ emissions from international shipping by ship type .....	92
Figure 5.2 3D representation of KCS (upper), KVLCC2 (middle) and BC (lower).....	93
Figure 5.3 Hull lines of KCS (upper), KVLCC2 (middle) and BC (lower).....	94
Figure 5.4 KP505 (left), KP458 (middle) and WB (right) propellers .....	95
Figure 5.5 The applied boundary conditions in CFD simulations of the flat plate having the same length as a ship .....	98
Figure 5.6 The geometry of the flat plate having the same length as a ship .....	99
Figure 5.7 The obtained $u_\tau$ distribution (upper) and $k^+$ distribution (lower) for the flat plate representing KCS, R1 H.....	102
Figure 5.8 The obtained $\Delta C_{F0}$ due to the presence of biofilm for the flat plate representing KCS (upper), KVLCC2 (middle) and BC (lower) .....	105
Figure 5.9 The obtained $\Delta C_{F0}$ due to the presence of hard fouling for the flat plate representing KCS (upper), KVLCC2 (middle) and BC (lower) .....	106
Figure 5.10 The profile view cross-section of the domain for KCS (upper left), KVLCC2 (middle left) and BC (lower left) and the top view cross-section of the domain for KCS (upper right), KVLCC2 (middle right) and BC (lower right).....	109
Figure 5.11 Volume mesh for the KCS hull, bow region (upper) and stern region (lower) ..	109
Figure 5.12 The obtained $y^+$ distributions in the first cell near the wall for smooth KCS (upper), KVLCC2 (middle) and BC (lower).....	110
Figure 5.13 The obtained $y^+$ distributions in the first cell near the wall for KCS (upper), KVLCC2 (middle) and BC (lower) fouled with the surface condition R2 B .....	111
Figure 5.14 The obtained $y^+$ distributions in the first cell near the wall for KCS (upper), KVLCC2 (middle) and BC (lower) fouled with the surface condition R1 H .....	111
Figure 5.15 The impact of biofilm on $\Delta C_F$ (upper) and $\Delta C_V$ (lower).....	128
Figure 5.16 The impact of hard fouling on $\Delta C_F$ (upper) and $\Delta C_V$ (lower).....	128
Figure 5.17 The impact of biofilm (upper) and hard fouling (lower) on $\Delta(1+k)$ .....	132
Figure 5.18 The impact of biofilm (upper) and hard fouling (lower) on $\Delta C_T$ .....	134
Figure 5.19 The impact of biofilm (upper) and hard fouling (lower) on $\Delta C_w$ for KCS and BC .....	135
Figure 5.20 The impact of biofilm (upper) and hard fouling (lower) on $\Delta C_w$ for KVLCC2	135
Figure 5.21 The decomposition of $R_T$ for KCS (upper), KVLCC2 (middle) and BC (lower) fouled with biofilm.....	136
Figure 5.22 The decomposition of $R_T$ for KCS (upper), KVLCC2 (middle) and BC (lower) fouled with hard fouling .....	137
Figure 5.23 The impact of biofilm (upper) and hard fouling (lower) on $\Delta(1-w_N)$ .....	138
Figure 5.24 The obtained circumferential averaged non-dimensional axial velocity distribution for KCS (upper), KVLCC2 (middle) and BC (lower) .....	138

Figure 5.25 The obtained $k^+$ distribution along KCS hull (upper), KVLCC2 hull (middle) and BC hull (lower) for R2 B.....	139
Figure 5.26 The obtained $k^+$ distribution along KCS hull (upper), KVLCC2 hull (middle) and BC hull (lower) for R1 H .....	140
Figure 5.27 The effect of hard fouling on the log-law velocity profile for KCS (upper), KVLCC2 (middle) and BC (lower).....	141
Figure 5.28 The obtained $\tau_w$ distribution along the smooth KCS hull (upper), KVLCC2 hull (middle) and BC hull (lower) .....	141
Figure 5.29 The obtained $\tau_w$ distribution along the KCS hull (upper), KVLCC2 hull (middle) and BC hull (lower) for R2 B.....	142
Figure 5.30 The obtained $\tau_w$ distribution along the KCS hull (upper), KVLCC2 hull (middle) and BC hull (lower) for R1 H.....	142
Figure 5.31 The obtained turbulent kinetic energy contours for smooth KCS hull (upper), KCS with R2 B (middle) and KCS with R1 H (lower) at the midship plane .....	143
Figure 5.32 The obtained turbulent kinetic energy contours for smooth KVLCC2 hull (upper), KVLCC2 with R2 B (middle) and KVLCC2 with R1 H (lower) at the midship plane .....	144
Figure 5.33 The obtained turbulent kinetic energy contours for smooth BC hull (upper), BC with R2 B (middle) and BC with R1 H (lower) at the midship plane.....	144
Figure 5.34 The obtained boundary layers for smooth KCS hull (upper), KCS with R2 B (middle) and KCS with R1 H (lower) at locations $x = 30$ m and $x = 50$ m .....	145
Figure 5.35 The obtained boundary layers for smooth KVLCC2 hull (upper), KVLCC2 with R2 B (middle) and KVLCC2 with R1 H (lower) at locations $x = 50$ m and $x = 70$ m .....	145
Figure 5.36 The obtained boundary layers for smooth BC hull (upper), BC with R2 B (middle) and BC with R1 H (lower) at locations $x = 17.5$ m and $x = 35$ m .....	146
Figure 5.37 The obtained $C_p$ distributions for smooth KCS hull (upper), KCS with R2 B (middle) and KCS with R1 H (lower) .....	147
Figure 5.38 The obtained $C_p$ distributions for smooth KVLCC2 hull (upper), KVLCC2 with R2 B (middle) and KVLCC2 with R1 H (lower).....	147
Figure 5.39 The obtained $C_p$ distributions for smooth BC hull (upper), BC with R2 B (middle) and BC with R1 H (lower) .....	147
Figure 5.40 The obtained $C_p$ distributions at the symmetry plane for smooth KCS hull (upper), KCS with R2 B (middle) and KCS with R1 H (lower) .....	149
Figure 5.41 The obtained $C_p$ distributions at the symmetry plane for smooth KVLCC2 hull (upper), KVLCC2 with R2 B (middle) and KVLCC2 with R1 H (lower).....	150
Figure 5.42 The obtained $C_p$ distributions at symmetry plane for the smooth BC hull (upper), BC with R2 B (middle) and BC with R1 H (lower).....	151
Figure 5.43 The obtained contours of the axial velocity at the symmetry plane for smooth KCS hull (upper), KCS with R2 B (middle) and KCS with R1 H (lower).....	152
Figure 5.44 The obtained contours of the axial velocity at the symmetry plane for smooth KVLCC2 hull (upper), KVLCC2 with R2 B (middle) and KVLCC2 with R1 H (lower).....	153
Figure 5.45 The obtained contours of the axial velocity at the symmetry plane for smooth BC hull (upper), BC with R2 B (middle) and BC with R1 H (lower).....	154

Figure 5.46 The obtained wave patterns around KCS (left), KVLCC2 (middle) and BC (right)	155
Figure 5.47 Longitudinal wave cuts at symmetry plane behind the KCS stern for S, R2 B and R1 H surface condition	156
Figure 5.48 Longitudinal wave cuts at symmetry plane behind the KVLCC2 stern for S, R2 B and R1 H surface condition	156
Figure 5.49 Longitudinal wave cuts at symmetry plane behind the BC stern for S, R2 B and R1 H surface condition	156
Figure 5.50 The obtained contours of $1 - w_N$ for smooth KCS and KCS with R2 B (left) and for smooth KCS and KCS with R1 H (right) in the propeller disc plane	157
Figure 5.51 The obtained contours of $1 - w_N$ for smooth KVLCC2 and KVLCC2 with R2 B (left) and for smooth KVLCC2 and KVLCC2 with R1 H (right) in the propeller disc plane	157
Figure 5.52 The obtained contours of $1 - w_N$ for smooth BC and BC with R2 B (left) and for smooth BC and BC with R1 H (right) in the propeller disc plane	157
Figure 5.53 The computational domain for WB propeller (upper), KP 505 (middle) and KP 458 (lower)	159
Figure 5.54 The propeller surface (left) and profile view (right) cross section of the volume mesh for KP 505 (upper), KP 458 (middle) and WB (lower)	159
Figure 5.55 The obtained $y^+$ distributions in the first cell near the wall for smooth KP 505 (left), KP 458 (middle) and WB (right)	160
Figure 5.56 The obtained $y^+$ distributions in the first cell near the wall for KP 505 (left), KP 458 (middle) and WB (right) fouled with the fouling condition R2 B	160
Figure 5.57 The obtained $y^+$ distributions in the first cell near the wall for KP 505 (left), KP 458 (middle) and WB (right) fouled with the fouling condition R1 H	161
Figure 5.58 The validation study for KP 505 (upper), KP 458 (middle) and WB (lower)	163
Figure 5.59 The impact of biofilm (R2 B) on the open water characteristics of KP 505	166
Figure 5.60 The impact of biofilm (R2 B) on the open water characteristics of KP 458	167
Figure 5.61 The impact of biofilm (R2 B) on the open water characteristics of WB	167
Figure 5.62 The impact of hard fouling (R1 H) on the open water characteristics of KP 505	167
Figure 5.63 The impact of hard fouling (R1 H) on the open water characteristics of KP 458	167
Figure 5.64 The impact of hard fouling (R1 H) on the open water characteristics of WB	168
Figure 5.65 The obtained $C_p$ distribution for smooth KP 505 (upper) and KP 505 fouled with R1 H (lower) on the symmetry plane	169
Figure 5.66 The obtained $C_p$ distribution for smooth KP 505 (upper) and KP 505 fouled with R1 H (lower) at $r = 0.75R$	169
Figure 5.67 The obtained $C_p$ distribution on the propeller surface for smooth KP 505 (left) and KP 505 fouled with R1 H (right)	170
Figure 5.68 The obtained nondimensionalised axial velocity distribution on the symmetry plane for smooth KP 505 (upper) and KP 505 fouled with R1 H (lower)	170
Figure 5.69 The obtained $\tau_w$ distribution for smooth KP 505 (left) and for KP 505 fouled with R1 H (right)	171

Figure 5.70 The obtained vorticity magnitudes for smooth KP 505 (upper) and for KP505 fouled with R1 H (lower) on the symmetry plane .....	172
Figure 5.71 The iso-surface of $Q$ -criterion, vorticity magnitude for smooth KP505 (upper) and for KP505 fouled with R1 H (lower) .....	172
Figure 5.72 The profile view cross-section of the domain for KCS (upper left), KVLCC2 (middle left) and BC (lower left) and the mesh refinement in stern region of KCS (upper right), KVLCC2 (middle right) and BC (lower right).....	174
Figure 5.73 The obtained $y^+$ distributions for KCS in the area where the virtual disk is located for resistance test (upper) and self-propulsion test (lower).....	175
Figure 5.74 The obtained $\Delta P_D$ due to the presence of biofilm (upper) and hard fouling (lower) .....	185
Figure 5.75 The obtained $\Delta n$ due to the presence of biofilm (upper) and hard fouling (lower) .....	186
Figure 5.76 The obtained $\Delta P_D$ due to the presence of biofilm for different speeds .....	187
Figure 5.77 The obtained $k^+$ distribution for the fouling condition R7 B at 19 kn.....	189
Figure 5.78 The impact of biofilm on $Q$ at different speeds .....	189
Figure 5.79 The impact of biofouling on $C_p$ distribution for the region near the stern for smooth KCS (upper), KCS with the fouling condition R2 B (middle) and KCS with the fouling condition R1 H (lower) .....	197
Figure 5.80 The impact of biofouling on $C_p$ distribution for the region near the stern for smooth KVLCC2 (upper), KVLCC2 with the fouling condition R2 B (middle) and KVLCC2 with the fouling condition R1 H (lower).....	198
Figure 5.81 The impact of biofouling on $C_p$ distribution for the area near the stern of smooth BC (upper), BC with the fouling condition R2 B (middle) and BC with the fouling condition R1 H (lower).....	199
Figure 5.82 The impact of biofouling on the velocity distribution downstream the propeller at the symmetry plane for smooth KCS (upper), KCS with the fouling condition R2 B (middle) and KCS with the fouling condition R1 H (lower) .....	200
Figure 5.83 The impact of biofouling on the velocity distribution downstream the propeller at the symmetry plane for smooth KVLCC2 (upper), KVLCC2 with the fouling condition R2 B (middle) and KVLCC2 with the fouling condition R1 H (lower).....	201
Figure 5.84 The impact of biofouling on the velocity distribution downstream the propeller at the symmetry plane for smooth BC (upper), BC with the fouling condition R2 B (middle) and BC with the fouling condition R1 H (lower).....	202
Figure 5.85 The obtained axial velocity contours ( $v_x/v$ ) at the plane $x = 2$ m for smooth KCS (upper), KCS with the fouling condition R2 B (middle) and KCS with the fouling condition R1 H (lower) .....	203
Figure 5.86 The obtained axial velocity contours ( $v_x/v$ ) at the plane $x = 2.5$ m for smooth KVLCC2 (upper), KVLCC2 with the fouling condition R2 B (middle) and KVLCC2 with the fouling condition R1 H (lower).....	204
Figure 5.87 The obtained axial velocity contours ( $v_x/v$ ) at the plane $x = 1.5$ m for smooth BC (upper), BC with the fouling condition R2 B (middle) and BC with the fouling condition R1 H (lower) .....	205

Figure 6.1 Flow chart of the proposed method .....	208
Figure 6.2 The obtained impact of biofilm on $\Delta P_D$ (upper), $\Delta P_E$ (middle) and $\Delta n$ (lower) .....	213
Figure 6.3 The obtained impact of biofilm on $\Delta P_D$ for KCS (upper), KVLCC2 (middle) and BC (lower).....	220
Figure 6.4 The obtained impact of biofilm on $\Delta P_E$ for KCS (upper), KVLCC2 (middle) and BC (lower).....	221
Figure 6.5 The obtained impact of biofilm on $\Delta n$ for KCS (upper), KVLCC2 (middle) and BC (lower) .....	221
Figure 6.6 The obtained impact of biofilm on $\Delta T$ and $\Delta Q$ for KCS (upper), KVLCC2 (middle) and BC (lower).....	222
Figure 6.7 The obtained impact of biofilm on $K_T$ for KP505 (upper), KP458 (middle) and WB (lower) .....	225
Figure 6.8 The obtained impact of biofilm on $10K_O$ for KP505 (upper), KP458 (middle) and WB (lower).....	226
Figure 6.9 The obtained impact of biofilm on $\eta_o$ for KP505 (upper), KP458 (middle) and WB (lower) .....	227
Figure 6.10 The obtained impact of biofilm on $\Delta J$ for KCS (upper), KVLCC2 (middle) and BC (lower).....	231
Figure A.1 Axial velocity contours obtained with: RKE (upper left), SKE (upper right), SSTKO (lower left) and RSM (lower right) turbulence models (adapted from [151]) .....	262
Figure A.2 The transversal velocity distribution obtained with: RKE (upper left), SKE (upper right), SSTKO (lower left) and RSM (lower right) (adapted from [151]) .....	262
Figure A.3 The longitudinal wave cuts along the centreline of the ship: stern (upper), bow (lower) (adapted from [151]).....	263
Figure A.4 The comparison between numerically and experimentally obtained circumferentially averaged non-dimensional axial velocity distribution without (upper) and with (lower) wall functions at model scale .....	265
Figure A.5 Comparison between nominal axial wake field obtained utilizing RKE (a), SSTKO (b), RSM (c) and experimentally (d).....	266
Figure A.6 Comparison between obtained circumferentially averaged non-dimensional axial velocity distribution with and without wall functions (adapted from [240]) .....	267
Figure A.7 Comparison between nominal axial wake field obtained without (left) and with (right) the application of wall functions.....	267
Figure A.8 Numerically obtained circumferentially averaged non-dimensional axial velocity distribution utilizing different turbulence models in full-scale (adapted from [240]) .....	269
Figure A.9 Contours of axial velocity in the propeller disc plane for model scale (left) and full-scale (right) obtained utilizing RKE (a), SSTKO (b) and RSM (c) (adapted from [240]).....	269

## List of Tables

Table 1.1 Fouling rating scale [40] .....	8
Table 2.1 Hull roughness fouling factor (adapted from [161]) .....	39
Table 4.1 Tested coating schemes [133] .....	64
Table 4.2 Characteristics of TCF facility test section .....	65
Table 4.3 Tested fouled plates.....	67
Table 4.4 The verification study for smooth plate .....	75
Table 4.5 The verification study for B6, C6 and AC6 .....	75
Table 4.6 The verification study for plates A3, B3, C3 and AC3 .....	76
Table 4.7 The validation study for smooth plate.....	76
Table 4.8 The validation study for B6, C6 and AC6.....	77
Table 4.9 The validation study for plates A3, B3, C3 and AC3 .....	78
Table 4.10 The comparison between $k_{\text{CFD}}^+$ and $k_{\text{EXP}}^+$ .....	81
Table 4.11 Plates after immersion period, fouling coverages [123] .....	83
Table 4.12 The number of cells used in CFD simulations .....	87
Table 4.13 The grid convergence study for tested plates .....	90
Table 4.14 The validation study for smooth plate.....	90
Table 4.15 The validation study for ABC, SPC, SIL1 and SIL2 plates.....	91
Table 5.1 The main particulars of the investigated ships .....	94
Table 5.2 The main particulars of the investigated propellers .....	95
Table 5.3 The investigated surface conditions .....	96
Table 5.4 The main particulars of flat plates having the same length as a ship .....	98
Table 5.5 The number of cells within CFD simulations for plates having the same length as a ship .....	99
Table 5.6 The obtained numerical uncertainties within FPS for plates fouled with biofilm .	100
Table 5.7 The obtained numerical uncertainties within FPS for plates fouled with hard fouling .....	101
Table 5.8 The validation study for smooth flat plates having the same length as a ship .....	102
Table 5.9 The comparison for flat plates having the same length as a ship fouled with biofilm .....	103
Table 5.10 The comparison for flat plates having the same length as a ship fouled with hard fouling .....	104
Table 5.11 The computational domain.....	108
Table 5.12 The number of cells within DBS and FSS .....	112
Table 5.13 The obtained grid uncertainties within FSS for ships fouled with biofilm .....	113
Table 5.14 The obtained time step uncertainties within FSS for ships fouled with biofilm ..	114
Table 5.15 The obtained grid uncertainties within FSS for ships fouled with hard fouling ..	115
Table 5.16 The obtained time step uncertainties within FSS for ships fouled with hard fouling .....	116
Table 5.17 The obtained $U_{SN}$ in the prediction of $R_T (U_{R_T})$ .....	117
Table 5.18 The obtained grid uncertainties for $R_F$ within DBS for ships fouled with biofilm .....	118



Table 5.19 The obtained grid uncertainties for $R_F$ within DBS for ships fouled with hard fouling	119
Table 5.20 The obtained grid uncertainties for $R_V$ within DBS for ships fouled with biofilm	120
Table 5.21 The obtained grid uncertainties for $R_V$ within DBS for ships fouled with hard fouling	121
Table 5.22 The obtained grid uncertainties for $1+k$ within DBS for ships fouled with biofilm	122
Table 5.23 The obtained grid uncertainties for $1+k$ within DBS for ships fouled with hard fouling	123
Table 5.24 The obtained $U_{SN}$ in the prediction of $R_W (U_{R_W})$	124
Table 5.25 The validation study for $C_T$	125
Table 5.26 The validation study for $C_F$	126
Table 5.27 The validation study for $1-w_N$	127
Table 5.28 The comparison of the obtained $C_{FR}$ and $\Delta C_F$ at the same $k/L$ values	130
Table 5.29 The impact of biofilm on $k_f$	130
Table 5.30 The impact of hard fouling on $k_f$	130
Table 5.31 The number of cells within CFD simulations of open water test	161
Table 5.32 The verification study for $K_T$	162
Table 5.33 The verification study for $10K_Q$	162
Table 5.34 The validation study for $J$ value around expected self-propulsion point	163
Table 5.35 The obtained changes in open water characteristics due to the presence of biofilm	166
Table 5.36 The obtained changes in open water characteristics due to the presence of hard fouling	166
Table 5.37 The number of cells within numerical simulations of self-propulsion test	176
Table 5.38 The obtained grid uncertainties in the prediction of $T$	176
Table 5.39 The obtained grid uncertainties in the prediction of $Q$	177
Table 5.40 The obtained grid uncertainties in the prediction of $n$	177
Table 5.41 The obtained grid uncertainties in the prediction of $P_D$	178
Table 5.42 The obtained grid uncertainties in the prediction of $J$	178
Table 5.43 The obtained temporal uncertainties in the prediction of $T$	179
Table 5.44 The obtained temporal uncertainties in the prediction of $Q$	180
Table 5.45 The obtained temporal uncertainties in the prediction of $n$	180
Table 5.46 The obtained temporal uncertainties in the prediction of $P_D$	181
Table 5.47 The obtained temporal uncertainties in the prediction of $J$	181
Table 5.48 The obtained $U_{SN}$ in the prediction of $T (U_T)$ , $Q (U_Q)$ , $n (U_n)$ , $P_D (U_{P_D})$ and $J (U_J)$	182
Table 5.49 The validation study for self-propulsion point	183
Table 5.50 The validation study for propulsion characteristics	184

Table 5.51 The obtained increases in $P_D$ and $P_E$ for biofilm and hard fouling.....	187
Table 5.52 The obtained speed reductions due to the presence of biofilm for KCS.....	189
Table 5.53 The impact of biofilm on the propulsion characteristics for KCS .....	193
Table 5.54 The impact of biofilm on the propulsion characteristics for KVLCC2 .....	194
Table 5.55 The impact of biofilm on the propulsion characteristics for BC.....	194
Table 5.56 The impact of hard fouling on the propulsion characteristics for KCS .....	195
Table 5.57 The impact of hard fouling on the propulsion characteristics for KVLCC2.....	195
Table 5.58 The impact of hard fouling on the propulsion characteristics for BC.....	196
Table 6.1 Input data for in-house numerical code.....	212
Table 6.2 The impact of biofilm on $K_T$ and $\Delta K_T$ in open water test.....	214
Table 6.3 The impact of biofilm on $K_Q$ and $\Delta K_Q$ in open water test.....	215
Table 6.4 The impact of biofilm on $\eta_o$ and $\Delta\eta_o$ in open water test.....	217
Table 6.5 The impact of biofilm on $1-t$ and $1-w$ .....	217
Table 6.6 The impact of biofilm on $K_T$ and $10K_Q$ .....	218
Table 6.7 The comparison between the obtained open water characteristics for KP505 propeller fouled with biofilm at $J = 0.7$ .....	223
Table 6.8 The comparison between the obtained open water characteristics for KP458 propeller fouled with biofilm at $J = 0.5$ .....	223
Table 6.9 The comparison between the obtained open water characteristics for WB propeller fouled with biofilm at $J = 0.56$ .....	224
Table 6.10 The obtained propulsion characteristics for KCS using PPM.....	229
Table 6.11 The obtained propulsion characteristics for KVLCC2 using PPM.....	229
Table 6.12 The obtained propulsion characteristics for BC using PPM .....	230
Table 6.13 The obtained $P_D$ using the newly proposed PPM and CFD approach.....	232
Table 6.14 The obtained $n$ using the newly proposed PPM and CFD approach .....	233
Table A.1 Validation of the obtained $R_T$ for design loading condition at design speed (adapted from [151]).....	258
Table A.2 Validation of the obtained numerical results in OWT (adapted from [151]).....	258
Table A.3 Validation of the obtained results for $n$ and $P_B$ (adapted from [151]) .....	259
Table A.4 Validation of the obtained propulsion characteristics for different turbulence models (adapted from [151]) .....	261
Table A.5 The comparison between numerically and experimentally obtained integral values of nominal wake .....	266
Table A.6 The comparison between numerically and experimentally obtained integral values of nominal wake in full-scale .....	269

## Nomenclature

### Latin

Symbol	Unit	Description
$A_x$	N/m <sup>3</sup>	constant in virtual disk model
$A_\theta$	N/m <sup>3</sup>	constant in virtual disk model
$B$	m	breadth
$B$	-	smooth wall log-law intercept
$c$	m	chord length
$C_A$	-	correlation allowance
$C_{AAS}$	-	air resistance coefficient
$C_B$	-	block coefficient
$C_D$	-	drag coefficient of propeller blade section
$c_{d,2d}$	-	section form drag
$CEFF$	-	AF coating effectiveness factor
$C_F$	-	frictional resistance coefficient
$C_f$	-	local skin frictional coefficient
$C_f$	-	frictional resistance coefficient for the flat plate in turbulent channel flow
$c_f$	-	contribution of the friction in the drag coefficient of propeller blade section
$C_{FR}$	-	frictional resistance coefficient for fouled or rough ship
$C_{FR,0}$	-	frictional resistance coefficient for fouled plate having the same length as a ship
$C_{F0}$	-	frictional resistance coefficient for the flat plate

<b>Symbol</b>	<b>Unit</b>	<b>Description</b>
$C_L$	-	lift coefficient of propeller blade section
$C_M$	-	midship section coefficient
$C_P$	-	pressure coefficient
$C_R$	-	residual resistance coefficient
$C_S$	-	service roughness resistance coefficient
$C_T$	-	total resistance coefficient
$C_V$	-	viscous resistance coefficient
$C_{VP}$	-	viscous pressure resistance coefficient
$D$	m	diameter
$e_a^{21}$	-	approximate error
$e_{ext}^{21}$	-	extrapolated error
$f_{bx}$	N/m <sup>3</sup>	body force component in axial direction
$f_{b\theta}$	N/m <sup>3</sup>	body force component in tangential direction
$F_D^*$	N	skin friction correction force
$Fn$	-	Froude number
$FOC$	t/h	fuel oil consumption
$f_\beta$	-	vortex-stretching modification factor
$f_{\beta^*}$	-	function used for free-shear modification
$f_1$	-	linear damping constant
$f_2$	-	quadratic damping constant
$g$	m/s <sup>2</sup>	gravity of the Earth
$GCI_{fine}^{21}$	-	grid convergence index

<b>Symbol</b>	<b>Unit</b>	<b>Description</b>
$H$	m	turbulent channel height
$h$	m	turbulent channel half height
$h$	$\mu\text{m}$	average roughness height
$HRF$	$\mu\text{m}/\text{port day}$	hull roughness factor
$J$	-	advance coefficient
$k$	$\mu\text{m}$	biofilm thickness
$k$	-	form factor
$k$	$\mu\text{m}$	roughness length scale
$k$	J/kg	turbulence kinetic energy
$k_{eff}$	$\mu\text{m}$	effective roughness length scale
$k_f$	-	factor which takes into account the effect of longitudinal and transversal pressure gradients
$k_p$	$\mu\text{m}$	blade roughness
$K_Q$	-	torque coefficient
$k_s$	$\mu\text{m}$	equivalent sand grain roughness height
$K_T$	-	thrust coefficient
$k_0$	J/kg	ambient turbulence value in the source terms that counteracts turbulence decay
$k^+$	-	roughness Reynolds number
$L$	m	length
$L_{plate}$	m	length of flat plate used in laboratory experiments of drag characterization
$L_{pp}$	m	length between perpendiculars
$L_{WL}$	m	waterline length

<b>Symbol</b>	<b>Unit</b>	<b>Description</b>
$n$	rps	propeller rotation rate
$n$	-	damping exponent
$N_{C1}$	-	number of the cells for fine grid
$N_{C2}$	-	number of the cells for medium grid
$N_{C3}$	-	number of the cells for coarse grid
$P$	m	propeller pitch
$p$	Pa	pressure
$\bar{p}$	Pa	mean pressure
$p_a$	-	apparent order of method
$P_B$	kW	brake power
$P_C$	-	peak count per unit length
$P_D$	kW	delivered power
$P_{DO}$	kW	delivered power in open water conditions
$P_E$	kW	effective power
$P_k$	Pa/s	production term
$PT$	-	number of port days
$P_T$	kW	thrust power
$P_\omega$	N/m <sup>4</sup>	production term
$Q$	kNm	propeller torque
$q_z^d$	N/m <sup>3</sup>	source term in the $z$ -momentum equation causing the vertical resistance to the vertical velocity component
$R$	m	radius
$r$	m	radial coordinate

<b>Symbol</b>	<b>Unit</b>	<b>Description</b>
$R_a$	$\mu\text{m}$	centreline average roughness height
$RD$	-	relative deviation
$R_F$	kN	frictional resistance of a ship
$R_{F0}$	kN	frictional resistance of a flat plate having the same length as a ship
$R_H$	m	propeller hub radius
$r_k$	-	position vector from the origin of the MRF to the centre of a control volume
$Rn$	-	Reynolds number
$Rn_L$	-	Reynolds number based on the flat plate length
$Rn_m$	-	Reynolds number based on channel height and bulk mean velocity
$Rn_\tau$	-	friction Reynolds number
$R_p$	m	propeller tip radius
$R_q$	$\mu\text{m}$	root-mean square roughness height
$R_R$	kN	residual resistance of a ship
$R_{sk}$	$\mu\text{m}$	skewness of the roughness elevation distribution
$R_T$	kN	total resistance of a ship
$R_t$	$\mu\text{m}$	height of the largest barnacle
$R_t$	$\mu\text{m}$	maximum peak to through height
$R_V$	kN	viscous resistance of a ship
$R_{VP}$	kN	viscous pressure resistance of a ship
$R_W$	kN	wave resistance of a ship

<b>Symbol</b>	<b>Unit</b>	<b>Description</b>
$R^2$	-	coefficient of determination
$r_{21}$	-	refinement ratio between fine and medium input parameter
$r_{32}$	-	refinement ratio between medium and coarse input parameter
$S$	$m^2$	wetted surface area
$Sd_4$	$\mu m$	mean spacing between zero crossings
$SFOC$	$g/kWh$	specific fuel oil consumption
$S_k$	$Pa/s$	user specified source terms
$S_\omega$	$N/m^4$	user specified source terms
$T$	$m$	draught
$T$	$kN$	propeller thrust
$T$	$s$	time required for the fluid to pass ship
$T$	$s$	turbulent time scale
$t$	-	thrust deduction fraction
$t$	$mm$	maximum thickness
$u$	$m/s$	velocity
$\bar{U}$	$m/s$	bulk mean velocity
$U_D$	-	experimental uncertainty
$U_G$	-	grid uncertainty
$U_I$	-	iteration uncertainty
$\bar{u}_i$	$m/s$	averaged velocity vector
$u_{pi}$	$m/s$	velocity relative to the moving reference frame
$U_{R_T}$	-	numerical uncertainty in the prediction of total resistance
$U_{R_V}$	-	numerical uncertainty in the prediction of viscous resistance



<b>Symbol</b>	<b>Unit</b>	<b>Description</b>
$U_{R_W}$	-	numerical uncertainty in the prediction of wave resistance
$U_{SN}$	-	numerical uncertainty
$U_T$	-	time step uncertainty
$\hat{u}_{\text{tangential}}$	m/s	wall tangential velocity vector
$U_V$	-	validation uncertainty
$u_z$	m/s	vertical velocity component
$u_{0i}$	m/s	absolute velocity
$U_{\Delta\varphi}$	-	numerical uncertainty in the prediction of changes of resistance characteristics due to the presence of biofouling
$u_\tau$	m/s	friction velocity
$U^+$	-	non-dimensional velocity
$u_\infty$	m/s	free-stream velocity
$u_*$	m/s	velocity scale
$V$	m <sup>3</sup>	cell volume
$v_A$	m/s	speed of the advance
$V_K$	kn	ship design speed
$v_R$	m/s	resultant velocity of the flow approaching the propeller blade section
$W$	m	channel width
$w$	-	wake fraction
$w_F$	-	frictional wake fraction
$w_P$	-	potential wake fraction
$w_R$	-	rudder effect on wake fraction

<b>Symbol</b>	<b>Unit</b>	<b>Description</b>
$w_w$	-	wave wake fraction
$x$	m	streamwise distance
$x$	m	wave propagation direction
$x_d$	m	thickness of the damping layer
$x_{ed}$	m	end coordinate of the damping layer
$x_{sd}$	m	start coordinate of the damping layer
$Z$	-	number of blades
$Z$	-	ratio of accumulated time to effective life of AF coating
$y$	m	distance from the wall
$y^+$	-	non-dimensional normal distance from the wall
%SC	-	percentage of surface coverage

## Greek

<b>Symbol</b>	<b>Unit</b>	<b>Description</b>
$\alpha_i$	-	volume fraction of $i$ -th fluid
$\beta$	-	$k - \omega$ turbulence model coefficient
$\beta^*$	-	$k - \omega$ turbulence model coefficient
$\Delta$	t	displacement
$\Delta$	m	thickness of the virtual disk
$\delta$	m	boundary layer thickness
$\Delta C_F$	-	roughness allowance
$\delta_{ij}$	-	Kronecker delta symbol
$\Delta t$	s	time step
$\Delta U^+$	-	roughness function

<b>Symbol</b>	<b>Unit</b>	<b>Description</b>
$\Delta U^{+}$	-	roughness function slope
$\Delta\phi$	-	change in certain hydrodynamic characteristic
$\varepsilon$	J/kgs	turbulent dissipation
$\eta_D$	-	quasi-propulsion efficiency coefficient
$\eta_H$	-	hull efficiency
$\eta_O$	-	open water efficiency
$\eta_R$	-	relative rotative efficiency
$\eta_S$	-	shaft efficiency
$\kappa$	-	von Karman constant
$\lambda$	-	scale
$\mu$	Pas	dynamic viscosity coefficient
$\mu_t$	Pas	eddy viscosity
$\nu$	m <sup>2</sup> /s	kinematic viscosity coefficient
$\pi$	-	Coles' wake parameter
$\vartheta$	°C	water temperature
$\rho$	kg/m <sup>3</sup>	fluid density
$\overline{\rho u_i' u_j'}$	Pa	Reynolds stress tensor
$\sigma_k$	-	inverse turbulent Schmidt numbers
$\sigma_\omega$	-	inverse turbulent Schmidt numbers
$\tau$	Pa	total shear stress
$\bar{\tau}_{ij}$	Pa	mean viscous stress tensor
$\tau_w$	Pa	wall shear stress
$\phi$	-	certain hydrodynamic characteristic

<b>Symbol</b>	<b>Unit</b>	<b>Description</b>
$\phi_{ext}^{21}$	-	extrapolated solution
$\phi_1$	-	solution obtained using fine input parameter
$\phi_2$	-	solution obtained using medium input parameter
$\phi_3$	-	solution obtained using coarse input parameter
$\omega$	$s^{-1}$	specific rate of dissipation of the turbulence kinetic energy
$\omega^+$	-	non-dimensional specific rate of dissipation of the turbulence kinetic energy
$\omega_{pj}$	$s^{-1}$	angular velocity
$\omega_0$	$s^{-1}$	ambient turbulence value in the source terms that counteracts turbulence decay

## Abbreviations

<b>Abbreviation</b>	<b>Description</b>
ABC	ablative copper
AF	antifouling
AHR	average hull roughness
AMBIO	advanced nanostructured surfaces for the control of biofouling
AMG	algebraic multigrid
ASTM	American Society for Testing and Materials
B	fouled with biofilm
BC	bulk carrier
CDP	controlled depletion polymer
CEAS	Computerised Engine Application System
CFD	Computational Fluid Dynamics
DBS	Double Body Simulation
DES	Detached Eddy Simulations
DNS	Direct Numerical Simulations
EEDI	Energy Efficiency Design Index
EEOI	Energy Efficiency Operational Indicator
EFD	Experimental Fluid Dynamics
ESD	Energy Saving Devices
EX	Extrapolated
EXP	Experimental
FR	Fouling rating
FR	fouling release
FSS	Free Surface Simulation
FVM	Finite Volume Method
GCI	Grid Convergence Index
GHG	Green House Gas
H	fouled with hard fouling
HRIC	High Resolution Interface Capturing scheme
IMO	International Maritime Organisation
ISO	International Organization for Standardization
ITTC	International Towing Tank Conference

KCS	Kriso Container Ship
KVLCC2	Korean Very Large Crude Carrier 2
LES	Large Eddy Simulations
LNG	Liquid Natural Gas
M	million
MRF	Moving Reference Frame
NSTM	Naval Ships' Technical Manual
OWT	open water test
PANS	Partially Averaged Navier-Stokes Simulations
PDMS	polydimethylsiloxane
PI	performance indicators
PIV	Particle Image Velocimetry
PPM	Performance Prediction Method
PV	performance values
R	rough
RANS	Reynolds Averaged Navier-Stokes
RKE	realizable $k - \varepsilon$ turbulence model
RSM	Reynolds Stress Model
RT	resistance test
S	smooth
SEEMP	ship energy efficiency management plan
SEM	scanning electron microscope
SIL	silicone
SKE	standard $k - \varepsilon$ turbulence model
SPC	self-polishing copolymer
SPP	self-propulsion point
SPT	self-propulsion test
SST	shear stress transport
SSTKO	$k - \omega$ shear stress transport turbulence model
TBL	turbulent boundary layer
TBT	tributyltin
TCF	turbulent channel flow
URANS	unsteady Reynolds averaged Navier-Stokes
USNA	United States Naval Academy
V&V	verification and validation

VOF            volume of fluid

WB            Wageningen

# 1. Introduction

## 1.1. General overview

Maritime transport has been the backbone of globalized trade and the manufacturing supply chain throughout history and it remained the most important mode of cargo transport nowadays. Thus more than 80% of world trade is carried out at sea with 51684 seagoing vessels of gross tonnage 1000 and above, which have almost 2 billion deadweight tonnage [1] and are registered in more than 150 countries. The future of this industry is prosperous due to increase in liberalisation of economy and in efficiency of shipping as mode of transport. The growth in international maritime trade is recorded in the last years, and in 2018 more than 11 billion tons were transported by maritime transport [2]. Based on the scientific consensus that global warming is taking place and that it is most probably caused by human made carbon dioxide (CO<sub>2</sub>), Kyoto Protocol which commits state parties to reduce greenhouse gas emissions was adopted by the end of 1997 and entered into force in 2005. As the global mean annual concentration of CO<sub>2</sub> has increasing trend and is already above 410 ppm, the reduction of CO<sub>2</sub> emission is necessary in many different sectors. Since almost entire world fleet is powered by carbon-based fuel, the emission of harmful gases is an inevitable occurrence. Third International Maritime Organisation (IMO) Green House Gas (GHG) study has pointed out that 2.6% of global CO<sub>2</sub> emission comes from international shipping. Furthermore, IMO has projected a significant increase in CO<sub>2</sub> emissions in the following decades. Thus, this study projected an increase by 50% up to 250% in the period to 2050 and this projection relies upon future economic and energy developments. The mitigation of the emissions growth can be made with further actions on energy efficiency of ships as well as their emissions [2]. Therefore, IMO has set a goal to reduce CO<sub>2</sub> emissions per transport work by at least 40% till 2030 and to pursue this effort towards 70% by 2050 in comparison to 2008 [3]. In this manner, IMO has introduced in 2013, regulations for the shipping industry in order to decrease harmful gases emission, such as the Energy Efficiency Design Index (EEDI), the Ship Energy Efficiency Management Plan (SEEMP), as well as the Energy Efficiency Operational Indicator (EEOI). Beside from GHG emission, maritime transport is contributing to emission of non GHG, which are also very harmful to environment.

There are many ways for decarbonisation of maritime transport including fuels, energy efficiency technologies, operations and policies [4]. Thus, there are six main groups of measures which have high potential for reduction of GHG emission: hull design, economy of scale, power and propulsion, speed, fuels and alternative energy sources and weather routing and scheduling [5]. Ship energy efficiency measures can be classified into two main categories, technological and operational measures. Technological measures for increasing ship energy efficiency are mostly contained of bulbous bow designs, the installation of Energy Saving Devices (ESD), tuning, derating and waste heat recovery of ship engines as well as the use of alternative or cleaner fuels [5]. It should be noted that some technological measures can only be considered for new ships, while others can be applied as retrofit measures. On the other hand, operational measures can be applied for both new and existing ships. Operational measures are speed optimization, voyage planning, fleet management and on-board energy management. Bouman et al. [5] have reviewed around 150 studies in order to present an extensive overview of the CO<sub>2</sub> emissions reduction potentials of ship energy efficiency measures. The obtained CO<sub>2</sub> emissions reduction potential from individual measures, which are divided into five main



categories are presented in Figure 1.1. It should be noted that economy of scale is put under hull design category, while speed, weather routing and scheduling are put under operational category.

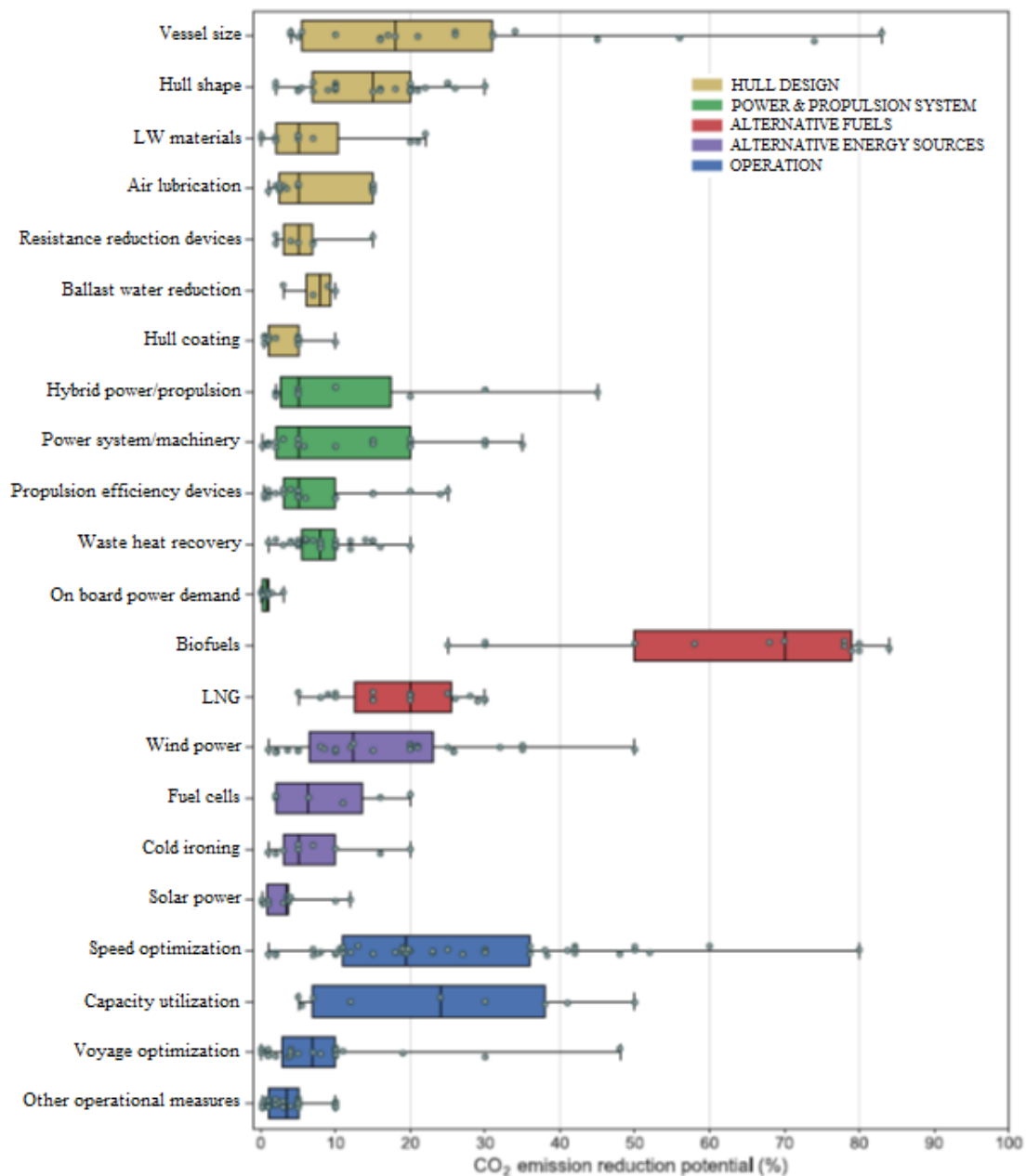


Figure 1.1 CO<sub>2</sub> emission reduction potential [5]

As can be seen from Figure 1.1, relatively large CO<sub>2</sub> emission reduction potential can be achieved with different energy efficiency measures. However, in order to implement a specific measure for energy savings, shipping companies evaluate the return on the investment [6]. Thus, the maritime transport industry has mostly ignored the use of alternative fuels and renewable energy sources and has mainly concentrated on other technological and operational measures [7]. For example, the systemic effects of large-scale adoption of biofuels reach well beyond reduction in CO<sub>2</sub> emissions during combustion. The use of Liquid Natural Gas (LNG) as a fuel could reduce CO<sub>2</sub> emissions, but would cause the increase of the leakage of methane from the engine, and methane is GHG as well [5]. Also, the capital costs related to the usage of

LNG as a fuel are higher when compared to oil-fuel equivalent; LNG storage tanks require twice the volume of the conventional bunker tanks; and there is the cost of adding port infrastructure. Even though fuel cell technologies offer the potential of CO<sub>2</sub> emission, the current fuel cell technology cannot provide enough power, which is required to propel large ships, i.e. fuel cells in the foreseeable future will not take a place of the existing main engines [8]. The use of soft and wing sails, kites, wind turbines and Flettner rotors can be very effective method for the reduction of CO<sub>2</sub> emission, especially at slower speeds and for smaller ships. However, due to unfamiliarity with technology, safety and reliability concerns, and a lack of demonstration, wind assistance as a measure for the reduction of CO<sub>2</sub> emission has still not been broadly applied [9]. As can be seen from Figure 1.1, solar assistance can provide lower CO<sub>2</sub> emission reduction potential than other alternative energy resources, and it is most efficient for smaller vessels which sail at lower speed and higher savings in fuel consumption and consequently CO<sub>2</sub> emission are unlikely to be cost effective. Cold ironing, i.e. the process of providing shoreside electrical power to a ship at berth while its main and auxiliary engines are turned off, can be applied to ships of any size. It can reduce CO<sub>2</sub> emission and the potential of CO<sub>2</sub> emission reduction is a function of a time spent in a port. However, it requires a supply of a shoreside electrical power and infrastructure costs related to this measure are significant. The highest CO<sub>2</sub> emission reduction potential within category of hull design measures target primarily the utilization of economies of scale, for example increasing the ship size causes the reduction of emissions per unit transport work. The optimization of the ship hull causes the reduction of ship resistance and thus the reduction of the fuel consumption. However, vessel size is predetermined with the law of the market, i.e. with the demand for a given cargo. Also, it is difficult to quantify the exact CO<sub>2</sub> emission reduction potential from the optimization of ship hull, as it is usually performed in the design stage in order to reduce fuel consumption. The implementation of light weighting materials has lower CO<sub>2</sub> emission reduction potential and it is questionable if it is cost effective, while air lubrication is still not market wide adopted as there are questions about its drag reduction performance beyond the laboratory, energy and economic cost benefit [10]. The proper selection of antifouling coating (AF) is important for the reduction of ship resistance for new ships, as well as during the exploitation for the prevention of biofouling. For measures in the category power and propulsion system, significant emission reductions can be obtained, Figure 1.1. Still, the medians of the estimated reductions are relatively low, which demonstrates the challenges and boundary conditions related to implementation of these measures. Thus, a truly integrated hybrid drivetrain varies considerably from a conventional set-up and optimal implementation is demanding, especially for technology which is in an early stage of its application [5]. The significance of operational measures was formalized with the introduction of SEEMP by IMO, assigning every ship operator/shipowner to set up a formal system for management and optimization of ship and fleet performance. The most important operational measures for reduction of CO<sub>2</sub> emission are speed reduction, weather routing and periodical cleaning of ship hull and screw propeller (in the following text propeller) [11]. Speed reduction, i.e. slow steaming is recognized as an operational measure which reduces the fuel consumption and in turn has led to significant decrease in carbon emissions [12], [13]. Slow steaming lengthens round-trip time by 10–20% depending on the service route and port times [14]. Even though longer transport times associated with slower speeds means more ships or load is required, a 10% reduction in speed may result in a total average emissions reduction of 19% [4], [15]. Regardless of this, the wide implementation of this operational measure is dependent on the fuel price, i.e. on the economic justification of its implementation [16] and on the market. Thus, if the market requires the

transportation of large quantities of goods within a limited time, it is unlikely that ship operator/shipowner will apply slow steaming approach. Also, if the fuel price is low, slow steaming is not sustainable, as the profit is reduced [16]. Additional problem related to slow steaming approach is the ‘split incentives problem’ since the fuel costs and costs related to longer voyage may be assigned to different agents [17]. Furthermore, there is a problem related to ship operation, as ships are operating in conditions that are significantly different to those for which they were designed and optimized [18]. Weather routing is important operational measure, as it has a potential to decrease harmful emissions, but also to increase safety of a voyage. However, weather conditions are exogenous, and exposure can only be minimized if voyage time increases [19]. The optimization of the maintenance schedule is important operational measure as ship operator/shipowner has a large degree of control over this measure. Thus, even though the rate of biofouling on the ship hull and propeller is mostly exogenous, the ship operator/shipowner can decide when to clean the hull or propeller [19]. The CO<sub>2</sub> emission reduction potential is substantial as biofouling is important contributor for an increase in CO<sub>2</sub> emission. Third IMO GHG study [2] has applied a fixed 9% increase in total resistance for all ships under the assumption that maintenance takes place every five years in order to restore initial hull roughness. Even though there is a large degree of uncertainty within this estimation, it represents the CO<sub>2</sub> emission reduction potential through the optimization of the maintenance schedule.

As said before, shipping companies evaluate the return on the investment and this evaluation is very complex. Therefore, the shipping industry seeks to find a general method or model for the assessment of the potential energy savings. The most important impediments in potential energy savings from the optimization of maintenance schedule, i.e. the proper timing for cleaning ship’s hull and propeller, are lack of information related to the potential benefits and impact of the cleaning on the ship resistance and propulsion characteristics, as well as the lack of information related to the economic impact of this operational measure [6]. These two impediments should not be considered as independent, but as dependent on each other. Thus, if the impact of hull and propeller cleaning on the ship resistance and propulsion characteristics is better understood, those knowledges could lead to new insights related to economic impact of hull and propeller cleaning. In that way, the return of the investment could be easily calculated, and the application of this operational measure leads to potential energy savings with reduction both in fuel consumption and GHG emission [20]. Therefore, the modelling and the assessment of the effect of biofouling on ship resistance and propulsion characteristics are very important as they can demonstrate the significance of the mitigation of biofouling, i.e. the hull and propeller cleaning [21]. Currently there are no reliable techniques which could provide ship operators/shipowners an assessment of the fuel penalty due to the presence of biofouling [22]. The goal of this thesis is to fill this gap through a development of a new model for the assessment of the biofouling effect on the ship resistance and propulsion characteristics.

## **1.2. Biofouling**

Biofouling is the accumulation of microorganisms, plants, algae or animals on wetted surfaces. It occurs in many different fields, including medical, marine and industrial field. However, shipping industry is the most affected by the settlement and the growth of biofouling organisms. Ship hull roughness is increased because of the presence of biofouling organisms. Thus, frictional resistance is increased, which results in increased fuel consumption, decreased ship speed and increased engine stress [23]. Biofouling represents a growing problem from both the

economic and environmental point of view. An important study related to economic impact of biofouling on a mid-sized naval surface ship is performed by Schultz et al. [24]. The authors have estimated the overall costs related with fouling for one fouling level present at ship to be around 1 million USD per year and they include costs related to painting and cleaning as those costs are much lower than the fuel costs. These costs for entire Arleigh Burke class destroyer DDG-51 over 15 years are estimated to be around 1 billion USD. Therefore, all costs related to the development, procurement and application, as well as relatively costly technical or management solutions for antifouling of ships are economically justified if they only slightly improve the fouling condition of a hull. Another problem related to ship biofouling is spreading of species across the world seas and consequently disruption and change of existing biological systems [25]. This problem is also recognized by the IMO, which adopted the guidelines for the control and management of ships' biofouling in order to reduce the transfer of invasive aquatic species by ships in 2011 [26]. Therefore, the biofouling management measures which will be carried on a ship should be written in a biofouling management plan, while records of biofouling management practices should be kept in a biofouling record book. IMO has recommended that every ship should have biofouling management plan and record book. What is more, IMO has advised ship owners/ship operators to undertake in-water inspection, cleaning and maintenance of a ship in order to maintain it as free of biofouling as practical. Thus, a valuable and adaptable way to investigate the condition of AF systems, as well as the fouling condition of a ship is in-water inspection. IMO has recommended that in-water inspection should be performed periodically as a general way of routine surveillance, augmented by specific inspections as required to address any situations of elevated risk. Also, in-water inspections should be planned before and after ship's inactivity periods or significant change of ship's operating profile, before in-water cleaning, after a known or suspected marine pest is discovered in a ship's internal seawater cooling systems as well as following damage of AF system. Another significant part of biofouling management is in-water cleaning. However, a special care should be given to in-water cleaning, as it can introduce various degrees of environmental risk, depending on the fouling condition, the amount of AF coating system residue released and the biocidal content of AF coating system. More attention is given to cleaning of fouling with lower fouling rates, as it can be cleaned with gentler techniques, which minimize degradation of AF coating system and thus minimize biocide release as well. Cleaning will improve ship resistance and propulsion characteristics, reduce fuel consumption and GHG emission. Oliveira and Granhag [27] have studied in-water cleaning and its effects on AF coatings. The authors have shown that with the application of minimal cleaning forces on AF coatings, either biocidal or non-biocidal, no significant damage or wear will be present at AF coatings. IMO has [26] recommended that the hull of a ship should be cleaned when practical, using soft methods if significant microfouling occurs. This will also lead to reduction of risk of spreading invasive aquatic species as macrofouling accumulation will be prevented. Namely, the settlement of fouling organisms on the wetted surface occurs in three stages, i.e. formation of a conditioning film, microfouling and macrofouling. Microfouling can be divided into two stages. The first stage of microfouling is formed from the mixture of the conditioning film and the slime of living and dead bacteria cells, while the secondary stage is formed when diatoms colonies, macroalgae and protozoa spores settlement increases [28]. Even though many studies were carried out regarding the settlement pattern of fouling on immersed surface, this question has still not been answered [29]. Van Mooy et al. [30] have shown that larger fouling organisms, i.e. macrofouling such as algae and tubeworms will settle earlier on the wetted surface covered with biofilm than on the unfouled wetted surface. However, macrofouling does not inevitably

require the presence of a microfouling on a surface to settle [31]. Biofouling growth on immersed surface is affected by various physical, chemical and biological processes including geographical location, distance from shore, depth, temperature and season, water current and tidal conditions, water quality and other factors. Fouling is generally more intense in tropical locations and this can be attributed to the continuous process of breeding and the higher temperature of seawater. However, it is important to note that it is not possible to predict the fouling communities on the basis of solely geographical location as fouling communities can be completely different at neighbouring locations. Physical and chemical parameters of sea water (salinity, temperature, organic content and light penetration) change significantly with depth and thus considerably affect the type and growth of fouling. As the rate of fouling is generally more important nearshore, it also decreases with increasing depth at any location. Fouling composition is greatly affected by temperature and seasons. The increase of the rate of fouling can be correlated to an increase in the temperature of sea water. In tropical waters fouling growth rate is at high and constant level throughout all seasons, while in temperate or cold waters, fouling growth rate is higher from April to September. Water current and tidal conditions are important for the settlement of fouling as water movement causes larvae movement as well, from the shore to the immersed surface. Water quality is important parameter which influences fouling growth rate. Thus, salinity, light, nutrients availability and silt influence the biology of species. Other factors which influence fouling growth rate are chemical signals, competition between species, human activities and the nature of the substrate (surface roughness, surface charge, hydrophobicity and nature of the material) [29].

Since the ancient times, fouling of the immersed surface was tried to be avoided. Currently, the most common method for the prevention of fouling on the immersed surface is the application of AF coating. Nevertheless, there are different methods for the prevention of fouling which include aeration and acoustic methods, but they are still not widely used [32], [33]. The real revolution of AF coatings commenced with the development of new synthetic petroleum-based resins in the 1940s, allowing the development of polymer-based coatings with better mechanical properties. In addition, AF coatings based on tributyltin (TBT) were developed in the 1950s and it was thought that fouling problem has been solved. Due to significant environmental concerns, TBT based coatings were firstly forbidden by the IMO in 2001 and thereafter banned worldwide in 2008 by the Rotterdam Convention. Consequently nowadays the development of a coating technology has been focused on discovering of the alternative AF agents and other AF strategies. Presently, there are two approaches in fouling prevention through the application of AF coatings, biocidal and non-biocidal coatings [28]. Biocidal coatings slowly leach the incorporated biocides into the water and in that way deter microorganisms from attaching to the surface [34]. Biocidal coatings can be divided into Controlled Depletion Polymer (CDP) and Self Polishing Copolymer (SPC) coatings. CDP coatings present traditional AF coatings based on a water soluble natural or synthetic pine rosin mixed with a biocide. The controlled dissolution of the rosin matrix releases the biocides. The recoating is problematic as insoluble materials accumulate over time at the surface in a leached layer. Furthermore, this slows down the release of biocide and therefore wall shear stress at the surface is needed for biocide release (present at the surface either because of ship is sailing or because of cleaning). SPC coatings are coatings based on an insoluble metallic or organic synthetic polymer that contains a biocide. These coatings have much smoother surface profile and thinner leached layer than CDP coatings due to good control of the dissolution rate, i.e. biocides. Biocide agents are currently based on copper, however this biocide agent will

probably be banned as well due to environmental concerns [35]. Therefore, the attention is now placed on the development of biocide free coatings [36]. One of the greatest efforts towards this path was carried out through a European Union research project entitled Advanced Nanostructured Surfaces for the Control of Biofouling (AMBIO) [37]. The goal of AMBIO was to develop new coatings which would prevent or reduce the adhesion of biofouling through nanostructuring in order to obtain the desired physical and chemical properties of the surface (non-stick properties) instead of using biocides, i.e. fouling release (FR) coatings. Commonly, FR coatings are based on silicone or fluoro-silicone and are typically applied on ships which sail often and at higher speeds [38]. The prevention of the adhesion or removing of biofouling from the wetted surfaces of slower vessels which sail at speed of 15 knots or lower, are challenging and therefore soft cleaning is needed for the removal of microfouling [39]. Removal of macrofouling, especially tubeworms or barnacles, which can attach a wetted surface of a ship if ship is stationary for some time, is impossible without cleaning.

Biofouling depends on various parameters and the prediction of time for successful prevention of fouling attachment at the immersed surfaces is still elusive [30]. Despite the use of effective AF systems and operational practices, undesirable amounts of biofouling may still accumulate during the intended lifetime of the AF system.

According to Naval Ships' Technical Manual (NSTM) [40], there are three types of biofouling: soft, hard and composite (combination of soft and hard fouling). Soft fouling is consisted of slime and grass (form of multicellular green and brown algae). Hard fouling is consisted of barnacles, tubeworms and calcareous deposits (deposition of magnesium and calcium carbonate on bare metal surfaces resulting from an active cathodic protection system). An important scale for description of fouling severity is presented in NSTM [40]. Fouling rating (FR) is described through fouling rating scale and fouling percentages. Thus, FR scale presents a rating number which is assigned to each of the 10 fouling patterns on a scale of 0 to 100 in 10-point increments (Table 1.1), while fouling percentage quantifies the density of fouling which covers a particular component or area of the hull.

The photographs of FR scale are shown in Figure 1.2 (soft fouling) and in Figure 1.3 (hard and composite fouling).



Figure 1.2 Fouling rating scale for soft fouling [40]



Figure 1.3 Fouling rating scale for hard and composite fouling [40]

Table 1.1 Fouling rating scale [40]

Type	FR	Description
Soft	0	A clean, foul-free surface.
Soft	10	Incipient slime, light shades of red and green. Bare metal and painted surfaces are visible beneath the fouling.
Soft	20	Advanced slime, slime as dark green patches with yellow or brown coloured areas. Bare metal and painted surfaces may be obscured by the fouling.
Soft	30	Grass as filaments up to 76 mm in length, projections up to 6.4 mm in height; or a flat network of filaments, green, yellow, or brown in colour; or soft non-calcareous fouling such as sea cucumbers, sea grapes, or sea squirts projecting up to 6.4 mm in height. The fouling cannot be easily wiped off by hand.
Hard	40	Calcareous fouling in the form of tubeworms less than 6.4 mm in diameter or height.
Hard	50	Calcareous fouling in the form of barnacles less than 6.4 mm in diameter or height.
Hard	60	Combination of tubeworms and barnacles, less than 6.4 mm in diameter or height.
Hard	70	Combination of tubeworms and barnacles, greater than 6.4 mm in diameter or height.
Hard	80	Tubeworms closely packed together and growing upright away from surface. Barnacles growing one on top of another, 6.4 mm or less in height. Calcareous shells appear clean or white in colour.
Hard	90	Dense growth of tubeworms with barnacles, 6.4 mm or greater in height; Calcareous shells brown in colour (oysters and mussels); or with slime or grass overlay.
Composite	100	All forms of fouling present, soft and hard, particularly soft sedentary animals without calcareous covering (tunicates) growing over various forms of hard growth.

### 1.3. The research problem definition

As already noted, there are many measures for increasing the ship energy efficiency. Ship operators/shipowners hesitate to implement them due to the lack of reliable data on their effect, i.e. data on the possible percentage savings due to implementation of certain measure [12], [41]. An accurate calculation of the return on investment is necessary for ship operators/shipowners to make a decision regarding the application of certain measure. The optimization of maintenance schedule is one of few measures over which ship operator/shipowner has a large degree of control. An accurate assessment of the impact of hull and propeller cleaning, i.e. biofouling, on ship resistance and propulsion characteristics will enable well assessment of economic aspect of this measure, what will lead to more accurate calculation of the return on investment. Namely, as AF coatings have a limited service life and cannot be applied or provide adequate protection to all parts of immersed hull surface, biofouling occurs in between dry-docking periods [42]. As a result, despite the duty cycle, biofouling will occupy immersed surface, but due to various duty cycles, miscellaneous fouling communities can be attached. In such a way, containerships which can be associated with relatively high speed and short immobile periods during loading and unloading of cargo are typically fouled with biofilm and algal communities, i.e. soft fouling [43]. On the other hand, ships which have long immobile periods as drill ships or naval vessels are often fouled with both microfouling and macrofouling. The condition of the hull and propeller as well as the presence of biofouling on the immersed surfaces can have a significant effect on the ship resistance and propulsion characteristics. IMO [44] has estimated that due to deterioration of hull and propeller the performance for certain typical merchant ships in between dry dockings can lead to 15-20% loss in the overall propulsive efficiency, leading to 15-20% increase in the fuel consumption if ship speed remains constant. Since 60-70% of the entire operational costs are related to fuel cost and as fouling of hull and propeller causes an increase in fuel consumption, the investigation of the fouling level and its influence on the ship performance is crucial for ship operators/shipowners [45]. Therefore, an accurate determination of the effect of biofouling on the ship resistance and propulsion characteristics is required for the optimization of the maintenance schedule. There is an increasing number of shipowners that are willing to invest in tools, which will give them the insights related to this impact [46].

In the literature, there are many studies related to the assessment of the effect of biofouling on the ship resistance and propulsion characteristics and those studies can be divided into several approaches [47]. One of the directions of research is oriented to the statistical studies or data driven models. The researchers based on the measured data analyse the impact of biofouling on the ship's performance [19], [48], [49], [50], [51]. Adland et al. [19] have evaluated empirically the impact of hull cleaning as well as dry-docking on ship energy efficiency on examples of Aframax crude oil tankers utilizing daily noon reports. The authors proposed a new methodology for the evaluation of the impact of ship cleaning on ship energy efficiency based on the comparison of fuel consumption before and after ship's cleaning. Krapp and Vranakis [49] have investigated 32 ships over 48 dry-docking intervals and concluded that a typical ship after 60 month of sailing has to use 36% more power than after the dry-docking. Coraddu et al. [50] have used deep extreme learning machines for the estimation of speed loss caused by biofouling of the hull and propeller based on the large amount of data collected from the on-board monitoring. For that purpose, a digital twin ship has been made and used for the calculation of the differences between the predicted and actual performance. A digital twin is



used for estimating the speed loss due to biofouling and the authors presented the effectiveness of their method and its accuracy in the prediction of speed loss due to biofouling. Notti et al. [51] have performed an analysis of a series of sea trials, which allowed the authors the quantitative and qualitative comparison of the fuel consumption. Thus, the authors have compared the fuel consumption before and after the application of fluoropolymer FR coating and noticed a reduction in the fuel consumption. Another approach is to study the impact of biofouling on a certain ship, or several ships, between dry-dockings, and then, after the detailed analysis of results make conclusions [52], [53], [54], [55]. Tarelko [53] has performed a long-term investigation of biofouling of the immersed surface between consecutive ship dockings. Thus, the author has measured ship speed, fuel consumption and propeller shaft torque over the time elapse from last docking of a sailing ship. The carried investigation can make a basis for decision making by a shipowner about economic justification of ship operation with relatively long-time intervals between consecutive dockings. Ballegooijen and Muntean [52] have presented the opportunities of full-scale measurement of propeller thrust for identifying fuel saving potentials and emission reductions on the example of containership in service. Coraddu et al. [54] have presented two data analysis unsupervised techniques which can be used for the prediction of the hull condition in an unsupervised fashion. The authors claimed that the proposed models can be used for easy and quick identification of maintenance requirements. Foteinos et al. [55] have estimated the effect of biofouling on ship performance through the propeller law coefficient and the fouling resistance coefficient over a dry-docking period for four sister ships, i.e. panamax bulk carriers. Both before mentioned approaches are based on the performance monitoring, either through noon reports, or through measurements of propeller thrust, torque, rotation rate or fuel consumption. The important document related to hull and propeller performance monitoring is [56]. ISO 19030 presents relatively simple and robust approach, which defines performance values (PV) and performance indicators (PI). PV are usually used for tracking the speed or power loss compared with a referent speed-power curve. Thereafter, the PV time series are utilized for the calculation of various PI, for example dry-docking performance, maintenance effect, etc [57]. ISO 19030 provides a unified methodology and measures for hull performance monitoring and it is rather simple and robust. Five main steps are required for the implementation of ISO 19030 approach. Those steps are obtaining speed-power reference curves, filtering the data, performing a wind correction, calculation of the PV and calculation of PI. Speed-power reference curves are obtained either from sea trial or towing tank test data or Computational Fluid Dynamics (CFD) simulations. The measured data is filtered for outliers and according to certain reference conditions. PV are calculated based on the measured values and a comparison with the reference curves, while PI are calculated utilizing the obtained PV. Although the approach is based on the actual measurements from ship operation, it has several shortcomings. In such a way, the filtering of the measured data is rather strict, i.e. if the wind force surpasses an upper limit of Beaufort 4 during the measurements, measured data should be discarded. As the most of the current monitoring approaches are not based on the continuous performance monitoring, a lot of data is lost due to this filtering, which is unfavourable. Another shortcoming is that this approach does not consider swell, which means that only wind waves are considered in this filtering. In this way, waves generated by the swell are not filtered, and since they are generated at the different location and time, they do not correspond to the actual wind conditions and therefore must be filtered as well [58]. Furthermore, the measured data is scattered, because they are collected during navigation. Conditions during navigation differ significantly from test run conditions, and therefore measured data should be corrected [59]. This correction is especially

difficult, since there is no practical approach for adequate quantification of the required added power in waves for the purpose of performance monitoring [58]. Additional shortcomings of this approach include problems related with variations of the reported average values, unintentional errors, as well as an intentional false reporting of the noon reports and are presented in [60]. Regardless of these shortcomings, the approach presented in ISO 19030 still represents the current best practice for performance monitoring [61]. Ship propulsion characteristics and consequently fuel consumption in service are affected by the surface conditions of both hull and propeller. For a proper management and evaluation of hull and propeller, a method for adequate evaluation of their separate performance is needed. However, this is still a demanding task and thus the most of performance monitoring approaches evaluate their combined performance [62]. Performance monitoring for ships in service is challenging as other parameters except hull and propeller surface condition have influence on speed-power performance of ship, for example various environmental and operational conditions. Generally, the separation of the effect of hull and propeller surface condition on the ship performance from all other influencing parameters can be done either through correction of all other significant factors or through filtering in order to obtain comparable conditions if the one has enough data available [62]. In order to reliably separate effect of the hull and propeller, propeller thrust measurements are necessary, and these measurements are very difficult and rare in commercial shipping nowadays. Van Ballegooijen and Helsloot [46] have proposed an approach for the separation of propeller and hull effects based on the definition of three PI, propulsion power loss ( $KPI_{H+P}$ ), hull power loss ( $KPI_H$ ) and propeller power loss ( $KPI_P$ ).  $KPI_{H+P}$  tracks changes in hull efficiency ( $\eta_H$ ), open water efficiency ( $\eta_o$ ), relative rotative efficiency ( $\eta_R$ ) and shaft efficiency ( $\eta_s$ ), while  $KPI_H$  tracks changes in the total resistance of a ship ( $R_T$ ) and thrust deduction fraction ( $t$ ). Finally  $KPI_P$ , which is defined as the difference between  $KPI_{H+P}$  and  $KPI_H$  tracks changes in wake fraction ( $w$ ),  $\eta_o$ ,  $\eta_R$  and  $\eta_s$ . Therefore, the approach proposed in [46] does not separate changes in the propeller and hull performance in total, as changes in  $w$  and  $\eta_R$  are related to hull surface conditions as well. Therefore, the further development of physical models for separation of roughness effects on hull and propeller are needed [63]. A new performance indicator is suggested within [64], which enables more reliable comparison between ships, more accurate comparison of a ship performance over time as well as the assessment of penalties in service conditions, which are not the same as were in past data (for example for slow steaming conditions). This indicator is based on the equivalent sand grain roughness approach and equivalent sand grain roughness is determined iteratively through comparison of the modelled roughness penalties using Granville similarity law scaling method (Section 2.3.3) and measured penalties.

In addition, there is an approach related to the investigation of the roughness effects on the flow around the immersed body and boundary layer which is formed around the immersed body. This approach is based on the wall similarity hypothesis, which states that roughness effects are limited to inner layer of turbulent boundary layer. Within this thesis, investigation of the effect of biofouling on the ship resistance and propulsion characteristics will be based on this approach. Therefore, a critical review of the current state of the art in this research field will be presented in the Section 2.

## 1.4. The research

### 1.4.1. Motivations behind this research

Regardless of the applied approach for the determination of the effect of biofouling on the ship resistance and propulsion characteristics, this determination is as evenly important as the improvement of the energy efficiency of existing ships through the application of new AF coatings, since it can demonstrate the importance of hull and propeller cleaning [21], [65], [66], [67], [68]. Namely, due to the complex identification of the actual contribution of biofouling to the decrease in ship performance, this determination is very valuable. Therefore, shipping companies have urged for the creation of a transparent and reliable standard for measuring hull and propeller performance [50]. Optimization of the maintenance schedule must consider the loss of the speed caused by the presence of biofouling in order to find the optimal balance between efficiency and costs. Therefore, an accurate assessment of the speed loss due to the presence of biofouling is required [69], [70]. In that sense, the International Towing Tank Conference (ITTC) has advised scientists to present new formulae or methods based on the experimental data to determine the effect of biofouling on ship resistance and propulsion characteristics [71]. Namely, currently ITTC proposes a method for the determination of this effect based on the roughness allowance ( $\Delta C_f$ ) [72], where roughness allowance is defined through equivalent sand grain roughness height ( $k_s$ ). As suggested in [73], different  $k_s$  values can be utilised, instead of utilising the standard value of 150  $\mu\text{m}$ , if roughness measurements are available, since this surface property is not directly measurable. Thus, within ITTC Performance Prediction Method (PPM) the effect of roughness, i.e. biofouling is taken into account only as an increase in the frictional resistance. Within [71] it is predicted that, due to variety of surface roughness on a ship related to coating, damage, slime and other types of fouling, a new formulation will include several formulations or at least one formulation but with parameters which depend on roughness type. Furthermore, it is claimed that the utilization of roughness function ( $\Delta U^+$ ), i.e. velocity shift function is the most likely candidate for the improvement of roughness allowance. The methods which use  $\Delta U^+$  are based on the boundary layer analysis. Until very recently, the most of studies related to the investigation of the biofouling effect on ship resistance characteristics were made using Granville similarity law scaling method. This method can only be utilized for the prediction of effect of biofouling on the frictional resistance of flat plates having the same length as a ship. As presented in Section 2, this method has several drawbacks and therefore a development of more comprehensive method, which could reliably predict the effect of biofouling on the ship resistance and propulsion characteristics, is required. This method will be based on the wall similarity hypothesis and the implementation of  $\Delta U^+$  model within the solver of CFD software package. In that way, the effect of biofouling, defined with a certain  $\Delta U^+$ , on each resistance component, propulsion characteristics, propeller open water characteristics and finally propeller operation point will be enabled.

Even though, the assessment of the effect of biofouling on the ship resistance and propulsion characteristics through the implementation of  $\Delta U^+$  model within the solver of CFD software will enable also a detail analysis of the flow around the investigated ship, it may be difficult for less experienced users to carry out CFD analysis. Furthermore, CFD analysis is consisted of three main steps: pre-processing, processing and post-processing, and consequently can have

burden of relatively high computational time. What is more, within the optimization of maintenance schedule it would be beneficial to have a rapid method for the estimation of the effect of biofouling on the ship resistance and propulsion characteristics. Namely, for this assessment by utilizing CFD, the user must carry out numerical simulations of resistance, open water and self-propulsion tests in full-scale. What is more, ITTC [71] has advised researchers to modify the current semi-empirical expressions used for the drag and lift coefficient of blade profiles in order to take into account coating effect or biofouling. In this sense, a new performance prediction method for the assessment of the effect of fouling on the ship resistance and propulsion characteristics, as well as for the assessment of the effect of fouling on the open water characteristics, would be beneficial. The purpose of this method is twofold, it will provide a rapid assessment of this effect and it can be used for comparison with the obtained CFD results. What is more, this method would provide more accurate prediction of roughness penalties than the ones obtained using only Granville similarity method for the prediction of the increase in the total resistance demonstrated in [64].

As already mentioned, regardless of the application of AF coating, biofouling on the immersed surface will be present. Thus, all AF coatings suffer from the slime occurrence, even in newly applied condition and this is even more highlighted for FR coatings as those coatings are non-biocidal and require shear stress to keep immersed surface without biofouling [71]. Consequently, one of the recommendations of [71] was to include the effect of slime on the performance predictions and in that way performance prediction would be widened in order to cover this effect, which represents an important issue for ships coated with FR coatings. What is more, the effect of slime is often neglected, since it is believed that the presence of slime will not have an important effect on the ship resistance and propulsion characteristics. This is evident from the definition of Antifouling Performance Index (API) proposed by Hempel, which ranges from 0 to 100%. Namely, even if 50% of the immersed surface is covered with slime, API is equal to 90%, meaning that AF coating has excellent performance [74]. Because of this, it would be beneficial to investigate the effect of slime on the ship resistance and propulsion characteristics, i.e. to propose a method for the prediction of this effect.

#### **1.4.2. Research objectives and hypothesis**

The objective of the proposed research is development of numerical procedure for the prediction of the effect of biofouling on the hydrodynamic characteristics of ship resistance and propulsion in calm water. This includes the effect on the ship resistance, wake and thrust deduction fractions, as well as the operating point of a propeller. Namely, using the proposed numerical procedure, the assessment of the effect of biofouling on each resistance component and propulsion characteristic, as well as the effect of biofouling on the open water characteristics will be enabled. The assessment of the effect of biofouling on the operating point of a propeller, i.e. on the delivered power and propeller rotation rate is very important as it can be related to fuel consumption and GHG emission.

The research is based on the following hypotheses:

1. Computational Fluid Dynamics methods can be used for the determination of ship hydrodynamic characteristics for different roughness conditions of wetted surface.
2. Roughness length scale can be expressed through easily measurable parameters, i.e. fouling height and percentage of coverage and non-uniform surface roughness effects can be described with sufficient accuracy utilizing the uniformly distributed sand grain roughness.

3. It is possible to develop a new numerical procedure for full-scale prediction of the hydrodynamic characteristics of ship resistance and propulsion for different fouling conditions of ship hull which would more comprehensively describe the effect of the biofouling than current methods based only on the roughness allowance.

As already noted, biofouling is dependent on many different parameters and prediction of how long will antifouling coating successfully prevent fouling has remained elusive [30]. Thus, it is still challenging to relate specific fouling conditions of ship and propeller and their development with real ships operating in the world seas. Therefore, this research will be focused on the investigation of potential effects of predetermined surface conditions on the hydrodynamic characteristics of ship resistance and propulsion in calm water. The future studies related to biofouling problems are needed for better understanding of time-dependent biofouling growth on the ship hull and propeller surfaces. One of the initial steps into development of time-dependent biofouling growth model is presented in [75].

In order to successfully achieve the main objective of this PhD thesis, several specific objectives should be accomplished. Firstly, a detail literature review related to the modelling of the effects of biofouling on the flow around the immersed body and boundary layer which is formed around the immersed body. This literature review will result with a definition of the gaps in the literature. The proposed numerical procedure will be based on the wall similarity hypothesis and the implementation of certain roughness function within the solver, i.e. software package for CFD analysis. Two fouling types will be analysed, slime as a representative of soft fouling and hard fouling. Fouling with a slime is of particular importance, as every AF coating suffers from slime occurrence and as recommended by ITTC, the effect of slime on ship performance should be analysed. Therefore, roughness function models should be proposed and implemented within the wall function of the solver. Thereafter, the applicability of a CFD model for the assessment of the effect of biofouling through employment of modified wall functions will be investigated and demonstrated. Afterwards, a numerical procedure for the prediction of the effect of biofouling on the ship resistance and propulsion in calm water will be developed and proposed. The verification and validation of the CFD model which enables the prediction of the effect of biofouling on ship resistance and propulsion characteristics will be performed. Sufficient grid size and time step, as well as the numerical uncertainty will be found on the basis of the verification procedure. Validation of the obtained numerical results for smooth surface condition will be performed by comparison with the extrapolated towing tank results. The obtained numerical results for rough surface conditions will be validated by comparison with the obtained increases in frictional and total resistance using Granville similarity law scaling method. The applicability of the proposed procedure will be shown on three merchant ships by carrying out CFD simulations of resistance, open water and self-propulsion tests at full-scale. This procedure will enable the assessment of the effect of biofouling on the delivered power and propeller rotation rate or decrease of ship speed if the delivered power is kept constant as for smooth surface condition, rather than on the effective power of a ship. A detail analysis of the obtained numerical results will be performed, and the effect of biofouling will be analysed.

The effect of the roughness and therefore biofouling within the current ITTC PPM is taken into account through the increase in frictional resistance. In PPM proposed by Kresic and Haskell [76], the effect of roughness is assessed through  $k_s$ , but predefinition of  $k_s$  for certain surface condition is required, which can be determined by hydrodynamic measurements. Therefore,

additional objective of this PhD thesis is to propose a new PPM, which combines Granville similarity law scaling method and roughness functions for the determination of the increase in frictional resistance due to the presence of biofouling. This PPM will enable a rapid assessment of the effect of biofouling on the ship resistance and propulsion characteristics. A comparison of the obtained numerical results with the results obtained with the proposed PPM will be performed and the applicability of PPM will be highlighted.

### **1.4.3. Scientific contribution of the research**

The research has resulted with a proposed numerical procedure, as well as with a PPM, which can be utilized for the assessment of the effect of biofouling on ship resistance and propulsion characteristics in calm water. This has enabled the determination of the effect of hull surface on the total, frictional, viscous pressure and wave resistance, as well as on the flow around ship hull and propeller. Furthermore, the effect of biofouling on open water characteristics, thrust deduction fraction, nominal wake fraction, open water and relative rotative efficiency and advance coefficient at self-propulsion point is assessed as well. In addition to the estimation of the operating point of a propeller, ship energy efficiency for different surface roughness conditions is enabled. The assessment of these effects can be utilized within the tools for the optimization of the maintenance schedule [63], where the prediction of the optimal timing for the maintenance is of crucial importance. The obtained results will show the importance of hull and propeller cleaning, i.e. the importance of keeping the hull and propeller free of fouling. The main scientific contributions are summarised as follows:

*Roughness function models for the prediction of frictional resistance of surface covered with diatomaceous biofilm are proposed and implemented in the CFD software.*

Since, all AF coatings suffer from the slime (biofilm) occurrence, and as ITTC has highlighted the importance of the prediction of the effect of slime on the ship performance, three roughness function models for diatomaceous biofilm are proposed. Roughness function models are proposed based on the experimentally determined roughness function values and the least squares method. After a detail verification and validation study, the prediction of the frictional resistance of the surfaces covered with biofilm using roughness measurements is enabled.

*Impact of diatomaceous biofilm on the ship resistance characteristics and nominal wake.*

Utilizing the proposed roughness function models within the numerical simulations of resistance test, the impact of biofilm on each resistance characteristic as well as nominal wake is assessed. The extensive quantification of numerical errors within the assessment of resistance characteristics and nominal wake is performed for the smooth surface condition and for surface covered with biofilm. It was shown that while frictional resistance coefficient and nominal wake fraction are increased due to the presence of biofilm, the form factor value is only slightly influenced, while wave resistance coefficient is decreased due to the presence of biofilm.

*Impact of diatomaceous biofilm on the ship propulsion characteristics.*

Utilizing the proposed roughness function models within the numerical simulations of resistance, open water and self-propulsion tests, the impact of biofilm on propulsion characteristics and speed reduction is assessed. It is shown that the presence of slime can have detrimental effect on the ship resistance and propulsion characteristics as well as on the open water characteristics of propeller and that fouling with slime should not be ignored. The

importance of the determination of the effect of biofilm on the delivered power rather than on the effective power is highlighted.

*Implementation of roughness function for the prediction of the impact of hard fouling on the flow around the hull.*

Roughness function for hard fouling proposed in the literature is implemented within the wall function of the software package. The applicability of the CFD model in the prediction of an increase in the frictional resistance of flat plate due to the presence of hard fouling is shown. Extensive verification and validation procedure are performed for the numerical simulations of towing tank experiments for a flat plate.

*Impact of hard fouling on the ship resistance characteristics and nominal wake.*

Utilizing the implemented roughness function for hard fouling within the numerical simulations of resistance test, the impact of hard fouling on the ship resistance characteristics and nominal wake is assessed. It was shown that frictional resistance coefficient of a ship fouled with hard fouling (fully rough surface) depends solely on the ratio between roughness length scale and ship length at high Reynolds number ( $Rn$ ). In addition it is shown that the form factor, wave resistance coefficient and nominal wake fraction decrease due to the presence of hard fouling.

*Impact of hard fouling on the ship propulsion characteristics.*

Utilizing the roughness function model for hard fouling within the numerical simulations of resistance, open water and self-propulsion tests, the impact of hard fouling on propulsion characteristics is assessed. It is shown that the presence of hard fouling can have extremely detrimental effects on the ship resistance and propulsion characteristics as well as open water characteristics of propeller. The importance of the determination of the effect of hard fouling on the delivered power rather than on the effective power is highlighted.

*Performance prediction method for fouled propeller surface.*

Performance prediction method for fouled propeller surface will be based on the combination of the Granville similarity law scaling method and roughness function for certain fouling condition, as well as on [76] changes in the thrust and torque coefficients. The applicability of the method will be shown on the examples of open water tests. Thus, the obtained thrust and torque coefficients and open water efficiency at different advance coefficients using the proposed method will be compared with the numerically obtained results. The proposed method will enable rapid assessment of the effect of biofouling on the propeller open water characteristics.

*Performance prediction method for fouled surfaces.*

A new performance prediction method for the assessment of the fouling effects on the ship resistance and propulsion characteristics is proposed. The method is based on the combination of the Granville similarity law scaling method, roughness function and ITTC Performance Prediction Method (PPM) [72]. The applicability of the proposed method is shown by comparison with CFD results. The proposed method is applicable to different ship types and allows a rapid assessment of the effect of fouling on the ship resistance and propulsion characteristics. Therefore, it can be used within tools for the optimization of the maintenance schedule.

## **1.5. Structure of the Thesis**

The rest of the thesis is organized as follows: in Section 2 a critical review regarding the roughness effects on the flow is given, in Section 3 methodology used in this thesis is demonstrated, in Section 4 roughness function models used in this thesis are presented, in Section 5 the obtained results regarding the impact of biofouling on the ship performance are shown, in Section 6 new performance prediction method for fouled surfaces is presented and finally in Section 7 conclusions drawn from this thesis are given.



## 2. Critical review – Roughness effects on the flow

As already noticed, the effect of biofouling on the ship resistance and propulsion characteristics can also be assessed through the investigation of the roughness effects on the flow around the immersed body and boundary layer which is formed around the immersed body. Within this section the main concepts regarding this investigation will be presented along with the current state of the art in this field.

### 2.1. Flow around immersed bodies

While fluid passes near the wall surface with no slip condition it adheres to it and consequently the motion of the fluid in a thin layer near the wall is decreased because of frictional forces. Within this thin layer, called boundary layer, the fluid velocity increases from zero at the no slip surface to its full value which matches to external frictionless flow, i.e. free-stream velocity ( $u_\infty$ ) [77]. Boundary layer thickness ( $\delta$ ) is defined as the position where the velocity ( $u$ ) parallel to the plate reaches 99% of  $u_\infty$ . The flow around the full-scale ship is turbulent and in order to comprehend it, the concept of turbulent boundary layer (TBL) must be well understood. However, even on a full-scale ship there are laminar, transition and turbulent region of boundary layer. The development of TBL can be nicely shown on the example of the flow around a flat plate, where no pressure gradient is present, Figure 2.1. Thus, at the first portion of the flat plate, the flow is laminar and as the flow advances along the plate, instability in the flow occurs, i.e. transition region occurs. Eventually, the fluctuations of velocity and pressure become more and more pronounced and the flow becomes turbulent. The length of the transition region varies, depending on various factors, but for a smooth flat plate  $Rn$  is the most critical one.  $Rn$  presents a ratio of inertial and viscous forces:

$$Rn = \frac{vL}{\nu} \quad (2.1)$$

where  $v$  is the mean velocity,  $L$  is the characteristic linear dimension and  $\nu$  is the kinematic viscosity coefficient of the fluid.

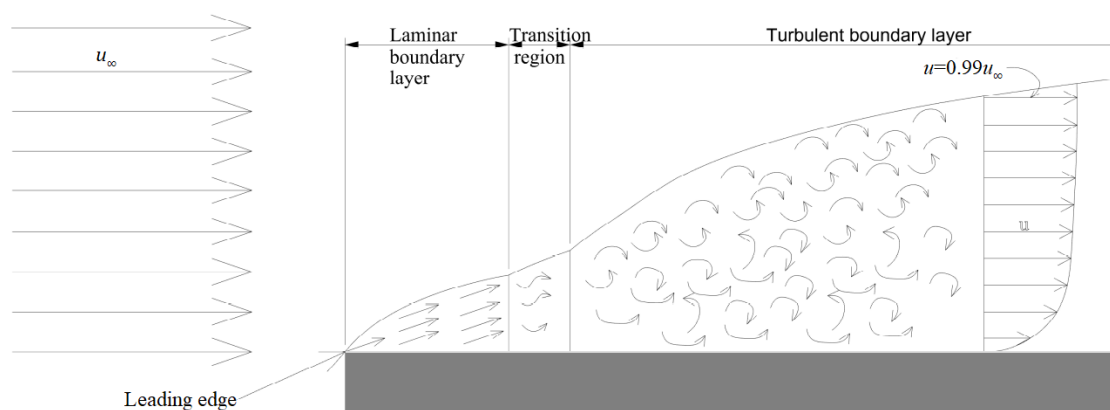


Figure 2.1 The development of TBL over the flat plate

TBL is consisted of inner and outer layer region. Inner layer region is divided into the viscous sublayer and the log-law region forming 10-20% of TBL near the wall and 70% of the velocity

variation occurs in the inner layer region [78]. Within this region, the local mean velocity ( $u$ ) depends solely on wall shear stress ( $\tau_w$ ), fluid density ( $\rho$ ), dynamic viscosity coefficient ( $\mu$ ) and distance from the wall ( $y$ ) and not upon freestream parameters. Thus, the fluid velocity can be expressed by the law of the wall (Figure 2.2):

$$U^+ = f(y^+) \tag{2.2}$$

where  $U^+$  is the non-dimensional velocity defined as the ratio between  $u$  and the friction velocity ( $u_\tau$ ) and  $y^+$  is the non-dimensional normal distance from the wall defined as follows:

$$y^+ = \frac{yu_\tau}{\nu} \tag{2.3}$$

The friction velocity is defined as follows:

$$u_\tau = \sqrt{\frac{\tau_w}{\rho}} \tag{2.4}$$

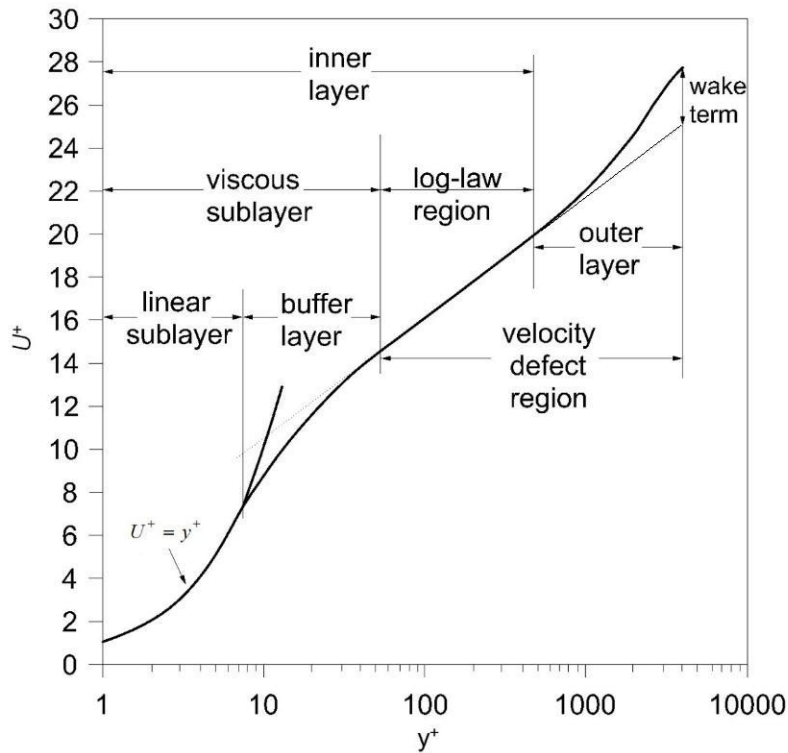


Figure 2.2 Law of the wall, adapted from [79]

Within TBL, total shear stress ( $\tau$ ) is made up of both viscous and turbulent stresses and this stress profile can be seen in Figure 2.3. As can be seen from Figure 2.2, viscous sublayer is consisted of two layers, linear sublayer and buffer layer. The thickness of viscous sublayer is generally agreed as  $5 \cdot \nu/u_\tau$ , where the quantity  $\nu/u_\tau$  represents the viscous length scale [80]. Within linear sublayer,  $\tau$  is almost constant and equal to  $\tau_w$ , i.e. viscous shear stress dominates and the velocity profile is linear:

$$U^+ = y^+ \tag{2.5}$$

The height of linear sublayer is not uniformly agreed, i.e. it varies from  $(3 \div 7) y^+$  [78], [80], [81]. Outside linear sublayer and up till  $y^+ < 30$ , buffer layer occurs, in which velocity profile departs from linearity. Within this layer both viscous and Reynolds stresses occur, and this is the region of the highest turbulence. The velocity profile is neither linear nor logarithmic, but a smooth merge between the two [80].

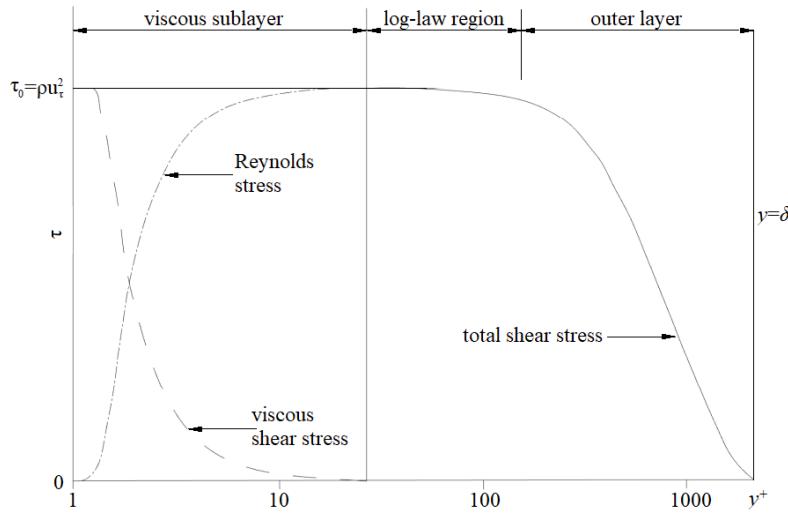


Figure 2.3 TBL shear stress profile, adapted from [82]

Log-law region occurs after the viscous sublayer and the upper end of this region depends on  $Rn$ . With the increase in  $Rn$ , the upper end of log-law region approaches to  $0.2 \delta$  [83]. Within this region,  $\tau$  is mainly affected by Reynolds stress, i.e. with the fluctuating velocity component ( $u'$ ) and the velocity distribution is defined as follows:

$$U^+ = \frac{1}{\kappa} \ln(y^+) + B \tag{2.6}$$

where  $\kappa$  is the von Karman constant and  $B$  is the smooth wall log-law intercept.

Various approaches have been utilized [84] to derive equation (2.6). Log-law region is associated with a constant velocity scale, i.e.  $u_\tau$  and characteristic lengths scale with  $y$ . Lately, there has been a strong discussion about the universality of  $\kappa$  [84], since this value has not been determined theoretically [85]. Thus, Nikuradse in 1930 proposed that  $\kappa$  is equal to 0.4 and  $B$  is equal to 5.5 and later on Coles and Hirst in 1968 suggested that  $\kappa$  is equal to 0.41 and  $B$  is equal to 5.0. From then till now various studies have pointed out different values of  $\kappa$  in the range from 0.384 to 0.44 [84], [85].

The remaining part of TBL is named outer layer, and here fluid motions are independent of fluid viscosity, while  $\tau$  is not constant and it decays to zero at the end of TBL. Thus, at the higher  $y^+$  values,  $U^+$  starts to rise above that predicted by the log-law and this is called the wake, Figure 2.2. The velocity defect law for a flat plate without pressure gradient can be written as follows:

$$\frac{u_\infty - u}{u_\tau} = f\left(\frac{y}{\delta}\right) \quad (2.7)$$

where  $u_\infty - u$  represents retardation of the flow due to wall effects.

Coles [80] has noted that the deviations of the outer layer above the log layer have a wake like shape when viewed from the freestream. The wake function is normalized to be zero at the wall and unity at  $y = \delta$ . By adding it to the log-law approximation of the both overlap, and outer layers the velocity distribution reads:

$$U^+ = \frac{1}{\kappa} \ln(y^+) + B + \frac{2\pi}{\kappa} f\left(\frac{y}{\delta}\right) \quad (2.8)$$

where  $\pi$  is Coles' wake parameter which is assumed to be 0.55 for zero pressure gradient and low free stream turbulence. The wake function  $f$  has two popular curve fits:

$$f\left(\frac{y}{\delta}\right) \approx \sin^2\left(\frac{\pi y}{2\delta}\right) \approx 3\left(\frac{y}{\delta}\right)^2 - 2\left(\frac{y}{\delta}\right)^3 \quad (2.9)$$

## 2.2. Effects of surface roughness. Roughness functions.

### 2.2.1. Wall roughness

The presence of roughness on the surface will lead to increased turbulence and fluid mixing in TBL and consequently increased turbulent and wall shear stresses. Surface roughness can be categorized either as k or d type and the most of rough surfaces are categorized as a k type [86]. For k type roughness effects on the flow scale with roughness height, while for d type roughness effects scale with the boundary layer thickness or pipe diameter [87]. Hull roughness presents k type roughness [88] and therefore the key parameter is the roughness length scale ( $k$ ) or  $k_s$ .

The roughness Reynolds number is defined as follows:

$$k^+ = \frac{ku_\tau}{\nu} \quad (2.10)$$

This parameter demonstrates the degree to which the surface roughness has an effect on the flow near the wall. In the turbulent flow, even a small roughness will break up the thin viscous sublayer and greatly increase the wall friction. Generally, there are three roughness regimes, hydraulically smooth, transition and completely rough regime. An extensive and systematic experiments on rough pipes have been performed by Nikuradse [77]. Nikuradse showed that in the region of the laminar flow, rough pipes have the same resistance as smooth ones, and frictional resistance does not depend on  $k_s$ , but on  $Rn$  only. Thus, if the roughness does not extend from laminar sublayer, the flow regime will be hydraulically smooth regime [77]. In the hydraulically smooth flow regime, the surface roughness is small enough and every perturbations of the flow caused by the presence of the roughness are damped by the viscosity. Nikuradse has shown that after certain  $k^+$  is exceeded, frictional resistance depends on both  $k_s$  and  $Rn$ , and the flow will be in transition regime. In transition flow regime, the surface roughness starts to produce pressure drag which leads to an increase in frictional drag [69]. Also, the curve of frictional resistance coefficient for rough pipe in transition regime deviates from the one for smooth pipe and after certain  $k^+$  is exceeded starts to depend solely on  $k_s$ , i.e.

completely rough regime. In the completely rough flow regime, the surface roughness is large enough and the drag on the wall is entirely produced by the pressure drag of the roughness [69]. For rough pipes which are covered inside as tightly as possible with sand roughness, Nikuradse has shown that the limits of flow regimes are  $k^+ < 5$  for hydraulically smooth regime,  $5 < k^+ < 70$  for transition regime and  $k^+ > 70$  for completely rough regime. However, real roughness can be described with significantly more parameters than  $k_s$  and therefore for the practical engineering purposes Moody chart has been developed [77], which can be used for the determination of frictional resistance coefficient ( $C_F$ ) if equivalent sand grain roughness height is known. From the Moody chart it can be clearly noticed that in the completely rough flow regime, frictional resistance coefficient for pipes depends solely on  $k_s / D$ . Determination of the equivalent  $k_s$  is not based on the roughness measurement, but on the hydrodynamic tests and can be expensive. Lately, Direct Numerical Simulations (DNS) have been applied for the prediction of equivalent  $k_s$  as well [89]. It is important to notice that different roughness types can generate various flow regime, even though the same  $k^+$  is present [69].

As the flow past ship represents external flow, it is more similar to the flow past a rough plate than to the flow in the rough pipe. For the case of rough plate, frictional resistance coefficient depends on the ratio  $k / \delta$ , rather than on  $k / Rn$  as for rough pipes [77]. This is important, as the ratio  $k / Rn$  for rough pipes is constant, while  $k / \delta$  for rough plates decreases along the plate. Therefore, the effect of roughness on the frictional resistance is different at the front of the plate and at the back portion. In the completely rough flow, the frictional resistance coefficient of the flat plate depends solely on the  $k / L$  ratio, where  $L$  is the length of flat plate.

While the surface roughness affects the inner layer region of TBL, the mean velocity and the turbulence intensity in the outer layer region are not affected by the surface conditions as assumed by the Townsend's wall similarity hypothesis [90]. This hypothesis claims that at sufficiently high  $Rn$ , the turbulent motions outside the roughness sublayer are independent of boundary condition at the wall, beside the fact that this boundary condition modifies the outer velocity and length scales [91], Figure 2.4. In order to this hypothesis be valid, the boundary layer thickness must be significantly higher than the roughness height. The roughness sublayer is thought to extend a few roughness heights from the wall [92], but this does not apply to all roughness types [93]. The Townsend's hypothesis is not only important to turbulence theoreticians but has wide application. Firstly, it allows the application of roughness function ( $\Delta U^+$ ), which relies on the similarity of the mean flow. Nowadays the CFD codes use  $\Delta U^+$  concept in order to take into account the effect of surface roughness on the flow. What is more, analytical approaches which are used for scaling up from laboratory to engineering scale are based on Townsend's hypothesis [91]. Within this thesis Townsend's wall similarity hypothesis is applied, as the effect of biofouling is taken into account through the implementation of  $\Delta U^+$  within the software package for CFD analysis.

In the literature, there is a debate about the Townsend' wall similarity hypothesis as some studies prove this hypothesis [91], [94], [95], [96], [97], [98], [100], while other studies show the effect of roughness in the outer layer [101] both experimentally and numerically. These discrepancies can be attributed to the effects of the relative roughness on the flow. Thus, if the relative roughness is sufficiently small, Townsend's hypothesis is valid. The similarity between smooth and rough wall data is noted in outer layer of TBL for 3D roughness elements if the

criteria for similarity is satisfied, i.e. relatively high  $Rn$  and relatively low roughness [102]. For example, Tsikata and Tachie [101] claim that lack of similarity in outer layer is observed due to relatively large roughness used in their study. Even though, Jimenez [102] proposed that Townsend's hypothesis is valid for  $\delta/k > 40$ , recently there are studies which show that even for higher roughness heights ( $k$ ), this hypothesis is valid. In [91] the authors have investigated the applicability of Townsend's hypothesis for rough surfaces with  $\delta/k$  from 110 to 16 and showed experimentally that it is valid for all investigated rough surfaces. Castro [103] have shown that Townsend's hypothesis holds for  $\delta/k > 5$ .

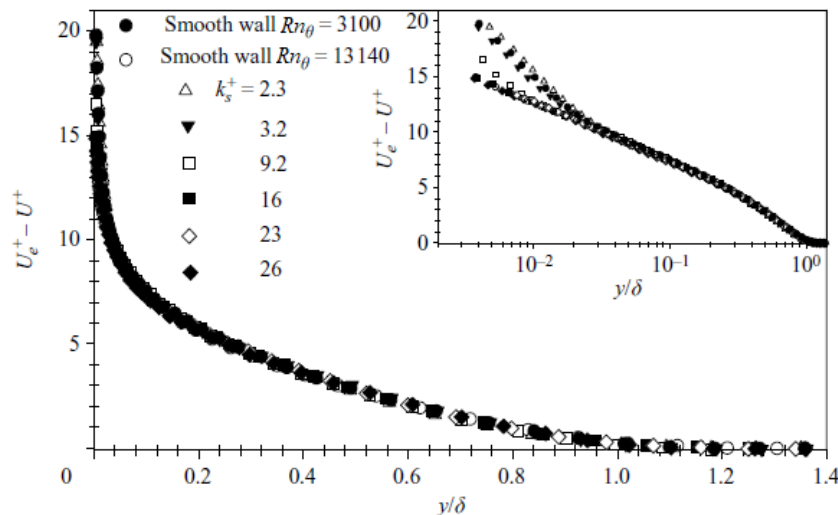


Figure 2.4 Velocity defect for smooth and rough walls, adapted from [94]

### 2.2.2. Roughness functions

The presence of roughness on the wall surface will lead to increase in turbulence and fluid mixing in TBL. Even the presence of small roughness will lead to break of viscous sublayer and will increase frictional resistance [80]. The log-law region will still exist, but  $U^+$  profile will change due to the presence of roughness and will become function of both  $y^+$  and  $k^+$ . The log-law velocity profile for rough surface is defined as follows [104]:

$$U^+ = \frac{1}{\kappa} \ln(y^+) + B - \Delta U^+ \quad (2.11)$$

where  $\Delta U^+$  is the roughness function.

Concept of the roughness function was proposed independently by Clauser and Hama, and they defined it as a downward shift of the mean velocity profile in the log-law [21]. Townsend's similarity hypothesis assumes that roughness effects are limited to inner layer and therefore  $U^+$  profile can be defined as follows [105], [106]:

$$U^+ = \frac{1}{\kappa} \ln(y^+) + B - \Delta U^+ + \frac{2\pi}{\kappa} f\left(\frac{y}{\delta}\right) \quad (2.12)$$

Thus, beside the increase in turbulent and wall shear stresses, the presence of roughness causes the decrease of  $U^+$  [78]. Roughness functions can be described as the differences between the velocity profile of the smooth and rough surfaces, Figure 2.5.

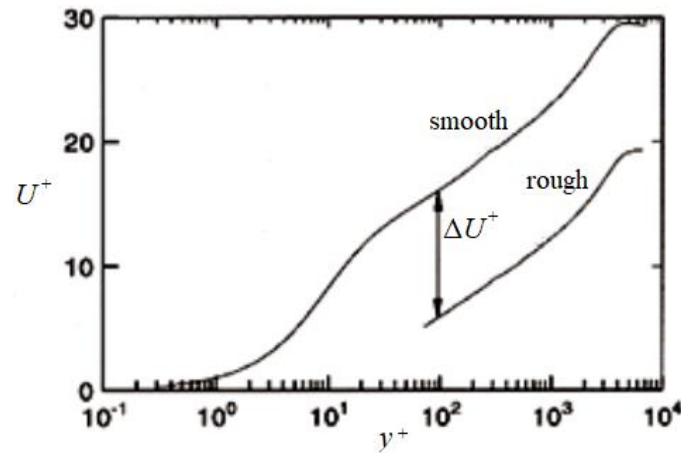


Figure 2.5 The roughness effect on the law of the wall (adapted from [107])

The determination of a universal relationship between the physical measures of an arbitrary surface and its  $\Delta U^+$  has still remain elusive [78]. Drag characterization of rough surface can be described as the determination of velocity decrement caused by the frictional resistance of the rough surface as a function of  $k^+$ .  $\Delta U^+$  as a function of  $k^+$  is unique for every surface [108]. Once  $\Delta U^+$  is determined experimentally for certain surface conditions, the effect of these surface conditions on the resistance of any arbitrary body can be assessed either through a similarity law analysis or a boundary layer code [109].

As said before,  $k^+$  is amongst the others a function of  $k$  and the choice of  $k$  is critical for the definition of  $\Delta U^+ = f(k^+)$ , i.e.  $\Delta U^+$  model. Since, the selection of  $k$  will not affect the  $\Delta U^+$  value, but only value of  $k^+$  (abscissa of  $\Delta U^+ = f(k^+)$ ),  $k$  is selected in a way that  $\Delta U^+$  values correspond to a predefined  $\Delta U^+$  model and that the observed behaviours are still deemed appropriate relative to each other [110]. As universal  $\Delta U^+$  does not exists, there is no single  $k$  which could characterize all types of roughness in all flow regimes [91]. Therefore, in order to determine the hydrodynamic effect of specified biofouling condition on a ship or marine structure,  $k$  for the certain biofouling condition must be assessed. Unfortunately, this surface property is not directly measurable and therefore ultimate objective of roughness research is to find relation between  $k$  and some easily measured surface properties [111]. Once the correlation between  $k$  and some easily measured surface properties is determined for certain surface condition, drag characterization is complete and  $\Delta U^+$  model can be implemented within boundary layer code and used for the prediction of the effect of this surface condition on the flow [104]. Recently, there has been a lot of studies dealing with drag characterization of various surface conditions which can occur during ship lifetime. Those studies have been traditionally performed experimentally, however with the development of CFD, there is an increasing number of numerical studies dealing with drag characterization. Numerical studies are either based on Reynolds Averaged Navier-Stokes (RANS) equations [112], [113], [114], Large Eddy Simulations (LES) [115], [116], [117] or DNS [118], [95], [89], [119].

A detail review of  $k$  in the fully rough regime is presented in [120]. The most of reviewed scales were developed for regular roughness, which limits their applicability for the assessment of the drag for many engineering flows. Therefore, Flack and Schultz [120] have proposed a new correlation for the determination of  $k$  in the fully rough flow regime for 3D irregular

roughness which depends on root-mean square roughness height ( $R_q$ ) and skewness of the roughness elevation distribution ( $R_{sk}$ ). Systematically generated surface roughness is investigated within [121]. Based on the obtained results, Barros et al. [121] concluded that some roughness parameters do not contribute significantly to the drag. The authors concluded that there is the necessity of surface filtering in order to identify the roughness parameters, i.e.  $k$  that contribute most significantly to the drag. Most of the studies which deal with drag characterization in the field of naval architecture are related to AF coatings. The important component within the measurement of surface roughness is the use of cut-off filter. Cut-off filter is a short pass filter which separates the waviness from the roughness through letting the high wave number components through. Based on cut-off length, roughness at various levels of magnification can be studied. The majority of studies published in the literature which deal with roughness and AF coatings do not acknowledge cut-off length and consequently the results cannot be compared [122]. Therefore, Howell and Behrends [122] highlighted the importance of developing international standard and the increase in awareness related to cut-off length and addressing it in the future studies. Schultz [123] has performed an experimental study in order to investigate the effect of surface condition on the frictional resistance coefficient for unfouled, fouled and cleaned condition of AF coatings. He investigated five different commercial AF coatings which were coated on the flat plates as well as three control surfaces, i.e. polished smooth surface, surface covered with 60-grit and 220-grit wet/dry sandpaper. He proposed three different  $k$ , for which he observed very good collapse with Grigson  $\Delta U^+$  model. Thus, two  $k$  were based on the centreline average roughness height ( $R_a$ ) (one for AF coatings and one for control surfaces), while one  $k$  was based on the height of the largest barnacle and percentage of the surface coverage with barnacles (for hard fouling). Flack et al. [124] have performed drag characterization of two surfaces coated with different AF coatings, 220-grit sandpaper and four surfaces which were sanded with sandpapers with various grit weights. The authors concluded that  $k$ , which is based on the maximum peak to trough height ( $R_t$ ), is the best for the prediction of the onset of roughness effects, i.e. the largest roughness features have the most influence for determination when a surface ceases to be hydraulically smooth. In the recent development of novel AF coatings based on nanotechnology, most emphasis is placed on understanding how the completely environmentally friendly FR coatings can control biofouling, while the hydrodynamic performance of these coatings has been overlooked. Therefore, Unal et al. [125] have performed boundary layer measurements on AF coatings developed during AMBIO project and highlighted the benefits from hydrodynamic point of view of these FR coatings related to the possible energy savings. Usta and Korkut [126] have shown that surface roughness of the flat plate, due to application of various AF coatings, can have significant effect on  $C_F$  of the flat plate. An extensive study related to the drag characterization of different commercial AF coatings is performed within [127]. Unal [127] has tested various roughness parameters which were determined using various low-pass filter window lengths and sampling lengths for the determination of  $k$ . From the obtained results an importance of cut-off length can be clearly noticed, i.e. depending on this length various roughness parameters are obtained for the same rough surface. Therefore, it is obvious that within the literature there are various  $k$  for AF coatings. Finally, the author has presented a new definition for  $k$  based on  $R_q$ ,  $R_{sk}$  and the mean spacing between zero crossings ( $Sd_4$ ). Yeginbayeva and Atlar [128] have studied boundary layer and drag characteristics of AF



coatings with various finishes, with the aim to simulate in-service conditions of AF coatings. For this purpose, the authors have applied three different AF coatings on normal (laboratory condition) finish of flat plate, as well as on rough flat plates. In order to mimic hull roughness ranges of ships, flat plates were abraded with sandpapers of 25-grit ('low' roughness density scenario) and 50-grit ('high' roughness density scenario). This approach of mimicking the levels of physical roughness experienced on hulls in service is based on the experience of International Paint Ltd and their analysis of hull roughness surveys. Based on the obtained results, the authors have proposed several  $k$  for AF coatings. The most successful roughness length scales in collapsing the obtained results onto Grigson  $\Delta U^+$  are based on  $R_a$  (coefficient of determination ( $R^2$ ) is equal to 0.87),  $R_t$  ( $R^2 = 0.89$ ) and  $R_q$  and the average wavelengths ( $\lambda_a$ ) ( $R^2 = 0.75$ ). Li et al. [129] have investigated the effect of  $\text{Cu}_2\text{O}$  particle size on roughness and hydrodynamic characteristics of biocidal AF coatings based on copper. The authors have proposed  $k$  based on  $R_t$  which can be used along with Colebrook type  $\Delta U^+$  of Aupoix [130]. Erbas [131] has investigated TBL and made drag characterization of new generation of AF coatings. The author has proposed  $k$  based on  $R_q$  and  $R_{sk}$  which can be used along with Colebrook type  $\Delta U^+$ .

Biofilm or slime occurs on the ship hull regardless of applied AF coating while ship is in service and that is why the importance of drag characterization of plates fouled with biofilm is very important. Schultz and Swain [78] have shown that the presence of biofilm causes the increase in frictional resistance and that this increase is dependent on biofilm composition and thickness. Holm et al. [132] have examined the differences amongst FR coatings and their drag penalties due to the presence of biofilms. An extensive study related to frictional resistance of FR coatings is presented in [133] and based on the obtained results, the authors proposed a new effective  $k$  for biofilms. Li et al. [134] have investigated the effect of biofilm on frictional resistance of flat plates coated with AF coatings with various sizes of  $\text{Cu}_2\text{O}$ . The analysis of the obtained results has indicated that biofilms had significant impacts by altering the surface microstructure, resulting in higher frictional resistance. Hartenberger et al. (2018) [135] have studied the drag performance characteristics of laboratory based biofilms, which were grown in a custom built slime farm, as well as rigid replicas of those slimes which were made by high resolution scanning and 3D printing facilities. Strong similarities in frictional behaviour between biofilm and its rigid replica, as well as biofilm and a surface covered with 80 grit sandpaper has noticed, which has led to conclusion that the compliance and motion of a biofilm may not play a significant role in drag production. Yeginbayeva et al. [136] have studied surface and hydrodynamic characteristics of biocidal, non-biocidal and hard AF coatings in the newly applied and fouling conditions. This study has demonstrated the effect of field grown fouling on the AF efficacy and drag performances. In addition to, a new  $k$  which can be used with Colebrook  $\Delta U^+$  based on fouling pattern (fouling rate), density (coverage) and surface free energy is presented. Boundary layer measurements over plates fouled with biofilm, using high resolution Particle Image Velocimetry (PIV), are performed in [137]. The obtained results have pointed out significant increase in skin friction, a downward shift in  $U^+$  profile as well as significantly higher  $k$  than the physical thickness of biofilm. Also, it was shown that the presence of biofilm causes the increase in turbulent kinetic energy and Reynolds shear stresses. A study [138] has demonstrated the applicability of flow cell for a representation of consistent

frictional resistance of hull surfaces, thus enabling the comparison of frictional resistance caused by surface roughness to the reference surface measurements. However, the authors have suggested that limiting roughness height must be investigated in future studies, as the above certain roughness height the wall bounded shear flow might be influenced by generation of bluff body wakes and mean velocity profile could be changed. A scanned and scaled test coupon coated with light calcareous tubeworms is reproduced for testing in the wind tunnel with the goal to determine  $k_s$  [111]. Thereafter, the authors have used the obtained  $k_s$  as an input for a method which numerically integrates the skin friction over the length of the boundary layer for the assessment of penalty in frictional resistance due to the presence of tubeworm fouling for two full-scale ships. Demirel et al. [139] have performed a series of towing tank measurements of flat plates covered with artificial barnacles in order to determine  $k$ , based on the barnacle height and percentage of surface coverage. The effect of barnacle settlement on frictional resistance ( $R_F$ ) as well as on the effective power ( $P_E$ ) is studied within [140] for six different ships. The obtained results showed that the settlement pattern does not affect  $R_F$  and  $P_E$  as much as was expected, particularly at the ship scale. Also, with an increase in percentage of surface coverage, this effect is even more minimized.

$\Delta U^+$  of real surfaces are expected to show behaviour that is in between the monotonic Colebrook and inflectional Nikuradse type  $\Delta U^+$  [21].  $U^+$  in TBL of smooth and rough pipes can be defined using following equations [141]:

$$U^+ = \frac{1}{\kappa} \ln(y^+) + B_1 \tag{2.13}$$

$$U^+ = \frac{1}{\kappa} \ln\left(\frac{y}{k_s}\right) + B_2 \tag{2.14}$$

where  $\kappa$  is equal to 0.4 while  $B_2$  has different values depending on the flow regime, Figure 2.6.

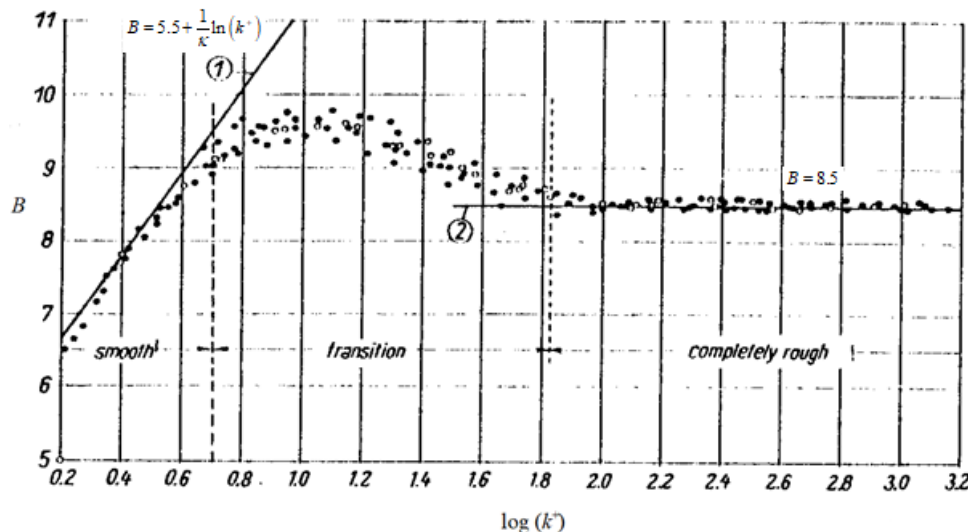


Figure 2.6 Constant  $B$  in terms of  $k^+$  for Nikuradse sand roughness (adapted from [77])

As can be seen from Figure 2.6, constant  $B$  for smooth surface ( $B_1$ ) is equal to 5.5. It should be noted that  $k^+$  is defined based on  $k_s$ .

Colebrook and White (1937) and Colebrook (1939) [78] demonstrated that  $\Delta U^+$  of some engineering surfaces could be written in the following form:

$$\Delta U^+ = A \ln(1+k^+) \quad (2.15)$$

In Figure 2.7. both Nikuradse and Colebrook  $\Delta U^+$  are shown, where Colebrook  $\Delta U^+$  is given by Hama with the log-constants of McKeon et al. [142]. From the same figure it can be seen that Colebrook  $\Delta U^+$  has monotonic behaviour and that  $\Delta U^+ > 0$  in whole range of  $k^+$ , while Nikuradse  $\Delta U^+$  tends toward hydraulically smooth flow regime ( $\Delta U^+ = 0$ ) in the flows at low  $k^+$  value and slight inflectional behaviour in transitional flow regime. At high  $k^+$  values, the flow reaches fully rough regime and both  $\Delta U^+$  tend toward fully rough asymptote [94].

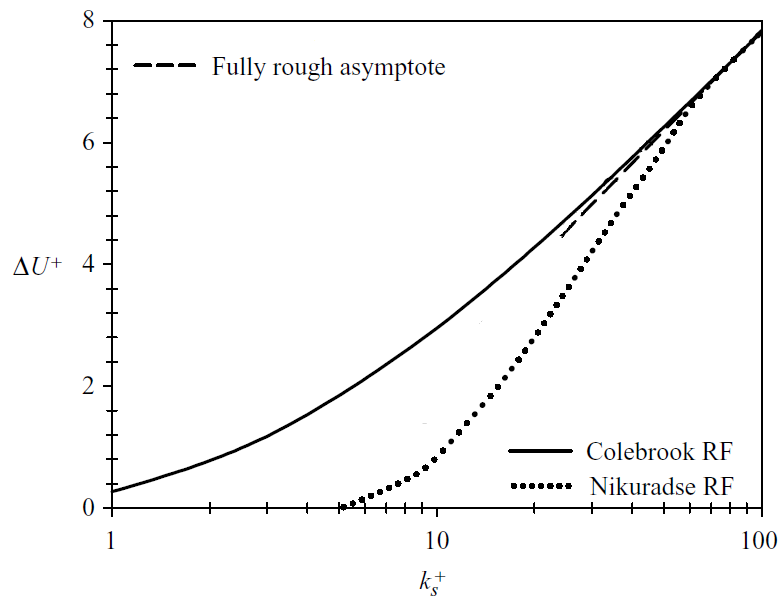


Figure 2.7  $\Delta U^+$  of Nikuradse and Colebrook

Grigson has proposed Colebrook type  $\Delta U^+$  for engineering surfaces with irregular roughness structures, which is applied for various surface conditions, including AF coatings [123], [110], [128], barnacles [139] and hard fouling [123] and this  $\Delta U^+$  is defined as follows [143]:

$$\Delta U^+ = \frac{1}{\kappa} \ln(1+k^+) \quad (2.16)$$

As said before, Townsend’s wall similarity hypothesis implies that surface roughness does not have any influence on outer layer, i.e. in outer layer it can be written:  $U_R(y) = U_S(y)$ . However,  $U^+$  profile in the outer layer of rough surface is still shifted downward when compared to  $U^+$  profile in outer layer of smooth surface and this is because of the fact that roughness has the influence on  $u_\tau$ . Based on this hypothesis, Hama [144] has shown by evaluating  $U^+$  profiles for rough (2.12) and smooth surface (2.8) for the same wall distance ( $y$ ) at the same value of  $Rn$  based on the displacement thickness ( $Rn_\delta$ ), that  $\Delta U^+$  can be defined as follows:

$$\Delta U^+ = \left( \sqrt{\frac{2}{C_f}} \right)_S - \left( \sqrt{\frac{2}{C_f}} \right)_R \quad (2.17)$$

where  $C_f$  is the local skin frictional coefficient defined as follows:

$$C_f = \frac{\tau_w}{\frac{1}{2}\rho U_\infty^2} = 2 \left( \frac{u_\tau}{U_\infty} \right)^2 \quad (2.18)$$

and subscripts S and R represent smooth and rough surfaces respectively.

An alternative method for the indirect determination of  $\Delta U^+$  is presented by Granville [145]. This method is based on Townsend's similarity hypothesis and  $C_F$  of rough flat plate is related to the local  $\tau_w$  and mean velocity profile at the trailing edge of the plate. It is also based on the comparison of frictional resistance coefficient for smooth ( $C_{FS}$ ) and rough surface ( $C_{FR}$ ) at the same value of  $Rn_L \cdot C_F$ , where  $Rn_L$  is the Reynolds number based on the flat plate length ( $L$ ). The resulting equations are as follows:

$$k^+ = \left( \frac{k}{L} \right) \left( \frac{Rn_L C_F}{2} \right) \left( \sqrt{\frac{2}{C_F}} \right)_R \left[ 1 - \frac{1}{\kappa} \left( \sqrt{\frac{C_F}{2}} \right)_R + \frac{1}{\kappa} \left( \frac{3}{2\kappa} - \Delta U^{+'} \right) \left( \frac{C_F}{2} \right)_R \right] \quad (2.19)$$

$$\Delta U^+ = \left( \sqrt{\frac{2}{C_F}} \right)_S - \left( \sqrt{\frac{2}{C_F}} \right)_R - 19.7 \left[ \left( \sqrt{\frac{C_F}{2}} \right)_S - \left( \sqrt{\frac{C_F}{2}} \right)_R \right] - \frac{1}{\kappa} \Delta U^{+'} \left( \sqrt{\frac{C_F}{2}} \right)_R \quad (2.20)$$

where  $\Delta U^{+'}$  is the roughness function slope, i.e. the slope of  $\Delta U^+$  as a function of  $\ln k^+$ .

Equations (2.19) and (2.20) are solved iteratively, and initially  $\Delta U^{+'}$  is set to zero. Based on this solution,  $\Delta U^{+'}$  is determined and this procedure is repeated until the solution converges [146].

It should be noted that there are other methods for the determination of  $\Delta U^+$  as well, but within this thesis only these two methods are mentioned since they are used for the determination of  $\Delta U^+$  values for fouling conditions investigated within this thesis.

Schultz and Myers [146] have compared three different experimental methods for the determination of  $\Delta U^+$  of several surfaces, i.e. velocity profile, rotating disk and towing plate methods. The obtained results showed good agreement between  $\Delta U^+$  obtained using velocity profile and towing plate method. Also, good agreement is achieved between  $\Delta U^+$  obtained using all three methods in fully rough flow regime. Therefore, the authors concluded that rotating disk method can be used as relatively economical method for the determination of the effect of surface roughness at high  $Rn$ . A detail review of experimental facilities used in drag characterization of AF coatings is presented in [108]. Thus, details of boundary layer measurements for flat plate in water tunnel, floating element force balance measurements, flat plate towing tank measurements, pipe flows, flat plate rectangular channels, rotating disks and rotating cylinders are presented. The authors have analysed advantages and disadvantages of the experimental facilities in terms of test type and duration, highest achievable  $\tau_w$  over test

surface, accuracy in skin friction measurement of test panels, parameters contributing to overall test quality, overall size and complexities associated with each test setups and overall cost for building and running the facility. Even though each experimental facility has certain advantages and disadvantages, the authors concluded that the flow channel facility is the best since it allows the high accuracy and simplicity in performing tests. What is more, high  $\tau_w$  over test surface can be achieved, which can be compared to the ones present at ship hull during navigation. More details regarding flat plate rectangular channels and flat plate towing tank measurements will be presented as these two experimental methods were used for the determination of  $\Delta U^+$  values for fouling conditions investigated within this thesis.

### 2.2.2.1. Turbulent channel flow facility

Turbulent Channel Flow (TCF) facility, i.e. flat plate rectangular channel, represents one of the experimental facilities used in drag characterization in which high  $\tau_w$  over test surface can be achieved. The high  $\tau_w$  over test surface can be achieved using water tunnel flat plate boundary layer measurements, pipe flows and rotating cylinders as well. TCF facilities have important advantage over pipe flows since their setup allows examination of the friction of flat plates, which are traditionally used for extrapolation from model to full-scale results. Also, coating of flat plates is simpler than coating of the interior of tested pipe, which is important in the determination of  $\Delta U^+$  values of coated surfaces. Another important advantage of TCF facility over pipe flow facility lies in the fact that TCF facility allows the possibility of growth of biofouling on flat panels, which are statically or dynamically immersed into sea water, and thereafter testing of the same panels for the purposes of drag characterization utilizing seawater. Within both facilities high  $\tau_w$  over test surface can be achieved and duration of experiment is similar (around 15 minutes), however the accuracy of the test results is higher within TCF facility but its cost is higher [108]. When compared to the rotating cylinders, using TCF facilities higher accuracy can be achieved, which can be attributed to the fact that once rotating cylinders are used there is no flow development length, velocity is constant along the test area and there are 3D effects of cylinders ends. On the other hand, test duration is slightly shorter (5 – 10 minutes) for rotating cylinders and rotating cylinder setup is significantly cheaper than TCF setup [108]. Water tunnel flat plate boundary layer measurements have similar accuracy as measurements in TCF, but test duration is significantly longer (2 – 3 hours) and overall cost for building and running the facility is higher [108]. In order to ensure 2D flow in duct it is important to have aspect ratio (ratio between channel width ( $W$ ) and height ( $H$ )) above 7:1 [108]). Thus, two-dimensionality of the flow along the centreline of the channel is ensured and there is no measurable spanwise variation in mean streamwise velocity. TCF facility at the United States Naval Academy (USNA) is shown in Figure 2.8. Within TCF  $\tau_w$  can be related to the streamwise pressure gradient as follows:

$$\tau_w = -\frac{H}{2} \frac{dp}{dx} \quad (2.21)$$

where streamwise pressure gradient can be measured using pressure taps. In equation (2.21),  $p$  is the static pressure and  $x$  is the streamwise distance.

Once  $\tau_w$  is determined, skin friction coefficient can be determined using following equation [147]:

$$C_f = \frac{\tau_w}{\frac{1}{2}\rho\bar{U}^2} = 2\left(\frac{u_\tau}{\bar{U}}\right)^2 \quad (2.22)$$

where  $\bar{U}$  is the bulk mean velocity.

Finally, using the similarity-law procedure for fully developed internal flows [145]  $\Delta U^+$  can be determined using equation (2.17). It should be noted that  $C_f$  must be evaluated at the same value of the friction Reynolds number ( $Rn_\tau$ ) which is defined as follows:

$$Rn_\tau = \frac{u_\tau h}{\nu} \quad (2.23)$$

where  $h$  is the channel half height.

Usually, there are several pressure taps, and the linearity of pressure gradient must be assured. The measurement of pressure should be done after assuring that the flow within TCF is fully turbulent, which can be done by comparison of the obtained mean velocity profile at certain location with the mean velocity profile obtained with DNS, as was done in [147]. Furthermore, TCF facility must be calibrated, which is done by comparison of the obtained  $C_f$  with the ones obtained using certain power law curve fit. Within [147] this calibration is performed by comparison of the obtained  $C_f$  values with [148]:

$$C_f = 0.0743Rn_m^{-1/4} \quad (2.24)$$

where  $Rn_m$  is the Reynolds number based on channel height and bulk mean velocity.

In order to obtain dynamically similar conditions during the experimental determination of  $\Delta U^+$ , in the channel or in the towing tank, and on the ship, the same  $k^+$  should be obtained. Since within TCF facility sea water can be used and the height of the fouling organism are assumed to be the same, only  $u_\tau$  must be matched for achieving dynamic similarity. If  $u_\tau$  is matched, the fouling organism will be exposed to the same mean velocity field and forces in TCF and at ship scale. Therefore, the fouling organism must be treated as a surface roughness element, meaning that it should be within the inner layer of the TBL for both TCF and the ship [109].

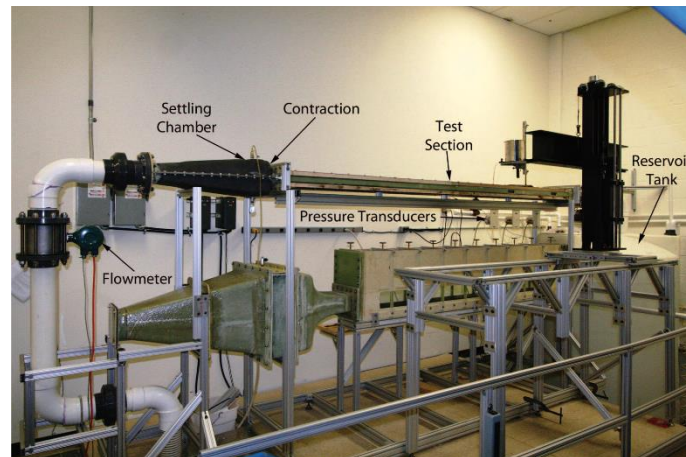


Figure 2.8 TCF facility at the United States Naval Academy (adapted from [147])

### 2.2.2.2. Flat plate towing tank measurements

The total resistance ( $R_T$ ) of flat plate can be decomposed into the residual ( $R_R$ ) and  $R_F$ .  $R_R$  is mostly composed of wave resistance ( $R_W$ ), as the viscous pressure resistance ( $R_{VP}$ ) can be considered negligible due to the fact that flat plate is very thin. During flat plate towing tank measurements,  $R_T$  is measured and in order to obtain  $R_F$  which is required for obtaining  $C_F$ , two methods can be applied. Thus, once  $R_T$  for smooth flat plate is determined,  $R_R$  can be determined as the difference between  $R_T$  and  $R_F$  which is determined using the Schoenherr friction line:

$$\frac{0.242}{\sqrt{C_F}} = \log(Rn C_F) \quad (2.25)$$

Another method for the determination of  $R_R$  is to measure  $R_T$  of a flat plate at two drafts, out of which one is usually significantly smaller than the other one. The difference between two measured  $R_T$  can be considered as  $R_F$  of the flat plate surface between those two drafts [123]. Once  $R_R$  is determined for smooth flat plate it can be considered that it is the same for rough flat plate. During the measurements precise alignment of the plate must be ensured in order to minimize the side force. This can be ensured by repeatedly towing the plate at constant velocity and adjusting the yaw angle in order to minimize the side force, which is measured using force transducer rotated 90° to the drag gauge [123]. Duration of test is around 30 seconds and it has very good accuracy with main uncertainties related to the effects of unsettled flow and poor alignment of plates [108]. Once  $C_F$  is determined it is used for the determination of  $\Delta U^+$  using equations (2.19) and (2.20).

## 2.3. Effects of surface roughness on the ship resistance and propulsion characteristics

### 2.3.1. Ship resistance and propulsion characteristics

Since  $R_T$  of full-scale ship cannot be measured directly, historically the determination of  $R_T$  has been performed using towing tank experiments and extrapolation procedure. Therefore, measured  $R_T$  of ship model is decomposed into several components, even though these components interact and the most of them cannot be measured individually [149]. The first decomposition of  $R_T$  was proposed by Froude in 1874, in which  $R_T$  is decomposed into  $R_F$  and  $R_R$ . By Froude, for the same Froude number ( $Fn$ ), the same residual resistance coefficient ( $C_R$ ) is obtained for both model and full-scale ship. Froude number is defined as the ratio between inertial and gravitational forces as follows:

$$Fn = \frac{v}{\sqrt{gL}} \quad (2.26)$$

where  $g$  is the gravity of the Earth.

This first decomposition of  $R_T$  allowed Froude the determination of  $R_T$  at full-scale using towing tank tests of ship models. Therefore, the first towing tank was built in Torquay, England in 1879 and soon other model basins were built in the rest of Europe and United States of America [149]. From back then, several methods of  $R_T$  decomposition were proposed and adapted into various extrapolation procedures. ITTC has proposed two PPM, in 1957 and 1978, which are mainly used in towing tanks across the world [149]. It should be noted that ITTC 1978 PPM has been slightly modified several times over the past years. The last version of ITTC 1978 PPM was published in 2017 within ITTC Recommended procedures [72]. Within this method, total resistance coefficient of a ship without bilge keels is given as:

$$C_T = (1+k)C_F + C_W + C_A + \Delta C_F + C_{AAS} \quad (2.27)$$

where  $k$  is the form factor determined with Prohaska method,  $C_F$  is the frictional resistance coefficient obtained using ITTC 1957 model-ship correlation line,  $C_W$  is the wave resistance coefficient, which is assumed to be the same for model and ship,  $C_A$  is the correlation allowance,  $\Delta C_F$  is the roughness allowance and  $C_{AAS}$  is the air resistance coefficient in full-scale.

ITTC 1957 model-ship correlation line is given with following equation:

$$C_F = \frac{0.075}{(\log Rn - 2)^2} \quad (2.28)$$

It should be noted that all resistance coefficients are obtained by dividing certain resistance component with  $\frac{1}{2}\rho v^2 S$ , where  $S$  is the wetted surface area. ITTC 1957 model-ship correlation line is derived for extrapolation purposes from model to full-scale. Using equation (2.28),  $C_F$  for 3D ship hull is obtained, which is different from the one obtained for the flat plate having the same length as a ship, equation (2.25). The difference between these two  $C_F$  values can be attributed to the longitudinal and transversal pressure gradients which are present on 3D ship hull due to longitudinal and transversal curvature of ship. The effect of longitudinal and transversal pressure gradients is accounted with  $k_f$ , i.e.  $C_F = k_f C_{F0}$  where  $C_F$  is frictional resistance coefficient for 3D ship hull, while  $C_{F0}$  is frictional resistance coefficient for the flat plate having the same length as a ship hull.

As can be seen from equation (2.27),  $C_A$  is separated from  $\Delta C_F$  and this separation was proposed in 1990 by the Performance Prediction Committee at 19<sup>th</sup> ITTC in Madrid. Thus,  $\Delta C_F$  takes into account the effect of roughness on  $R_T$  [72]:

$$\Delta C_F = 0.044 \left[ \left( \frac{k_s}{L_{WL}} \right)^{1/3} - 10Rn^{-1/3} \right] + 0.000125 \quad (2.29)$$

where  $L_{WL}$  is the waterline length and  $k_s$  is the roughness of hull surface. It should be noted that if roughness measurements are not available, ITTC recommends using  $k_s = 150 \mu\text{m}$ . However, it seems that the recent development of AF coatings has enabled lower values of  $k_s$ .



Thus, Seok and Park [150] have measured average hull roughness (AHR) of the car ferry, and it was equal to 81  $\mu\text{m}$ , which resulted in lower estimation of  $C_T$  for -1.7% at the speed of 21 knots. It is important to highlight that the equation (2.29) is proposed for determining the effect of coating roughness only.

$C_A$  is supposed to account for the effects which are not considered with PPM as well as to account for all assumptions made within PPM. ITTC [72] has defined  $C_A$  as follows:

$$C_A = 0.001(5.68 - 0.6 \log Rn) \quad (2.30)$$

However, it is also recommended that each institution should maintain its own correlation allowance.

Since the complete hydrodynamic similarity between model and full-scale ship cannot be achieved, experimentally obtained results are subjected to scale effects [151]. Lately, there has been a lot of discussion related to the scale effects on  $k$  and  $C_w$ . Pereira et al. (2017) [152] have shown that  $k$  value depends on the scale and that scaling of the viscous resistance coefficient ( $C_v$ ) is not reliable. The authors have determined  $1+k$  value as the ratio of  $C_v$ , obtained using Double Body Simulation (DBS) and  $C_f$  obtained using ITTC 1957 model-ship correlation line. Still, Raven et al. [153] have pointed out that once Grigson friction line is utilized,  $k$  value is independent on scale in the case of a containership and only slightly is dependent on scale for tanker. In addition to scale effects on  $k$  value, viscous effects on the stern wave system exists thus influencing wave resistance, as lower stern wave causes less radiated wave energy, i.e. lower  $R_w$  [153]. Due to the presence of viscous effects, the stern wave system is reduced and since viscous effects are relatively higher at the model scale, reduction in wave system is higher as well.

Open water characteristics are hydrodynamic characteristics of a propeller in uniform flow with a steady load. They are obtained for several advance coefficients ( $J$ ), which are defined as follows:

$$J = \frac{v_A}{nD} \quad (2.31)$$

where  $v_A$  is the speed of the advance,  $n$  is the propeller rotation rate and  $D$  is the propeller diameter.

Open water characteristics include thrust coefficient, torque coefficient and open water efficiency which are defined as follows:

$$K_T = \frac{T}{\rho n^2 D^4} \quad (2.32)$$

$$K_Q = \frac{Q}{\rho n^2 D^5} \quad (2.33)$$

$$\eta_o = \frac{J K_T}{2\pi K_Q} \quad (2.34)$$

where  $T$  is the propeller thrust and  $Q$  is the propeller torque.

Beside the scale effects on the ship resistance characteristics, scale effects are present on propulsion characteristics as well as on open water characteristics. As claimed by Helma [154] across the various towing tank institutions, four main scaling procedures are used for scaling open water characteristics obtained in model scale: no scaling, ITTC 1978 PPM, Lerbs-Meyne method and strip method. It should be noted that within ITTC 1957 PPM no scaling is applied for the obtained open water characteristics in model scale. Using ITTC 1978 PPM [72], open water characteristics for full-scale are calculated as follows:

$$K_{TS} = K_{TM} - \Delta K_T \quad (2.35)$$

$$K_{QS} = K_{QM} - \Delta K_Q \quad (2.36)$$

where subscripts S and M are representing ship and model scale and  $\Delta K_T$  and  $\Delta K_Q$  are obtained as follows:

$$\Delta K_T = -\Delta C_D \cdot 0.3 \cdot \frac{P}{D} \cdot \frac{c \cdot Z}{D} \quad (2.37)$$

$$\Delta K_Q = \Delta C_D \cdot 0.25 \cdot \frac{c \cdot Z}{D} \quad (2.38)$$

where  $P$  is the propeller pitch,  $D$  is the propeller diameter,  $c$  is the chord length,  $Z$  is the number of blades, while  $\Delta C_D$  is determined as the difference between  $C_{DM}$  and  $C_{DS}$ , which are calculated as follows:

$$C_{DM} = 2 \left( 1 + 2 \frac{t}{c} \right) \left[ \frac{0.044}{(Rn_{c0})^{1/6}} - \frac{5}{(Rn_{c0})^{2/3}} \right] \quad (2.39)$$

$$C_{DS} = 2 \left( 1 + 2 \frac{t}{c} \right) \left( 1.89 + 1.62 \log \frac{c}{k_p} \right)^{-2.5} \quad (2.40)$$

where  $t$  is the maximum thickness,  $k_p$  is the blade roughness (standard value is 30  $\mu\text{m}$ ) and  $Rn_{c0}$  is the local  $Rn$  defined as follows:

$$Rn_{c0} = \frac{v_R c}{\nu} \quad (2.41)$$

where  $v_R$  is the resultant velocity of the flow.

All geometric characteristics are defined for the representative blade section at  $0.75R$  and  $Rn_{c0}$  is calculated for the same radius.

Due to operation of the propeller behind the ship, the velocities of the flow over the hull surface are increased and consequently the local pressure field over the aft part of the hull surface is reduced. Because of this, resistance is increased and  $T$  is higher than  $R_T$  and this increase is accounted through thrust deduction fraction:

$$t = 1 - \frac{R_T}{T} \quad (2.42)$$

The loss of the axial velocity in the propeller disc plane when compared with  $v$  is accounted through wake fraction:

$$w = 1 - \frac{v_A}{v} \quad (2.43)$$

Once  $w$  and  $t$  are determined, hull efficiency can be calculated as follows:

$$\eta_H = \frac{1-t}{1-w} \quad (2.44)$$

The quasi-propulsive efficiency coefficient can be determined with following equation:

$$\eta_D = \eta_H \eta_O \eta_R \quad (2.45)$$

where  $\eta_R$  is the relative rotative efficiency calculated with:

$$\eta_R = \frac{K_{QO}}{K_{QB}} \quad (2.46)$$

where  $K_{QO}$  and  $K_{QB}$  are torque coefficients obtained in open water conditions and behind the hull in self-propulsion test. It should be noted that the propeller efficiency behind the ship hull can be determined as the product of  $\eta_R$  and  $\eta_O$ .

The quasi-propulsive efficiency coefficient can be written in another way as follows:

$$\eta_D = \frac{P_E}{P_T} \frac{P_T}{P_{DO}} \frac{P_{DO}}{P_D} \quad (2.47)$$

where  $P_E$  is the effective power,  $P_T$  is the thrust power,  $P_{DO}$  is the delivered power in open water conditions and  $P_D$  is the delivered power.

While from practical viewpoint  $t$  is independent on scale [155],  $w$  is subjected to scale effects [152]. Wake fraction coefficient for full-scale ship is assessed using the following equation [72]:

$$w_S = (t + w_R) + (w_M - t - w_R) \frac{(1+k)C_{FS} + \Delta C_F}{(1+k)C_{FM}} \quad (2.48)$$

where  $w_R$  stands for the rudder effect on  $w$  and it is taken as 0.04 if there is no estimation for it.

Within ITTC 1978 [72] it is considered that  $\eta_R$  is the same for model and full-scale ship. Using this procedure, a curve defined with parameter  $K_T / J^2$  can be drawn in open water diagram for full-scale propeller and  $J$  for full-scale ship can be obtained as an intersection of this curve and curve  $K_T = f(J)$ . Thereafter,  $n$  and  $P_D$  in full-scale can be obtained easily.

A detail comparison of ITTC 1957 PPM and three versions of ITTC 1978 PPM is presented in [151] for three different loading conditions and at two speeds for handymax bulk carrier. The obtained results for brake power ( $P_B$ ) have shown maximum deviations between methods equal to 1.5% for design loading condition, 0.7% for scantling loading condition and 4.9% for

ballast loading condition at the design speeds and equal to 1.1% for design loading condition, 1.1% for scantling loading condition and 3.8% for ballast loading condition at the slow steaming speeds. The obtained results of  $n$  have shown maximum deviations between methods equal to 0.4% for design loading condition, 0.6% for scantling loading condition and 0.9% for ballast loading condition at the design speeds and equal to 0.8% for design loading condition, 0.5% for scantling loading condition and 0.9% for ballast loading condition at the slow steaming speeds. The obtained differences amongst PPM are found for all propulsion characteristics as well [151] and the highest deviations are obtained for  $w$ , which was expected as ITTC 1957 does not consider scale effects for  $w$ . Thus, the obtained results for  $1-w$  have shown maximum deviations between methods equal to 6.3% for design loading condition, 4.4% for scantling loading condition and 11% for ballast loading condition at the design speeds and equal to 6.5% for design loading condition, 4.6% for scantling loading condition and 11.9% for ballast loading condition at the slow steaming speeds. From the obtained results it is clear that significantly different ship resistance and propulsion characteristics at full-scale can be obtained with the application of different PPM. Within this thesis ITTC 1978 PPM [72] is used for the extrapolation of the towing tank results and further comparison with the numerically obtained ship resistance and propulsion characteristics in full-scale for smooth surface. Therefore,  $\Delta C_F$  is taken to be zero as within CFD simulations for smooth surface no surface roughness is taken into account.

### **2.3.2. The influence of surface roughness on ship resistance and propulsion characteristics – PPM perspective**

$R_F$  is generally the largest part of  $R_T$  and it is caused by viscosity of the fluid. Thus, for new and slow speed ships,  $R_F$  can account up to 85% of  $R_T$ .  $R_F$  is significantly affected by the presence of surface roughness consisting of coating roughness as well as added roughness due to coating degradation and the presence of fouling. Thus, ships with severe fouling condition may require twice the power as with a smooth surface condition [149]. Good coating condition is essential for low fuel consumption and Munk (2006) has estimated that only 1/3 of the world fleet has good coating condition with less than 20% of roughness penalty when compared with smooth surface condition [149]. Obviously, the assessment of the effect of surface roughness on ship resistance and propulsion characteristics is very important and this effect has been investigated for almost 150 years. One of the first studies related to this effect is performed by Froude, when he investigated roughness effects by comparison of frictional resistance obtained for smooth flat plate and flat plate with various surface conditions [156]. Detailed historical overview of the studies related to investigation of surface roughness effects on ship performance is given in [157]. Thus, in the beginning of research of this topic, hull fouling and corrosion often have been seen as the same problem. With the development of anticorrosive coatings, hull fouling has been considered as the main influential parameter which causes the increase of surface roughness. This has changed with the invention of SPC coatings based on TBT, which could successfully prevent hull fouling for longer periods of time. Therefore, the interest of researchers has turned into the investigation of the effect of coating roughness on the ship performance. However, as TBT coatings are now banned, researchers started once again to investigate the impact of hull fouling on the ship performance. Throughout the past several decades, ITTC has followed the research related to the effect of surface roughness on ship performance and consequently modified equation for roughness allowances. Thus, in ITTC

1978 PPM roughness allowance is determined with the Bowden and Davison equation [21] as follows:

$$\Delta C_F = 0.105 \left( \frac{h}{L} \right)^{1/3} - 0.00064 \quad (2.49)$$

where  $h$  is the average roughness height.

Even though this formulation for the prediction of  $\Delta C_F$  has been criticized just after its adoption, it remained in ITTC PPM until 1990. The main flaws of this equation are that it was used for both correlation and roughness allowance as well as that it did not take into account the effect of various ship speeds, i.e.  $Rn$ . In 1990, this equation was replaced with equation (2.29) proposed by Townsin and Dey [21]. Since then the equation for roughness allowance has remained the same. In 26<sup>th</sup> ITTC meeting, more attention to this problem was given by assembling a Special Committee on Surface Treatment. As already stated in section 1, the committee [71] has advised researchers to develop new formulae or methods based on the experimental data for the determination of the effect of biofouling on ship resistance and propulsion characteristics. Until new formulae or method is proposed, ITTC still recommends using equation (2.29) for the roughness allowance, since this is the most suitable option for the time being. Furthermore, it was shown that roughness function used to generate Bowden or Townsin type formulation for the full-scale ship using CFD analysis is one of the best candidates for a new prediction method. In 2011, ITTC has separated roughness allowance from correlation allowance [158], which is from then on calculated with equation (2.30), as suggested at 19<sup>th</sup> ITTC meeting back in 1990. At the last ITTC meeting held in Wuxi, 2017 there was a discussion related to influence of ship hull surface degradation due to fouling and aging on the ship performance. ITTC [159] has concluded that for the improvement of the in-service performance as well as for minimization of shipping related emissions, prediction models, monitoring and mitigation measures are required. As already mentioned, degradation of hull surface can be estimated by different approaches, and ITTC [159] has categorized them into ‘direct’ and ‘indirect’ types. Direct types directly target the surface quality of the hull by roughness measurements, while in-direct methods are based on the performance monitoring for the assessment of the level of surface degradation. It is noted that the surface condition of propellers should be considered as well. ITTC has stated that systematic evaluation of degraded hull surface samples could provide good basis for the relation between direct and in-direct methods in the future.

It should be noted that equation (2.49) is proposed based on the sea trials of real ships, while equation (2.29) is based on the roughness measurements of rough painted surfaces and their statistical analysis [157]. Therefore, these equations are mainly proposed for the estimation of  $\Delta C_F$  for clean coating condition of ship hull and not for the estimation of the effect of fouling on  $\Delta C_F$ . However, they can be applied for the prediction of ship performance in service, if roughness measurements are available. Kresic and Haskell [76] have proposed a method for the estimation of ship and propeller performance in service, i.e. for deteriorated hull and propeller surface condition. They have defined service roughness resistance coefficient as follows:

$$C_S = \Delta C_{F \text{ service}} - \Delta C_{F \text{ trial}} \quad (2.50)$$

where both  $\Delta C_F$  are obtained using equation (2.49) where  $h$  is equal to 150  $\mu\text{m}$  for trial condition and  $h$  for service condition is the total hull roughness which can be estimated using certain factors which determine either daily or monthly increase in roughness. Thus, the total hull roughness is consisted of initial roughness (150  $\mu\text{m}$ ), hull roughness from service, hull roughness from dockings and fouling equivalent roughness. Kresic and Haskell [76] used assumption given by Townsin et al. [160] for the estimation of hull roughness from service as average 2.8  $\mu\text{m}/\text{month}$ . This increase can be attributed to corrosion and various mechanical damages of hull. Also, Kresic and Haskell used for the determination of hull roughness from dockings value 14  $\mu\text{m}/\text{dry docking}$ , which is based on the analysis of the published data [160]. Fouling equivalent roughness is estimated with expression derived in [161]:

$$h_{\text{fouling}} = C \cdot HRF \cdot PT \cdot CEFF \quad (2.51)$$

where  $C$  is the factor equal to 1 for sides and 0.75 for bottom,  $HRF$  is the hull roughness factor given in  $\mu\text{m}/\text{port day}$  (Table 2.1),  $PT$  is the number of port days and  $CEFF$  is the AF coating effectiveness factor determined as follows:

$$CEFF = 1 - \left[ 2.72 / e^Z - 0.24(Z - 1)^{0.263} \right] \quad (2.52)$$

where  $Z$  is the ratio of accumulated time to effective life of AF coating.

Table 2.1 Hull roughness fouling factor (adapted from [161])

Qualitative Fouling Severity Scale	Fouling Severity	$HRF$ , $\mu\text{m}/\text{port day}$
0	clean	0
2	trace	$5.334 \cdot 10^{-4}$
4	trace to light	$7.849 \cdot 10^{-3}$
6	light	$3.828 \cdot 10^{-2}$
8	light to moderate	0.1178
10	moderate	0.2822
12	moderate to severe	0.5755
14	severe	1.052

The effect of hull roughness in service on  $t$  and  $\eta_R$  within Kresic and Haskell method [76] is assumed to be negligible. While the assumption that  $t$  is independent on the surface condition is based on the tests conducted on model and full-scale ships for various roughness conditions performed in [162], Kresic and Haskell [76] suggested that the assumption for  $\eta_R$  should be checked by measuring torque in behind and open-water conditions for both smooth and rough propellers. On the other hand, the authors have proposed equation for the determination of  $w$  in service as follows:

$$w_{\text{service}} = t + (w_{\text{trial}} - t) \left( 1 + \frac{C_s}{(1+k)C_{F \text{ trial}}} \right) \quad (2.53)$$

where  $w_{\text{trial}}$  is determined based on the equations (2.48) and (2.49) and  $C_{F \text{ trial}}$  is determined by ITTC 1957 model-ship correlation line. This equation is based on the fact that only friction wake fraction is changed due to the presence of roughness and that potential part of wake fraction is independent of roughness. Namely, wake fraction can be divided into potential ( $w_p$ ), frictional ( $w_f$ ) and wave wake fraction ( $w_w$ ). Thus,  $w_p$  arises in inviscid fluid due to the fact that as the streamlines close in aft, there is a rise in pressure and decrease in velocity in the propeller disc plane, while  $w_f$  arises due to the effect of friction and boundary layer that develops along the hull. Finally,  $w_w$  arises due to the influence of the subsurface orbital motions of the waves and for single screw ships this component is small [73]. Thus, if it is assumed that  $w_p = t$  and that  $w_w$  is negligible, it is obvious that only  $w_f = w - t$  is changed due to the presence of roughness.

The presence of surface roughness on ship propeller influences propeller efficiency in a way that the drag of blades is increased, while circulation is decreased. Because of increase in the drag of blades  $K_Q$  increases. Due to decrease in circulation, lift coefficient of the blade decreases causing the decrease in  $K_T$  [76]. Kresic and Haskell [76] have estimated roughness effects on open water characteristics as follows:

$$K_{T \text{ service}} = K_{T \text{ trial}} - \Delta K_{TD} - \Delta K_{TL} \quad (2.54)$$

$$K_{Q \text{ service}} = K_{Q \text{ trial}} - \Delta K_{QD} - \Delta K_{QL} \quad (2.55)$$

where  $\Delta K_{TD}$  and  $\Delta K_{QD}$  are changes in  $K_T$  and  $K_Q$  as a result of increased drag of blades which are estimated according to equations (2.37) and (2.38) and  $\Delta C_D = C_{D \text{ service}} - C_{D \text{ trial}}$  ( $C_D$  is determined according to equation (2.40)),  $\Delta K_{TL}$  and  $\Delta K_{QL}$  are changes in  $K_T$  and  $K_Q$  as a result of decreased lift of blades which are determined as follows:

$$\Delta K_{TL} = \Delta C_L \cdot \frac{c \cdot Z}{D} \cdot \frac{0.733 + 0.132J^2}{\sqrt{1 + 0.18(P/D)^2}} \quad (2.56)$$

$$\Delta K_{QL} = \Delta C_L \cdot \frac{c \cdot Z}{D} \cdot \frac{0.117 + 0.021J^2}{\sqrt{1 + 0.18(P/D)^2}} \quad (2.57)$$

where  $\Delta C_L$  is the change in the lift coefficient determined with  $\Delta C_L = -1.1\Delta C_D$  as proposed by ITTC [72].

Kresic and Haskell [76] have estimated the roughness effects on the open water characteristics according to ITTC 1978 PPM and based on the work of Lindgren and Bjarne [163], Aucher [164] and Lerbs [165]. Kresic and Haskell have faced with a problem related to the determination of an average roughness of the propeller blades for various stages in service, since very little is known about the change in propeller blade roughness with the time in operation, particularly when fouling is present. Therefore, the authors have presented

recommendations for the estimation of propeller blade roughness in service. Using the proposed method, hull roughness determined with equation (2.51) and recommendations for the estimation of propeller blade roughness, the one can estimate the effect of surface roughness on the ship performance. However, it should be noted that  $h$  determined with equation (2.51) largely depends on factors used as an input and they depend on various parameters and cannot be described with such simple factors. What is more, the recommendations, proposed by the authors, for the determination of propeller roughness height in service are questionable as they do not have any support in actual measurements of propeller roughness in service. Regardless of this, Kresic and Haskell method for the assessment of the roughness effect on the ship performance is very important, because it allows the assessment even if total roughness height is known. Unfortunately, the determination of roughness height which could be used as hull and propeller roughness requires hydrodynamic measurements, as various roughness types have different  $\Delta U^+ = f(k^+)$ .

Generally, the effect of surface roughness on the propeller performance may be divided into the effect of surface deterioration and fouling. The effect of surface deterioration can be adequately represented with surface roughness. Thus, within ITTC PPM 1978 [72], the impact of surface deterioration on the propeller performance can be assessed through variation of propeller blade roughness ( $k_p$ ). In order to accurately represent roughness of propeller blades, relatively sophisticated measurement devices are required [71], as well as a proper definition of average  $k_p$ . A procedure for the assessment of average  $k_p$  based on the propeller roughness measurements is presented in [166]. In this procedure, each blade surface is subdivided into a number of roughly uniform radial strips and at each radial strip three roughness measurements of mean line average roughness amplitude ( $R_a$ ) and peak count per unit length ( $Pc$ ) are taken with cut off length equal to 2.5 mm. Thereafter, characteristic roughness parameter is calculated, and it is used for the determination of weighted average, i.e.  $k_p$ . Thus, roughness closer to propeller tip has a much greater influence than the same roughness near the blade root. Differently from the surface deterioration, the effect of fouling cannot be easily described and the determination of fouling effects on the propeller performance is more complicated, since theoretical and experimental work done on this topic are rather scarce [71]. The attempt of the assessment of effects of fouling release coating and various surface roughness in numerical simulations of open water test utilizing lifting surface method is performed by Atlar et al. [167]. The effects of fouling release coating are simulated through appropriate selection of  $C_D$  for the propeller blade section. The authors have varied characteristic roughness parameter according to Rubert gauge surfaces and calculated the increase in  $C_F$  and  $C_D$ . In his PhD thesis, Candries [168] has determined a characteristic roughness parameter for propeller coated with fouling release coating using the roughness measurements. After performing open water tests, he concluded that  $\eta_o$  of a propeller coated with fouling release coating was similar to to the new or well-polished blade surface. On the other hand,  $\eta_o$  was significantly reduced for rougher propeller blade surfaces. The effects of propeller fouling on the propeller performance are documented in the literature. Thus, Glover [169] showed that due to frictional loss caused by a surface deterioration or fouling can be up to 15% of the total propeller losses. Kan et al. [162] showed that the effects of propeller fouling are significant and higher than those of surface roughness in terms of power penalty.



### 2.3.3. Granville similarity law scaling method

Granville has utilized Townsend’s similarity hypothesis in order to develop a similarity law scaling procedure for the assessment of the roughness effects of a certain roughness type on  $R_F$  of any arbitrary body covered with the same roughness type [145], [170]. The method utilises the experimentally obtained  $\Delta U^+$  for certain roughness type. Graphical representation of this procedure is given in Figure 2.9. which is consisted of following steps:

1. Schoenherr friction line is plotted within the graph  $C_F$  versus  $\log Rn$ .
2.  $k^+$  is assumed and  $\Delta U^+$  is calculated or read off from plot  $\Delta U^+$  versus  $k^+$ .
3. Schoenherr friction line is shifted in positive  $\log Rn$  direction by  $\Delta U^+ \kappa / \ln 10$  and  $C_{FR}$  curve is obtained.
4. Line of constant  $L_{plate}^+$  is plotted in  $C_F$  versus  $\log Rn$  graph.
5. Line of constant  $L_{plate}^+$  is shifted in positive  $\log Rn$  direction by  $\log(L_{ship} / L_{plate})$  and  $L_{ship}^+$  curve is obtained.
6. If the intersection of  $C_{FR}$  and  $L_{ship}^+$  curve is located at  $\log Rn_{ship}$  the procedure is finished and  $C_{FR_{ship}}$  can be read off. Otherwise, the one has to return to step 2 and assume different value of  $k^+$ .

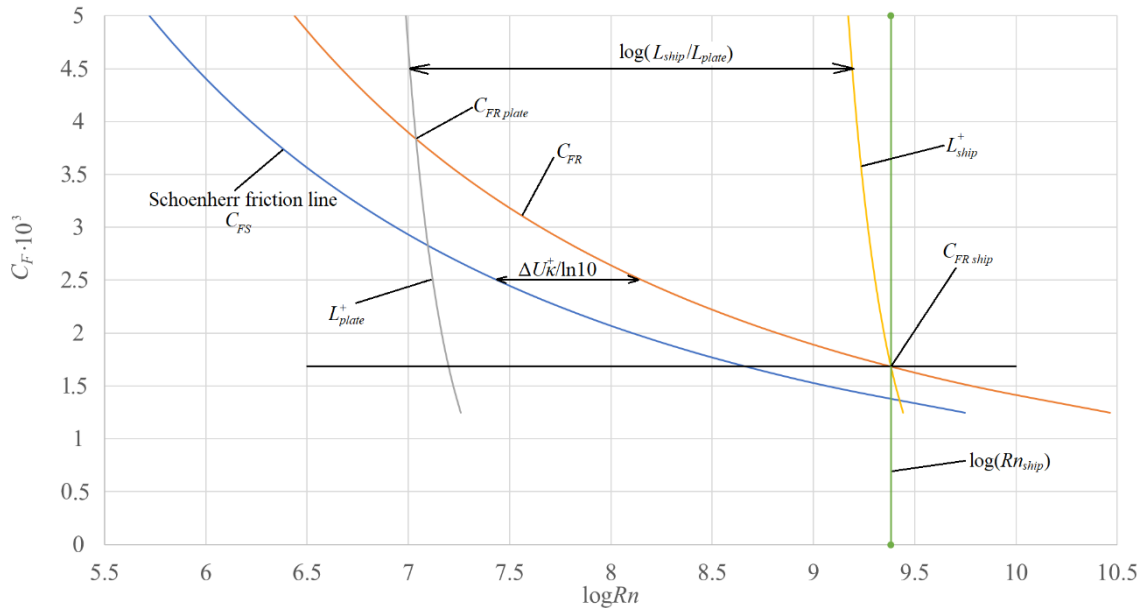


Figure 2.9 Granville similarity law scaling procedure

Line of constant  $L_{plate}^+$  satisfies following equation:

$$Rn = \frac{L_{plate}^+}{\sqrt{\frac{C_F}{2} \left( 1 - \frac{1}{\kappa} \sqrt{\frac{C_F}{2}} \right)}} \quad (2.58)$$

where  $L_{\text{plate}}^+$  is defined as follows:

$$L_{\text{plate}}^+ = \frac{L_{\text{plate}} U_\tau}{\nu} = \frac{L_{\text{plate}} k^+}{k} \quad (2.59)$$

where  $L_{\text{plate}}$  is the length of flat plate used in laboratory experiments of drag characterization.

Granville similarity law scaling procedure is iterative procedure which include several numerical procedures. In order to obtain reliable predictions of  $C_{FR}$  for a given surface condition, the computer code was developed for robust and fast determination of  $C_{FR}$ . The in-house code was developed in Python [171] and within it  $\Delta U^+$  models are implemented. The numerical code is written using libraries SciPy and NumPy and the input parameters for this code are roughness length scale, selection of roughness function model, ship length (preferably  $L_{WL}$ ) and ship speed. The user can choose whether to determine  $C_{FR}$  for ship sailing in the sea (at 15°C) or for some other fluid density and dynamic viscosity coefficient. Based on this input, the code provides  $C_{FR}$  as well as  $k^+$  value for a ship. The numerical code is based on finding the intersection of  $C_{FR}$  and  $L_{\text{ship}}^+$  curve is located at  $\log Rn_{\text{ship}}$ .

Granville similarity law scaling method has been used within many scientific papers published in the literature, for example [69], [123], [172].

Kiosidou et al. [173] have performed towing tank tests of smooth flat plate and ship model, as well as rough ones which were covered with sandpapers of 40 and 80 grit. The obtained  $\Delta U^+$  exhibited Nikuradse behaviour, which has verified the validity of the experiments. The obtained results for flat plate were extrapolated to full-scale values using the Granville similarity law scaling method, while the obtained results for ship model were extrapolated using the newly proposed method based on the equation (2.60) for rough plates. It should be noted that the results of the Schlichting resistance formula for rough plates are presented graphically [77], but for fully rough flow regime following equation is derived:

$$C_F = \left( 1.89 + 1.62 \log \left( \frac{l}{k_s} \right) \right)^{-2.5} \quad (2.60)$$

which is valid for  $10^2 < l/k_s < 10^6$ , where  $l$  is the flat plate length.

The extrapolation method based on the Schlichting formula is applied for two length scales and therefore two version of methods are used. In the first version of the method,  $l/k_s$  determined from flat plate towing tests is kept constant for both model and ship  $Rn$ . In the second version,  $l/k_s$  from flat plate towing tests is used for calculation of  $C_F$  in model scale, whereas the extrapolation in ship scale was based on  $L/k_s$ , where  $L$  is the ship length. The highest  $C_T$  is predicted using constant  $l/k_s$  value, followed by Granville similarity law scaling method and the lowest  $C_T$  is predicted using  $l/k_s$  value for model and  $L/k_s$  for full-scale. Granville scaling method determines  $\Delta C_F$  which is added to  $C_T$  for smooth hull, while the proposed method determines  $C_T$  with an application of Froude methodology in rough condition, i.e.  $C_R$  is

determined within towing tank experiments for a rough ship model. Upper and lower limit of the predicted  $C_T$  are provided with the two versions of the proposed method [173].

#### **2.3.4. The influence of surface roughness on ship resistance and propulsion characteristics – CFD perspective**

Until very recently, there were only few studies dealing with the prediction of the roughness effects on ship performance based on CFD models. Thus, Patel [174] in 1998 claimed that the most complex problems for CFD are flows at full-scale  $Rn$  which consider surface roughness. Due to complex geometry of biofouling it is impossible to make an actual representation of biofouling within numerical simulation. However, if drag characterization of rough surface is known,  $\Delta U^+$  model can be either used for the implementation within wall function or used to change turbulence boundary conditions in the CFD software [174].

CFD models which can include roughness effects have several advantages over the Granville similarity law scaling method as they can simulate this phenomenon using the fully non-linear method. Thus, CFD model can predict non-uniform distribution of  $u_\tau$  across the surface, which will result in non-uniform distribution of  $k^+$ . As  $\Delta U^+$  values vary with  $k^+$ , within CFD simulation various  $\Delta U^+$  values across the surface will be used. If one compares the prediction of roughness effects on  $C_F$  of flat plate using CFD model and Granville similarity law scaling method, non-uniform distribution of  $k^+$  across the flat plate surface presents an important advantage over the Granville method, where only one value of  $k^+$  is assumed for a flat plate. Therefore, more accurate  $C_F$  of flat plate will be obtained using CFD model [21]. Another obvious advantage of CFD model over Granville method is that CFD enables the assessment of the roughness effect on the ship resistance and propulsion characteristics, while Granville method can only predict the increase in  $C_F$  for a plate having the same length as a ship. Furthermore, CFD allows a detail analysis of the flow, which enables various insights related to the roughness effects on the flow around ship. The possibilities of CFD model which can account for roughness effect in the problems related to ship hydrodynamics are presented in the following sections.

An extensive numerical study dealing with the aspects of including roughness effects in the  $k-\omega$  Shear Stress Transport (SST) turbulence model has been performed within [175]. Eca and Hoekstra [175] have investigated three types of implementation out of which two included modification of boundary conditions and one included implementation of  $\Delta U^+$  model within wall function. The authors have demonstrated that uniform roughness effects, i.e. sand grain roughness, on  $C_F$  of flat plates at full-scale  $Rn$  (corresponding to  $Rn$  of a ship) can be accurately simulated with all three types of implementation. Ohashi [176] has performed a numerical study of roughness effects for flat plate at various  $Rn$ , as well as for full-scale tanker ship. He carried out numerical simulations using two low  $Rn$  roughness models which are based on the two-equation turbulence model, as well as using wall function method. Low  $Rn$  roughness models modify the boundary condition of  $\omega$  on a wall surface using the function for roughness effect, while wall function which accounts for roughness effect is developed based on the assumption of local equilibrium. Ohashi showed that the wall function method is better approach to account for roughness effects in the numerical simulation of self-propulsion test at full-scale  $Rn$  than low  $Rn$  roughness models, since the obtained numerical uncertainties for

the prediction of  $C_T$  and pressure coefficient ( $C_p$ ) are significantly lower. Within this study, the roughness effects are accounted using the wall function approach. As can be seen from the recent studies published in the literature, wall function approach which accounts for roughness effects within numerical simulations related to ship hydrodynamics has prevailed over the low  $Rn$  roughness models.

Date and Turnock in 1999 [177] have investigated the necessary conditions for the assessment of  $C_F$  for a flat plate at model and full-scale  $Rn$ . The authors demonstrated that the effect of surface roughness on  $C_F$  can be predicted using CFD through the modification of the log-layer constant. Leer-Andersen and Larsson (2003) [178] have used boundary layer method within CFD code Shipflow, which uses the potential flow module along with the equations for boundary layer. The authors employed  $\Delta U^+$  within the boundary layer equations and investigated the roughness effect on  $C_F$  of full-scale tanker. Towing tank experiments of flat plates coated with two commercial AF coatings as well as numerical simulations of viscous flow around those flat plates have been performed within [179]. In order to numerically simulate the effect of surface roughness related to different AF coating applications, the authors used  $\Delta U^+$  which was implemented in commercial software package STAR-CCM+ [180]. CFD model for the prediction of the effects of fouling as well as AF coating roughness on the drag and lift coefficients of NACA 4424 air foil and one submarine hull was proposed within [181]. Thus, the fouling was modelled by setting small conical shapes on the surface, as was done in the experiment, while AF coating roughness was modelled through implemented  $\Delta U^+$  model which considers the uniform  $k_s$ . The authors showed that CFD can be used for modelling the fouling effects. Castro et al. [182] have performed Unsteady RANS (URANS) simulations of Kriso Container Ship (KCS) in full-scale operating in self-propulsion conditions. The authors considered the effect of hull roughness through implementation of  $\Delta U^+$  within the wall function. They suggested  $k_s$  for sea trial condition by equalizing the sum of  $C_F$  and  $\Delta C_F$ , proposed by ITTC, with  $C_F$  for a flat plate in fully rough regime, equation (2.60). Vargas and Shan [183] have developed CFD model based on the equivalent sand grain roughness approach, i.e. they have implemented Nikuradse  $\Delta U^+$  model within solver NavyFOAM. The authors validated CFD model by comparison of the numerically obtained  $C_F$  against the experimentally obtained values published in [123]. Thus, the developed CFD model could predict the effect of uniform sand grain roughness on the frictional resistance of any arbitrary body. Kid et al. [184] have presented new ship powering prediction models, which are based on the combination of the assessment of total roughness and CFD simulations. The total roughness, which is consisted of coating, hull and fouling roughness cannot be measured directly, but it is represented with  $k_s$ . For the prediction of fouling roughness, expressed as  $k_s$ , the authors reviewed ship operational profiles and based on the ship performance in three different performance scenarios they defined various  $k_s$ . Thereafter, the authors carried out CFD simulations with various  $k_s$  in order to predict the influence of  $k_s$  on the ship resistance and nominal wake. Thus, the proposed method can be considered as bottom up approach, in which the observation related to previous application of AF coatings and ship performances were used for the assessment of ship powering in the future. However, the development of reliable fouling roughness model based on the database of previous ship performance is very difficult, as the fouling development

depends on various parameters. Currently there is no reliable time dependent biofouling growth model. One of the initial steps into development of time-dependent biofouling growth model is presented in [75], where the authors have proposed biofouling growth model based on the static immersion data. Goedicke [185] have performed numerical simulations of resistance and self-propulsion tests for the smooth surface condition and for three roughness conditions characterized with arbitrarily selected  $k_s$ . He obtained significant roughness effects on the ship resistance and propulsion characteristics and therefore recommended that the roughness effects should be investigated not only for resistance but propulsion characteristics as well. Seok and Park [186] have used  $\Delta U^+$  model implemented within STAR-CCM+ to simulate the roughness effect on ship resistance. The authors investigated roughness effects for four different  $k_s$  on the increase in ship resistance for three different ships in model scale.

Until recently, the roughness effects on the ship resistance and propulsion characteristics within CFD models was investigated using the uniform sand grain roughness approach and the authors did not attempt to employ  $\Delta U^+$  model, which would be more appropriate for real engineering surfaces. Demirel [21] within his PhD thesis proposed a novel combined CFD/Experimental Fluid Dynamics (EFD) method for the determination of the roughness effects of coatings and fouling on the ship resistance characteristics. This method is based upon drag characterization of rough surface and thereafter the implementation of  $\Delta U^+ = f(k^+)$  within wall function of the CFD solver. Demirel et al. [110] have implemented Grigson  $\Delta U^+$  model within the wall function of the solver in order to represent the surface condition of AF coatings. The implemented  $\Delta U^+$  model was proposed by Schultz [123] along with roughness length scale  $k = 0.17R_a$ , after the drag characterization of AF coatings. The developed CFD model was validated by comparison of the numerically obtained  $C_f$  for various AF coatings with experimentally obtained ones published in [123]. Karabulut et al. [187] have implemented the same  $\Delta U^+$  model and used the same roughness length scale in order to numerically investigate hydrodynamic performance of AF coatings. Firstly the authors validated their CFD model, which can account for roughness effects, and thereafter performed DBS simulations for KCS coated with various AF coatings. They found an increase in frictional resistance due to roughness around 3–5 %. A newly proposed wall function approach based on the implementation of single  $\Delta U^+$  model for different fouling conditions has been presented in [188]. Demirel et al. [188] have proposed  $\Delta U^+$  model representing a typical coating and different fouling conditions based on  $\Delta U^+$  versus  $k^+$  graph presented in [69]. The developed CFD model was used for the assessment of the effect of a typical coating and different fouling conditions on the ship resistance characteristics. The obtained results led to conclusion that the wave resistance and wave patterns were significantly affected by roughness. The authors assumed that form factor is independent of roughness presence. It should be noted that the proposed  $\Delta U^+$  model as an input requires a value of  $k$ , which has been determined for only six different surface conditions in [69]. The authors claimed that investigated surface conditions and the proposed  $\Delta U^+$  model did not represent all types of fouling conditions. Therefore, the authors proposed that future work should be focused on the investigation into the range of applicability of the selected  $k$  for the present conditions. The proposed  $\Delta U^+$  model for a typical coating and different fouling conditions has been used within [65] in order to determine the negative effects of biofouling on the open water characteristics of Potsdam propeller. The

obtained results showed that with an increase in  $k$ , i.e. increase in fouling severity,  $K_T$  decreases while  $K_O$  increases causing significant decrease in  $\eta_o$  up to 30% for heavy calcareous fouling condition. The authors suggested that within the future studies, rather than using a single  $k$  for representation of a limited number of fouling conditions, a graduated approach should be developed for representation of any fouling condition. This could be done by performing drag characterization for various fouling conditions. Ostman et al. [189] have analysed the influence of the application of various coatings on  $C_V$  of Korean Very Large Crude Carrier 2 (KVLCC2). The authors performed drag characterization of rough plates whose aim was to mimic typical real application processes, i.e. an optimal new build condition; dry dock situation with some underlying spot repair roughness and poor coating application; and the extreme case with severe underlying roughness accumulated from several dry dockings and very poor application of the coating. Thereafter, the authors implemented  $\Delta U^+$  model within wall function and carry out DBS. The possibilities of different coating application were recognized in terms of reduction in  $C_F$  for low-cost. Thus, coating with low roughness (more expensive) can be applied in the areas where local skin friction coefficient is high, while in other areas coating with higher roughness and application procedures resulting in higher roughness (cheaper) could be applied. Vargas et al. [190] have analysed the effects of various surface conditions on  $C_T$  of DTMB 5415 model. The authors used modified Nikuradse  $\Delta U^+$ , for which they have proposed curve fit for constant  $B$ . Vargas et al. [191] have extended their study and analysed the roughness effect on  $C_T$  of DTMB 5415 in full-scale. The authors divided a ship hull into sections in order to analyse both homogenous and heterogenous fouling conditions. Thus, they studied the possibilities of partial cleaning of the ship hull and concluded that the benefits of partial cleaning of the hull depend on the initial surface condition of the hull. However, it should be noted that the authors used relation between fouling conditions and  $k_s$  presented in [69], but did not use the same  $\Delta U^+$  model as was used in [69]. Since there is no universal  $\Delta U^+$  model which could describe all surface conditions, drag characterization should be performed before implementation of  $\Delta U^+$  model within wall function [192].

Speranza et al. [192] have presented a combined EFD/CFD method for the assessment of roughness effect on ship resistance. Using EFD for the same values of  $k^+$  which would appear on the ship hull, the authors performed drag characterization. In order to obtain appropriate  $\Delta U^+$  model, following formulations was proposed:

$$\Delta U^+ = A \ln \left( B + \frac{ku_\tau}{\nu} \right) \quad (2.61)$$

where  $k$  is determined hydrodynamically and  $A$  and  $B$  are the dimensionless parameters.

The parameters  $k$ ,  $A$  and  $B$  are determined using the least squares method if the certain surface condition is tested at three or more  $k^+$  values. However, it should be noted that  $k$  cannot be selected arbitrarily as it is correlated with specific unscalable roughness topology (for example slime or barnacles). After the fitting of  $\Delta U^+$ , the authors implemented it in wall function of solver and performed numerical simulations of viscous flow around Wigley hull. The authors showed that once the surface condition does not follow established correlation between surface roughness and  $k_s$ , the method based on drag characterization and fitting of

$\Delta U^+$  model to the obtained  $\Delta U^+$  values provides higher accuracy in comparison with the approaches using the uniform sand grain roughness.

Song et al. [193], [68] have implemented Grigson  $\Delta U^+$  model within the commercial software package STAR-CCM+ and utilized  $k$  for barnacles developed in [139]. The authors validated their CFD model, which can account for the effects of barnacle fouling, by comparison of the numerically obtained  $C_F$  values for fouled flat plates with experimental ones. Thus, they established CFD model which can represent the barnacles on the hull, rudder and propeller surfaces [68]. The effect of barnacle fouling on the ship resistance characteristics and flow around KCS has been investigated in [193], while the effect of barnacle fouling on open water characteristics of KP505 has been studied in [67]. In [68], the authors have analysed the effect of barnacle fouling on the propulsion characteristics of KCS for various fouling conditions with barnacles. Andersson et al. [194] have reviewed and compared various methods presented in the literature for the modelling hull roughness. Thus, the authors investigated the effect of several types of roughness, including newly coated surfaces, surfaces with poor coating application or coating damages and surfaces covered with light slime on increase in viscous resistance and change in wake field for KVLCC2. The authors highlighted that within the literature there is no convergence towards universal roughness function or method for the determination of the roughness length scale for the investigated surface condition. Consequently, in order to create reliable CFD model for the prediction of the effect of certain surface condition on the ship performance, drag characterization of that surface condition must be performed. Mikkelsen and Walther [195] have shown the importance of including the effect of hull and propeller roughness directly within the CFD model, through the modification of the wall functions. In that way the authors obtained lower relative deviations between numerical results and speed trial measurements in comparison with the traditional approach, which includes roughness effects through a force determined by an empirical equation. Therefore, the authors concluded that inclusion of a roughness model directly into the wall function could be a more precise approach than the traditional approach, originally designed for towing tank extrapolation.

Garcia et al. [196] have performed drag characterization of four fouling resistance coatings during two years of exposure to sea water. The authors prepared a CFD model which could account for fouling effects using the implemented roughness model and appropriately selected  $k_s$  based on the drag characterization study. Finally, frictional and total resistance were assessed for a hull surface with the experimentally investigated coatings.

The validity of the roughness modelling in CFD with wall function approach has been reviewed shown in [197]. Using the previously developed  $\Delta U^+$  model based on drag characterization, the authors performed CFD simulations of towed flat plate and KCS. The obtained numerical results were compared with the results of towing tank experiments for both rough and smooth flat plate and KCS at several values of  $Rn$ . The satisfactory agreement was obtained, and it was concluded that CFD with wall function approach could adequately assess the roughness effect on the both frictional and total resistance of the 3D hull.

## 3. Methodology

### 3.1. Approach

The main aim of this study is to develop CFD model which can simulate the effects of biofouling on the flow around immersed fouled surface. Using this model, the effects of biofouling on the ship resistance and propulsion characteristics can be determined. Additionally, a new performance prediction method for fouled surfaces is proposed, which allows the rapid assessment of the effects of biofouling on the ship resistance and propulsion characteristics. The flow chart representing the methodology followed in this study is shown in Figure 3.1. Firstly, studies related to drag characterization of various surfaces covered with biofilm and hard fouling are found from the literature [123], [133]. Within [123], Schultz has proposed  $\Delta U^+$  model for hard fouling which can be used along with the proposed roughness length scale for hard fouling. On the other hand, in [133], the authors have proposed roughness length scale for biofilm and provided  $\Delta U^+$  and  $k^+$  values for certain surface conditions fouled with biofilm. Using the provided  $\Delta U^+$  and  $k^+$  values from the literature and least square method,  $\Delta U^+$  models for biofilm were proposed, which can be used along with roughness length scale proposed in [133]. Thereafter,  $\Delta U^+$  models could be implemented within the wall function of CFD software package and in that way CFD model which could take into account the effects of biofouling was developed. As already noted, a code was developed for the assessment of  $C_F$  using Granville similarity law scaling method and within this code  $\Delta U^+$  models were implemented. The newly proposed performance prediction method presented in Section 6 requires several numerical procedures as well as steps to assess the effect of biofouling on the resistance and propulsion characteristics. Therefore, in order to minimize potential errors during calculations using the new method, as well as to allow rapid assessment of these effects, an in-house code was developed in Python [171]. Within this code,  $\Delta U^+$  models are implemented as well. However, it should be noted that calculations with both Granville similarity law scaling method and newly proposed performance prediction method can be performed without  $\Delta U^+$  models, i.e. with the plot of  $\Delta U^+$  and  $k^+$  values for a given surface condition. In order to validate the proposed CFD model, numerical simulations of the drag characterization studies are performed. Namely, for the purpose of drag characterization,  $C_F$  for smooth and rough surfaces is measured with certain method for the determination of  $\Delta U^+$ . In this thesis, fouling with biofilm and hard fouling are analysed. Results of drag characterization for surfaces fouled with biofilm obtained using TCF facility are taken from [133], while results of drag characterization for surfaces fouled with hard fouling obtained using towing tank tests of flat plates are taken from [123]. Therefore, CFD simulations for the purposes of validation study include simulations of the flow in TCF facility and simulations of the towing of the flat plate. Firstly, an extensive verification study is performed for all CFD simulations for the purposes of validation study and the simulation uncertainties are determined. Then, the numerically obtained  $C_F$  for both smooth and rough plates are compared with the experimentally obtained ones and in that way the CFD model is validated. Thereafter, numerical simulations of the flow around flat plates having the same length as ships (flat plates in full-scale) are performed for both smooth and rough surfaces and the obtained  $C_F$  are compared with the ones obtained using Granville similarity law scaling method. In order to determine the



effect of biofouling on the resistance, open water and propulsion characteristics, following numerical simulations are performed: double body simulations (DBS), as well as simulations of resistance (RT), open water (OWT) and self-propulsion tests (SPT). It should be noted that double body simulations do not include free surface effects into account. Even though  $C_F$  obtained using DBS for both smooth and rough surfaces can be used for the calculation of  $\Delta C_F$  and compared with  $\Delta C_F$  obtained using Granville similarity law scaling method, within Figure 3.1, this comparison is not included. Namely, the one should bear in mind that using Granville similarity law scaling method  $\Delta C_F$  is obtained for flat plate, while using DBS  $\Delta C_F$  is obtained for 3D ship hull. Consequently, these increases will not be the same if there is an effect of biofouling on  $k_f$ , i.e. if the biofouling will cause the change in  $k_f$ . The results of numerical simulations of DBS, RT, OWT and SPT for various surface conditions are analysed and used for the determination of the effect of biofouling on resistance, open water and self-propulsion characteristics. The obtained results are compared with the ones obtained using the newly proposed method. It should be noted that verification study is performed within CFD simulations of RT, OWT and SPT as well and that simulation uncertainties are determined. Furthermore, the applicability of CFD model for the prediction of effects of biofouling on the flow characteristics around the fouled ship hull is shown. More details regarding the performed numerical simulations will be presented in Sections 4 and 5.

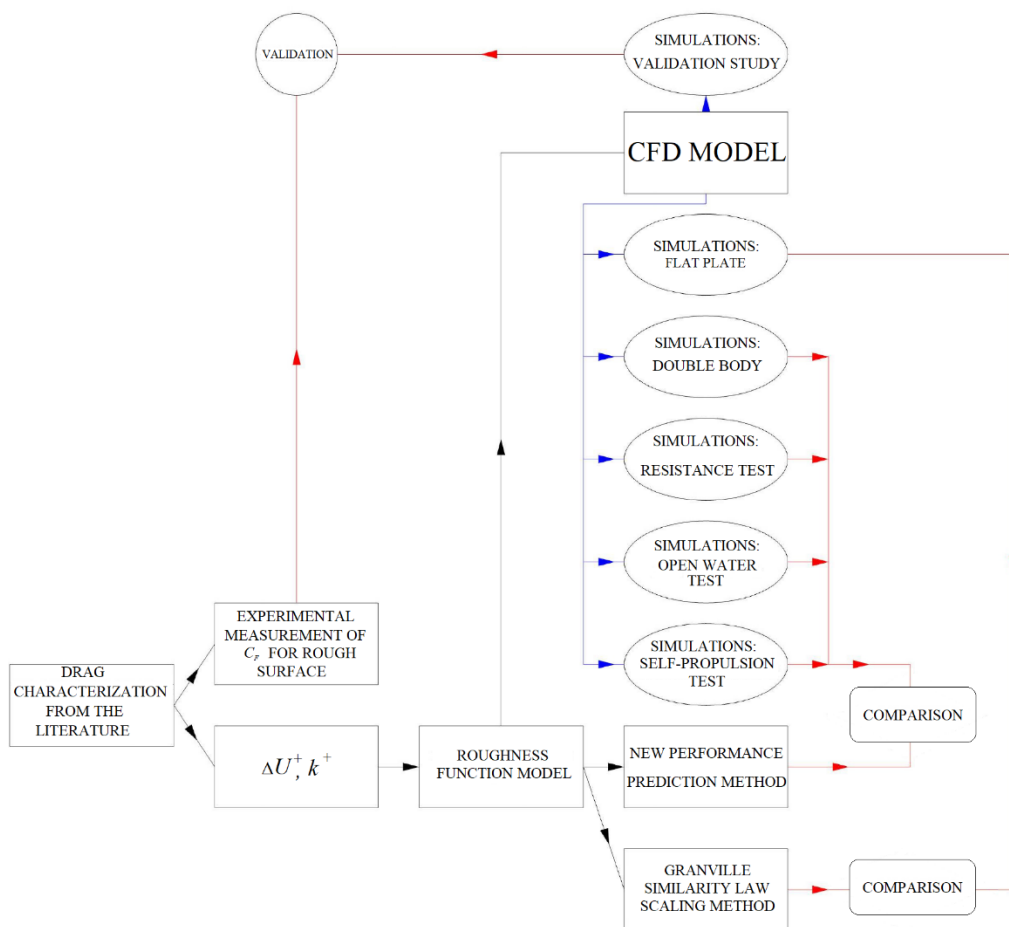


Figure 3.1 The flow chart representing methodology of this study

## 3.2. Numerical modelling

### 3.2.1. Governing equations

The proposed CFD model which can account for the effects of biofouling on the ship resistance, open water and self-propulsion characteristics is developed within commercial software package STAR-CCM+ [180]. Numerical simulations are performed for incompressible viscous flow of Newtonian fluid. In general, the motion of viscous flow can be depicted using continuity equation and Navier-Stokes equations, which are derived from the law of conservation of mass and the law of conservation of momentum as well as by the introduction of constitutive equations. Constitutive equations divide stress in the fluid on the pressure and viscous term. However, for turbulent flows, these equations do not have analytical solutions, as turbulent flows are in nature stochastic [198]. Accordingly, these equations are solved numerically either using RANS, LES, Detached Eddy Simulations (DES), Partially Averaged Navier-Stokes Simulations (PANS) or DNS. For engineering purposes, where averaged physical quantities are of interest, utilization of RANS equations presents a reasonable choice between the accuracy and computational efficiency. Consequently, RANS equations are widely used within the literature in the problems related to ship hydrodynamics [199], [200], [201], [202], [203]. Within this thesis, RANS and averaged continuity equations are utilized for the quantitative characterization of the developed turbulent flow. In the turbulent flow, each physical quantity can be decomposed into a mean and fluctuating part. RANS and averaged continuity equations are derived after applying Reynolds averaging to Navier-Stokes and continuity equations. Those equations are presented as follows [198]:

$$\frac{\partial(\rho\bar{u}_i)}{\partial t} + \frac{\partial}{\partial x_j}(\rho\bar{u}_i\bar{u}_j + \overline{\rho u_i' u_j'}) = -\frac{\partial\bar{p}}{\partial x_i} + \frac{\partial\bar{\tau}_{ij}}{\partial x_j} \quad (3.1)$$

$$\frac{\partial(\rho\bar{u}_i)}{\partial x_i} = 0 \quad (3.2)$$

where  $\bar{u}_i$  is the averaged velocity vector,  $\overline{\rho u_i' u_j'}$  is the Reynolds stress tensor,  $\bar{p}$  is the mean pressure and  $\bar{\tau}_{ij}$  is the mean viscous stress tensor given as:

$$\bar{\tau}_{ij} = \mu \left( \frac{\partial\bar{u}_i}{\partial x_j} + \frac{\partial\bar{u}_j}{\partial x_i} \right) \quad (3.3)$$

It should be noted that for incompressible flow in equations (3.1) and (3.2)  $\rho$  can be written outside the partial derivation since  $\rho = \text{const.}$ , i.e. equation (3.2) can be written without  $\rho$ .

However, since Navier-Stokes equations are nonlinear, velocity fluctuations will still appear in RANS equations in the nonlinear term, i.e. Reynolds stress tensor, from the convective acceleration. Therefore, equations (3.1) and (3.2) present an unclosed set of equations. In order to derive equations which contain only mean velocity and pressure, Reynolds stress tensor should be modelled as a function of the mean flow. This problem is known as the closure problem, which is solved by application of certain turbulence model. Within the literature, several turbulence model have been proposed for closure of RANS and continuity equations, classified in two basic approaches: eddy viscosity and Reynolds stress transport models. The

eddy viscosity models are based on the assumption that turbulence effects can be explained as an increased viscosity [198]:

$$-\overline{\rho u'_i u'_j} = \mu_t \left( \frac{\partial \bar{u}_i}{\partial x_j} + \frac{\partial \bar{u}_j}{\partial x_i} \right) - \frac{2}{3} \rho \delta_{ij} k \quad (3.4)$$

where  $\mu_t$  is the eddy viscosity and  $\delta_{ij}$  is the Kronecker delta symbol and  $k$  is the turbulent kinetic energy defined as follows:

$$k = \frac{1}{2} \overline{u'_i u'_i} \quad (3.5)$$

The most applied eddy viscosity turbulence models in the problems of ship hydrodynamics are  $k-\omega$  SST and  $k-\varepsilon$  turbulence models, which represent two equations turbulence models. However, there are some applications of one equation turbulence models, for example Spalart-Allmaras or Menter. Eddy-viscosity turbulence models are isotropic, and anisotropic models are either of the algebraic stress or Reynolds stress type [204]. It should be noted that eddy-viscosity models have several deficiencies in complex, 3D flows which are frequently present in problems related to the ship hydrodynamics. Regardless of this, currently they are most commonly applied models and this can be attributed to their lower requirement for computational power. Namely, in Reynolds stress transport models, differential equations are defined for each individual component of the symmetric Reynolds stress tensor and in that way complex interactions in turbulent flow fields can be resolved more reliably. Besides six equations for Reynolds stress tensor, one equation is required for the isotropic turbulent dissipation ( $\varepsilon$ ). Consequently, Reynolds stress transport models require more computational power than eddy-viscosity turbulence models, which in case of  $k-\omega$  SST and  $k-\varepsilon$  turbulence models require two additional equation for closing the set of equations (3.1) and (3.2).

Within this thesis  $k-\omega$  SST turbulence model is chosen for the closure of the set of equations (3.1) and (3.2) after detail investigations related to the application of different turbulence models in the prediction of ship resistance, open water and self-propulsion characteristics described in Appendix A.

$k-\omega$  SST turbulence model is two equation model which solves two transport equations, one for  $k$  and one for the specific dissipation rate ( $\omega$ ) [151]:

$$\frac{\partial}{\partial t}(\rho k) + \frac{\partial(\rho u_j k)}{\partial x_j} = P_k - \beta^* \rho f_{\beta^*} (\omega k - \omega_0 k_0) + \frac{\partial}{\partial x_j} \left[ (\mu + \sigma_k \mu_t) \frac{\partial k}{\partial x_j} \right] + S_k \quad (3.6)$$

$$\frac{\partial}{\partial t}(\rho \omega) + \frac{\partial(\rho u_j \omega)}{\partial x_j} = P_\omega - \beta \rho f_\beta (\omega^2 - \omega_0^2) + \frac{\partial}{\partial x_j} \left[ (\mu + \sigma_\omega \mu_t) \frac{\partial \omega}{\partial x_j} \right] + S_\omega \quad (3.7)$$

where  $u_j$  is the velocity vector,  $S_k$  and  $S_\omega$  are user specified source terms,  $k_0$  and  $\omega_0$  are the ambient turbulence value in the source terms that counteracts turbulence decay,  $\sigma_k$  and  $\sigma_\omega$  are the inverse turbulent Schmidt numbers,  $P_k$  and  $P_\omega$  are turbulent production terms,  $\beta$  and  $\beta^*$  are model coefficients,  $f_\beta$  is the vortex stretching modification factor,  $f_{\beta^*}$  is the function used for free-shear modification. Eddy viscosity is given as follows:

$$\mu_t = \rho k T \quad (3.8)$$

where  $T$  is the turbulent time scale.

The roughness effects can be included within  $k - \omega$  SST turbulence model with or without wall functions. If the roughness effects are accounted for without wall functions either  $\omega$  wall value should be set according to non-dimensional roughness length scale in wall coordinates combined with a modification of the eddy-viscosity limiter or the relations between  $k$  and  $\omega$  wall boundary conditions and roughness length scale should be defined [175]. In this thesis roughness effects are accounted for with wall functions, which are used for providing algebraic approximations of velocity and turbulence quantities in the inner layer of TBL. Thus, except for obtaining the velocity in the inner layer of TBL using  $U^+$  distribution, wall functions are used for obtaining  $\tau_w$  values for the mean velocity components and describing the distribution of non-dimensional specific turbulent dissipation ( $\omega^+$ ) and non-dimensional production of turbulent kinetic energy ( $P_k^+$ ). In that way, the wall treatment within STAR-CCM+ [180] is used for calculation of  $\tau_w$  and for imposing values for the turbulence quantities on the centroids of the near wall cells. Namely,  $\tau_w$  is calculated using  $u_\tau$  determined as follows:

$$u_\tau = \frac{u_*}{U^+} |\hat{u}_{\text{tangential}}| \quad (3.9)$$

where  $u_*$  is the velocity scale and  $\hat{u}_{\text{tangential}}$  is the wall tangential velocity vector. It should be noted that  $u_*$  and  $U^+$  are approximated using wall functions. The value of  $u_*$  is calculated as a product of the fourth root of model coefficient  $\beta^*$  and square root of  $k$ .

At the wall surface, normal velocity gradient for  $k$  and  $\omega$  at the wall are set to zero. Also, in the near wall cells, the transport equations for  $k$  and  $\omega$  are solved using imposed values for  $P_k$  and  $\omega$ . Thus, within  $k - \omega$  SST turbulence model, two non-dimensional quantities are imposed,  $P_k^+$  and  $\omega^+$  which are calculated as follows:

$$P_k^+ = \frac{1}{\kappa y^+} \quad (3.10)$$

$$\omega^+ = \frac{1}{\sqrt{\beta^*} \kappa y^+} \quad (3.11)$$

The value of the certain turbulence quantity is derived by equating the non-dimensional definition of the turbulence quantity with its algebraic approximation as provided by the applied wall function.

More details related to  $k - \omega$  SST turbulence model can be found within [205].

### 3.2.2. Finite Volume method

Finite Volume Method (FVM) is utilized for representation and evaluation of partial differential equations in the form of algebraic equations. Thus, governing equations are transformed into a system of algebraic equations through the discretization in time and space. The computational domain is therefore subdivided into finite number of control volumes by grid. The utilization

of both structured and unstructured grid is allowed with FVM, but since unstructured grid significantly simplifies grid generation for complex geometries, unstructured hexahedral mesh is used within numerical simulations. It is created using STAR-CCM+ meshing tools: surface remesher, automatic surface repair, prism layer mesher and trimmed cell mesher. Surface remesher is utilized for the improvement of the overall quality and optimization of the imported triangulated surface (re-triangularization), which will be used for volume mesh generation. Re-triangularization is based on a target edge length and feature refinement that is based on surface and curvature proximity. After surface has been remeshed, geometric type problems which may appear are repaired using automatic surface repair. Trimmed cell mesher is used for the generation of hexahedral mesh. Trimmed cell mesher uses a template mesh generated from hexahedral cells, from which it cuts or trims the core mesh using the input surface. However, before the core mesh is generated, a subsurface at specified prism layer thickness value is created. Prism layer cells are orthogonal prismatic cells next to wall surfaces or boundaries, defined with prism layer thickness, number of cells within prism layer, size distribution of the cells and function for the generation of distribution (within this thesis geometric progression is used). Custom mesh controls are applied in the parts of computational domain, where the mesh refinement is required. Thus, in numerical simulations where free surface effects are taken into account, the mesh is refined for capturing Kelvin wake and near the free surface. Also, mesh is refined near the investigated geometry (either flat plate or ship). More details regarding the mesh refinement will be presented in Sections related to CFD simulations. After the generation of the core mesh with refinements, prism layer mesh is created by extruding the cell faces from the core mesh to the initial surface [206]. It should be noted that all mesh parameters are defined as relative values of the cell base size except prism layer thickness which is set as absolute value. In this way, for grid sensitivity studies remeshing is greatly simplified while keeping the same  $y^+$  value in the first cells near the wall in all meshes. The analysed physical time interval is subdivided into an arbitrary number of subintervals called time steps.

In numerical simulations where free surface effects are not considered there is no need for temporal discretization, as unsteady term from RANS equations is equal to zero. On the other hand, free surface simulations are carried out as unsteady calculations, using implicit unsteady solver. Governing equations are solved using the segregated flow solver, which solves them in a sequential manner. Momentum and continuity equations are linked using predictor-corrector approach. Rhie-Chow type of pressure velocity coupling combined with SIMPLE algorithm is used to obtain pressure and velocity fields. Pressure-correction equation is used for the fulfilment of the mass conservation constraint on the velocity field and it is obtained from the continuity equation and the momentum equations in a way that a predicted velocity field is sought to fulfil the continuity equation, which is accomplished through pressure correction. Pressure as a variable is obtained using the pressure-correction equation [205]. A second order upwind scheme is utilized for the discretization of convection terms in RANS equations, while first order temporal scheme is used for temporal discretization. Reconstruction gradients are computed using Hybrid Gauss-Least Squares Method. The discrete linear system is iteratively solved using Algebraic Multigrid (AMG) solver. The convergence is improved through under relaxation in each time step using Gauss-Seidel relaxation scheme. Free surface simulations are initialized with the initial velocity and pressure field, while double body simulations are initialized with imposed velocity.

### 3.2.3. Volume of fluid method

Within numerical simulations which include free surface effects, Volume of Fluid (VOF) method combined with High Resolution Interface Capturing scheme (HRIC) is utilized for tracking sharp interfaces and locating the free surface. Thus, the distribution and the movement of the interface of immiscible phases are predicted with VOF method. The important assumption of this modelling approach is that the mesh resolution is fine enough to determine the location and the shape of the interface between the phases. This method is based on the volume fraction of  $i$ -th fluid ( $\alpha_i$ ), which is defined as a ratio between volume of the  $i$ -th fluid in cell and the volume of the cell and it is assessed using averaged continuity equation. Thus, within cell, sum of all  $\alpha_i$  must be one. Since in free surface simulations only two fluids are considered, transport equation for  $\alpha_i$  is solved only for the first fluid ( $\alpha_1$ ) and  $\alpha_i$  of the second fluid ( $\alpha_2$ ) is adjusted in a way that  $\alpha_1 + \alpha_2 = 1$ . Physical properties depend on the presence of the fluid in a particular cell and are calculated according to the following equation:

$$X = \sum_i \alpha_i X_i \quad (3.12)$$

Water and air represent a system of immiscible phases, i.e. fluids are always separated by a sharp interface. HRIC is designed to mimic the convective transport of immiscible fluid components and therefore it presents a scheme which is suited for tracking sharp interfaces. In order to assure that HRIC scheme is used regardless of the selected time step, the values of upper and lower Courant number limit in HRIC scheme are set to be larger than the maximum Courant number obtained in simulation. It should be noted that Courant number for one dimensional case is defined as a ratio of the product of the velocity magnitude and time step and the length interval.

In free surface simulations it is important to eliminate the possible wave reflections at the domain boundaries and this can be accomplished using several approaches. Nowadays, the most frequently used ones are grid damping and damping layer approaches. The elimination of possible wave reflections using grid damping approach is achieved using progressively larger cells towards the corresponding boundary, where reflection is anticipated. On the other hand, this elimination using damping layer approach is achieved through the introduction of damping zone near the boundary, where reflection is anticipated. In damping zone momentum sinks are introduced within the governing equations, in order to damp the waves that propagate through the zone. Even though both approaches are successfully used within literature, damping layer approach is more predictable with respect to damping quality, since for sufficiently fine discretization it is independent on grid, time step, temporal and spatial discretization schemes, unlike the grid damping approach [207]. Therefore, within this thesis the possible reflection of VOF waves is eliminated utilizing damping layer approach. Choi and Yoon method of VOF waves damping [208] is implemented within STAR-CCM+. This method introduces the source term in the  $z$ -momentum equation causing the vertical resistance to the vertical velocity component ( $u_z$ ):

$$q_z^d = \rho (f_1 + f_2 |u_z|) \frac{e^\kappa - 1}{e^1 - 1} u_z \quad (3.13)$$

$$\kappa = \left( \frac{x - x_{sd}}{x_{ed} - x_{sd}} \right)^n \quad (3.14)$$

where  $f_1$  is the linear damping constant set as 10,  $f_2$  is the quadratic damping constant set as 10),  $n$  is the damping exponent set as 2,  $x$  is the wave propagation direction,  $x_{sd}$  is the start and  $x_{ed}$  is the end coordinate of the damping layer.

Thickness of the damping layer (damping zone) is determined as:

$$x_d = |x_{ed} - x_{sd}| \quad (3.15)$$

and it is set to be equal to representative length.

Within free surface simulations with symmetry boundary condition, VOF wave damping is applied to inlet, outlet, and side boundary, while within free surface simulations where whole computational domain is modelled, VOF wave damping is applied to inlet, outlet, left side and right side boundaries.

### 3.2.4. Moving reference frame method

Moving Reference Frame (MRF) is the reference frame that can rotate and translate with the respect to the stationary reference frame. MRF method assumes that the angular velocity of the body is constant and that the mesh is rigid. Also, it applies a steady state approximation to a transient problem leading to time-averaged results. This method is applied in many problems, but in the field of ship hydrodynamics it is mostly used for numerical simulation of open water test. Thus, computational domain is subdivided into the stationary and rotational parts. The absolute velocity ( $u_{oi}$ ) is related to the velocity relative to the moving reference frame ( $u_{pi}$ ) as follows [205]:

$$u_{oi} = u_{pi} + \varepsilon_{ijk} \omega_{pj} r_k \quad (3.16)$$

where  $\omega_{pj}$  is the angular velocity and  $r_k$  is the position vector from the origin of the MRF to the centre of a control volume.

Equations (3.1) and (3.2) in MRF written with relative velocity for incompressible flows can be written as follows [205]:

$$\frac{\partial u_{pi}}{\partial x_i} = 0 \quad (3.17)$$

$$\frac{\partial u_{pi}}{\partial t} + u_j \frac{\partial u_{pi}}{\partial x_j} + \varepsilon_{ijk} \frac{d\omega_{pj}}{dt} r_k + 2\varepsilon_{ijk} \omega_{pj} u_{pk} + \varepsilon_{ijk} \varepsilon_{jlm} \omega_{pl} \omega_{pm} r_k = -\frac{1}{\rho} \frac{\partial p}{\partial x_i} + \nu \frac{\partial^2 u_{pi}}{\partial x_j \partial x_j} \quad (3.18)$$

Owen et al. [65] have investigated application of various methods for propeller representation in numerical simulations of open water tests. Thus, the authors have studied the differences between steady MRF, unsteady MRF as well as unsteady sliding mesh methods. In the sliding mesh approach the whole computational domain rotates about an axis. In that way, transient calculations, which produce time accurate results that require higher computational power are represented. According to the obtained results, Owen et al. [65] have concluded that the application of unsteady MRF only slightly improves the accuracy of the results in comparison

with the application of steady MRF. However, the application of unsteady MRF causes significant increase in computational time and therefore the application of unsteady MRF is unnecessary. What is more, since the results obtained using sliding mesh and MRF methods showed only minor differences, steady MRF can be considered as a reasonable compromise between the accuracy and required computational power. In this thesis, numerical simulations of open water test are performed using steady MRF method and therefore unsteady term from equation (3.18) is equal to zero.

### 3.2.5. Body force method

The body force propeller method is utilised for modelling the effects of a propeller in numerical simulations of self-propulsion test and in that way propeller geometry is not resolved. Body force method is based on a uniform distribution of volume force over the cylindrical virtual disk which varies only in radial directions. Components of this volume force follow the Goldstein optimum [205]:

$$f_{bx} = A_x r^* \sqrt{1 - r^*} \quad (3.19)$$

$$f_{b\theta} = A_\theta \frac{r^* \sqrt{1 - r^*}}{r^* (1 - r_h') + r_h'} \quad (3.20)$$

where  $f_{bx}$  is the body force component in axial direction,  $f_{b\theta}$  is the body force component in tangential direction and  $r^*$  is defined as follows:

$$r^* = \frac{r' - r_h'}{1 - r_h'} \quad (3.21)$$

where  $r'$  and  $r_h'$  are determined as follows:

$$r' = \frac{r}{R_p} \quad (3.22)$$

$$r_h' = \frac{R_H}{R_p} \quad (3.23)$$

where  $r$  is the radial coordinate,  $R_p$  is the propeller tip radius and the  $R_H$  is the propeller hub radius.

The constants  $A_x$  and  $A_\theta$  in equations (3.19) and (3.20) are computed as:

$$A_x = \frac{105}{8} \cdot \frac{T}{\pi \Delta (3R_H + 4R_p)(R_p - R_H)} \quad (3.24)$$

$$A_\theta = \frac{105}{8} \cdot \frac{Q}{\pi \Delta R_p (3R_H + 4R_p)(R_p - R_H)} \quad (3.25)$$

where  $T$  is the thrust,  $Q$  is the torque and  $\Delta$  is the thickness of the virtual disk.

For the computation of body forces, several inputs are required including propeller open water characteristics, the virtual disc properties including  $R_p$ ,  $R_H$ ,  $\Delta$  and the position of the virtual disc within the computational domain, the direction of the propeller rotational axis, and the



direction of rotation. Furthermore, the inflow velocity should be specified and within numerical simulations of self-propulsion test, the inflow velocity is specified using inflow velocity plane, i.e. by setting inflow plane radius and offset. Inflow plane radius is set as  $1.1R$ , while inflow plane offset is set as  $0.1D$ . The velocities and densities at this plane are volume averaged and then projected onto the normal plane of the virtual disk to yield one average density value ( $\rho_{\text{inflow plane}}$ ) and average velocity vector value ( $v_{\text{inflow plane}}$ ). However, the averaged inflow velocity is influenced by the propeller induced velocity. Namely, the propeller can increase the velocity artificially at the inflow leading to over-prediction of performance and therefore induced velocity is corrected within numerical simulations of self-propulsion test. In this way, more accurate results are obtained, which is reflected in more accurate prediction of wake fraction.

Numerical simulation of self-propulsion test is performed for certain operating point, which can be specified either by  $n$ ,  $T$  or  $Q$ . In this thesis, operating point is set using  $T$  ( $T_{\text{operating point}}$ ) and in that way self-propulsion point can be assessed using only one simulation. Namely, self-propulsion point in full-scale is obtained once propeller thrust is equal to total resistance during self-propulsion conditions. In order to improve convergence, in the first part of numerical simulation  $T_{\text{operating point}}$  is set to be  $R_T / (1-t)$ , where  $R_T$  is obtained from resistance test and  $t$  is estimated. For numerical simulations for rough surfaces,  $t$  is assumed to be the same for smooth surface, for which  $t$  is estimated according to similar ship. In the second part of numerical simulation,  $T_{\text{operating point}}$  is set to be equal to  $R_T$  during self-propulsion conditions. In that way, once total resistance or thrust force become steady, self-propulsion point is obtained. It should be noted that the final result will not depend on the estimated value of  $t$  used in the first part of simulation, it will only affect the time required for achieving convergence.

Using the given  $T$ ,  $J$  is calculated numerically by solving equation  $f(J) = K_T - K_T'$ , where  $K_T$  is evaluated from open water characteristics and  $K_T'$  is evaluated from:

$$K_T' = \frac{J^2 T_{\text{operating point}}}{\rho_{\text{inflow plane}} v_{\text{inflow plane}}^2 D^2} \quad (3.26)$$

After  $J$  is estimated,  $K_T$  and  $K_Q$  are interpolated from the specified propeller open water characteristics. Thereafter,  $T$  and  $Q$  are calculated as follows:

$$T = \frac{K_T \rho v_{\text{inflow plane}}^2 D^2}{J^2} \quad (3.27)$$

$$Q = \frac{K_Q \rho v_{\text{inflow plane}}^2 D^2}{J^2} \quad (3.28)$$

Finally, with  $T$  and  $Q$  available,  $f_{bx}$  and  $f_{b\theta}$  are calculated using equations (3.19) and (3.20). Required computational time using body force method is significantly reduced in comparison with rigid body simulation, where required time step is very low, and more cells are required for a proper discretization of propeller geometry. Since, transient occurrences are not of prime interest within this study, but averaged propulsion characteristics, body force method is acceptable.

### 3.2.6. Verification and validation studies

Verification and Validation (V&V) studies are independent procedures that are utilised together in order to determine the accuracy and reliability of numerical simulations. The aim of V&V studies is to secure that implemented methodology provides reasonable results for a certain range of problems.

#### 3.2.6.1. The verification study

The verification study is the process for evaluating the correctness of solving the governing equations. It is performed using multiple numerical solutions for certain physical quantity ( $\phi$ ) with systematic parameter refinement by varying the  $i$ -th input parameter and holding all other parameters constant [209]. The input parameters investigated within this thesis are grid spacing and time step. It should be noted that a refinement ratio between input parameters does not have to be uniform [209]. Within this thesis three different grid sizes and fine time step were utilized in grid sensitivity studies, while within time step sensitivity studies, three different time steps are utilized along with fine mesh as done in [199]. A refinement ratio for time step is equal to 2, as three utilized time steps are equal to  $T/50$ ,  $T/100$  and  $T/200$ , where  $T$  is defined as the ratio between characteristic length and velocity. It should be noted that medium and fine time steps correspond to lower and upper limits of range of time steps prescribed by ITTC [210]. Also, as shown in [151], the numerical solution obtained with  $T/200$  had very low relative deviation from the numerical solution obtained with  $T/2000$ , even for rough surface. Hence, in order to reduce the required computational time,  $T/200$  is chosen as the finest time step.

A refinement ratio for grid size is calculated as follows:

$$r_{21} = \sqrt[3]{\frac{N_{C1}}{N_{C2}}} \quad (3.29)$$

$$r_{32} = \sqrt[3]{\frac{N_{C2}}{N_{C3}}} \quad (3.30)$$

where  $N_{C1}$ ,  $N_{C2}$  and  $N_{C3}$  are the number of the cells for fine, medium and coarse grid respectively, obtained with uniform refinement.

The verification study is undertaken in order to estimate sufficient grid spacing and time step, as well as to assess the numerical uncertainty ( $U_{SN}$ ). After the verification study has been completed, all numerical simulations are performed with fine input parameters, i.e. with fine grid and fine time steps.  $U_{SN}$  is calculated using the Grid Convergence Index (GCI) method, which relies on Richardson extrapolation and it is recommended by the American Society of Mechanical Engineers as well as by the American Institute of Aeronautics and Astronautics [199]. Even though GCI method was firstly proposed for the determination of grid uncertainties ( $U_G$ ), it can be also used for the estimation of time step uncertainties ( $U_T$ ) [199], [211], [212].

$U_{SN}$  is determined as follows:

$$U_{SN}^2 = U_I^2 + U_G^2 + U_T^2 \quad (3.31)$$

where  $U_I$  is the iteration uncertainty and it is considered to be negligible in comparison with  $U_G$  and  $U_T$ , as proven in [152].

The apparent order of method is calculated with following equation:

$$p_a = \frac{1}{\ln(r_{21})} \left| \ln \left| \frac{\varepsilon_{32}}{\varepsilon_{21}} \right| + q(p_a) \right| \quad (3.32)$$

where  $\varepsilon_{32} = \phi_3 - \phi_2$ ,  $\varepsilon_{21} = \phi_2 - \phi_1$  and  $\phi_i$  is the numerical solution obtained with  $i$ -th grid and  $q(p_a)$  is given with:

$$q(p_a) = \ln \left( \frac{r_{21}^{p_a} - s}{r_{32}^{p_a} - s} \right) \quad (3.33)$$

$$s = \operatorname{sgn} \left( \frac{\varepsilon_{32}}{\varepsilon_{21}} \right) \quad (3.34)$$

The extrapolated solution is obtained as follows:

$$\phi_{ext}^{21} = \frac{r_{21}^{p_a} \phi_1 - \phi_2}{r_{21}^{p_a} - 1} \quad (3.35)$$

The approximate and extrapolated errors are calculated by following equations:

$$e_a^{21} = \left| \frac{\phi_1 - \phi_2}{\phi_1} \right| \quad (3.36)$$

$$e_{ext}^{21} = \left| \frac{\phi_{ext}^{21} - \phi_1}{\phi_{ext}^{21}} \right| \quad (3.37)$$

The grid convergence index for fine input parameter is calculated by:

$$GCI_{fine}^{21} = \frac{1.25e_a^{21}}{r_{21}^{p_a} - 1} \cdot 100\% \quad (3.38)$$

### 3.2.6.2. The validation study

The validation study is the process for evaluating the correctness of the description of the actual problem with the proposed model and methodology, i.e. governing equations. Within the validation study, the obtained numerical solutions for certain  $\phi$  are compared with the available numerical or experimental data. If numerical simulations are performed in full-scale, available experimental data should be extrapolated. Relative deviations between numerical ( $\phi_{CFD}$ ) and extrapolated results ( $\phi_{EX}$ ) are obtained with the following equation:

$$RD = \frac{\phi_{CFD} - \phi_{EX}}{\phi_{EX}} \cdot 100\% \quad (3.39)$$

Equation (3.39) can be easily altered, if numerical simulations are performed in a same scale as experiment by changing  $\phi_{EX}$  value with the obtained experimental value ( $\phi_{EXP}$ ).

In order to determine whether validation has been achieved,  $RD$  is compared with validation uncertainty, which is calculated as follows [209]:

$$U_V^2 = U_{SN}^2 + U_D^2 \quad (3.40)$$

where  $U_D$  is the experimental uncertainty.

Thus, if  $RD$  is lower than  $U_V$ , the combination of all the errors in numerical simulation and experiment is smaller than  $U_V$  and one can conclude that the validation is achieved at  $U_V$  level.

## 4. Development and validation of roughness function models for biofouling

### 4.1. Roughness function model for biofilm

#### 4.1.1. Biofilm

A biofilm is an aggregation of microbial cells that is irreversibly attached to a surface, i.e. cannot be removed by gentle rinsing, and placed within a matrix of primarily polysaccharide material. Aside of microbial cells, within the biofilm matrix noncellular materials can also be present, like mineral crystals, clay or silt particles, blood components, corrosion particles and this depends on the surroundings in which the biofilm is grown. They can be formed on a various surfaces, for example living tissues, indwelling medical devices, industrial or potable water system piping, natural aquatic systems, marine and offshore structures, etc [213]. Within shipping industry, fouling with biofilm is often referred to as slime. Microbial cells are located randomly within a matrix with pores, i.e. voids, through which nutrient flow is present [214]. The presence of biofilm on the immersed surface increases the rate of biofouling [30]. What is more, the presence of biofilm causes the increase of the corrosion process, which can be attributed to the increase in surface roughness [38]. A detailed investigation related to biofilms is enabled with the development of the electron microscope, which enabled high resolution photo microscopy at much higher magnification in comparison with the light microscope [213]. Thus, Scanning Electron Microscope (SEM) produces images of a sample by scanning the surface with a focused beam of electrons and in that way enables high resolution photos at high magnifications. In Figure 4.1 top view and cross sections of the fouled flat plates with biofilm, coated with different sized  $\text{Cu}_2\text{O}$  particles are presented. Thus, the presence of biofilm after 4.5 months of immersion in sea water can be clearly noticed on  $\text{Cu}_2\text{O}$  particles, Figure 4.1.

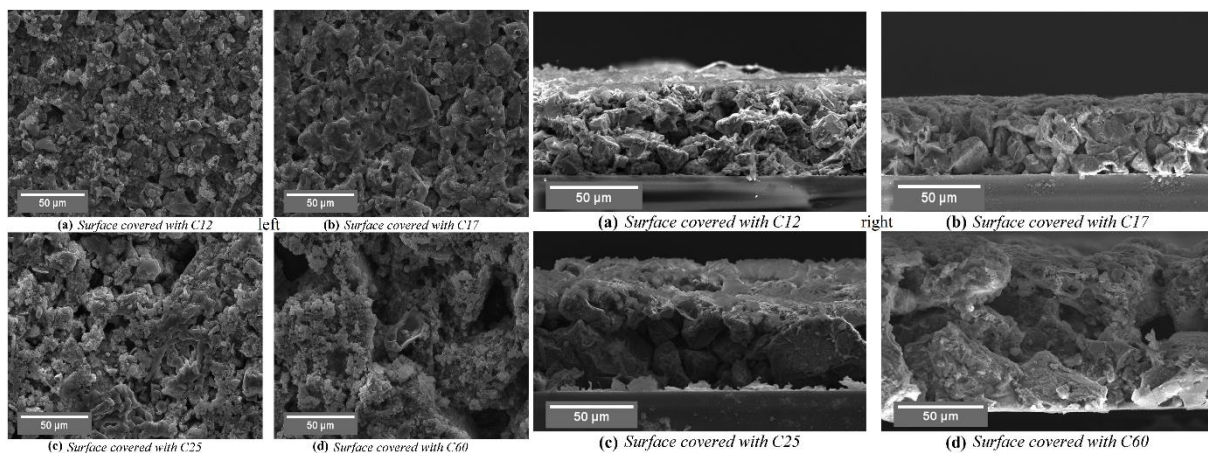


Figure 4.1 SEM top-view (left) and cross sections (right) of the specimens covered with biofilm after 4.5 month of immersion (adapted from [134])

Biofilms are characterized with its heterogeneity, both spatial and temporal as well as with non-uniform distribution over a surface [29]. They are flexible, have variable density and height and due to production of extracellular polymeric substances, rich interactions with the fluid flow over the biofilm are present. What is more, biofilms can be modified and displaced due to the flow, which can make resistance characteristics of biofilm time dependant, even at steady flow

velocity [133]. Also, the species distribution of organisms in the biofilm varies with the level of turbulence [134]. Consequently, the modelling of the flow as well as the determination of resistance for biofilm covered surfaces are difficult and therefore a subject of many forthcoming research. The effects of macrofouling are far better comprehended than the effects of microfouling [157]. Even though biofilms are flexible, the compliance and motion of a biofilm do not seem to have important role in drag production [134]. FR and biocidal coatings can help in the control of hard fouling, however these coatings are often proven to be ineffective in prevention of slime fouling [215]. Thus, slime can be found on the most of immersed surfaces and is often first type of biofouling to occur. Biofilms are primarily consisted of bacterial cells and diatoms, a unicellular algae, embedded within viscoelastic extracellular polymeric substances [216], however the dominant species in biofilm are usually diatoms. Biofilm adhesion, diatom abundance and diatom diversity were found to be significantly different between static and dynamic treatments [217]. Therefore, Zargiel et al. [217] have recommended that test panels should be cycled between static and dynamic conditions in order to more realistically model a ship's cycle in the open ocean. However, the drag forces are similar for the fouling communities that are developed under static and dynamic conditions [218].

Presently, there is no generally accepted approach for assessing the effects of a given biofilm covered surface on the resistance. Biofilms extract energy from the flow in two ways, by means of the roughness of the biofilm and the flapping streamers. Because of this, biofilm has a larger effective roughness length scale than the physical roughness. Also, a large spatial heterogeneity in the turbulence and momentum transport over the bed is present, even though the biofilm is uniform in coverage [137]. Schultz et al. [133] have carried out the experiments in a fully developed TCF facility with the aim to investigate the impact of diatomaceous slime on the frictional resistance.

#### **4.1.2. Experiments in TCF**

Schultz et al. [133] have studied the impact of biofilms on the frictional drag of FR coating system with a goal of developing robust roughness length scale, which would allow the estimation of hydrodynamic effects of biofilm with solely physical measurements of the biofilm. For that purpose, the authors carried out drag characterization of three modern FR coatings in the clean, as-applied condition and after fouling with diatomaceous biofilm for periods of 3 and 6 months. Test plates were coated typically, with full coating scheme including a primer, a tie-coat and FR coating. Additionally, a set of uncoated acrylic control (AC) surfaces was also examined. Thus, in total eight plates were tested, as each coating scheme listed in Table 4.1 was applied to two replicate test panels.

Biofilms within [133] were grown under dynamic conditions within dynamic biofilm exposure facility. The facility was lighted for 18 h per day, while it was kept dark during the rest of a day. It was kept at a constant temperature of 25 °C and exposure cycle was varied during the exposure period, i.e. one-week of static exposure and then three weeks of dynamic exposure. This was done in order to mimic a reasonable ship operational profile. Dynamic biofilm exposure facility was filled with artificial seawater having salinity of 15 ppt and tank was inoculated with a diatomaceous biofilm collected from a rubber panel which was exposed in the Indian River Lagoon near Sebastian Inlet, Florida, USA for 4.5 years. The biofilm was consisted of diatoms from four genera, typically found in biofilms on hulls of ships in-service. Before measurement of frictional resistance coefficients of tested plates within TCF, all plates were exposed to flow at the highest velocity used during hydrodynamic tests. In this way, all

loosely attached biofilm was dislodged before start of hydrodynamic test. It should be noted that in service, loosely attached biofilm is also dislodged from the ship hull.

Table 4.1 Tested coating schemes [133]

Coating scheme	Product technology	Symbol	Tested after the exposure of 3 months	Tested after the exposure of 6 months
International Intersleek <sup>®</sup> 700	a silicone FR coating system	A	A3	A6
International Intersleek <sup>®</sup> 900	a fluoropolymer FR coating system	B	B3	B6
International Intersleek <sup>®</sup> 1100SR	fluoropolymer FR coating system formulated to resist slime fouling	C	C3	C6
acrylic control	uncoated	AC	AC3	AC6

After hydrodynamic tests, grown biofilms on each test plate were measured in terms of biofilm thickness ( $k$ ) and percentage of surface coverage ( $\%SC$ ). Biofilm thickness was measured only on parts of plate where biofilm was present. Both measured  $k$  and  $\%SC$  have shown variation both in treatments as well as among treatments. After hydrodynamic tests, grown biofilm on each plate was sampled, and it was concluded that all samples included the taxa with which the facility was initially inoculated.

Hydrodynamic tests were made in TCF facility at USNA shown in Figure 2.8, and tests covered a large  $Rn$  range. The large  $Rn$  range allowed achieving a wide range of the wall shear stress, as well as performing the drag characterization over a whole range of flow regimes. The sketch of TCF facility is presented in Figure 4.2 and the main characteristics of TCF test section are given within Table 4.2. As aspect ratio  $W/H$  is high, i.e. it is equal to 8, two-dimensional flow in TCF facility is assured [147]. Turbulence is stimulated using square bars located on the top and bottom walls at the entrance to the test section, which provided 15% blockage as recommended by Durst et al. [219]. This blockage provided adequate turbulence stimulation along with fast recovery to streamwise self-similarity. As explained in 2.2.2.1,  $\Delta U^+$  value for certain surface condition in TCF facility is actually determined with pressure gradient, which is used for the determination of skin friction coefficient ( $C_f$ ). Pressure gradient was measured with two pressure taps, located  $90H$  and  $110H$  downstream of the location where turbulence is stimulated at the inlet. It should be noted that nine pressure taps were present in the test section during hydrodynamic tests and that linearity of pressure gradient was achieved with a coefficient of determination ( $R^2$ ) above 0.995. As can be seen from Figure 4.2, two tested plates are placed within TCF during hydrodynamic test, i.e. two replicate test panels, thus forming the top and bottom walls of the test section. Thus, the flow is firstly developed over smooth walls for a distance of  $60H$  from the inlet and as the first measurement of pressure is done at  $90H$  from the inlet, there was a  $30H$  roughness fetch, which is sufficient to re-establish fully developed conditions in terms of both the mean flow and Reynolds stresses [133]. The flow was fully developed, which was confirmed by velocity measurements at locations where

pressure was measured, i.e. at  $90H$  and  $110H$  downstream from the inlet, as the mean velocity profiles at these two locations collapsed. The resulting wall shear stress, shown in Table 4.2, is given for the smooth surface condition. This range of wall shear stress created conditions which are similar to average conditions on a smooth ship hull during sail. Experimental uncertainty in determination of the measured quantities was calculated using the method presented in [220], which takes into account both precision and bias. The overall experimental uncertainty in the determination of  $C_f$  was equal to  $\pm 8\%$  at the lowest  $Rn_m$  ( $Rn_m = 10000$ ), but rapidly dropped to  $\pm 1.2\%$  for  $Rn_m \geq 40000$ . The overall experimental uncertainty in the determination of  $\Delta U^+$  was equal to  $\pm 3.8\%$  or  $\pm 0.15$ , whichever was greater.

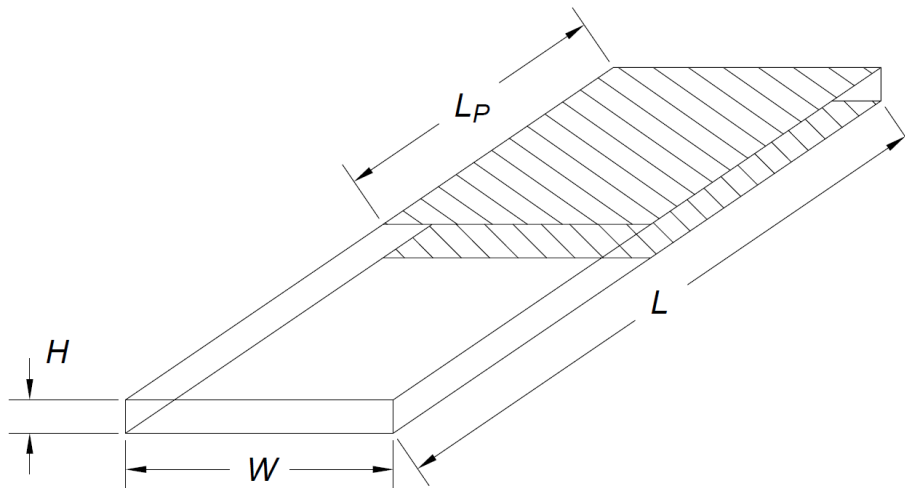


Figure 4.2 The sketch of TCF (adapted from [104])

Table 4.2 Characteristics of TCF facility test section

Characteristic	Value
Length ( $L$ )	3.1 m
Length of flat plate ( $L_p$ )	1.52 m
Width ( $W$ )	0.2 m
Height ( $H$ )	0.025 m
Wetted surface of flat plate ( $S$ )	$0.304 \text{ m}^2$
Bulk mean velocity ( $\bar{U}$ )	0.4 – 11 m/s
Water temperature ( $\vartheta$ )	$22 \pm 0.5 \text{ }^\circ\text{C}$
$Rn_m$	10000 – 300000
Wall shear stress ( $\tau_w$ )	0.6 – 206 Pa



### 4.1.3. Roughness length scale and roughness functions for biofilm

Schultz et al. [133] determined skin friction coefficients for smooth wall, clean and fouled plates after 3 and 6 months of exposure in dynamic biofilm exposure facility. Since for determination of roughness length scale and roughness function for biofilm,  $C_f$  for smooth wall and fouled plates are utilised, more attention was given to these plates. However, it should be noted that all clean plates have quite similar hydrodynamic performance, and very subtle differences in the obtained  $C_f$  are likely occurred due to coating application rather than differences in surface roughness of different coatings. At ship scale, all these surfaces are expected to operate in the hydraulically smooth regime, or nearly so. It should be noted that resulting surface roughness for clean plates is significantly smoother than typically achieved in dry dock (laboratory conditions), i.e. have better finish than coating systems in an actual hull application. The hydrodynamic tests in TCF for fouled plates after 3 months of exposure were performed for  $16Rn_m$  in the range from 10000 to 110000, for fouled plates after 6 months of exposure for  $28Rn_m$  in the range from 10000 to 190000, while for smooth wall (S) were performed for  $41Rn_m$  in the range from 10000 to 300000 and the obtained  $C_f$  are presented in Figure 4.3. The obtained  $C_f$  for fouled plates even after 3 months of exposure pointed out significant increase in  $C_f$  in comparison with  $C_f$  for smooth plates after  $Rn_m > 30000$ . Fouled plates after 3 months of exposure exhibited a decrease in  $C_f$  values with increasing  $Rn_m$ , meaning that these surfaces did not yet reach fully rough flow regime. This could be attributed to the fact that maximum  $Rn_m$  of the performed hydrodynamic tests was too low for the achievement of fully rough flow regime. However, even not all fouled plates after 6 months of exposure (A6 and B6), which were tested at higher  $Rn_m$  values, did not reach fully rough flow regime, Figure 4.3. Therefore, this could be indicative of a fundamental change in flow regimes strongly related to percentage of surface coverage with biofilm than to biofilm thickness [133]. Thus, surfaces with a mean %SC above 25% displayed fully rough frictional behaviour, while surfaces with lower mean %SC did not and it therefore appeared that a fundamental flow regime change occurred for a surfaces with low %SC. Tested flat plates along with their biofilm thickness ( $k$ ), %SC, effective roughness length scale ( $k_{eff}$ ) and  $\Delta U^+$  model are shown in Table 4.3. It should be noted that  $k$  and %SC presented in Table 4.3 represent mean values taken from [133], while  $k_{eff}$  values represent round values obtained using equation (4.1). As said before, the fully rough flow regime is present once frictional resistance is almost entirely formed from drag due to the roughness presence, i.e. when viscous shear stress becomes negligible and therefore  $C_f$  or  $C_F$  is independent on  $Rn$ . Thus, it has appeared that once %SC < 25%, the viscous shear stress on the clean areas of the surface contributes to  $C_f$ , even at higher  $Rn_m$ . However, since the tested plates in the baseline condition were hydraulically smooth over the  $Rn_m$  range, for which the hydrodynamic tests were performed, it is uncertain if this would occur on surfaces with elevated baseline roughness [133].

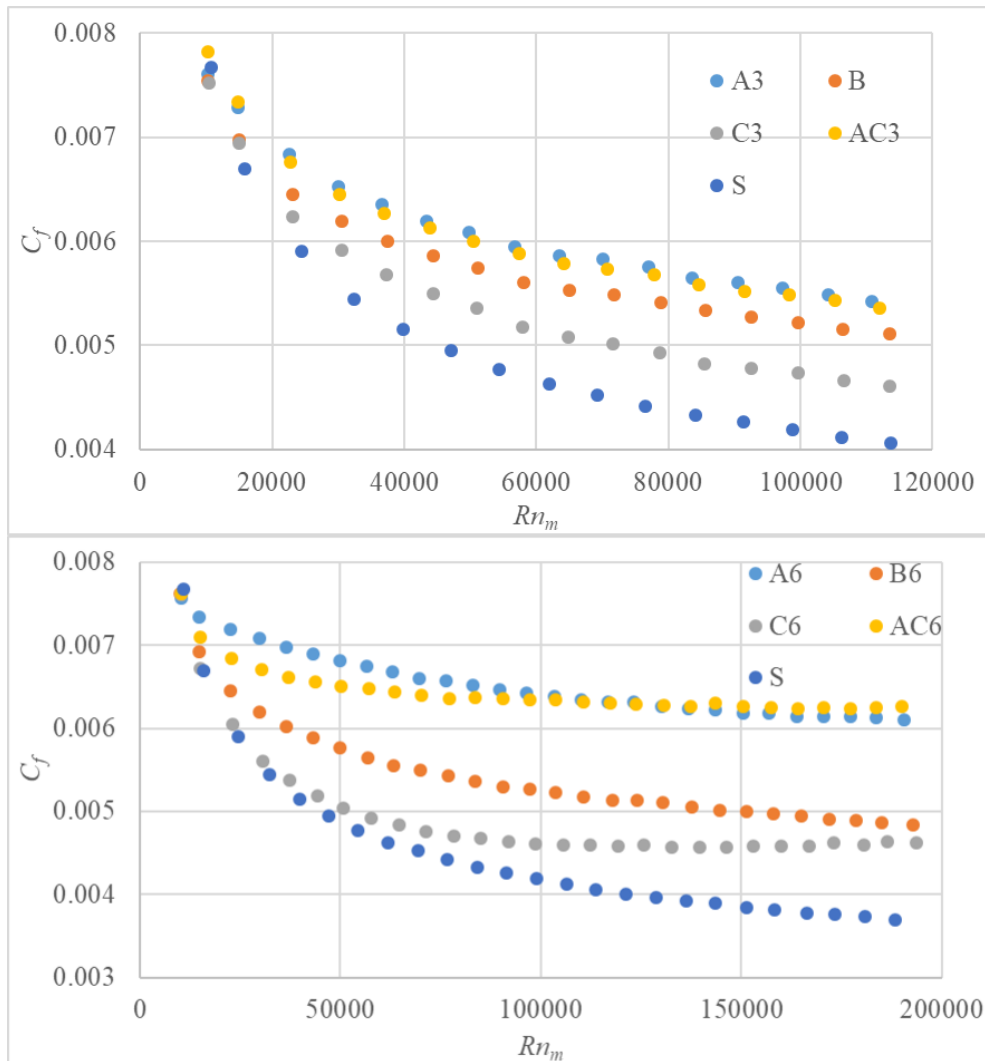


Figure 4.3 The experimentally obtained  $C_f$  for fouled flat plates after 3 months (upper) and 6 months (lower) of exposure [133]

Table 4.3 Tested fouled plates

Fouled plate	$k$ , $\mu\text{m}$	%SC, %	$k_{eff}$ , $\mu\text{m}$	$\Delta U^+$ model
A3	545	19.6	135	(4.3)
B3	443	11.8	85	(4.3)
C3	574	6.4	80	(4.4)
AC3	527	18.1	125	(4.3)
A6	520	14.2	108	/
B6	443	13.7	90	(4.3)
C6	98	49.2	35	(4.2)
AC6	392	27.8	115	(4.2)

After the determination of  $C_f$ , Schultz et al. [133] calculated  $\Delta U^+$  values with equation (2.17) using  $C_{fS}$  and  $C_{fR}$  at the same value of  $Rn_\tau$ . The plot of the obtained  $\Delta U^+$  values versus  $k^+$  defined using mean biofilm height has led to conclusion that  $k$  solely is not adequate for collapsing  $\Delta U^+$  values of biofilm covered surfaces into one function. Also,  $\Delta U^+$  shape has quite varied among the tested surfaces. In order to propose a single roughness length scale, which would be adequate for collapsing  $\Delta U^+$  values into one curve, only plates which reached fully rough flow regime are analysed, i.e. C6 and AC6. Thereafter, Schultz et al. [133] determined  $k_s$  using Nikuradse  $\Delta U^+$  model for fully rough flow regime. Thus, the obtained  $k_s$  for C6 is equal to  $35\mu\text{m}$  and for AC6 is equal to  $115\mu\text{m}$  and these values may be referred as very light slime and light slime if compared with the obtained  $k_s$  presented in [69]. However, it should be noted that within [133] biofilm was grown under dynamic conditions and before hydrodynamic tests all loosely attached biofilm was dislodged. On the other hand,  $k_s$  values presented in [69] were based on towing tank tests of statically immersed plates [123] and biofilms grown under static conditions tend to be thicker and with more uniform coverage than biofilms grown under dynamic conditions. Schultz et al. [133] have also proposed correlation between parameters  $k$  and %SC with  $k_s$ , i.e. they have proposed new effective roughness length scale for biofilm covered surfaces:

$$k_{eff} = 0.55k\sqrt{\%SC} \quad (4.1)$$

Using equation (4.1), with some easily measured parameters, the one can obtain roughness length scale without carrying out hydrodynamic tests. Thus,  $k^+$  is defined using  $k_{eff}$ . The plot of the obtained  $\Delta U^+$  values versus  $k^+$  for fouled plates with %SC > 25% is shown within Figure 4.4. Using  $\Delta U^+$  values presented in Figure 4.4 and the least squares method, a suitable  $\Delta U^+$  model is fitted:

$$\Delta U^+ = \begin{cases} \frac{1}{\kappa} \ln(0.27767k^+) & \text{for } k^+ \geq 3.61 \\ 0 & \text{for } k^+ < 3.61 \end{cases} \quad (4.2)$$

where  $\kappa$  is equal to 0.42.

The proposed  $\Delta U^+$  model, shown in equation (4.2), can be easily implemented within the wall function of CFD software package STAR-CCM+ [180]. As it can be seen from Figure 4.4, the proposed  $\Delta U^+$  model has excellent accordance with the experimentally obtained  $\Delta U^+$  values for higher  $k^+$  values, while for lower  $k^+$  values, the proposed  $\Delta U^+$  model reasonably corresponds the experimental data. However, in the range of  $k^+$  values from 2 to 4,  $\Delta U^+$  model underestimates the experimentally obtained  $\Delta U^+$  values, due to the fact that least squares method considered both experimentally obtained  $\Delta U^+$  values at higher and lower  $k^+$  values. This allowed the development of unique  $\Delta U^+$  model for both fouled surfaces with %SC > 25%, i.e. C6 and AC6. It should be noted that  $\tau_w$  values on the hull are typically above 50 Pa at design speed for most of unfouled ships. Since  $u_\tau$  for rough surfaces is higher than for smooth surfaces, the range of  $k^+$  values on the hull of full-scale ships are often above 4.5, even

for smaller  $k_{eff}$  values. Thus, it can be concluded that the proposed  $\Delta U^+$  model for biofilm covered surfaces with  $\%SC > 25\%$  can be used for reliable determination of the increase in frictional resistance for higher  $k^+$  values, which are common on full-scale ships during sailing.

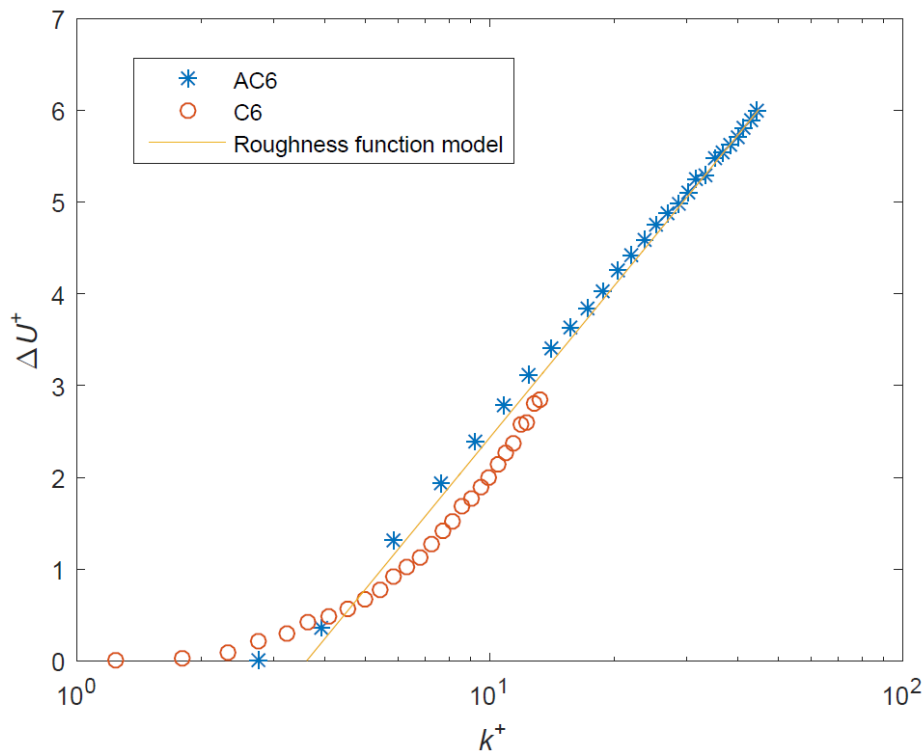


Figure 4.4 The comparison between the proposed  $\Delta U^+$  model and experimentally [133] obtained  $\Delta U^+$  values for  $\%SC > 25\%$  (adapted from [104])

While for surfaces covered with biofilm with  $\%SC > 25\%$ , the flow at higher  $Rn_m$  reaches fully rough flow regime, if  $\%SC < 25\%$  the flow in the patches between the islands of biofilm, relaxes to a state which is more similar to the flow over a smooth wall. In those areas, viscous stress is noticeable, even at higher  $Rn_m$  [133]. Consequently, the flow around surface covered with biofilm with  $\%SC < 25\%$  is more complex than the flow around surface covered with biofilm with  $\%SC > 25\%$  and  $\Delta U^+$  model will change. The uncertainty in the prediction of frictional resistance of surface covered with biofilm with  $\%SC < 25\%$  using proposed  $\Delta U^+$  models, shown with equations (4.3) and (4.4), is somewhat higher than for surfaces with  $\%SC > 25\%$  and  $\Delta U^+$  model shown with equation (4.2), as experimental data [133] for surfaces with  $\%SC < 25\%$  are scattered, Figure 4.5. It should be noted that  $k^+$  for surfaces with  $\%SC < 25\%$  is also defined using  $k_{eff}$ , even though  $k_{eff}$  is originally proposed for surfaces with  $\%SC > 25\%$ , as in [133]. Even though it appears that  $k_{eff}$  is ineffective in collapsing  $\Delta U^+$  values into one  $\Delta U^+$  model for all tested surfaces with  $\%SC < 25\%$ , Schultz et al. [133] concluded that this can be attributed to the three distinct  $\Delta U^+$  shapes that are presented by these surfaces covered with biofilm, rather than a shortcoming in  $k_{eff}$  as a scaling parameter. Three different  $\Delta U^+$  shapes are marked in Figure 4.5 with different symbols, i.e. \*, o and +. Furthermore, as said before the selection of roughness length scale will not affect the  $\Delta U^+$

value, but only the value of  $k^+$  (abscissa of  $\Delta U^+ = f(k^+)$ ). Therefore,  $k$  can be selected in a way that  $\Delta U^+$  values correspond to a predefined  $\Delta U^+$  model while the observed behaviours are still deemed appropriate relative to each other.

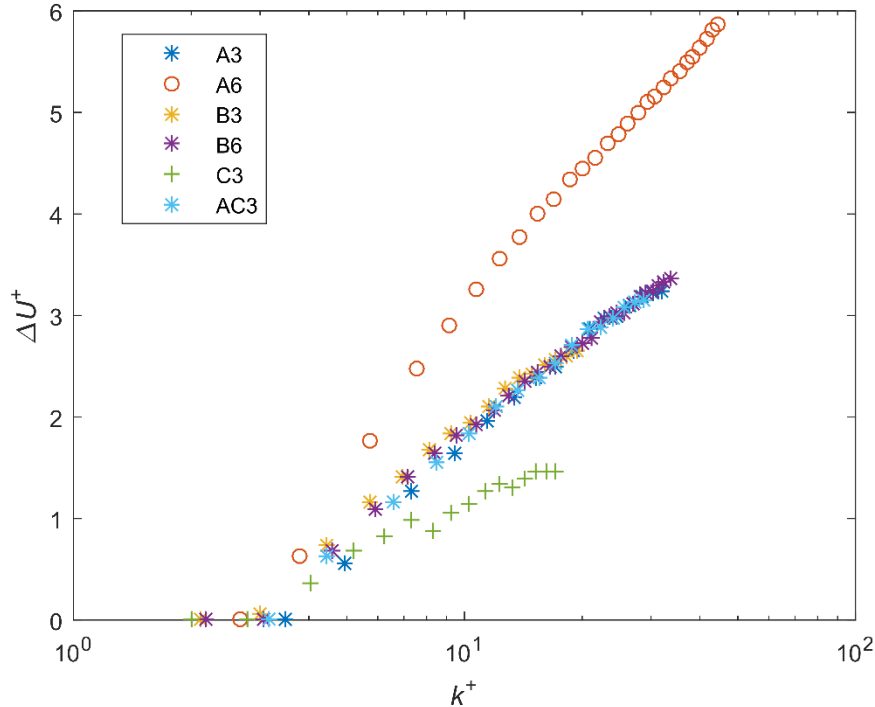


Figure 4.5 The plot of  $\Delta U^+$  versus  $k^+$  for surfaces with  $\%SC < 25\%$  (adapted from [104])

By considering Figure 4.5, it can be seen that the highest  $\Delta U^+$  slope is obtained for the fouled plate A6, although it does not have the highest  $\%SC$ , while the smallest  $\Delta U^+$  slope is obtained for the fouled plate B6, which has the smallest  $\%SC$ . The rest of the fouled plates with  $\%SC < 25\%$ , i.e. A3, B3, AC3 and B6, clearly display the same  $\Delta U^+$  behaviour, Figure 4.5. Therefore, in order to propose  $\Delta U^+$  model as accurate as possible, within this thesis two  $\Delta U^+$  models are proposed for surfaces with  $\%SC < 25\%$ , one for surfaces with  $10\% < \%SC < 25\%$ , and the other one for  $\%SC < 10\%$ .

$\Delta U^+$  model for surfaces with  $10\% < \%SC < 25\%$  is defined using experimentally obtained  $\Delta U^+$  values for fouled plates A3, B3, AC3 and B6 and the least squares method, Figure 4.6. This  $\Delta U^+$  model can be easily implemented within the wall function of CFD software package STAR-CCM+ and is defined with:

$$\Delta U^+ = \begin{cases} \frac{1}{\kappa} \ln(1.14492 + 0.0988k^+) & \text{for } k^+ \geq 4.5 \\ 0 & \text{for } k^+ < 4.5 \end{cases} \quad (4.3)$$

where  $\kappa$  is equal to 0.42.

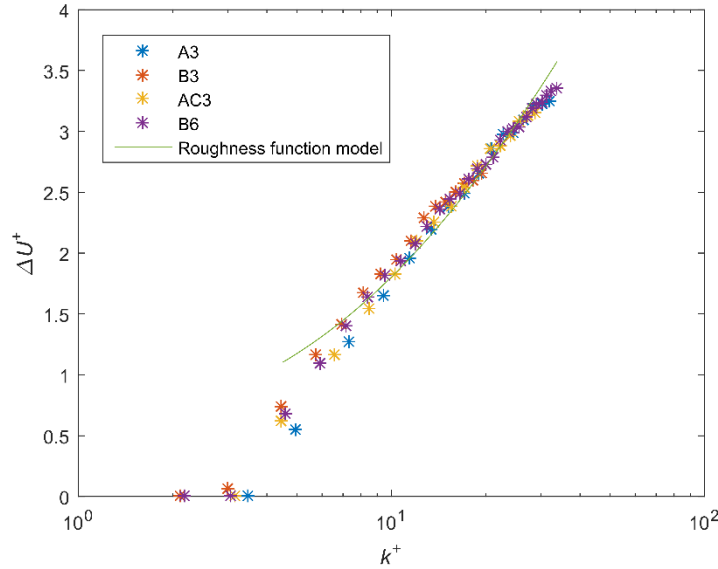


Figure 4.6 The comparison between the proposed  $\Delta U^+$  model and experimentally [133] obtained  $\Delta U^+$  values for  $10\% < \%SC < 25\%$  (adapted from [104])

The satisfactory agreement between  $\Delta U^+$  model presented with equation (4.3) and experimentally obtained  $\Delta U^+$  values for  $10\% < \%SC < 25\%$  is accomplished. Still, in the definition of  $\Delta U^+$  model presented with equation (4.3), experimentally obtained  $\Delta U^+$  values for fouled plate A6 are not taken into account and therefore this  $\Delta U^+$  model has higher uncertainty for assessment of the impact of biofilm on the frictional resistance than  $\Delta U^+$  model presented with equation (4.2). This was expected, as the flow around the surfaces covered with biofilm with  $\%SC < 25\%$  is more complex than the flow around the surfaces covered with biofilm with  $\%SC > 25\%$ , as discussed earlier. As claimed by Schultz et al. [133], the physical nature of the impact of biofilm on the frictional resistance is far from well understood and therefore for obtaining more reliable  $\Delta U^+$  model for surfaces covered with biofilm, additional drag characterization studies should be performed. Nevertheless, the proposed  $\Delta U^+$  model presented with equation (4.3) can be valuable in the determination of the increase in frictional resistance or resistance for biofilm covered surfaces with  $10\% < \%SC < 25\%$ . The obtained results of increase in the resistance can be considered as a minimal, since  $\Delta U^+$  values for the fouled plate A6 are higher than  $\Delta U^+$  values for the rest of fouled plates with  $10\% < \%SC < 25\%$ , Figure 4.5.

For surfaces covered with biofilm with  $\%SC < 10\%$ ,  $\Delta U^+$  model is defined using experimentally obtained  $\Delta U^+$  values for fouled plate C3 [133] and the least squares method:

$$\Delta U^+ = \begin{cases} \frac{1}{\kappa} \ln(1.06492 + 0.05332k^+) & \text{for } k^+ \geq 4 \\ 0 & \text{for } k^+ < 4 \end{cases} \quad (4.4)$$

where  $\kappa$  is equal to 0.42.

The satisfactory agreement between  $\Delta U^+$  model presented with equation (4.4) and experimentally obtained  $\Delta U^+$  values for  $\%SC < 10\%$  is accomplished, Figure 4.7.

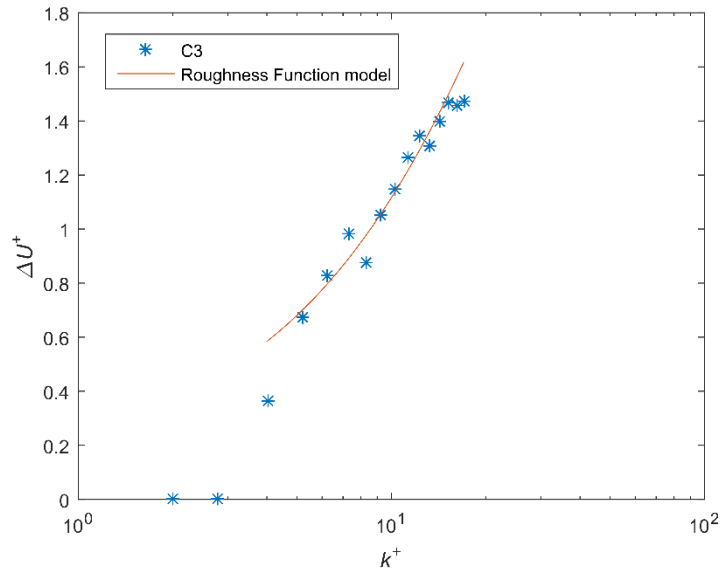


Figure 4.7 The comparison between the proposed  $\Delta U^+$  model and experimentally [133] obtained  $\Delta U^+$  values for %SC <10% (adapted from [104])

From Figure 4.4, Figure 4.6 and Figure 4.7 it can be identified that the highest relative deviations between  $\Delta U^+$  values obtained using the proposed  $\Delta U^+$  models and experimentally obtained  $\Delta U^+$  values are present for lower  $k^+$  values. Namely,  $\Delta U^+$  model given with equation (4.2) for  $k^+ < 4$  underestimates experimentally obtained  $\Delta U^+$  values. On the other hand,  $\Delta U^+$  models given with equations (4.3) and (4.4) at lower  $k^+$  values overestimate the experimentally obtained  $\Delta U^+$  values. As already mentioned,  $k^+$  values on the hull surfaces of full-scale ships at design speed are often above 4.5 even for smaller  $k_{eff}$  values. What is more, even if lower  $k^+$  values are present, the increase in the frictional resistance will be almost negligible, as  $\Delta U^+$  values for lower  $k^+$  values are very low. Accordingly, the proposed  $\Delta U^+$  models can be used for reliable determination of the increase in frictional resistance.

#### 4.1.4. CFD model for simulation of biofilm effects on the flow around biofilm covered surface – validation

In order to develop CFD model which can account for biofilm effects on the flow around biofilm covered surface, the proposed  $\Delta U^+$  models, shown with equations (4.2), (4.3) and (4.4) are implemented within the wall function of CFD solver. All CFD simulations are therefore performed with the application of wall functions. After the implementation, CFD simulations of the flow in TCF facility are prepared in order to numerically simulate the performed experiments [133] at several  $Rn$  values. Thereafter, verification and validation studies are performed and finally validation uncertainties are compared with the obtained relative deviations from experimental results.

Computational domain is consisted of TCF facility test section, shown in Figure 4.2. The flow within TCF facility is modelled as a steady phenomenon and therefore unsteady term in equation (3.1) is equal to zero. Details related to numerical model are shown in Section 3. The applied boundary conditions are shown in Figure 4.8.

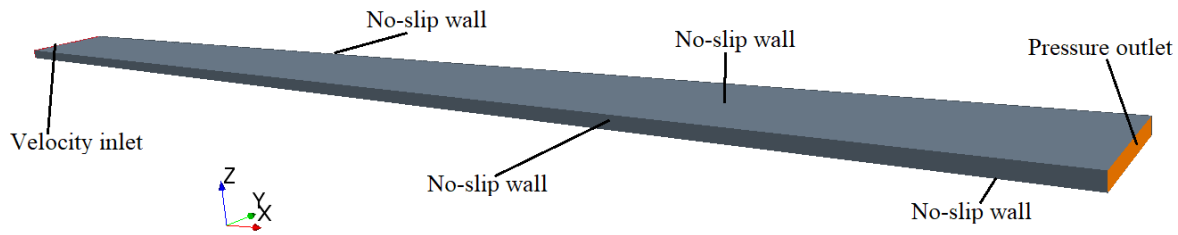


Figure 4.8 The applied boundary conditions in CFD simulations of TCF

The computational domain is discretized using unstructured hexahedral mesh and for the purpose of verification study, three meshes are made, i.e. coarse, medium and fine. Since plates which were exposed for 3 months were tested in  $Rn_m$  range from 10000 to 110000, plates which were exposed for 6 months in the range from 10000 to 190000 and smooth plates in the range from 10000 to 300000, CFD simulations for fouled plates after 3 months of exposure are performed for four  $Rn_m$ , while for fouled plates after 6 months of exposure and smooth plates for seven  $Rn_m$ . Thus, CFD simulations of TCF for plates A3, B3, C3 and AC3 are performed for bulk mean velocities ( $\bar{U}$ ) equal to 1, 2, 3 and 4 m/s, while CFD simulations of TCF for plates S, B6, C6 and AC6 for  $\bar{U}$  equal to 1, 2, 3, 4, 5, 6 and 7 m/s. Depending on  $Rn_m$ , i.e.  $\bar{U}$ , the number of cells used for coarse (0.35-0.5 M), medium (0.7-1 M) or fine mesh (1.4-2 M) has varied, because of the different discretization of near wall mesh. Cut-cell grid with prism layer mesh on the walls is used, with a goal to ensure that  $y^+$  value of the first cell near the wall is around 50, as recommended within [110] for both smooth and rough plates. Also, for rough plates the first cell height is set to be higher than  $2k_{eff}$ , i.e.  $y^+ > k^+$ , because otherwise  $C_F$  would be underestimated [175]. Therefore, the mesh generation is done carefully for each  $Rn_m$  and transition from prism layer cells to the core mesh is made appropriately, Figure 4.9. The obtained  $y^+$  distribution at the upper plate, B3 for TCF at  $Rn_m = 107527$  is shown in Figure 4.10.

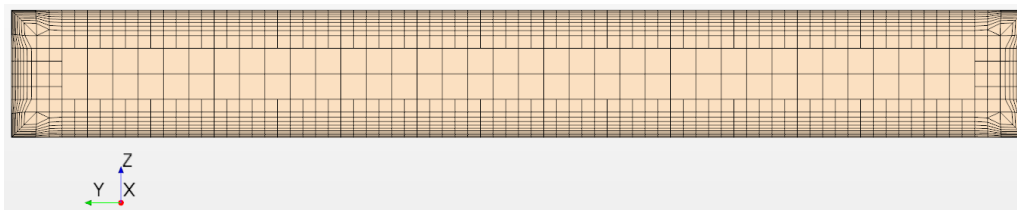


Figure 4.9 The cross section of the fine mesh used in CFD simulations of TCF (adapted from [104])

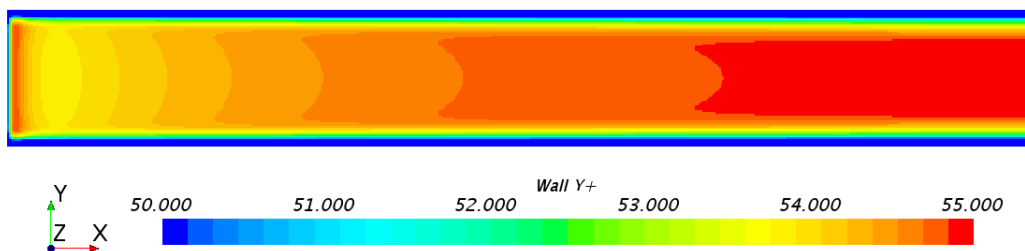


Figure 4.10 The obtained  $y^+$  distribution at B3 plate in TCF at  $Rn_m = 107527$



The verification study is carried out for all tested plates at all  $Rn_m$  and grid uncertainty is calculated using GCI method. It is performed for frictional resistance and the obtained results are presented in Table 4.4,

Table 4.5 and Table 4.6. As can be seen from these tables, the obtained grid uncertainties are relatively low with the highest  $GCI_{\text{fine}}^{21}$  obtained for C3 at the lowest  $\bar{U}$  and it equals to 3.3%. Generally, higher  $GCI_{\text{fine}}^{21}$  are obtained at lower  $\bar{U}$ , which is in accordance with experimental uncertainty. CFD simulations of TCF are stopped after 1000 iterations when all residuals dropped at least eight orders of magnitude. Therefore, iterative uncertainty is considered as negligible and grid uncertainty is equal to numerical uncertainty since CFD simulations of TCF are performed as steady simulations.

After an extensive verification study, the validation study is performed by comparison with the experimental results published in [133]. Thus, numerically obtained frictional resistance coefficients for plates ( $C_{f,\text{CFD}}$ ) are compared with experimentally obtained ones ( $C_{f,\text{EXP}}$ ). It should be noted that  $C_{f,\text{CFD}}$  are calculated using  $\phi_{\text{ext}}^{21}$  solution, while  $RD$  are calculated using equation (3.39). The validation study is performed for all tested plates at all  $Rn_m$  and the obtained results are presented in Table 4.7, Table 4.8 and Table 4.9. Within these tables,  $U_v$  calculated with equation (3.40) are shown. Experimental uncertainty for  $\bar{U} = 1$  m/s is calculated using linear interpolation of the reported  $U_D$  values [133] and it is equal to 4.2%. For other  $\bar{U}$  values,  $U_D$  is equal to 1.2%, as reported in [133].

As can be seen from Table 4.7, Table 4.8 and Table 4.9, the obtained  $RD$  are very low and mainly below 1.5%. For smooth plate, the highest  $RD$  is obtained for  $\bar{U} = 7$  m/s and it is equal to 1.2%. All obtained  $RD$  for smooth plate are lower than  $U_v$  and therefore the validation is achieved at  $U_v$  level for all tested  $Rn_m$ . The obtained results of validation study for plates which were exposed for 3 months are presented within Table 4.9. It can be seen that the obtained  $RD$  are lower than 1.5% for all tested plates at all  $Rn_m$ . All obtained  $RD$  for plates which were exposed for 3 months are lower than  $U_v$  and therefore the validation is achieved at  $U_v$  level for all tested  $Rn_m$ , except for B3 at  $\bar{U} = 3$  m/s. Namely the highest  $RD$  for plates which were exposed for 3 months is obtained for B3 at  $\bar{U} = 3$  m/s and it is equal to -1.532% and this value is slightly above  $U_v$ , which is equal to 1.276%. The obtained results of validation study for plates which were exposed for 6 months are presented within Table 4.8. It can be seen that the obtained  $RD$  are lower than 3.25% for all tested plates at all  $Rn_m$ . For plate B6, the obtained  $RD$  are lower than 1.25% at all  $Rn_m$  and lower than  $U_v$ . Therefore, the validation is achieved at  $U_v$  level for all tested  $Rn_m$  for plate B6. For plate C6 slightly higher  $RD$  are obtained, however they are lower than 2% except at  $\bar{U} = 4$  m/s, where the highest  $RD$  is obtained and it is equal to 3.246%. The validation for plate C6 is achieved at  $U_v$  level for all tested  $Rn_m$ , except at  $\bar{U} = 4$  m/s and  $\bar{U} = 5$  m/s, where the obtained  $RD$  are slightly higher than  $U_v$ . For plate AC6 the obtained  $RD$  are lower than 1% and therefore lower than  $U_v$  as well at all tested

$\bar{U}$ , except at  $\bar{U} = 7$  m/s, where the obtained  $RD$  is equal to -1.931%. Thus, the validation is achieved at  $U_v$  level for all tested  $\bar{U}$  for plate AC6, except at  $\bar{U} = 7$  m/s, where  $RD$  is slightly higher than  $U_v$ .

Table 4.4 The verification study for smooth plate

$\bar{U}$ , m/s	$\phi_3$ , N	$\phi_2$ , N	$\phi_1$ , N	$p_a$	$\phi_{ext}^{21}$ , N	$GCI_{fine}^{21}$ , %
1	0.8461	0.8535	0.8571	2.120	0.8646	1.102
2	2.8743	2.8924	2.9009	1.981	2.9197	0.814
3	5.9169	5.9472	5.9588	2.968	5.9738	0.316
4	9.7968	9.9417	9.9535	9.559	9.9557	0.028
5	14.7548	14.8199	14.8355	5.081	14.8444	0.075
6	20.4482	20.5495	20.5595	8.734	20.5617	0.013
7	26.9637	27.1136	27.1205	11.895	27.1212	0.003

Table 4.5 The verification study for B6, C6 and AC6

B6						
$\bar{U}$ , m/s	$\phi_3$ , N	$\phi_2$ , N	$\phi_1$ , N	$p_a$	$\phi_{ext}^{21}$ , N	$GCI_{fine}^{21}$ , %
1	0.9487	0.9538	0.9584	2.883	0.9649	0.850
2	3.3700	3.3913	3.4022	1.351	3.4369	1.274
3	7.1761	7.2254	7.2434	2.750	7.2685	0.434
4	12.3724	12.4556	12.4802	3.609	12.5041	0.239
5	18.8600	19.0091	19.0328	6.406	19.0419	0.059
6	26.6982	26.9099	26.9294	8.592	26.9335	0.019
7	35.7962	36.1067	36.0652	7.864	36.0547	0.036
C6						
$\bar{U}$ , m/s	$\phi_3$ , N	$\phi_2$ , N	$\phi_1$ , N	$p_a$	$\phi_{ext}^{21}$ , N	$GCI_{fine}^{21}$ , %
1	0.8461	0.8535	0.8571	2.114	0.8647	1.107
2	2.9050	2.9253	2.9357	1.335	2.9693	1.428
3	6.4200	6.4614	6.4779	2.409	6.5052	0.526
4	11.3603	11.4341	11.4569	3.448	11.4803	0.256
5	17.6195	17.7537	17.7752	6.386	17.7834	0.058
6	25.2516	25.4464	25.4639	8.686	25.4675	0.018
7	34.1703	34.4631	34.4445	10.626	34.4421	0.009
AC6						
$\bar{U}$ , m/s	$\phi_3$ , N	$\phi_2$ , N	$\phi_1$ , N	$p_a$	$\phi_{ext}^{21}$ , N	$GCI_{fine}^{21}$ , %
1	0.9835	0.9905	0.9941	0.924	1.0132	2.391
2	3.8469	3.8747	3.8891	1.289	3.9375	1.554
3	8.5504	8.6224	8.6471	3.008	8.6778	0.444
4	15.1214	15.2481	15.2849	3.685	15.3196	0.284
5	23.4178	23.648	23.6856	6.312	23.7002	0.077
6	33.5345	33.858	33.861	17.372	33.8611	0.000
7	45.3282	45.7927	45.6289	4.209	45.5078	0.332

Table 4.6 The verification study for plates A3, B3, C3 and AC3

A3						
$\bar{U}$ , m/s	$\phi_3$ , N	$\phi_2$ , N	$\phi_1$ , N	$p_a$	$\phi_{ext}^{21}$ , N	$GCI_{fine}^{21}$ , %
1	0.9839	0.9905	0.9938	1.044	1.009	1.908
2	3.5417	3.5649	3.5769	1.357	3.6144	1.313
3	7.6014	7.6568	7.6766	2.860	7.7027	0.426
4	13.1768	13.2718	13.2992	3.701	13.3249	0.242
B3						
$\bar{U}$ , m/s	$\phi_3$ , N	$\phi_2$ , N	$\phi_1$ , N	$p_a$	$\phi_{ext}^{21}$ , N	$GCI_{fine}^{21}$ , %
1	0.9403	0.9470	0.9531	2.668	0.9624	1.225
2	3.3496	3.3707	3.3815	1.348	3.4159	1.272
3	7.1248	7.1734	7.1912	2.738	7.2162	0.435
4	12.2743	12.3561	12.3804	3.599	12.404	0.239
C3						
$\bar{U}$ , m/s	$\phi_3$ , N	$\phi_2$ , N	$\phi_1$ , N	$p_a$	$\phi_{ext}^{21}$ , N	$GCI_{fine}^{21}$ , %
1	0.8949	0.9036	0.9081	0.906	0.9323	3.324
2	3.1455	3.1645	3.1726	2.085	3.1880	0.607
3	6.5899	6.6322	6.6479	2.663	6.6709	0.432
4	11.2623	11.3317	11.3527	3.532	11.3736	0.230
AC3						
$\bar{U}$ , m/s	$\phi_3$ , N	$\phi_2$ , N	$\phi_1$ , N	$p_a$	$\phi_{ext}^{21}$ , N	$GCI_{fine}^{21}$ , %
1	0.9764	0.9829	0.9861	1.048	1.001	1.888
2	3.5052	3.5280	3.5397	1.358	3.5766	1.302
3	7.5120	7.5660	7.5854	2.835	7.6114	0.428
4	13.0088	13.1012	13.1281	3.682	13.1534	0.241

Table 4.7 The validation study for smooth plate

$\bar{U}$ , m/s	$Rn_m$	$10^3 C_{f,CFD}$	$10^3 C_{f,EXP}$	$RD$ , %	$U_V$ , %
1	26882	5.703	5.762	-1.023	4.342
2	53763	4.814	4.789	0.531	1.450
3	80645	4.378	4.381	-0.065	1.241
4	107527	4.104	4.131	-0.659	1.200
5	134409	3.916	3.927	-0.281	1.202
6	161290	3.767	3.800	-0.861	1.200
7	188172	3.651	3.695	-1.200	1.200

Table 4.8 The validation study for B6, C6 and AC6

B6					
$\bar{U}$ , m/s	$Rn_m$	$10^3 C_{f,CFD}$	$10^3 C_{f,EXP}$	$RD$ , %	$U_v$ , %
1	26882	6.364	6.288	1.210	4.285
2	53763	5.667	5.694	-0.481	1.750
3	80645	5.327	5.394	-1.250	1.276
4	107527	5.154	5.183	-0.561	1.224
5	134409	5.024	5.076	-1.036	1.201
6	161290	4.934	4.976	-0.828	1.200
7	188172	4.853	4.839	0.291	1.201
C6					
$\bar{U}$ , m/s	$Rn_m$	$10^3 C_{f,CFD}$	$10^3 C_{f,EXP}$	$RD$ , %	$U_v$ , %
1	26882	5.703	5.805	-1.766	4.344
2	53763	4.896	4.976	-1.600	1.865
3	80645	4.767	4.723	0.945	1.310
4	107527	4.732	4.584	3.246	1.227
5	134409	4.692	4.599	2.019	1.201
6	161290	4.666	4.611	1.198	1.200
7	188172	4.636	4.640	-0.089	1.200
AC6					
$\bar{U}$ , m/s	$Rn_m$	$10^3 C_{f,CFD}$	$10^3 C_{f,EXP}$	$RD$ , %	$U_v$ , %
1	26882	6.682	6.748	-0.971	4.833
2	53763	6.492	6.483	0.148	1.963
3	80645	6.359	6.39	-0.485	1.279
4	107527	6.315	6.298	0.262	1.233
5	134409	6.253	6.275	-0.357	1.202
6	161290	6.204	6.236	-0.515	1.200
7	188172	6.125	6.246	-1.931	1.245

It can be concluded that satisfactory agreement between numerical and experimental  $C_f$  is obtained for all tested  $Rn_m$ . In addition to, the proposed CFD model, as well as proposed  $\Delta U^+$  models, can correctly assess the impact of biofilm on the increase in  $C_f$  even for surfaces covered with biofilm, which have small difference in  $k_{eff}$ . Thus, CFD model successfully predicted the differences in  $C_f$  between plates A3 ( $k_{eff} = 135 \mu\text{m}$ ) and AC3 ( $k_{eff} = 125 \mu\text{m}$ ), as well as between plates B3 ( $k_{eff} = 85 \mu\text{m}$ ) and B6 ( $k_{eff} = 90 \mu\text{m}$ ). It should be noted that plates A3, AC3, B3 and B6 have  $10\% < \%SC < 25\%$ , i.e. the same  $\Delta U^+$  model (4.3). Thus, it can be seen from Table 4.8 and Table 4.9 that  $C_f$  increases with the increase in  $k_{eff}$ , if the same  $\Delta U^+$  model is used. Another important part of the validation of the proposed CFD model, for simulation of biofilm effects on the flow around biofilm covered surface, is to examine whether CFD model can reliably determine  $k^+$ . Namely, this is substantial as  $\Delta U^+$  depends solely on

$k^+$  and if  $k^+$  is determined accurately,  $C_f$  or  $C_F$  will be also accurately determined [110]. In CFD simulations,  $u_\tau$  distribution even on the flat plate surface is not uniform and this can be seen in Figure 4.11. Therefore,  $k^+$  values along the surface vary as well, which represents a valuable benefit in comparison with Granville similarity law scaling method and because of this, the impact of roughness on any arbitrary body is more accurately assessed using CFD than Granville similarity law scaling method [188].

Table 4.9 The validation study for plates A3, B3, C3 and AC3

A3					
$\bar{U}$ , m/s	$Rn_m$	$10^3 C_{f,CFD}$	$10^3 C_{f,EXP}$	$RD$ , %	$U_v$ , %
1	26882	6.655	6.652	0.034	4.613
2	53763	5.960	6.012	-0.871	1.779
3	80645	5.645	5.695	-0.878	1.273
4	107527	5.493	5.439	0.996	1.224
B3					
$\bar{U}$ , m/s	$Rn_m$	$10^3 C_{f,CFD}$	$10^3 C_{f,EXP}$	$RD$ , %	$U_v$ , %
1	26882	6.348	6.292	0.884	4.375
2	53763	5.632	5.695	-1.105	1.749
3	80645	5.288	5.371	-1.532	1.276
4	107527	5.113	5.130	-0.328	1.223
C3					
$\bar{U}$ , m/s	$Rn_m$	$10^3 C_{f,CFD}$	$10^3 C_{f,EXP}$	$RD$ , %	$U_v$ , %
1	26882	6.149	6.058	1.504	5.356
2	53763	5.257	5.289	-0.617	1.345
3	80645	4.889	4.890	-0.021	1.275
4	107527	4.688	4.642	0.995	1.222
AC3					
$\bar{U}$ , m/s	$Rn_m$	$10^3 C_{f,CFD}$	$10^3 C_{f,EXP}$	$RD$ , %	$U_v$ , %
1	26882	6.602	6.576	0.406	4.605
2	53763	5.897	5.948	-0.848	1.770
3	80645	5.578	5.624	-0.816	1.274
4	107527	5.422	5.395	0.495	1.224

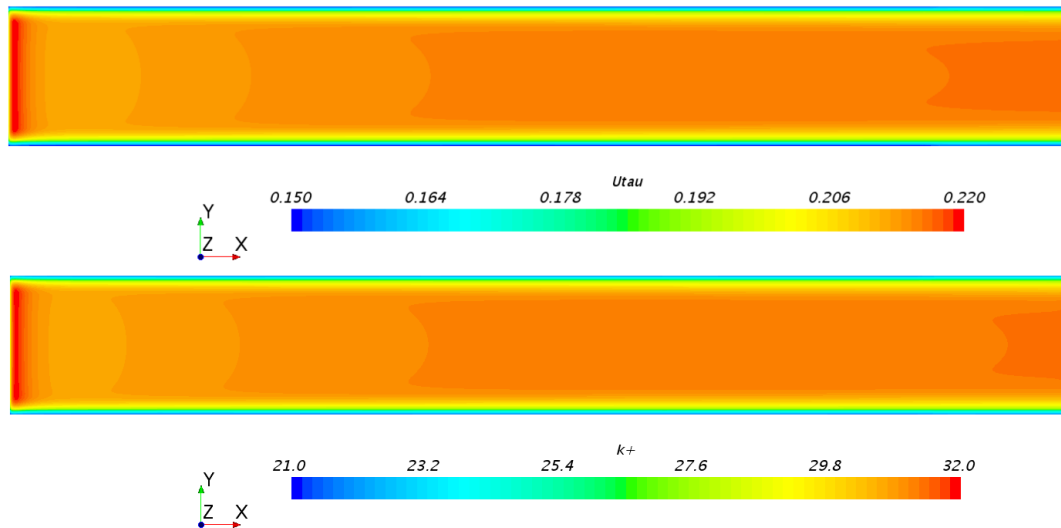


Figure 4.11 The obtained  $u_\tau$  (upper) and  $k^+$  (lower) distributions for plate A3 at  $\bar{U} = 4$  m/s

The comparison between numerically ( $k_{CFD}^+$ ) and experimentally ( $k_{EXP}^+$ ) obtained  $k^+$  values for fouled plates is shown in Figure 4.12 (for plates which were exposed for 3 months) and in Figure 4.13 (for plates which were exposed for 6 months). As,  $k^+$  values vary along the plate,  $k_{CFD}^+$  is obtained as the average value of the obtained  $k^+$  values at the plate surface.  $k_{EXP}^+$  is obtained combining equations (2.10) and (2.22). Furthermore, the comparison between  $k_{CFD}^+$  and  $k_{EXP}^+$  along with the obtained  $RD$  is presented within

Table 4.10. It should be noted that  $k_{CFD}^+$  is calculated using fine mesh. The obtained  $RD$  are very low and the highest  $RD$  is obtained for AC6 for the lowest tested  $\bar{U} = 1$  m/s and it is equal to -1.837%. Experimental uncertainty for the prediction of  $k_{EXP}^+$  is the same as for prediction of  $C_f$ , as  $k_{EXP}^+$  is determined using  $C_f$ . Since  $U_D$  at the lowest tested  $\bar{U}$  is equal to 4.2%, and for other  $\bar{U}$  is equal to 1.2%, it is evident that the obtained  $RD$  are mostly below  $U_D$  values. Therefore, it can be concluded that  $k^+$  for surfaces covered with biofilm can be determined correctly using the proposed CFD model for a given  $k_{eff}$ . Since  $k^+$  values are well predicted utilizing the proposed CFD model, correct  $\Delta U^+$  values will be utilized for the assessment of the impact of biofilm on the flow. Also, it is shown that the proposed CFD model can accurately predict the increase in  $C_f$  due to the presence of biofilm even if surfaces have small differences in  $k_{eff}$ . Therefore, the proposed CFD model, as well as proposed  $\Delta U^+$  models, can be used for reliable assessment of the impact of biofilm on the flow around any immersed surface covered with biofilm [104]. This assessment can be made using the surface roughness measurements, i.e. biofilm thickness and percentage of surface coverage, rather than determining roughness length scale by hydrodynamic tests. However, it should be noted that before drawing any definitive conclusion regarding the assessment of the impact of biofilm on the flow, further experimental studies are needed, considering the deficiency of the experimental data concerning these effects. The proposed CFD model, i.e.  $\Delta U^+$  models, can be considered as a robust model,

which can be utilised for the assessment of the diatomaceous biofilm based on the available experimental data.

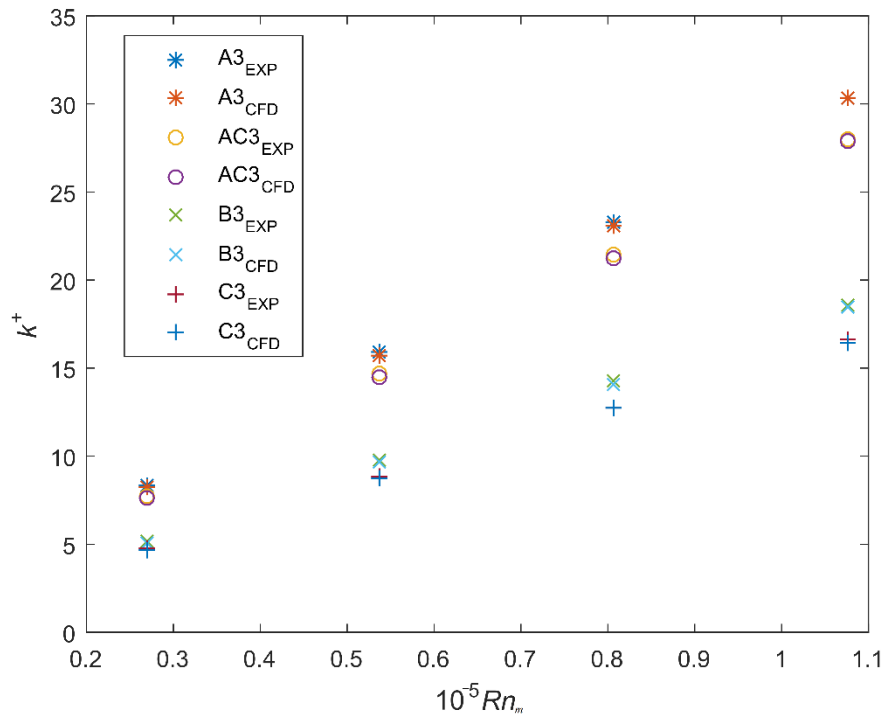


Figure 4.12 The comparison between  $k_{CFD}^+$  and  $k_{EXP}^+$  for plates that were exposed for 3 months (adapted from [104])

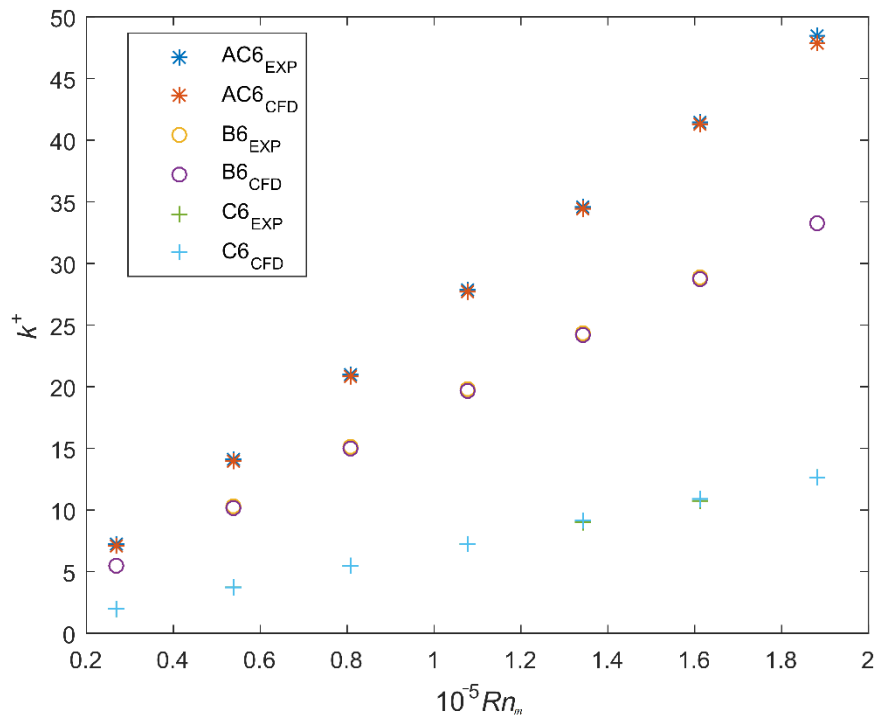


Figure 4.13 The comparison between  $k_{CFD}^+$  and  $k_{EXP}^+$  for plates that were exposed for 6 months (adapted from [104])

Table 4.10 The comparison between  $k_{CFD}^+$  and  $k_{EXP}^+$

Plate	A3			B3		
$\bar{U}$ , m/s	$k_{CFD}^+$	$k_{EXP}^+$	$RD$ , %	$k_{CFD}^+$	$k_{EXP}^+$	$RD$ , %
1	8.288	8.373	-1.008	5.110	5.137	-0.516
2	15.728	15.913	-1.161	9.629	9.750	-1.241
3	23.045	23.244	-0.853	14.044	14.238	-1.361
4	30.336	30.321	0.050	18.429	18.551	-0.655
Plate	C3			AC3		
$\bar{U}$ , m/s	$k_{CFD}^+$	$k_{EXP}^+$	$RD$ , %	$k_{CFD}^+$	$k_{EXP}^+$	$RD$ , %
1	4.695	4.740	-0.931	7.645	7.713	-0.885
2	8.778	8.848	-0.786	14.488	14.655	-1.145
3	12.709	12.774	-0.505	21.211	21.405	-0.904
4	16.424	16.600	-1.058	27.908	27.952	-0.157
Plate	B6			C6		
$\bar{U}$ , m/s	$k_{CFD}^+$	$k_{EXP}^+$	$RD$ , %	$k_{CFD}^+$	$k_{EXP}^+$	$RD$ , %
1	5.427	5.431	-0.082	1.997	2.030	-1.673
2	10.227	10.331	-1.011	3.695	3.760	-1.722
3	14.924	15.077	-1.016	5.488	5.469	0.333
4	19.592	19.738	-0.743	7.299	7.218	1.127
5	24.199	24.384	-0.758	9.093	8.995	1.092
6	28.786	28.922	-0.470	10.884	10.811	0.679
7	33.311	33.311	-0.002	12.66	12.686	-0.206
Plate	AC6					
$\bar{U}$ , m/s	$k_{CFD}^+$	$k_{EXP}^+$	$RD$ , %			
1	7.060	7.192	-1.837			
2	13.969	14.091	-0.869			
3	20.833	20.93	-0.461			
4	27.702	27.816	-0.409			
5	34.491	34.606	-0.330			
6	41.237	41.445	-0.502			
7	47.860	48.409	-1.135			

## 4.2. Roughness function model for hard fouling

### 4.2.1. Hard fouling

Generally, biofouling can be classified into microfouling and macrofouling. As said before, the occurrence of microfouling, i.e. biofilm, is inevitable regardless of the applied AF coating and this is even more highlighted for FR coatings as those coatings are non-biocidal and require shear stress to keep immersed surface without biofouling [71]. The presence of microfouling on the immersed surface will foster the rate of macrofouling on that immersed surface. Macrofouling is usually of greater concern for marine structures than microfouling, due to its larger impact on the performance [29]. In addition, biofouling and therefore macrofouling as well, can be classified into soft and hard fouling. Soft fouling is consisted of both microfouling and macrofouling, i.e. of both biofilm and grass [40]. While hard species have a solid skeleton,



for example shell or a calcareous tube, which protects the body within, soft species have no such protection. The texture of soft organisms, i.e. seaweed, hydroid, soft coral, sponge and anemone, can vary a lot from quite flexible to very rigid bodies. Hard fouling has rigid texture and it can be consisted of mussels, barnacles, oysters, tubeworms and encrusting sponges [29]. The dominant forms of hard fouling are barnacles and tubeworms [40]. Together soft and hard fouling form a composite fouling, which is usually present at hull surface after long immobile periods. Macrofouling, in particular hard fouling has significantly higher adhesion strength than microfouling [221]. Barnacles have three phases of adhesion: temporary in which the cypris larva explores a surface, thereafter the larva produces a settlement cement and lastly the metamorphosed adult barnacle produces a stronger cement which leads to permanent settlement [221]. Therefore, once barnacles are settled, without application of external forces related to grooming or cleaning barnacles cannot be removed or dislodged. Hard fouling forms rigid structures on immersed surfaces and thus drag characterization of such surface is simpler than for flexible structures.

#### 4.2.2. Experiments in towing tank

Schultz [123] has carried out experimental study in order to investigate the impact of various coating conditions on the frictional resistance. He performed a drag characterization study for five ship hull coatings in the unfouled, fouled and cleaned conditions. Thus, he tested two polydimethylsiloxane (PDMS) silicone coatings (SIL 1 and SIL2), ablative copper coating (ABC) and two self-polishing copolymer (SPC) coatings, one based on copper and other based on TBT. AF coatings were applied according to the suggestion of coating manufacturer, i.e. firstly the surfaces of tested flat plates were adequately prepared, thereafter primer and tie-coat were applied and finally AF coatings were applied. Additionally, Schultz has tested three control surfaces, i.e. polished smooth flat plate and flat plate covered with 60-grit and 220-grit wet/dry sandpaper. Only plates coated with AF coatings were tested in three conditions, while control surfaces were tested only in unfouled conditions, i.e. prior to immersion. Since within this thesis the impact of hard fouling is analysed, more details regarding the fouled conditions are provided while the details regarding testing in unfouled and cleaned condition can be found in [123]. Immersion of plates coated with AF coatings was performed near the confluence of the Severn River and the Chesapeake Bay (Annapolis, Maryland, USA) for 287 days. The plates were held vertically at 0.2 m below the mean low water level, the water temperature at the exposure site ranged from 1–27 °C and salinity from 4–10 ppt during the immersion period. After the immersion, the fouling coverage was evaluated according to American Society for Testing and Materials (ASTM) [222] and is presented in Table 4.11.

After the immersion, the drag characterization of fouled plates was performed in the towing tank facility at the USNA Hydromechanics Laboratory. The main dimensions of towing tank are length of 115 m, width 7.9 m and depth 4.9 m. The towing velocity was varied between 2 and 3.8 m/s, leading to  $Rn$  range  $(2.8–5.5) \cdot 10^6$  and the precision uncertainty for the mean velocity measurement was 0.02% over the tested velocity range. The towing tank experiments were performed in fresh water and water temperature was monitored to within  $\pm 0.05$  °C during experiments. As claimed by Schultz [123] before and after the hydrodynamic testing of fouled plates there were no visual difference in fouling and invertebrate organisms remained alive. Furthermore, as the salinity of estuarine water was low, Schultz claimed that testing in fresh water did not caused undue stress on the fouling or had significant influence on the obtained results. The plates used in towing tank testing were made of stainless steel and had length equal

to 1.52 m, height 0.76 m and width 3.2 mm with filleted leading and trailing edges to a radius of 1.6 mm. During towing tank tests, turbulence was not stimulated, and precise alignment of the plate is ensured with side force. For each plate and  $Rn$ , towing tank tests were repeated thrice and the obtained frictional resistance of two faces of plate ( $L = 1.52$  m and  $T = 0.565$  m) are calculated as the means of these three tests.

Table 4.11 Plates after immersion period, fouling coverages [123]

AF coating	Total fouling coverage, %	Surface coverage with slime, %	Surface coverage with hydroids, %	Surface coverage with barnacles (%SC), %	Height of the largest barnacle ( $R_t$ ), mm	Fouling description
ABC	76	75	0	1	5	Dense layer of diatomaceous and bacterial slime with very isolated barnacles
SPC copper (SPC)	73	65	3	4	5	Moderate layer of diatomaceous and bacterial slime with isolated barnacles
SPC TBT	70	70	0	0	0	Light layer of diatomaceous and bacterial slime
SIL 1	75	10	5	60	6	Uniform coverage of barnacles
SIL 2	95	15	5	75	7	Uniform coverage of barnacles

Experimental uncertainty in the determination of the measured quantities was calculated using the method presented in [220]. The overall experimental uncertainty in the determination of  $C_F$  was equal to  $\pm 5\%$  at  $Rn = 2.8 \cdot 10^6$  and  $\pm 2\%$  at  $Rn = 5.5 \cdot 10^6$ . The overall experimental uncertainty in the determination of  $\Delta U^+$  was equal to  $\pm 16\%$  or  $\pm 0.2$ , whichever was greater at  $Rn = 2.8 \cdot 10^6$  and  $\pm 6\%$  or  $\pm 0.1$ , whichever was greater at  $Rn = 5.5 \cdot 10^6$ . The overall uncertainty for other  $Rn$  within tested range was estimated using linear interpolation of the reported  $U_D$  values for these two  $Rn$ . Thus, the overall experimental uncertainty in the determination of  $C_F$  is equal to  $\pm 3.5\%$  at  $Rn = 4.2 \cdot 10^6$ .

#### 4.2.3. Roughness length scale and roughness function for hard fouling

Schultz [123] has determined frictional coefficients for unfouled, fouled and cleaned plates after 287 days of exposure. Since for the determination of roughness length scale and roughness function for hard fouling,  $C_F$  for smooth and fouled plates are utilised, more attention is given to these plates. What is more, SPC TBT plate did not have any hard fouling on its surface and therefore the results obtained for this plate were not utilized for the determination of roughness

length scales and roughness function for hard fouling, Table 4.11. Towing tank tests are performed for each plate for seven  $Rn$  in the range  $(2.8-5.5) \cdot 10^6$  and the obtained results are presented in Figure 4.14.

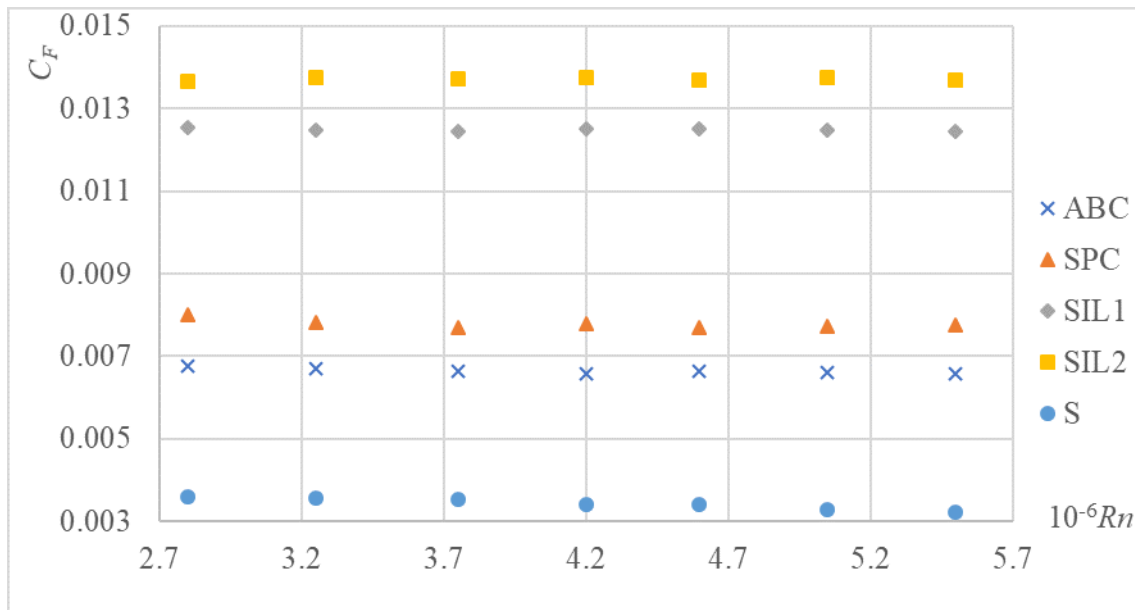


Figure 4.14 The experimentally obtained  $C_F$  for fouled plates [123]

As can be seen from Figure 4.14, significantly higher values of  $C_F$  are obtained for fouled plates ABC, SPC copper (SPC), SIL1 and SIL2 than for smooth plate (S) over the entire  $Rn$  range. The highest increase in  $C_F$  was obtained for SIL1 and SIL2, which had the highest barnacles as well as the highest percentage of surface coverage with barnacles. For those plates,  $C_F$  is increased three to four times in comparison with smooth plate. SIL1 and SIL2 plates represented plates coated with FR coating, which is designed for ships which sail at higher speeds. In that way fouling is released due to the wall shear stress which occurs during the sailing. Therefore, in order to FR coating be effective, certain wall shear stress must be present at the immersed surface. Thus, the slime will inevitably occur on the immersed surface coated with FR coating during immobile periods. If this immobile period is short, the adhesion strength of fouling, which has covered immersed surface, is low and consequently the fouling will be released from the surface coated with FR coating during sailing. However, if immobile period is long as in case of static immersion tests carried by Schultz [123], hard fouling will occur at the immersed surface, which has significantly higher adhesion strength. Therefore, hard fouling cannot be easily released, even from surface coated with FR coating and consequently substantial increases in  $C_F$  will be obtained. Obviously, the presence of hard fouling caused considerable increase in  $C_F$ , even for plates SPC and ABC which had %SC equal to 4% and 1% respectively and these increases ranged from 87% - 138% in comparison with S plate. As claimed by Schultz [123], the obtained significant increases in  $C_F$  are in line with the results from previously performed experiments of the resistance tests for classic pontoon covered with barnacles [223] and pipe flow experiments over barnacles [178].

Schultz [123] used the obtained  $C_F$  for smooth and fouled plates for the determination of  $\Delta U^+$  and  $k^+$  values for fouled plates with hard fouling using equations (2.19) and (2.20). As, the

selection of  $k$  will not affect the  $\Delta U^+$  value, but only the value of  $k^+$  (abscissa of  $\Delta U^+ = f(k^+)$ ),  $k$  is selected in a way that  $\Delta U^+$  values correspond to a predefined Grigson  $\Delta U^+$  model, shown with equation (2.16). For the development of relation for the determination of  $k$  for surfaces fouled with hard fouling, Schultz [123] assumed that the height of the largest barnacles ( $R_t$ ) had dominant effect on drag and that the effect of increased surface coverage with barnacles (%SC) was the largest for small %SC and smaller for large %SC. Mentioned presumptions were based on the experimentally obtained  $C_F$  within his study [123], on the pipe flow experiments [178] and the observations for typical roughness types [224], [225]. Thus, Schultz has proposed relation for the determination of  $k$  for surfaces fouled with hard fouling:

$$k = 0.059 R_t \sqrt{\%SC} \quad (4.5)$$

With equation (4.5), Schultz has obtained excellent collapse with Grigson  $\Delta U^+$  model ( $R^2 = 0.98$ ), as shown in Figure 4.15.

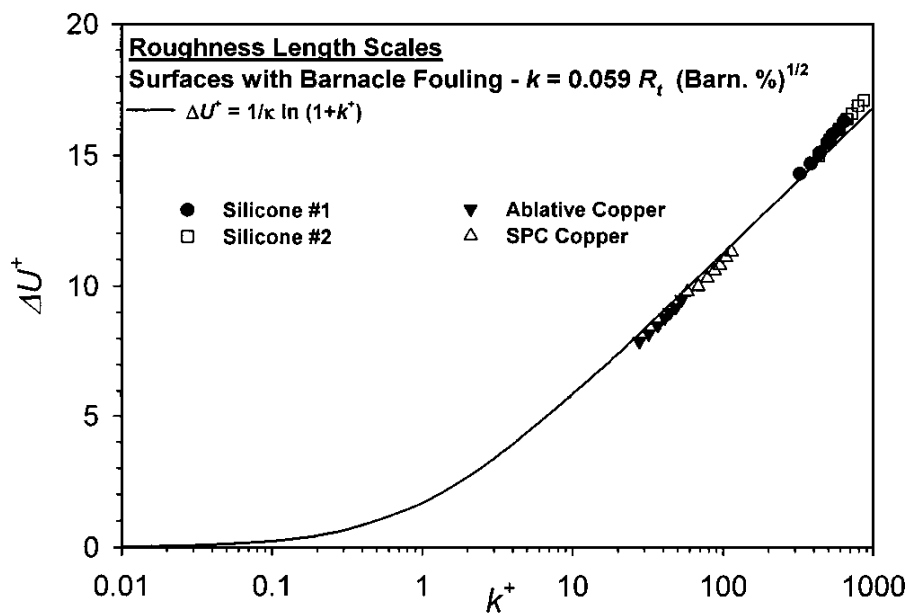


Figure 4.15 The plot of  $\Delta U^+$  versus  $k^+$  for fouled plates adapted from [123]

The proposed relation for the determination of  $k$  for surfaces fouled with hard fouling is different from the one presented in [139], developed for barnacles. This difference is discussed within [139] and may be attributed to the existence of slime and hydroid accumulations seen on the plates investigated in [123], whereas rough plates investigated within [139] have been covered with artificial barnacles only. Therefore, it can be concluded that the proposed relation presented with equation (4.5) is developed for hard fouling, even though it depends on physical characteristics of barnacles. As claimed by Schultz [123], further drag characterizations of range of surfaces fouled with hard fouling are required in order to assess the validity of scaling presented with equation (4.5).

#### 4.2.4. CFD model for simulation of hard fouling effects on the flow around surface covered with hard fouling – validation

In order to develop CFD model which can account for hard fouling effects on the flow around surface covered with hard fouling, Grigson  $\Delta U^+$  model, shown with equation (2.16) is implemented within the wall function of CFD solver. All CFD simulations are therefore performed with the application of wall functions. After the implementation, CFD simulations of towing tank experiments corresponding to the ones performed by Schultz [123] are performed for three  $Rn$  values. Thereafter, verification and validation studies are performed and finally validation uncertainties are compared with the obtained relative deviations from experimental results.

As CFD simulations are made in a way that they reproduce performed towing tank experiments [123], computational domain is created with respect to towing tank dimensions, Figure 4.16. As can be seen from Figure 4.16, bottom and side boundaries are placed at 4.9 m and 3.95 m away from the plate in order to accurately represent towing tank facility, while inlet, outlet and top boundaries are placed sufficiently far from flat plate in order to avoid their influence on the obtained results [210]. Furthermore, in order to prevent reflection from inlet and outlet boundaries, VOF wave damping is applied at these two boundaries, as explained in subsection 3.2.3. Within CFD simulations of performed towing tank test, VOF wave damping length is set as a plate length ( $L$ ). In order to reduce computational burden, only half of computational domain is modelled, and symmetry condition is applied at symmetry plane. CFD simulations are performed using Unsteady RANS (URANS) equations and more details related to computational model are given in Section 3. The applied boundary conditions are shown in Figure 4.16. Thus, from Figure 4.16 it can be seen that for side and bottom boundaries no slip wall boundary conditions are applied and this was done in order to reproduce performed towing tank experiments, i.e. in order to represent tank bottom and side. It should be noted that same boundary conditions are applied within [110], where the authors also reproduced Shultz's experiments [123], but for purpose of validation of their CFD model for the frictional resistance prediction of AF coatings.

CFD simulations are performed for each tested plate at three towing speeds: the lowest tested speed (2 m/s), the highest tested speed (3.8 m/s) and at 3 m/s. Unstructured hexahedral mesh is used for the discretization of computational domain and three meshes are generated for each tested plate and at each tested speed. The roughness length scales for tested fouled plates are obtained using equation (4.5) and are as follows: for ABC is equal to 0.295 mm, for SPC is equal to 0.59 mm, for SIL1 is equal to 2.7421 mm, while for SIL2 is equal to 3.5767. Prism layer mesh is generated in a way that  $y^+$  value is kept above 50 and above  $k^+$ . For plates SIL1 and SIL2, which have significantly higher  $k$  than ABC and SPC plates, prism layer mesh is set according to condition  $y^+ > k^+$ . Thus, for SIL1 and SIL2 plates the same prism layer mesh is used for all three tested speeds. On the other hand, ABC and SPC plates have lower  $k$  values. Because of this, prism layer mesh for those plates is generated according to condition  $y^+ > 50$ , as was done for S plate. Since, the same prism layer mesh should be used at all tested speeds for SIL1 and SIL2 plates, it was decided to keep the same prism layer mesh for ABC, SPC and S plates as well, regardless of the tested speed, as was done in [110]. Beside prism layer mesh, a special care is given to meshing the plate, especially leading and trailing edges where mesh surface refinements are applied in order to accurately represent leading and trailing edges to a

radius of 1.6 mm. Also, mesh is refined around the plate, free surface, as well as in the wake region in order to accurately capture Kelvin wake. The applied refinements can be seen within Figure 4.17. The number of cells used in CFD simulations is shown in Table 4.12, while the obtained  $y^+$  distribution for S plate is shown in Figure 4.18.

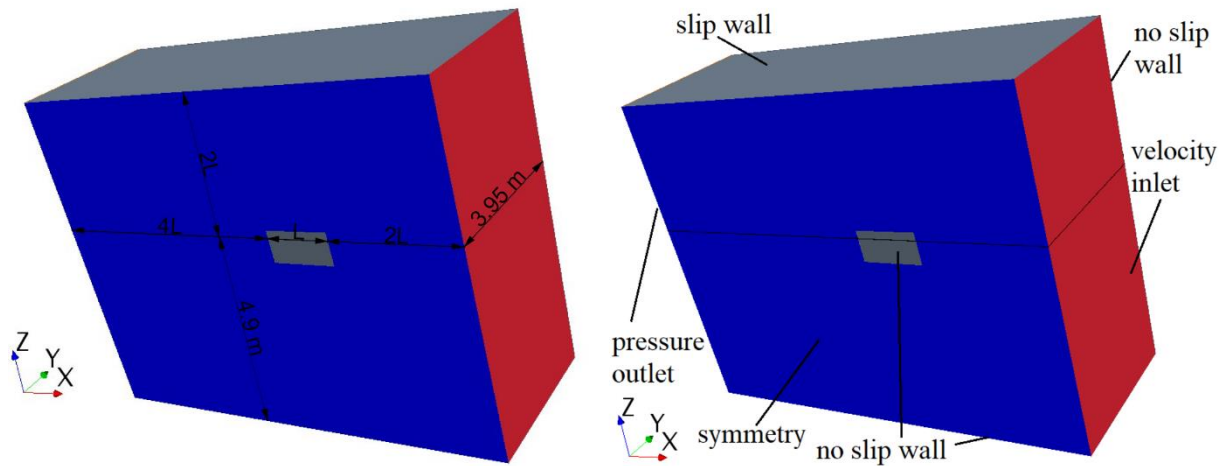


Figure 4.16 The definition of computational domain boundaries (left) and applied boundary conditions (right) in CFD simulations

Table 4.12 The number of cells used in CFD simulations

Plate	Coarse, M	Medium, M	Fine, M
S	0.8	1.5	2.7
ABC	0.8	1.5	2.7
SPC	0.8	1.5	2.7
SIL 1	0.5	0.8	1.4
SIL 2	0.5	0.8	1.3

The verification study is carried out for all tested plates at all  $Rn$  and grid and time step uncertainties are calculated using GCI method. It should be noted that iterative uncertainty is considered to be negligible. The verification study is performed for frictional resistance and the obtained results of grid convergence study are shown in Table 4.13. The obtained results of temporal convergence study indicated that time step uncertainty is negligible as the highest obtained  $U_T$  is lower than 0.08%. Therefore, it can be concluded that  $U_G$  is the only source of numerical uncertainty for these CFD simulations. As can be seen from Table 4.13, the obtained  $U_G$  are relatively low and the highest  $U_G$  is obtained for S plate at  $v = 3$  m/s and it is below 2.9%. Also from this table, it can be seen that higher  $U_G$  are obtained for S, ABC and SPC plates than for SIL1 and especially SIL2 plates. Namely,  $C_F$  and thus  $R_F$  of flat plate depends on  $\tau_w$ , i.e. on  $u_\tau$ .  $C_F$  for flat plate depends solely on  $Rn$  if the flow is in hydraulically smooth regime (S plate), while  $C_F$  depends on the ratio  $k/L$  if the flow is in fully rough regime. As can be seen from Figure 4.14, experimentally obtained  $C_F$  for fouled plates depends solely on  $k/L$ . The same results are obtained using CFD simulations of performed towing tank experiments. Since, the plate length is the same for all fouled plates,  $C_F$  for fouled plates depends solely on  $k$ . Within CFD simulations of performed towing tank experiments, the

impact of hard fouling is considered through implementation of Grigson  $\Delta U^+$  model for which  $\Delta U^+$  value depends solely on  $k^+$ , as  $\kappa$  is constant. For that reason, it can be concluded that  $C_F$  for fouled plates depends on  $k^+$  values across the fouled plate. Since  $u_\tau$  is the only parameter which can vary due to change in mesh density (all other parameters which define  $k^+$  are constant for a given fouling condition), the change in  $u_\tau$  will have direct influence on the change in  $C_F$  and consequently on  $U_G$ . Relative change in  $u_\tau$  values across plate due to different mesh density is significantly lower for SIL1 and SIL2 plates as  $u_\tau$  values across SIL1 and SIL2 plates are significantly higher than for ABC and SPC plates, due to higher  $k$ . Thus, significantly lower relative change in  $C_F$  will be obtained for SIL1 and SIL2 plates as well. As  $GCI_{\text{fine}}^{21}$  is defined relatively, due to the fact that  $e_a^{21}$  is defined relatively,  $GCI_{\text{fine}}^{21}$  will be significantly lower for SIL1 and especially for SIL2 plates.

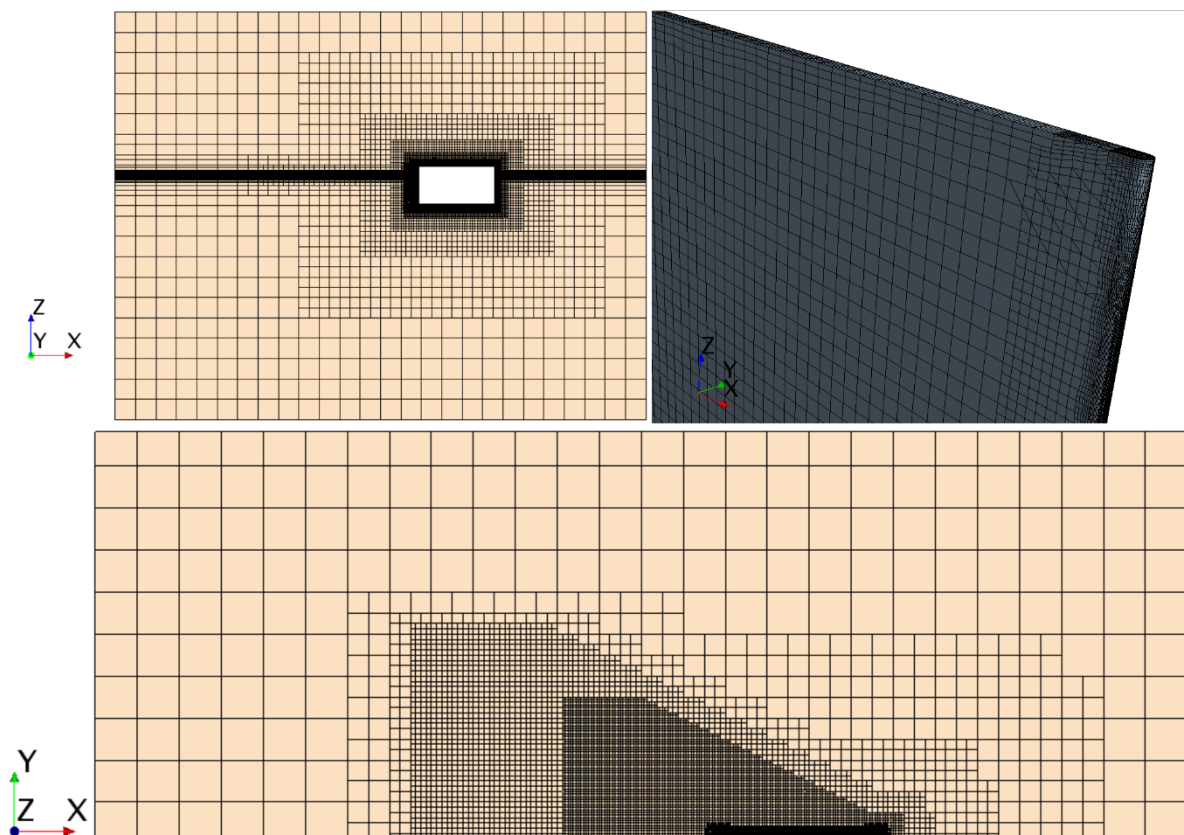


Figure 4.17 The profile view cross section of the volume mesh (upper left), refinement around plate leading edge (upper right) and top view cross section of the volume mesh (lower)

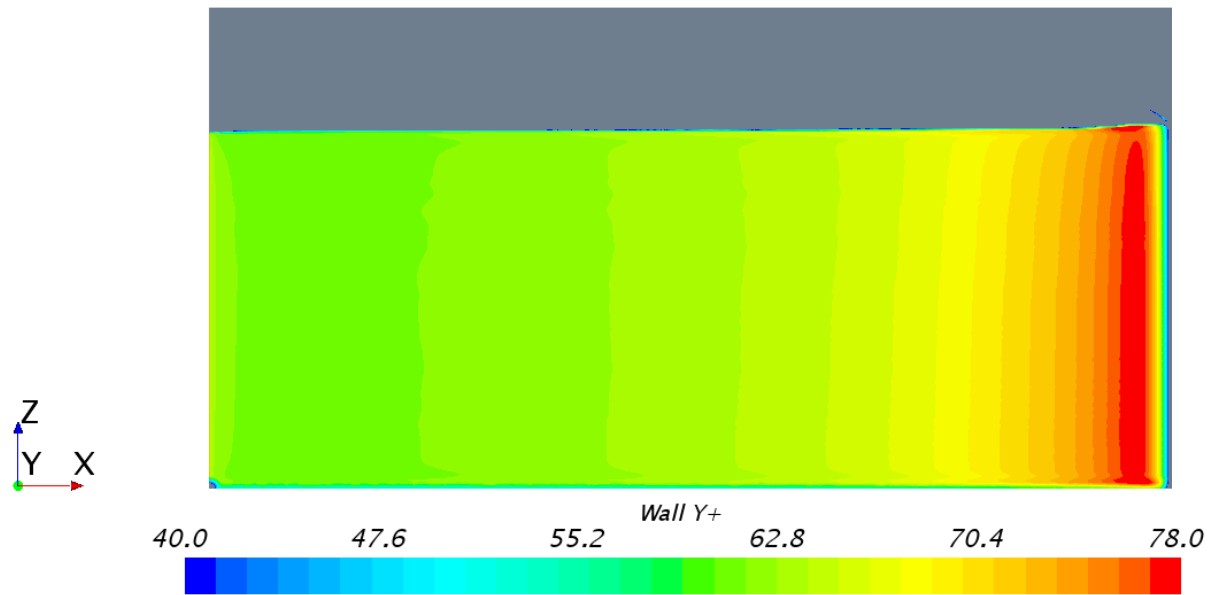


Figure 4.18 The obtained  $y^+$  distribution at S plate in CFD simulations of towing tank tests at  $Rn = 2.8 \cdot 10^6$

After an extensive verification study, the validation study is performed by comparison with the experimental results published in [123]. Thus, numerically obtained frictional resistance coefficients for plates ( $C_{F,CFD}$ ) are compared with experimental ones ( $C_{F,EXP}$ ). It should be noted that  $C_{F,CFD}$  are calculated using  $\phi_{ext}^{21}$  solution, while  $RD$  are calculated using equation (3.39). The validation study is performed for all tested plates at all  $Rn$  and the obtained results for  $C_{F,CFD}$ ,  $C_{F,EXP}$ ,  $RD$  and  $U_v$  are presented within Table 4.14 and Table 4.15.

As can be seen from Table 4.14 and Table 4.15, the obtained  $RD$  are low and mainly below 2%. For S plate, the highest  $RD$  is obtained for  $v = 3$  m/s and it is equal to -1.97%. All obtained  $RD$  for S plate are lower than  $U_v$  and therefore the validation is achieved at  $U_v$  level for all three  $Rn$ . In Table 4.15 the obtained results of validation study for fouled plates are presented and it can be seen that all obtained  $RD$  for fouled plates are lower than  $U_v$  and therefore the validation is achieved at  $U_v$  level for all three  $Rn$ . The highest  $RD$  for ABC plate is achieved for  $v = 2$  m/s and it is equal to -2%, while the highest  $RD$  for SPC plate is achieved also for  $v = 2$  m/s and it is equal to -3.8%. It was expected that  $RD$  will be the highest at lowest  $v$ , since  $U_D$  is the highest. The highest obtained  $RD$  for SIL1 plate is achieved at  $v = 3.8$  m/s, however it is quite low, i.e. equal to 0.77%, while the highest obtained  $RD$  for SIL2 plate is achieved at  $v = 2$  m/s and it is equal to 1.25%.

It can be concluded that satisfactory agreement between numerically and experimentally obtained  $C_F$  is achieved and that the proposed CFD model for simulation of hard fouling effects on the flow around surface covered with hard fouling is validated.



Table 4.13 The grid convergence study for tested plates

S						
$v$ , m/s	$\phi_3$ , N	$\phi_2$ , N	$\phi_1$ , N	$p_a$	$\phi_{ext}^{21}$ , N	$GCI_{fine}^{21}$ , %
2	5.9172	5.9874	6.0268	2.286	6.1008	1.536
3	12.4511	12.5989	12.6952	1.537	12.9852	2.855
3.8	19.3210	19.5823	19.7151	2.854	19.9040	1.198
ABC						
$v$ , m/s	$\phi_3$ , N	$\phi_2$ , N	$\phi_1$ , N	$p_a$	$\phi_{ext}^{21}$ , N	$GCI_{fine}^{21}$ , %
2	11.0187	11.2186	11.3017	3.776	11.3830	0.899
3	24.6668	25.1446	25.3404	3.847	25.5270	0.920
3.8	39.7677	40.4963	40.8379	3.258	41.2464	1.250
SPC						
$v$ , m/s	$\phi_3$ , N	$\phi_2$ , N	$\phi_1$ , N	$p_a$	$\phi_{ext}^{21}$ , N	$GCI_{fine}^{21}$ , %
2	12.8558	13.0900	13.1800	4.166	13.2566	0.727
3	28.8283	29.3685	29.5737	4.223	29.7450	0.724
3.8	46.8164	47.3107	48.2240	4.160	49.0030	2.019
SIL1						
$v$ , m/s	$\phi_3$ , N	$\phi_2$ , N	$\phi_1$ , N	$p_a$	$\phi_{ext}^{21}$ , N	$GCI_{fine}^{21}$ , %
2	20.4960	21.4196	21.5842	10.380	21.6147	0.176
3	45.9161	47.9904	48.3786	10.094	48.4550	0.197
3.8	73.9155	77.2523	77.9347	9.574	78.0849	0.241
SIL2						
$v$ , m/s	$\phi_3$ , N	$\phi_2$ , N	$\phi_1$ , N	$p_a$	$\phi_{ext}^{21}$ , N	$GCI_{fine}^{21}$ , %
2	22.6365	23.7822	23.8175	21.627	23.8184	0.005
3	50.7469	53.3010	53.3584	23.577	53.3595	0.002
3.8	81.6464	85.7996	85.9493	20.658	85.9539	0.007

Table 4.14 The validation study for smooth plate

$v$ , m/s	$10^3 C_{F,CFD}$	$10^3 C_{F,EXP}$	$RD$ , %	$U_V$ , %
2	3.542	3.605	-1.746	5.231
3	3.351	3.418	-1.970	4.517
3.8	3.201	3.226	-0.772	2.331

Table 4.15 The validation study for ABC, SPC, SIL1 and SIL2 plates

ABC				
$v$ , m/s	$10^3 C_{F,CFD}$	$10^3 C_{F,EXP}$	$RD$ , %	$U_V$ , %
2	6.609	6.747	-2.050	5.080
3	6.587	6.594	-0.108	3.619
3.8	6.634	6.576	-0.868	2.359
SPC				
$v$ , m/s	$10^3 C_{F,CFD}$	$10^3 C_{F,EXP}$	$RD$ , %	$U_V$ , %
2	7.697	8.000	-3.793	5.053
3	7.675	7.784	-1.394	3.574
3.8	7.881	7.756	1.615	2.842
SIL1				
$v$ , m/s	$10^3 C_{F,CFD}$	$10^3 C_{F,EXP}$	$RD$ , %	$U_V$ , %
2	12.549	12.543	0.046	5.003
3	12.503	12.508	-0.039	3.506
3.8	12.558	12.462	0.773	2.014
SIL2				
$v$ , m/s	$10^3 C_{F,CFD}$	$10^3 C_{F,EXP}$	$RD$ , %	$U_V$ , %
2	13.829	13.658	1.247	5.000
3	13.769	13.748	0.152	3.500
3.8	13.824	13.694	0.950	2.000

## 5. The impact of biofouling on the ship performance

### 5.1. Case study – the investigated ships and fouling conditions

Within this section, the impact of biofouling on the ship performance is investigated on the example of three commercial ships: one containership, oil tanker and bulk carrier. The CO<sub>2</sub> emissions from international shipping by ship type determined using the bottom-up method [2] are presented within Figure 5.1. Containerships, bulk carriers and tankers together account for almost 62% of total CO<sub>2</sub> emissions from international shipping and therefore those three types of ships are selected for a case study within this thesis.

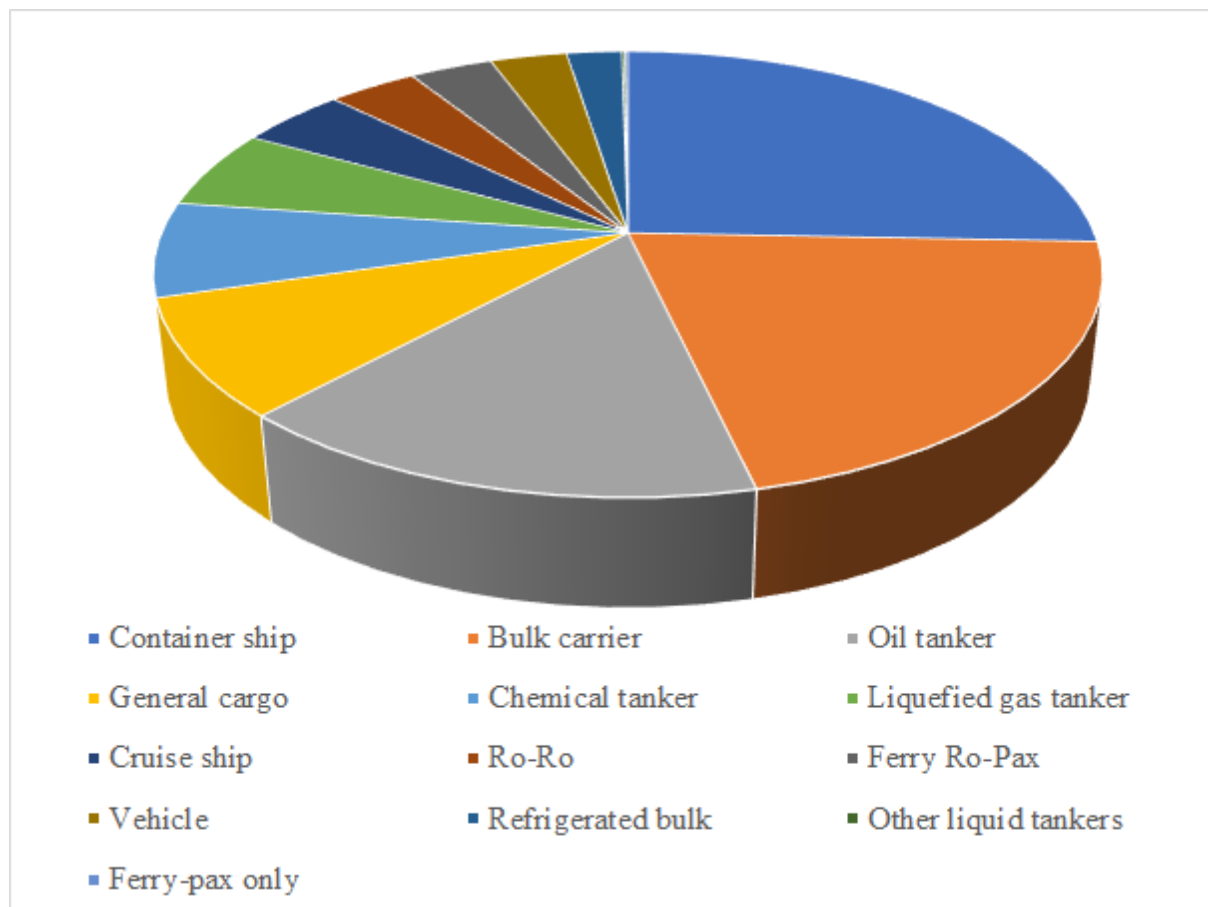


Figure 5.1 Bottom-up CO<sub>2</sub> emissions from international shipping by ship type

Kriso Container Ship (KCS) was designed with an aim to represent a modern container ship with a bulbous bow that can carry 3600 TEU containers [226]. KCS represents a panamax container ship. The Korea Research Institute for Ships and Ocean Engineering (KRISO) carried out an extensive towing tank experiments in order to determine resistance, mean flow data and free surface waves [226]. Self-propulsion tests were performed at the Ship Research Institute (now NMRI) in Tokyo and the obtained results were reported in the Proceedings of the CFD Workshop Tokyo in 2005 [227]. Thereafter, resistance tests in waves were also carried out by NMRI. Experimental data for pitch, heave and added resistance are available from Force/Dmi measurements published in [228]. It should be noted that full-scale ship has never been built.

Kriso Very Large Crude-oil Carrier 2 (KVLCC2) was designed with an aim to represent a large oil tanker that can transport 300000 tons of crude oil and it represents the second variant of KRISO tanker with more U-shaped stern frame lines in comparison with KVLCC. KVLCC2 represents a very large crude carrier. KRISO carried out an extensive towing tank experiments in order to ascertain resistance, mean flow data, free surface waves as well as self-propulsion tests [226]. Added resistance in short waves for KVLCC2 was experimentally determined by Bingjie and Steen [229]. It should be noted that full-scale ship has never been built.

While KCS and KVLCC2 represent ships which were designed for research purposes with the aim to form the benchmark database for CFD validation, Bulk Carrier (BC) ship was designed for the ship owner, however in the end it was not built. BC represents a typical handymax bulk carrier. An extensive towing tank experiments including resistance tests, self-propulsion tests, as well as nominal wake measurements were performed in Brodarski institute [230]. Resistance tests were performed for four different loading conditions, while self-propulsion tests were performed using the stock propeller and the British method for three different loading conditions.

3D representation of KCS, KVLCC2 and BC is shown in Figure 5.2, while hull lines of KCS, KVLCC2 and BC are given in Figure 5.3.

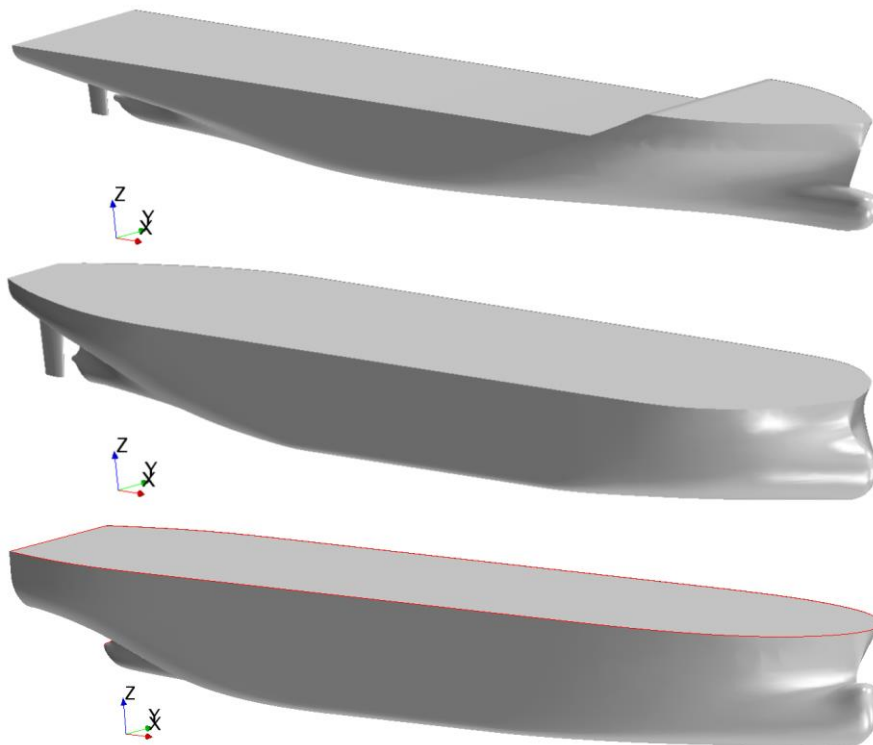


Figure 5.2 3D representation of KCS (upper), KVLCC2 (middle) and BC (lower)

As can be seen from Figure 5.2 and Figure 5.3, all three ships have bulbous bow and transom stern. KVLCC2 and BC have fuller hull form, while KCS has more slender hull form. The main particulars of the investigated ships are shown in Table 5.1. It should be noted that values presented in Table 5.1 correspond to full-scale values, since within this thesis the impact of biofouling on the ship performance is investigated for full-scale ships.

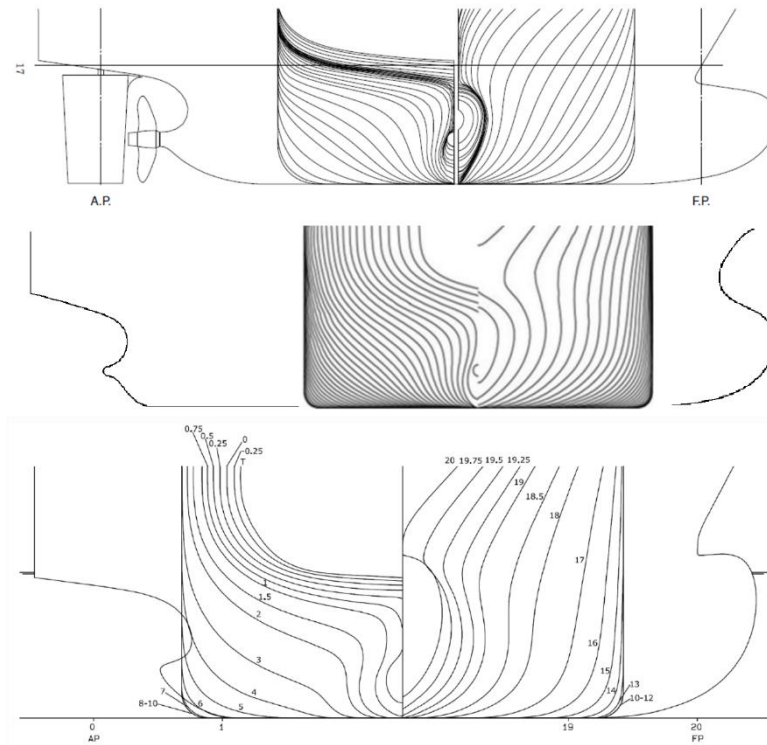


Figure 5.3 Hull lines of KCS (upper), KVLCC2 (middle) and BC (lower)

Table 5.1 The main particulars of the investigated ships

Parameter	KCS	KVLCC2	BC
length between perpendiculars ( $L_{pp}$ ), m	230	320	175
length of waterline ( $L_{WL}$ ), m	232.5	325.5	182.69
Breadth ( $B$ ), m	32.2	58	30
Draught ( $T$ ), m	10.8	20.8	9.9
Displacement ( $\Delta$ ), t	53382.8	320750	41775
Area of wetted surface ( $S$ ), m <sup>2</sup>	9645	27467	7351.9
Block coefficient ( $C_B$ )	0.6505	0.8098	0.7834
Midship section coefficient ( $C_M$ )	0.9849	0.9980	0.9958
Froude number ( $Fn$ )	0.26	0.1423	0.2026
Ship design speed ( $V_K$ ), kn	24	15.5	16.32
Propeller center, longitudinal location from fore perpendicular ( $x/L_{pp}$ )	0.9825	0.9797	0.9800
Propeller center, vertical location from waterline ( $-z/T$ )	0.62037	0.72115	0.6800
model scale ( $\lambda$ )	31.6	58	25.2

Experimental self-propulsion tests were carried out using propeller KP505 for KCS, KP458 for KVLCC2 and one stock propeller from Wageningen series (WB) for BC [230]. KP505 and

KP468 were designed by KRISO and experimental results of open water tests were published in [227], [231]. Furthermore, these propellers are widely used in academic and comparative purposes since their geometry is readily available. The main particulars of the investigated propellers are shown in Table 5.2., while the geometries of propellers can be seen in Figure 5.4. It should be noted that tested propellers do not have radial rake and that they are right handed propellers. Towing tank tests for all three investigated propellers are performed at  $Rn$  which are above  $Rn = 2 \cdot 10^5$  as prescribed by ITTC [72].



Figure 5.4 KP505 (left), KP458 (middle) and WB (right) propellers

Table 5.2 The main particulars of the investigated propellers

Propeller	KP505	KP458	WB
$D$ , m	7.900	9.860	6.199
$P$ , m	7.505	7.085	5.294
$Z$	5	4	4
$c$ , m	2.844	2.233	1.633
$t$ , m	0.132	0.131	0.168
Hub ratio	0.180	0.155	0.179
model scale ( $\lambda$ )	31.6	58	25.2

Previously validated  $\Delta U^+$  models for biofilm and hard fouling are used for the analysis of the impact of biofouling on the ship performance. As already noted, biofouling can be divided into soft fouling, hard fouling and composite fouling. The fouling with biofilm can be considered as soft fouling, which inevitably occurs on the immersed surfaces. On the other hand, the presence of hard fouling on the immersed surfaces is possible during long immobile periods. The presence of biofilm increases the rate of biofouling, however hard fouling can occur even without the presence of biofilm. During drag characterization of fouled flat plates Schultz noticed the presence of both slime and barnacles on the investigated plates. Consequently, roughness length scale, which he proposed can be considered as a roughness length scale for composite fouling. However, since proposed roughness length scale depends only on the height of the largest barnacle and percentage of surface coverage with barnacles, he proclaimed that developed scale can be used for hard fouling as the main fouling effects are related to barnacles. Within this thesis, this roughness length scale is used for the description of hard fouling effects.

Further studies are required for distinguishing the effects of slime, i.e. soft fouling and hard fouling once both types of fouling are present and, in that way, a new roughness length scale for composite fouling could be proposed. In this thesis, the impact of biofilm and hard fouling on the ship performance is studied separately.

An investigation related to biofouling of ships' hulls and propellers has been carried out within [232]. In that study, the authors analysed the fouling community on the immersed surfaces of seven ships using video footage. The obtained results showed that hard fouling has lower percentage of coverage of both hull and propeller surfaces (up to 3%) than soft fouling (up to 85%). Thus, barnacles and tubeworms occurred in isolated patches, generally in areas of hull with scratches in the coating or metal on uncoated propellers as well as drydocking support strips. Since it is expected that the presence of hard fouling will cause more detrimental effect on the ship performance than biofilm, higher percentages of surface coverage with hard fouling are not expected, i.e. if the higher %*SC* is present, hull or propeller cleaning would be necessary, since the ship energy efficiency would be drastically reduced. In this thesis, eight surface conditions for biofilm (R1 B – R8 B) and six surface conditions for hard fouling (R1 H – R6 H) are investigated, Table 5.3.

Table 5.3 The investigated surface conditions

Surface condition	$k$ , $\mu\text{m}$	% <i>SC</i> , %	$k_{eff}$ , $\mu\text{m}$	$\Delta U^+$ model
R1 B	100	50	39	eq. (4.2)
R2 B	500	50	195	eq. (4.2)
R3 B	100	25	27.5	eq. (4.2)
R4 B	500	25	137.5	eq. (4.2)
R5 B	100	15	21.3	eq. (4.3)
R6 B	500	15	106.5	eq. (4.3)
R7 B	100	5	12.3	eq. (4.4)
R8 B	500	5	61.5	eq. (4.4)
Surface condition	$R_t$ , mm	% <i>SC</i> , %	$k$ , $\mu\text{m}$	$\Delta U^+$ model
R1 H	7	25	2065.00	eq. (2.16)
R2 H	5	25	1475.00	eq. (2.16)
R3 H	7	5	923.50	eq. (2.16)
R4 H	5	5	659.64	eq. (2.16)
R5 H	7	1	413.00	eq. (2.16)
R6 H	5	1	295.00	eq. (2.16)

As can be seen from Table 5.3, the values of roughness length scale for hard fouling are higher than the ones for biofilm. As already noted, these values are important for the discretization of the prism layer near the rough wall, as the first cell near the wall must have height higher than  $2k$ .

## 5.2. The impact of biofouling on the frictional resistance of the flat plate having the same length as a ship

Equivalent flat plate is the flat plate which has the same length and wetted surface area as full-scale ship. The term “equivalent flat plate” was firstly introduced by Froude in 1870’s. Namely, William Froude had carried out the first investigations related to skin friction of a ship by towing flat plates of different lengths. The plates were fully immersed in order to eliminate as much residuary resistance as possible, so that the total measured resistance consisted only of the frictional resistance. In that way he developed an empirical formula for the relation between frictional resistance, wetted surface area and speed. Froude is the most credited for the introduction of model-ship similarity laws in the ship hydrodynamics. His decomposition of the total resistance of a ship is in some way still in use nowadays. Froude decomposed the total resistance of a ship on the frictional resistance of an equivalent flat plate ( $R_{F0}$ ) and residuary resistance ( $R_R$ ). The main assumption of Froude’s decomposition is that residuary resistance coefficient ( $C_R$ ) of the model and ship are the same. ITTC 1957 PPM, which is being used in many towing tank institutions nowadays, relies on the Froude’s decomposition of the total resistance. The main modification is that frictional resistance coefficient of an equivalent flat plate is replaced with ITTC 1957 model-ship correlation line. By the development of fluid mechanics, as well as ship hydrodynamics it has been shown by various scientist that frictional resistance coefficient of smooth flat plate depends solely on  $Rn$ . Therefore, for a given speed and kinematic viscosity coefficient, it is clear that  $C_{F0}$  depends solely on flat plate length. Consequently, in the determination of  $C_{F0}$  for flat plate, an equivalent flat plate can be replaced with flat plate having the same length as a ship. The development of computers, as well as CFD, created the preconditions for carrying out numerical simulations in full-scale.

In this thesis, the impact of biofouling on the frictional resistance of the flat plate having the same length as a ship is investigated. Firstly, an extensive verification study is performed for all investigated surface conditions, including smooth surface conditions. The goal of the verification study is to determine numerical uncertainty, as well as to determine sufficient grid spacing. Thereafter, the obtained results using fine mesh are compared with the results obtained with the Schoenherr friction line for smooth plates and results obtained using Granville similarity law scaling method.

### 5.2.1. Numerical modelling and verification study

CFD simulations are performed as a steady DBS, since flat plate having the same length as a ship is fully immersed in water in order to eliminate wave resistance. In order to avoid influence of the boundaries on the obtained solution, the boundaries are placed far enough from the flat plate according to [210]. Thus, the outlet boundary is set to distance  $2.5L$ , inlet boundary to distance  $L$ , while other boundaries to distance  $1.5L$ , where  $L$  is the length of the flat plate. The applied boundary conditions in CFD simulations of the flat plate having the same length as a ship are shown in Figure 5.5. As can be seen, only a quarter of computational domain is modelled, since top boundary is placed on the half of the plate height. Therefore, two symmetry conditions are applied, one on the top boundary and the other on the plane which corresponds to symmetry plane of a flat plate. Thus, on these two boundaries, the normal velocity of the boundary is zero as well as the gradient of the physical quantity of the flow. Slip wall boundary



condition is applied at the bottom and side boundary. On a slip wall, the fluid slides along the wall without any shear forces. At the wall surface, i.e. the surface of a flat plate, no-slip wall boundary condition is applied, which represents an impermeable surface that confines fluid or solid regions. On a no-slip wall, the fluid moves at the same velocity as the wall, i.e. in CFD simulations performed within this thesis velocity at the wall surface is equal to zero as well as the normal gradient of pressure. Pressure outlet is applied at the outlet boundary. It is an outflow condition which imposes the pressure at outlet boundary. The variables of outlet boundary are generally unknown, but since the boundary is usually far away from the analysed surface, the changes in physical variables are small. Except for the pressure, the normal gradient of other physical variables is zero and the values of those variables are obtained by extrapolation from the interior of the solution domain. The velocity inlet boundary is applied at the inlet boundary. This boundary condition is usually used as an inflow condition, where the distributions of velocity and fluid properties are known. Thus, the incoming velocity is set, while the pressure is obtained by reconstructed gradient interpolation.

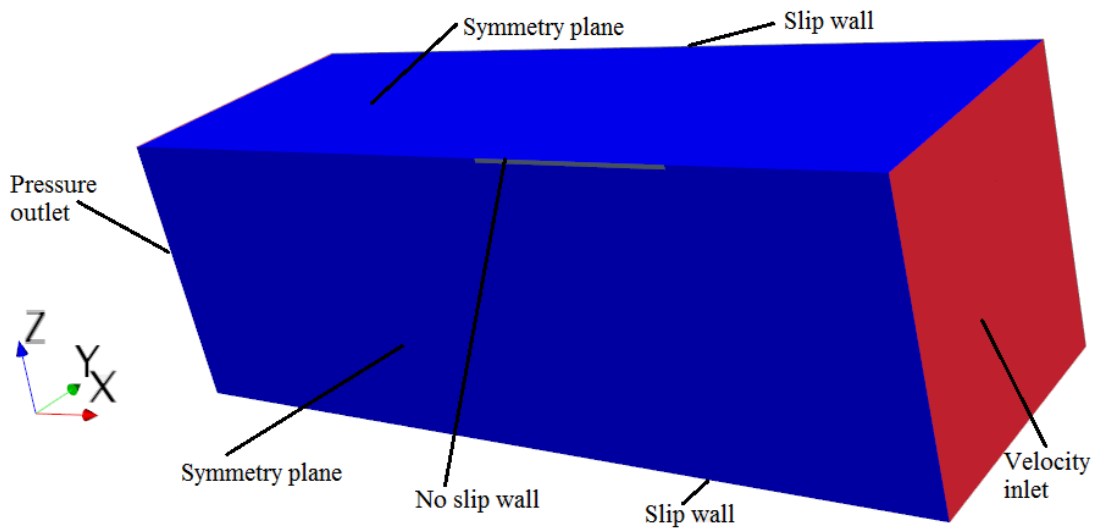


Figure 5.5 The applied boundary conditions in CFD simulations of the flat plate having the same length as a ship

The computational domain is discretized utilizing a cut-cell grid with prism layer mesh on the walls. The mesh is refined near the plate edges, as well as around the plate. More details regarding discretization are given in 3.2.2. The main particulars of the investigated plates are shown in Table 5.4, while the geometry of the flat plate is given in Figure 5.6. As can be seen from Table 5.4, length of flat plate is equal to  $L_{wl}$ .

Table 5.4 The main particulars of flat plates having the same length as a ship

Plate	KCS	KVLCC2	BC
$L$ , m	232.5	325	182.69
$B$ , m	9	9	9
$R$ , m	0.016	0.023	0.013
$S$ , m <sup>2</sup>	4200.208	5889.418	3305.798

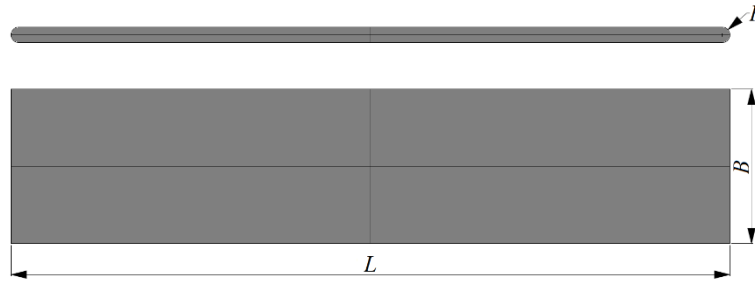


Figure 5.6 The geometry of the flat plate having the same length as a ship

Three meshes are created for the purpose of verification study: coarse, medium and fine mesh. The mesh is refined systematically, as all mesh parameters (except prism layer) are set as relative values of the cell base size and the refinement is performed by changing the of cell base size. The number of cells for the investigated plates is given in Table 5.5. It should be noted that number of cells for CFD simulations with hard fouling varies amongst the investigated surface conditions, because of different discretization of prism layer mesh. Within Table 5.5, the number of cells is given for the surface condition R6 H. It should be noted that the average value of  $y^+$  in the first cells near the wall for smooth flat plate representing KCS (KCS plate) is equal to 159.61, for smooth flat plate representing KVLCC2 (KVLCC2 plate) is equal to 157.60 and for smooth flat plate representing BC (BC plate) is equal to 295.74. The average value of  $y^+$  in the first cells near the wall for fouled plates is higher than for smooth plates as explained in subsection 5.3.1.

Table 5.5 The number of cells within CFD simulations for plates having the same length as a ship

Case	KCS – biofilm	KVLCC2 – biofilm	BC – biofilm
Coarse mesh	0.5 M	0.19 M	0.44 M
Medium mesh	1.06 M	0.33 M	0.76 M
Fine mesh	2.5 M	0.51 M	1.36 M
Case	KCS – hard fouling	KVLCC2 – hard fouling	BC – hard fouling
Coarse mesh	0.38 M	0.33 M	0.27 M
Medium mesh	0.59 M	0.51 M	0.47 M
Fine mesh	0.95 M	0.78 M	0.8 M

Since all flat plate simulations (FPS) are stopped after 1000 iterations, when all residuals drop at least eight orders of magnitude, the iterative uncertainty can be considered as negligible. Therefore, numerical uncertainties obtained within flat plate simulations consist only of grid uncertainties, as these simulations are performed as steady ones. The verification study is performed using  $R_{F0}$  as a key variable. The obtained results of the verification study are shown in Table 5.6 and Table 5.7. As can be seen from Table 5.6 and Table 5.7 the obtained numerical uncertainties are relatively low, i.e. below 5.1%. Significantly lower numerical uncertainties for CFD simulations are obtained for KCS plate fouled with biofilm than for KVLCC2 and BC plates fouled with biofilm. Thus, for KCS plate fouled with biofilm, the highest obtained  $GCI_{fine}^{21}$  is equal to 0.036%, for KVLCC2 5.086%, while for BC 1.782%. This was expected

since the highest number of cells is used for CFD simulations of KCS plates, followed by BC plate and lastly KVLCC2 plate, Table 5.5. From Table 5.7 it can be seen that similar numerical uncertainties are obtained for every tested plate fouled with hard fouling. Thus, for KCS plate fouled with hard fouling, the highest obtained  $GCI_{fine}^{21}$  is equal to 0.379%, for KVLCC2 0.458%, while for BC 0.388%. This was also expected, since the number of cells used in CFD simulations for plates fouled with hard fouling is similar. Based on the results presented in Table 5.6 and Table 5.7, it can be concluded that the implementation of  $\Delta U^+$  model within the wall function of CFD solver did not lead to an increase in numerical uncertainty.

Table 5.6 The obtained numerical uncertainties within FPS for plates fouled with biofilm

KCS plate					
Surface condition	$\phi_3$ , kN	$\phi_2$ , kN	$\phi_1$ , kN	$\phi_{ext}^{21}$ , kN	$GCI_{fine}^{21}$ , %
S	111.249	111.935	112.060	112.082	0.024
R1 B	126.744	127.539	127.584	127.586	0.002
R2 B	155.731	156.406	156.374	156.373	0.001
R3 B	121.519	122.300	122.369	122.374	0.005
R4 B	148.646	149.381	149.363	149.363	0.000
R5 B	118.435	119.174	119.261	119.270	0.010
R6 B	131.243	132.013	132.033	132.033	0.000
R7 B	111.376	112.041	112.186	112.218	0.036
R8 B	120.292	121.045	121.122	121.129	0.007
KVLCC2 plate					
Surface condition	$\phi_3$ , kN	$\phi_2$ , kN	$\phi_1$ , kN	$\phi_{ext}^{21}$ , kN	$GCI_{fine}^{21}$ , %
S	62.611	63.745	65.407	67.156	3.343
R1 B	67.476	68.938	70.784	73.664	5.086
R2 B	82.662	84.446	86.752	90.117	4.849
R3 B	64.736	66.132	67.898	70.643	5.053
R4 B	78.957	80.670	82.862	86.147	4.955
R5 B	62.616	63.832	65.436	67.647	4.224
R6 B	71.147	72.640	74.552	77.415	4.801
R7 B	62.611	63.745	65.407	67.156	3.343
R8 B	66.225	67.587	69.325	71.960	4.751
BC plate					
Surface condition	$\phi_3$ , kN	$\phi_2$ , kN	$\phi_1$ , kN	$\phi_{ext}^{21}$ , kN	$GCI_{fine}^{21}$ , %
S	42.813	43.121	43.922	44.512	1.681
R1 B	46.821	47.181	48.13	48.816	1.782
R2 B	57.709	58.144	59.334	60.142	1.701
R3 B	44.863	45.207	46.106	46.762	1.777
R4 B	55.050	55.47	56.607	57.392	1.735
R5 B	43.113	43.417	44.239	44.808	1.608
R6 B	49.208	49.576	50.549	51.246	1.725
R7 B	42.813	43.121	43.922	44.512	1.681
R8 B	45.537	45.873	46.763	47.402	1.709

Table 5.7 The obtained numerical uncertainties within FPS for plates fouled with hard fouling

KCS plate					
Surface condition	$\phi_3$ , kN	$\phi_2$ , kN	$\phi_1$ , kN	$\phi_{ext}^{21}$ , kN	$GCI_{fine}^{21}$ , %
S	107.690	110.644	111.553	111.891	0.379
R1 H	268.680	274.424	274.948	274.988	0.018
R2 H	252.573	258.285	258.628	258.648	0.010
R3 H	232.240	237.814	238.453	238.533	0.042
R4 H	219.033	224.597	225.124	225.173	0.028
R5 H	202.252	207.863	208.526	208.598	0.044
R6 H	192.258	197.650	198.366	198.456	0.057
KVLCC2 plate					
Surface condition	$\phi_3$ , kN	$\phi_2$ , kN	$\phi_1$ , kN	$\phi_{ext}^{21}$ , kN	$GCI_{fine}^{21}$ , %
S	63.745	65.407	65.941	66.182	0.458
R1 H	148.568	152.175	151.400	151.174	0.186
R2 H	139.796	143.169	142.706	142.622	0.073
R3 H	128.339	131.779	131.984	131.997	0.013
R4 H	121.010	124.595	124.853	124.872	0.019
R5 H	112.609	115.925	116.308	116.355	0.051
R6 H	107.148	110.286	110.711	110.774	0.072
BC plate					
Surface condition	$\phi_3$ , kN	$\phi_2$ , kN	$\phi_1$ , kN	$\phi_{ext}^{21}$ , kN	$GCI_{fine}^{21}$ , %
S	41.940	42.813	43.121	43.254	0.388
R1 H	100.917	103.053	103.248	103.264	0.020
R2 H	93.993	95.958	96.289	96.348	0.076
R3 H	86.337	88.142	88.640	88.803	0.230
R4 H	81.435	83.173	83.662	83.827	0.246
R5 H	74.928	77.075	77.622	77.792	0.274
R6 H	71.173	73.232	73.781	73.963	0.309

### 5.2.2. The validation study and comparison with Granville similarity law scaling method

After the verification study, the obtained results for smooth flat plates are validated with the results obtained using equation (2.25), Table 5.8. As can be seen from Table 5.8, the obtained  $RD$  are small, i.e. below 2.75%. The validation study is performed for six smooth plates in total. The number of cells used in flat plate simulations for smooth plate varies depending on the fouling condition, i.e. biofilm or hard fouling. Lower  $RD$  are obtained for cases where higher number of cells are used. Thus, for smooth KCS and BC plates (biofilm) and KVLCC2 plate (hard fouling) obtained  $RD$  are lower in comparison with smooth KCS and BC plates (hard fouling) and KVLCC2 plate (biofilm).

After the validation study, the obtained  $C_{F0}$  for fouled flat plates are compared with the ones obtained using Granville similarity law scaling method, Table 5.9 and Table 5.10. As can be seen from Table 5.9, the obtained  $RD$  between  $C_{F0}$  obtained by CFD approach and Granville similarity law scaling method are low. Thus, for KCS plate, the highest  $RD$  is obtained for the surface condition R2 B and it is equal to -2.775%, for KVLCC2 plate, the highest  $RD$  is

obtained also for the surface condition R2 B and it is equal to -3.163%, while for BC plate, the highest  $RD$  is obtained for the surface condition R2 B and it is equal to -2.045%. On the other hand, the obtained  $RD$  between  $C_{F0}$  obtained by CFD approach and Granville similarity law scaling method for hard fouling are somewhat higher, Table 5.10. Thus, for KCS plate, the highest  $RD$  is obtained for the surface condition R1 H and it is equal to -7.181%, for KVLCC2 plate, the highest  $RD$  is obtained for the surface condition R1 H and it is equal to -6.825%, while for BC plate, the highest  $RD$  is obtained for the surface condition R2 H and it is equal to -9.097%. The higher  $RD$  between  $C_{F0}$  obtained by CFD approach and Granville similarity law scaling method for hard fouling were expected. Namely, CFD approach represents fully non-linear method, which can predict non-uniform distribution of  $u_\tau$  across the surface, and consequently non-uniform distribution of  $k^+$  as well. Since  $\Delta U^+$  values vary with  $k^+$ , within CFD simulation various  $\Delta U^+$  values across the surface are applied. If one looks the prediction of roughness effects on  $C_{F0}$  by CFD approach and Granville similarity law scaling method, non-uniform distribution of  $k^+$  across the flat plate surface presents an important advantage over the Granville method, where only one value of  $k^+$  is assumed for whole flat plate. These differences between non-uniform distribution of  $k^+$  and only one value of  $k^+$  will be even more highlighted for surfaces fouled with more severe fouling, as roughness length scale will be higher and consequently  $k^+$  as well. Since hard fouling presents a fouling with significantly higher fouling rating scale than biofilm, higher  $RD$  between  $C_{F0}$  obtained by CFD approach and Granville similarity law scaling method were expected.

Table 5.8 The validation study for smooth flat plates having the same length as a ship

Plate	$10^3 \cdot C_{F0}^{fine}$	$10^3 \cdot C_{F0}^{Schoenherr}$	$RD, \%$
KCS – biofilm	1.365	1.377	-0.867
KVLCC2 – biofilm	1.362	1.393	-2.232
BC – biofilm	1.470	1.484	-0.939
KCS – hard fouling	1.359	1.377	-1.316
KVLCC2 – hard fouling	1.373	1.393	-1.435
BC – hard fouling	1.443	1.484	-2.746

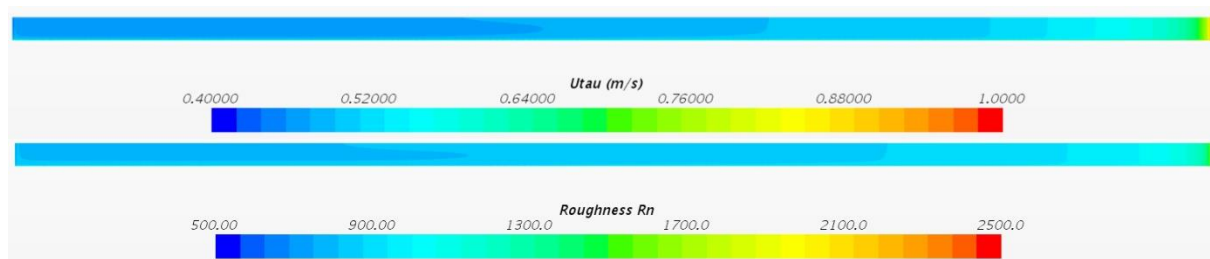


Figure 5.7 The obtained  $u_\tau$  distribution (upper) and  $k^+$  distribution (lower) for the flat plate representing KCS, R1 H

Table 5.9 The comparison for flat plates having the same length as a ship fouled with biofilm

KCS plate			
Surface condition	$10^3 \cdot C_{F0}^{fine}$	$10^3 \cdot C_{F0}^{Granville}$	$RD, \%$
R1 B	1.554	1.563	-0.572
R2 B	1.905	1.959	-2.775
R3 B	1.490	1.490	0.031
R4 B	1.819	1.862	-2.299
R5 B	1.453	1.471	-1.217
R6 B	1.608	1.631	-1.382
R7 B	1.366	1.377	-0.755
R8 B	1.475	1.492	-1.137
KVLCC2 plate			
Surface condition	$10^3 \cdot C_{F0}^{fine}$	$10^3 \cdot C_{F0}^{Granville}$	$RD, \%$
R1 B	1.474	1.501	-1.810
R2 B	1.807	1.866	-3.163
R3 B	1.414	1.433	-1.338
R4 B	1.726	1.776	-2.858
R5 B	1.363	1.393	-2.190
R6 B	1.553	1.590	-2.378
R7 B	1.362	1.393	-2.233
R8 B	1.444	1.474	-2.069
BC plate			
Surface condition	$10^3 \cdot C_{F0}^{fine}$	$10^3 \cdot C_{F0}^{Granville}$	$RD, \%$
R1 B	1.611	1.621	-0.603
R2 B	1.986	2.027	-2.045
R3 B	1.543	1.543	0.009
R4 B	1.894	1.931	-1.874
R5 B	1.481	1.484	-0.224
R6 B	1.692	1.714	-1.313
R7 B	1.470	1.484	-0.939
R8 B	1.565	1.584	-1.168

Beside comparison of  $C_{F0}$  values obtained by CFD approach and Granville similarity law scaling method, it is interesting to compare the obtained increases in  $C_{F0}$  ( $\Delta C_{F0}$ ) due to the presence of fouling. As can be seen from Figure 5.8, the obtained  $\Delta C_{F0}$  due to the presence of biofilm by CFD approach and Granville similarity law scaling method are similar. Thus, for the most severe investigated fouling condition (R2 B), the obtained  $\Delta C_{F0}$  for KCS plate is equal to 39.5% (CFD) and 42.3% (Granville), for KVLCC2 plate is equal to 32.6% (CFD) and 33.9% (Granville) and for BC plate is equal to 35.1% (CFD) and 36.6% (Granville). It should be noted that for other surface conditions these differences are lower. From the obtained results it is clear that the highest  $\Delta C_{F0}$  are obtained for KCS plate, followed by BC plate and lastly KVLCC2 plate. The obtained differences in  $\Delta C_{F0}$  due to the presence of hard fouling by CFD approach

and Granville similarity law scaling method are somewhat higher (Figure 5.9), as was expected. Thus, for the most severe investigated fouling condition (R1 H), the obtained  $\Delta C_{F0}$  for KCS plate is equal to 146.5% (CFD) and 162.0% (Granville), for KVLCC2 plate is equal to 129.6% (CFD) and 142.9% (Granville) and for BC plate is equal to 139.4% (CFD) and 154.9% (Granville). It should be noted that for other surface conditions these differences are lower, except for BC plate and the surface condition R2 H, where the obtained  $\Delta C_{F0}$  for is equal to 123.3% (CFD) and 138.9% (Granville). It should be noted that these discrepancies can be related to high  $y^+$  values obtained within numerical simulations for fouled plates. Thus, these discrepancies would be probably lower if  $\Delta C_{F0}$  was calculated using  $C_{F0}$  values for fouled and smooth plate obtained using the same  $y^+$  values in the first cell near the wall. The obtained  $\Delta C_{F0}$  due to the presence of hard fouling are in accordance with  $\Delta C_{F0}$  due to the presence of heavy calcareous fouling determined within [188]. Thus, in [188], the authors determined  $\Delta C_{F0}$  equal to 164.32% for KCS plate by CFD approach and  $\Delta C_{F0}$  equal to 171% by Granville similarity law scaling method, which is in accordance with the results obtained within this thesis.

Table 5.10 The comparison for flat plates having the same length as a ship fouled with hard fouling

KCS plate			
Surface condition	$10^3 \cdot C_{F0}^{fine}$	$10^3 \cdot C_{F0}^{Granville}$	$RD, \%$
R1 H	3.349	3.608	-7.181
R2 H	3.150	3.385	-6.949
R3 H	2.904	3.105	-6.457
R4 H	2.742	2.925	-6.258
R5 H	2.540	2.699	-5.897
R6 H	2.416	2.553	-5.358
KVLCC2 plate			
Surface condition	$10^3 \cdot C_{F0}^{fine}$	$10^3 \cdot C_{F0}^{Granville}$	$RD, \%$
R1 H	3.153	3.384	-6.825
R2 H	2.972	3.183	-6.643
R3 H	2.749	2.925	-6.042
R4 H	2.600	2.760	-5.790
R5 H	2.422	2.553	-5.124
R6 H	2.306	2.418	-4.658
BC plate			
Surface condition	$10^3 \cdot C_{F0}^{fine}$	$10^3 \cdot C_{F0}^{Granville}$	$RD, \%$
R1 H	3.455	3.782	-8.633
R2 H	3.223	3.545	-9.097
R3 H	2.967	3.245	-8.587
R4 H	2.800	3.054	-8.308
R5 H	2.598	2.815	-7.713
R6 H	2.469	2.660	-7.181

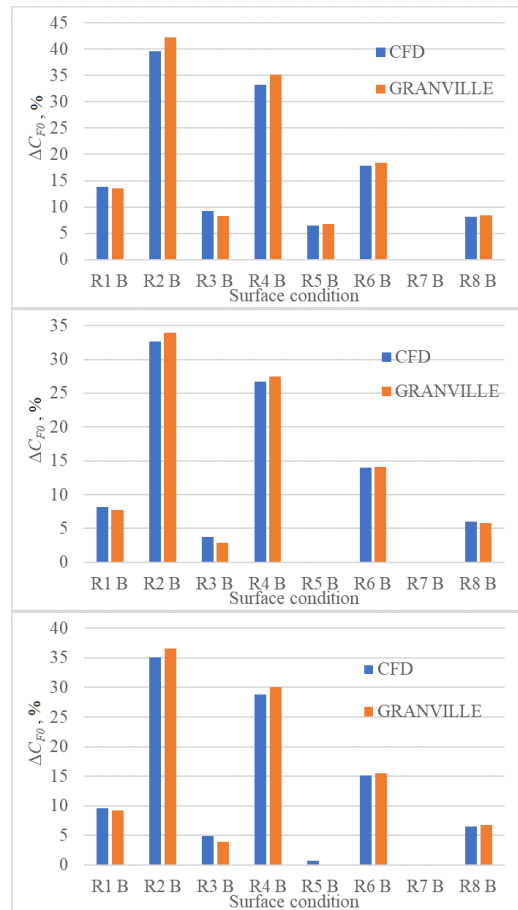


Figure 5.8 The obtained  $\Delta C_{F0}$  due to the presence of biofilm for the flat plate representing KCS (upper), KVLCC2 (middle) and BC (lower)

As already known,  $C_{F0}$  for fully rough regime at high  $Rn$  depends solely on the ratio  $k/L$ , i.e.  $C_{F0,R} = f(k/L)$  [233]. The confirmation of this can be seen from Table 5.10 if  $C_{F0,R}$  values obtained for the same values of  $k/L$  are compared. Thus,  $RD$  between  $C_{F0,R}$  for KVLCC2 plate for R2 H and  $C_{F0,R}$  for KCS plate for R1 H is equal to -0.09% ( $k/L = 6.344 \cdot 10^{-6}$ ),  $RD$  between  $C_{F0,R}$  for KVLCC2 plate for R4 H and  $C_{F0,R}$  for KCS plate for R3 H is equal to -0.24% ( $k/L = 2.837 \cdot 10^{-6}$ ) and  $RD$  between  $C_{F0,R}$  for KVLCC2 plate for R6 H and  $C_{F0,R}$  for KCS plate for R5 H is equal to -0.25% ( $k/L = 1.269 \cdot 10^{-6}$ ). Obviously, the obtained  $\Delta C_{F0}$  for the same  $k/L$  will not be the same if the plates were tested at various  $Rn$  values, since  $\Delta C_{F0}$  depends on  $C_{F0}$  for smooth plate, which is dependent on  $Rn$ . Therefore, additional CFD simulations are performed for KCS plate at  $Rn$  which corresponds to  $Rn$  of KVLCC2 plate. Using  $C_{F0}$  of smooth KCS plate at  $Rn$  which corresponds to  $Rn$  of KVLCC2 plate, the obtained  $\Delta C_{F0}$  for KCS plate are equal to 129.19% (R2 H), 99.50% (R4 H) and 75.79% (R6 H). The obtained  $\Delta C_{F0}$  for KVLCC2 plate are equal to 129.6% (R1 H), 100.16% (R3 H) and 76.38% (R5 H). It is clear that these  $\Delta C_{F0}$  are almost the same and probably within numerical and modelling uncertainties of CFD approach. Therefore, it is clear



that  $k/L$  is the key parameter which effects  $C_{F0,R}$  for fully rough regime at high  $Rn$  values [234].

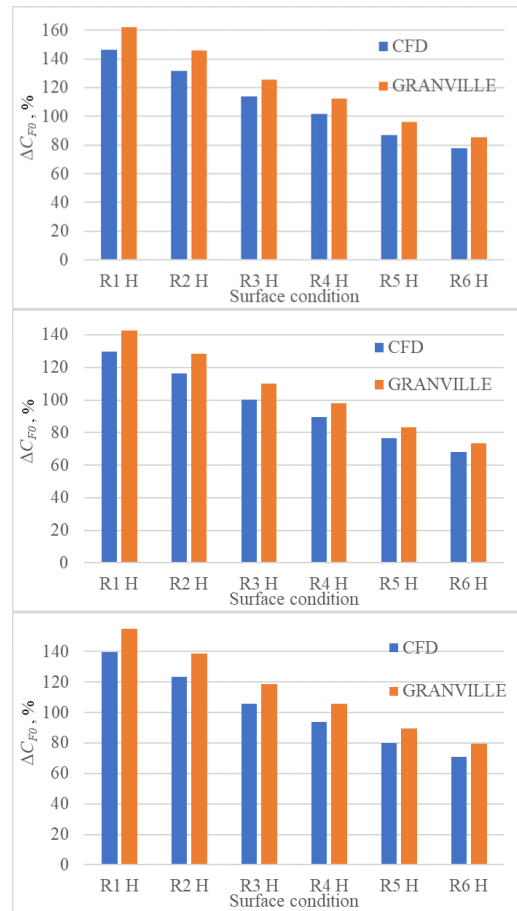


Figure 5.9 The obtained  $\Delta C_{F0}$  due to the presence of hard fouling for the flat plate representing KCS (upper), KVLCC2 (middle) and BC (lower)

### 5.3. The impact of biofouling on the resistance characteristics and nominal wake

Historically, the determination of the total resistance of a ship has been performed using towing tank experiments and extrapolation procedure. For that purpose the total resistance is decomposed into several components presented in Section 2.3.1. Thus, the form factor is usually determined by Prohaska’s method,  $C_F$  by ITTC 1957 model-ship correlation line and  $C_w$  by subtracting the calculated  $C_T$  of ship model using the measured data with  $C_V$  of ship model. The development of computers, as well as CFD have enabled detailed numerical investigations related to ship hydrodynamics. Lately, CFD is being used not only for research purposes, but for industrial purposes as well, both for design and operational analysis. When  $R_T$  is determined by CFD simulations based on the viscous flow theory,  $C_T$  is divided into  $C_F$  and the pressure resistance coefficient ( $C_p$ ). This also represents a physical decomposition of the total resistance, which is based on the knowledge that water acts on a ship with continuously distributed surface forces, i.e. tangential stresses and hydrodynamic pressure in normal direction. In order to obtain common resistance characteristics, the method described in [206],

[153] is used. Thus,  $R_T$  of a ship is obtained by CFD simulations of the viscous flow around a ship hull, including the free surface effects, i.e. Free Surface Simulations (FSS). In these simulations, VOF method will be applied for tracking and locating the free surface.  $R_V$  is obtained by DBS, which do not take free surface effects into account. In DBS, the flow around deeply immersed double body model or ship is simulated and thus the obtained  $R_T$  is equal to  $R_V$ .  $R_F$  is obtained by integrating the tangential stresses over the wetted surface, while  $R_{VP}$  is obtained by integrating the pressure over the wetted surface in DBS.  $R_W$  is obtained by subtracting  $R_T$  obtained in FSS and  $R_V$  obtained in DBS. It should be noted that the mesh used in DBS and FSS should be similar [235]. The Granville similarity law scaling method allows the prediction of the impact of biofouling on the frictional resistance. Historically, it was considered that the biofouling, i.e. roughness does not have any impact on the other resistance components except on the frictional resistance. However, the development of CFD model which can account for the effects of roughness allows the investigation of the impact of various surface conditions on each component of  $R_T$ .

Wake field of a ship represents an important parameter in the overall propulsive efficiency and the wake can be classified into either effective or nominal wake. The influence of surface conditions on the nominal wake of a ship is relatively modestly investigated, since it is very difficult to measure nominal wake of a ship at full-scale. The measurement of the nominal wake at model scale is carried out during towing tank experiments using either Prandtl-Pitot tube or laser doppler flowmetry. The nominal wake of a ship can be presented visually, through circumferentially averaged nominal wake at certain radii and with an integral value. As described within Appendix A, after a detail investigation related to nominal wake, it was decided to use wall functions along with  $k-\omega$  SST turbulence model for the assessment of nominal wake in full-scale. The nominal wake of a full-scale ship obtained from FSS can be represented visually, as circumferentially averaged nominal wake at certain radii and as an integral value.

### 5.3.1. Numerical modelling and verification study

Two types of CFD simulations are performed for the purpose of study related to the impact of biofouling on the ship resistance characteristics, i.e. DBS and FSS. DBS are performed as steady simulations, in which the free surface is replaced with the symmetry boundary condition. In that way, there are no free surface effects, i.e. wave making, and therefore the obtained  $R_T$  is equal to  $R_V$ . FSS are performed as unsteady simulations, as the free surface effects are taken into account. Only half of the computational domain is taken into account, since the symmetry condition is applied on the symmetry plane of a ship. In DBS, only quarter of domain is taken into account, as symmetry condition is applied on the symmetry plane of a ship and on the top boundary. Boundaries of computational domain are placed far enough from the ship in order to avoid their influence on the obtained solution [210], Table 5.11. What is more, VOF wave damping is applied within FSS as explained in detail in Section 3.2.3. The applied boundary conditions are given in Table 5.11 as well. It should be noted that the same boundary conditions are used in [188], [193], [236]. The boundary conditions for FSS are chosen to represent the full-scale ship being towed in a deep-water condition, while the boundary conditions for DBS are chosen to represent the deeply immersed full-scale ship being towed.

As can be seen from Table 5.11, the domain boundaries for DBS are placed at the same distances from the ship as in FSS, except the top boundary, which is placed at the waterline plane. This is done in order to have similar mesh in DBS and FSS, what is important for a proper decomposition of  $R_T$  [153]. The computational domain is discretized using the same mesh sizes and mesh refinements, except refinement regarding free surface effects, as within DBS free surface effects are not considered. The prism layer mesh is discretized in the same way, i.e. with the same number of prism layer cells, same prism layer stretching as well as the same prism layer thickness. In addition to, the same boundary conditions are applied for FSS, except the boundary condition at the top boundary, where symmetry condition is applied, thus allowing a significant reduction in the cell number. Namely, the initial flow velocity at side, bottom, inlet and top boundaries is set to the velocity of the flat wave, i.e. a ship speed, in the negative  $x$ -direction. The selection of the velocity inlet for the top and side of the domain in FSS therefore allows the flow at the top and side of the domain to be parallel to the outlet boundary, which prevents reflections from these boundaries, similarly to slip wall boundary condition. The representation of the deep water is allowed by the application of a velocity boundary condition at bottom boundary in FSS, i.e. slip wall boundary condition at bottom boundary in DBS.

The computational domain is discretized with a cut-cell grid with prism layer mesh on the walls using the automatic mesh generator in STAR-CCM+. The cell size at hull surface within DBS and FSS is set as  $1/1000L_{pp}$ , thus allowing very fine discretization of the hull geometry. The mesh is refined using the volumetric mesh controls, which ensured finer grids in the critical regions. Thus, in the area around the hull and rudder, near the bow and stern region, as well as in the wake generated by the ship finer grids are generated. Additionally, in FSS the mesh is refined in the area where the free surface is expected and it is divided into three refinement regions, in order to allow gradual transition from very fine mesh to coarse mesh. Furthermore, the refinement for capturing Kelvin wake pattern is made. Since within this thesis, the impact of biofouling is accounted via implementation of roughness function within the wall function of the solver, wall functions are used in DBS and FSS. The application of wall functions within full-scale FSS is common in the literature [182], [188], [237]. As already explained, an appropriate near-wall mesh resolution is applied to wall surfaces with no-slip boundary conditions based on the roughness height values corresponding to each fouling condition. For this reason, the near-wall cell numbers varied for certain of the fouling conditions. More details regarding the computational domain discretization can be found in subsection 3.2.2.

Table 5.11 The computational domain

Boundary	DBS		FSS	
	Boundary condition	Distance from a ship	Boundary condition	Distance from a ship
Side	Slip wall	$2.75L_{pp}$	Velocity inlet	$2.75L_{pp}$
Bottom	Slip wall	$2.5L_{pp}$	Velocity inlet	$2.5L_{pp}$
Inlet	Velocity inlet	$1.5L_{pp}$	Velocity inlet	$1.5L_{pp}$
Outlet	Pressure outlet	$3L_{pp}$	Pressure outlet	$3L_{pp}$
Top	Symmetry	/	Velocity inlet	$1.5L_{pp}$
Ship hull	No slip wall	/	No slip wall	/

Cross-sections of the discretized computational domains used in FSS are shown in Figure 5.10. From this figure, the refinements along the location of free surface, around the ship hull and for capturing the Kelvin wake can be observed. A very fine discretization of the hull surface can be noticed in Figure 5.11, where the volume mesh for the KCS hull is shown.

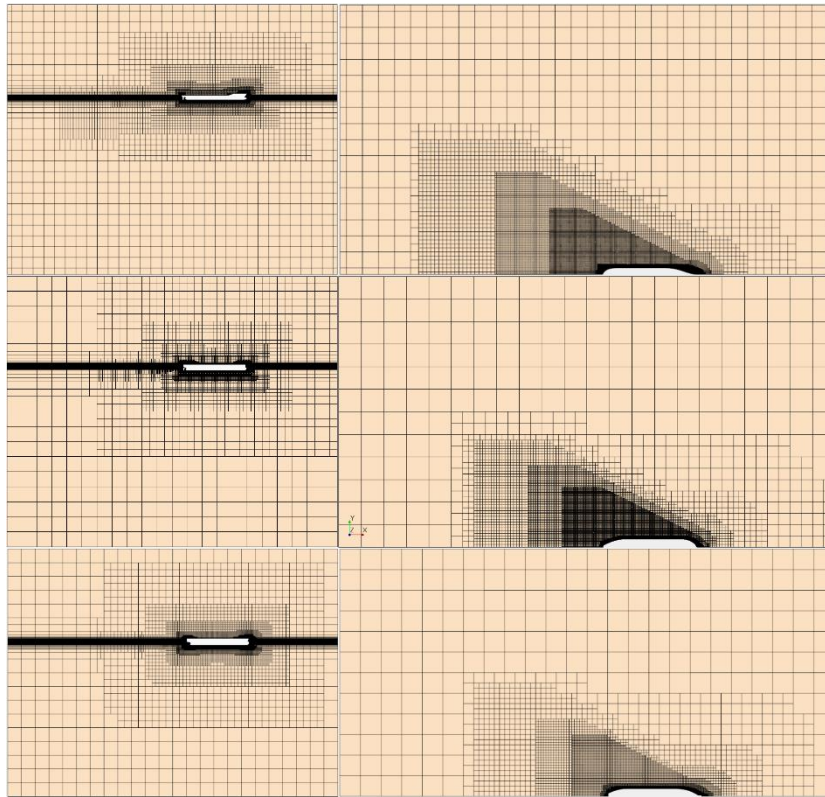


Figure 5.10 The profile view cross-section of the domain for KCS (upper left), KVLCC2 (middle left) and BC (lower left) and the top view cross-section of the domain for KCS (upper right), KVLCC2 (middle right) and BC (lower right)

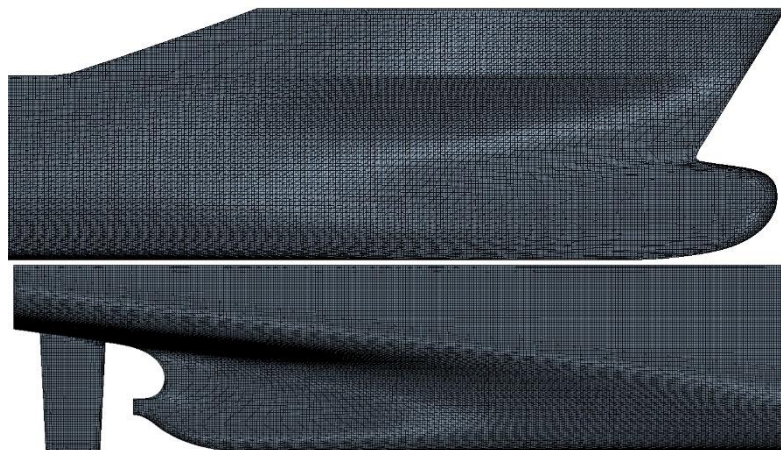


Figure 5.11 Volume mesh for the KCS hull, bow region (upper) and stern region (lower)

The obtained  $y^+$  distributions in the first cell near the wall for smooth KCS, KVLCC2 and BC are shown in Figure 5.12. The average value of  $y^+$  in the first cells near the wall below free surface for smooth KCS is equal to 164.16, for KVLCC2 to 168.96 and for BC to 308.37. It should be noted that boundary layer of a ship has extended log-law and outer region [109].

Since, log-law region extends up to 15% of the boundary layer thickness, the  $y^+$  value for full-scale ship, where log-law region is still present, is significantly higher than for ship model. Therefore, the obtained  $y^+$  distributions in the first cell near the wall for full-scale ships are satisfactory. The presence of fouling will cause the increase in  $y^+$  values in the first cells near the wall even though  $y$  values of the first cell has remained the same. This can be seen from Figure 5.13, where the obtained  $y^+$  distributions in the first cell near the wall for full-scale ships fouled with biofilm are shown (R2 B). Namely, since  $k_{eff}$  values of surface conditions fouled with biofilm are relatively small (Table 5.3),  $y$  values of the first cell within DBS and FSS for ships fouled with biofilm have remained the same as in DBS and FSS for smooth ships. The average value of  $y^+$  in the first cells near the wall below free surface for KCS is equal to 194.16, KVLCC2 to 200.00 and for BC to 357.54 for the surface condition R2B. Therefore, it is clear that  $u_\tau$ , i.e.  $\tau_w$  rises due to the presence of fouling and that depending on the surface condition  $y^+$  values along the wetted surface will vary, regardless the same  $y$  values of the first cell in FSS of smooth ships. The obtained  $y^+$  distributions for ships fouled with hard fouling are even higher for two reasons. The first reason is that higher  $y$  values of the first cell must be used, as  $k$  values are higher and  $y$  must be higher than  $k$ . Another reason is that hard fouling is more severe fouling type than biofilm and consequently  $\Delta U^+$  values will be higher. This will result with higher  $u_\tau$  values along the wetted surface of ship fouled with hard fouling in comparison with ship fouled with biofilm. The obtained  $y^+$  distributions in the first cell near the wall for full-scale ships fouled with hard fouling are shown for the surface condition R1 H, Figure 5.14. The average value of  $y^+$  in the first cells near the wall below free surface for KCS is equal to 1308.87, KVLCC2 to 810.99 and for BC to 1480.10 for the surface condition R1 H. These significantly higher  $y^+$  are justified, since for the surface condition R1 H  $k$  is equal to 2.065 mm, being very large value. Even higher  $y^+$  in the first cell near the wall are obtained for KCS fouled with heavy calcareous fouling in [21]. It should be noted that within DBS the same  $y^+$  values in the first cell near the wall are obtained since the same prism layer mesh is applied.

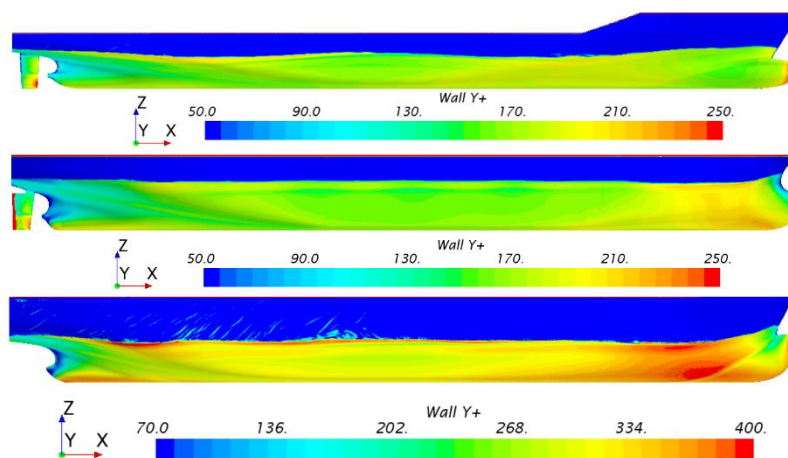


Figure 5.12 The obtained  $y^+$  distributions in the first cell near the wall for smooth KCS (upper), KVLCC2 (middle) and BC (lower)

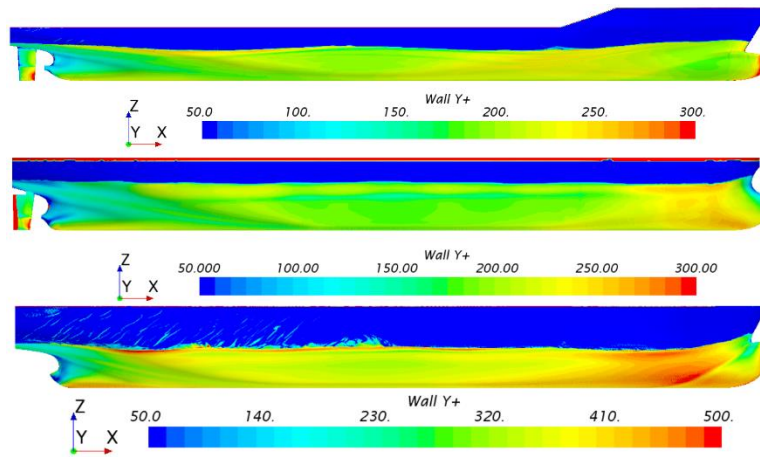


Figure 5.13 The obtained  $y^+$  distributions in the first cell near the wall for KCS (upper), KVLCC2 (middle) and BC (lower) fouled with the surface condition R2 B

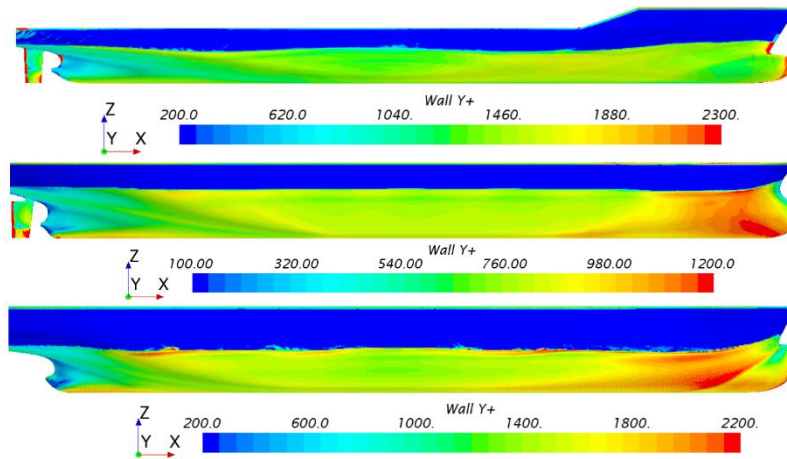


Figure 5.14 The obtained  $y^+$  distributions in the first cell near the wall for KCS (upper), KVLCC2 (middle) and BC (lower) fouled with the surface condition R1 H

Three meshes are generated for the purpose of the verification study: coarse, medium and fine mesh. The mesh is refined systematically, as all mesh parameters (except prism layer) are set as a relative values of cell base size and the refinement is performed through a change of cell base size. The number of cells used for the investigated ships is given in Table 5.12. It should be noted that the number of cells for CFD simulations with the hard fouling varied amongst the investigated surface conditions, since prism layer is discretized in a different way amongst the investigated surface conditions. Within Table 5.12, the number of cells is given for the surface condition R6 H.

Within DBS and FSS, iterative uncertainties are considered to be negligible as done in [152]. Therefore, numerical uncertainties obtained within DBS consist only of grid uncertainties. On the other hand, numerical uncertainties obtained within FSS are consisted of grid and time step uncertainties. Simulation numerical uncertainties for FSS are calculated using equation (3.31). It should be noted that  $U_G$  and  $U_T$  are obtained as a product of the obtained numerical solution using fine mesh ( $\phi_1$ ) and  $GCI_{fine}^{21}$ . Both temporal and grid convergence studies are performed for FSS with  $R_T$  as a key variable. The grid convergence study for DBS is performed with  $R_F$ ,  $R_V$  and  $1+k$  as key variables. As a result of the performed verification study numerical

uncertainties for the determination of  $R_T$ ,  $R_F$ ,  $R_V$  and  $1+k$  are obtained. It should be noted that  $1+k$  is determined as  $R_V / R_F$ . For the determination of wave resistance, both  $R_T$  and  $R_V$  should be known. Therefore, numerical uncertainties in the prediction of  $R_W$  are obtained analogously to equation (3.31) as follows [20]:

$$U_{R_W}^2 = \sqrt{U_{R_T}^2 + U_{R_V}^2} \tag{5.1}$$

where  $U_{R_T}$  is the numerical uncertainty in the prediction of  $R_T$  with FSS and is consisted of both grid and temporal uncertainties and  $U_{R_V}$  is the numerical uncertainty in the prediction of  $R_V$  with DBS.

Table 5.12 The number of cells within DBS and FSS

DBS			
Case	KCS – biofilm	KVLCC2 – biofilm	BC – biofilm
Coarse mesh	1.21 M	0.46 M	0.65 M
Medium mesh	2.35 M	0.90 M	1.40 M
Fine mesh	4.60 M	1.70 M	3.10 M
Case	KCS – hard fouling	KVLCC2 – hard fouling	BC – hard fouling
Coarse mesh	0.64 M	0.90 M	0.35 M
Medium mesh	1.21 M	1.70 M	0.77 M
Fine mesh	2.35 M	3.36 M	1.63 M
FSS			
Case	KCS – biofilm	KVLCC2 – biofilm	BC – biofilm
Coarse mesh	1.92 M	0.68 M	1.07 M
Medium mesh	3.69 M	1.32 M	2.29 M
Fine mesh	7.25 M	2.47 M	4.98 M
Case	KCS – hard fouling	KVLCC2 – hard fouling	BC – hard fouling
Coarse mesh	1.01 M	1.32 M	0.55 M
Medium mesh	1.89 M	2.47 M	1.20 M
Fine mesh	3.66 M	5.06 M	2.59 M

The numerical uncertainty in the prediction of changes of resistance characteristics due to the presence of biofouling are calculated as follows:

$$U_{\Delta\varphi}^2 = \sqrt{U_S^2 + U_R^2} \tag{5.2}$$

where  $U_s$  is the numerical uncertainty in the prediction of certain resistance characteristic for smooth surface condition ( $\phi$ ) and  $U_R$  is the numerical uncertainty in the prediction of certain resistance characteristic for rough surface condition.

More details regarding the verification study and used time steps within temporal convergence studies can be found in Section 3.2.6.1.

Table 5.13 The obtained grid uncertainties within FSS for ships fouled with biofilm

KCS						
Surface condition	$\phi_3$ , kN	$\phi_2$ , kN	$\phi_1$ , kN	$\phi_{ext}^{21}$ , kN	$GCI_{fine}^{21}$ , %	$U_G$ , kN
S	1596.364	1569.604	1560.162	1555.423	0.380	5.924
R1 B	1753.746	1711.316	1708.092	1707.852	0.018	0.299
R2 B	1993.858	1973.866	1969.524	1968.416	0.070	1.385
R3 B	1699.400	1669.912	1660.716	1656.876	0.289	4.799
R4 B	1946.104	1915.774	1906.756	1903.240	0.230	4.395
R5 B	1665.686	1633.094	1627.558	1626.519	0.080	1.299
R6 B	1781.080	1755.748	1747.568	1743.974	0.257	4.492
R7 B	1599.638	1577.092	1564.850	1551.639	1.055	16.514
R8 B	1677.984	1653.032	1648.328	1647.324	0.076	1.255
KVLCC2						
Surface condition	$\phi_3$ , kN	$\phi_2$ , kN	$\phi_1$ , kN	$\phi_{ext}^{21}$ , kN	$GCI_{fine}^{21}$ , %	$U_G$ , kN
S	1712.626	1635.220	1647.384	1649.906	0.191	3.152
R1 B	1822.702	1787.740	1765.326	1716.209	3.478	61.397
R2 B	2157.540	2136.920	2107.800	2051.207	3.356	70.741
R3 B	1793.786	1734.238	1703.542	1665.088	2.822	48.068
R4 B	2057.600	2038.520	2024.980	1982.652	2.613	52.910
R5 B	1718.636	1677.560	1653.298	1611.213	3.182	52.606
R6 B	1923.176	1894.580	1835.248	1788.039	3.215	59.011
R7 B	1707.108	1669.782	1647.530	1607.968	3.002	49.453
R8 B	1753.736	1733.330	1719.710	1685.713	2.471	42.496
BC						
Surface condition	$\phi_3$ , kN	$\phi_2$ , kN	$\phi_1$ , kN	$\phi_{ext}^{21}$ , kN	$GCI_{fine}^{21}$ , %	$U_G$ , kN
S	602.835	583.898	580.334	579.550	0.169	0.980
R1 B	651.529	635.830	627.206	617.315	1.971	12.364
R2 B	776.254	755.313	748.863	746.135	0.455	3.409
R3 B	631.245	614.102	605.590	597.662	1.636	9.910
R4 B	746.659	726.374	721.105	719.349	0.304	2.195
R5 B	616.828	597.592	589.462	583.821	1.196	7.051
R6 B	678.389	657.958	653.842	652.857	0.188	1.232
R7 B	603.518	587.981	580.422	573.654	1.458	8.460
R8 B	638.182	619.991	611.914	605.805	1.248	7.636

The obtained results of both grid and temporal convergence studies for FSS are shown in Table 5.13, Table 5.14, Table 5.15 and Table 5.16. It should be noted that within these tables the obtained  $R_T$  are doubled as only half of the ship is simulated. After  $U_G$  and  $U_T$  are obtained,



$U_{SN}$  in the prediction of  $R_T$  are calculated using equation (3.31), Table 5.17. The obtained results of grid convergence studies for DBS are shown in Table 5.18, Table 5.19, Table 5.20, Table 5.21, Table 5.22 and Table 5.23. The uncertainties in the prediction of certain resistance characteristic is given in the last column. As for FSS, the obtained numerical results from DBS are doubled as only quarter of double body is simulated. Once  $U_{SN}$  in the prediction of  $R_T$  ( $U_{R_T}$ ) and  $U_{SN}$  in the prediction of  $R_V$  ( $U_{R_V}$ ) are determined,  $U_{SN}$  in the prediction of  $R_W$  ( $U_{R_W}$ ) can be calculated according to equation (5.1). The obtained  $U_{R_W}$  are presented in Table 5.24.

Table 5.14 The obtained time step uncertainties within FSS for ships fouled with biofilm

KCS						
Surface condition	$\phi_3$ , kN	$\phi_2$ , kN	$\phi_1$ , kN	$\phi_{ext}^{21}$ , kN	$GCI_{fine}^{21}$ , %	$U_T$ , kN
S	1575.631	1564.573	1560.162	1557.234	0.235	3.660
R1 B	1750.377	1719.698	1708.092	1701.030	0.517	8.827
R2 B	1988.972	1972.523	1969.524	1968.855	0.042	0.836
R3 B	1678.997	1665.586	1660.716	1657.939	0.209	3.472
R4 B	1936.646	1911.732	1906.756	1905.514	0.081	1.552
R5 B	1668.542	1638.706	1627.558	1620.907	0.511	8.314
R6 B	1769.237	1752.299	1747.568	1745.734	0.131	2.292
R7 B	1582.295	1566.904	1564.850	1564.534	0.025	0.396
R8 B	1663.112	1652.058	1648.328	1646.428	0.144	2.374
KVLCC2						
Surface condition	$\phi_3$ , kN	$\phi_2$ , kN	$\phi_1$ , kN	$\phi_{ext}^{21}$ , kN	$GCI_{fine}^{21}$ , %	$U_T$ , kN
S	1679.300	1658.780	1647.380	1633.130	1.081	17.812
R1 B	1824.584	1814.990	1765.326	1753.435	0.842	14.864
R2 B	2210.960	2135.920	2107.800	2090.947	0.999	21.066
R3 B	1717.224	1724.708	1703.542	1691.964	0.850	14.472
R4 B	2075.540	2043.780	2024.980	1997.708	1.683	34.090
R5 B	1690.870	1666.700	1653.298	1636.618	1.261	20.850
R6 B	1876.558	1867.320	1835.248	1822.273	0.884	16.219
R7 B	1690.098	1678.374	1647.530	1628.617	1.435	23.641
R8 B	1741.502	1726.518	1719.710	1714.041	0.412	7.086
BC						
Surface condition	$\phi_3$ , kN	$\phi_2$ , kN	$\phi_1$ , kN	$\phi_{ext}^{21}$ , kN	$GCI_{fine}^{21}$ , %	$U_T$ , kN
S	584.139	579.625	580.334	580.466	0.028	0.165
R1 B	629.605	630.667	627.206	625.673	0.306	1.917
R2 B	756.470	746.424	748.863	749.645	0.131	0.978
R3 B	613.137	604.964	605.590	605.642	0.011	0.065
R4 B	732.196	721.403	721.105	721.097	0.001	0.011
R5 B	591.705	587.777	589.462	590.727	0.268	1.582
R6 B	655.007	655.093	653.842	653.749	0.018	0.117
R7 B	581.507	581.357	580.422	580.243	0.039	0.224
R8 B	619.014	612.762	611.914	611.781	0.027	0.166

Table 5.15 The obtained grid uncertainties within FSS for ships fouled with hard fouling

KCS						
Surface condition	$\phi_3$ , kN	$\phi_2$ , kN	$\phi_1$ , kN	$\phi_{ext}^{21}$ , kN	$GCI_{fine}^{21}$ , %	$U_G$ , kN
S	1639.638	1596.364	1569.604	1532.043	2.991	46.952
R1 H	3051.452	3069.500	3073.322	3074.234	0.037	1.140
R2 H	2957.920	2940.320	2928.180	2905.394	0.973	28.482
R3 H	2847.570	2758.106	2729.960	2718.386	0.530	14.468
R4 H	2637.838	2616.434	2605.672	2596.045	0.462	12.034
R5 H	2443.956	2459.356	2451.840	2444.969	0.350	8.589
R6 H	2380.346	2352.290	2352.168	2352.168	0.000	0.001
KVLCC2						
Surface condition	$\phi_3$ , kN	$\phi_2$ , kN	$\phi_1$ , kN	$\phi_{ext}^{21}$ , kN	$GCI_{fine}^{21}$ , %	$U_G$ , kN
S	1635.220	1647.384	1610.246	1589.466	1.613	25.975
R1 H	3543.920	3563.150	3557.500	3555.376	0.075	2.655
R2 H	3356.088	3370.410	3360.040	3334.161	0.963	32.349
R3 H	3142.630	3110.550	3115.760	3116.538	0.031	0.972
R4 H	3007.110	2945.100	2955.560	2957.213	0.070	2.066
R5 H	2803.822	2771.060	2762.080	2759.636	0.111	3.055
R6 H	2639.580	2637.280	2637.100	2637.090	0.000	0.013
BC						
Surface condition	$\phi_3$ , kN	$\phi_2$ , kN	$\phi_1$ , kN	$\phi_{ext}^{21}$ , kN	$GCI_{fine}^{21}$ , %	$U_G$ , kN
S	648.418	602.835	583.898	569.505	3.081	17.991
R1 H	1256.130	1260.748	1252.756	1241.987	1.075	13.462
R2 H	1191.318	1189.990	1175.158	1173.809	0.143	1.686
R3 H	1106.148	1105.220	1092.158	1091.260	0.103	1.123
R4 H	1061.058	1052.394	1039.866	1015.109	2.976	30.946
R5 H	989.582	991.448	973.264	971.341	0.247	2.403
R6 H	948.236	943.490	931.358	924.183	0.963	8.969

From the results of the verification study of FSS (Table 5.13, Table 5.14, Table 5.15 and Table 5.16), where  $R_T$  is used as a key variable, it can be concluded that time step uncertainties are lower than grid uncertainties. Regarding  $U_G$  related to the prediction of  $R_T$  for smooth ships and ships fouled with biofilm, the lowest  $U_G$  are obtained for KCS, than for BC and lastly for KVLCC2. This was expected, since the computational domain is discretized with the largest number of cells for KCS, followed by BC and KVLCC2, Table 5.12. The lowest  $U_T$  related to the prediction of  $R_T$  for smooth ships and ships fouled with biofilm are obtained for BC, than for KCS and lastly for KVLCC2. It should be noted that temporal convergence studies are performed using fine mesh, and three time steps defined in Section 3.2.6.1, i.e.  $T/50, T/100$  and  $T/200$ .

Table 5.16 The obtained time step uncertainties within FSS for ships fouled with hard fouling

KCS						
Surface condition	$\phi_3$ , kN	$\phi_2$ , kN	$\phi_1$ , kN	$\phi_{ext}^{21}$ , kN	$GCI_{fine}^{21}$ , %	$U_T$ , kN
S	1596.082	1595.146	1569.604	1568.632	0.077	1.215
R1 H	3113.140	3115.534	3073.322	3070.784	0.103	3.172
R2 H	2962.880	2956.740	2928.180	2920.358	0.334	9.777
R3 H	2772.270	2778.520	2729.960	2722.787	0.328	8.967
R4 H	2641.060	2638.400	2605.672	2602.777	0.139	3.619
R5 H	2488.600	2492.200	2451.840	2447.887	0.202	4.941
R6 H	2393.660	2390.840	2352.168	2349.126	0.162	3.802
KVLCC2						
Surface condition	$\phi_3$ , kN	$\phi_2$ , kN	$\phi_1$ , kN	$\phi_{ext}^{21}$ , kN	$GCI_{fine}^{21}$ , %	$U_T$ , kN
S	1598.660	1605.908	1610.246	1616.713	0.502	8.083
R1 H	3567.180	3566.830	3557.500	3557.136	0.013	0.455
R2 H	3373.320	3364.020	3360.040	3357.062	0.111	3.722
R3 H	3122.200	3111.040	3115.760	3119.219	0.139	4.324
R4 H	2984.540	2955.420	2955.560	2955.561	0.000	0.001
R5 H	2775.280	2758.220	2762.080	2763.209	0.051	1.411
R6 H	2611.200	2637.960	2637.100	2637.071	0.001	0.036
BC						
Surface condition	$\phi_3$ , kN	$\phi_2$ , kN	$\phi_1$ , kN	$\phi_{ext}^{21}$ , kN	$GCI_{fine}^{21}$ , %	$U_T$ , kN
S	594.318	584.566	583.898	583.849	0.011	0.061
R1 H	1281.062	1280.160	1252.756	1251.823	0.093	1.166
R2 H	1198.104	1181.802	1175.158	1170.587	0.486	5.713
R3 H	1104.980	1094.054	1092.158	1091.760	0.046	0.498
R4 H	1067.702	1046.128	1039.866	1037.305	0.308	3.201
R5 H	998.956	982.330	973.264	962.392	1.396	13.59
R6 H	988.790	942.402	931.358	927.907	0.463	4.314

Generally, the obtained  $U_G$  related to the prediction of  $R_T$  for smooth ships and ships fouled with biofilm are low and the highest  $GCI_{fine}^{21}$  for KCS is equal to 1.055%, for BC to 1.971% and for KVLCC2 to 3.478%. The obtained  $U_T$  related to the prediction of  $R_T$  for smooth ships and ships fouled with biofilm are even lower and the highest  $GCI_{fine}^{21}$  for KCS is equal to 0.517%, for BC to 0.306% and for KVLCC2 to 1.683%. Regarding  $U_G$  related to the prediction of  $R_T$  for smooth ships and ships fouled with hard fouling, the lowest  $U_G$  are obtained for KVLCC2, than for KCS and lastly for BC. This was also expected, since the computational domain is discretized with the largest number of cells for KVLCC2, followed by KCS and BC, Table 5.12. The lowest  $U_T$  related to the prediction of  $R_T$  for smooth ships and ships fouled with biofilm are obtained for KCS, than for KVLCC2 and lastly for BC. Generally, the obtained  $U_G$  related to the prediction of  $R_T$  for smooth ships and ships fouled with hard fouling are low

and the highest  $GCI_{fine}^{21}$  for KCS is equal to 2.991%, for BC to 3.081% and for KVLCC2 to 1.613%.

Table 5.17 The obtained  $U_{SN}$  in the prediction of  $R_T$  ( $U_{R_T}$ )

	KCS		KVLCC2		BC	
Surface condition	$U_{R_T}$ , kN	$U_{R_T}$ , %	$U_{R_T}$ , kN	$U_{R_T}$ , %	$U_{R_T}$ , kN	$U_{R_T}$ , %
S	6.964	0.446	18.089	1.098	0.993	0.171
R1 B	8.832	0.517	63.170	3.578	12.512	1.995
R2 B	1.618	0.082	73.811	3.502	3.547	0.474
R3 B	5.923	0.357	50.199	2.947	9.910	1.636
R4 B	4.661	0.244	62.941	3.108	2.195	0.304
R5 B	8.415	0.517	56.587	3.423	7.227	1.226
R6 B	5.043	0.289	61.199	3.335	1.237	0.189
R7 B	16.519	1.056	54.813	3.327	8.463	1.458
R8 B	2.686	0.163	43.083	2.505	7.638	1.248
	KCS		KVLCC2		BC	
Surface condition	$U_{R_T}$ , kN	$U_{R_T}$ , %	$U_{R_T}$ , kN	$U_{R_T}$ , %	$U_{R_T}$ , kN	$U_{R_T}$ , %
S	46.967	2.992	27.203	1.689	17.991	3.081
R1 H	3.371	0.110	2.693	0.076	13.512	1.079
R2 H	30.114	1.028	32.562	0.969	5.957	0.507
R3 H	17.021	0.623	4.432	0.142	1.228	0.112
R4 H	12.566	0.482	2.066	0.070	31.111	2.992
R5 H	9.909	0.404	3.365	0.122	13.801	1.418
R6 H	3.802	0.162	0.038	0.001	9.953	1.069

The obtained  $U_T$  related to the prediction of  $R_T$  for smooth ships and ships fouled with hard fouling are even lower and the highest  $GCI_{fine}^{21}$  for KCS is equal to 0.334%, for BC to 1.396% and for KVLCC2 to 0.502%. The obtained  $U_{R_T}$ , which are consisted of both  $U_G$  and  $U_T$ , are shown in Table 5.17. As can be seen from Table 5.17, the lowest  $U_{R_T}$  for smooth ships and ships fouled with biofilm are obtained for KCS, while for smooth ships and ships fouled with hard fouling are obtained for KVLCC2. Thus, the highest  $U_{R_T}$  for smooth KCS and KCS fouled with biofilm is equal to 1.056%, for BC to 1.995% and for KVLCC2 to 3.578%. The highest  $U_{R_T}$  for smooth KCS and KCS fouled with hard fouling is equal to 2.992%, for BC to 3.081% and for KVLCC2 to 1.689%.

The obtained  $U_G$  for DBS are equal to  $U_{SN}$ , since the grid uncertainty is the only uncertainty within DBS. Thus, the obtained  $GCI_{fine}^{21}$  within Table 5.18 and Table 5.19 represent  $U_{R_F}$ , the obtained  $GCI_{fine}^{21}$  within Table 5.20 and Table 5.21 represent  $U_{R_V}$  and the obtained  $GCI_{fine}^{21}$  within Table 5.22 and Table 5.23 represent  $U_{1+k}$ .

Table 5.18 The obtained grid uncertainties for  $R_F$  within DBS for ships fouled with biofilm

KCS						
Surface condition	$\phi_3$ , kN	$\phi_2$ , kN	$\phi_1$ , kN	$\phi_{ext}^{21}$ , kN	$GCI_{fine}^{21}$ , %	$U_{R_F}$ , kN
S	1059.200	1066.388	1069.684	1072.994	0.387	4.137
R1 B	1209.394	1218.940	1223.156	1227.099	0.403	4.929
R2 B	1477.148	1491.522	1498.768	1507.582	0.735	11.018
R3 B	1160.286	1169.270	1173.104	1176.472	0.359	4.210
R4 B	1413.434	1426.538	1431.544	1435.176	0.317	4.540
R5 B	1126.896	1134.978	1138.884	1143.236	0.478	5.440
R6 B	1248.634	1258.676	1263.742	1269.914	0.611	7.715
R7 B	1060.048	1067.106	1070.528	1074.366	0.448	4.797
R8 B	1145.448	1153.908	1157.980	1162.480	0.486	5.625
KVLCC2						
Surface condition	$\phi_3$ , kN	$\phi_2$ , kN	$\phi_1$ , kN	$\phi_{ext}^{21}$ , kN	$GCI_{fine}^{21}$ , %	$U_{R_F}$ , kN
S	1242.385	1283.312	1303.498	1327.397	2.292	29.874
R1 B	1382.682	1392.822	1415.496	1430.696	1.342	19.000
R2 B	1684.690	1698.834	1724.750	1750.104	1.838	31.693
R3 B	1327.854	1337.352	1359.294	1373.195	1.278	17.377
R4 B	1611.500	1624.636	1649.816	1672.298	1.703	28.102
R5 B	1283.892	1294.404	1314.454	1332.534	1.719	22.600
R6 B	1452.272	1462.994	1486.080	1502.633	1.392	20.691
R7 B	1274.761	1283.312	1303.498	1315.824	1.182	15.407
R8 B	1351.426	1360.898	1382.511	1396.498	1.265	17.485
BC						
Surface condition	$\phi_3$ , kN	$\phi_2$ , kN	$\phi_1$ , kN	$\phi_{ext}^{21}$ , kN	$GCI_{fine}^{21}$ , %	$U_{R_F}$ , kN
S	408.724	410.574	414.05	418.431	1.323	5.476
R1 B	449.142	451.384	455.294	461.155	1.609	7.326
R2 B	551.754	555.210	559.280	589.625	6.782	37.931
R3 B	430.558	432.662	436.464	441.700	1.499	6.545
R4 B	526.828	529.946	533.985	550.447	3.854	20.578
R5 B	415.876	417.910	421.412	426.831	1.607	6.773
R6 B	470.740	473.124	477.068	483.832	1.772	8.455
R7 B	408.730	410.572	414.05	418.386	1.309	5.420
R8 B	435.560	437.622	441.342	446.484	1.456	6.428

The obtained  $U_{R_F}$  for smooth ships and ships fouled with biofilm are low and the highest  $GCI_{fine}^{21}$  for KCS is equal to 0.735%, for BC to 6.782% and for KVLCC2 to 2.292%, while for smooth ships and ships fouled with hard fouling the highest  $GCI_{fine}^{21}$  for KCS is equal to 3.118%, for BC to 1.915% and for KVLCC2 to 0.318%. The obtained  $U_{R_F}$  for smooth ships and ships fouled with biofilm are low and the highest  $GCI_{fine}^{21}$  for KCS is equal to 0.558%, for BC to 0.126% and for KVLCC2 to 0.618%, while for smooth ships and ships fouled with hard fouling the highest  $GCI_{fine}^{21}$  for KCS is equal to 2.405%, for BC to 2.266% and for KVLCC2 to 0.395%.

The obtained  $U_{1+k}$  for smooth ships and ships fouled with biofilm are low and the highest  $GCI_{fine}^{21}$  for KCS is equal to 0.930%, for BC to 1.825% and for KVLCC2 to 1.979%, while for smooth ships and ships fouled with hard fouling the highest  $GCI_{fine}^{21}$  for KCS is equal to 4.150%, for BC to 1.841% and for KVLCC2 to 0.204%. Generally, it can be concluded that the obtained  $U_G$ , i.e.  $U_{SN}$ , in the prediction of resistance characteristics with DBS are low.

Table 5.19 The obtained grid uncertainties for  $R_F$  within DBS for ships fouled with hard fouling

KCS						
Surface condition	$\phi_3$ , kN	$\phi_2$ , kN	$\phi_1$ , kN	$\phi_{ext}^{21}$ , kN	$GCI_{fine}^{21}$ , %	$U_{R_F}$ , kN
S	1052.894	1060.479	1066.388	1085.011	2.183	23.279
R1 H	2549.860	2584.604	2606.868	2643.973	1.779	46.382
R2 H	2400.380	2434.250	2455.964	2491.966	1.832	45.003
R3 H	2211.400	2244.288	2266.952	2313.078	2.543	57.657
R4 H	2095.240	2124.560	2144.646	2184.793	2.340	50.183
R5 H	1946.608	1971.466	1988.832	2025.714	2.318	46.102
R6 H	1852.672	1876.155	1893.728	1940.971	3.118	59.054
KVLCC2						
Surface condition	$\phi_3$ , kN	$\phi_2$ , kN	$\phi_1$ , kN	$\phi_{ext}^{21}$ , kN	$GCI_{fine}^{21}$ , %	$U_{R_F}$ , kN
S	1283.315	1303.656	1310.918	1314.257	0.318	4.174
R1 H	2901.020	2934.440	2946.720	2952.529	0.246	7.261
R2 H	2740.300	2774.100	2783.260	2786.038	0.125	3.472
R3 H	2538.780	2572.020	2578.920	2580.410	0.072	1.862
R4 H	2406.520	2438.620	2445.760	2447.448	0.086	2.110
R5 H	2246.280	2277.640	2284.260	2285.723	0.080	1.828
R6 H	2141.840	2172.240	2178.900	2180.444	0.089	1.930
BC						
Surface condition	$\phi_3$ , kN	$\phi_2$ , kN	$\phi_1$ , kN	$\phi_{ext}^{21}$ , kN	$GCI_{fine}^{21}$ , %	$U_{R_F}$ , kN
S	399.572	408.724	410.574	411.062	0.149	0.610
R1 H	961.364	970.096	975.366	990.308	1.915	18.678
R2 H	885.492	905.216	911.292	914.373	0.423	3.851
R3 H	816.282	833.609	841.031	847.392	0.945	7.951
R4 H	772.164	787.772	794.882	801.709	1.074	8.533
R5 H	717.117	732.035	738.446	743.963	0.934	6.896
R6 H	682.170	696.604	702.392	706.815	0.787	5.529

Table 5.20 The obtained grid uncertainties for  $R_v$  within DBS for ships fouled with biofilm

KCS						
Surface condition	$\phi_3$ , kN	$\phi_2$ , kN	$\phi_1$ , kN	$\phi_{ext}^{21}$ , kN	$GCI_{fine}^{21}$ , %	$U_{R_v}$ , kN
S	1193.934	1181.916	1176.504	1171.254	0.558	6.563
R1 B	1352.276	1343.546	1341.226	1340.246	0.091	1.225
R2 B	1639.186	1637.304	1638.374	1639.861	0.113	1.859
R3 B	1301.084	1290.370	1287.216	1285.680	0.149	1.920
R4 B	1570.846	1566.242	1565.556	1565.414	0.011	0.177
R5 B	1265.900	1255.194	1250.826	1247.283	0.354	4.429
R6 B	1395.326	1387.522	1385.118	1383.868	0.113	1.562
R7 B	1194.960	1182.774	1177.666	1173.321	0.461	5.431
R8 B	1285.510	1275.416	1271.362	1268.162	0.315	4.000
KVLCC2						
Surface condition	$\phi_3$ , kN	$\phi_2$ , kN	$\phi_1$ , kN	$\phi_{ext}^{21}$ , kN	$GCI_{fine}^{21}$ , %	$U_{R_v}$ , kN
S	1596.823	1598.304	1599.314	1602.187	0.225	3.591
R1 B	1763.376	1725.744	1729.928	1730.537	0.044	0.761
R2 B	2106.480	2079.900	2091.800	2102.149	0.618	12.936
R3 B	1700.570	1661.408	1664.548	1664.873	0.024	0.407
R4 B	2022.940	1993.680	2003.820	2009.667	0.365	7.309
R5 B	1650.678	1612.476	1613.204	1613.222	0.001	0.023
R6 B	1842.876	1806.549	1811.903	1814.998	0.214	3.869
R7 B	1638.832	1598.304	1599.675	1599.735	0.005	0.076
R8 B	1727.228	1688.218	1691.605	1691.986	0.028	0.476
BC						
Surface condition	$\phi_3$ , kN	$\phi_2$ , kN	$\phi_1$ , kN	$\phi_{ext}^{21}$ , kN	$GCI_{fine}^{21}$ , %	$U_{R_v}$ , kN
S	497.242	489.850	488.324	487.961	0.093	0.454
R1 B	544.978	538.150	537.334	537.234	0.023	0.126
R2 B	666.548	661.900	663.386	664.053	0.126	0.834
R3 B	523.020	515.940	514.858	514.680	0.043	0.222
R4 B	636.996	631.864	632.133	632.147	0.003	0.017
R5 B	506.328	499.004	497.576	497.260	0.079	0.395
R6 B	570.708	564.208	563.608	563.369	0.053	0.299
R7 B	497.340	489.860	488.350	488.001	0.089	0.436
R8 B	529.080	521.928	520.776	520.574	0.048	0.252

Table 5.21 The obtained grid uncertainties for  $R_V$  within DBS for ships fouled with hard fouling

KCS						
Surface condition	$\phi_3$ , kN	$\phi_2$ , kN	$\phi_1$ , kN	$\phi_{ext}^{21}$ , kN	$GCI_{fine}^{21}$ , %	$U_{R_V}$ , kN
S	1213.372	1194.455	1181.916	1159.174	2.405	28.427
R1 H	2806.460	2829.174	2842.362	2859.535	0.755	21.467
R2 H	2646.520	2667.114	2678.292	2690.745	0.581	15.566
R3 H	2444.680	2462.246	2473.190	2489.982	0.849	20.99
R4 H	2320.140	2333.004	2340.640	2351.033	0.555	12.991
R5 H	2160.800	2168.258	2171.526	2173.929	0.138	3.004
R6 H	2060.640	2065.620	2068.978	2075.379	0.387	8.002
KVLCC2						
Surface condition	$\phi_3$ , kN	$\phi_2$ , kN	$\phi_1$ , kN	$\phi_{ext}^{21}$ , kN	$GCI_{fine}^{21}$ , %	$U_{R_V}$ , kN
S	1598.306	1598.806	1601.528	1602.262	0.057	0.918
R1 H	3501.840	3541.180	3554.640	3560.349	0.201	7.136
R2 H	3308.680	3345.480	3356.380	3360.124	0.139	4.680
R3 H	3067.820	3100.080	3111.020	3115.667	0.187	5.809
R4 H	2911.600	2940.300	2950.420	2954.986	0.193	5.708
R5 H	2722.140	2747.080	2756.500	2761.229	0.214	5.911
R6 H	2598.720	2620.700	2631.420	2639.744	0.395	10.405
BC						
Surface condition	$\phi_3$ , kN	$\phi_2$ , kN	$\phi_1$ , kN	$\phi_{ext}^{21}$ , kN	$GCI_{fine}^{21}$ , %	$U_{R_V}$ , kN
S	506.826	489.850	488.324	488.166	0.040	0.198
R1 H	1160.101	1159.632	1173.364	1173.584	0.023	0.274
R2 H	1074.586	1084.042	1090.310	1105.367	1.726	18.821
R3 H	995.126	999.323	1006.502	1015.121	1.070	10.774
R4 H	943.410	944.065	950.948	951.567	0.081	0.774
R5 H	880.873	878.579	883.064	886.603	0.501	4.423
R6 H	839.490	837.792	839.330	854.547	2.266	19.021



Table 5.22 The obtained grid uncertainties for  $1+k$  within DBS for ships fouled with biofilm

KCS						
Surface condition	$\phi_3$	$\phi_2$	$\phi_1$	$\phi_{ext}^{21}$	$GCI_{fine}^{21}, \%$	$U_{1+k}$
S	1.127	1.108	1.100	1.092	0.930	0.010
R1 B	1.118	1.102	1.097	1.093	0.424	0.005
R2 B	1.110	1.098	1.093	1.090	0.385	0.004
R3 B	1.121	1.104	1.097	1.093	0.460	0.005
R4 B	1.111	1.098	1.094	1.091	0.273	0.003
R5 B	1.123	1.106	1.098	1.091	0.798	0.009
R6 B	1.117	1.102	1.096	1.091	0.611	0.007
R7 B	1.127	1.108	1.100	1.092	0.879	0.010
R8 B	1.122	1.105	1.098	1.091	0.766	0.008
KVLCC2						
Surface condition	$\phi_3$	$\phi_2$	$\phi_1$	$\phi_{ext}^{21}$	$GCI_{fine}^{21}, \%$	$U_{1+k}$
S	1.285	1.245	1.227	1.208	1.979	0.024
R1 B	1.275	1.239	1.222	1.204	1.818	0.022
R2 B	1.250	1.224	1.213	1.202	1.126	0.014
R3 B	1.281	1.242	1.225	1.206	1.882	0.023
R4 B	1.255	1.227	1.215	1.202	1.260	0.015
R5 B	1.286	1.246	1.227	1.208	1.947	0.024
R6 B	1.269	1.235	1.219	1.203	1.619	0.020
R7 B	1.286	1.245	1.227	1.209	1.865	0.023
R8 B	1.278	1.241	1.224	1.207	1.715	0.021
BC						
Surface condition	$\phi_3$	$\phi_2$	$\phi_1$	$\phi_{ext}^{21}$	$GCI_{fine}^{21}, \%$	$U_{1+k}$
S	1.217	1.193	1.179	1.162	1.825	0.022
R1 B	1.213	1.192	1.180	1.166	1.511	0.018
R2 B	1.208	1.192	1.186	1.183	0.354	0.004
R3 B	1.215	1.192	1.180	1.164	1.675	0.020
R4 B	1.209	1.192	1.184	1.176	0.838	0.010
R5 B	1.217	1.194	1.181	1.165	1.664	0.020
R6 B	1.212	1.193	1.181	1.169	1.349	0.016
R7 B	1.217	1.193	1.179	1.163	1.777	0.021
R8 B	1.215	1.193	1.180	1.165	1.623	0.019

Table 5.23 The obtained grid uncertainties for  $1+k$  within DBS for ships fouled with hard fouling

KCS						
Surface condition	$\phi_3$	$\phi_2$	$\phi_1$	$\phi_{ext}^{21}$	$GCI_{fine}^{21}, \%$	$U_{1+k}$
S	1.152	1.126	1.108	1.072	4.150	0.046
R1 H	1.101	1.095	1.090	1.080	1.133	0.012
R2 H	1.103	1.096	1.091	1.077	1.573	0.017
R3 H	1.105	1.097	1.091	1.076	1.758	0.019
R4 H	1.107	1.098	1.091	1.075	1.882	0.021
R5 H	1.110	1.100	1.092	1.067	2.879	0.031
R6 H	1.112	1.101	1.093	1.070	2.611	0.029
KVLCC2						
Surface condition	$\phi_3$	$\phi_2$	$\phi_1$	$\phi_{ext}^{21}$	$GCI_{fine}^{21}, \%$	$U_{1+k}$
S	1.245	1.226	1.222	1.220	0.132	0.002
R1 H	1.207	1.207	1.206	1.204	0.204	0.002
R2 H	1.207	1.206	1.206	1.206	0.000	0.000
R3 H	1.208	1.205	1.206	1.207	0.047	0.001
R4 H	1.210	1.206	1.206	1.206	0.010	0.000
R5 H	1.212	1.206	1.207	1.207	0.007	0.000
R6 H	1.213	1.206	1.208	1.208	0.024	0.000
BC						
Surface condition	$\phi_3$	$\phi_2$	$\phi_1$	$\phi_{ext}^{21}$	$GCI_{fine}^{21}, \%$	$U_{1+k}$
S	1.268	1.198	1.189	1.188	0.150	0.002
R1 H	1.207	1.195	1.203	1.221	1.841	0.022
R2 H	1.214	1.198	1.196	1.196	0.010	0.000
R3 H	1.219	1.199	1.197	1.196	0.028	0.000
R4 H	1.222	1.198	1.196	1.196	0.024	0.000
R5 H	1.228	1.200	1.196	1.195	0.096	0.001
R6 H	1.231	1.203	1.195	1.192	0.350	0.004

The obtained  $U_{R_w}$  (Table 5.24) are significantly higher than numerical uncertainties in the prediction of other resistance components, which was expected since  $R_w$  is obtained from  $R_T$  and  $R_v$ . If considered in a relative way, i.e. as the ratio between  $U_{R_w}$  and  $R_w$ , the highest  $U_{R_w}$  are obtained for KVLCC2. Thus, the highest obtained  $U_{R_w}$  for smooth ships and ships fouled with biofilm are for KVLCC2 equal to 468.350%, for BC to 13.923% and for KCS to 4.491%, while for smooth ships and ships fouled with hard fouling the highest  $U_{R_w}$  for KCS is equal to 14.161%, for BC to 35.000% and for KVLCC2 to 898.815%. Significantly higher  $U_{R_w}$  obtained for KVLCC2 can be ascribed to the fact that  $R_w$  for KVLCC2 is very low, i.e. almost negligible. Therefore, the obtained relative values of  $U_{R_w}$  for KVLCC2 are very high. If analysed as an absolute value, the highest  $U_{R_w}$  for smooth ships and ships fouled with biofilm are obtained for

KVLCC2, while for smooth ships and ships fouled with hard fouling the highest  $U_{R_w}$  are obtained for KCS.

Finally, from the obtained results of the verification study, it can be clearly seen that the implementation of  $\Delta U^+$  models within the wall function did not lead to any increase in  $U_{SN}$  related to the prediction of resistance characteristics.

Table 5.24 The obtained  $U_{SN}$  in the prediction of  $R_w$  ( $U_{R_w}$ )

	KCS		KVLCC2		BC	
Surface condition	$U_{R_w}$ , kN	$U_{R_w}$ , %	$U_{R_w}$ , kN	$U_{R_w}$ , %	$U_{R_w}$ , kN	$U_{R_w}$ , %
S	9.569	2.494	18.442	38.365	1.092	1.187
R1 B	8.917	2.431	63.175	178.471	12.513	13.923
R2 B	2.464	0.744	74.936	468.350	3.644	4.263
R3 B	6.227	1.667	50.201	128.740	9.913	10.926
R4 B	4.664	1.367	63.364	299.452	2.196	2.468
R5 B	9.509	2.524	56.587	141.136	7.237	7.876
R6 B	5.280	1.457	61.322	262.675	1.273	1.411
R7 B	17.389	4.491	54.813	114.540	8.474	9.204
R8 B	4.818	1.278	43.085	153.299	7.642	8.385
	KCS		KVLCC2		BC	
Surface condition	$U_{R_w}$ , kN	$U_{R_w}$ , %	$U_{R_w}$ , kN	$U_{R_w}$ , %	$U_{R_w}$ , kN	$U_{R_w}$ , %
S	54.900	14.161	27.219	312.215	17.993	18.826
R1 H	21.730	9.409	7.627	266.684	13.515	17.023
R2 H	33.899	13.566	32.897	898.815	19.741	23.267
R3 H	27.024	10.525	7.307	154.147	10.844	12.660
R4 H	18.074	6.820	6.070	118.099	31.121	35.000
R5 H	10.354	3.694	6.802	121.896	14.492	16.067
R6 H	8.859	3.128	10.405	183.184	21.468	23.328

### 5.3.2. The validation study

After the verification study, the obtained  $R_T$  using fine mesh for smooth surface condition for all three ships are validated with the extrapolated values based on ITTC 1978 PPM [72] using towing tank results published in the literature [226], [230], [231]. The validation study is performed for six smooth ships in total. Namely, as can be seen from Table 5.12, the number of cells used in FSS for smooth ship has varied depending on the fouling condition, i.e. biofilm or hard fouling.  $C_T$  for full-scale ship is determined according to equation (2.27). It should be noted that for the purpose of this extrapolation,  $C_A$ ,  $\Delta C_F$  and  $C_{AAS}$  are considered to be zero. Furthermore, the form factor for KCS is taken as 0.1, as in [188], for KVLCC2 is taken as 0.16, as in [226] and presented in [238], while for BC is taken as 0.179 which is obtained using DBS. It should be noted that the form factor for KCS obtained using DBS in this study is equal to 0.1, while for KVLCC2 is equal to 0.22. The numerically obtained form factor value for KVLCC2 in this study is similar to the numerically obtained one in [236], where the authors have obtained

form factor for KVLCC2 equal to 0.21 using DBS. The obtained results of the validation study for  $C_T$  are shown in Table 5.25. In addition to, within Table 5.25 the results from other CFD studies published in the literature are shown. Thus,  $C_T^{\text{CFD LITERATURE}}$  for KCS is taken from [188], while  $C_T^{\text{CFD LITERATURE}}$  for KVLCC2 is taken from [152]. It should be noted that within [152] DBS for KVLCC2 were performed using various turbulence models and consequently various  $C_V$  were obtained. Within Table 5.25,  $C_T^{\text{CFD LITERATURE}}$  from the study [152] is obtained as the sum of  $C_V$  obtained by  $k-\omega$  SST turbulence model at full-scale and experimentally obtained  $C_W$ . As can be seen, the obtained  $RD$  between numerically obtained results ( $C_T^{\text{CFD}}$ ) and extrapolated results ( $C_T^{\text{EX}}$ ) are relatively low. The highest  $RD$  is obtained for smooth KVLCC2, prepared for the analysis of the impact of biofilm and it is equal to 6.5%. For KCS and KVLCC2 using CFD simulations with higher cell number lower  $RD$  are obtained, while for BC lower  $RD$  is obtained for smooth BC prepared for the analysis of the impact of hard fouling where lower cell number is used. Beside  $C_T$ ,  $C_F^{\text{CFD}}$  calculated using  $R_F$ , which is obtained from DBS are validated with ITTC 1957 model-ship friction line and Grigson friction line. For  $10^8 < Rn < 4 \cdot 10^9$  Grigson friction line reads [239]:

$$C_F^{\text{GRIGSON}} = \left[ 1.032 + 0.02816(\log Rn - 8) - 0.006273(\log Rn - 8)^2 \right] \cdot \frac{0.075}{(\log Rn - 2)^2} \quad (5.3)$$

The validation study for  $C_F$  is presented in Table 5.26. As can be seen from Table 5.26, the obtained  $RD$  are relatively low, i.e. the highest  $RD$  between  $C_F^{\text{CFD}}$  and  $C_F^{\text{ITTC 1957}}$  is obtained for KVLCC2 prepared for the analysis of the impact of hard fouling and it is equal to 4.894%. Also, it can be seen that lower  $RD$  are obtained between  $C_F^{\text{CFD}}$  and  $C_F^{\text{GRIGSON}}$ . Thus, the highest  $RD$  between  $C_F^{\text{CFD}}$  and  $C_F^{\text{GRIGSON}}$  is obtained for KCS prepared for the analysis of the impact of hard fouling and it is equal to 1.989%. This was expected since Grigson friction line can be considered as the most accurate friction line currently [239].

Table 5.25 The validation study for  $C_T$

Ship	$10^3 \cdot C_T^{\text{CFD}}$	$10^3 \cdot C_T^{\text{EX}}$	$RD, \%$	$10^3 \cdot C_T^{\text{CFD LITERATURE}}$ [152], [188]	$RD, \%$
KCS – biofilm	2.092	2.053	+1.812	2.097	-0.247
KVLCC2 – biofilm	1.839	1.727	+6.500	1.852	-0.699
BC – biofilm	2.183	2.296	-4.922	/	/
KCS – hard fouling	2.104	2.053	+2.429	2.097	+0.357
KVLCC2 – hard fouling	1.798	1.727	+4.100	1.852	-2.937
BC – hard fouling	2.197	2.296	-4.338	/	/

Table 5.26 The validation study for  $C_F$ 

Ship	$10^3 \cdot C_F^{\text{CFD}}$	$10^3 \cdot C_F^{\text{ITTC 1957}}$	$RD, \%$	$10^3 \cdot C_F^{\text{GRIGSON}}$	$RD, \%$
KCS – biofilm	1.434	1.378	+4.104	1.459	-1.686
KVLCC2 – biofilm	1.455	1.395	+4.300	1.477	-1.452
BC – biofilm	1.558	1.491	+4.470	1.574	-1.002
KCS – hard fouling	1.430	1.378	+3.783	1.459	-1.989
KVLCC2 – hard fouling	1.463	1.395	+4.894	1.477	-0.891
BC – hard fouling	1.545	1.491	+3.593	1.574	-1.833

Finally, the obtained integral values of nominal wake ( $w_N$ ) within FSS are validated, Table 5.27. However, since  $1-w_N$ , as well as nominal wake distribution is subjected to significant scale effects [152], measured  $1-w_N$  at model scale have to be scaled using certain scaling method. In this thesis,  $1-w_N$  is scaled using ITTC 1978 PPM, i.e. equation (2.48). It should be noted that  $\Delta C_F$  is taken to be zero, while  $w_{N,M}$  and  $t$  are obtained from towing tank results [226], [230]. In addition to within Table 5.27, the results from other CFD studies published in the literature are shown [240], [182], [152]. As can be seen, satisfactory agreement between  $1-w_N^{\text{CFD}}$  and  $1-w_N^{\text{EX}}$  is achieved. Thus, for KCS the highest  $RD$  is obtained for KCS prepared for the analysis of the impact of hard fouling and is equal to 2.176%, for KVLCC2 the highest  $RD$  is obtained for KVLCC2 prepared for the analysis of the impact of hard fouling and is equal to 1.847% and for BC the highest  $RD$  is obtained for BC prepared for the analysis of the impact of hard fouling and is equal to 7.892%. Also, satisfactory agreement between  $1-w_N^{\text{CFD}}$  and  $1-w_N^{\text{CFD LITERATURE}}$  is achieved as well. Thus, for KCS the highest  $RD$  is obtained for KCS prepared for the analysis of the impact of biofilm and is equal to 3.496%, for KVLCC2 the highest  $RD$  is obtained for KVLCC2 prepared for the analysis of the impact of hard fouling and is equal to 9.907% and for BC the highest  $RD$  is obtained for BC prepared for the analysis of the impact of biofilm and is equal to 0.127%. Relatively higher  $RD$  between  $1-w_N^{\text{CFD}}$  and  $1-w_N^{\text{CFD LITERATURE}}$  [152] for KVLCC2 can be ascribed to the fact that within [152] only DBS are considered. Thus, the obtained  $1-w_N^{\text{CFD LITERATURE}}$  [152] did not take into account the free surface effects.

Table 5.27 The validation study for  $1 - w_N$ 

Ship	$1 - w_N^{\text{CFD}}$	$1 - w_N^{\text{EX}}$	$RD, \%$	$1 - w_N^{\text{CFD LITERATURE}}$ [152], [182], [240]	$RD, \%$
KCS – biofilm	0.784	0.768	+2.043	0.812	-3.496
KVLCC2 – biofilm	0.676	0.687	-1.651	0.749	-9.727
BC – biofilm	0.705	0.655	+7.636	0.706	-0.127
KCS – hard fouling	0.785	0.768	+2.176	0.812	-3.370
KVLCC2 – hard fouling	0.675	0.687	-1.847	0.749	-9.907
BC – hard fouling	0.707	0.655	+7.892	0.706	+0.111

### 5.3.3. Results of the analysis of the impact of biofouling on the resistance characteristics and nominal wake

Once validated, the CFD model can be used for the prediction of the impact of biofouling on the resistance characteristics and nominal wake by following equation:

$$\Delta\phi = \frac{\phi_R - \phi_S}{\phi_S} \cdot 100\% \quad (5.4)$$

where  $\phi_R$  is the certain resistance characteristic for rough surface condition and  $\phi_S$  is the certain resistance characteristic for smooth surface condition both obtained using fine mesh.

Firstly, DBS are performed in order to study the impact of biofouling on the increase in  $C_F$  ( $\Delta C_F$ ) and  $C_V$  ( $\Delta C_V$ ) and the obtained results are presented in Figure 5.15 and Figure 5.16. It should be noted that within these figures, the numerical uncertainty in the prediction of  $\Delta C_F$  and  $\Delta C_V$  is presented in a form of error bars. As can be seen from Figure 5.15 and Figure 5.16, the significant increase in  $C_F$  is determined due to the presence of biofouling. Thus, the increase in  $C_F$  due to the presence of biofilm for KCS ranges from 0.08% for surface condition R7 B to 40.11% for R2 B, for KVLCC2 from 0% for surface condition R7 B to 32.32% for R2 B and for BC from 0% for surface condition R7 B to 35.08% for R2 B. The increase in  $C_F$  due to the presence of hard fouling for KCS ranges from 77.58% for surface condition R6 H to 144.46% for R1 H, for KVLCC2 ranges from 66.21% for surface condition R6 H to 124.78% for R1 H and for BC ranges from 71.08% for surface condition R6 H to 137.56% for R1 H. From Figure 5.15 and Figure 5.16 it is clear that the obtained  $\Delta C_F$  are significantly higher than numerical uncertainties in the prediction of  $\Delta C_F$ , except for surface condition R5 B for KVLCC2 and BC and R7 B for all three ships, where the obtained  $\Delta C_F$  are very small. The highest  $\Delta C_F$  are obtained for KCS for all investigated surface conditions, followed by BC and KVLCC2. This can be attributed to the fact that  $\Delta C_F$  is defined relatively as the ratio of the

increase in  $C_F$  and  $C_{FS}$ . Namely,  $C_{FS}$  for KCS is significantly lower than for BC and therefore  $\Delta C_F$  is higher. However, if  $C_{FR}$  are compared, the highest are obtained for BC, which has the highest  $k_{eff}/L$  or  $k/L$  value.

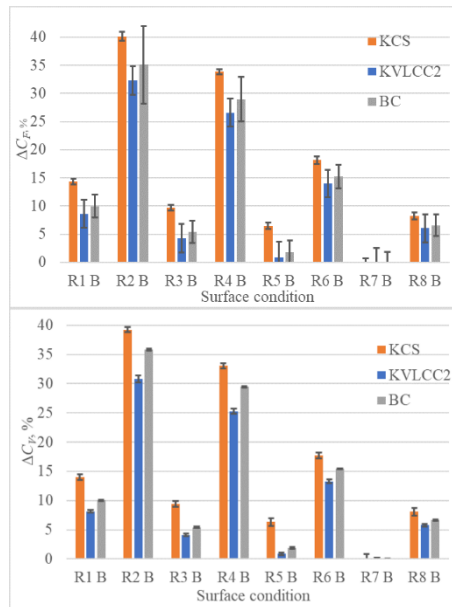


Figure 5.15 The impact of biofilm on  $\Delta C_F$  (upper) and  $\Delta C_V$  (lower)

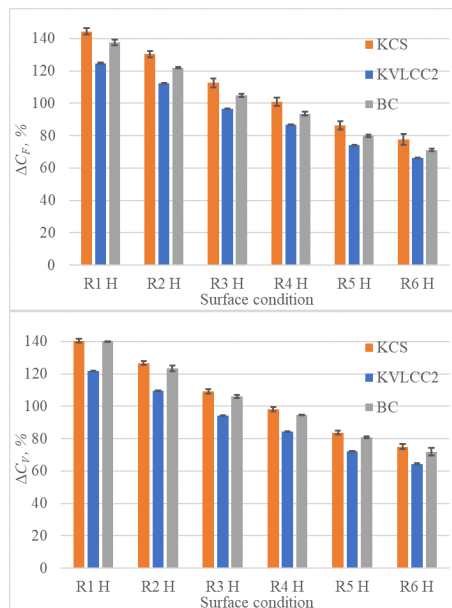


Figure 5.16 The impact of hard fouling on  $\Delta C_F$  (upper) and  $\Delta C_V$  (lower)

In order to compare  $C_{FR}$  and  $\Delta C_F$  at the same  $k/L$  values for different ships, additional CFD simulations are carried out, i.e. FPS and DBS for smooth KCS are carried out at  $Rn$  which corresponds to  $Rn$  of KVLCC2. In that way  $\Delta C_F$  are determined at the same  $Rn$  values for both ships. In Table 5.28 the obtained results are shown along with  $RD$  which are determined as follows:

$$RD = \frac{C_{FR, KVLCC2} - C_{FR, KCS}}{C_{FR, KCS}} \cdot 100\% \quad (5.5)$$

In order to have the same  $k/L$  values for KCS and KVLCC2, different surface conditions are analysed, i.e. for KVLCC2: R1 H, R3 H and R5 H, while for KCS: R2 H, R4 H and R6 H. From the obtained results presented in Table 5.28, it is evident that  $RD$  are very low and therefore it can be concluded that  $C_{FR}$  for fully rough regime at high  $Rn$  values depends solely on  $k/L$  value. Even though Shin and Song [241], [242] have shown the influence of favourable and adverse pressure gradients on frictional resistance coefficient for rough flat plate ( $C_{FOR}$ ), within this thesis it is shown that  $C_{FR}$  is mainly influenced by the parameter  $k/L$ . Shin and Song [241], [242] investigated the impact of pressure gradient on frictional resistance coefficient for smooth flat plate ( $C_{FOS}$ ) and  $C_{FOR}$ . The authors performed experiments in the wind tunnel facility, with moveable aluminium flat plate and thus pressure gradient was achieved. They concluded that favourable pressure gradient caused the increase in  $C_{FOR}$ , while adverse pressure gradient caused the decrease in  $C_{FOR}$ . In this thesis, DBS are performed for 3D ship forms and both favourable and adverse pressure gradients are present at the ship hull. Therefore the effects of pressure gradients are moderated, since the effects of favourable and adverse pressure gradients are contrary. Because of that, it can be concluded that for fully rough regime at high  $Rn$  value, both  $C_{FOR}$  (for flat plate) and  $C_{FR}$  (for 3D ship) depend only on  $k/L$  value [234]. Beside the impact of biofouling on  $C_F$ , it is interesting to analyse the impact of biofouling on  $k_f$ , i.e. on the factor which takes into account longitudinal and transversal curvature of the ship form. In this thesis,  $k_f$  is obtained as a ratio between  $C_F$  obtained in DBS and  $C_{F0}$  obtained in FPS. The obtained impact of biofouling on  $k_f$  using fine mesh is shown in Table 5.29 and Table 5.30. As can be seen, the impact of biofilm on  $k_f$  is very low and for the most of investigated surface conditions, the presence of biofilm causes the increase in  $k_f$  value. Also it can be seen from Table 5.29 that the impact of biofilm is similar amongst the investigated ships. The highest  $\Delta k_f$  due to the presence of biofilm is obtained for BC fouled with R5 B and it is equal to 1.049%. On the other hand, the impact of hard fouling on  $k_f$  is slightly more pronounced and the presence of hard fouling causes the decrease in  $k_f$  value. The impact of hard fouling on  $k_f$  is most pronounced for KVLCC2, which has the highest  $C_B$ , i.e. KVLCC2 has more fuller ship form than BC and KCS. As  $k_f$  is the factor which takes into account longitudinal and transversal curvature of the ship form, and those curvatures caused the pressure gradients, it can be concluded that more significant effects of pressure gradient on  $C_F$  are present for KVLCC2 than for KCS and BC. The highest  $\Delta k_f$  due to the presence of hard fouling is obtained for KVLCC2 fouled with R1 H and it is equal to -2.098%.

Even though from the obtained results presented in Table 5.29 and Table 5.30 it can be seen that the presence of biofouling has certain impact on  $k_f$ , the obtained  $\Delta k_f$  are very low, especially when compared with  $\Delta C_F$  and within the numerical and modelling uncertainties of the proposed CFD model.



Factor  $k_f$  can have practical importance for more reliable scaling of the obtained results using the Granville similarity law scaling method. Namely, using the Granville similarity method, one can obtain increases in  $C_{F0}$  for the flat plate having the same length as a ship. In order to obtain  $C_{FR}$  for 3D ship hull, which is required in the extrapolation procedure, one can multiply  $k_f$  and  $C_{F0R}$ . In that way, more comprehensive extrapolation method will be enabled, which can be of importance in the determination of increases in  $R_T$  with the Granville method. For the purpose of practical extrapolation, one can assume that  $k_f$  is the same for smooth and rough surface, as is usually done for form factor and  $C_w$  when the Granville method is used for the assessment of the effect of biofouling on  $R_T$ .

Table 5.28 The comparison of the obtained  $C_{FR}$  and  $\Delta C_F$  at the same  $k/L$  values

$10^6 k/L$	KCS		KVLCC2		$RD, \%$
	$10^3 \cdot C_{FR}$	$\Delta C_F, \%$	$10^3 \cdot C_{FR}$	$\Delta C_F, \%$	
6.344	3.256	127.40	3.250	126.18	-0.218
2.837	2.844	98.58	2.840	97.69	-0.125
1.269	2.511	75.34	2.512	74.87	0.051

Table 5.29 The impact of biofilm on  $k_f$

Surface condition	KCS		KVLCC2		BC	
	$k_f$	$\Delta k_f, \%$	$k_f$	$\Delta k_f, \%$	$k_f$	$\Delta k_f, \%$
S	1.039	/	1.068	/	1.060	/
R1 B	1.044	0.434	1.072	0.343	1.063	0.346
R2 B	1.043	0.407	1.066	-0.239	1.060	-0.011
R3 B	1.044	0.429	1.073	0.455	1.064	0.419
R4 B	1.043	0.405	1.067	-0.094	1.060	0.066
R5 B	1.040	0.041	1.077	0.796	1.071	1.049
R6 B	1.042	0.270	1.069	0.023	1.061	0.114
R7 B	1.039	-0.034	1.068	0.000	1.060	0.000
R8 B	1.041	0.155	1.069	0.068	1.061	0.115

Table 5.30 The impact of hard fouling on  $k_f$

Surface condition	KCS		KVLCC2		BC	
	$k_f$	$\Delta k_f, \%$	$k_f$	$\Delta k_f, \%$	$k_f$	$\Delta k_f, \%$
S	1.041	/	1.066	/	1.070	/
R1 H	1.032	-0.818	1.043	-2.098	1.062	-0.784
R2 H	1.034	-0.663	1.045	-1.895	1.064	-0.603
R3 H	1.035	-0.550	1.047	-1.713	1.067	-0.351
R4 H	1.037	-0.345	1.050	-1.464	1.068	-0.214
R5 H	1.038	-0.229	1.053	-1.210	1.069	-0.085
R6 H	1.039	-0.134	1.055	-1.002	1.070	-0.016

As can be seen from Figure 5.15 and Figure 5.16, the significant increase in  $C_V$  is obtained due to the presence of biofouling. Thus, the increase in  $C_V$  due to the presence of biofilm for KCS ranges from 0.10% for surface condition R7 B to 39.26% for R2 B, for KVLCC2 from 0.02% for surface condition R7 B to 30.79% for R2 B and for BC from 0.01% for surface condition R7 B to 35.85% for R2 B. The increase in  $C_V$  due to the presence of hard fouling for KCS ranges from 75.05% for surface condition R6 H to 140.49% for R1 H, for KVLCC2 from 64.31% for surface condition R6 H to 121.95% for R1 H and for BC from 71.88% for surface condition R6 H to 140.28% for R1 H. From Figure 5.15 and Figure 5.16 it is clear that the obtained  $\Delta C_V$  are significantly higher than numerical uncertainties in the prediction of  $\Delta C_V$ , except for surface condition R7 B for all three ships, where the obtained  $\Delta C_V$  are very small. The highest  $\Delta C_V$  are obtained for KCS for all investigated surface conditions, followed by BC and KVLCC2. Generally, the obtained  $\Delta C_V$  are slightly lower than the obtained  $\Delta C_F$  since the impact of biofouling on  $1+k$  is present. In this thesis,  $1+k$  is determined as a ratio between  $R_V$  and  $R_F$  obtained using DBS. The obtained impact of biofouling on  $1+k$  is shown in Figure 5.17. As can be seen, the impact of biofouling causes the decrease in  $1+k$  for KCS and KVLCC2, while for BC it causes the increase in  $1+k$  values. The obtained change in  $1+k$  due to the presence of biofilm for KCS ranges from 0.02% for surface condition R7 B to -0.61% for R2 B, for KVLCC2 from 0.02% for surface condition R7 B to -1.15% for R2 B and for BC from 0.01% for surface condition R7 B to 0.57% for R2 B. The obtained change in  $1+k$  due to the presence of hard fouling for KCS ranges from -1.42% for surface condition R6 H to -1.62% for R1 H, for KVLCC2 from -1.14% for surface condition R6 H to -1.26% for R1 H and for BC from 0.47% for surface condition R6 H to 1.15% for R1 H. The obtained  $\Delta(1+k)$  due to the presence of biofilm are lower than the obtained numerical uncertainties in the prediction of  $\Delta(1+k)$ . Since the obtained  $\Delta(1+k)$  are low it can be concluded that the impact of biofilm on  $1+k$  is negligible. On the other hand, the obtained  $\Delta(1+k)$  due to the presence of hard fouling are higher than the obtained numerical uncertainties in the prediction of  $\Delta(1+k)$ , except for KCS at all investigated surface conditions and for BC fouled with surface condition R1 H. Regardless of this, the other obtained  $\Delta(1+k)$  are low and probably below the modelling uncertainty of the CFD model and therefore for the purpose of practical extrapolation it is justified to assume that  $1+k$  values are independent on the presence of roughness without significantly compromising the accuracy of the extrapolation.

After the analysis of the impact of biofouling using DBS, FSS are performed in order to investigate the impact of biofouling on  $C_T$ . The obtained  $\Delta C_T$  due to the presence of biofouling are shown in Figure 5.18. The increase in  $C_T$  due to the presence of biofilm for KCS ranges from 0.30% for surface condition R7 B to 26.24% for R2 B, for KVLCC2 from 0.01% for surface condition R7 B to 27.95% for R2 B and for BC from 0.02% for surface condition R7 B to 29.04% for R2 B. The increase in  $C_T$  due to the presence of hard fouling for KCS ranges from 49.86% for surface condition R6 H to 95.80% for R1 H, for KVLCC2 from 63.77% for surface condition R6 H to 120.93% for R1 H and for BC from 59.51% for surface condition R6 H to 114.55% for R1 H. The obtained  $\Delta C_T$  are higher than the obtained numerical uncertainties

in the prediction of  $\Delta C_T$  for all test cases except for KVLCC2 fouled with surface condition R5 B and for all three ships fouled with surface condition R7 B. Roughness penalties due to the presence of biofilm vary for various ship forms. For example for surface conditions R2 B, R4 B and R6 B the highest  $\Delta C_T$  are obtained for BC. On the other hand for surface conditions R1 B, R3 B, R5 B, R7 B and R8 B the highest  $\Delta C_T$  are obtained for KCS. For surface conditions R1 B, R3 B, R5 B, R7 B and R8 B the lowest  $\Delta C_T$  are obtained for KVLCC2. This can be attributed to the fact that lower  $k^+$  values are obtained along the KVLCC2 hull caused by lower  $u_\tau$  values since investigations for KVLCC2 are performed for the lowest speed. More details regarding this will be presented in Section 5.3.4. Obviously, the fact that  $k^+$  distribution along the KVLCC2 hull is significantly lower than for other two ships is more important than a fact that KVLCC2 has higher portion of  $R_F$  in  $R_T$ . The importance of  $k^+$  values along the hull are even more highlighted for ships fouled with biofilm, since below certain threshold  $k^+$  values  $\Delta U^+$  models for biofilm are equal to zero, i.e. there is no influence of biofilm on the flow around the hull. In the case of hard fouling the highest  $\Delta C_T$  are obtained for KVLCC2 for all investigated surface conditions, followed by BC and lastly KCS. Since hard fouling is significantly severe fouling condition,  $k^+$  values are significantly higher than for biofilm. The highest  $\Delta C_T$ , which are obtained for KVLCC2 can be explained with the fact that KVLCC2 has the highest portion of  $R_F$  in  $R_T$  and that  $R_F$  is most significantly affected due to the presence of fouling.

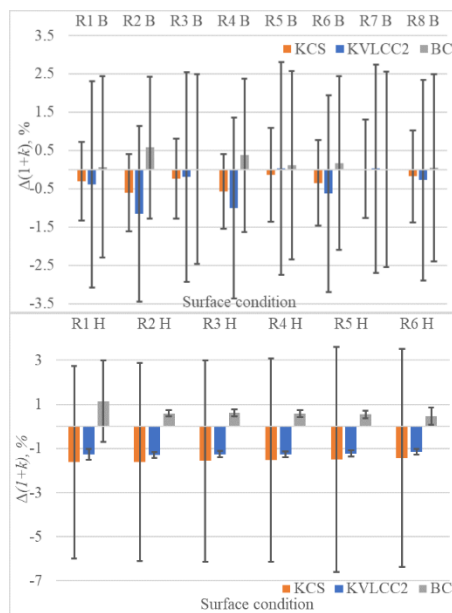


Figure 5.17 The impact of biofilm (upper) and hard fouling (lower) on  $\Delta(1+k)$

However, there is also additional explanation regarding this. Within Figure 5.19 and Figure 5.20 the obtained  $\Delta C_w$  are shown. The obtained  $\Delta C_w$  due to the presence of biofilm for KCS ranges from 0.92% for surface condition R7 B to -13.69% for R2 B, for KVLCC2 from -0.45% for surface condition R7 B to -66.72% for R2 B and for BC from 0.07% for surface condition R7 B to -7.10% for R2 B. The obtained  $\Delta C_w$  due to the presence of hard fouling for KCS ranges from -26.95% for surface condition R6 H to -40.43% for R1 H, for KVLCC2 from

-34.85% for surface condition R6 H to -67.19% for R1 H and for BC from -3.71% for surface condition R6 H to -16.93% for R1 H. From Figure 5.19 and Figure 5.20, it can be seen that the effect of biofouling on  $C_w$  is significant and it causes the decrease in  $C_w$ . The obtained  $\Delta C_w$  are higher than the obtained numerical uncertainties in the prediction of  $\Delta C_w$  for KCS fouled with hard fouling and R1 B, R2 B, R4 B and R6 B, as well as for BC fouled with R2 B, R4 B and R6 B. It should be noted that if more cells were used in FSS and DBS for BC fouled with hard fouling, numerical uncertainties in the prediction of  $\Delta C_w$  would be lower and probably lower than the obtained  $\Delta C_w$ . On the other hand, numerical uncertainties in the prediction of  $\Delta C_w$  are higher for all investigated surface conditions than the obtained  $\Delta C_w$  for KVLCC2, Figure 5.20. Very high numerical uncertainties obtained for the prediction of  $\Delta C_w$  for KVLCC2 can be attributed to the fact that the obtained uncertainties are presented in relative way. Namely, the numerical uncertainties shown in figures, where the impact of biofouling on certain resistance characteristic is shown, are represented with error bars which are defined as a percentage of certain value. Thus for a case of the impact of biofouling on  $\Delta C_w$ , numerical uncertainty in the prediction of  $\Delta C_w$  for surface condition R1 H is defined as the ratio of  $U_{\Delta R_w}$ , calculated using equation (5.2) and the absolute value of  $R_w$  for surface condition R1 H. Since  $R_w$  for KVLCC2 is almost negligible as proven in [226], the obtained relative uncertainties are very high. Also, numerical uncertainties in the prediction of  $R_w$  are higher than for other resistance components, since for prediction of  $R_w$ , both  $R_T$  and  $R_V$  should be known, as shown with equation (5.1). Regardless of the fact that for some surface conditions the numerical uncertainties in the prediction of  $\Delta C_w$  are higher than the obtained  $\Delta C_w$ , a clear trend from Figure 5.19 and Figure 5.20 can be noticed, i.e. the presence of biofouling on the ship hull causes the decrease in  $R_w$ . This represent an important finding, as until recently it was considered that the roughness only affects  $R_F$  of a ship. Recently, the same finding is presented in the literature [188], [193], [197]. The fact that the presence of biofouling causes the decrease in  $R_w$  is more important for the ships with higher portion of  $R_w$  in  $R_T$ . Also, for more severe fouling conditions the impact of biofouling on  $R_w$  is more pronounced. Thus, for KCS the impact of biofouling on  $R_w$ , i.e. the decrease in  $R_w$ , will reduce the fouling penalty  $\Delta C_T$ , while for KVLCC2 the impact of biofouling on  $R_w$ , will not have important influence on  $\Delta C_T$ , as a portion of  $R_w$  in  $R_T$  for KVLCC2 is negligible. This is another reason why the impact of hard fouling on  $\Delta C_T$  is more pronounced for KVLCC2, than for KCS and BC.

From the obtained results it is clear that the effect of biofouling on each resistance characteristic is different. Therefore, it would be beneficial to investigate the portion of each resistance component in  $R_T$  for various fouling conditions. The decomposition of  $R_T$  for investigated ships along with the portion of each resistance component in  $R_T$  are shown in Figure 5.21 and Figure 5.22. From these two figures several interesting trends can be noticed. For example, the portion of  $R_{F0}$  in  $R_T$  is significantly increased due to the presence of biofouling. Thus, due to the presence of biofilm this portion for KCS varies from 65.2% for S to 72.1% for R2 B, for KVLCC2 from 74.1% for S to 76.8% for R2 B and for BC from 67.3% for S to 70.5% for

R2 B. Due to the presence of hard fouling the portion of  $R_{F0}$  in  $R_T$  for KCS varies from 64.6% for S to 81.3% for R1 H, for KVLCC2 from 76.4% for S to 79.4% for R1 H and for BC from 65.7% for S to 73.3% for R1 H. The slight differences in the portion of certain resistance component in  $R_T$  for smooth surface condition are obtained, which can be related to different meshes used in FSS and DBS. The portion of  $R_{F0}$  in  $R_T$  has increased the most for KCS due to the presence of biofouling. The portion of  $R_F - R_{F0}$  in  $R_T$  has mainly remained the same regardless of the presence of biofouling. It should be noted that the portion of  $R_F - R_{F0}$  in  $R_T$  due to the presence of biofouling has slightly increased for KCS and BC, while for KVLCC2 has slightly decreased. Similar trend is obtained for the portion of  $R_{VP}$  in  $R_T$ . Even though the portions of  $R_F - R_{F0}$  in  $R_T$  and  $R_{VP}$  in  $R_T$  decrease due to the presence of biofouling for KVLCC2, it should be noted that the absolute values of  $R_F - R_{F0}$  and  $R_{VP}$  increase. On the other hand, the effect of biofouling on  $R_W$  causes the decrease in  $R_W$ . Consequently, the portion of  $R_W$  in  $R_T$  is significantly reduced and due to the presence of biofilm this portion for KCS varies from 24.6% for S to 16.8% for R2 B, for KVLCC2 from 2.9% for S to 0.8% for R2 B and for BC from 15.9% for S to 11.4% for R2 B. Due to the presence of hard fouling the portion of  $R_W$  in  $R_T$  for KCS varies from 24.7% for S to 7.5% for R1 H, for KVLCC2 from 0.5% for S to 0.1% for R1 H and for BC from 16.4% for S to 6.3% for R1 H. From Figure 5.22 it is clear that  $R_T$  for KVLCC2 due to the presence of hard fouling is the most affected, as the portion of  $R_V$  in  $R_T$  is the highest and  $R_V$  increases due to the presence of biofouling. The portion of  $R_V$  in  $R_T$  for KVLCC2 is above 99%, while this portion for KCS varies from 75.3% for S to 92.49% for R1 H, and for BC from 83.63% for S to 93.66% for R1 H.

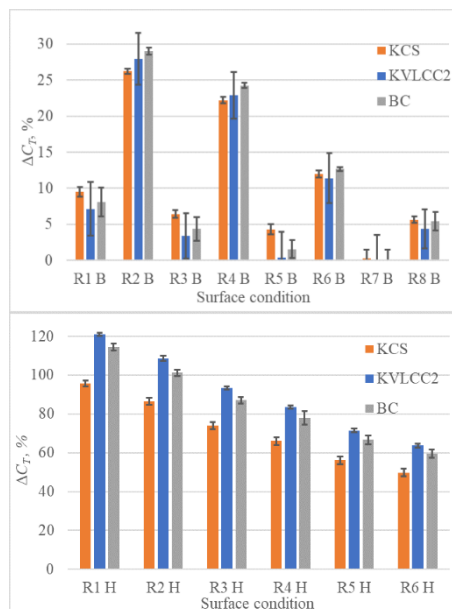


Figure 5.18 The impact of biofilm (upper) and hard fouling (lower) on  $\Delta C_T$

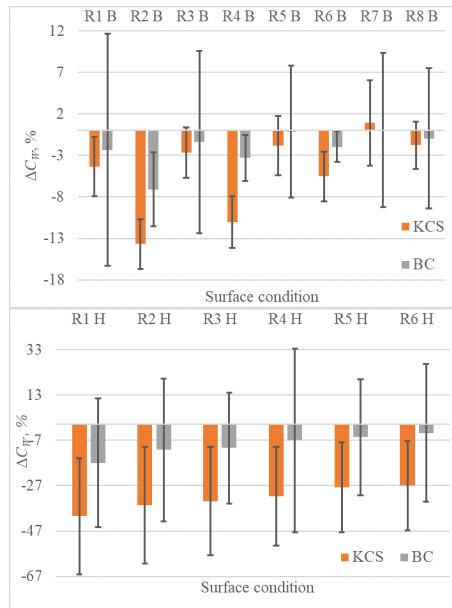


Figure 5.19 The impact of biofilm (upper) and hard fouling (lower) on  $\Delta C_w$  for KCS and BC

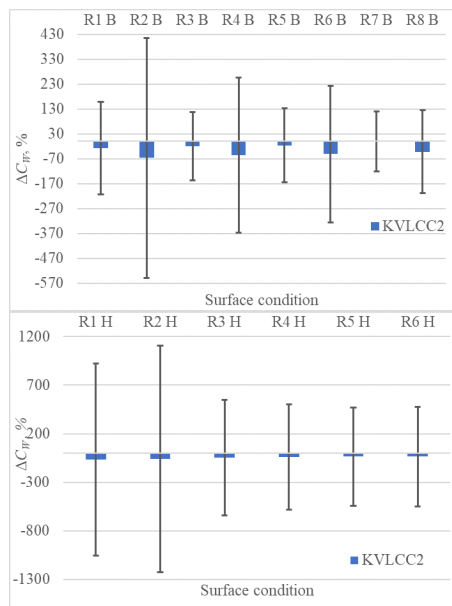


Figure 5.20 The impact of biofilm (upper) and hard fouling (lower) on  $\Delta C_w$  for KVLCC2

To sum up the impact of biofouling on the ship resistance characteristics is various for each resistance characteristics. Thus, the presence of biofouling causes significant increase in  $C_{F0}$  and consequently in  $C_F$  and  $C_V$  as well, since the impact of biofouling on  $k_f$  and  $1+k$  is relatively low. On the other hand, the presence of biofouling causes the decrease in  $C_w$  and this effect is more pronounced for fouling with higher fouling rating scale, i.e. higher severity, as well as for the ship having higher portion of  $R_w$  in  $R_T$ . Thus, for the purposes of practical extrapolation, one can estimate the increase in  $C_{F0}$  using the Granville similarity law scaling method and  $k_f$  obtained for smooth ship to obtain the increase in  $C_F$ . Furthermore, since the impact of biofouling on  $1+k$  is very low, for the purposes of practical extrapolation the increase in  $C_V$  can be obtained as well. In addition to for lower fouling rating scales it can be considered

that the impact of biofouling on  $C_w$  is negligible, especially if the portion of  $R_w$  in  $R_T$  is relatively low, since this assumption will not lead to high errors. However, for hard fouling or other type of fouling with high fouling rating scale, the impact of biofouling on  $C_w$  is important and should not be neglected. Finally, it has been shown that fouling effects as well as the penalties related to the presence of biofouling may not always be the most pronounced for fuller ship forms, i.e. for ships which sail at lower  $Fn$ . Namely, the ships which sail at lower  $Fn$  have the higher portion of  $R_f$  in  $R_T$  than ships which sail at higher  $Fn$ . Even though for fouling with higher fouling rating, for example hard fouling, the impact of biofouling will be more pronounced for fuller ship forms, for fouling with lower fouling rating, for example biofilm this may not be a case. Namely for ships which sail at lower  $Fn$ , lower  $k^+$  values will be obtained which will result in lower  $\Delta U^+$  values. What is more, below certain threshold  $k^+$  value,  $\Delta U^+$  will be equal to zero. Therefore, the impact of biofouling with lower fouling rating scale could be more pronounced for ships which sail at higher  $Fn$ . More explanation regarding this will be presented in Section 5.3.4, where the impact of biofouling on the flow around the fouled ship hull is shown.



Figure 5.21 The decomposition of  $R_T$  for KCS (upper), KVLCC2 (middle) and BC (lower) fouled with biofilm



Figure 5.22 The decomposition of  $R_r$  for KCS (upper), KVLCC2 (middle) and BC (lower) fouled with hard fouling

The impact of biofouling is not limited to the impact on the ship resistance characteristics. Thus, among other, biofouling affects the flow around ship hull and in that way nominal wake distribution as well. Within Figure 5.23 the impact of biofouling on  $1-w_N$  is shown. The obtained  $\Delta(1-w_N)$  due to the presence of biofilm for KCS ranges from -0.02% for surface condition R7 B to -4.70% for R2 B, for KVLCC2 from -0.14% for surface condition R7 B to -6.64% for R2 B and for BC from 0.02% for surface condition R7 B to -7.10% for R2 B. The obtained  $\Delta(1-w_N)$  due to the presence of hard fouling for KCS ranges from -9.02% for surface condition R6 H to -17.84% for R1 H, for KVLCC2 from -16.69% for surface condition R6 H to -32.62% for R1 H and for BC from -14.99% for surface condition R6 H to -30.45% for R1 H. It is clear that the effect of biofouling on  $\Delta(1-w_N)$  is significant and that biofouling causes the decrease in  $\Delta(1-w_N)$ . Within [20], numerical uncertainties in the prediction of  $\Delta(1-w_N)$  are estimated for KCS and BC fouled with biofilm for fouling conditions presented in Table 5.3. For the most of investigated surface conditions, i.e. R1 B, R2 B, R4 B and R6 B in the case



of KCS and for R1 B, R2 B, R3 B, R4 B, R6 B and R8 B in the case of BC, the obtained  $\Delta(1-w_N)$  are higher than numerical uncertainties in the prediction of  $\Delta(1-w_N)$ .

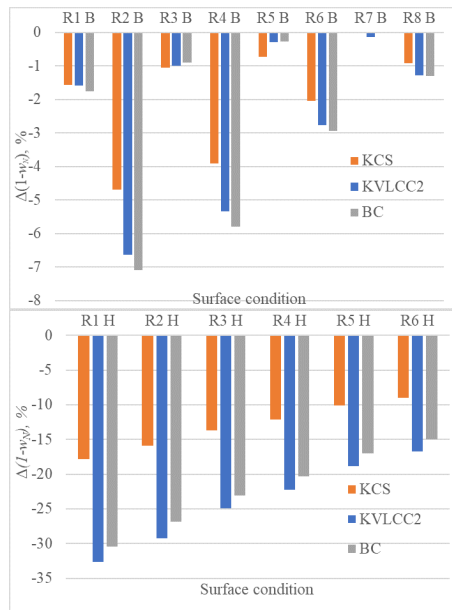


Figure 5.23 The impact of biofilm (upper) and hard fouling (lower) on  $\Delta(1-w_N)$

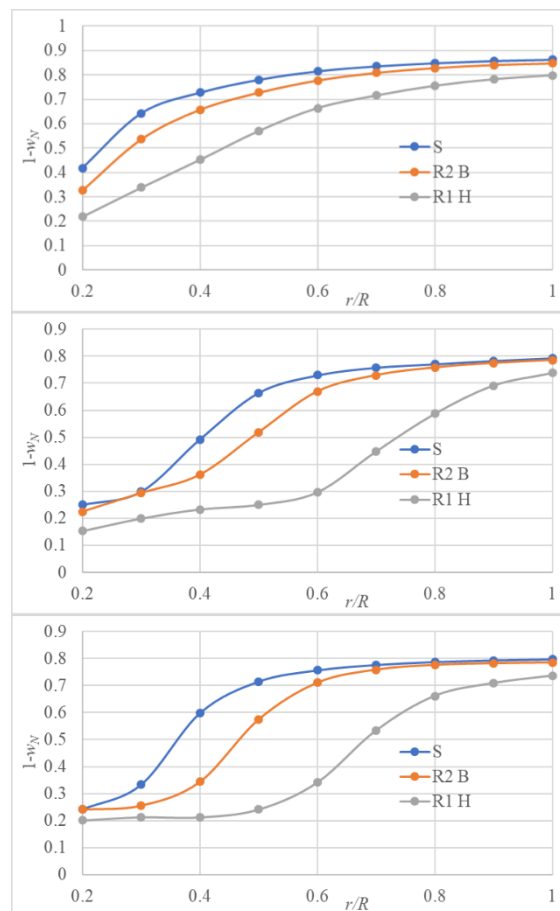


Figure 5.24 The obtained circumferential averaged non-dimensional axial velocity distribution for KCS (upper), KVLCC2 (middle) and BC (lower)

The obtained circumferential averaged non-dimensional axial velocity distribution for smooth surface condition, R2 B and R1 H are shown in Figure 5.24. The surface conditions R2 B and R1 H are selected since they represent the most severe fouling conditions amongst investigated fouling conditions for biofilm and hard fouling, respectively. As can be seen from Figure 5.24, the impact of biofouling on the circumferential averaged non-dimensional axial velocity distribution is the most highlighted for  $r/R$  in the range from 0.4 to 0.7 for KVLCC2 and BC, while for KCS for  $r/R$  in the range from 0.2 to 0.5. At higher  $r/R$ , for example  $r/R > 0.8$ ,  $\Delta(1-w_N)$  is significantly lower and it is almost negligible in the case of surface condition R2 B. Generally, it can be concluded from Figure 5.23 and Figure 5.24 that circumferential averaged non-dimensional axial velocity distributions as well as  $1-w_N$  for KVLCC2 and BC are significantly more affected due to the presence of biofouling than for KCS.

### 5.3.4. The impact of biofouling on the flow around the ship hull

One of the important benefits of CFD lies in the possibility of detail analysis of the flow around the ship hull. This benefit can be utilized for a detail analysis of the flow around the fouled ship hull and in that way allow different insights related to the fouling effects on the flow around the ship hull. Within this subsection, the obtained results using fine mesh for smooth, R2 B and R1 H surface conditions are presented. As already noted,  $k^+$  values along the KCS hull are higher than  $k^+$  values along the KVLCC2 and BC hull due to the fact that  $u_\tau$  values along the KCS hull are higher, since KCS is investigated at higher speed. The obtained  $k^+$  distributions for R2 B and R1 H are shown in Figure 5.25 and Figure 5.26, respectively. The average value of  $k^+$  in the first cells near the wall below free surface for KCS with R2 B is equal to 64.01, KVLCC2 with R2 B to 40.25 and for BC with R2 B to 44.42. The average value of  $k^+$  in the first cells near the wall below free surface for KCS with R1 H is equal to 889.41, KVLCC2 with R1 H to 554.43 and for BC with R1 H to 621.29. It should be noted that the obtained  $k^+$  values along the investigated hulls are lower than  $y^+$  values, which is a necessary condition for a valid prediction of  $C_F$ . Due to higher  $k^+$  values along the KCS hull, higher  $\Delta U^+$  values are obtained as well. The higher  $\Delta U^+$  values caused the higher  $\Delta C_F$  for KCS than for KVLCC2 and BC, as shown in Figure 5.15 and Figure 5.16.

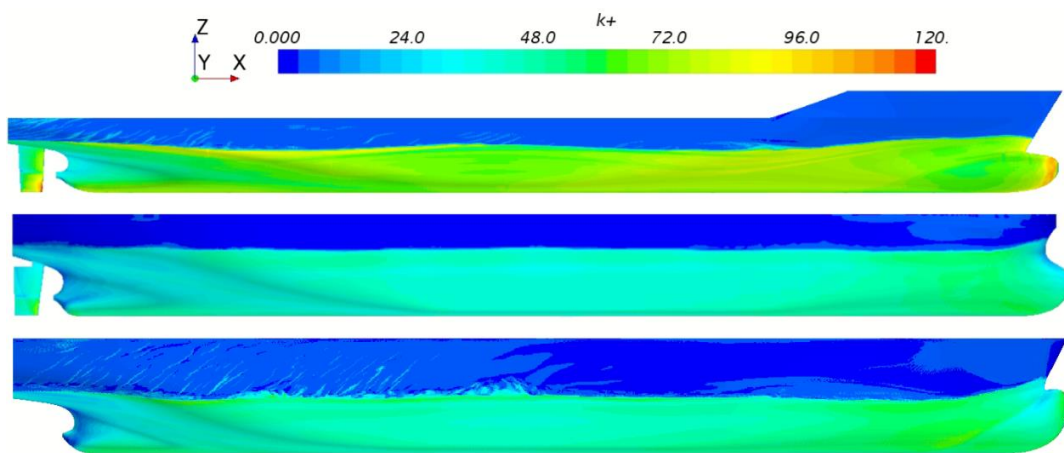


Figure 5.25 The obtained  $k^+$  distribution along KCS hull (upper), KVLCC2 hull (middle) and BC hull (lower) for R2 B

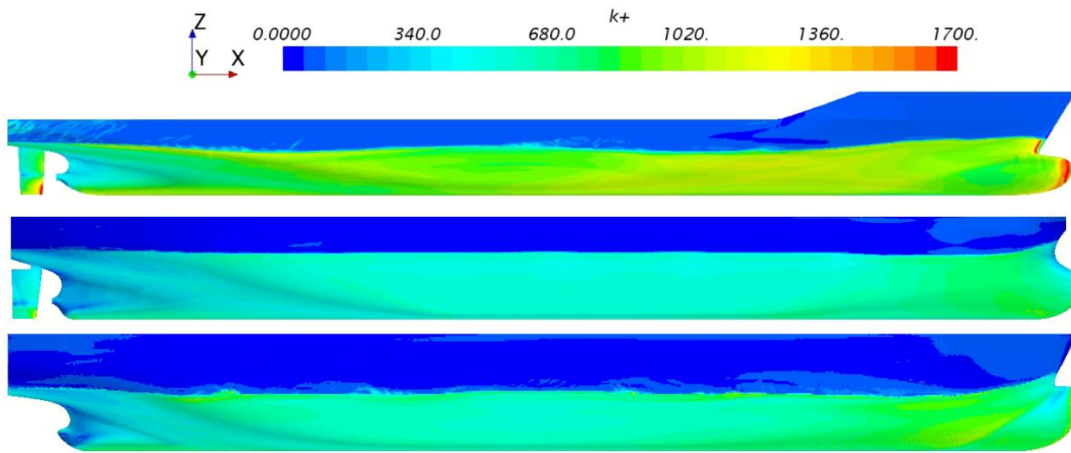


Figure 5.26 The obtained  $k^+$  distribution along KCS hull (upper), KVLCC2 hull (middle) and BC hull (lower) for R1 H

As already noted,  $\Delta U^+$  causes the downward shift of the mean velocity profile in the log-law region. In order to investigate the proper implementation of  $\Delta U^+$  model within the wall function, the log-law velocity profiles for ships fouled with hard fouling are investigated. In that way, the effect of hard fouling on the log-law velocity profiles can be clearly seen. Within Figure 5.27,  $U^+ - y^+$  plots for smooth KCS, KVLCC2 and BC, as well as for KCS, KVLCC2 and BC fouled with hard fouling are presented. The effect of hard fouling on the log-law velocity profiles is presented rather than the effect of biofilm, since hard fouling is defined with single  $\Delta U^+$  model and in that way more clear representation of this effect is enabled. The plots shown in Figure 5.27 are obtained using FSS, for the location at the hull surface amid ship and at  $z = 0.7T$ .  $U^+$  and  $y^+$  values are extracted from the cells within boundary layer, whose thickness is defined as 99% of the ship speed. It should be noted that  $x$  axis in Figure 5.27 is logarithmic. Several interesting phenomena can be noticed, from Figure 5.27. Namely, the log-law velocity profile is significantly decreased due to the presence of hard fouling. For the higher roughness length scale, i.e. for the higher fouling severity, this decrease is larger as well. The highest decrease in the log-law velocity profile is therefore obtained for the fouling condition R1 H. In addition to, from Figure 5.27 it is clear that the highest decrease in the log-law velocity profile, i.e. the highest  $\Delta U^+$  values are obtained for KCS, which can be ascribed to the highest  $k^+$  values, Figure 5.26. This decrease in the log-law velocity profile causes an increase in  $C_F$ . Furthermore, from Figure 5.27 it can be seen that  $y^+$  value of the first cell near the wall increases with the increase of surface roughness, what was expected since the first cell near the wall has larger wall distance for rough surface ( $y > k$ ). Also, for rough surface higher  $u_\tau$  values are obtained and consequently,  $y^+$  value of the first cell near the wall is even higher. Nevertheless, it is clear that the first cell near the both smooth and rough wall lies within the log-law region of the boundary layer. Lastly, the boundary layer of a ship has extended log-law and outer region as discussed in [109], i.e. the log-law region extends up to 15% of the boundary layer thickness, meaning that  $y^+$  value for full-scale ship, where the log-law region is still present, is significantly higher than for a ship model or flat plate which is used in drag characterization. Regardless the large difference in the boundary layer thickness between flat plate used in the drag characterization and full-scale ship, the matching of the mean velocity

profiles in the inner layer is present, since the growth of the boundary layer along a ship occurs primarily in the log-law and outer layer [109].

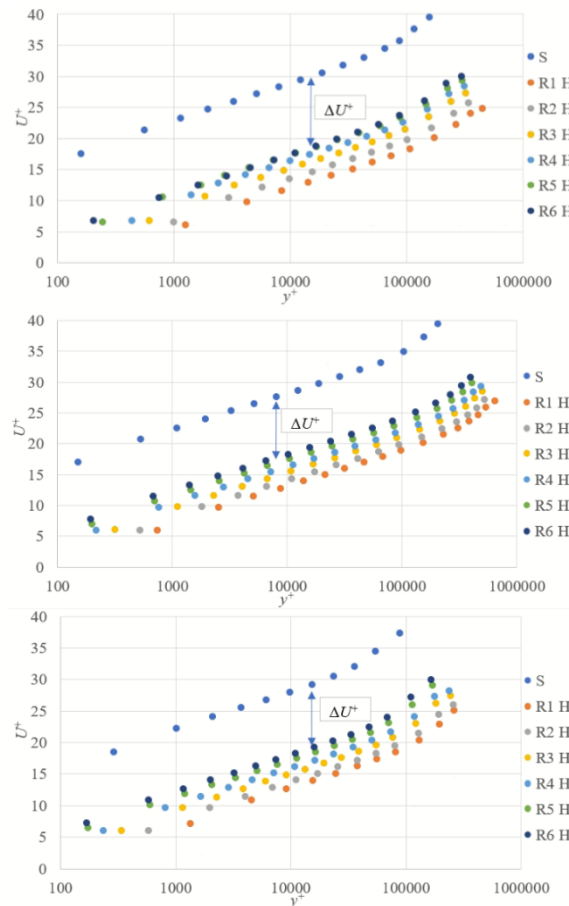


Figure 5.27 The effect of hard fouling on the log-law velocity profile for KCS (upper), KVLCC2 (middle) and BC (lower)

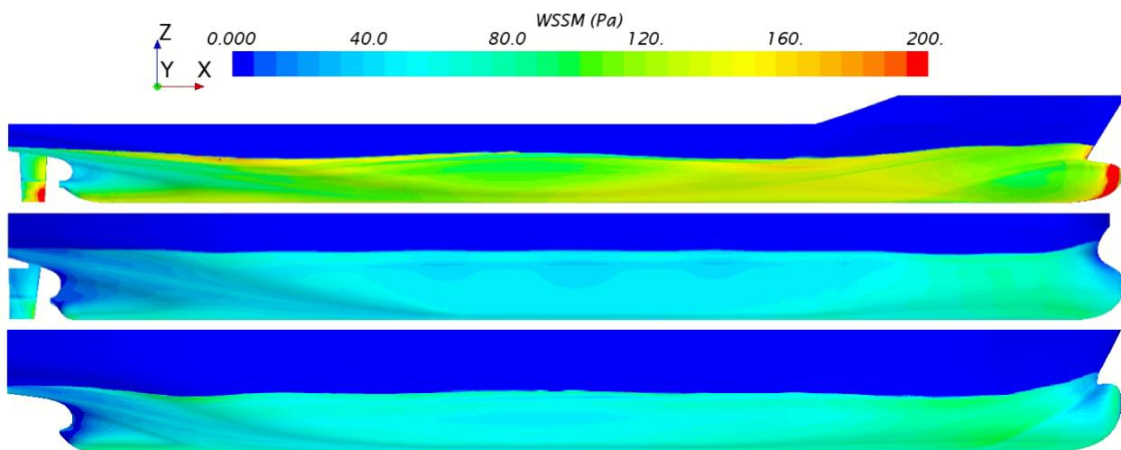


Figure 5.28 The obtained  $\tau_w$  distribution along the smooth KCS hull (upper), KVLCC2 hull (middle) and BC hull (lower)

As noted,  $R_f$  is obtained by integrating the tangential stresses over the wetted surface in DBS. Obviously, the distribution of  $\tau_w$  along the ship hull is of crucial importance in the determination of  $R_f$ . Thus, the increase in  $\tau_w$  values along the fouled hull will affect  $R_f$ . The

obtained  $\tau_w$  distributions along the smooth, hull with the fouling condition R2 B and R1 H, for all investigated ships are shown in Figure 5.28, Figure 5.29 and Figure 5.30. The average value of  $\tau_w$  below free surface for smooth KCS is equal to 110.86 Pa, KVLCC2 to 47.94 Pa and for BC to 56.94 Pa. The average value of  $\tau_w$  below free surface for KCS with R2 B is equal to 154.85 Pa, KVLCC2 with R2 B to 63.23 Pa and for BC with R2 B to 77.06 Pa. The average value of  $\tau_w$  below free surface for KCS with R1 H is equal to 269.80 Pa, KVLCC2 with R1 H to 107.98 Pa and for BC with R1 H to 135.76 Pa. From Figure 5.28 it is clear that the highest  $\tau_w$  values are obtained for KCS, which was expected since KCS is investigated for the highest speed, i.e. 24 kn. It should be noted that the same trend can be seen from Figure 5.29 and Figure 5.30. Furthermore, the obtained  $\Delta\tau_w$  due to the presence of biofouling are also the highest for KCS, followed by BC and KVLCC2. Thus, due to the presence of biofilm, i.e. R2 B, the obtained  $\Delta\tau_w$  for KCS is equal to 39.68%, for KVLCC2 to 31.9% and for BC to 35.35%. Due to the presence of hard fouling, i.e. R1 H, the obtained  $\Delta\tau_w$  for KCS is equal to 143.37%, for KVLCC2 to 125.24% and for BC to 138.44%. Due to the fact that  $\Delta\tau_w$  is directly related to  $\Delta C_F$ , it is obvious that the highest  $\Delta C_F$  are obtained for KCS.

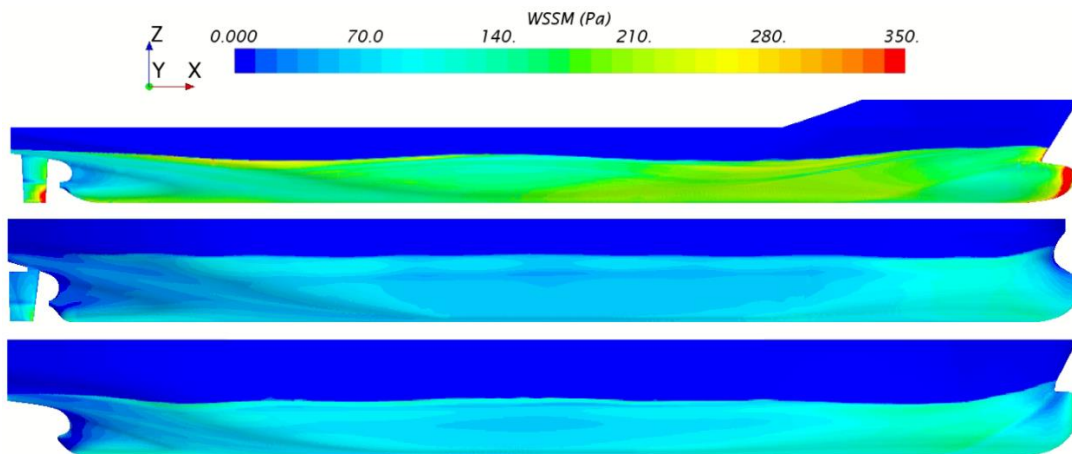


Figure 5.29 The obtained  $\tau_w$  distribution along the KCS hull (upper), KVLCC2 hull (middle) and BC hull (lower) for R2 B

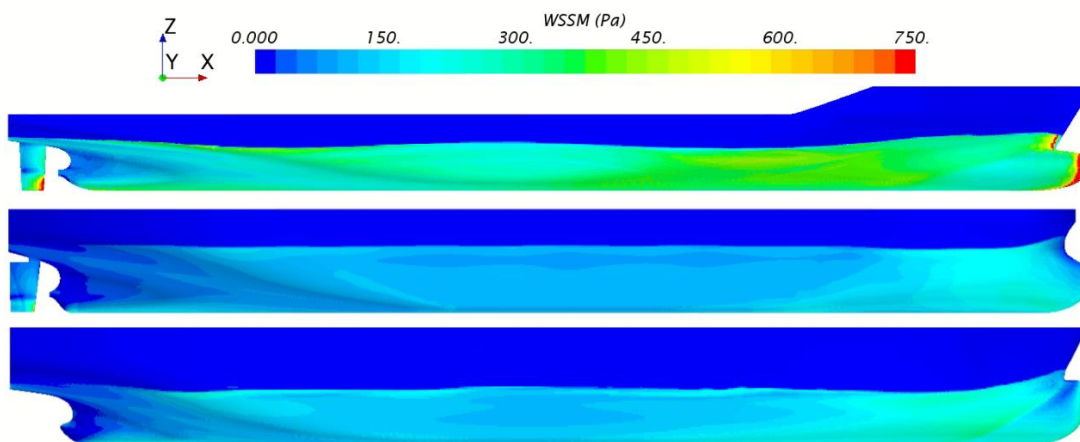


Figure 5.30 The obtained  $\tau_w$  distribution along the KCS hull (upper), KVLCC2 hull (middle) and BC hull (lower) for R1 H

The increase in  $\tau_w$  is related with an increase in turbulent kinetic energy, i.e. turbulence is increased due to the presence of roughness, which implicates that turbulent stress and  $\tau_w$  are increased as well [78]. The increase in turbulent kinetic energy and  $\tau_w$  leads to a decrease in the velocity within the turbulent boundary layer, i.e. turbulent boundary layer thickness increases due to the presence of roughness [188]. The obtained turbulent kinetic energy contours for smooth ships, ships fouled with R2 B and R1 H at the midship plane are shown in Figure 5.31, Figure 5.32 and Figure 5.33. It is clear that the presence of biofilm and especially hard fouling causes significant increase in the turbulent kinetic energy near the hull surface. This increase in turbulence results in increased boundary layer thickness as can be seen from Figure 5.34, Figure 5.35 and Figure 5.36. Within those figures, boundary layers, which are defined as the distance between the hull surface and the point where the axial velocity magnitude of the flow reaches the proportion of 0.99 of the ship speed, are presented. The increase in the boundary layer thickness due to the presence of biofouling or roughness obtained within this thesis is in line with previously published experimental results in the literature [93], [94]. This finding also highlights the importance of keeping the hull free of biofouling, since the increase in turbulent kinetic energy and  $\tau_w$  leads to an increase in  $R_F$ .



Figure 5.31 The obtained turbulent kinetic energy contours for smooth KCS hull (upper), KCS with R2 B (middle) and KCS with R1 H (lower) at the midship plane

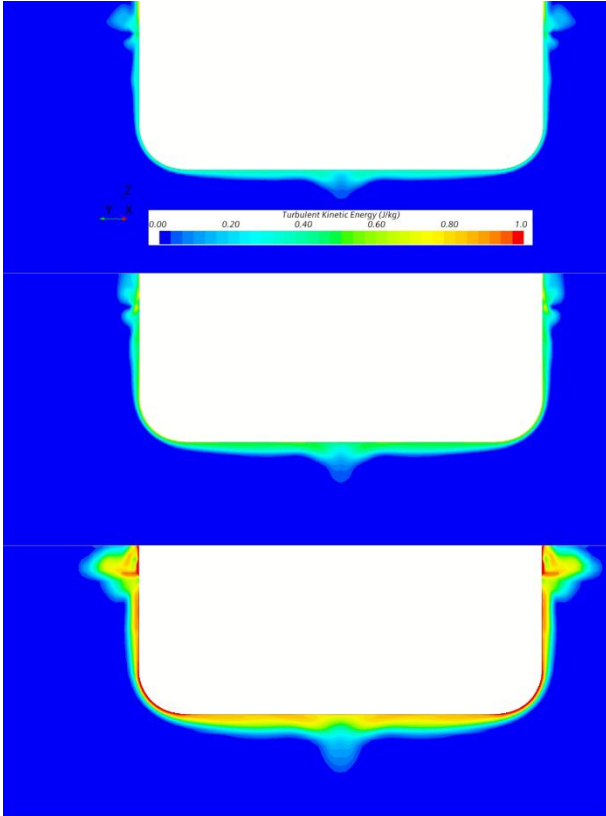


Figure 5.32 The obtained turbulent kinetic energy contours for smooth KVLCC2 hull (upper), KVLCC2 with R2 B (middle) and KVLCC2 with R1 H (lower) at the midship plane

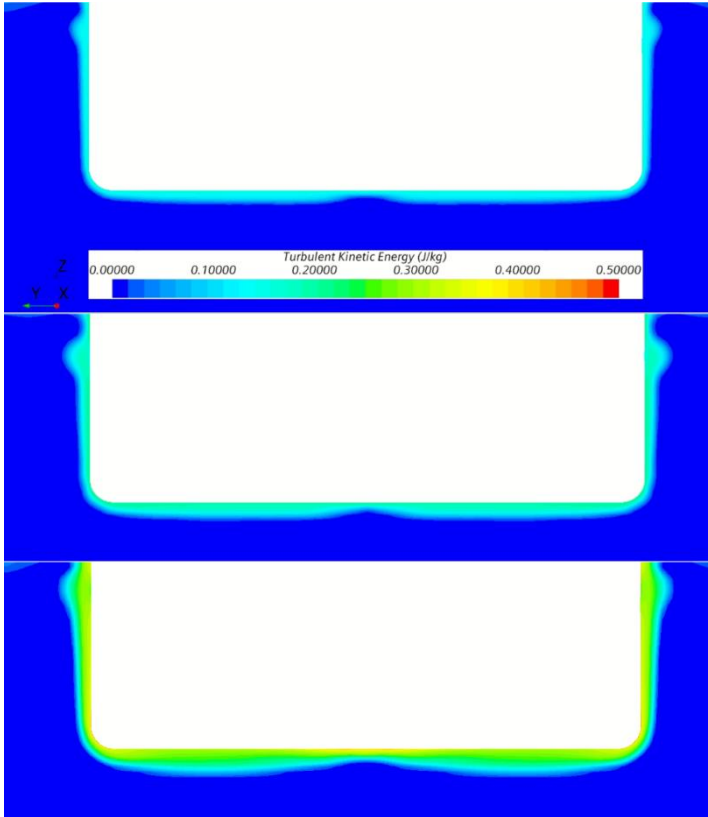


Figure 5.33 The obtained turbulent kinetic energy contours for smooth BC hull (upper), BC with R2 B (middle) and BC with R1 H (lower) at the midship plane

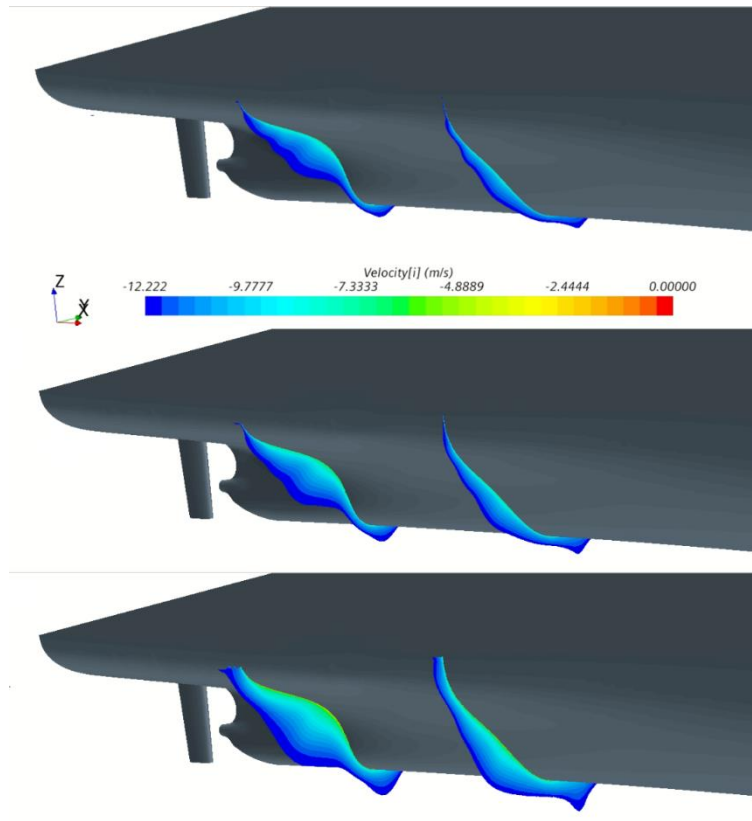


Figure 5.34 The obtained boundary layers for smooth KCS hull (upper), KCS with R2 B (middle) and KCS with R1 H (lower) at locations  $x = 30$  m and  $x = 50$  m

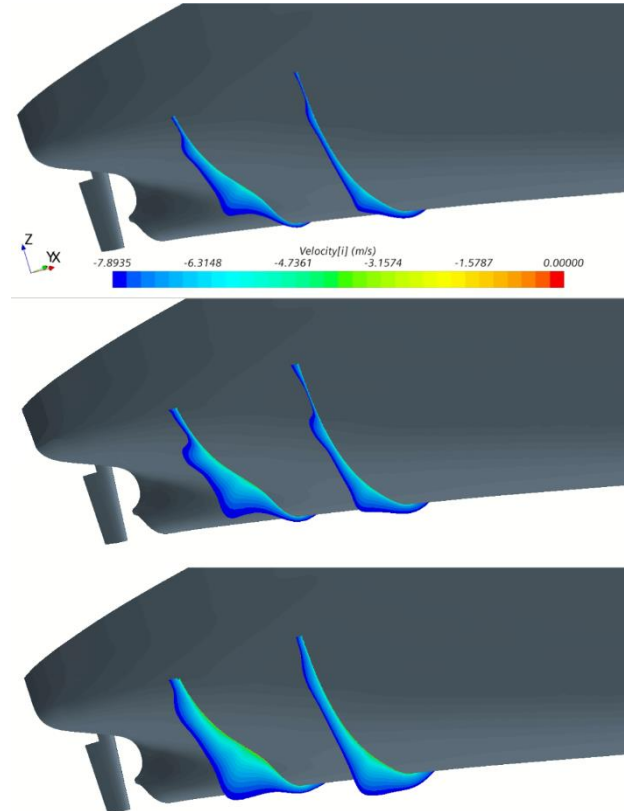


Figure 5.35 The obtained boundary layers for smooth KVLCC2 hull (upper), KVLCC2 with R2 B (middle) and KVLCC2 with R1 H (lower) at locations  $x = 50$  m and  $x = 70$  m



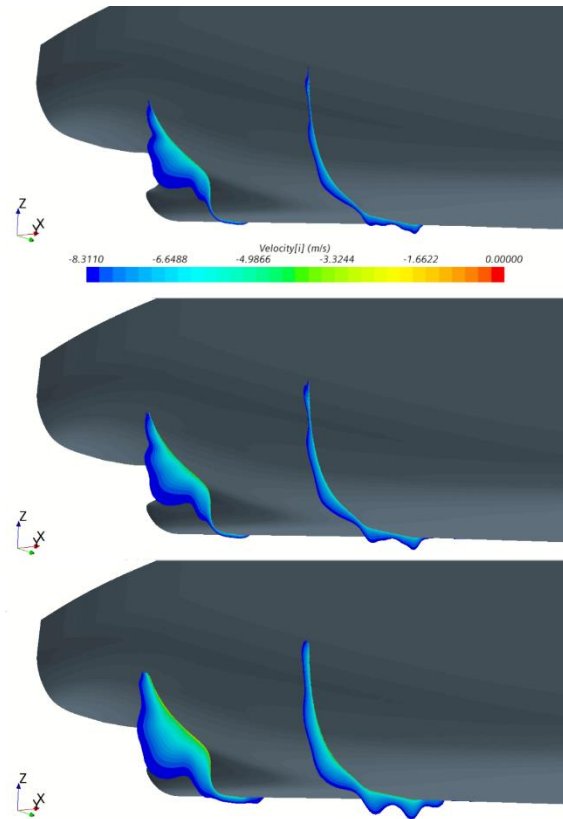


Figure 5.36 The obtained boundary layers for smooth BC hull (upper), BC with R2 B (middle) and BC with R1 H (lower) at locations  $x = 17.5$  m and  $x = 35$  m

The obtained distributions of dynamic pressure coefficient ( $C_p$ ) along the wetted surface for smooth, R2 B and R1 H surface conditions are presented in Figure 5.37, Figure 5.38 and Figure 5.39 respectively. It should be noted that  $C_p$  is defined as a ratio of hydrodynamic pressure and  $\frac{1}{2}\rho v^2$ . From these figures it can be noticed that the pressure recovery at the stern is reduced due to the presence of biofouling, which results in the increase in  $R_{vp}$ , as observed in the Section 5.3.3. Also, it can be seen that the pressure at the fore part of the rudder is increased due to the presence of biofouling. This can be attributed to the reduced flow velocity behind the stern, which can be noticed in Figure 5.43, Figure 5.44 and Figure 5.45. In addition to, the obtained  $C_p$  distributions from the bow to the midship are similar for smooth and fouled hull. This finding is also obtained within [193] and it denotes that  $C_p$  distribution is not significantly affected by the biofouling unless an adverse pressure gradient occurs near the stern shoulder. This supports the assumption that  $C_R$  of the flat plates is not significantly affected by the surface roughness. Generally, it can be concluded that  $\tau_w$  distribution is more affected than  $C_p$  distribution due to the presence of biofouling, which was expected since the highest impact of biofouling is obtained for  $C_F$ .

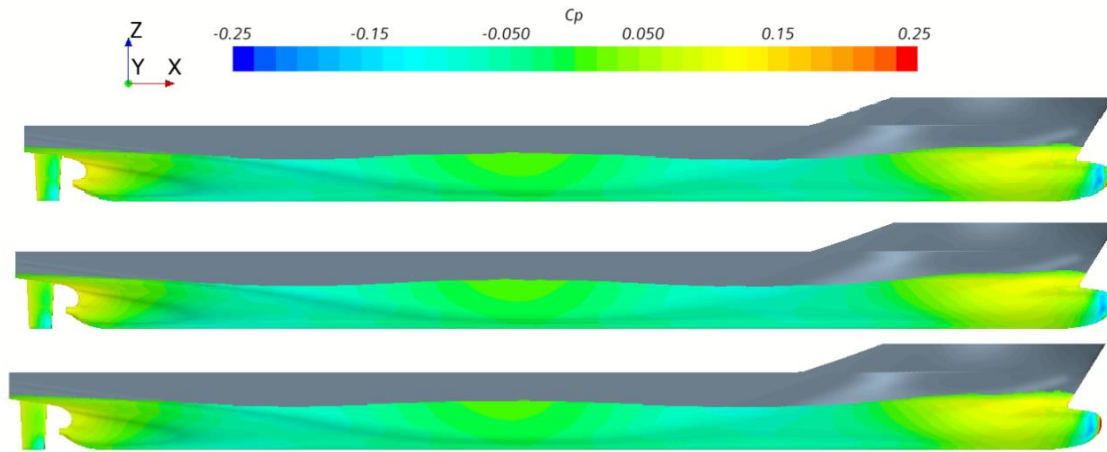


Figure 5.37 The obtained  $C_p$  distributions for smooth KCS hull (upper), KCS with R2 B (middle) and KCS with R1 H (lower)

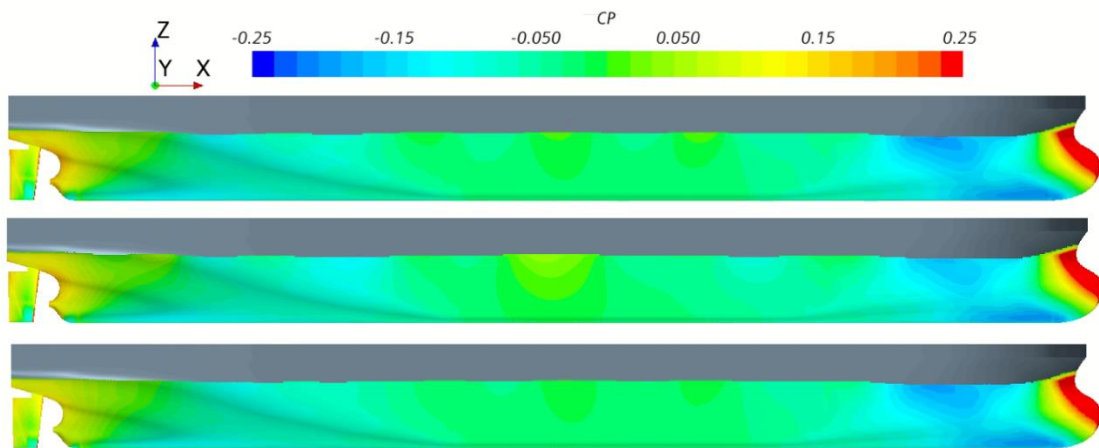


Figure 5.38 The obtained  $C_p$  distributions for smooth KVLCC2 hull (upper), KVLCC2 with R2 B (middle) and KVLCC2 with R1 H (lower)

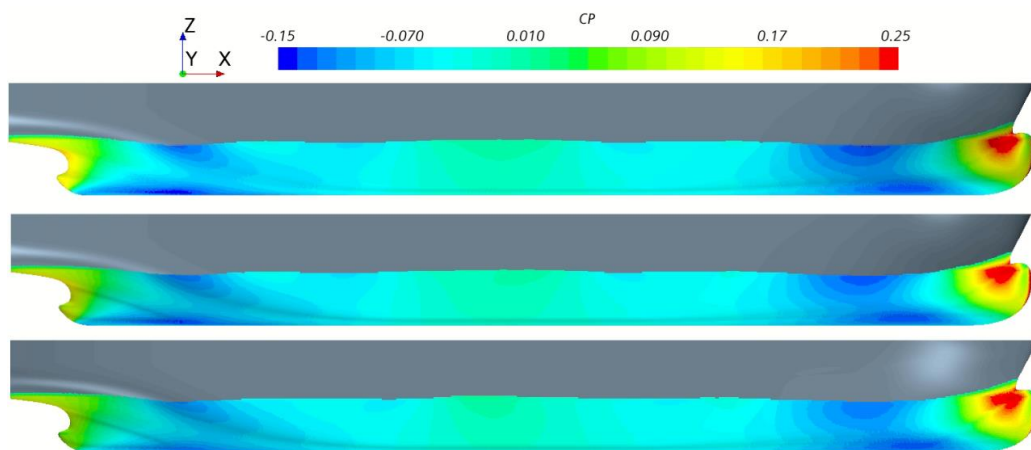


Figure 5.39 The obtained  $C_p$  distributions for smooth BC hull (upper), BC with R2 B (middle) and BC with R1 H (lower)

The obtained  $C_p$  distributions at the symmetry plane near the stern of the investigated ships for smooth, R2 B and R1 H surface conditions are shown in Figure 5.40, Figure 5.41 and Figure 5.42, respectively. From these figures it is clear that the presence of biofouling causes the

decrease in the  $C_p$  values downstream the ship hull. Due to the decrease in the  $C_p$  values downstream the hull, the wave elevations behind the stern for fouled ships are reduced, as shown in Figure 5.47, Figure 5.48 and Figure 5.49.

The obtained contours of the axial velocity at the symmetry plane near the stern for smooth, R2 B and R1 H surface conditions for investigated ships are shown in Figure 5.43, Figure 5.44 and Figure 5.45, respectively. As can be seen from these figures, the velocity downstream the hull is reduced due to the presence of biofouling. This decrease of velocity enlarges the wake field of the ship. It should be noted that the most reduction in the flow velocity is obtained for KVLCC2, followed by BC and KCS.

One of the interesting findings presented in subsection 5.3.3 is that the presence of biofouling causes the decrease in  $R_w$ . Therefore, it is worth to investigate the impact of biofouling on the wave profiles of the investigated ships. The obtained wave patterns for smooth, R2 B and R1 H surface conditions around the investigated ships are shown in Figure 5.46. By comparing the obtained wave amplitudes it can be seen that wave amplitudes are reduced due to the presence of biofouling. The obtained reduction in the wave amplitudes is in accordance with the obtained reductions in  $C_w$  due to the presence of biofouling. It should be noted that the highest reduction in wave amplitudes is obtained for KCS, then for BC, while for KVLCC2, the wave amplitudes almost remain the same regardless of surface conditions. Higher reduction of wave amplitudes and consequently  $C_w$  for KCS than for BC and KVLCC2, can be attributed to higher  $k^+$  and  $\Delta U^+$  values along KCS hull and consequently higher viscosity effects. Namely, the obtained reductions in wave amplitudes can be attributed to the effect of viscosity on the wave system, as already explained in [188]. Thus, these effects caused the decrease in wave amplitudes resulted in lower  $C_w$ .

In order to represent the impact of biofouling on the wave amplitudes more clearly, the obtained longitudinal wave cuts in the symmetry plane behind the stern of KCS, KVLCC2 and BC are shown in Figure 5.47, Figure 5.48 and Figure 5.49, respectively. The obtained longitudinal wave cuts in the symmetry plane for S, R2 B and R1 H surface conditions are shown. It should be noted that the obtained longitudinal wave cuts in the bow region are not influenced by the presence of biofouling. On the other hand, as can be seen from Figure 5.47, Figure 5.48 and Figure 5.49 the obtained wave amplitudes are reduced in the wake region due to the presence of biofouling. This finding suggests that the effect of biofouling on the wave pattern of the ship is present in the wake region, where the viscous effects are important as noted in [182]. The reduction of the stern wave system due to viscous effects on  $R_w$  and wave systems is in accordance with the results presented in [153]. From Figure 5.47, Figure 5.48 and Figure 5.49 it is evident that the highest reduction in the wave amplitude is obtained for KCS, as already explained.

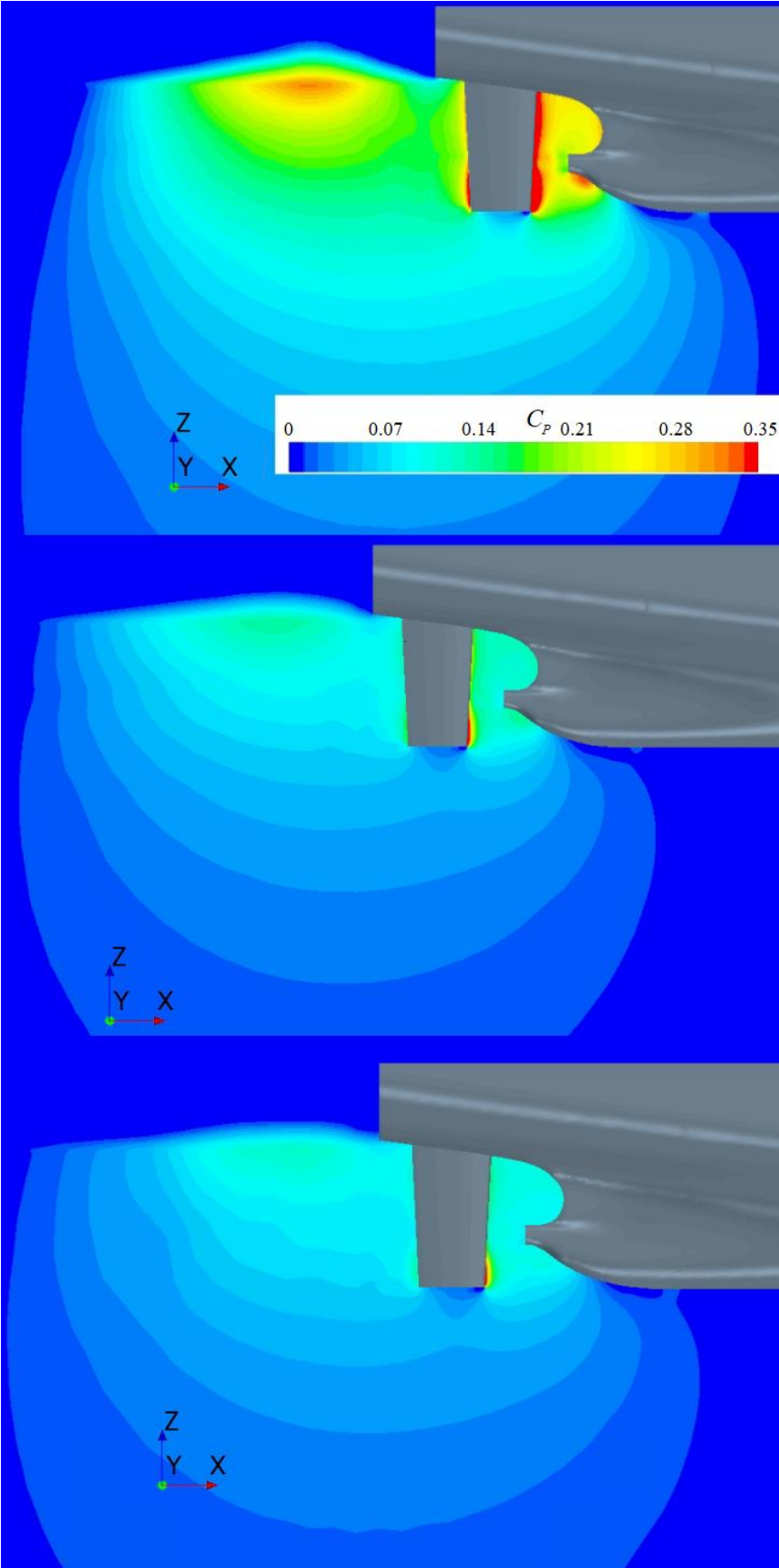


Figure 5.40 The obtained  $C_p$  distributions at the symmetry plane for smooth KCS hull (upper), KCS with R2 B (middle) and KCS with R1 H (lower)

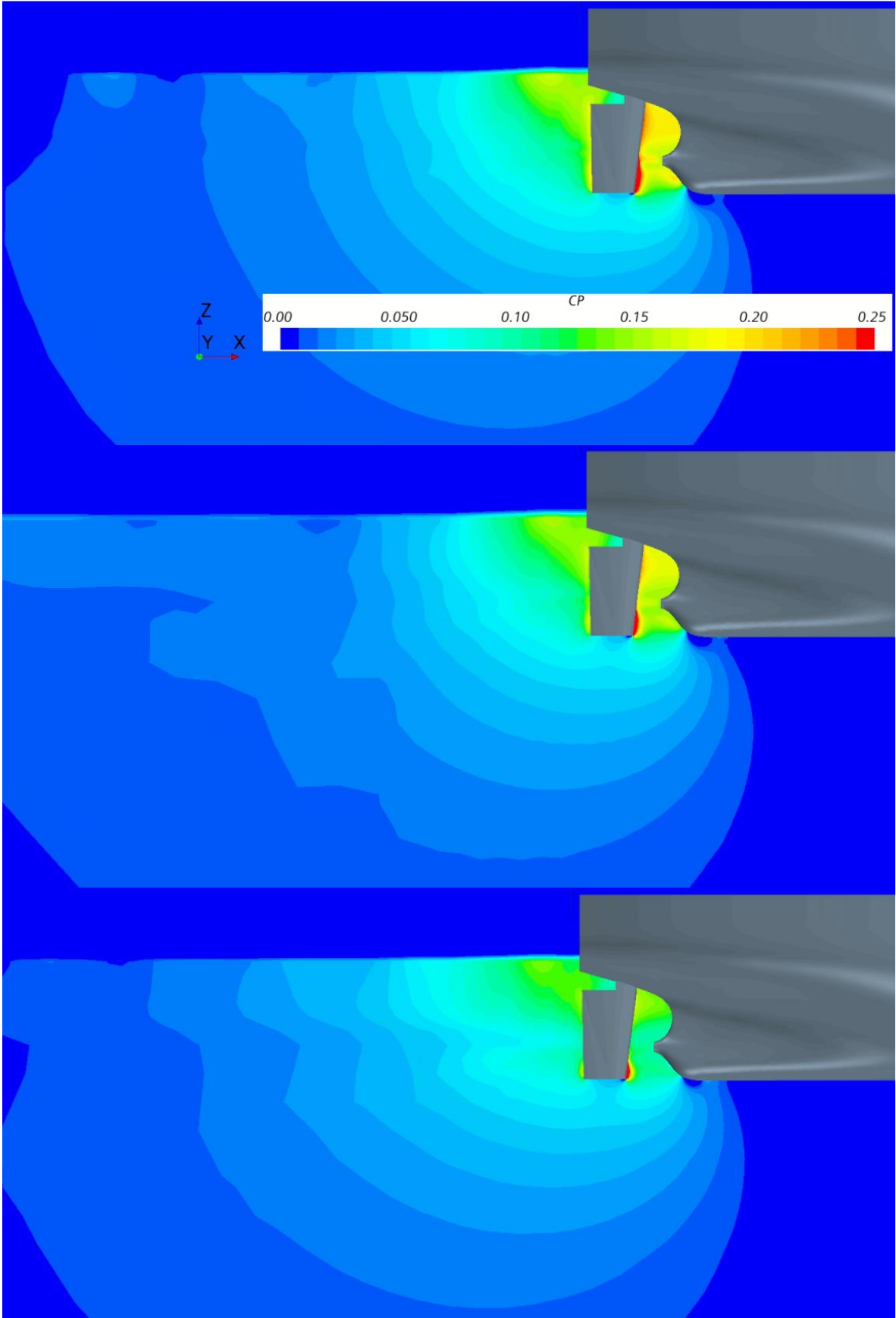


Figure 5.41 The obtained  $C_p$  distributions at the symmetry plane for smooth KVLCC2 hull (upper), KVLCC2 with R2 B (middle) and KVLCC2 with R1 H (lower)

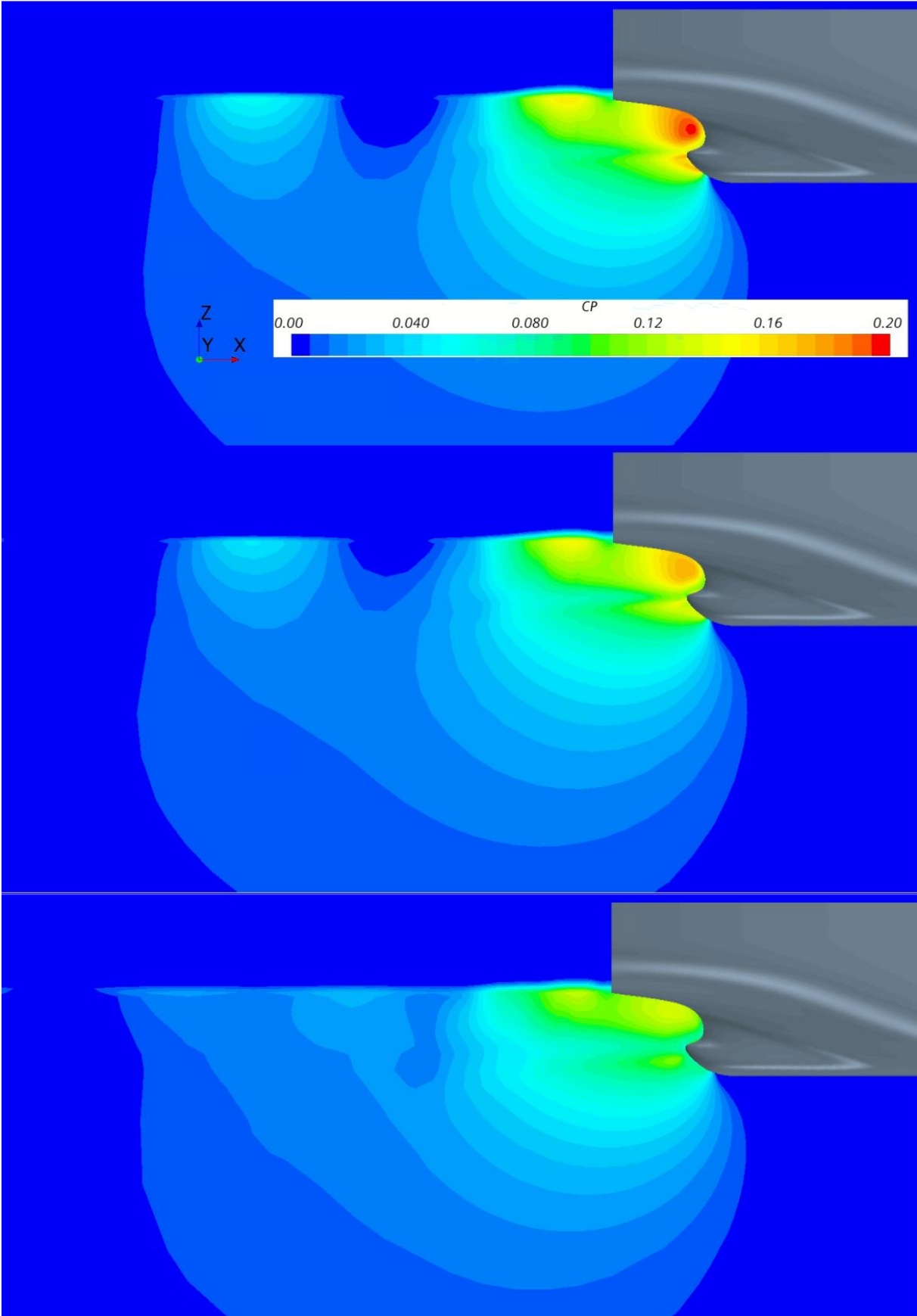


Figure 5.42 The obtained  $C_p$  distributions at symmetry plane for the smooth BC hull (upper), BC with R2 B (middle) and BC with R1 H (lower)

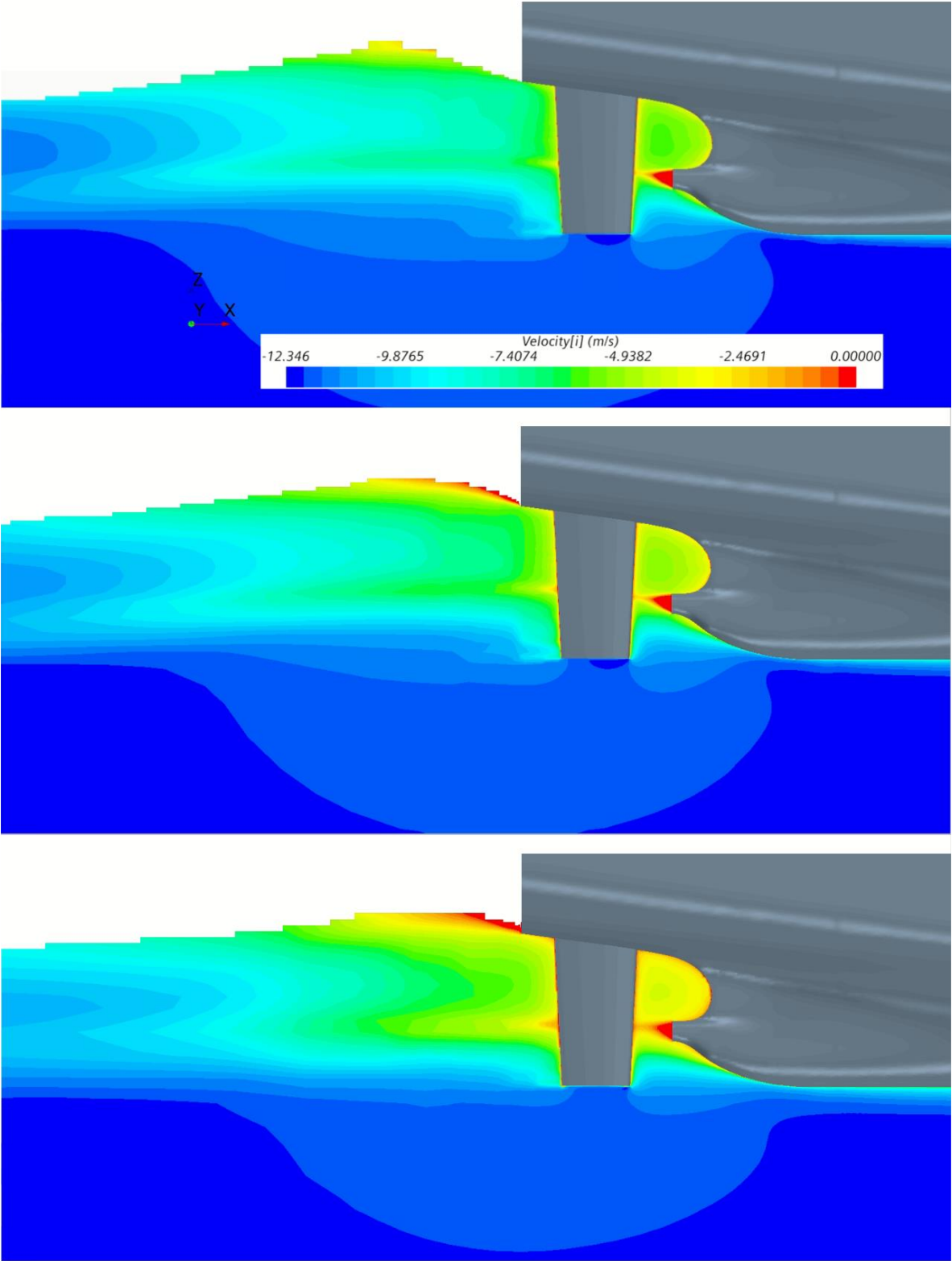


Figure 5.43 The obtained contours of the axial velocity at the symmetry plane for smooth KCS hull (upper), KCS with R2 B (middle) and KCS with R1 H (lower)

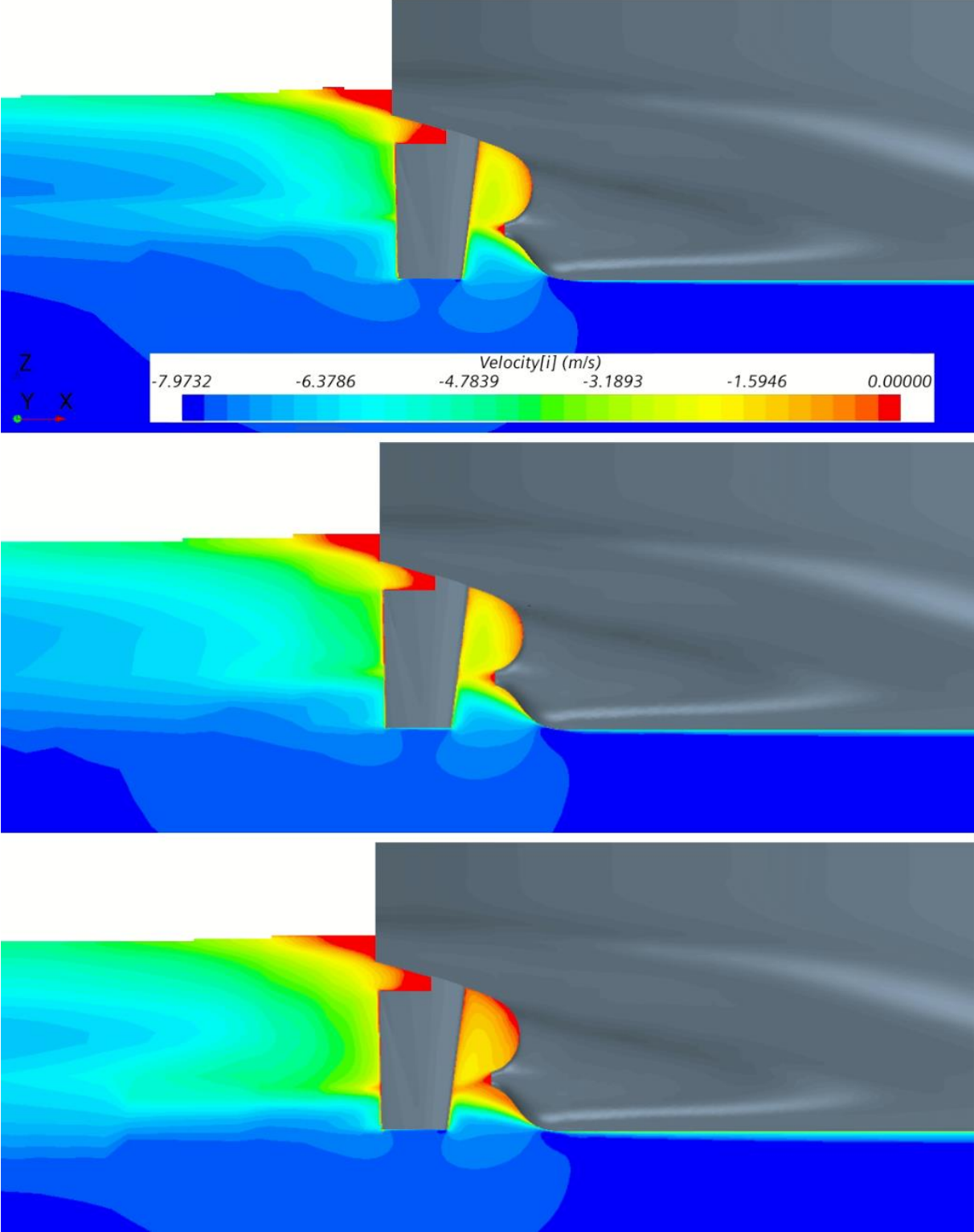


Figure 5.44 The obtained contours of the axial velocity at the symmetry plane for smooth KVLCC2 hull (upper), KVLCC2 with R2 B (middle) and KVLCC2 with R1 H (lower)



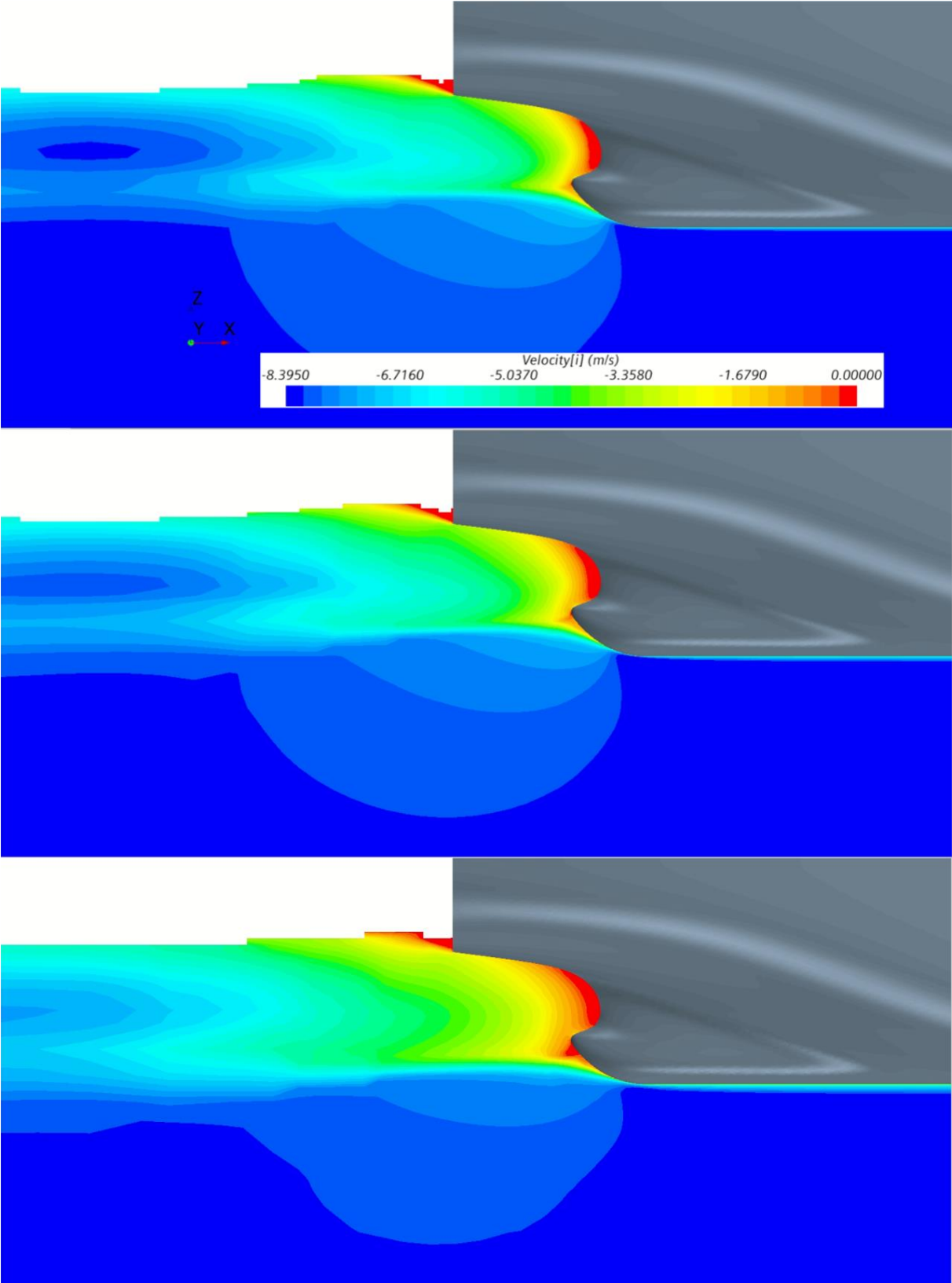


Figure 5.45 The obtained contours of the axial velocity at the symmetry plane for smooth BC hull (upper), BC with R2 B (middle) and BC with R1 H (lower)

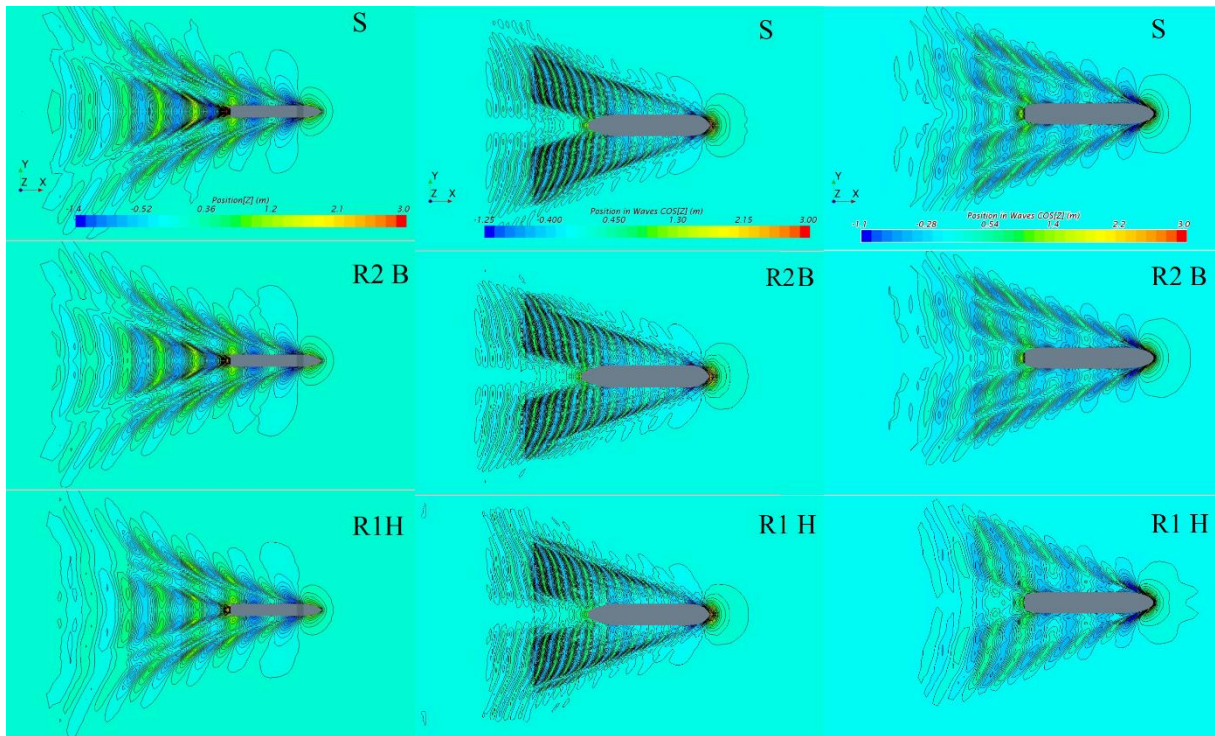


Figure 5.46 The obtained wave patterns around KCS (left), KVLCC2 (middle) and BC (right) As already presented in Figure 5.23 and Figure 5.24, the presence of biofouling decreases the integral value of  $1-w_N$ , and causes the downward shift of the circumferential averaged non-dimensional axial velocity distribution. From Figure 5.50, Figure 5.51 and Figure 5.52 it can be seen that the presence of biofouling causes the significant reduction of the flow in the propeller disc plane. Within these figures, the obtained contours of  $1-w_N$  for smooth, R2 B and R1 H surface conditions are presented. It should be noted that  $1-w_N$  is obtained as the ratio between axial velocity ( $v_x$ ) and the ship speed. The highest reduction of the flow in the propeller disc plane due to the presence of biofilm (R2 B) is obtained for BC, while due to the presence of hard fouling (R1 H) is obtained for KVLCC2. The reduction in the flow due to the presence of biofouling can be associated with an increase in turbulence, i.e. turbulent and wall shear stress which lead to a decrease in the velocity in the turbulent boundary layer. The decelerated inflow velocity at the propeller disc plane causes the altering of the propeller  $J$  and consequently affects the propeller efficiency, i.e.  $\eta_o$ . More discussion regarding this will be presented in the following sections.

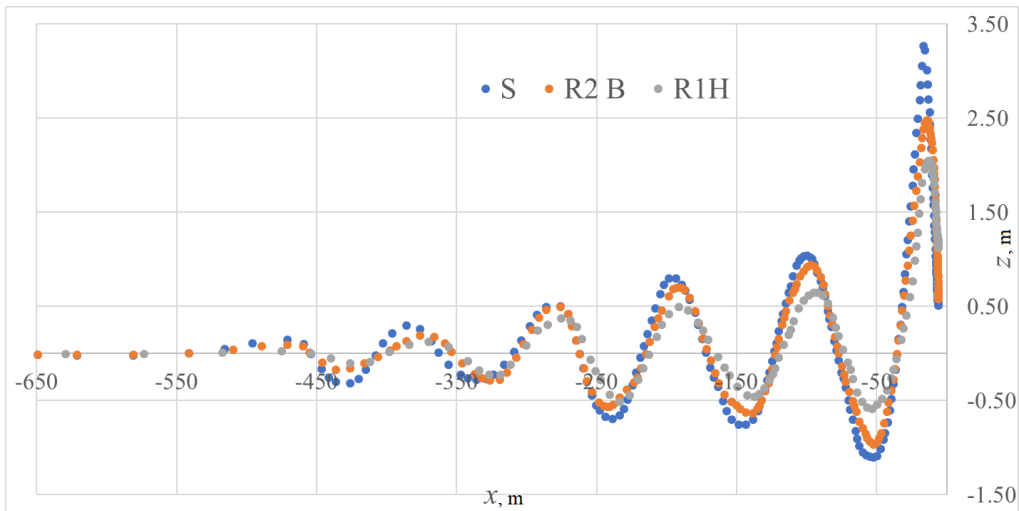


Figure 5.47 Longitudinal wave cuts at symmetry plane behind the KCS stern for S, R2 B and R1 H surface condition

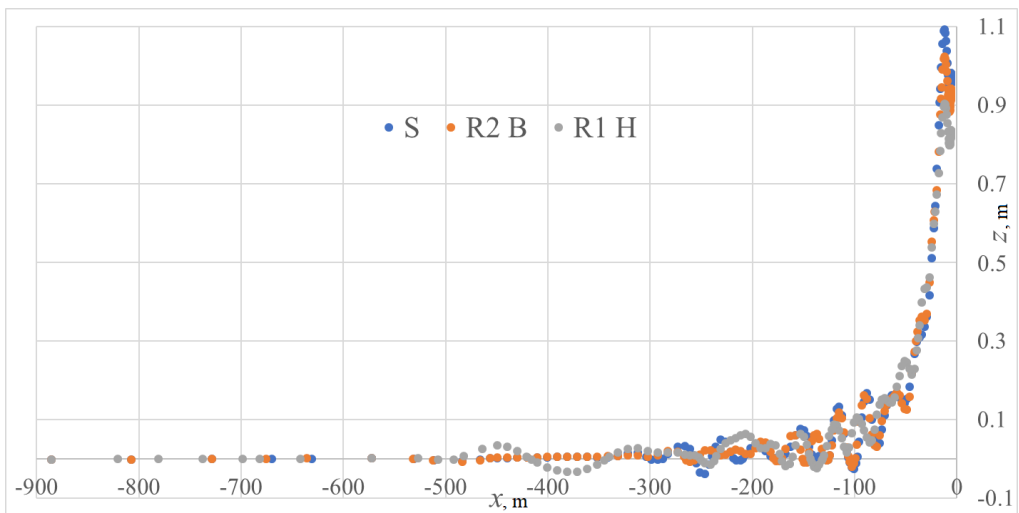


Figure 5.48 Longitudinal wave cuts at symmetry plane behind the KVLCC2 stern for S, R2 B and R1 H surface condition

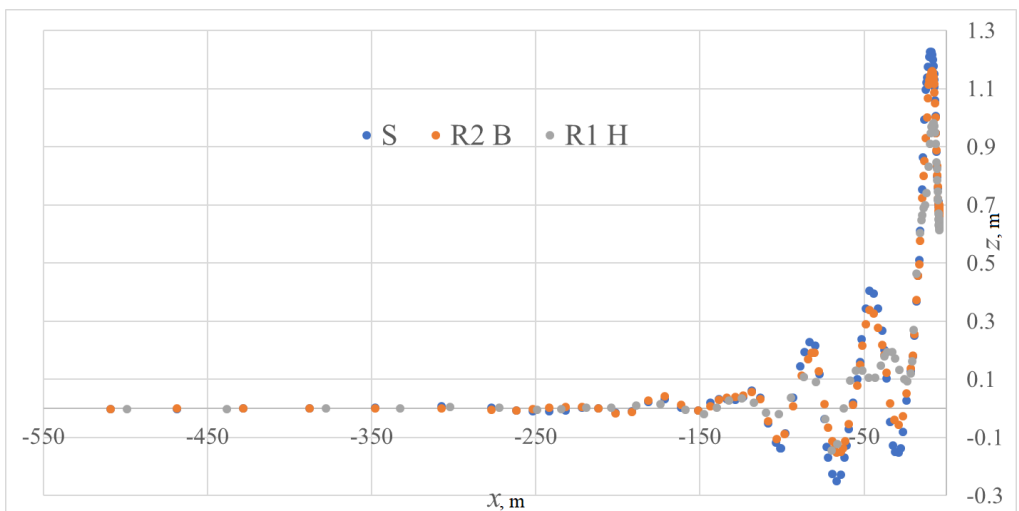


Figure 5.49 Longitudinal wave cuts at symmetry plane behind the BC stern for S, R2 B and R1 H surface condition

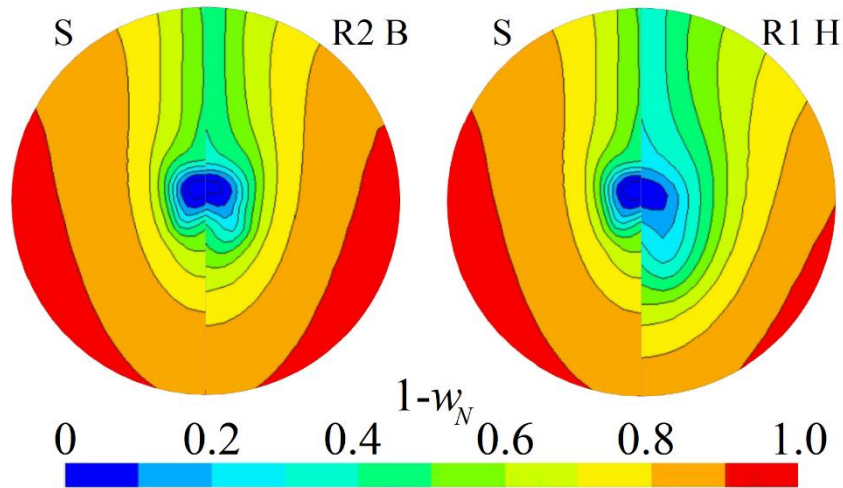


Figure 5.50 The obtained contours of  $1-w_N$  for smooth KCS and KCS with R2 B (left) and for smooth KCS and KCS with R1 H (right) in the propeller disc plane

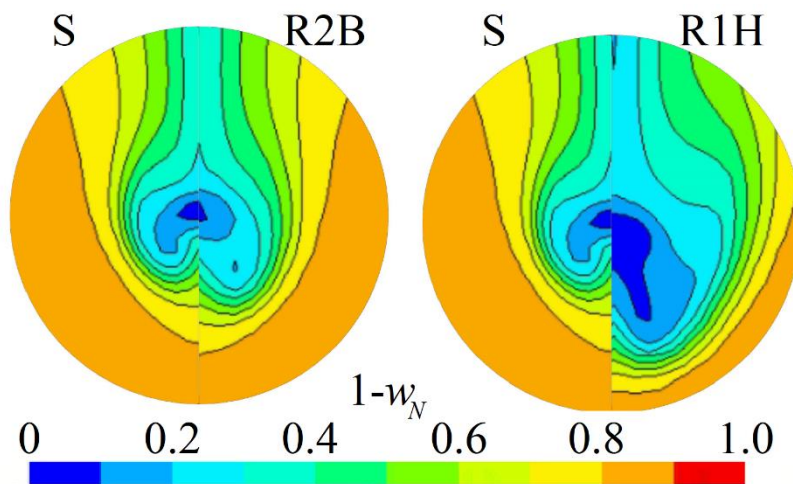


Figure 5.51 The obtained contours of  $1-w_N$  for smooth KVLCC2 and KVLCC2 with R2 B (left) and for smooth KVLCC2 and KVLCC2 with R1 H (right) in the propeller disc plane

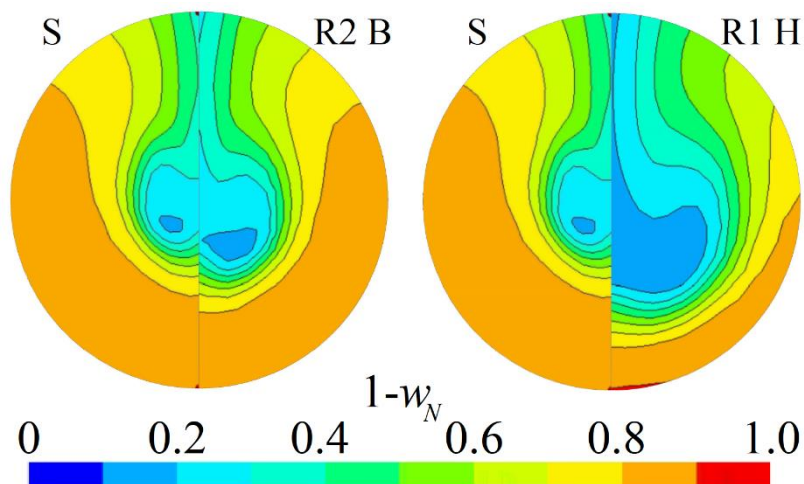


Figure 5.52 The obtained contours of  $1-w_N$  for smooth BC and BC with R2 B (left) and for smooth BC and BC with R1 H (right) in the propeller disc plane

## 5.4. The impact of biofouling on the open water characteristics

In the analysis of the impact of biofouling on the ship performance, the effect of the propeller surface condition is frequently neglected [71]. Even though, the impact of the propeller fouling condition on the ship performance is lower than the impact of hull fouling condition, if analysed per unit area the impact of propeller fouling condition is significantly more important [243]. Thus, only slightly lower CO<sub>2</sub> reduction potential can be achieved with propeller polishing in comparison with hull cleaning, which is significantly more expensive [244]. What is more, a greater reduction in CO<sub>2</sub> emission can be accomplished with propeller polishing in comparison with weather routing or optimization of water flow. Consequently, propeller cleaning can be used as a relatively cheap and effective method for the reduction of fuel consumption and GHG emission. Thus, high return related to the increased ship performance is enabled with propeller cleaning and this is recognized by many ship operators or ship owners. However, it is important to find adequate timing for propeller cleaning, which depends on the propeller performance. As already noted, the effect of surface roughness on the propeller performance may be subdivided into the effect of surface deterioration and fouling. Although the effect of surface deterioration is described in [72], the effect of fouling is not described. Therefore, ITTC [71] has recommended researchers to investigate the effect of biofouling on the propeller performance, i.e. to extend the propeller performance prediction method with effects of biofouling. Furthermore, ITTC highlighted the importance of including at least the effect of slime on the propeller performance, since it is usually present on the propeller surfaces and it affects the propeller performance.

In this thesis, the impact of biofouling on the open water characteristics is investigated for three different propellers presented in Table 5.2 and two types of biofouling. In order to simulate the effect of biofilm and hard fouling on the open water characteristics,  $\Delta U^+$  models for biofilm and hard fouling are implemented within the wall function of CFD solver.

### 5.4.1. Numerical modelling and verification study

As described in subsection 3.2.4, CFD simulations of open water test are performed using MRF method and carried out as steady simulations. The computational domain is created as a cylinder and two regions are defined, rotating and static region. Domain boundaries are placed sufficiently far from the investigated propeller in order to avoid their influence on the obtained results, Figure 5.53. The applied boundary conditions are velocity inlet for inlet boundary, pressure outlet for outlet boundary, no-slip wall for propeller and shaft surfaces and slip wall for lateral surface of the computational domain.

The computational domain is discretized using the unstructured hexahedral mesh. The special care is taken for the discretization of propeller blade surfaces. Thus, the mesh is refined along the leading and trailing edges of the propeller in order to make an appropriate demarcation between the suction and pressure side of the propeller. In addition to, isotropic mesh refinements are applied around the investigated propellers. Finally, the prism layer cells near the wall are generated in a way that  $y^+$  are higher than 30 and  $k^+$  values, as already explained. The volume meshes used in CFD simulations of open water test are shown in Figure 5.54.

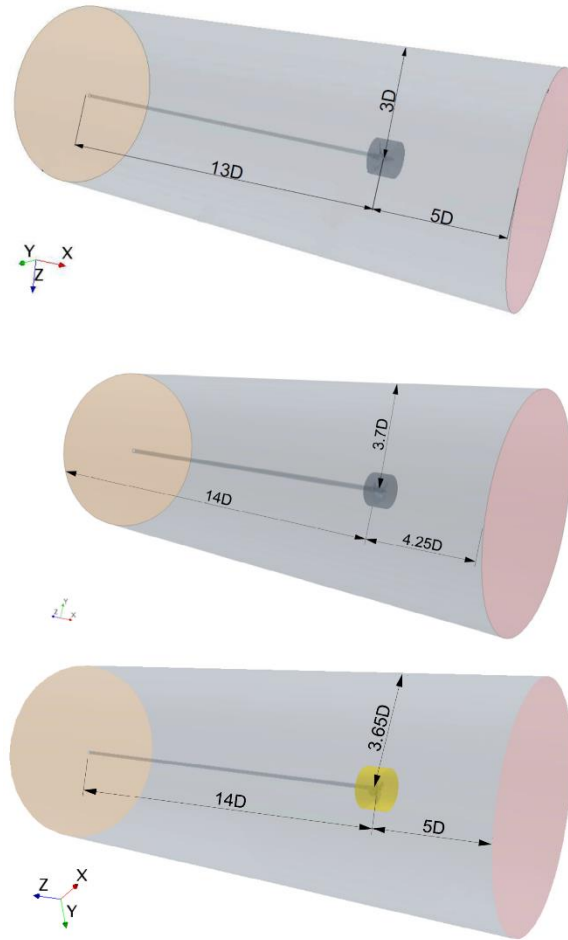


Figure 5.53 The computational domain for WB propeller (upper), KP 505 (middle) and KP 458 (lower)

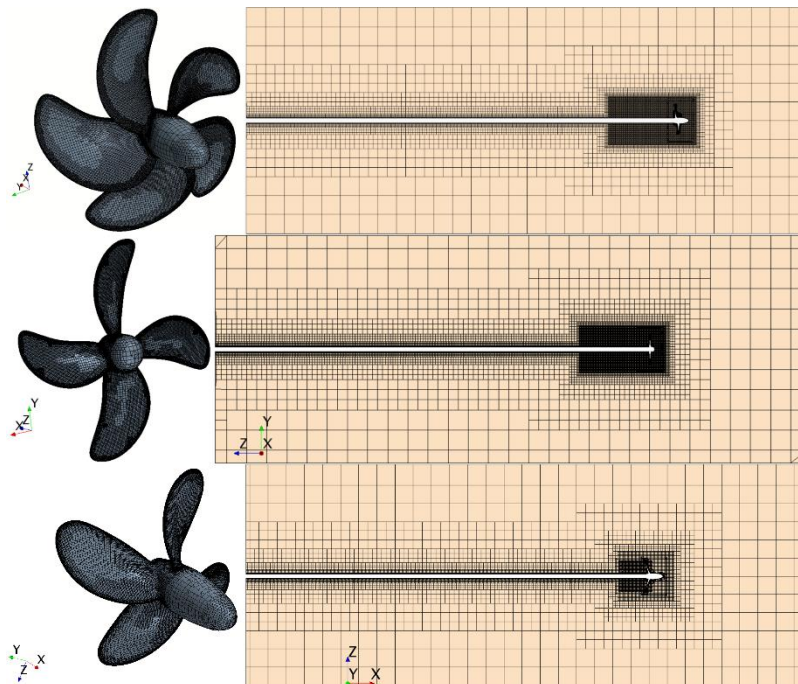


Figure 5.54 The propeller surface (left) and profile view (right) cross section of the volume mesh for KP 505 (upper), KP 458 (middle) and WB (lower)

CFD simulations are performed for full-scale propellers at eight  $J$  values for KP505 propeller, seven  $J$  values for KP458 propeller and eleven  $J$  values for WB propeller in a way that  $n = 1.5$  rps is kept constant while  $v_A$  is changed through iterations.

The obtained  $y^+$  distributions in the first cell near the wall for smooth KP 505, KP 458 and WB in full-scale are shown in Figure 5.55. The average value of  $y^+$  in the first cells near the wall for smooth KP 505 is equal to 179.15, KP 458 to 211.37 and for WB to 98.76. The obtained  $y^+$  distributions in the first cell near the wall for full-scale propellers fouled with biofilm are shown (R2 B) in Figure 5.56. The average value of  $y^+$  in the first cells near the wall for KP 505 fouled is equal to 236.76, KP 458 to 282.91 and for WB to 182.82, all fouled with R2 B. The obtained  $y^+$  distributions in the first cell near the wall for propellers fouled with hard fouling (R1 H) are shown in Figure 5.57. It can be seen that they are higher than the ones for biofilm. The average value of  $y^+$  in the first cells near the wall for KP 505 is equal to 3705.32, KP 458 to 4451.94 and for WB to 3086.02, all fouled with R1 H. As can be seen from Figure 5.55, Figure 5.56 and Figure 5.57, the obtained  $y^+$  values at the propeller surfaces vary depending on the location on the propeller blade, i.e. radius. The significantly higher  $y^+$  values obtained for propellers fouled with R1 H are justified since the fouling condition R1 H represents very severe fouling conditions. Owen et al. [65] have also obtained  $y^+$  values above 1000 for model scale propeller fouled with calcareous fouling.

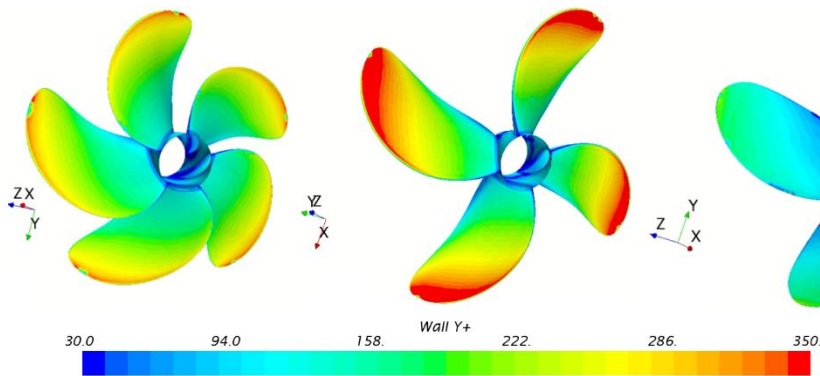


Figure 5.55 The obtained  $y^+$  distributions in the first cell near the wall for smooth KP 505 (left), KP 458 (middle) and WB (right)

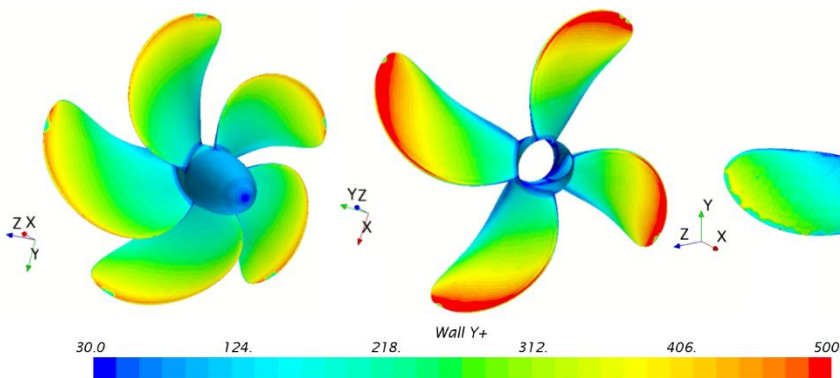


Figure 5.56 The obtained  $y^+$  distributions in the first cell near the wall for KP 505 (left), KP 458 (middle) and WB (right) fouled with the fouling condition R2 B

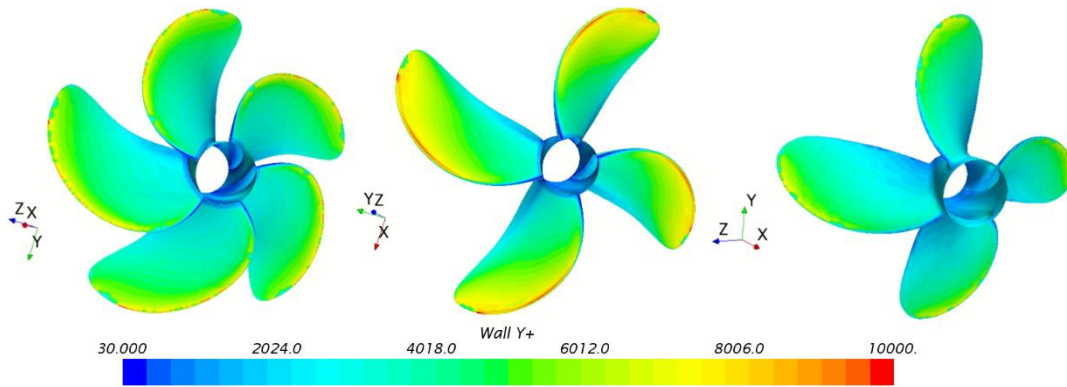


Figure 5.57 The obtained  $y^+$  distributions in the first cell near the wall for KP 505 (left), KP 458 (middle) and WB (right) fouled with the fouling condition R1 H

Three meshes are created for the verification study: coarse, medium and fine mesh. It should be noted that numerical uncertainty for CFD simulations of open water test is consisted only of grid uncertainty, as CFD simulations are performed as steady simulations and iterative uncertainty is considered to be negligible, since all residuals dropped at least five orders of magnitude. The verification study is performed for  $J$  value around the expected self-propulsion point and for surface conditions S, R2 B and R1 H. For that purpose, the mesh is refined systematically and the number of cells used for the investigated propellers is given in Table 5.31. It should be noted that the number of cells used for fine mesh in CFD simulations with hard fouling varied amongst investigated surface conditions, because of different discretization of prism layer mesh. Within Table 5.31, the number of cells is given for the surface condition R1 H. It should be noted that  $K_T$  and  $K_Q$  are used as key variables in the verification study.

Table 5.31 The number of cells within CFD simulations of open water test

Propeller \ Mesh	KP 505 – S & R2 B	KP 458 – S & R2 B	WB – S & R2 B
Coarse mesh	3.5 M	2.4 M	2.2 M
Medium mesh	5.1 M	3.3 M	3.5 M
Fine mesh	7.1 M	5.3 M	5 M
Propeller \ Mesh	KP 505 – R1 H	KP 458 – R1 H	WB – R1 H
Coarse mesh	2.3 M	1.8 M	1.6 M
Medium mesh	3.5 M	2.3 M	2.4 M
Fine mesh	5.3 M	3.9 M	3.4 M

The obtained results of the verification study are presented in Table 5.32 and Table 5.33. As can be seen from these tables, relatively low numerical uncertainties are obtained and in line with numerical uncertainties of other CFD studies regarding open water test [65], [67]. Numerical uncertainties obtained for smooth and fouled propellers are relatively close, i.e. the numerical uncertainty did not increase due to the roughness effects.



Table 5.32 The verification study for  $K_T$ 

Propeller	$J$	$\phi_3$	$\phi_2$	$\phi_1$	$\phi_{ext}^{21}$	$GCI_{fine}^{21}, \%$
KP505 S	0.7	0.18068	0.18047	0.18058	0.18071	0.092
KP505 R2B	0.7	0.17415	0.17397	0.17400	0.17400	0.006
KP505 R1H	0.6	0.20722	0.20665	0.20668	0.20668	0.001
KP458 S	0.5	0.18513	0.18576	0.18478	0.18264	1.443
KP458 R2B	0.5	0.17763	0.17816	0.17727	0.17568	1.124
KP458 R1H	0.4	0.15868	0.15883	0.15725	0.15698	0.217
WB S	0.56	0.17468	0.17338	0.17250	0.16758	3.565
WB R2B	0.56	0.16857	0.16813	0.16789	0.16727	0.464
WB R1 H	0.4	0.20876	0.20855	0.20878	0.21098	1.317

Table 5.33 The verification study for  $10K_Q$ 

Propeller	$J$	$\phi_3$	$\phi_2$	$\phi_1$	$\phi_{ext}^{21}$	$GCI_{fine}^{21}, \%$
KP505 S	0.7	0.29436	0.29386	0.29387	0.29387	0.000
KP505 R2B	0.7	0.30506	0.30422	0.30376	0.30282	0.384
KP505 R1H	0.6	0.40234	0.40168	0.40249	0.40615	1.136
KP458 S	0.5	0.21219	0.21268	0.21169	0.21045	0.729
KP458 R2B	0.5	0.21459	0.21478	0.21361	0.21326	0.202
KP458 R1H	0.4	0.22703	0.22713	0.22533	0.22512	0.115
WB S	0.56	0.24312	0.24120	0.23910	0.23372	2.815
WB R2B	0.56	0.24867	0.24757	0.24613	0.24402	1.070
WB R1 H	0.4	0.32578	0.32591	0.32531	0.32524	0.024

It should be noted that the remaining CFD simulations regarding the assessment of the effect of biofouling on the open water characteristics are performed using a fine mesh.

#### 5.4.2. The validation study

After the verification study, the obtained open water characteristics using a fine mesh for smooth surface condition for all three propellers are validated with the towing tank results published in the literature [230], [231], [245]. It should be noted that numerical open water tests are performed in full-scale. Towing tank tests for all three investigated propellers are performed at  $Rn$  above  $Rn = 2 \cdot 10^5$  as prescribed by ITTC [72]. In Figure 5.58, the comparison between numerically and experimentally obtained open water characteristics is shown. Also, within Table 5.34 the comparison between numerically and experimentally obtained open water characteristics for  $J$  value around expected self-propulsion point is presented.

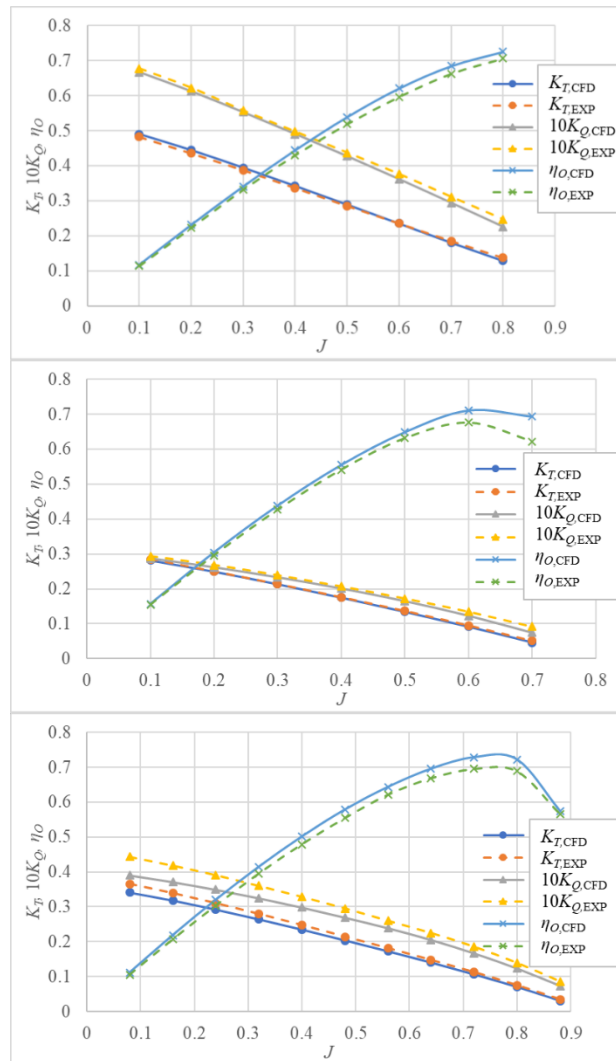


Figure 5.58 The validation study for KP 505 (upper), KP 458 (middle) and WB (lower)

Table 5.34 The validation study for  $J$  value around expected self-propulsion point

Propeller	$J$	$K_T^{EXP}$	$K_T^{CFD}$ (RD, %)	$10K_Q^{EXP}$	$10K_Q^{CFD}$ (RD, %)	$\eta_o^{EXP}$	$\eta_o^{CFD}$ (RD, %)
KP505	0.6	0.2350	0.2348 (-0.095)	0.3760	0.3611 (-3.976)	0.5968	0.6210 (4.401)
KP505	0.7	0.1850	0.1804 (-2.485)	0.3110	0.2936 (-5.601)	0.6627	0.6846 (3.301)
KP458	0.4	0.1757	0.1749 (-0.469)	0.2067	0.2006 (-2.941)	0.5411	0.5549 (2.547)
KP458	0.5	0.1344	0.1342 (-1.682)	0.1721	0.1646 (-4.385)	0.6312	0.6490 (2.827)
WB	0.48	0.2144	0.2038 (-4.944)	0.2956	0.2693 (-8.897)	0.5541	0.5781 (4.339)
WB	0.56	0.1811	0.1725 (-4.749)	0.2599	0.2391 (-8.003)	0.6210	0.6430 (3.537)

As can be seen from Table 5.34 and Figure 5.58, satisfactory agreement between numerically and experimentally obtained open water characteristics is achieved for all investigated propellers. Regarding the obtained open water characteristics for KP 505, it should be noted that similar  $RD$  are obtained in [182], where the authors also have performed CFD simulations of full-scale KP505 and obtained slightly higher  $\eta_o$  in comparison with experimental model scale results. For KP 458, the obtained  $RD$  between numerical and experimental open water characteristics are the lowest. For KP 458 the highest  $RD$  is obtained at the highest investigated  $J$  value, which is higher than  $J$  value for which the curve  $\eta_o$  has its maximum and therefore it is unlikely that propeller will operate at this  $J$  value. Regarding the comparison of the obtained open water characteristics for WB, it should be noted that slightly higher  $RD$  are obtained, especially at lower  $J$  values. At higher  $J$  values, i.e. around  $J$  value for self-propulsion point, the obtained  $RD$  are lower. Since, CFD simulations are performed for full-scale propellers and experiments for model scale, the scale effects could be one of the reasons related to the obtained  $RD$ . Namely, it is still not certain whether scale effects should be taken into account for scaling the obtained open water characteristics from model to full-scale. Thus, currently there are four main scaling procedures which are used across the model basins for scaling the measured open water characteristics: no scaling, ITTC 1978 PPM, Lerbs – Meyne method and strip method [154]. The numerically obtained open water characteristics for smooth full-scale WB are compared with the extrapolated open water characteristics using the method proposed in [246] based on ITTC 1978 PPM. It should be noted that  $RD$  for  $K_T$  were equal to 5.676% at  $J = 0.48$  and 5.547% at  $J = 0.56$ , for  $10K_Q$  were equal to 6.256% at  $J = 0.48$  and 4.746% at  $J = 0.56$ , while for  $\eta_o$  were equal to -0.546% at  $J = 0.48$  and 0.765% at  $J = 0.56$ .

#### 5.4.3. Results of the analysis of the impact of biofouling on the open water characteristics

After the validation study, the obtained open water characteristics for fouled propellers are compared with ones for smooth propellers in order to investigate the impact of biofouling on the open water characteristics. The obtained changes in open water characteristics are determined using the equation (5.4). The impact of biofilm and hard fouling on the open water characteristics are investigated at eight  $J$  values for KP505 propeller, seven  $J$  values for KP458 propeller and eleven  $J$  values for WB propeller. The obtained changes in the open water characteristics due to the presence of biofouling are shown in Table 5.35 and Table 5.36. Due to extensiveness of the obtained results,  $\Delta K_T$ ,  $\Delta K_Q$  and  $\Delta \eta_o$  are presented only for  $J$  value around self-propulsion point within these tables. The obtained impact of biofilm (R2 B) on the open water characteristics is shown in Figure 5.59, Figure 5.60 and Figure 5.61, while the obtained impact of hard fouling (R1 H) on the open water characteristics is shown in Figure 5.62, Figure 5.63 and Figure 5.64. From these figures it is evident that the impact of biofouling on the open water characteristics is more highlighted at higher  $J$  values, i.e. with an increase in  $J$ , the obtained changes in open water characteristics increase as well. Because of this, ships that operate at higher  $J$  values will experience a greater effect on performance in comparison with ships that operate at lower  $J$ . Since the change in open water characteristic is defined in relation with open water characteristic for smooth propeller (equation (5.4)), higher changes at higher  $J$  were expected, since with an increase in  $J$  value, the  $K_T$  and  $K_Q$  values decrease. Also, it is clear that the presence of biofouling has caused decrease in  $K_T$  and increase in  $10K_Q$

, which in turn has caused a significant reduction in  $\eta_o$ . Even though the presence of biofilm is often ignored [247], from Table 5.35 it is evident that the presence of slime has caused important decrease in propeller performance for open water conditions. Thus, for the fouling condition R2 B, which represents the most severe investigated surface condition for fouling with biofilm, the obtained  $\Delta K_T$  for  $J$  value around self-propulsion point for KP 505 is equal to -3.645%, for KP 458 to -4.832% and for WB to -2.673%. The obtained  $\Delta K_Q$  for  $J$  value around self-propulsion point for KP 505 is equal to 3.365%; for KP 458 to 1.816% and for WB to 2.940%, while the obtained  $\Delta \eta_o$  for KP 505 is equal to -6.782%, for KP 458 to -6.529% and for WB to -5.491%. The obtained  $\Delta \eta_o$  show the importance of propeller cleaning even if only slime is present. As noted in [71], slime can be relatively easily wiped off propeller without significant damage of the propeller coating and therefore underwater cleaning of slime should be considered as relatively easy, efficient and cheap method for the reduction of fuel consumption and GHG emissions. While the impact of biofilm on open water characteristics is moderate, the impact of hard fouling is substantial. Thus, for the fouling condition R1 H, which represents the most severe investigated surface condition for fouling with hard fouling, the obtained  $\Delta K_T$  for  $J$  value around self-propulsion point for KP 505 is equal to -12.05%; for KP 458 to -14.45% and for WB to -12.09%. The obtained  $\Delta K_Q$  for  $J$  value around self-propulsion point for KP 505 is equal to 11.37%, for KP 458 to 7.46% and for WB to 11.19%, while the obtained  $\Delta \eta_o$  for KP 505 is equal to -21.03%, for KP 458 to -20.39% and for WB to -20.93%. The obtained results show the importance of propeller cleaning which can enable significant savings in the fuel consumption and GHG emissions. However, the cleaning of hard fouling from the propeller surfaces can cause damage of the coating and consequently the potential savings will be reduced since the propeller roughness will increase. Furthermore, antifouling performance of the damaged coating is reduced and therefore the fouling will occur faster. In addition to, underwater cleaning of propeller fouled with hard fouling is more difficult than the one fouled with biofilm, as hard fouling has higher adhesion strength and for some cases dry-docking is required, which increases the costs of propeller cleaning. Regardless of this, the potential savings in fuel consumption and GHG emissions are very high and therefore the propeller cleaning is recommended.

As can be seen from Figure 5.59, Figure 5.60, Figure 5.61, Figure 5.62, Figure 5.63 and Figure 5.64, due to the presence of fouling  $J$  value at which maximum  $\eta_o$  is obtained is reduced in comparison with smooth propeller. For example for smooth WB propeller,  $J$  value at which maximum  $\eta_o$  is obtained is around 0.77, while for WB propeller fouled with hard fouling (R1 H) is around 0.64.

The analysis of the rate of change in open water characteristics due to the presence of hard fouling is made. This analysis is made for hard fouling, since it is described with one  $\Delta U^+$  model and therefore it is relatively easy to analyse the rate of change in open water characteristics due to an increase in the fouling severity using the obtained results for investigated surface conditions. It can be observed that the rate of change becomes smaller as the fouling severity increases. This is in agreement with the behaviour of the full-scale measurements as discussed in [248] and the same behaviour is obtained in CFD study [67].

Table 5.35 The obtained changes in open water characteristics due to the presence of biofilm

Propeller <i>J</i>	KP 505 <i>J</i> = 0.7			KP 458 <i>J</i> = 0.5			WB <i>J</i> = 0.56		
	$\Delta K_T$ , %	$\Delta K_Q$ , %	$\Delta \eta_o$ , %	$\Delta K_T$ , %	$\Delta K_Q$ , %	$\Delta \eta_o$ , %	$\Delta K_T$ , %	$\Delta K_Q$ , %	$\Delta \eta_o$ , %
R1 B	-1.579	1.710	-3.233	-2.284	0.958	-3.211	-1.040	1.514	-2.555
R2 B	-3.645	3.365	-6.782	-4.832	1.816	-6.529	-2.673	2.940	-5.491
R3 B	-1.214	1.428	-2.605	-1.835	0.818	-2.632	-0.795	1.215	-2.025
R4 B	-3.130	2.974	-5.927	-4.222	1.591	-5.721	-2.212	2.696	-4.818
R5 B	-0.559	0.782	-1.330	-0.935	0.434	-1.364	-0.428	0.614	-1.076
R6 B	-1.709	1.738	-3.388	-2.397	0.96	-3.324	-1.168	1.561	-2.726
R7 B	-0.182	0.363	-0.543	-0.394	0.186	-0.579	-0.153	0.274	-0.466
R8 B	-0.780	0.977	-1.740	-1.238	0.536	-1.764	-0.569	0.789	-1.387

Table 5.36 The obtained changes in open water characteristics due to the presence of hard fouling

Propeller <i>J</i>	KP 505 <i>J</i> = 0.6			KP 458 <i>J</i> = 0.4			WB <i>J</i> = 0.48		
	$\Delta K_T$ , %	$\Delta K_Q$ , %	$\Delta \eta_o$ , %	$\Delta K_T$ , %	$\Delta K_Q$ , %	$\Delta \eta_o$ , %	$\Delta K_T$ , %	$\Delta K_Q$ , %	$\Delta \eta_o$ , %
R1 H	-12.05	11.37	-21.03	-14.45	7.46	-20.39	-12.09	11.19	-20.93
R2 H	-10.77	9.56	-18.55	-12.81	6.11	-17.83	-11.18	9.75	-19.07
R3 H	-9.24	7.66	-15.69	-11.66	4.69	-15.62	-10.10	7.65	-16.49
R4 H	-8.13	6.49	-13.73	-9.72	3.81	-13.03	-9.39	6.34	-14.79
R5 H	-6.85	5.30	-11.54	-8.20	2.99	-10.87	-8.47	4.75	-12.62
R6 H	-6.22	4.66	-10.39	-7.44	2.59	-9.77	-7.86	3.77	-11.21

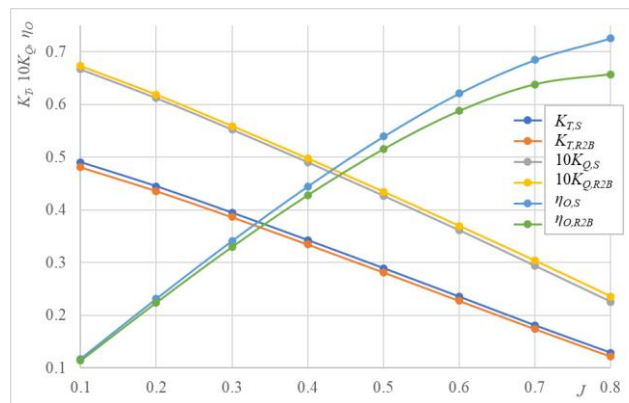


Figure 5.59 The impact of biofilm (R2 B) on the open water characteristics of KP 505

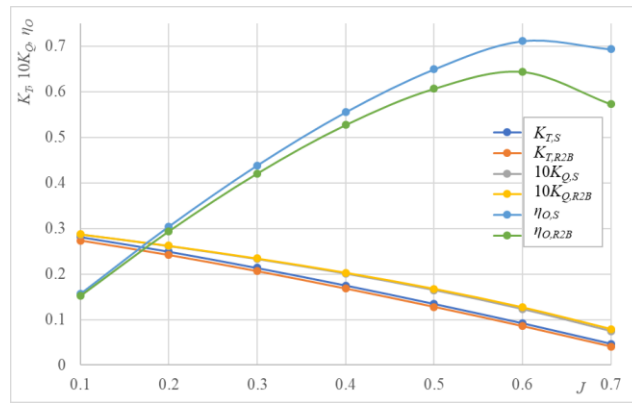


Figure 5.60 The impact of biofilm (R2 B) on the open water characteristics of KP 458

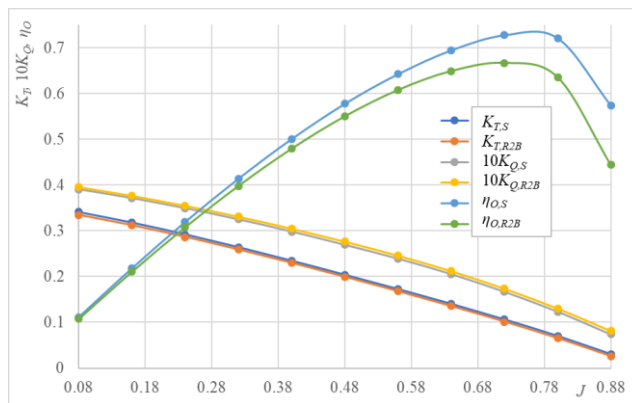


Figure 5.61 The impact of biofilm (R2 B) on the open water characteristics of WB

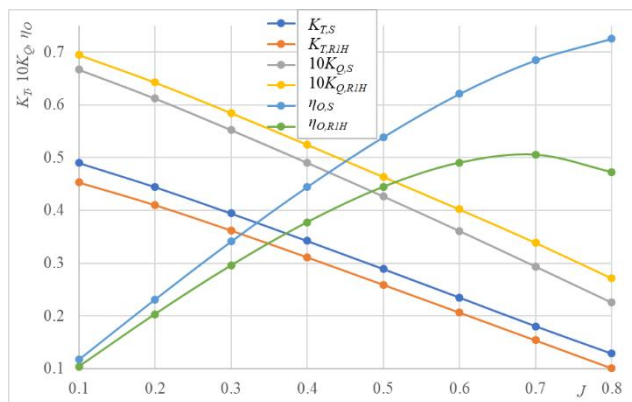


Figure 5.62 The impact of hard fouling (R1 H) on the open water characteristics of KP 505

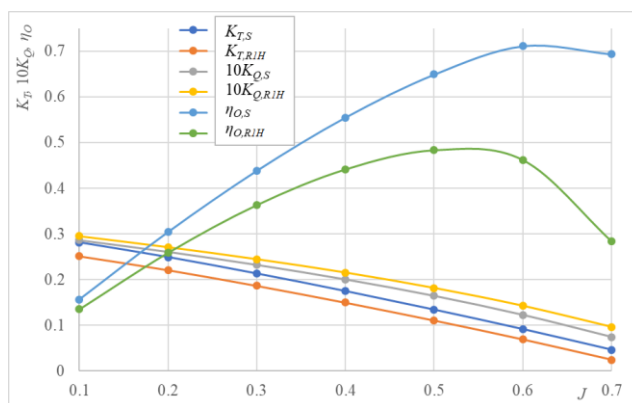


Figure 5.63 The impact of hard fouling (R1 H) on the open water characteristics of KP 458

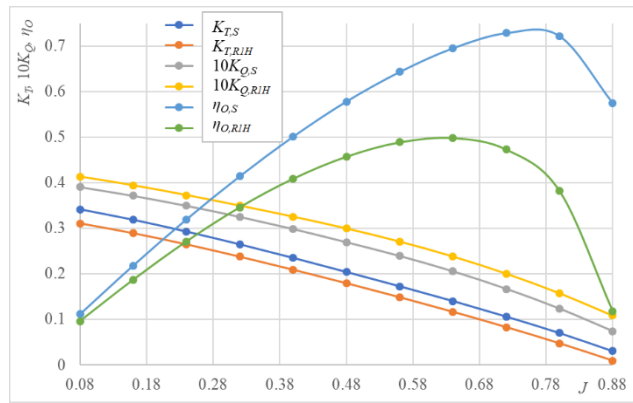


Figure 5.64 The impact of hard fouling (R1 H) on the open water characteristics of WB

#### 5.4.4. The impact of biofouling on the flow around the fouled propeller

Within this subsection, the impact of hard fouling on the flow around KP 505 in open water conditions is analysed in detail. It was decided to present the effect of hard fouling on the flow around the propeller, since it represents a fouling with higher fouling severity than biofilm and therefore its effect is more pronounced, and it is more easily noticed. The impact of biofilm on the flow around fouled propeller has the same trend as the impact of hard fouling, however these effects are less notable. It should be noted that the impact of biofouling is similar for all investigated propellers and due to the extensiveness of the results only the impact of fouling with R1 H on the flow around KP 505 is analysed, since it represents the most severe investigated fouling condition.

Firstly, the impact of hard fouling on the pressure distribution is investigated and the obtained results are presented on the symmetry plane (Figure 5.65), at  $r = 0.75R$  (Figure 5.66) and on the propeller surface (Figure 5.67). The pressure distribution is presented using the pressure coefficient ( $C_p$ ), which is defined as a ratio between pressure and  $\frac{1}{2}\rho v^2$ . It should be noted that the nondimensional velocities in Figure 5.65, Figure 5.66 and Figure 5.67 are not the same, i.e. in Figure 5.65 and Figure 5.67 advance velocity ( $v_A$ ) is applied, while in Figure 5.66 the resultant velocity of the flow approaching the propeller blade section ( $v_R$ ) at  $r = 0.75R$  is applied. Within figures the distributions of  $C_p$  are presented for smooth KP 505 and KP 505 fouled with R1 H at  $J = 0.7$ . As can be seen from Figure 5.65, the presence of fouling on the propeller surface significantly reduces the pressure difference between the pressure and suction sides of propeller. Thus, the obtained  $C_p$  values upstream of a propeller are lower and downstream are higher for smooth propeller. Because of this, pressure components in the propeller thrust and torque decrease for fouled propeller [67]. This reduction in the obtained  $C_p$  values between propeller face and back sides can be noticed in Figure 5.66 as well. Thus, the absolute values of  $C_p$  around smooth blade section are higher, which is the most noticeable around trailing edge of propeller. The decrease in the obtained  $C_p$  values on the propeller surfaces due to the presence of biofouling can be noticed in Figure 5.67. Due to decrease in pressure difference between the pressure and suction sides of the propeller, the lift coefficient of the blade section ( $C_L$ ) decreases. Consequently, the decrease in  $K_T$  for fouled propeller is obtained.

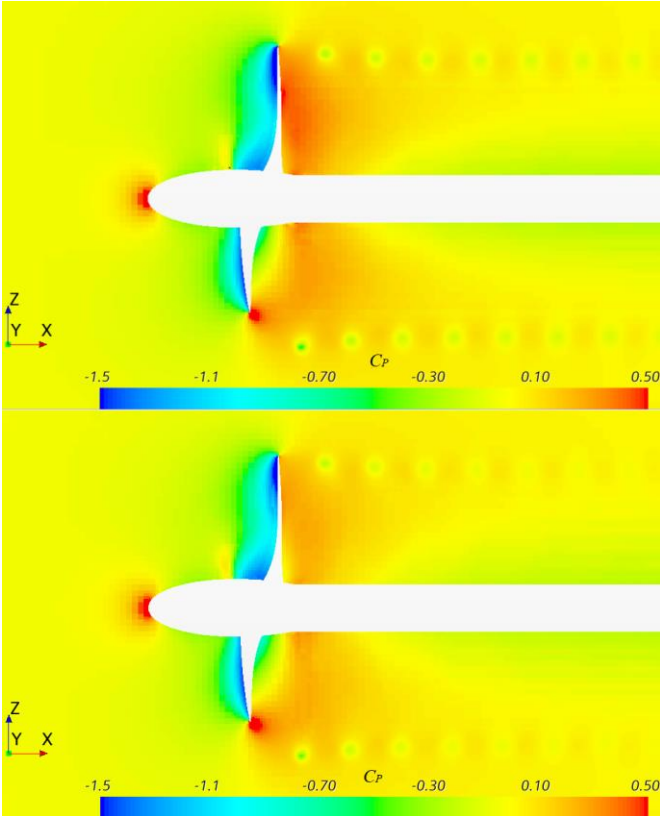


Figure 5.65 The obtained  $C_p$  distribution for smooth KP 505 (upper) and KP 505 fouled with R1 H (lower) on the symmetry plane

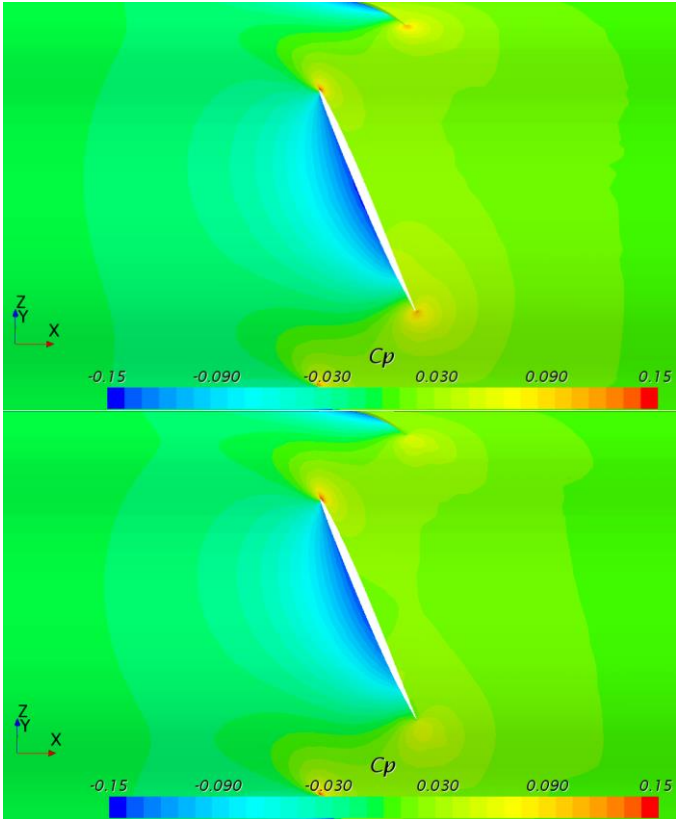


Figure 5.66 The obtained  $C_p$  distribution for smooth KP 505 (upper) and KP 505 fouled with R1 H (lower) at  $r = 0.75R$



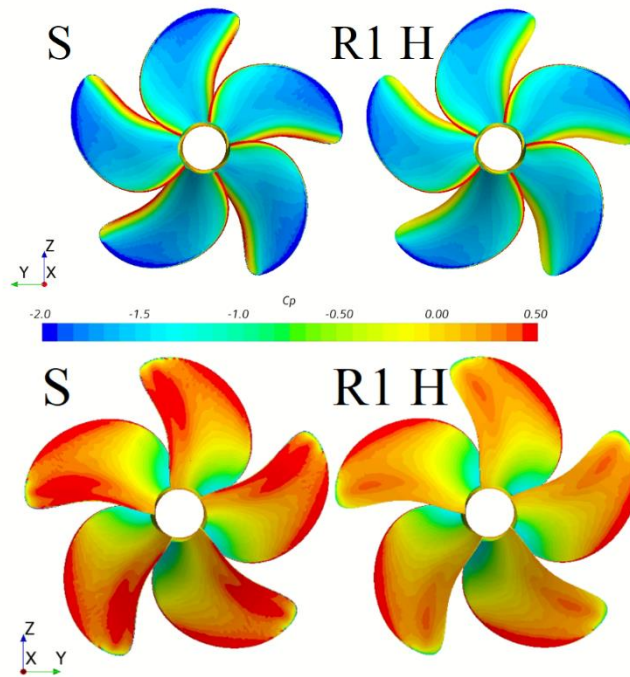


Figure 5.67 The obtained  $C_p$  distribution on the propeller surface for smooth KP 505 (left) and KP 505 fouled with R1 H (right)

The obtained axial velocity distribution on the symmetry plane for smooth KP 505 and KP 505 fouled with R1 H at  $J = 0.7$  is presented in Figure 5.68. It should be noted that the presented distribution is nondimensionalised with  $v_A$ . This distribution is related to the pressure distribution and from Figure 5.68 it is clear that the values of  $v_x/v_A$  are lower for fouled propeller as well as that the distribution of  $v_x/v_A$  is more scattered.

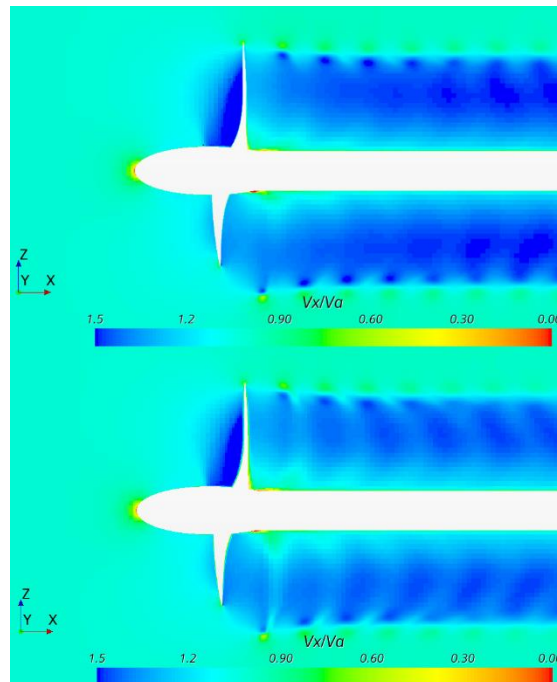


Figure 5.68 The obtained nondimensionalised axial velocity distribution on the symmetry plane for smooth KP 505 (upper) and KP 505 fouled with R1 H (lower)

In Figure 5.69, the obtained  $\tau_w$  distribution at  $J = 0.7$  for smooth KP 505 and KP 505 fouled with R1 H are shown. It is clear that significantly higher  $\tau_w$  values are obtained for fouled propeller, which in turn causes higher drag coefficients ( $C_D$ ) of the blades. The increase in skin friction of the propeller blades leads to an increase in  $K_Q$ . Thus, the obtained decrease in  $K_T$  values and increase in  $K_Q$  values, presented in subsection 5.4.3, due to the presence of biofouling have physical background related to pressure distribution around the propeller and wall shear stress distribution on the propeller surface. Because of decrease in  $K_T$  and increase in  $K_Q$  values,  $\eta_o$  values significantly decrease as can be seen from equation (2.34).

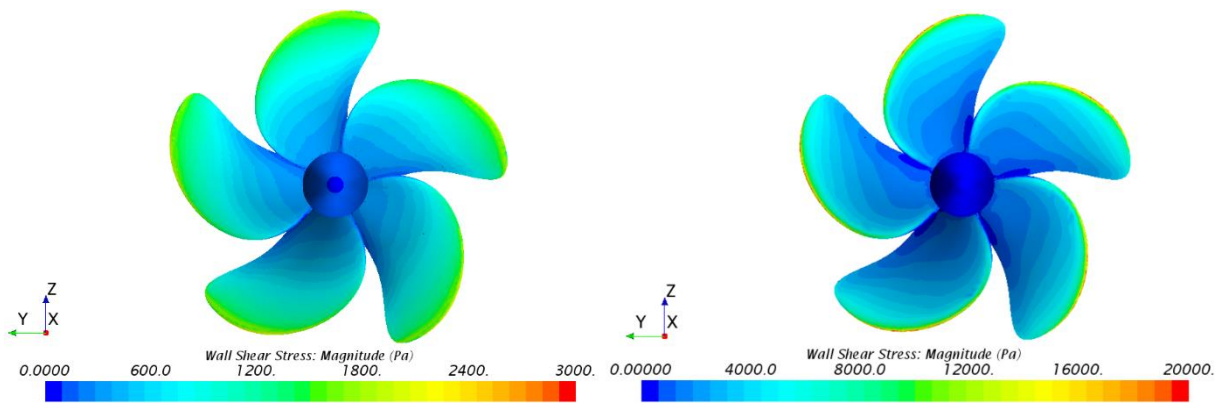


Figure 5.69 The obtained  $\tau_w$  distribution for smooth KP 505 (left) and for KP 505 fouled with R1 H (right)

The obtained distributions of the vorticity magnitudes on the symmetry plane for smooth KP 505 and for KP 505 fouled with R1 H at  $J = 0.7$  are presented in Figure 5.70. Similarly to the obtained nondimensionalised axial velocity distribution on the symmetry plane, the distribution of vorticity magnitudes for fouled KP 505 is also more scattered in comparison with smooth KP 505. Generally, due to the presence of biofouling the strength of vortices is reduced and consequently the vortices dissipate earlier for fouled propeller. However, in the vicinity of propeller, the vorticity magnitudes are higher for fouled propeller in comparison with smooth propeller. More clear representation of the impact of biofouling on the vorticity magnitudes can be noticed in Figure 5.71, where the iso-surfaces of  $Q$  - criterion ( $Q = 10 \text{ s}^{-2}$ ) for smooth KP 505 and for KP505 fouled with R1 H are shown. From this figure it can be easily noticed that the tip and hub vortices dissipate earlier for fouled KP 505, as well as that that the vortices near the fouled KP 505 are stronger than the vortices near the smooth KP 505.

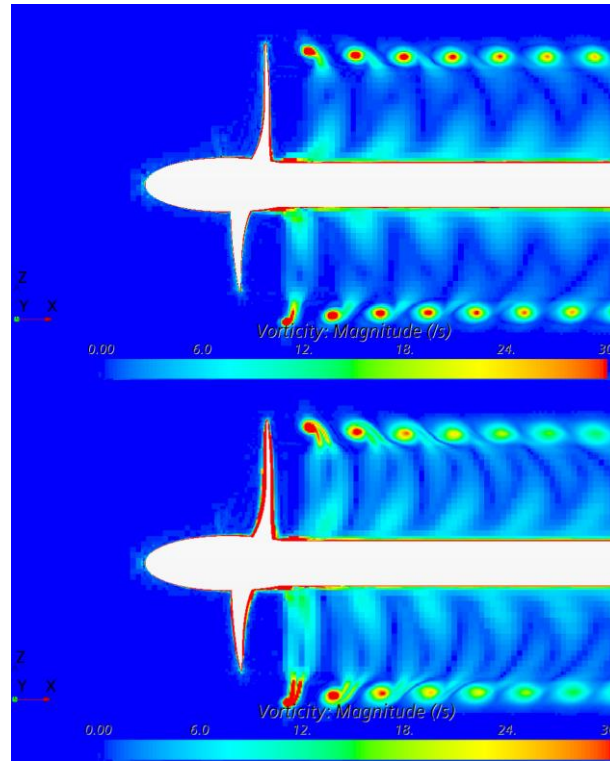


Figure 5.70 The obtained vorticity magnitudes for smooth KP 505 (upper) and for KP505 fouled with R1 H (lower) on the symmetry plane

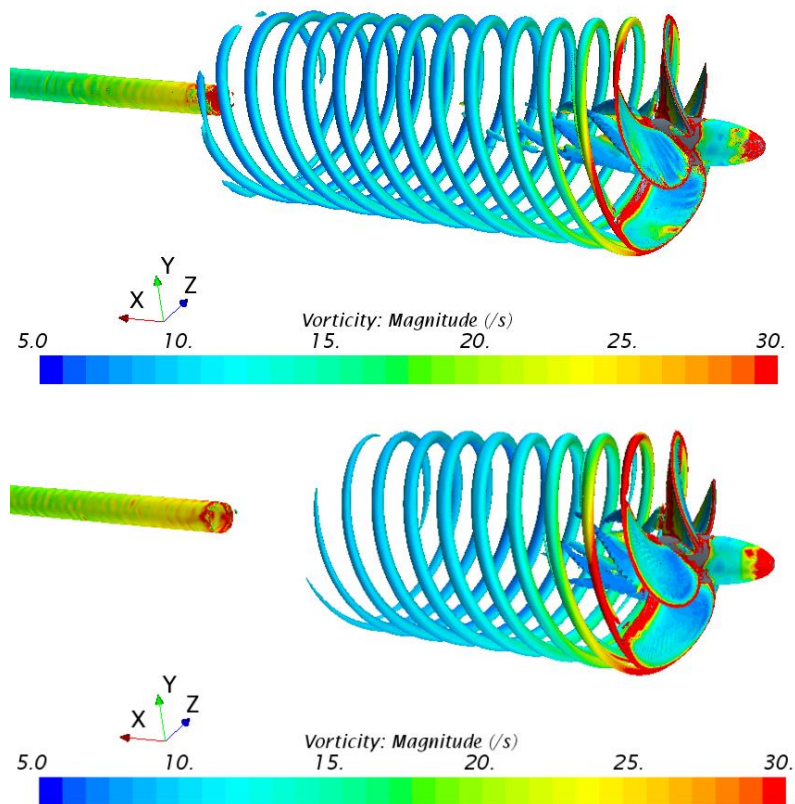


Figure 5.71 The iso-surface of  $Q$ -criterion, vorticity magnitude for smooth KP505 (upper) and for KP505 fouled with R1 H (lower)

## 5.5. The impact of biofouling on the propulsion characteristics

Historically, the impact of biofouling on the ship performance was taken into account with an increase in  $C_F$ , which resulted with an increase in  $R_T$ . Because of the increase in  $R_T$ ,  $P_E$  increases as well, however it was considered that the propulsion efficiency is not affected due to the presence of biofouling, i.e. it was assumed that the increase in  $P_E$  corresponds to the increase in  $P_B$ . This was justified with an assumption that the effect of biofouling on  $\eta_H$  and on  $\eta_o$  cancel each other out [64]. Within this subsection, the impact of biofouling on the propulsion characteristics is investigated using the obtained results from resistance, open water and self-propulsion tests. The obtained results show the importance of analysing the impact of biofouling on each resistance and propulsion component solely, i.e. that the impact of biofouling on  $P_B$  and  $P_E$  are not the same. Furthermore, the obtained results present the impact of biofouling on the propeller operating point, which enables the assessment of the increase in the fuel consumption if the installed engine is known [249]. The increase in the fuel consumption due to the presence of biofouling can be used as a performance indicator which could indicate an appropriate time for hull or propeller cleaning. Namely, the costs related to an increase in the fuel consumption can be easily calculated. Based on these costs, more informed decision regarding the proper timing of hull and propeller cleaning can be made, since fuel costs represent 60–70% of the entire operational cost [45]. Therefore, the assessment of the impact of biofouling on the resistance and propulsion characteristics is as equally important as the improvement of the energy efficiency of existing ships through the application of new AF coatings, since it can point out the importance of hull and propeller cleaning [68]. Consequently, there is an increasing number of shipowners or ship operators that are willing to invest in tools, which will give them the insights related to this impact [46].

Due to the presence of biofouling, two scenarios can occur, either  $P_B$  increases if the ship speed is maintained, or ship speed decreases if  $P_B$  is maintained the same as for smooth surface condition. In this thesis, the increase in  $P_B$  due to the presence of biofouling is analysed. However, on the example of KCS, it is shown how the decrease in ship speed due to the presence of biofilm can be estimated.

### 5.5.1. The numerical modelling and verification study

In order to develop a CFD model which can simulate the effect of biofouling on the propulsion characteristics several steps should be carried out. Firstly,  $\Delta U^+$  model for certain biofouling type must be implemented in the wall function of the CFD solver. After the validation of the developed CFD model, numerical simulations of resistance, open water and self-propulsion tests should be carried out. Within this subsection numerical modelling of self-propulsion tests as well as the performed verification studies related to numerical simulations of self-propulsion tests are described. Through the analysis of the obtained results of resistance, open water and self-propulsion tests, the impact of biofouling on the propulsion characteristics is determined. The investigated fouling conditions are presented in Table 5.3 and for the analysis of the impact of biofouling on the propulsion characteristics it is considered that both ship and propeller are fouled with the same fouling condition. Using the same methodology it is relatively easy to investigate the case in which the ship and propeller are fouled with different fouling condition. This would be interesting for a case in which ship is fouled and propeller is cleaned or vice

versa. In that way the separate effect of hull or propeller cleaning on the ship performance could be assessed.

FSS of self-propulsion tests are performed for the purpose of study related to the impact of biofouling on the ship propulsion characteristics. In these simulations the whole computational domain is taken into account. The boundaries of the computational domain are placed at the same distances as in resistance tests, Table 5.11. Also, the same boundary conditions and the parameters related to VOF wave damping as in resistance tests are applied within CFD simulations of self-propulsion tests. Since the whole computational domain is analysed in numerical simulations of self-propulsion test, the boundary at the symmetry plane in the resistance test is replaced with side boundary placed at the same distance as the other side boundary. Also, the symmetry boundary condition utilized in FSS of resistance test is replaced with velocity inlet at the side boundary.

The computational domain is discretized utilizing a cut-cell grid with prism layer mesh on the walls using the automatic mesh generator in STAR-CCM+. The mesh is refined using the same volumetric mesh controls as used in resistance tests, except in the region where the virtual disk is located. Namely, FSS of self-propulsion tests are performed using the body force method and more details regarding this method can be found in subsection 3.2.5. The refinement in the region where virtual disk is located is made as a cylindrical refinement with the radius equal to  $1.05D$  and length equal to  $5D$  downstream and  $4D$  upstream from propeller. More details regarding the computational domain discretization can be found in subsections 3.2.2 and 5.3.1. Cross-sections of the discretized computational domains used in FSS of self-propulsion tests are shown in Figure 5.72. In this figure, the refinement in the region where the virtual disk is located can be clearly seen.

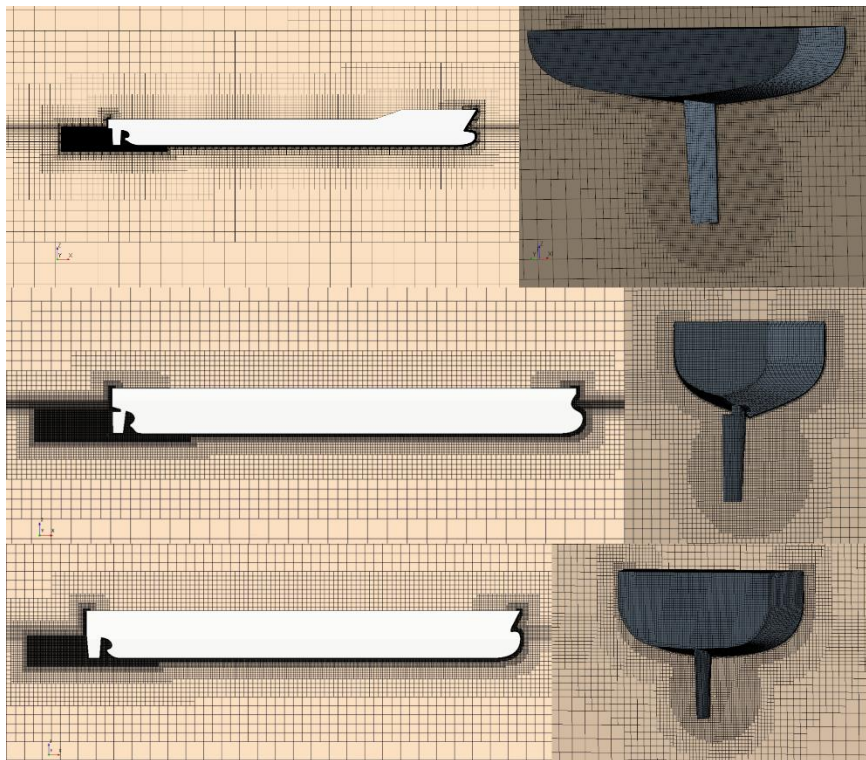


Figure 5.72 The profile view cross-section of the domain for KCS (upper left), KVLCC2 (middle left) and BC (lower left) and the mesh refinement in stern region of KCS (upper right), KVLCC2 (middle right) and BC (lower right)

The obtained  $y^+$  distributions are very similar to the ones obtained in the resistance tests, except in the area where the virtual disk is located, as can be seen from Figure 5.73. This was expected, since the propeller affects the velocity and pressure distribution only in the region extending two propeller diameters upstream [250]. Thus, due to the propeller operation, the obtained  $y^+$  distribution are mostly affected downstream of the propeller, i.e. on the rudder.

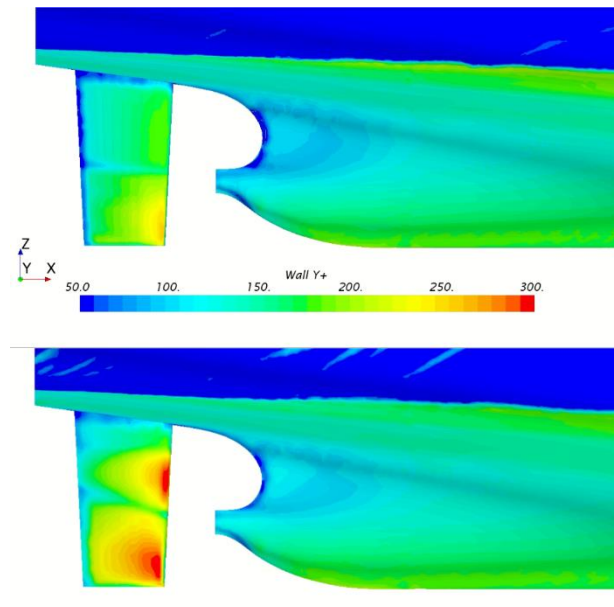


Figure 5.73 The obtained  $y^+$  distributions for KCS in the area where the virtual disk is located for resistance test (upper) and self-propulsion test (lower)

The verification study is performed for both grid size and time step for the smooth surface condition and fouling conditions R2 B and R1 H for all three ships. For the purpose of verification study for grid size, three meshes are generated. Similarly as for resistance tests, the mesh is refined systematically. The number of cells used for investigated ships is given in Table 5.37. It should be noted that the number of cells for numerical simulations with hard fouling varied amongst investigated surface conditions, because of different discretization of prism layer mesh. The number of cells for the surface condition R1 H is given in Table 5.37. In numerical simulations of self-propulsion tests, iterative uncertainties are negligible and therefore the obtained numerical uncertainties consist only of grid and time step uncertainties. Numerical uncertainties are calculated using equation (3.31). Both temporal and grid convergence study are performed using  $T$ ,  $Q$ ,  $n$ ,  $P_D$  and  $J$  as key variables. More details regarding the verification study and used time steps within temporal convergence studies can be found in subsection 3.2.6.1.

The obtained results of both grid and temporal convergence studies are shown in Table 5.38 – Table 5.47. After  $U_G$  and  $U_T$  are obtained,  $U_{SN}$  in the prediction of thrust ( $U_T$ ), torque ( $U_Q$ ), propeller rotation rate ( $U_n$ ), delivered power ( $U_{P_D}$ ) and advance coefficient ( $U_J$ ) are calculated using equation (3.31), Table 5.48. As can be seen from these tables, relatively low numerical uncertainties are obtained and in line with numerical uncertainties of other CFD studies regarding self-propulsion test [68], [195], [251]. Numerical uncertainties obtained for smooth and fouled propellers are relatively close, i.e. the numerical uncertainty did not increase due to the roughness effects.

The obtained  $U_T$ ,  $U_Q$ ,  $U_n$ ,  $U_{P_d}$  and  $U_J$ , which are consisted of both  $U_G$  and  $U_T$ , are shown in Table 5.48. As can be seen from Table 5.48, the lowest  $U_{SN}$  for smooth and fouled ships are obtained for KCS, which was expected since  $U_G$  are higher than  $U_T$  and the mesh for KCS had more cells than for KVLCC2 and BC. The highest  $U_{SN}$  is obtained for the prediction of  $U_{P_d}$  for BC fouled with R1 H and it is equal to 7.421% and the other obtained  $U_{SN}$  are lower than 5.5%. It should be noted that remaining numerical simulations of self-propulsion tests are carried out using fine mesh and fine time step.

Table 5.37 The number of cells within numerical simulations of self-propulsion test

Case	KCS – S & R2 B	KVLCC2 – S & R2 B	BC – S & R2 B
Coarse mesh	2.12 M	1.23 M	0.96 M
Medium mesh	4.19 M	2.74 M	2.20 M
Fine mesh	8.47 M	5.25 M	5.06 M
Case	KCS – R1 H	KVLCC2 – R1 H	BC – R1 H
Coarse mesh	1.89 M	1.14 M	0.89 M
Medium mesh	3.83 M	2.54 M	2.01 M
Fine mesh	7.54 M	4.86 M	4.61 M

Table 5.38 The obtained grid uncertainties in the prediction of  $T$

KCS						
Surface condition	$\phi_3$ , kN	$\phi_2$ , kN	$\phi_1$ , kN	$\phi_{ext}^{21}$ , kN	$GCI_{fine}^{21}$ , %	$U_G$ , kN
S	1903.77	1877.34	1810.89	1763.46	3.273	59.281
R2 B	2388.80	2306.17	2284.48	2247.91	2.001	45.709
R1 H	3669.43	3630.48	3605.91	3557.73	1.670	60.226
KVLCC2						
Surface condition	$\phi_3$ , kN	$\phi_2$ , kN	$\phi_1$ , kN	$\phi_{ext}^{21}$ , kN	$GCI_{fine}^{21}$ , %	$U_G$ , kN
S	2276.43	2015.69	2009.71	2009.41	0.019	0.374
R2 B	2963.66	2586.3	2568.93	2556.22	0.619	15.890
R1 H	4557.62	4308.72	4390.60	4442.50	1.478	64.872
BC						
Surface condition	$\phi_3$ , kN	$\phi_2$ , kN	$\phi_1$ , kN	$\phi_{ext}^{21}$ , kN	$GCI_{fine}^{21}$ , %	$U_G$ , kN
S	829.63	813.35	763.94	739.27	4.037	30.839
R2 B	1024.29	1029.49	984.48	951.57	4.179	41.143
R1 H	1616.88	1644.82	1592.13	1532.04	4.717	75.107

From the results of the verification study of self-propulsion tests (Table 5.38 – Table 5.47), it can be concluded that the time step uncertainties are lower than the grid uncertainties. It should be noted that temporal convergence studies are performed using fine mesh and three time steps defined in subsection 3.2.6.1, i.e.  $T/50$ ,  $T/100$  and  $T/200$ . Generally, the obtained  $U_G$  related

to the prediction of  $T$  for smooth and fouled ships are low and the highest  $GCI_{fine}^{21}$  for KCS is equal to 3.273%, for BC to 4.717% and for KVLCC2 to 1.478%. The obtained  $U_T$  related to the prediction of  $T$  for smooth and fouled ships are lower or similar to  $U_G$  and the highest  $GCI_{fine}^{21}$  for KCS is equal to 0.807%, for BC to 3.499% and for KVLCC2 to 1.529%.

Table 5.39 The obtained grid uncertainties in the prediction of  $Q$

KCS						
Surface condition	$\phi_3$ , kNm	$\phi_2$ , kNm	$\phi_1$ , kNm	$\phi_{ext}^{21}$ , kNm	$GCI_{fine}^{21}$ , %	$U_G$ , kNm
S	2529.02	2425.59	2367.02	2297.29	3.682	87.157
R2 B	3182.16	3112.81	3077.59	3044.24	1.354	41.684
R1 H	5405.54	5309.65	5272.49	5246.48	0.617	32.512
KVLCC2						
Surface condition	$\phi_3$ , kNm	$\phi_2$ , kNm	$\phi_1$ , kNm	$\phi_{ext}^{21}$ , kNm	$GCI_{fine}^{21}$ , %	$U_G$ , kNm
S	2636.24	2347.23	2405.55	2426.08	1.067	25.663
R2 B	3487.87	3105.22	3125.32	3127.28	0.078	2.449
R1 H	5873.47	5646.49	5685.13	5696.53	0.251	14.247
BC						
Surface condition	$\phi_3$ , kNm	$\phi_2$ , kNm	$\phi_1$ , kNm	$\phi_{ext}^{21}$ , kNm	$GCI_{fine}^{21}$ , %	$U_G$ , kNm
S	692.46	683.142	645.14	632.60	2.429	15.673
R2 B	872.58	875.92	836.82	833.10	0.555	4.646
R1 H	1513.26	1542.42	1490.39	1423.40	5.618	83.731

Table 5.40 The obtained grid uncertainties in the prediction of  $n$

KCS						
Surface condition	$\phi_3$ , rpm	$\phi_2$ , rpm	$\phi_1$ , rpm	$\phi_{ext}^{21}$ , rpm	$GCI_{fine}^{21}$ , %	$U_G$ , rpm
S	100.982	99.686	99.341	99.225	0.146	0.145
R2 B	105.346	104.288	104.159	104.143	0.020	0.021
R1 H	118.374	117.672	117.376	117.137	0.255	0.299
KVLCC2						
Surface condition	$\phi_3$ , rpm	$\phi_2$ , rpm	$\phi_1$ , rpm	$\phi_{ext}^{21}$ , rpm	$GCI_{fine}^{21}$ , %	$U_G$ , rpm
S	73.068	70.484	70.858	70.951	0.164	0.117
R2 B	79.832	76.695	76.560	76.548	0.019	0.015
R1 H	95.356	93.902	93.963	93.968	0.007	0.006
BC						
Surface condition	$\phi_3$ , rpm	$\phi_2$ , rpm	$\phi_1$ , rpm	$\phi_{ext}^{21}$ , rpm	$GCI_{fine}^{21}$ , %	$U_G$ , rpm
S	101.830	101.580	99.541	99.251	0.364	0.362
R2 B	108.700	108.852	107.074	106.906	0.196	0.210
R1 H	130.805	132.033	131.120	128.345	1.661	2.160



Table 5.41 The obtained grid uncertainties in the prediction of  $P_D$

KCS						
Surface condition	$\phi_3$ , MW	$\phi_2$ , MW	$\phi_1$ , MW	$\phi_{ext}^{21}$ , MW	$GCI_{fine}^{21}$ , %	$U_G$ , MW
S	26.744	25.321	24.624	24.009	3.123	0.769
R2 B	35.105	33.995	33.568	33.323	0.915	0.307
R1 H	67.008	65.429	64.807	64.361	0.860	0.558
KVLCC2						
Surface condition	$\phi_3$ , MW	$\phi_2$ , MW	$\phi_1$ , MW	$\phi_{ext}^{21}$ , MW	$GCI_{fine}^{21}$ , %	$U_G$ , MW
S	20.172	17.325	17.850	18.017	1.174	0.209
R2 B	29.159	24.940	25.057	25.063	0.033	0.008
R1 H	58.651	55.524	55.940	56.036	0.214	0.120
BC						
Surface condition	$\phi_3$ , MW	$\phi_2$ , MW	$\phi_1$ , MW	$\phi_{ext}^{21}$ , MW	$GCI_{fine}^{21}$ , %	$U_G$ , MW
S	7.384	7.267	6.725	6.573	2.825	0.190
R2 B	9.933	9.985	9.383	9.325	0.769	0.072
R1 H	20.778	21.326	20.301	19.112	7.318	1.486

Table 5.42 The obtained grid uncertainties in the prediction of  $J$

KCS						
Surface condition	$\phi_3$	$\phi_2$	$\phi_1$	$\phi_{ext}^{21}$	$GCI_{fine}^{21}$	$U_G$
S	0.7196	0.7215	0.7293	0.7319	0.452	0.0033
R2 B	0.6647	0.6655	0.6701	0.6760	1.100	0.0074
R1 H	0.5476	0.5442	0.5452	0.5456	0.094	0.001
KVLCC2						
Surface condition	$\phi_3$	$\phi_2$	$\phi_1$	$\phi_{ext}^{21}$	$GCI_{fine}^{21}$	$U_G$
S	0.4428	0.4603	0.4573	0.4564	0.248	0.0011
R2 B	0.3958	0.4116	0.4068	0.3955	3.451	0.0140
R1 H	0.3066	0.3128	0.3099	0.3068	1.257	0.0039
BC						
Surface condition	$\phi_3$	$\phi_2$	$\phi_1$	$\phi_{ext}^{21}$	$GCI_{fine}^{21}$	$U_G$
S	0.5160	0.5209	0.5328	0.5414	1.997	0.0106
R2 B	0.4632	0.4622	0.4711	0.4776	1.723	0.0081
R1 H	0.3593	0.3580	0.3591	0.3649	2.041	0.0073

The obtained  $U_G$  related to the prediction of  $Q$  for smooth and fouled ships are also low and the highest  $GCI_{fine}^{21}$  for KCS is equal to 3.682%, for BC to 5.618% and for KVLCC2 to 1.067%. The obtained  $U_T$  related to the prediction of  $Q$  for smooth and fouled ships are also low and the highest  $GCI_{fine}^{21}$  for KCS is equal to 1.048%, for BC to 1.962% and for KVLCC2 to 2.588%. The obtained  $U_G$  related to the prediction of  $n$  for smooth and fouled ships are the lowest

amongst investigated key variables and the highest  $GCI_{fine}^{21}$  for KCS is equal to 0.255%, for BC to 1.661% and for KVLCC2 to 0.164%. Interestingly, the obtained  $U_T$  related to the prediction of  $n$  for smooth ships and fouled ships are higher than  $U_G$  and the highest  $U_T$  for KCS is equal to 1.048%, for BC to 2.909% and for KVLCC2 to 3.613%. The obtained  $U_G$  related to the prediction of  $P_D$  for smooth and fouled ships are slightly higher than for the other investigated key variables and the highest  $GCI_{fine}^{21}$  for KCS is equal to 3.123%, for BC to 7.318% and for KVLCC2 to 1.173%. The obtained  $U_T$  related to the prediction of  $P_D$  for smooth and fouled ships are lower than  $U_G$  related to the prediction of  $P_D$  and the highest  $GCI_{fine}^{21}$  for KCS is equal to 1.366%, for BC to 3.390% and for KVLCC2 to 1.502%. Finally, the obtained  $U_G$  related to the prediction of  $J$  for smooth and fouled ships are low and the highest  $GCI_{fine}^{21}$  for KCS is equal to 1.100%, for BC to 2.041% and for KVLCC2 to 3.451%. The obtained  $U_T$  related to the prediction of  $J$  for smooth and fouled ships are low as well and the highest  $GCI_{fine}^{21}$  for KCS is equal to 0.451%, for BC to 3.199% and for KVLCC2 to 0.703%.

Table 5.43 The obtained temporal uncertainties in the prediction of  $T$

KCS						
Surface condition	$\phi_3$ , kN	$\phi_2$ , kN	$\phi_1$ , kN	$\phi_{ext}^{21}$ , kN	$GCI_{fine}^{21}$ , %	$U_T$ , kN
S	1833.25	1827.69	1810.89	1802.58	0.574	10.388
R2 B	2303.81	2298.95	2284.48	2277.16	0.400	9.147
R1 H	3611.92	3621.12	3605.91	3582.67	0.807	29.104
KVLCC2						
Surface condition	$\phi_3$ , kN	$\phi_2$ , kN	$\phi_1$ , kN	$\phi_{ext}^{21}$ , kN	$GCI_{fine}^{21}$ , %	$U_T$ , kN
S	2025.11	2018.75	2009.71	1988.26	1.334	26.816
R2 B	2585.99	2545.97	2568.93	2599.83	1.504	38.626
R1 H	4371.42	4347.51	4390.60	4444.32	1.529	67.146
BC						
Surface condition	$\phi_3$ , kN	$\phi_2$ , kN	$\phi_1$ , kN	$\phi_{ext}^{21}$ , kN	$GCI_{fine}^{21}$ , %	$U_T$ , kN
S	774.04	784.54	763.94	742.56	3.499	26.730
R2 B	976.76	981.39	984.48	990.72	0.792	7.801
R1 H	1609.60	1597.42	1592.13	1588.07	0.319	5.077

Table 5.44 The obtained temporal uncertainties in the prediction of  $Q$

KCS						
Surface condition	$\phi_3$ , kNm	$\phi_2$ , kNm	$\phi_1$ , kNm	$\phi_{ext}^{21}$ , kNm	$GCI_{fine}^{21}$ , %	$U_T$ , kNm
S	2400.11	2389.56	2367.02	2347.18	1.048	24.805
R2 B	3095.52	3089.30	3077.59	3064.31	0.539	16.595
R1 H	5285.22	5292.91	5272.49	5260.15	0.292	15.417
KVLCC2						
Surface condition	$\phi_3$ , kNm	$\phi_2$ , kNm	$\phi_1$ , kNm	$\phi_{ext}^{21}$ , kNm	$GCI_{fine}^{21}$ , %	$U_T$ , kNm
S	2359.02	2345.67	2405.55	2422.73	0.893	21.475
R2 B	3100.11	3097.47	3125.32	3128.237	0.117	3.646
R1 H	5693.22	5654.27	5685.13	5802.85	2.588	147.148
BC						
Surface condition	$\phi_3$ , kNm	$\phi_2$ , kNm	$\phi_1$ , kNm	$\phi_{ext}^{21}$ , kNm	$GCI_{fine}^{21}$ , %	$U_T$ , kNm
S	652.95	658.76	645.14	635.01	1.962	12.661
R2 B	841.28	844.18	836.82	832.02	0.716	5.990
R1 H	1499.91	1496.65	1490.39	1483.59	0.571	8.503

Table 5.45 The obtained temporal uncertainties in the prediction of  $n$

KCS						
Surface condition	$\phi_3$ , rpm	$\phi_2$ , rpm	$\phi_1$ , rpm	$\phi_{ext}^{21}$ , rpm	$GCI_{fine}^{21}$ , %	$U_T$ , rpm
S	99.697	99.577	99.341	99.094	0.311	0.309
R2 B	104.384	104.293	104.159	103.871	0.346	0.361
R1 H	117.477	117.628	117.376	116.999	0.401	0.471
KVLCC2						
Surface condition	$\phi_3$ , rpm	$\phi_2$ , rpm	$\phi_1$ , rpm	$\phi_{ext}^{21}$ , rpm	$GCI_{fine}^{21}$ , %	$U_T$ , rpm
S	70.490	70.249	70.858	71.255	0.701	0.496
R2 B	76.507	76.190	76.560	78.773	3.613	2.766
R1 H	94.492	93.715	93.963	94.079	0.154	0.145
BC						
Surface condition	$\phi_3$ , rpm	$\phi_2$ , rpm	$\phi_1$ , rpm	$\phi_{ext}^{21}$ , rpm	$GCI_{fine}^{21}$ , %	$U_T$ , rpm
S	99.638	100.066	99.541	97.225	2.909	2.896
R2 B	107.294	107.156	107.074	106.954	0.140	0.150
R1 H	130.805	130.529	130.073	129.374	0.672	0.874

Table 5.46 The obtained temporal uncertainties in the prediction of  $P_D$

KCS						
Surface condition	$\phi_3$ , MW	$\phi_2$ , MW	$\phi_1$ , MW	$\phi_{ext}^{21}$ , MW	$GCI_{fine}^{21}$ , %	$U_T$ , MW
S	25.058	24.918	24.624	24.355	1.366	0.336
R2 B	33.837	33.740	33.569	33.342	0.846	0.284
R1 H	65.020	65.198	64.807	64.479	0.633	0.410
KVLCC2						
Surface condition	$\phi_3$ , MW	$\phi_2$ , MW	$\phi_1$ , MW	$\phi_{ext}^{21}$ , MW	$GCI_{fine}^{21}$ , %	$U_T$ , MW
S	17.413	17.256	17.850	18.064	1.502	0.268
R2 B	24.838	24.714	25.057	25.251	0.968	0.243
R1 H	56.335	55.490	55.940	56.454	1.147	0.642
BC						
Surface condition	$\phi_3$ , MW	$\phi_2$ , MW	$\phi_1$ , MW	$\phi_{ext}^{21}$ , MW	$GCI_{fine}^{21}$ , %	$U_T$ , MW
S	6.813	6.903	6.725	6.542	3.390	0.228
R2 B	9.452	9.473	9.383	9.357	0.352	0.033
R1 H	20.546	20.458	20.301	20.101	1.233	0.250

Table 5.47 The obtained temporal uncertainties in the prediction of  $J$

KCS						
Surface condition	$\phi_3$	$\phi_2$	$\phi_1$	$\phi_{ext}^{21}$	$GCI_{fine}^{21}$ , %	$U_T$
S	0.7269	0.7279	0.7293	0.7319	0.451	0.0033
R2 B	0.6689	0.6691	0.6701	0.6702	0.028	0.0002
R1 H	0.5457	0.5442	0.5452	0.5466	0.335	0.0018
KVLCC2						
Surface condition	$\phi_3$	$\phi_2$	$\phi_1$	$\phi_{ext}^{21}$	$GCI_{fine}^{21}$ , %	$U_T$
S	0.4596	0.4600	0.4573	0.4569	0.114	0.0005
R2 B	0.4092	0.4099	0.4068	0.4059	0.277	0.0011
R1 H	0.3107	0.3116	0.3099	0.3082	0.703	0.0022
BC						
Surface condition	$\phi_3$	$\phi_2$	$\phi_1$	$\phi_{ext}^{21}$	$GCI_{fine}^{21}$ , %	$U_T$
S	0.5312	0.5276	0.5328	0.5444	2.719	0.0145
R2 B	0.4706	0.4737	0.4711	0.4591	3.199	0.0151
R1 H	0.3590	0.3590	0.3591	0.3591	0.007	0.0000

The obtained  $U_T$ ,  $U_Q$ ,  $U_n$ ,  $U_{P_b}$  and  $U_J$ , which are consisted of both  $U_G$  and  $U_T$ , are shown in Table 5.48. As can be seen from Table 5.48, the lowest  $U_{SN}$  for smooth and fouled ships are obtained for KCS, which was expected since  $U_G$  are higher than  $U_T$  and the mesh for KCS had more cells than for KVLCC2 and BC. The highest  $U_{SN}$  is obtained for the prediction of  $U_{P_b}$  for BC fouled with R1 H and it is equal to 7.421% and the other obtained  $U_{SN}$  are lower than

5.5%. It should be noted that remaining numerical simulations of self-propulsion tests are carried out using fine mesh and fine time step.

Table 5.48 The obtained  $U_{SN}$  in the prediction of  $T (U_T)$ ,  $Q (U_Q)$ ,  $n (U_n)$ ,  $P_D (U_{P_D})$  and  $J (U_J)$

	KCS		KVLCC2		BC	
Surface condition	$U_T$ , kN	$U_T$ , %	$U_T$ , kN	$U_T$ , %	$U_T$ , kN	$U_T$ , %
S	60.185	3.323	26.819	1.334	40.811	5.342
R2 B	46.615	2.041	41.766	1.626	41.876	4.254
R1 H	66.890	1.855	93.365	2.126	75.279	4.728
	KCS		KVLCC2		BC	
Surface condition	$U_Q$ , kNm	$U_Q$ , %	$U_Q$ , kNm	$U_Q$ , %	$U_Q$ , kNm	$U_Q$ , %
S	90.618	3.828	33.463	1.391	20.148	3.123
R2 B	44.866	1.458	4.392	0.141	7.578	0.906
R1 H	35.982	0.682	147.836	2.600	84.162	5.647
	KCS		KVLCC2		BC	
Surface condition	$U_n$ , rpm	$U_n$ , %	$U_n$ , rpm	$U_n$ , %	$U_n$ , rpm	$U_n$ , %
S	0.341	0.343	0.510	0.720	2.918	2.932
R2 B	0.361	0.346	2.766	3.613	0.258	0.241
R1 H	0.558	0.475	0.145	0.154	2.331	1.791
	KCS		KVLCC2		BC	
Surface condition	$U_{P_D}$ , MW	$U_{P_D}$ , %	$U_{P_D}$ , MW	$U_{P_D}$ , %	$U_{P_D}$ , MW	$U_{P_D}$ , %
S	0.839	3.409	0.340	1.906	0.297	4.413
R2 B	0.418	1.246	0.243	0.969	0.079	0.846
R1 H	0.692	1.068	0.653	1.167	1.506	7.421
	KCS		KVLCC2		BC	
Surface condition	$U_J$	$U_J$ , %	$U_J$	$U_J$ , %	$U_J$	$U_J$ , %
S	0.0047	0.638	0.0012	0.273	0.0180	3.374
R2 B	0.0074	1.101	0.0141	3.462	0.0171	3.633
R1 H	0.0019	0.348	0.0045	1.440	0.0073	2.041

### 5.5.2. The validation study

After the verification study has been performed, the obtained propulsion characteristics using fine mesh for smooth surface condition for all three ships are validated with the extrapolated values of towing tank results published in the literature [226], [230], [231], [252]. As for the resistance tests, experimental results are extrapolated using ITTC 1978 PPM. It should be noted that the extrapolation is performed for smooth full-scale ship and propeller. Consequently, there is no difference between ITTC 1978 PPM and ITTC 1999 PPM, since  $\Delta C_F$  is equal to zero [151]. The obtained results of the validation study for self-propulsion point, which is defined with  $n$  and  $P_D$  for all three investigated ships are presented in Table 5.49. As can be seen from

Table 5.49, satisfactory agreement between numerical and extrapolated results for self-propulsion point is obtained. Thus, the obtained  $RD$  between numerical and extrapolated  $n$  are lower than 1.8%, while the obtained  $RD$  for  $P_D$  are lower than 5.7% for all three ships. The validation study for propulsion characteristics is presented in Table 5.50. Thus, the obtained  $RD$  for  $1-t$  are lower than 3.7%, for  $1-w$  are lower than 7.4% and for  $\eta_H$  are lower than 5.6% for all investigated ships. It should be noted that slightly higher  $RD$  for  $1-w$  is obtained only for BC and this can be attributed to the application of body force method. However, this  $RD$  is in line with previously published studies related to numerical simulations of self-propulsion tests, where virtual disk model is applied [253], [254]. The obtained  $RD$  for  $\eta_o$  are lower than 3.1%, for  $\eta_B$  are lower than 3.8%, for  $\eta_R$  are lower than 2.9% and for  $\eta_D$  are lower than 6.2%. It should be noted that slightly higher  $RD$  for  $\eta_D$  is obtained only for KCS. Within [182], the authors performed full-scale self-propulsion test for KCS using discretized propeller and  $\eta_D$  was equal to 0.766, which is also lower than the extrapolated result.  $RD$  between the obtained  $\eta_D$  and  $\eta_D$  obtained in [182] is equal to -3.394%. In Table 5.50, the validation for the obtained  $J$ ,  $K_T$  and  $K_Q$  for self-propulsion point is presented as well. It can be seen that the obtained  $RD$  for  $J$  are lower than 5.7%, for  $K_T$  are lower than 4.1% and for  $K_Q$  are lower than 3.4% for all investigated ships. Generally, the obtained  $RD$  between numerically obtained self-propulsion point and propulsion characteristics and extrapolated values can be attributed to various aspects. For example, insufficiently accurate prediction of the nominal wake, as well as underestimation of the propeller performance in open water test can be directly related to the difference in the prediction of  $J$  for self-propulsion point, which then leads to difference in the prediction of other propulsion characteristics. Furthermore, the modelling error should also be considered, since in the body force method the effect of propeller is modelled, i.e. propeller is not discretized. In addition to there is a numerical error as well, which is related to the utilized mesh and time step. Lastly, there are also aspects regarding the applied PPM for the extrapolation of towing tank results. Namely, in [151] four different PPM were compared, and it was shown that extrapolated values can significantly vary with respect to the applied PPM. Thus, it was shown that for BC, extrapolated value of  $P_D$  can vary up to 1.5%, for  $n$  up to 0.4%, for  $1-t$  up to 0.5%,  $1-w$  up to 6.3%, for  $\eta_R$  up to 1.1% and for  $\eta_B$  up to 2.6%. In addition to these variations, the experimental uncertainty should also be considered. Considering all before mentioned aspects, it can be concluded that satisfactory agreement is achieved for self-propulsion points and all propulsion characteristics.

Table 5.49 The validation study for self-propulsion point

	$n_{CFD}$ , rpm	$n_{EX}$ , rpm	$RD$ , %	$P_{D,CFD}$ , MW	$P_{D,EX}$ , MW	$RD$ , %
KCS	99.341	100.359	-1.014	24.624	25.511	-3.476
KVLCC2	70.858	71.417	-0.784	17.850	18.929	-5.701
BC	99.541	101.351	-1.786	6.725	6.961	-3.392

Table 5.50 The validation study for propulsion characteristics

Propulsion characteristic	KCS		KVLCC2		BC	
	EX	CFD (RD, %)	EX	CFD (RD, %)	EX	CFD (RD, %)
$1-t$	0.853	0.867 (1.613)	0.810	0.820 (1.199)	0.794	0.764 (-3.722)
$1-w$	0.803	0.773 (-3.476)	0.695	0.668 (-3.904)	0.705	0.653 (-7.418)
$\eta_H$	1.062	1.122 (5.596)	1.165	1.227 (5.310)	1.126	1.171 (3.992)
$\eta_o$	0.690	0.700 (1.485)	0.620	0.600 (-3.146)	0.623	0.622 (-0.112)
$\eta_B$	0.698	0.702 (0.565)	0.623	0.600 (-3.752)	0.642	0.623 (-2.964)
$\eta_R$	1.011	1.002 (-0.906)	1.005	0.998 (-0.626)	1.030	1.000 (-2.855)
$\eta_D$	0.741	0.787 (6.193)	0.726	0.736 (1.359)	0.722	0.729 (0.910)
$J$	0.750	0.729 (-2.786)	0.472	0.457 (-3.145)	0.565	0.533 (-5.734)
$K_T$	0.161	0.165 (2.954)	0.155	0.149 (-4.055)	0.179	0.183 (2.312)
$10K_Q$	0.275	0.274 (-0.477)	0.187	0.180 (-3.449)	0.251	0.250 (-0.609)

### 5.5.3. Results of the analysis of the impact of biofouling on the propulsion characteristics

After the verification and validation studies, numerical simulations of self-propulsion test for fouled ships are performed. The investigated fouling conditions are presented in Table 5.3 and the obtained changes in certain propulsion characteristic are determined with equation (5.4).

The obtained increases in  $P_B$  due to the presence of biofouling are the same as the obtained increases in  $P_D$ , since it is considered that mechanical losses have remained the same. The obtained  $\Delta P_D$  and  $\Delta n$  due to the presence of biofouling are presented in Figure 5.74 and Figure 5.75, respectively. As can be seen from Figure 5.74, the obtained  $\Delta P_D$  due to the presence of biofilm are significant and for the most severe investigated fouling condition (R2 B) are equal to 36.3% for KCS, 40.4% for KVLCC2 and 39.5% for BC. Even for the surface condition R7 B, which represents the fouling condition with the smallest  $k_{eff}$  value, the obtained  $\Delta P_D$  are equal to 1.4% for KCS, 0.4% for KVLCC2 and 2.6% for BC. Therefore, it is clear that the presence of biofilm on the immersed surfaces, i.e. on the hull and propeller, should not be ignored as it can lead to significant increase in  $P_D$  and consequently in the fuel consumption. The obtained  $\Delta P_D$  due to the presence of biofilm are the highest as follows: for KCS for surface conditions R1 B, R3 B, R5 B, R8 B, for BC for surface condition R6 B and R7 B, for KVLCC2 for surface conditions R2 B and R4 B.  $\Delta P_D$  depends on the many aspects related to the fouling and hydrodynamic characteristics of a ship. For example,  $\Delta P_D$  depends on the obtained  $k^+$  values along the ship hull, which are the highest for KCS. However, it also depends on the

portion of  $R_f$  (which is the most affected by the presence of biofouling amongst resistance components) in  $R_T$  as well, which is the highest for KVLCC2. This is obviously the most dominant aspect regarding the increase in  $P_D$  for more severe fouling conditions such as hard fouling. Thus, the highest increases in  $P_D$  due to the presence of hard fouling are obtained for KVLCC2, Figure 5.74. The obtained  $\Delta P_D$  due to the presence of hard fouling are substantial and for the most severe investigated fouling condition (R1 H) are equal to 163.2% for KCS, 213.4% for KVLCC2 and 201.9% for BC. Even for the surface condition R6 H, which represents the fouling condition with the smallest  $k$  value, the obtained  $\Delta P_D$  are equal to 75.0% for KCS, 90.7% for KVLCC2 and 90.6% for BC. The presence of biofouling causes the increase in  $n$  as well, which can be noticed from Figure 5.75. The obtained  $\Delta n$  due to the presence of biofilm for the fouling condition R2 B are equal to 4.9% for KCS, 8.0% for KVLCC2 and 7.6% for BC, while for the fouling condition R7 B are equal to 0.1% for KCS, 0.1% for KVLCC2 and 0.4% for BC. These increases are significantly higher if the hard fouling is present and for the fouling condition R1 H are equal to 18.2% for KCS, 32.6% for KVLCC2 and 30.7% for BC, while for R6 H are equal to 9.4% for KCS, 16.7% for KVLCC2 and 16.6% for BC.

It is interesting to compare the obtained increases in  $P_D$  and  $P_E$  in order to show the importance of the assessment of the impact of biofouling on the propulsion characteristics. Thus the obtained  $\Delta P_D$  and  $\Delta P_E$  are shown in Table 5.51. From the presented results in Table 5.51, it is clear that the obtained  $\Delta P_D$  are significantly higher than  $\Delta P_E$ . This is especially highlighted for fouling with hard fouling, where the obtained  $\Delta P_D$  are almost two times higher than the obtained  $\Delta P_E$ . This points out the importance of the assessment of the impact of biofouling on  $P_D$  rather than on  $P_E$ , which most of the current studies do not consider. Obviously, one of the reasons why the obtained  $\Delta P_D$  are significantly higher than  $\Delta P_E$  can be attributed to a decrease in propeller performance related to propeller fouling. However, as it will be shown in the following text, even if propeller is cleaned the obtained  $\Delta P_D$  would be higher than  $\Delta P_E$ .

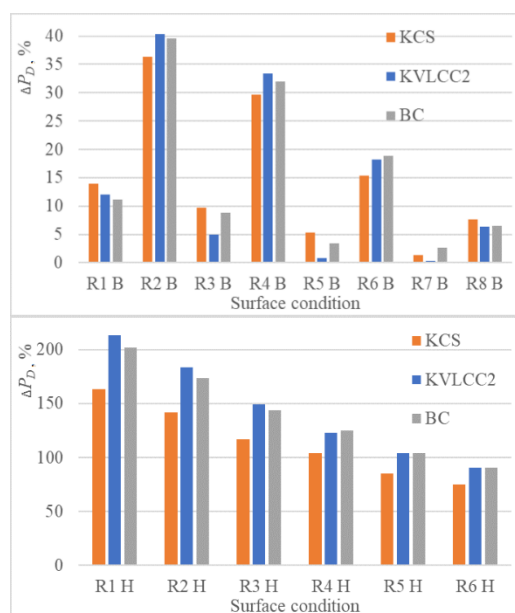


Figure 5.74 The obtained  $\Delta P_D$  due to the presence of biofilm (upper) and hard fouling (lower)



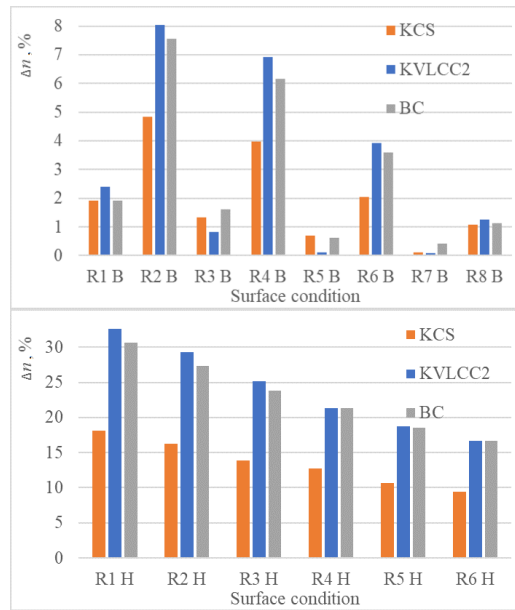


Figure 5.75 The obtained  $\Delta n$  due to the presence of biofilm (upper) and hard fouling (lower) It should be highlighted that  $\Delta P_E$  and  $\Delta P_D$  are obtained by comparison with smooth hull and propeller surfaces. Since the hull and propeller surfaces are not smooth in the future work it would be beneficial to determine these increases in comparison with surface condition typical as applied AF coating. Thus, the obtained increases would be slightly lower, which could be of importance for biofilm, where the obtained  $\Delta P_D$  for some of the investigated fouling conditions (R5 B and R7 B) would probably be negligible. Due to the presence of hard fouling the installed engine will not be able to deliver  $P_D$  and because of this ship will not be able to achieve the design speed. Therefore, the ship speed will decrease, and this decrease can be estimated if  $P_D$  is kept the same as for the smooth surface condition. This will also occur for certain more severe fouling conditions with biofilm (R2 B and R4 B) and even for fouling conditions with lower fouling severity, since the sea margin is most commonly taken as 15%. Namely, it is upon ship operator or shipowner to decide whether to reduce the ship speed, rather than having a large fuel penalty keeping the ship speed constant. In order to estimate the speed reduction, additional numerical simulations of self-propulsion test should be performed at lower ship speeds. In order to represent the approach for determination of speed loss due to the presence of biofilm, additional numerical simulations are performed for KCS at two additional speeds, i.e. 19 kn and 14 kn. It should be noted that the same approach could be applied for other ships or other fouling conditions. After the numerical simulations are finished, the second polynomial is fitted to the obtained data and finally attainable speed is determined for constant value of  $P_D$ , equal to the one obtained for the smooth surface condition. The obtained  $P_D$  for the smooth surface conditions are equal to 24.624 MW for 24 kn, 10.535 MW for 19 kn and 4.284 MW for 14 kn. The obtained  $\Delta P_D$  due to the presence of biofilm for different speeds are shown in Figure 5.76. From this figure, a significant  $\Delta P_D$  can be noticed for fouling conditions R2 B and R4 B. Following this,  $\Delta P_D$  for fouling conditions R6 B and R1 B is more than two times lower when compared to  $\Delta P_D$  for R2 B, while for fouling conditions R3 B, R8 B and R5 B,  $\Delta P_D$  is even

lower. Lastly,  $\Delta P_D$  for R7 B is almost negligible as this fouling condition has the lowest  $k_{eff}$  value.

Table 5.51 The obtained increases in  $P_D$  and  $P_E$  for biofilm and hard fouling

Surface condition	KCS		KVLCC2		BC	
	$\Delta P_E$ , %	$\Delta P_D$ , %	$\Delta P_E$ , %	$\Delta P_D$ , %	$\Delta P_E$ , %	$\Delta P_D$ , %
R1 B	9.029	13.968	7.159	11.980	8.894	11.170
R2 B	25.756	36.326	27.948	40.377	29.357	39.527
R3 B	6.391	9.770	3.409	4.916	5.173	8.828
R4 B	22.055	29.678	22.921	33.422	24.401	32.008
R5 B	4.045	5.346	0.359	0.775	2.345	3.351
R6 B	11.859	15.354	11.404	18.242	12.684	18.881
R7 B	0.477	1.396	0.009	0.357	0.699	2.635
R8 B	5.315	7.693	4.390	6.302	6.181	6.468
R1 H	95.802	163.187	116.291	213.398	114.55	201.878
R2 H	86.555	141.684	104.592	183.393	101.261	173.469
R3 H	73.927	117.104	88.818	149.590	87.046	144.022
R4 H	66.008	104.384	78.774	122.792	78.090	124.937
R5 H	56.208	85.320	68.210	104.036	66.684	103.822
R6 H	49.857	75.029	60.089	90.724	59.507	90.602

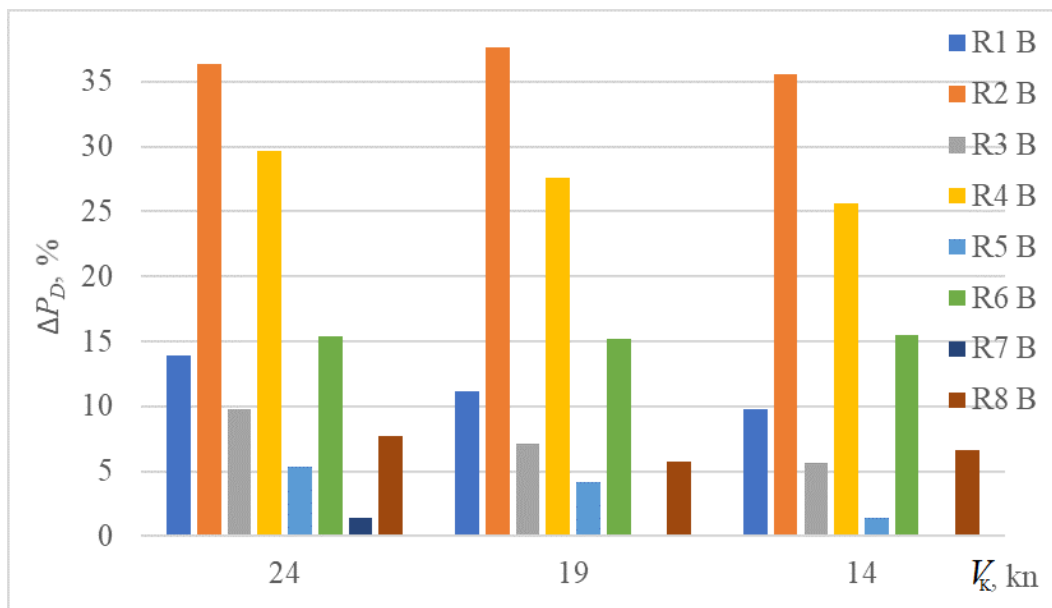


Figure 5.76 The obtained  $\Delta P_D$  due to the presence of biofilm for different speeds

The obtained speed reductions for KCS due to the presence of biofilm are calculated for two speeds, 24 kn and 19 kn and presented in Table 5.52. As can be seen from Table 5.52, the obtained speed reduction for the design speed ranges from -0.384% (R7 B) to -8.411% (R2B), while for the slow steaming speed ranges from 0% (R7 B) to -8.567% (R2 B). For the design speed the speed reduction is lower than 0.5 kn for fouling conditions R5 B, R7 B and R8 B, and lower than 1 kn for R1 B, R3 B and R6 B, while for R2 B and R4 B is higher than 1 kn. For the slow steaming speed the speed reduction is around or lower than 0.5 kn for fouling conditions R1 B, R3 B, R5 B, R7 B and R8 B, lower than 1 kn for fouling conditions R6 B, while for R2

B and R4 B is higher than 1 kn. Generally, higher  $\Delta V_K$  are obtained for the design speed, except for fouling condition R2 B for which higher  $\Delta V_K$  are obtained for the slow steaming speed, even though the portion of  $R_F$  in  $R_T$  is higher for the slow steaming speed. The higher  $\Delta V_K$  for the design speed can be ascribed to the fact that at slow steaming speed  $u_r$  values along the ship hull are lower than  $u_r$  values at the design speed. Since  $k^+$  is a function of  $u_r$ , the same is obtained for  $k^+$  values and therefore higher  $\Delta U^+$  values for the design speed are obtained, which obviously caused the higher  $\Delta V_K$ . However, only for the surface condition R2 B which represents the most severe investigated fouling condition, the obtained  $\Delta V_K$  for the slow steaming speed is higher than for the design speed. Thus, only for this surface condition the fact that the portion of  $R_F$  in  $R_T$  is higher at 19 kn than at 24 kn was more important for  $\Delta V_K$  than the fact that  $\Delta U^+$  values are lower at 19 kn than at 24 kn. It should be noted that the obtained  $\Delta V_K$  for fouling conditions with lower  $k_{eff}$  values are very low, or even negligible, for example the obtained  $\Delta V_K$  for the slow steaming speed and fouling condition R7 B is equal to 0%. The obtained  $\Delta V_K$  for R7 B at 19 kn is negligible because of the obtained  $k^+$  values along the ship hull. Namely, the flow around ship hull for low  $k^+$  values is in the hydraulically smooth regime and  $\Delta U^+$  is equal to 0. The threshold  $k^+$  value for which  $\Delta U^+$  is equal to 0 for biofilm with %SC < 10% is equal to 4. The obtained  $k^+$  distribution for the fouling condition R7 B at 19 kn is shown in Figure 5.77. It should be noted that only  $k^+$  values above the threshold value are presented in Figure 5.77. It is obvious that the most of the obtained  $k^+$  values are below 4, meaning that the flow on the largest part of the wetted surface of KCS is in the hydraulically smooth regime. Areas where the obtained  $k^+$  are higher than 4 cover only small part of the wetted surface, and therefore they did not have any effect on  $\Delta P_D$ . Generally, the obtained speed reductions due to the presence of biofilm are significant and account up to -8.5% for the fouling condition R2 B.

The speed reductions presented in Table 5.52 are obtained for constant value of  $P_D$  equal to the one obtained for the smooth surface condition. However, these speed reductions could be even higher, which can be seen from Figure 5.78, where the impact of biofilm on  $Q$  at different speeds is presented. Namely, for the reduced speed for the fouled ship keeping  $P_D$  the same as for smooth ship,  $Q$  will be higher while  $n$  will be lower. This can be easily seen from Figure 5.78, if the  $Q$  value for the fouling condition R2 B at 22 kn and for the smooth surface condition at 24 kn are read off from diagram. Thus, for the smooth surface condition at 24 kn  $Q$  is equal to 2367 kNm, while for R2 B fouling condition at 22 kn  $Q$  is equal to 2510 kNm, which is 6% higher. Consequently, if the engine cannot provide sufficient  $Q$ , either  $P_D$  has to be reduced according to the engine characteristic curve, or additional gear system is needed, which is not desirable. This behaviour was expected, since for the fouled hull and propeller, the propeller curve shifts to the left towards lower values of  $n$ , i.e. the propeller curve behaves as heavy loaded [255]. Thus, for the more severe fouling condition (for example hard fouling), the engine would not be able to provide sufficient  $Q$ . Therefore, in the approach for the prediction of the speed reduction due to the presence of hard fouling, engine characteristic curve must be taken into account.

Table 5.52 The obtained speed reductions due to the presence of biofilm for KCS

Reference speed	24 kn (design speed)		19 kn (slow steaming speed)	
	$V_K$ , kn	$\Delta V_K$ , %	$V_K$ , kn	$\Delta V_K$ , %
R1 B	23.15	-3.541	18.48	-2.760
R2 B	21.98	-8.411	17.37	-8.567
R3 B	23.39	-2.546	18.66	-1.807
R4 B	22.34	-6.932	17.79	-6.378
R5 B	23.65	-1.455	18.79	-1.082
R6 B	23.05	-3.949	18.28	-3.812
R7 B	23.91	-0.384	19.00	0.000
R8 B	23.51	-2.040	18.72	-1.492

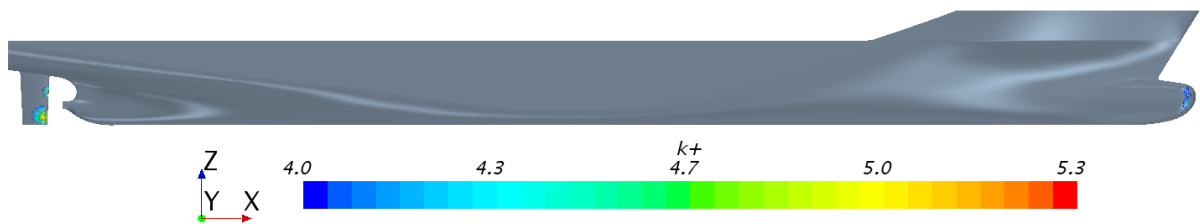


Figure 5.77 The obtained  $k^+$  distribution for the fouling condition R7 B at 19 kn

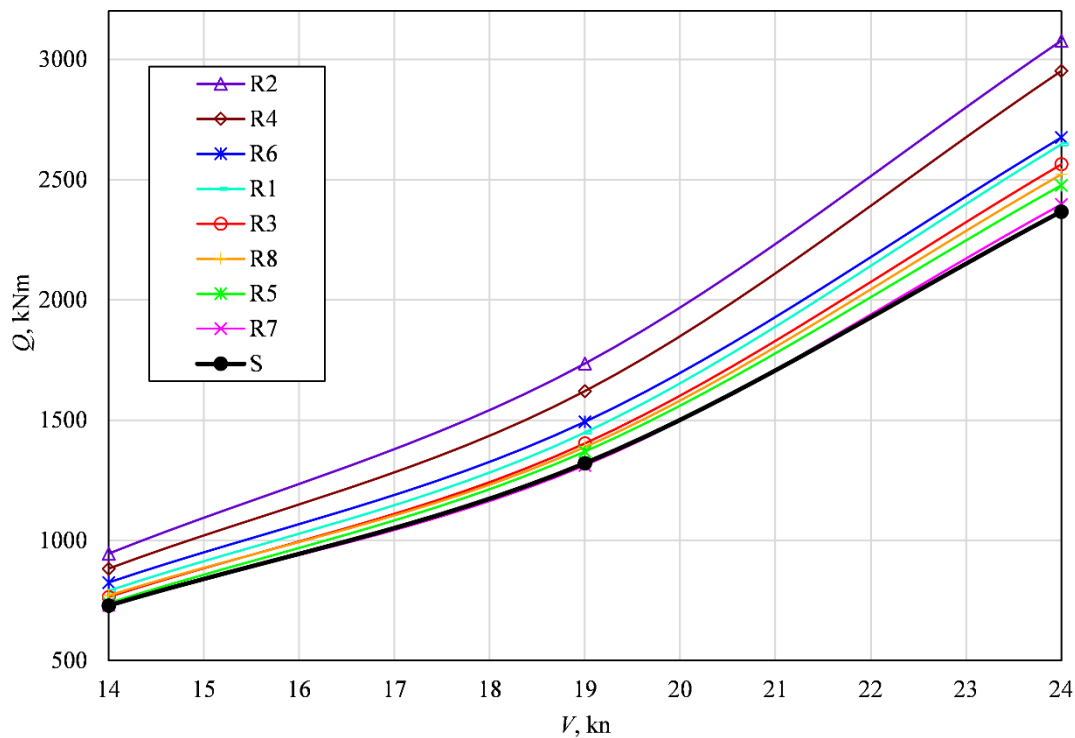


Figure 5.78 The impact of biofilm on  $Q$  at different speeds

After the impact of biofouling on  $\Delta P_D$  and  $\Delta V_K$  has been determined, the impact of biofouling on the propulsion characteristics is analysed for the constant speed: 24 kn for KCS, 15.5 kn for KVLCC2 and 16.32 kn for BC. Within Table 5.53 – Table 5.58, the obtained propulsion characteristics, as well as the impact of biofouling on propulsion characteristics are shown for all three investigated ships. As can be seen from these tables, some propulsion characteristics

are significantly affected by the presence of biofouling, while for some of them this impact is negligible. Thus, the impact of biofouling on  $\eta_R$  is minimal, i.e. it is lower than 0.5% for all investigated fouling conditions and ships. The impact of biofilm on  $1-t$  is minimal as well, since the obtained impact for all investigated fouling conditions for biofilm and all ships is lower than 0.5%. This confirms the hypothesis made by Townsin et al. [166], which assumes that the impact of biofouling on  $\eta_R$  and  $1-t$  is negligible. However, the obtained results show slight impact of hard fouling on  $1-t$ . Interestingly, due to the presence of hard fouling  $1-t$  value for KCS and KVLCC2 decreases, while for BC increases. Thus, due to the presence of hard fouling (R1 H),  $1-t$  value for KCS decreases by 1.67%, for KVLCC2 by 1% and for BC is increased by 2.95%. The value  $1-t$  depends on many different parameters, i.e. on the fouling penalties: related to an increase in  $R_T$ , propeller performance, as well as hull and propeller interaction. Furthermore, it depends on the obtained  $J$  value for the self-propulsion point, as  $K_T$  value depends on  $J$ . Obviously, the assessment of the effect of biofouling on  $1-t$  value is very complex. It should be noted that the obtained impact of hard fouling is within the obtained numerical uncertainty in the prediction of  $R_T$  and  $T$ . Additionally, in the prediction of  $1-t$  value the modelling error is present related to turbulence modelling, modelling of the effect of ship propeller with the virtual disk method etc. Therefore, in order to accurately predict this impact, the numerical uncertainty as well as the modelling error should be reduced through the application of more dense grids and lower time steps, as well as through discretization of the propeller itself. In that way, more accurate assessment of the impact of biofouling on  $1-t$  would be achieved. Based on the obtained results within this thesis, it can be concluded that the impact of biofilm on  $1-t$  value is negligible, while the impact of hard fouling is present, however it is relatively low. On the other hand, the impact of biofouling on  $1-w$  is significant and detrimental, since it causes the decrease in  $1-w$  value. Due to the presence of biofilm the obtained decreases in  $1-w$  values range from -0.06% (R7 B) to -3.66% (R2 B) for KCS, from -0.01% (R7 B) to -3.89% (R2 B) for KVLCC2 and from -0.61% (R5 B) to -4.89% (R2 B) for BC. This impact is significantly more pronounced for hard fouling and the obtained decreases in  $1-w$  values range from -6.99% (R6 H) to -11.7% (R1 H) for KCS, from -6.29% (R6 H) to -10.1% (R1 H) for KVLCC2 and from -8.46% (R6 H) to -12.0% (R1 H) for BC. The highest impact of biofouling on  $1-w$  value is obtained for BC. The numerical uncertainty in the prediction of  $1-w$  value can be related to the numerical uncertainty in the prediction of  $J$  and  $n$  both for smooth and fouled ships. Therefore, it can be concluded that for investigated biofilm fouling conditions with higher fouling severity and all hard fouling conditions, the obtained impact of biofouling on  $1-w$  value is higher than the numerical uncertainty in the prediction of  $1-w$  value. For fouling conditions with lower  $k_{eff}$  values, the numerical uncertainty in the prediction of  $\Delta(1-w)$  is higher than  $\Delta(1-w)$  itself, however a clear trend, i.e. the decrease in  $1-w$  value is obtained for all investigated fouling conditions. This decrease can be ascribed to slower flow around the area where the propeller is operating and the flow slows down due to thicker boundary layer, as ship hull is fouled (Figure 5.34 – Figure 5.36, Figure 5.43 – Figure 5.45). The decrease in  $1-w$  has beneficial effect on  $\eta_H$ , equation (2.44). Thus, due to the presence of biofilm the obtained  $\Delta\eta_H$  values range from 0.25% (R7 B) to 3.48% (R2 B) for KCS, from -0.04% (R7 B) to 4.15% (R2 B) for KVLCC2 and from 0.73% (R7 B) to 5.54% (R2 B) for BC. This impact is significantly more pronounced for hard fouling and the obtained  $\Delta\eta_H$

values range from 6.13% (R6 H) to 11.3% (R1 H) for KCS, from 6.11% (R6 H) to 10.2% (R1 H) for KVLCC2 and from -11.3% (R6 H) to 16.9% (R1 H) for BC. The highest impact of biofouling on  $\eta_H$  value is obtained for BC. The numerical uncertainty in the prediction of  $\Delta\eta_H$  value is related to numerical uncertainties in the prediction of  $1-t$  and  $1-w$  values. From the obtained results it can be concluded that the impact of hard fouling on  $\Delta\eta_H$  is higher than the numerical uncertainty in the prediction of  $\Delta\eta_H$ . Also, a clear trend for the impact of biofilm on  $\Delta\eta_H$  value can be noticed, since for all investigated conditions and all ships, except for KVLCC2 fouled with the surface condition R7 B it has been shown that the presence of biofilm causes an increase in  $\eta_H$  value. Regardless of the fact that the decrease in  $1-w$  value has beneficial effect on  $\eta_H$ , in general the decrease in  $1-w$  value has detrimental effect on  $\eta_D$  and  $P_D$ . Namely, the decrease in  $1-w$  value means that the flow around propeller is slower and consequently the propeller operating point is changed compared with the one for smooth hull surface. Therefore,  $J$  for the self-propulsion point is decreased, since the speed of advance is lower. Furthermore,  $J$  for the self-propulsion point is decreased, due to the increase in  $n$  as well, Figure 5.75. Due to the presence of biofilm the obtained decreases in  $J$  values for the self-propulsion point range from -0.18% (R7 B) to -8.12% (R2 B) for KCS, from -0.10% (R7 B) to -11.1% (R2 B) for KVLCC2 and from -1.47% (R7 B) to -11.6% (R2 B) for BC. This impact is significantly more pronounced for hard fouling and the obtained decreases in  $J$  values for the self-propulsion point range from -15.0% (R6 H) to -25.3% (R1 H) for KCS, from -19.7% (R6 H) to -32.2% (R1 H) for KVLCC2 and from -21.5% (R6 H) to -32.6% (R1 H) for BC. The highest impact of biofouling on  $J$  value for self-propulsion point is obtained for BC. The obtained impact of biofouling on  $\Delta J$  for biofilm fouling conditions with higher fouling severity and for all investigated hard fouling conditions is higher than the numerical uncertainty in the prediction of  $\Delta J$  value. For fouling conditions with lower  $k_{eff}$  values, the numerical uncertainty in the prediction of  $\Delta J$  is higher than  $\Delta J$  itself, however a clear trend, i.e. the decrease in  $J$  value is obtained for all investigated fouling conditions and all ships. The decrease in  $J$  value is unfavourable, as KP 505, KP 458 and WB operate at  $J$  value which is lower than  $J$  value for which  $\eta_o$  has its maximum value. It should be noted that it is common for all ship propellers to operate at  $J$  value which is lower than  $J$  value for which  $\eta_o$  has its maximum value. Consequently, the decrease in  $J$  value causes the decrease in  $\eta_o$  value as well, which is related to the detrimental effect of biofouling on the open water characteristics as well. Thus, the obtained decreases in  $\eta_o$  values are higher than the obtained increases in  $\eta_H$  values. Due to the presence of biofilm the obtained decreases in  $\eta_o$  values range from -0.71% (R7 B) to -10.6% (R2 B) for KCS, from -0.31% (R7 B) to -12.5% (R2 B) for KVLCC2 and from -1.94% (R5 B) to -12.2% (R2 B) for BC. This impact is significantly more pronounced for hard fouling and the obtained decreases in  $\eta_o$  values range from -19.2% (R6 H) to -32.9% (R1 H) for KCS, from -21.1% (R6 H) to -37.3% (R1 H) for KVLCC2 and from -24.9% (R6 H) to -39.2% (R1 H) for BC. The obtained decreases in  $\eta_B$  values are similar to the ones obtained for  $\eta_o$  values, as the impact of biofouling on  $\eta_R$  value is negligible. Therefore the presence of biofouling therefore has two detrimental effects on  $\eta_o$  value, i.e. on the open water characteristics and on the propeller operating point. The impact of biofouling on the propeller operating point can be

equally meaningful as the impact of biofouling on the open water characteristics. The importance of the impact of biofouling on the propeller operating point can be seen from the obtained impact of biofouling on  $K_T$  values. Thus, even though the presence of biofouling on the propeller surfaces causes the decrease in  $K_T$  value, due to the impact of biofouling on the propeller operating point,  $K_T$  value increases. The obtained  $\Delta K_T$  values due to the presence of biofilm range from 0.04% (R7 B) to 14.8% (R2 B) for KCS, from -0.11% (R7 B) to 9.49% (R2 B) for KVLCC2 and from 0.22% (R7 B) to 11.4% (R2 B) for BC. This impact is significantly more pronounced for hard fouling and the obtained increases in  $K_T$  values range from 26.8% (R6 H) to 42.6% (R1 H) for KCS, from 18.2% (R6 H) to 24.2% (R1 H) for KVLCC2 and from 15.1% (R6 H) to 22.1% (R1 H) for BC. The numerical uncertainty in the prediction of  $\Delta K_T$  is consisted of uncertainties in the prediction of  $T$  and  $n$  for both smooth and fouled ship. It can be concluded that the obtained impact of biofouling on  $K_T$  is higher than the obtained numerical uncertainty in the prediction of  $\Delta K_T$  for biofilm with higher  $k_{eff}$  values, as well as for hard fouling. However, a clear trend i.e. an increase in  $K_T$  due to the presence of biofouling is obtained for all fouling conditions and all ships, except for KVLCC2 fouled with the fouling condition R7 B. The presence of biofouling on hull and propeller surfaces causes an increase in  $K_Q$  values due to two reasons. Firstly, due to the presence of biofouling on propeller surfaces  $K_Q$  values for open water conditions are higher in comparison with the smooth surface condition and secondly due to the change in  $J$  for the self-propulsion point  $K_Q$  value increases. The obtained increases in  $K_Q$  values due to the presence of biofilm range from 1.03 % (R7 B) to 18.3% (R2 B) for KCS, from 0.10% (R7 B) to 11.3% (R2 B) for KVLCC2 and from 1.38% (R7 B) to 12.1% (R2 B) for BC. This impact is significantly more pronounced for hard fouling and the obtained increases in  $K_Q$  values range from 33.6% (R6 H) to 59.6% (R1 H) for KCS, from 20.0% (R6 H) to 34.4% (R1 H) for KVLCC2 and from 20.2% (R6 H) to 35.3% (R1 H) for BC. The numerical uncertainty in the prediction of  $\Delta K_Q$  is consisted of uncertainties in the prediction of  $Q$  and  $n$  for both smooth and fouled ship. It can be concluded that the obtained impact of biofouling on  $K_Q$  is higher than the obtained numerical uncertainty in the prediction of  $\Delta K_Q$  for biofilm with higher  $k_{eff}$  values, as well as for hard fouling conditions. However, a clear trend i.e. an increase in  $K_Q$  due to the presence of biofouling is obtained for all fouling conditions and all ships. Finally, from Table 5.53 – Table 5.58, it is clear that the presence of biofouling on the hull and propeller surfaces causes a significant decrease in  $\eta_D$  values, which is obtained since the decreases in  $\eta_B$  values are higher than the increases in  $\eta_H$  values. The obtained decreases in  $\eta_D$  values due to the presence of biofilm range from -0.91% (R7 B) to -7.75% (R2 B) for KCS, from -0.35% (R7 B) to -8.85% (R2 B) for KVLCC2 and from -0.27% (R8 B) to -7.29% (R2 B) for BC. This impact is even more pronounced for hard fouling and the obtained reduction in  $\eta_D$  values range from -14.4% (R6 H) to -25.6% (R1 H) for KCS, from -16.1% (R6 H) to -31.0% (R1 H) for KVLCC2 and from -16.3% (R6 H) to -28.9% (R1 H) for BC. The impact of biofouling on  $\eta_D$  value is the highest for KVLCC2 for the most of the investigated fouling conditions. Since the impact of biofouling on  $\eta_D$  value is not negligible,

the increases in  $P_E$  and  $P_D$  are not the same and therefore it is necessary to investigate the impact of biofouling on  $P_D$  rather than on  $P_E$ . It should be noted that the results presented in this subsection are obtained for the presence of biofouling on both the propeller and hull surfaces. For a case when the propeller surfaces are cleaned and the ship hull is fouled, the obtained results, i.e. trends may not be the same. Thus, Song et al. [68] have obtained slight increases in  $\eta_D$  values due to the presence of barnacles at hull surfaces, i.e. with a clean propeller. This can be attributed to the fact that the authors have obtained higher increases in  $\eta_H$  values due to the presence of barnacles than the decreases in  $\eta_B$  values due to the change in operating point. Because of these reasons, the analysis of the impact of biofouling on the propulsion characteristics is very important, i.e. the assessment of biofouling on the resistance characteristics and  $P_E$  is not enough.

With the application of the proposed CFD approach within numerical simulations of self-propulsion test, the impact of biofouling on the propeller operating point defined with  $n$  and  $P_D$  can be estimated. With these results and the specific fuel oil consumption ( $SFOC$ ) of the installed engine, the fuel oil consumption ( $FOC$ ) can be calculated. The  $SFOC$  values depend on the engine load, speed, as well as engine optimization strategy. The  $SFOC$  values for MAN engines can be obtained from the MAN Computerised Engine Application System (CEAS) [256]. Once  $FOC$  values have been determined and under the assumption of complete combustion, the  $CO_2$  emission can be determined by multiplying the obtained  $FOC$  values with the carbon conversion factor [246].

Table 5.53 The impact of biofilm on the propulsion characteristics for KCS

Propulsion characteristic	S	R1 B	R2 B	R3 B	R4 B	R5 B	R6 B	R7 B	R8 B
$1-t$ $\Delta(1-t)$	0.867	0.863 -0.42%	0.864 -0.31%	0.868 0.12%	0.870 0.33%	0.866 -0.10%	0.870 0.35%	0.868 0.20%	0.865 -0.19%
$1-w$ $\Delta(1-w)$	0.773	0.762 -1.34%	0.744 -3.66%	0.767 -0.78%	0.749 -3.04%	0.768 -0.58%	0.760 -1.69%	0.772 -0.06%	0.767 -0.71%
$\eta_H$ $\Delta\eta_H$	1.122	1.132 0.92%	1.161 3.48%	1.132 0.91%	1.161 3.47%	1.127 0.48%	1.145 2.07%	1.125 0.25%	1.128 0.52%
$\eta_O$ $\Delta\eta_O$	0.700	0.665 -5.05%	0.626 -10.6%	0.674 -3.72%	0.638 -8.87%	0.689 -1.56%	0.666 -4.82%	0.695 -0.71%	0.682 -2.56%
$\eta_B$ $\Delta\eta_B$	0.702	0.665 -5.21%	0.625 -10.9%	0.674 -3.96%	0.638 -9.04%	0.690 -1.71%	0.666 -5.00%	0.693 -1.16%	0.682 -2.72%
$\eta_R$ $\Delta\eta_R$	1.002	1.000 -0.17%	0.999 -0.23%	0.999 -0.24%	1.000 -0.19%	1.000 -0.15%	1.000 -0.18%	0.997 -0.45%	1.000 -0.17%
$\eta_D$ $\Delta\eta_D$	0.787	0.753 -4.33%	0.726 -7.75%	0.763 -3.08%	0.741 -5.88%	0.777 -1.24%	0.763 -3.03%	0.780 -0.91%	0.770 -2.21%
$J$ $\Delta J$	0.729	0.706 -3.19%	0.670 -8.12%	0.714 -2.09%	0.680 -6.74%	0.720 -1.27%	0.703 -3.66%	0.728 -0.18%	0.716 -1.77%
$K_T$ $\Delta K_T$	0.165	0.174 5.42%	0.190 14.8%	0.171 3.47%	0.186 12.5%	0.170 2.71%	0.177 7.04%	0.165 0.04%	0.171 3.30%
$10K_Q$ $\Delta 10K_Q$	0.274	0.294 7.67%	0.323 18.3%	0.288 5.47%	0.316 15.4%	0.282 3.17%	0.297 8.55%	0.276 1.03%	0.285 4.31%



Table 5.54 The impact of biofilm on the propulsion characteristics for KVLCC2

Propulsion characteristic	S	R1 B	R2 B	R3 B	R4 B	R5 B	R6 B	R7 B	R8 B
$1-t$ $\Delta(1-t)$	0.820	0.819 -0.04%	0.820 0.10%	0.821 0.17%	0.820 0.04%	0.820 0.02%	0.820 -0.02%	0.819 -0.05%	0.821 0.16%
$1-w$ $\Delta(1-w)$	0.668	0.662 -0.91%	0.642 -3.89%	0.664 -0.64%	0.651 -2.50%	0.668 -0.01%	0.657 -1.66%	0.668 -0.01%	0.661 -1.06%
$\eta_H$ $\Delta\eta_H$	1.227	1.238 0.88%	1.278 4.15%	1.237 0.81%	1.259 2.61%	1.228 0.02%	1.248 1.66%	1.227 -0.04%	1.242 1.23%
$\eta_o$ $\Delta\eta_o$	0.601	0.571 -4.97%	0.526 -12.5%	0.588 -2.04%	0.539 -10.2%	0.597 -0.44%	0.555 -7.64%	0.600 -0.31%	0.585 -2.54%
$\eta_B$ $\Delta\eta_B$	0.600	0.569 -5.14%	0.525 -12.5%	0.586 -2.23%	0.538 -10.2%	0.597 -0.44%	0.556 -7.32%	0.598 -0.31%	0.582 -2.99%
$\eta_R$ $\Delta\eta_R$	0.998	0.997 -0.17%	0.998 -0.01%	0.996 -0.20%	0.998 -0.03%	1.000 0.20%	1.002 0.34%	0.997 -0.16%	0.994 -0.47%
$\eta_D$ $\Delta\eta_D$	0.736	0.704 -4.31%	0.671 -8.85%	0.725 -1.44%	0.678 -7.87%	0.733 -0.41%	0.693 -5.78%	0.733 -0.35%	0.723 -1.80%
$J$ $\Delta J$	0.457	0.443 -3.23%	0.407 -11.1%	0.451 -1.45%	0.417 -8.81%	0.457 -0.11%	0.433 -5.38%	0.457 -0.10%	0.447 -2.28%
$K_T$ $\Delta K_T$	0.149	0.152 2.26%	0.163 9.49%	0.151 1.56%	0.160 7.48%	0.149 0.15%	0.153 3.15%	0.148 -0.11%	0.151 1.67%
$10K_Q$ $\Delta 10K_Q$	0.180	0.188 4.32%	0.201 11.3%	0.185 2.37%	0.197 9.15%	0.181 0.48%	0.190 5.32%	0.181 0.10%	0.185 2.42%

Table 5.55 The impact of biofilm on the propulsion characteristics for BC

Propulsion characteristic	S	R1 B	R2 B	R3 B	R4 B	R5 B	R6 B	R7 B	R8 B
$1-t$ $\Delta(1-t)$	0.764	0.768 0.43%	0.767 0.38%	0.761 -0.38%	0.768 0.45%	0.767 0.38%	0.761 -0.49%	0.762 0.34%	0.768 0.42%
$1-w$ $\Delta(1-w)$	0.653	0.640 -1.90%	0.621 -4.89%	0.641 -1.73%	0.625 -4.18%	0.649 -0.61%	0.630 -3.48%	0.646 -1.06%	0.645 -1.13%
$\eta_H$ $\Delta\eta_H$	1.171	1.199 2.37%	1.236 5.54%	1.187 1.37%	1.228 4.84%	1.183 0.99%	1.207 3.10%	1.179 0.73%	1.189 1.57%
$\eta_o$ $\Delta\eta_o$	0.622	0.598 -3.88%	0.546 -12.2%	0.592 -4.81%	0.559 -10.2%	0.611 -1.87%	0.571 -8.21%	0.606 -2.61%	0.613 -1.47%
$\eta_B$ $\Delta\eta_B$	0.622	0.596 -4.31%	0.547 -12.2%	0.593 -4.67%	0.560 -10.1%	0.610 -1.94%	0.572 -8.07%	0.606 -2.60%	0.611 -1.81%
$\eta_R$ $\Delta\eta_R$	1.000	0.996 -0.45%	1.001 0.08%	1.002 0.16%	1.002 0.14%	0.999 -0.08%	1.002 0.16%	1.000 0.01%	0.997 -0.35%
$\eta_D$ $\Delta\eta_D$	0.729	0.714 -2.05%	0.676 -7.29%	0.704 -3.36%	0.687 -5.76%	0.722 -0.97%	0.691 -5.21%	0.715 -1.89%	0.727 -0.27%
$J$ $\Delta J$	0.533	0.513 -3.73%	0.471 -11.6%	0.515 -3.29%	0.481 -9.73%	0.526 -1.23%	0.496 -6.83%	0.525 -1.47%	0.521 -2.22%
$K_T$ $\Delta K_T$	0.183	0.191 4.42%	0.204 11.4%	0.187 2.26%	0.201 9.91%	0.184 0.69%	0.193 5.53%	0.184 0.22%	0.189 3.41%
$10K_Q$ $\Delta 10K_Q$	0.250	0.262 5.06%	0.280 12.1%	0.259 3.74%	0.275 10.4%	0.253 1.43%	0.267 6.95%	0.253 1.38%	0.257 2.97%

Table 5.56 The impact of hard fouling on the propulsion characteristics for KCS

Propulsion characteristic	S	R1 H	R2 H	R3 H	R4 H	R5 H	R6 H
$1-t$ $\Delta(1-t)$	0.867	0.852 -1.67%	0.857 -1.15%	0.858 -1.07%	0.858 -1.06%	0.856 -1.28%	0.856 -1.29%
$1-w$ $\Delta(1-w)$	0.773	0.682 -11.7%	0.690 -10.8%	0.699 -9.56%	0.707 -8.54%	0.714 -7.64%	0.719 -6.99%
$\eta_H$ $\Delta\eta_H$	1.122	1.249 11.3%	1.243 10.8%	1.227 9.39%	1.214 8.19%	1.199 6.89%	1.191 6.13%
$\eta_o$ $\Delta\eta_o$	0.700	0.470 -32.9%	0.489 -30.2%	0.514 -26.6%	0.527 -24.8%	0.553 -21.1%	0.566 -19.2%
$\eta_B$ $\Delta\eta_B$	0.702	0.469 -33.2%	0.489 -30.3%	0.514 -26.8%	0.527 -24.9%	0.553 -21.1%	0.566 -19.3%
$\eta_R$ $\Delta\eta_R$	1.002	0.998 -0.40%	1.000 -0.16%	0.999 -0.29%	1.000 -0.18%	1.001 -0.11%	1.000 -0.16%
$\eta_D$ $\Delta\eta_D$	0.787	0.585 -25.6%	0.607 -22.8%	0.630 -19.9%	0.639 -18.8%	0.663 -15.7%	0.674 -14.4%
$J$ $\Delta J$	0.729	0.545 -25.3%	0.560 -23.3%	0.579 -20.6%	0.592 -18.9%	0.609 -16.5%	0.620 -15.0%
$K_T$ $\Delta K_T$	0.165	0.236 42.6%	0.231 39.6%	0.224 35.6%	0.218 32.0%	0.214 29.3%	0.210 26.8%
$10K_Q$ $\Delta 10K_Q$	0.274	0.436 59.6%	0.420 53.7%	0.402 47.0%	0.390 42.7%	0.374 36.9%	0.365 33.6%

Table 5.57 The impact of hard fouling on the propulsion characteristics for KVLCC2

Propulsion characteristic	S	R1 H	R2 H	R3 H	R4 H	R5 H	R6 H
$1-t$ $\Delta(1-t)$	0.820	0.812 -1.00%	0.812 -0.91%	0.813 -0.88%	0.813 -0.79%	0.814 -0.66%	0.815 -0.56%
$1-w$ $\Delta(1-w)$	0.668	0.600 -10.1%	0.608 -9.02%	0.613 -8.19%	0.616 -7.75%	0.620 -7.17%	0.626 -6.29%
$\eta_H$ $\Delta\eta_H$	1.227	1.352 10.2%	1.337 8.91%	1.325 7.96%	1.320 7.55%	1.313 7.01%	1.302 6.11%
$\eta_o$ $\Delta\eta_o$	0.601	0.377 -37.3%	0.397 -34.0%	0.421 -29.9	0.448 -25.4%	0.461 -23.3%	0.474 -21.1%
$\eta_B$ $\Delta\eta_B$	0.600	0.376 -37.4%	0.397 -33.7%	0.420 -29.9%	0.447 -25.4%	0.462 -23.0%	0.474 -20.9%
$\eta_R$ $\Delta\eta_R$	0.998	0.997 -0.10%	1.002 0.35%	0.998 -0.02%	0.998 -0.02%	1.003 0.44%	1.001 0.28%
$\eta_D$ $\Delta\eta_D$	0.736	0.508 -31.0%	0.531 -27.8%	0.557 -24.4%	0.590 -19.8%	0.607 -17.6%	0.618 -16.1%
$J$ $\Delta J$	0.457	0.310 -32.2%	0.322 -29.7%	0.336 -26.6%	0.348 -24.0%	0.357 -21.8%	0.367 -19.7%
$K_T$ $\Delta K_T$	0.149	0.185 24.2%	0.183 23.4%	0.181 21.7%	0.182 22.4%	0.178 20.1%	0.176 18.2%
$10K_Q$ $\Delta 10K_Q$	0.180	0.242 34.4%	0.236 31.0%	0.230 27.4%	0.225 24.7%	0.220 21.8%	0.216 20.0%

Table 5.58 The impact of hard fouling on the propulsion characteristics for BC

Propulsion characteristic	S	R1 H	R2 H	R3 H	R4 H	R5 H	R6 H
$1-t$ $\Delta(1-t)$	0.764	0.787 2.95%	0.785 2.76%	0.782 2.31%	0.781 2.22%	0.779 1.95%	0.779 1.88%
$1-w$ $\Delta(1-w)$	0.653	0.575 -12.0%	0.579 -11.3%	0.583 -10.7%	0.590 -9.68%	0.595 -8.89%	0.598 -8.46%
$\eta_H$ $\Delta\eta_H$	1.171	1.369 16.9%	1.356 15.8%	1.341 14.5%	1.325 13.2%	1.310 11.9%	1.303 11.3%
$\eta_o$ $\Delta\eta_o$	0.622	0.378 -39.2%	0.396 -36.4%	0.416 -33.1%	0.436 -30.0%	0.456 -26.8%	0.468 -24.9%
$\eta_B$ $\Delta\eta_B$	0.622	0.378 -39.2%	0.396 -36.4%	0.417 -33.1%	0.435 -30.1%	0.455 -26.9%	0.468 -24.8%
$\eta_R$ $\Delta\eta_R$	1.000	1.000 -0.03%	0.999 -0.09%	1.001 0.10%	0.999 -0.14%	0.999 -0.15%	1.001 0.10%
$\eta_D$ $\Delta\eta_D$	0.729	0.518 -28.9%	0.536 -26.4%	0.559 -23.4%	0.577 -20.8%	0.596 -18.2%	0.61 -16.3%
$J$ $\Delta J$	0.533	0.359 -32.6%	0.371 -30.3%	0.384 -27.8%	0.397 -25.6%	0.410 -23.1%	0.418 -21.5%
$K_T$ $\Delta K_T$	0.183	0.224 22.1%	0.221 20.8%	0.219 19.3%	0.217 18.4%	0.213 16.4%	0.211 15.1%
$10K_Q$ $\Delta 10K_Q$	0.250	0.338 35.3%	0.331 32.5%	0.321 28.6%	0.314 26.0%	0.306 22.5%	0.300 20.2%

#### 5.5.4. The impact of biofouling on the flow around the fouled ship hull in the self-propulsion test

Within this subsection, the impact of biofouling on the flow around the fouled ship hull in self-propulsion test is presented. Since the propeller has influence on the velocity and pressure distribution only in the region extending two propeller diameters upstream [151], [250], only the region including this region and region downstream the propeller is analysed. It should be noted that velocity, pressure and wall shear stress distributions are almost the same in the remaining regions around the fouled hull as in the resistance test, presented in subsection 5.3.4.

Pressure distributions are non-dimensionalised by dividing pressure with  $\frac{1}{2}\rho v^2$  and shown for the region near the stern of KCS (Figure 5.79), KVLCC2 (Figure 5.80) and BC (Figure 5.81). Similarly to the impact of biofouling on the  $C_p$  distribution near the stern obtained within the resistance tests, the presence of biofouling causes the decrease in  $C_p$  values near the stern of investigated ships. This can be clearly seen if the obtained  $C_p$  distribution for smooth ship is compared to the one for ship with the fouling condition R1 H.

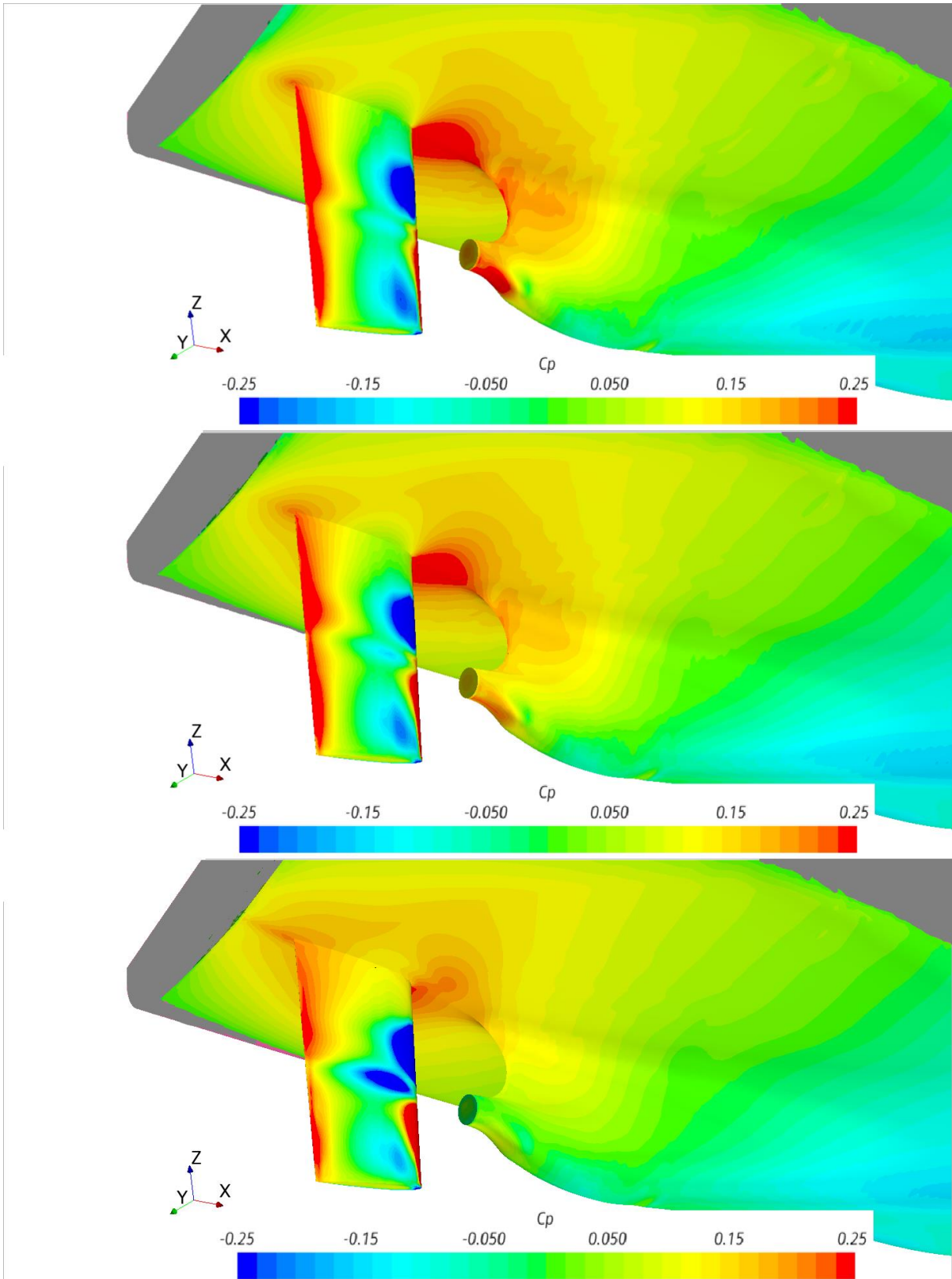


Figure 5.79 The impact of biofouling on  $C_p$  distribution for the region near the stern for smooth KCS (upper), KCS with the fouling condition R2 B (middle) and KCS with the fouling condition R1 H (lower)

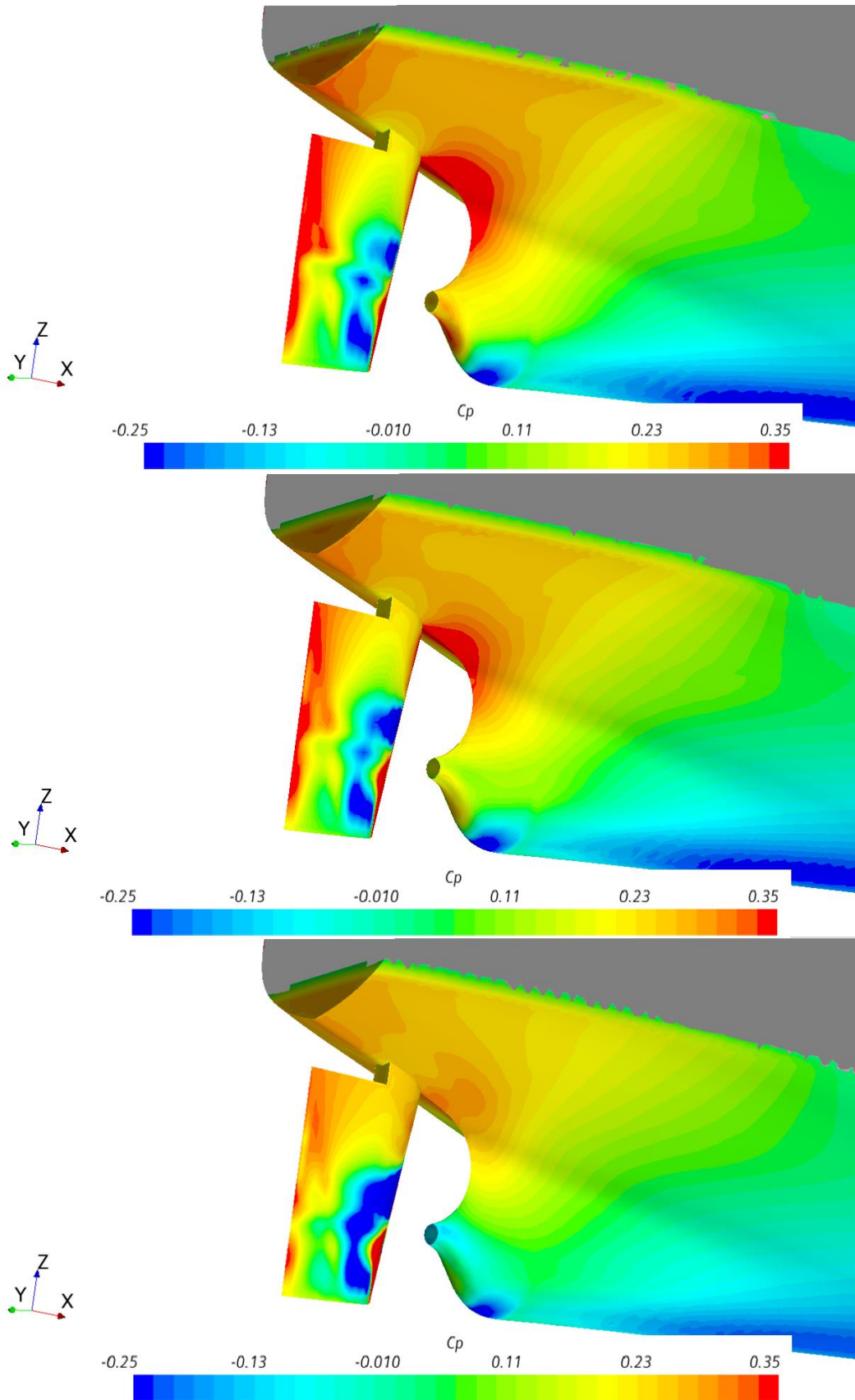


Figure 5.80 The impact of biofouling on  $C_p$  distribution for the region near the stern for smooth KVLCC2 (upper), KVLCC2 with the fouling condition R2 B (middle) and KVLCC2 with the fouling condition R1 H (lower)

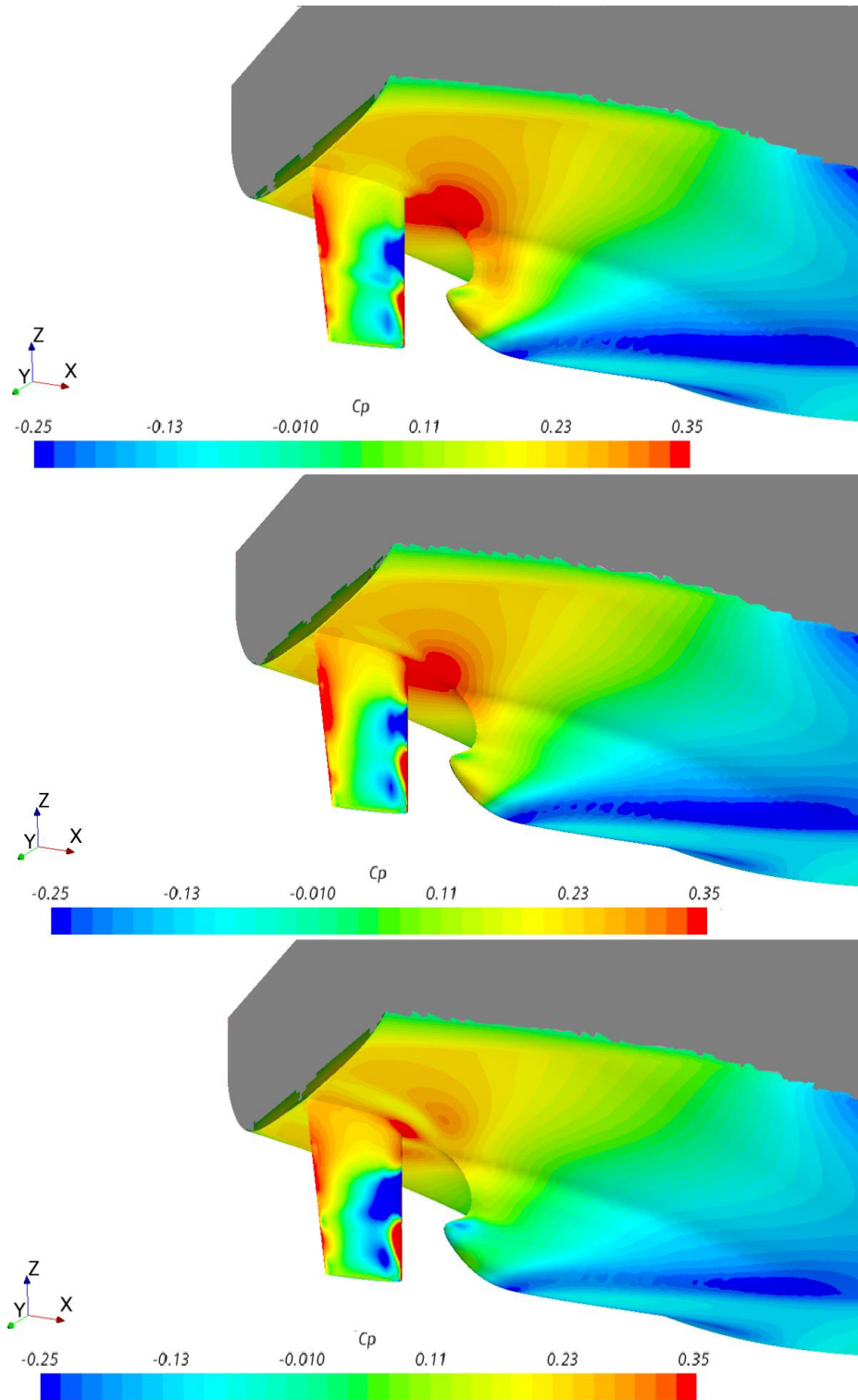


Figure 5.81 The impact of biofouling on  $C_p$  distribution for the area near the stern of smooth BC (upper), BC with the fouling condition R2 B (middle) and BC with the fouling condition R1 H (lower)

While the impact of biofouling on  $C_p$  distribution is the same in resistance and self-propulsion tests, this is not the case for the impact of biofouling on the velocity distribution downstream the propeller. In Figure 5.82, Figure 5.83 and Figure 5.84 the obtained velocity distributions downstream the propeller at the symmetry plane for smooth ships, ships with the fouling

condition R2 B and ships with the fouling condition R1 H are presented. From these figures, it is clear that due to the presence of biofouling, the flow downstream the propeller is accelerated, which can be ascribed to the increase in  $n$  due to biofouling, Figure 5.75. Thus, the propeller in fouled condition accelerates the flow more than in smooth condition, since the self-propulsion point for fouled conditions is reached at higher  $n$  due to the detrimental effect of the hull and propeller biofouling. This can be easily noticed from Figure 5.82, Figure 5.83 and Figure 5.84, where the blue region, which represents more accelerated flow, is significantly darker for fouled conditions than for smooth conditions. On the other hand, upstream the propeller the presence of biofouling causes the decrease in the velocity distribution, which as expected. Thus, the wake fractions for fouled conditions are higher in comparison with smooth conditions, as presented in Table 5.53 – Table 5.58.

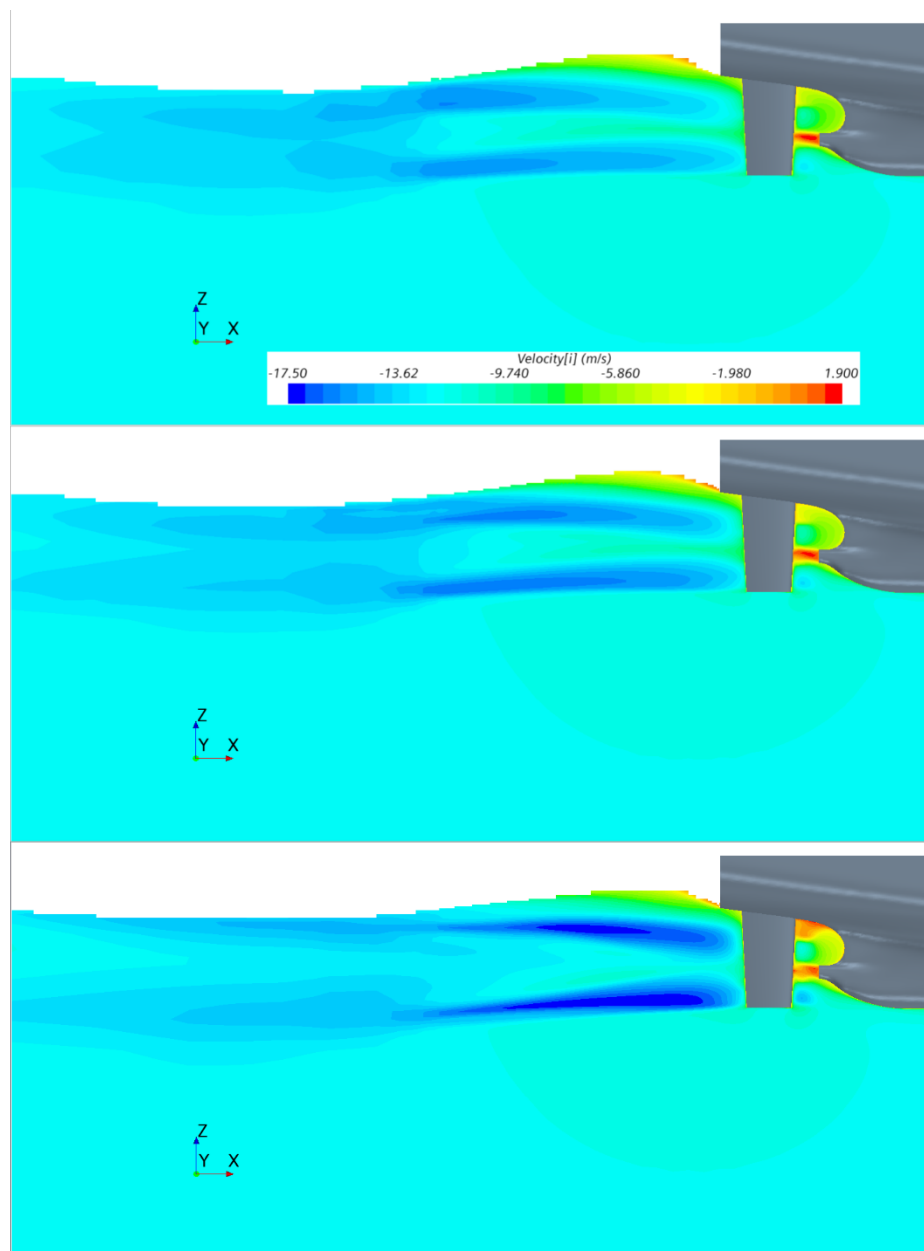


Figure 5.82 The impact of biofouling on the velocity distribution downstream the propeller at the symmetry plane for smooth KCS (upper), KCS with the fouling condition R2 B (middle) and KCS with the fouling condition R1 H (lower)

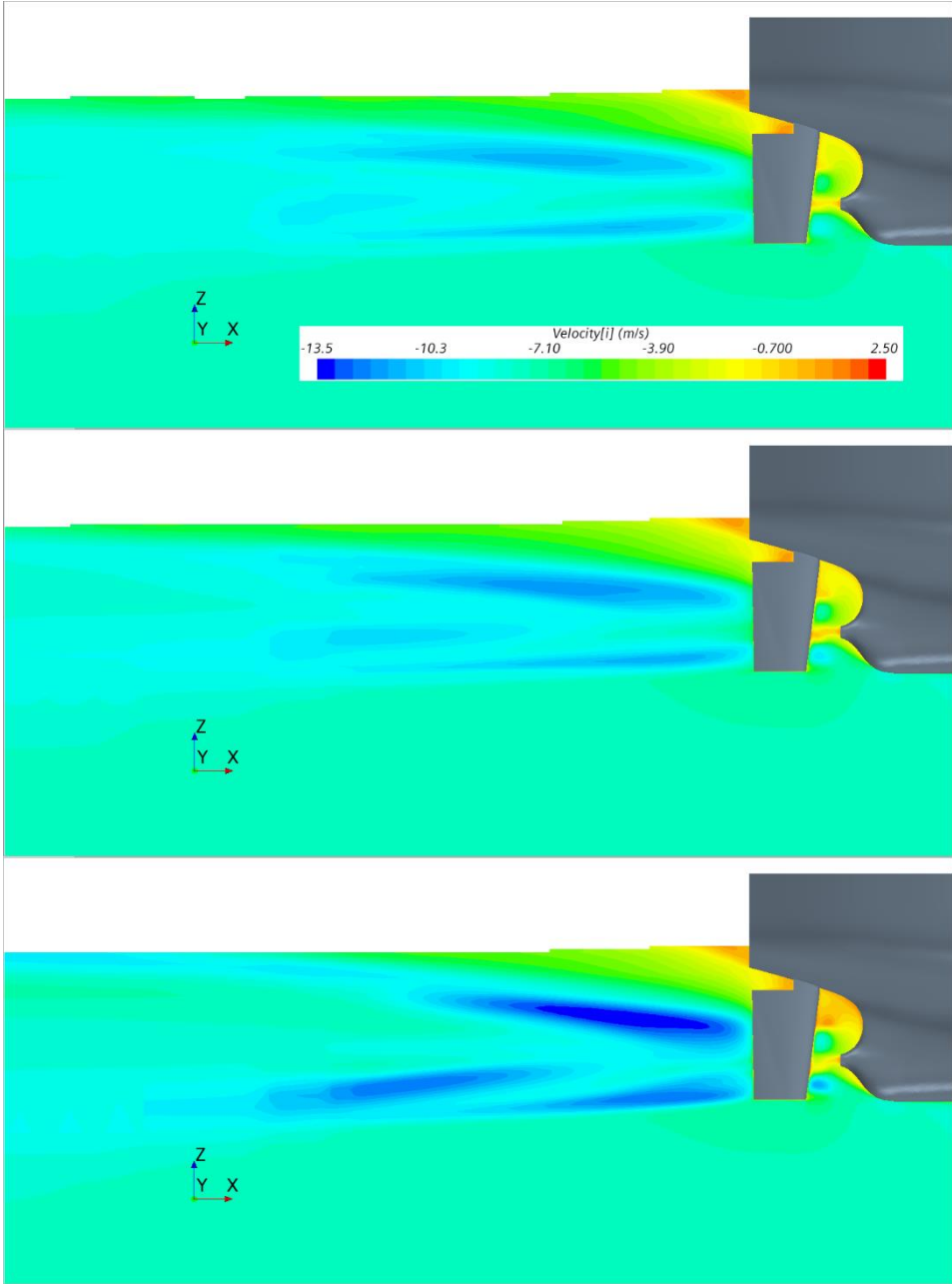


Figure 5.83 The impact of biofouling on the velocity distribution downstream the propeller at the symmetry plane for smooth KVLCC2 (upper), KVLCC2 with the fouling condition R2 B (middle) and KVLCC2 with the fouling condition R1 H (lower)



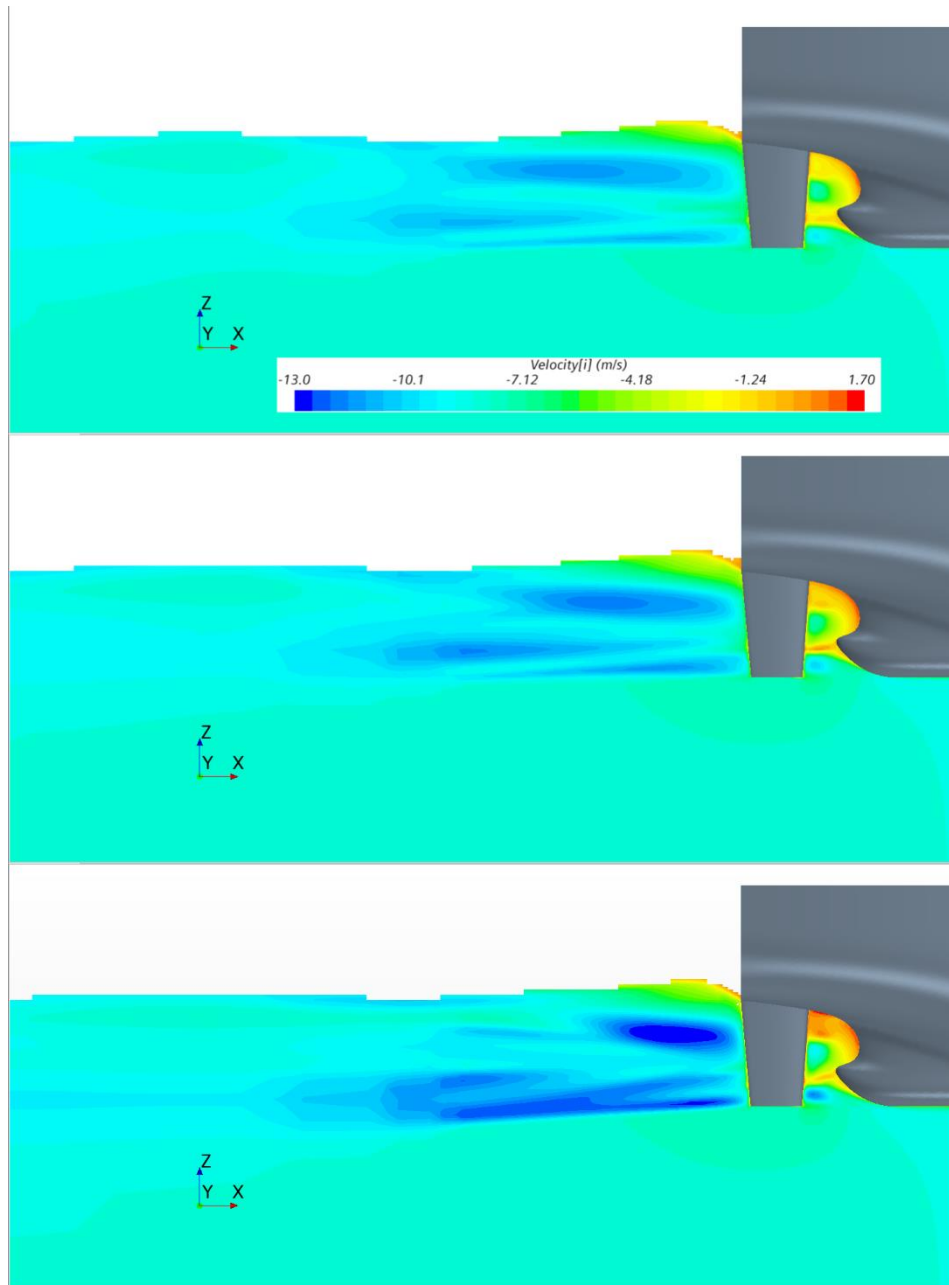


Figure 5.84 The impact of biofouling on the velocity distribution downstream the propeller at the symmetry plane for smooth BC (upper), BC with the fouling condition R2 B (middle) and BC with the fouling condition R1 H (lower)

Within Figure 5.85, Figure 5.86 and Figure 5.87 the obtained axial velocities non-dimensionalised with  $v$  are presented. From these figures the impact of biofouling can be noticed. Thus, due to the presence of biofouling, the axial velocity is accelerated downstream the propeller, which is evident if the obtained axial velocity contours for smooth ship are compared with the ones for ship with the fouling condition R1 H.

The impact of biofouling on the other distributions and flow characteristics, such as  $k^+$  and  $\tau_w$  distributions, turbulent kinetic energy contours, boundary layer thickness, wave patterns, wave heights etc., is the same as presented in subsection 5.3.4. Obviously, the before-mentioned distributions and flow characteristics are slightly different within self-propulsion test in comparison to the ones obtained within resistance test downstream the propeller and in the

region extending two propeller diameters upstream. Namely, the propeller accelerates the flow and consequently increases the rate of shear in the boundary layer. In that way, the propeller increases the frictional resistance of the ship hull and reduces the pressure over the stern of the hull causing the increase in the pressure resistance. Because of this, the propeller alters the resistance of the ship and therefore the thrust exceeds the ship resistance. This can be explained as a resistance augment, but usually it is defined as thrust deduction through thrust deduction fraction, equation (2.42) [73].

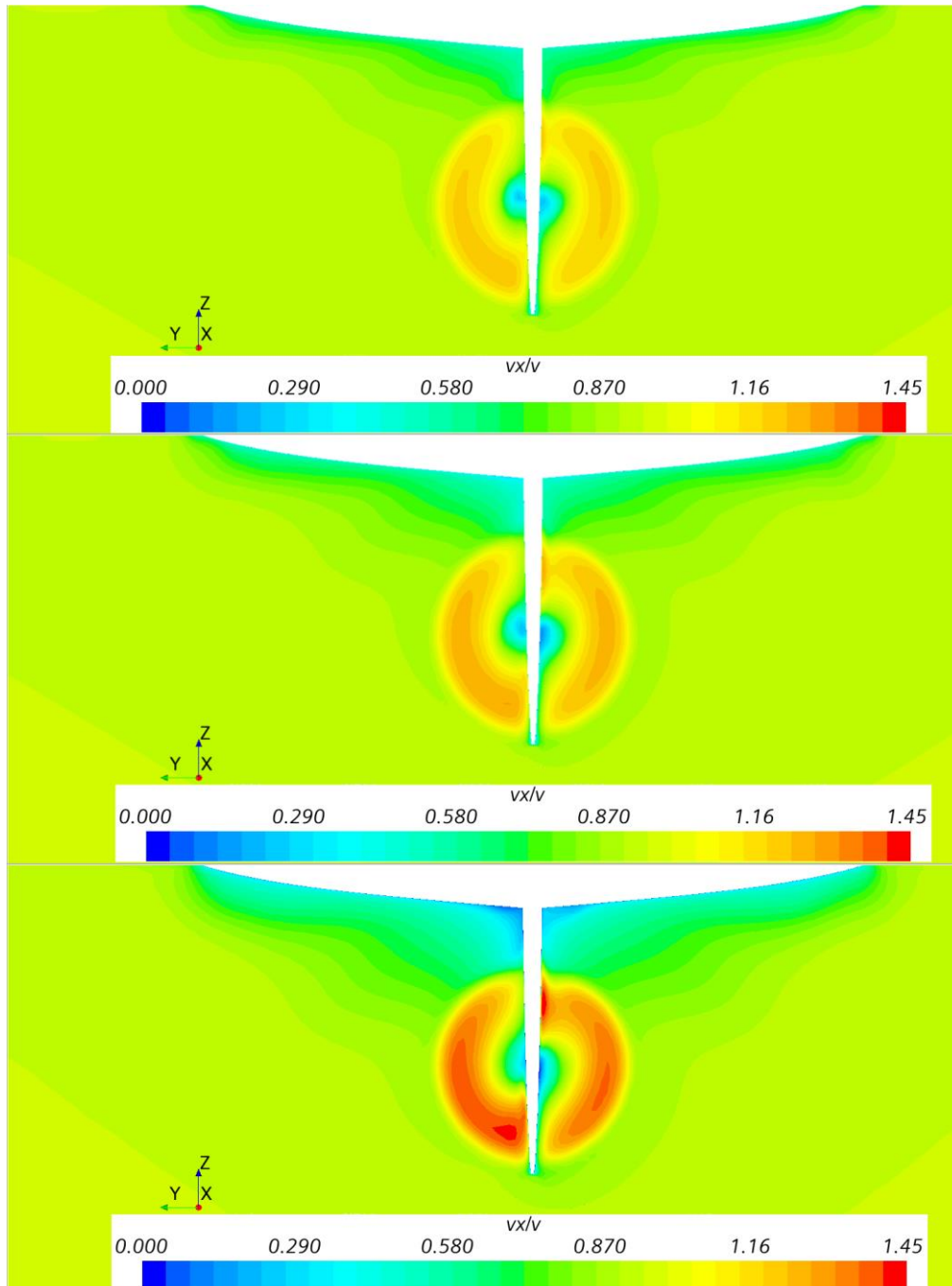


Figure 5.85 The obtained axial velocity contours ( $v_x/v$ ) at the plane  $x = 2$  m for smooth KCS (upper), KCS with the fouling condition R2 B (middle) and KCS with the fouling condition R1 H (lower)

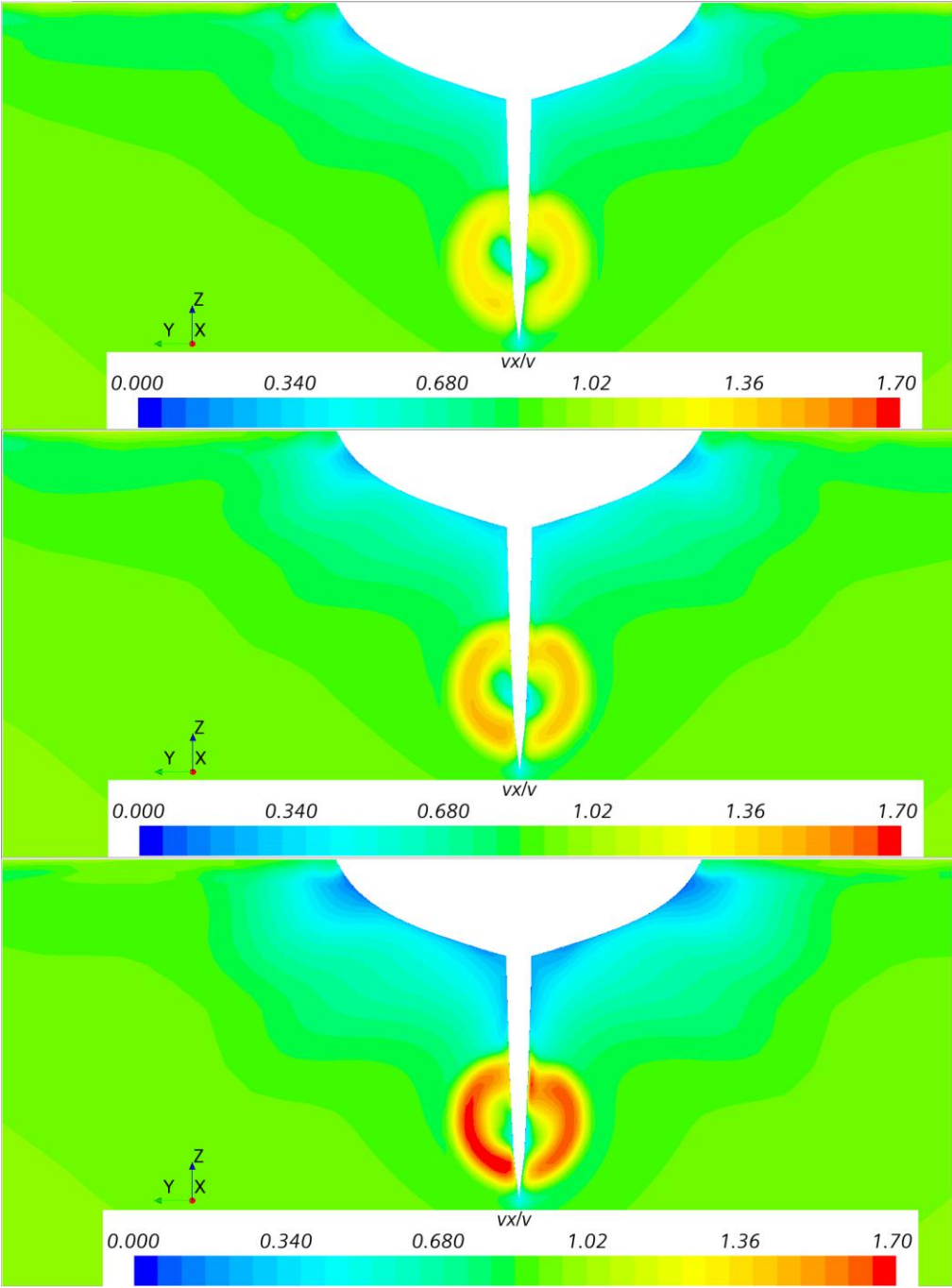


Figure 5.86 The obtained axial velocity contours ( $v_x/v$ ) at the plane  $x = 2.5$  m for smooth KVLCC2 (upper), KVLCC2 with the fouling condition R2 B (middle) and KVLCC2 with the fouling condition R1 H (lower)

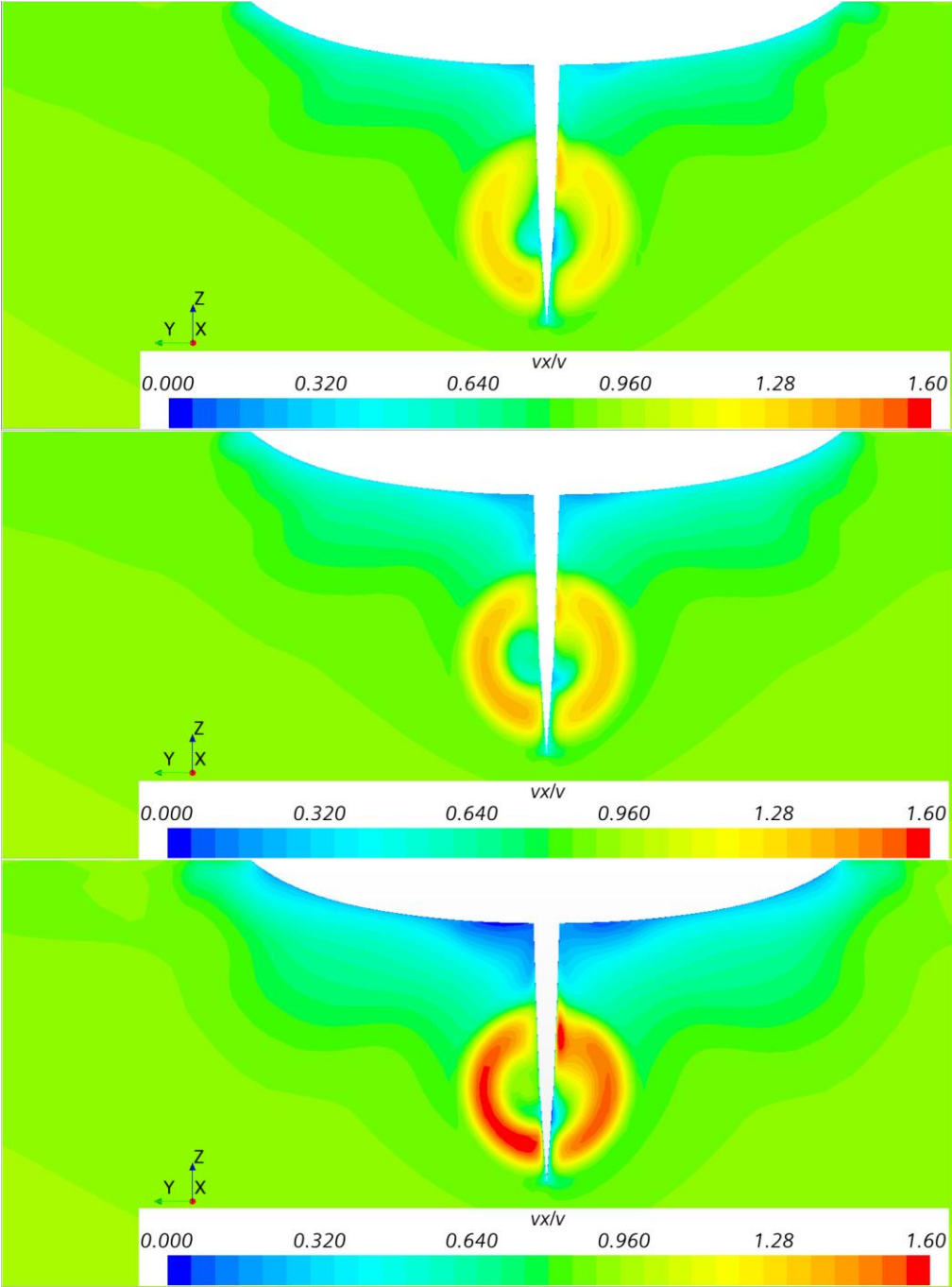


Figure 5.87 The obtained axial velocity contours ( $v_x/v$ ) at the plane  $x = 1.5$  m for smooth BC (upper), BC with the fouling condition R2 B (middle) and BC with the fouling condition R1 H (lower)

## 6. The performance prediction method for fouled surfaces

It is known that hull and propeller surface condition is important for the ship fuel consumption, however it is decisive that ship operators or ship owners carry out hull and propeller cleaning optimally. Thus, delayed hull and propeller cleaning add costs due to increased fuel consumption, while early or too often cleanings can be costly over time. In order to accurately optimize the ship and propeller maintenance schedule it is crucial to estimate the impact of biofouling or surface roughness on the ship performance. The accurate assessment of this impact will enable ship operator or ship owner relatively easy prediction of costs as well as savings on potential maintenance. What is more, due to reduction of the fuel consumption GHG emission will be reduced as well and IMO requirements will be more easily fulfilled. The assessment of the impact of biofouling on the ship performance can be performed in various ways as described in subsection 1.3. The application of CFD approach is one of the most comprehensive ways to analyse this impact. Nevertheless, it is important to notice that it may be challenging for less experienced users to perform such study [172]. Moreover, even for experienced users, numerical simulations require significant computational effort and certain time for pre-processing and post-processing. This can be important drawback, since in the optimization of maintenance schedule, it is important to rapidly determine the impact of biofouling on the ship performance. Thus, for a given fouling or surface condition it is important to estimate the fuel consumption rapidly and thereafter the performance indicator in order to decide whether it is necessary to clean the ship hull or propeller. Oliveira et al. [64] proposed the application of  $k_s$  and  $\Delta U^+$  model presented in [188] as a novel performance indicator within ISO 19030 method [56]. In that way, a comparison amongst ships, increased accuracy in comparison of a ship to itself over time and the assessment of penalties under operating conditions which differ from the past data is enabled. However, the authors have assumed that  $\Delta P_E$  and  $\Delta P_D$  due to the presence of biofouling are the same, i.e. that the impact of biofouling on the propulsion efficiency is negligible. As presented in subsection 5.5.3,  $\Delta P_D$  is higher than  $\Delta P_E$  in case of fouled hull and propeller. What is more, even if propeller is clean, the wake field around fouled ship is different from the wake field around smooth ship (subsection 5.3.4) and consequently propeller behind the fouled hull will operate at different  $J$ . Because of this, the assumption that  $\Delta P_E$  and  $\Delta P_D$  due to the presence of biofouling are the same will lead to certain errors. Accordingly, the robust performance prediction method for fouled surfaces which could determine  $\Delta P_D$  reliably is required. Based on the detail literature review and obtained results within this thesis, the newly proposed performance prediction method for fouled surfaces is proposed and presented in this section.

### 6.1. The newly proposed performance prediction method for fouled surfaces

The current performance prediction methods proposed by ITTC consider roughness effects through roughness allowance and these effects are related to coating roughness. Roughness allowance is defined with  $k_s$  and as suggested in [73] if  $k_s$  values are determined for a given surface condition, different  $k_s$  values can be utilized instead of the standard value of 150  $\mu\text{m}$ . It is very important to notice that  $k_s$  value cannot be determined with roughness measurements, but with hydrodynamic measurements which cannot be performed for a ship in service. As

claimed in [71], due to variety of surface roughness on a ship related to applied coating, damage, slime or other types of fouling, a new formulation for performance prediction will include several formulations or at least one formulation but with roughness type dependent parameters. Furthermore, the utilization of  $\Delta U^+$  is the most likely candidate for the improvement of roughness allowance [71]. In that sense, a new performance prediction method for fouled surfaces is proposed, however this method can be extended on rough surfaces as well if the  $\Delta U^+$  model for a given surface condition is known. The newly proposed method is proposed on the basis of ITTC 1978 PPM as well as PPM proposed by Kresic and Haskell [76], however it accounts the increases in  $C_F$  using the Granville similarity law scaling method. In that way, if  $\Delta U^+$  model for a given surface condition is known, the impact of biofouling on the ship performance can be determined utilizing the proposed method and roughness measurements. The applicability of the proposed method will be demonstrated in this thesis for one fouling type, i.e. biofilm. It should be noted that the proposed method relies on the certain assumptions and therefore it has certain limitations and that it is more suitable for fouling types with lower fouling severities as it will be explained in the following text.

The ITTC 1978 PPM represents an extrapolation procedure which can be used for the assessment of ship resistance and propulsion characteristics based on the performed towing tank experiments. The proposed method can be applied using two different input data: either towing tank measurements, i.e. resistance, open water and self-propulsion tests using the British method, or CFD results for the smooth surface condition for a full-scale ship. The method differs slightly depending on the input data. Firstly, the method using towing tank measurements as the input data will be presented.

The flow chart of the proposed method can be seen in Figure 6.1. It should be noted that subscript M refers to model scale and S to full-scale. As can be seen from this figure, the procedure starts with the extrapolation of total resistance, i.e. the assessment of total resistance for fouled surface. Total resistance coefficient for fouled or rough full-scale ship is determined as follows:

$$C_{TR} = (1+k)C_{FR} + C_W \quad (6.1)$$

where  $C_{FR}$  is the frictional resistance coefficient for fouled or rough full-scale ship calculated as follows:

$$C_{FR} = C_{FS} + \Delta C_F \quad (6.2)$$

where  $C_{FS}$  is determined with ITTC 1957 model-ship correlation line, equation (2.28), and  $\Delta C_F$  is determined as:

$$\Delta C_F = C_{F0R} - C_{F0S} \quad (6.3)$$

where  $C_{F0R}$  is the frictional resistance coefficient for the rough flat plate having the same length as a ship obtained using the Granville similarity law scaling method and  $C_{F0S}$  is the frictional resistance coefficient for the smooth flat plate having the same length as a ship obtained using the Schoenherr friction line, equation (2.25).

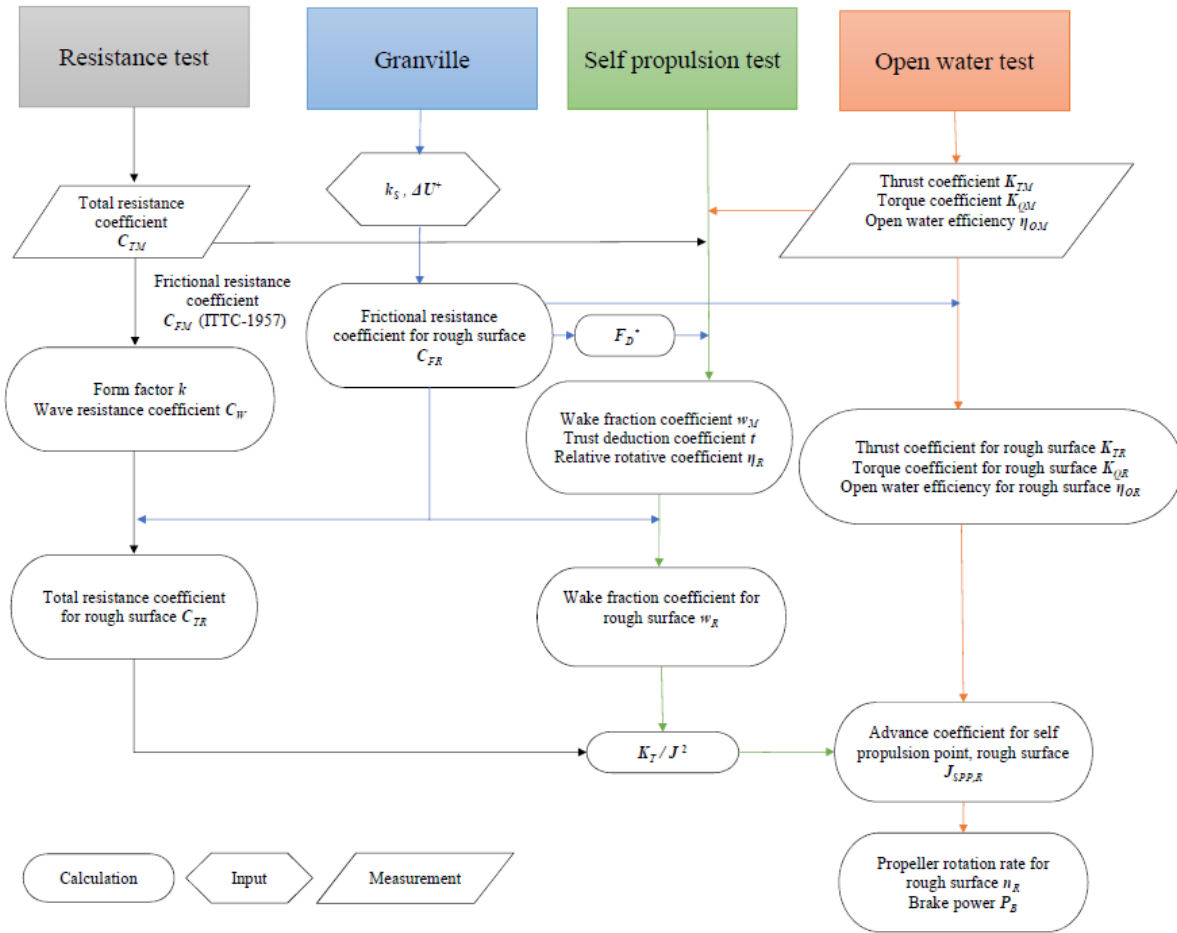


Figure 6.1 Flow chart of the proposed method

Once  $C_{FR}$  is obtained, the skin friction correction force can be determined as follows:

$$F_D^* = \frac{1}{2} \rho v_M^2 S_M (C_{FM} - C_{FR}) \quad (6.4)$$

where  $v_M$  is the model speed and  $S_M$  is the wetted surface of ship model.

This force is applied to the ship model as an external assisting tow force during towing tank measurements in order to achieve the theoretically correct propeller loads during self-propulsion test. It takes into account the difference in skin friction coefficients between the ship model and full-scale ship [257]. Thus, self-propulsion point is obtained once  $F_D^* = R_T - T$ . Since  $C_{FR}$  is dependent on the fouling condition it is important that self-propulsion tests are carried out using the British method, i.e. the load varying method. In that case, the self-propulsion point can be defined for various fouling conditions. It should be noted that  $F_D^*$  is defined in the same way as in ITTC 1978 PPM, however  $C_{FR}$  is defined using the Granville similarity law scaling method.

For the self-propulsion point  $t_M$ ,  $\eta_{RM}$  and  $w_M$  values are obtained. One of the assumptions within this performance prediction method is that  $t_M$  and  $\eta_{RM}$  values are the same as for the fouled ship in full-scale, as done in [76] and demonstrated within [162]. Since the scale effects

on  $t_M$  [155] and  $\eta_{RM}$  values are negligible, within ITTC 1978 PPM it is assumed that  $t_M$  and  $\eta_{RM}$  values are the same as for the full-scale ship. As presented in Section 5.5, the impact of biofilm and hard fouling on  $\eta_R$  and  $1-t$  is negligible. Furthermore, the impact of hard fouling on  $1-t$  is minimal and within the numerical uncertainty of the prediction of  $1-t$ . Consequently, the assumption that  $t_M$  and  $\eta_{RM}$  values are the same as for the fouled ship in full-scale is valid. The impact of biofouling or roughness on  $w$  is accounted as follows:

$$w_R = (t + 0.04) + (w_M - t - 0.04) \frac{C_{FR}}{C_{FM}} \quad (6.5)$$

The first term on the right hand side of equation (6.5) is an inviscid wake component, which is considered to be independent on the biofouling or roughness presence, while the second term is a viscous wake component, which is scaled using  $C_F$ .

The impact of biofouling or roughness on the open water characteristics is considered in the same way as presented in [76]:

$$K_{TR} = K_{TS} - \Delta K_{TD} - \Delta K_{TL} \quad (6.6)$$

$$K_{QR} = K_{QS} - \Delta K_{QD} - \Delta K_{QL} \quad (6.7)$$

where  $K_{TS}$  and  $K_{QS}$  are the thrust and torque coefficient for full-scale smooth propeller,  $\Delta K_{TD}$  and  $\Delta K_{QD}$  are the changes in thrust and torque coefficients as a result of increased drag coefficient ( $C_D$ ) of the propeller blade sections and  $\Delta K_{TL}$  and  $\Delta K_{QL}$  are the changes in thrust and torque coefficients as a result of reduced lift coefficient ( $C_L$ ) of the propeller blade sections. It should be noted that  $\Delta K_{TD}$  and  $\Delta K_{QD}$  values are obtained using the equations (2.37) and (2.38), while  $\Delta K_{TL}$  and  $\Delta K_{QL}$  are obtained using the equations (2.56) and (2.57).

As presented in Section 5.4 due to the presence of biofouling on the propeller surfaces,  $C_D$  of the propeller blade sections will increase, which may be attributed to the increased  $\tau_w$  on the propeller surfaces. On the other hand, due to the presence of biofouling on the propeller surfaces,  $C_L$  will decrease, which may be attributed to the decreased pressure difference between pressure and suction side of fouled propeller in comparison with smooth one. In order to obtain correct  $\Delta K_{TD}$ ,  $\Delta K_{QD}$ ,  $\Delta K_{TL}$  and  $\Delta K_{QL}$ ,  $\Delta C_D$  is calculated as  $C_{DS} - C_{DR}$  and  $\Delta C_L = -1.1\Delta C_D$ . It is known that  $C_D$  of the propeller blade sections can be divided as follows [154]:

$$C_D = 2c_{d,2d}c_f \quad (6.8)$$

where  $c_{d,2d}$  is the section form drag calculated as  $c_{d,2d} = 1 + 2\frac{t}{c}$  and  $c_f$  is the contribution of the friction. It should be noted that  $t$  represents the maximum thickness at radius  $0.75R$ , while  $c$  represents the chord length at radius  $0.75R$ .



Within the newly proposed method it is considered that the impact of biofouling on  $c_{d,2d}$  is negligible as done in [76]. On the other hand,  $c_f$  for fouled propeller is taken to be the same as the frictional resistance coefficient of the fouled flat plate having a length equal to  $c$  and calculated for the resultant velocity of the flow approaching the propeller blade section ( $v_R$ ) at radius  $0.75R$  in full-scale using the Granville similarity law scaling method. This represents the main difference from the method proposed in [76], where the authors estimated  $C_{DR}$  according to equation (2.40). In equation (2.40) the contribution of friction in the drag coefficient of propeller blade sections, i.e.  $c_f$  is taken into account with equation for the frictional resistance coefficient of rough flat plate [77]. In that way it is justified to take  $c_f$  as  $C_F$  for fouled flat plate calculated using the Granville similarity law scaling method.

Thrust and torque coefficients for full-scale smooth propeller ( $K_{TS}, K_{QS}$ ) are calculated using ITTC 1978 PPM, equations (2.35), (2.36), (2.37) and (2.38). Since in this thesis, the impact of biofouling on the resistance, open water and self-propulsion characteristics is determined as the obtained change in certain hydrodynamic characteristic in comparison with the smooth surface condition,  $C_{DS}$  is determined as follows:

$$C_{DS} = 2 \left( 1 + \frac{t}{c} \right) C_{FS} \quad (6.9)$$

where  $C_{FS}$  is the frictional resistance coefficient of the flat plate having the same length as the chord length at radius  $0.75R$  obtained for  $v_R$  using the Schoenherr friction line. It should be noted that  $C_{DM}$  is obtained using equation (2.39).

In this way, the impact of biofouling on the propeller performance in open water conditions obtained using the newly proposed method will be assessed in comparison with the smooth surface condition.

The load of the full-scale propeller for fouled ship is calculated as follows:

$$\frac{K_{TR}}{J^2} = \frac{S}{2D^2} \frac{C_{TR}}{(1-t)(1-w_R)^2} \quad (6.10)$$

Using the load of the full-scale propeller for fouled ship,  $J$  for the self-propulsion point of fouled ship and propeller ( $J_{SPP,R}$ ) is read off from the open water diagram for full-scale fouled propeller. With the obtained  $J_R$ ,  $n_R$  can be easily calculated and the delivered power for fouled condition is determined as follows:

$$P_{DR} = 2\pi n_R Q_R \quad (6.11)$$

where  $Q_R$  is the propeller torque for the fouled propeller and ship.

The newly proposed PPM for fouled surfaces presented with Figure 6.1 can be comprehend as an extrapolation procedure. For the input data extensive towing tank measurements must be available. One of the example of such input data is given in [230], where the extensive towing tank measurements for BC are given. Thus, the applicability of the proposed method will be

presented for BC by the comparison of the resistance, open water and propulsion characteristics obtained using the newly proposed method and CFD approach. It has to be mentioned that the newly proposed method can be utilised with CFD results as input data obtained for the smooth surface condition in full-scale. The benefits of doing so are twofold. Firstly, CFD can be considered as a valuable tool for the determination of the ship performance [159]. Thus, CFD baselines are the most appropriate for fulfilment of the high requirements of ISO performance monitoring standard [56]. Consequently, CFD is explicitly allowed for obtaining power-speed-draught-trim database for specific ship within procedure for performance monitoring described in ISO 19030 [258]. Secondly, in this way the best comparison between the obtained results using the CFD approach and newly proposed method is enabled, since the same input data will be utilised for the assessment of the impact of biofouling on the ship performance.

If the CFD results obtained for the smooth surface condition in full-scale are used as an input data, the newly proposed method is only slightly modified. Thus,  $C_{TR}$  is determined in the same way using equation (6.1), except the fact that  $1+k$ ,  $C_{FS}$  and  $C_W$  are obtained from CFD simulations. The values of  $t$  and  $\eta_R$  for the fouled ship are considered to be the same as the ones obtained in CFD simulations for smooth full-scale ship and  $w_R$  is determined as follows:

$$w_R = (t + 0.04) + (w_S - t - 0.04) \frac{C_{FR}}{C_{FM}} \quad (6.12)$$

where  $w_S$  is determined by numerical simulations for the smooth full-scale ship.

The impact of biofouling on the propeller performance in open water conditions is taken into account through equations (6.6) and (6.7), where  $K_{TS}$  and  $K_{QS}$  are determined by numerical simulations for the smooth full-scale ship. Finally, the propeller load can be determined using equation (6.10) and once  $J_{SPP,R}$  is read off from diagram,  $n_R$  and  $P_{DR}$  can be easily determined. The applicability of the proposed method once CFD results for the smooth surface condition in full-scale are used as an input data is shown by comparison with CFD approach. Thus, the obtained impact of biofouling on the resistance, open water and propulsion characteristics using the proposed performance prediction method (PPM) and CFD approach are compared and this comparison is presented in the following section.

As can be seen, the newly proposed PPM for fouled surfaces is consisted of several numerical operations, which may generate numerical errors, if performed manually for each investigated fouling condition and ship. Therefore, an in-house numerical code is developed using Python [171] to allow robust and fast solution. The developed code requires several input data presented in Table 6.1. The code is developed for a case when full-scale CFD results are used as an input data and. Once all input data is imported, the code determines the resistance, open water and propulsion characteristics for the required fouling condition in short time using before mentioned equations and Granville similarity law scaling method. Namely, for the determination of  $\Delta C_{F0}$ , the numerical code firstly calculates  $C_{F0S}$  and  $C_{F0R}$  for the flat plate having the same length as a ship using Granville similarity law scaling method and Schoenherr friction line as presented in Section 2.3.3. Thereafter the code calculates  $C_{FR}$  using equation (6.2),  $R_W$ ,  $C_{TR}$  and determines the impact of biofouling on propeller open water characteristics. After that,  $w_R$  using equation (6.12) is calculated which is used for the calculation of propeller

load using equation (6.10). Once propeller load for fouled propeller is determined, code finds an intersection, i.e.  $J_{SPP,R}$ , between propeller load curve and curve for thrust coefficient of a fouled propeller. For this  $J_{SPP,R}$  value  $K_{QR}$  can be determined using  $\eta_R$  and finally  $P_{DR}$  and  $n_R$  can be determined.

Table 6.1 Input data for in-house numerical code

Data type	Input data
ship and propeller	ship speed, waterline length, wetted surface area, chord length and maximum thickness at radius $r = 0.75R$ , propeller diameter, pitch and number of blades
fluid and flow properties	density, dynamic viscosity, von Karman constant
surface condition of a ship	fouling height, percentage of surface coverage and fouling type
resistance characteristics for smooth ship	form factor, total resistance, frictional resistance
open water characteristics for smooth propeller	thrust and torque coefficients determined for several advance coefficients
self-propulsion characteristics	thrust deduction fraction, relative rotative efficiency and wake fraction

## 6.2. The impact of biofouling on the ship performance obtained using the newly proposed PPM

Within this subsection the obtained results using the newly proposed PPM are presented. Furthermore, the results are compared with the ones obtained using the CFD approach in order to demonstrate the applicability of the proposed method. This subsection is divided into two parts: in the first part the results from the towing tank measurements are utilised as an input data, while in the second part the CFD results for the smooth full-scale ship are utilised as an input data for PPM.

### 6.2.1. The impact of biofouling on the ship performance obtained using the newly proposed PPM and towing tank measurements as an input data

A wooden model of BC in a scale  $\lambda = 25.2$  was subjected to extensive towing tank measurements [230]. Resistance and self-propulsion tests were performed in Brodarski institute, Zagreb in the towing tank No 1, which has length equal to 276.3 m, width 12.5 m and depth 6m. It should be noted that no blockage effects were taken into account due to relatively large dimensions of the towing tank and the fact that ship model was investigated at low  $Fn$ . Resistance tests were performed at various  $Fn$  in order to obtain the resistance curve. Self-propulsion tests were carried out by means of the British method at seven velocities with the stock propeller. The stock propeller is WB propeller presented in Table 5.2, made in scale  $\lambda = 25.2$ . During open water test the rotational speed of the propeller was kept constant ( $n = 18.01$  rps), while the advance velocity was varied. In that way, the whole range of  $J$  was examined. The towing tank results are extrapolated to full-scale values using the newly proposed PPM. It should be noted that the obtained extrapolated values slightly deviate from

the ones presented in subsection 5.5.2, since open water characteristics for full-scale smooth propeller were scaled for the purpose of the newly proposed PPM, as previously mentioned. Thus, the obtained  $RD$  between extrapolated and CFD results for  $P_D$  is equal to 1.20%, for  $n$  is equal to 1.68% and for  $R_T$  is equal to 5.25%. In addition to the obtained  $RD$  between extrapolated and CFD results for  $T$  is equal to 1.80%, for  $Q$  to -0.47%, for  $J$  to 5.94%, for  $1-w$  to 7.73%, for  $1-t$  to 3.39%, for  $\eta_r$  to 3.82%, for  $\eta_o$  to 4.38% and for  $\eta_D$  to 4.00%.

The obtained impact of biofilm on  $\Delta P_D$ ,  $\Delta P_E$  and  $\Delta n$  is presented in Figure 6.2. From this figure it can be seen that satisfactory agreement between the results obtained using the newly proposed PPM and CFD is achieved. Thus, due to the presence of biofilm, the increase in  $P_D$  vary from 0.40% (PPM) and 2.63% (CFD) for R7 B up to 42.12% (PPM) and 39.53% (CFD) for R2 B, while the increase in  $P_E$  vary from 0.00% (PPM) for R5 B and R7 B and 0.70% (CFD) for R7 B up to 27.85% (PPM) and 29.36% (CFD) for R2 B. From the obtained results it is clear that  $\Delta P_D$  and  $\Delta P_E$  are not the same as already noted. The increase in  $n$  due to the presence of biofilm ranges from 0.06% (PPM) and 0.41% (CFD) for R7 B up to 8.02% (PPM) and 7.57% (CFD) for R2 B.

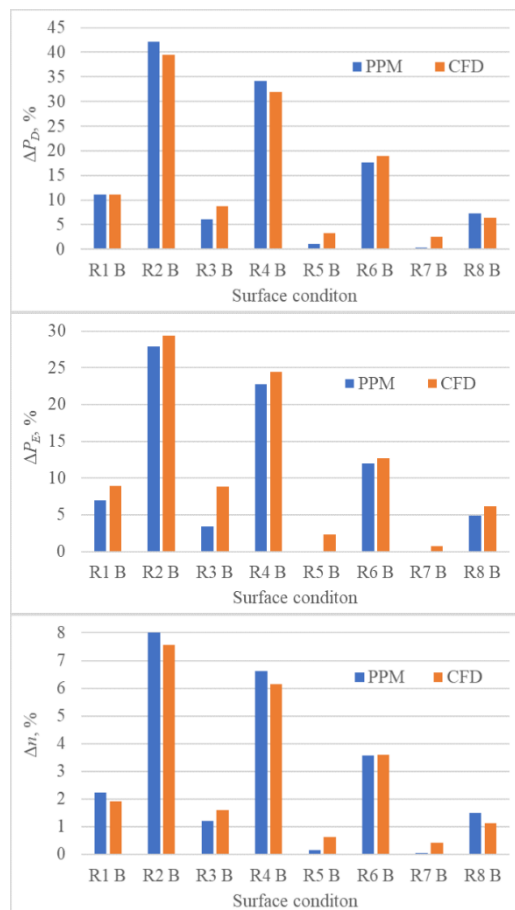


Figure 6.2 The obtained impact of biofilm on  $\Delta P_D$  (upper),  $\Delta P_E$  (middle) and  $\Delta n$  (lower)

The impact of biofilm on the open water characteristics is presented in Table 6.2 - Table 6.4 for three  $J$  values around the self-propulsion point. From these tables it can be seen that low  $RD$  between the open water characteristics using the newly proposed PPM and CFD are obtained. Thus, the highest  $RD$  between certain open water characteristic obtained using newly proposed

PPM and CFD is achieved for smooth propeller at  $J = 0.48$  and for  $10K_Q$ . This  $RD$  is equal to 6.26% and all other  $RD$  are below this value. In addition to, the obtained  $K_T$  and  $10K_Q$  values using the newly proposed PPM are higher than the obtained  $K_T$  and  $10K_Q$  values using CFD for both smooth and fouled conditions. Consequently, the obtained  $\Delta K_T$ ,  $\Delta(10K_Q)$  and  $\Delta\eta_o$  are almost the same for both methods. This highlights the importance of using the same input data for testing the applicability of the newly proposed method, i.e. it can be assumed that if the same input data is used for both methods the obtained  $RD$  would be lower. Therefore in the following section, the same input data for PPM and CFD approach will be used in order to prove this assumption. However, it should be noted that slightly higher decrease in  $K_T$  and slightly lower increase in  $10K_Q$  values are obtained using newly proposed PPM in comparison with CFD, which resulted in very similar prediction of  $\Delta\eta_o$ .

Table 6.2 The impact of biofilm on  $K_T$  and  $\Delta K_T$  in open water test

	$K_T$ $J = 0.48$	$K_T$ $J = 0.56$	$K_T$ $J = 0.64$	$\Delta K_T, \%$ $J = 0.48$	$\Delta K_T, \%$ $J = 0.56$	$\Delta K_T, \%$ $J = 0.64$
CFD S	0.2038	0.1725	0.1401	/	/	/
EX S ( $RD$ )	0.2154 (5.676%)	0.1821 (5.547%)	0.1485 (5.974%)	/	/	/
CFD R1 B	0.2022	0.1707	0.1381	-0.797	-1.040	-1.407
EX R1 B ( $RD$ )	0.2130 (5.375%)	0.1797 (5.276%)	0.1461 (5.755%)	-1.080	-1.294	-1.611
CFD R2 B	0.1994	0.1679	0.1353	-2.167	-2.673	-3.421
EX R2 B ( $RD$ )	0.2099 (5.275%)	0.1765 (5.153%)	0.1429 (5.588%)	-2.539	-3.037	-3.772
CFD R3 B	0.2026	0.1711	0.1386	-0.605	-0.795	-1.095
EX R3 B ( $RD$ )	0.2136 (5.434%)	0.1803 (5.330%)	0.1466 (5.814%)	-0.833	-0.999	-1.244
CFD R4 B	0.2002	0.1687	0.1361	-1.770	-2.212	-2.871
EX R4 B ( $RD$ )	0.2107 (5.261%)	0.1774 (5.151%)	0.1437 (5.609%)	-2.156	-2.580	-3.205
CFD R5 B	0.2031	0.1718	0.1392	-0.347	-0.428	-0.608
EX R5 B ( $RD$ )	0.2145 (5.598%)	0.1811 (5.463%)	0.1475 (5.946%)	-0.422	-0.507	-0.634
CFD R6 B	0.2019	0.1705	0.1379	-0.914	-1.168	-1.553
EX R6 B ( $RD$ )	0.2129 (5.427%)	0.1796 (5.326%)	0.1459 (5.804%)	-1.148	-1.375	-1.711
CFD R7 B	0.2035	0.1722	0.1397	-0.142	-0.153	-0.254
EX R7 B ( $RD$ )	0.2150 (5.661%)	0.1817 (5.507%)	0.1481 (5.987%)	-0.157	-0.191	-0.242
CFD R8 B	0.2029	0.1715	0.1390	-0.458	-0.569	-0.786
EX R8 B ( $RD$ )	0.2142 (5.578%)	0.1809 (5.448%)	0.1472 (5.931%)	-0.551	-0.662	-0.826

Also, from Table 6.2 - Table 6.4 it can be seen that even though fouling conditions slightly differ in terms of  $k_{eff}$ , the obtained  $\Delta K_T$ ,  $\Delta(10K_Q)$  and  $\Delta\eta_o$  differ among various fouling conditions for both methods. This proves the applicability of the proposed PPM, as well as the

applicability of the CFD approach for capturing the effects of biofilm on open water characteristics even for fouling conditions which have slight variation in  $k_{eff}$ . Thus, the applicability of the newly proposed PPM in the prediction of changes in open water characteristics due to the presence of the biofilm is demonstrated.

Table 6.3 The impact of biofilm on  $K_Q$  and  $\Delta K_Q$  in open water test

	$10K_Q$ $J = 0.48$	$10K_Q$ $J = 0.56$	$10K_Q$ $J = 0.64$	$\Delta(10K_Q), \%$ $J = 0.48$	$\Delta(10K_Q), \%$ $J = 0.56$	$\Delta(10K_Q), \%$ $J = 0.64$
CFD S	0.269	0.239	0.205	/	/	/
EX S (RD)	0.286 (6.256%)	0.250 (4.746%)	0.215 (4.893%)	/	/	/
CFD R1 B	0.273	0.243	0.209	1.466	1.514	1.702
EX R1 B (RD)	0.289 (5.733%)	0.253 (4.309%)	0.218 (4.428%)	0.966	1.091	1.251
CFD R2 B	0.277	0.246	0.212	2.760	2.940	3.395
EX R2 B (RD)	0.293 (5.750%)	0.257 (4.358 %)	0.222 (4.420 %)	2.270	2.559	2.929
CFD R3 B	0.272	0.242	0.208	1.179	1.215	1.359
EX R3 B (RD)	0.288 (5.800%)	0.253 (4.359%)	0.217 (4.486%)	0.745	0.841	0.966
CFD R4 B	0.276	0.246	0.212	2.557	2.696	3.083
EX R4 B (RD)	0.292 (5.605%)	0.256 (4.213%)	0.221 (4.288%)	1.928	2.173	2.489
CFD R5 B	0.271	0.241	0.207	0.580	0.614	0.679
EX R5 B (RD)	0.287 (6.042%)	0.252 (4.551%)	0.216 (4.699%)	0.377	0.428	0.493
CFD R6 B	0.273	0.243	0.209	1.496	1.561	1.768
EX R6 B (RD)	0.289 (5.765%)	0.253 (4.331%)	0.218 (4.440%)	1.027	1.159	1.329
CFD R7 B	0.270	0.240	0.206	0.251	0.274	0.286
EX R7 B (RD)	0.287 (6.139%)	0.251 (4.628%)	0.216 (4.790%)	0.140	0.161	0.188
CFD R8 B	0.271	0.241	0.207	0.746	0.789	0.882
EX R8 B (RD)	0.288 (5.989%)	0.252 (4.505%)	0.217 (4.643%)	0.493	0.558	0.642

The impact of biofilm on the propulsion characteristics obtained using newly proposed PPM and CFD is presented in Table 6.5 and Table 6.6. As can be seen from Table 6.5 the obtained  $1-t$  and  $1-w$  using newly proposed PPM are higher than the ones obtained using CFD. It should be noted that the obtained  $RD$  between  $1-t$  using newly proposed PPM and CFD are relatively low and the highest  $RD$  is obtained for R6 B and it is equal to 4.316%. Higher  $RD$  between  $1-w$  obtained using newly proposed PPM and CFD are obtained and the highest  $RD$  is obtained for R2 B and it is equal to 11.449%. Higher  $RD$  were expected and can be ascribed to inability of body force method to estimate precisely the interaction between ship hull and propeller, since the propeller is not discretized, and only its effects are modelled [246]. Thus, higher  $RD$  between numerical and experimental results for  $1-w$  have been noticed in other studies as well [253], [254]. On the other hand, the obtained  $K_T$  and  $10K_Q$  in self-propulsion

test using newly proposed PPM are lower than the ones obtained using CFD, Table 6.6. The obtained  $RD$  between  $K_T$  and  $K_Q$  obtained using the newly proposed PPM and CFD are relatively low. Thus,  $RD$  for  $K_T$  are lower than 4.06% and for  $K_Q$  than 5%. The prediction of  $K_T$  and  $10K_Q$  depends on many parameters, including resistance, open water and propulsion characteristics. Namely, the accuracy of prediction of the propeller load defined with equation (6.10) depends on accurate assessment of  $C_T$  and  $1-t$  and  $1-w$ . Also, in order to find  $J$  value for the self-propulsion point as accurate as possible, which defines  $K_T$  and  $10K_Q$ , the accurate assessment of propeller open water characteristics is important as well. Therefore, it can be concluded that the obtained  $RD$  for  $K_T$  and  $10K_Q$  are satisfactory.

It should be noted that if towing tank results are used as an input, firstly those results must be extrapolated to full-scale and thereafter fouling effects are determined. Because of this, the obtained  $RD$  for  $1-t$  and  $1-w$ , as well as for  $K_T$  and  $10K_Q$  are higher. This can be clearly seen if the obtained results for  $1-t$ ,  $1-w$ ,  $K_T$  and  $10K_Q$  obtained using newly proposed PPM and CFD are compared for smooth hull and propeller. Therefore, in order to represent the applicability of the proposed PPM in the prediction of fouling effects solely, the same input values should be used. Thus, in the following subsection the obtained results using full-scale CFD simulations will be used as an input data. In that way, the scale effects are eliminated, and only fouling effects are considered.

As can be seen from Table 6.5 and Table 6.6, the obtained changes in  $1-t$ ,  $1-w$ ,  $K_T$  and  $10K_Q$  due to the presence of biofilm obtained using newly proposed PPM and CFD are relatively similar. Thus, both methods have predicted very low  $\Delta(1-t)$  and the highest discrepancy between these methods is obtained for R6 B, where CFD has predicted decrease in  $1-t$  equal to -0.489% and PPM has predicted increase in  $1-t$  equal to 0.404%. PPM has predicted lower decreases in  $1-w$  in comparison with the CFD approach and the highest discrepancy between these methods is obtained for R2 B, where CFD has predicted decrease in  $1-w$  equal to -4.892% and PPM has predicted decrease in  $1-w$  equal to -1.606%. Both methods have predicted an increase in  $K_T$  and  $10K_Q$  due to the presence of biofilm, except for R5 B and R7 B for PPM, where very slight decrease in  $K_T$  is obtained. It should be noted that the obtained increases are relatively similar. Thus, the highest discrepancy between the newly proposed PPM and CFD approach in the prediction of  $\Delta K_T$  is obtained for R2 B, where CFD has predicted increase in  $K_T$  equal to 11.374% and PPM equal to 8.545%. The obtained increases in  $10K_Q$  are even more similar, i.e. the highest discrepancy between the newly proposed PPM and CFD approach in the prediction of  $(\Delta 10K_Q)$  is obtained for R3 B, where CFD has predicted increase in  $K_Q$  equal to 3.735% and PPM equal to 2.392%. It should be noted that a slime represents a fouling with low roughness length scale and because of this the most of the numerically obtained changes in the propulsion characteristics are lower than the simulation uncertainty.

Table 6.4 The impact of biofilm on  $\eta_o$  and  $\Delta\eta_o$  in open water test

	$\eta_o$ $J = 0.48$	$\eta_o$ $J = 0.56$	$\eta_o$ $J = 0.64$	$\Delta\eta_o, \%$ $J = 0.48$	$\Delta\eta_o, \%$ $J = 0.56$	$\Delta\eta_o, \%$ $J = 0.64$
CFD S	0.5781	0.6430	0.6951	/	/	/
EX S (RD)	0.5750 (-0.546%)	0.6479 (0.765%)	0.7023 (1.030%)	/	/	/
CFD R1 B	0.5650	0.6266	0.6736	-2.270	-2.555	-3.096
EX R1 B (RD)	0.5633 (-0.298%)	0.6326 (0.968%)	0.6824 (1.312%)	-2.027	-2.359	-2.826
CFD R2 B	0.5502	0.6077	0.6490	-4.833	-5.491	-6.630
EX R2 B (RD)	0.5479 (-0.409%)	0.6126 (0.802%)	0.6565 (1.159%)	-4.702	-5.456	-6.511
CFD R3 B	0.5677	0.6300	0.6780	-1.803	-2.025	-2.460
EX R3 B (RD)	0.5660 (-0.306%)	0.6361 (0.971%)	0.6869 (1.311%)	-1.566	-1.824	-2.188
CFD R4 B	0.5535	0.6120	0.6547	-4.257	-4.818	-5.813
EX R4 B (RD)	0.5519 (-0.285%)	0.6178 (0.941%)	0.6633 (1.307%)	-4.006	-4.652	-5.555
CFD R5 B	0.5726	0.6361	0.6859	-0.962	-1.076	-1.318
EX R5 B (RD)	0.5704 (-0.379%)	0.6419 (0.913%)	0.6944 (1.232%)	-0.796	-0.931	-1.121
CFD R6 B	0.5642	0.6255	0.6721	-2.414	-2.726	-3.302
EX R6 B (RD)	0.5626 (-0.279%)	0.6317 (0.994%)	0.6812 (1.347%)	-2.152	-2.505	-3.000
CFD R7 B	0.5756	0.6400	0.6911	-0.433	-0.466	-0.579
EX R7 B (RD)	0.5733 (-0.410%)	0.6457 (0.881%)	0.6992 (1.182%)	-0.297	-0.352	-0.429
CFD R8 B	0.5710	0.6341	0.6833	-1.235	-1.387	-1.694
EX R8 B (RD)	0.5690 (-0.348%)	0.6401 (0.943%)	0.6920 (1.272%)	-1.039	-1.213	-1.459

Table 6.5 The impact of biofilm on  $1-t$  and  $1-w$

Surface condition	$1-t_{CFD}$	$1-w_{CFD}$	$1-t_{EX}$ RD, %	$1-w_{EX}$ RD, %	$\Delta(1-t_{CFD})$ , %	$\Delta(1-w_{CFD})$ , %	$\Delta(1-t_{EX})$ , %	$\Delta(1-w_{EX})$ , %
S	0.764	0.653	0.790 3.389%	0.703 7.726%	/	/	/	/
R1 B	0.768	0.640	0.792 3.196%	0.700 9.340%	0.426%	-1.895%	0.238%	-0.426%
R2 B	0.767	0.621	0.798 3.965%	0.692 11.449%	0.378%	-4.892%	0.938%	-1.606%
R3 B	0.761	0.641	0.791 3.908%	0.702 9.396%	-0.383%	-1.730%	0.117%	-0.207%
R4 B	0.768	0.625	0.796 3.698%	0.694 10.906%	0.454%	-4.181%	0.755%	-1.353%
R5 B	0.767	0.649	0.790 3.002%	0.703 8.385%	0.376%	-0.608%	0.000%	0.000%
R6 B	0.761	0.630	0.793 4.316%	0.698 10.791%	-0.489%	-3.484%	0.404%	-0.739%
R7 B	0.762	0.646	0.790 3.740%	0.703 8.884%	-0.338%	-1.063%	0.000%	0.000%
R8 B	0.768	0.645	0.791 3.977%	0.701 8.628%	0.423%	-1.127%	0.169%	-0.300%



Table 6.6 The impact of biofilm on  $K_T$  and  $10K_Q$

Surface condition	$K_{T,CFD}$	$10K_{Q,CFD}$	$K_{T,EX}$ <i>RD</i> , %	$10K_{Q,EX}$ <i>RD</i> , %	$\Delta K_{T,CFD}$ , %	$\Delta(10K_{Q,CFD})$ , %	$\Delta K_{T,EX}$ , %	$\Delta(10K_{Q,EX})$ , %
S	0.183	0.250	0.180 -1.557%	0.240 -3.756%	/	/	/	/
R1 B	0.191	0.262	0.184 -3.759%	0.250 -4.711%	4.419%	5.055%	2.084%	4.013%
R2 B	0.204	0.280	0.196 -4.058%	0.271 -3.201%	11.374%	12.102%	8.545%	12.748%
R3 B	0.187	0.259	0.182 -2.950%	0.246 -5.002	2.257%	3.735%	0.811%	2.392%
R4 B	0.201	0.275	0.193 -4.024%	0.266 -3.463%	9.906%	10.370%	7.152%	10.706%
R5 B	0.184	0.253	0.180 -2.538%	0.242 -4.558%	0.693%	1.428%	-0.310%	0.583%
R6 B	0.193	0.267	0.188 -2.949%	0.254 -4.724%	5.528%	6.949%	4.035%	5.874%
R7 B	0.184	0.253	0.180 -1.883%	0.241 -4.856%	0.215%	1.379%	-0.117%	0.220%
R8 B	0.189	0.257	0.183 -3.231%	0.246 -4.140	3.407%	2.972%	1.649%	2.561%

### 6.2.2. The impact of biofouling on the ship performance obtained using the newly proposed PPM and full-scale CFD results as an input data

The proper demonstration of the applicability of the newly proposed PPM for fouled surfaces can be shown if full-scale CFD results are used as an input data as described earlier. The newly proposed PPM is then only slightly altered. Thus, total resistance coefficient for fouled or rough surface is calculated according to equation (6.1) and the procedure is described in Section 6.1, however  $C_F$ ,  $1+k$  and  $C_W$  are determined from full-scale CFD simulations for smooth surface. It should be noted that  $C_F$  and  $1+k$  are determined from DBS and it is assumed that  $1+k$  and  $C_W$  are independent on the presence of fouling. Also,  $t$  and  $\eta_R$  are considered to be the same for smooth and fouled surface and wake fraction coefficient for fouled surface is determined as follows:

$$w_R = (t + 0.04) + (w_S - t - 0.04) \frac{C_{FR}}{C_{FS}} \quad (6.13)$$

where  $w_S$  is the wake fraction for smooth ship and  $C_{FS}$  is the frictional resistance coefficient for smooth ship obtained using full-scale numerical simulations.

The impact of biofouling on the open water characteristics is taken into account using equations (6.6) and (6.7). Obviously, the obtained open water characteristics using full-scale numerical simulations represent  $K_{TS}$  and  $K_{QS}$ . It should be noted that  $\Delta K_{TD}$  and  $\Delta K_{QD}$  values are obtained using equations (2.37) and (2.38), while  $\Delta K_{TL}$  and  $\Delta K_{QL}$  are obtained using equations (2.56) and (2.57). However,  $\Delta C_D$  is determined as the difference between  $C_{DS}$  and  $C_{DR}$ , where  $C_{DS}$  is determined according to equation (6.9), while  $C_{DR}$  is determined as:

$$C_{DR} = 2 \left( 1 + \frac{t}{c} \right) C_{FR} \quad (6.14)$$

where  $C_{FR}$  is the frictional resistance coefficient of the fouled flat plate having the same length as the chord length at radius  $0.75R$  obtained for  $v_R$  using the Granville similarity law scaling method.

Thereafter, the propeller load is determined according to equation (6.10) and  $J_R$  for the self-propulsion point can be determined using the open water characteristics for fouled propeller. Finally,  $n_R$  can be easily determined and  $P_{D,R}$  is calculated according to equation (6.11). As it can be noticed, the newly proposed PPM is almost the same if as an input towing tank results or full-scale CFD results are used. The only difference when using full-scale CFD results, is that the scaling of those results is avoided.

In order to demonstrate the applicability of the newly proposed PPM for fouled surfaces, the obtained results using the newly proposed PPM and CFD approach are compared for all three investigated ships.

The obtained impact of biofilm on  $\Delta P_D$ ,  $\Delta P_E$  and  $\Delta n$  is presented in Figure 6.3, Figure 6.4 and Figure 6.5. From Figure 6.3, it can be seen that satisfactory agreement between the results obtained using the newly proposed PPM and CFD is achieved. Thus, due to the presence of biofilm,  $\Delta P_D$  for KCS range from 0.89% (PPM) and 1.40% (CFD) for R7 B up to 43.44% (PPM) and 36.33% (CFD) for R2 B, for KVLCC2 from 0.46% (PPM) and 0.36% (CFD) for R7 B up to 40.86% (PPM) and 40.38% (CFD) for R2 B and for BC from 0.37% (PPM) and 0.41% (CFD) for R7 B up to 42.79% (PPM) and 39.53% (CFD) for R2 B. Although for all ships satisfactory agreement between  $\Delta P_D$  obtained using the newly proposed PPM and CFD is obtained, it is clear that the highest discrepancies in  $\Delta P_D$  obtained using the newly proposed PPM and CFD are obtained for KCS. This can be attributed to the fact that KCS has the highest portion of  $R_w$  in  $R_T$  and since within proposed PPM it is considered that  $R_w$  is not affected due to the presence of fouling, the obtained  $\Delta P_D$  for KCS are most affected by this assumption. Namely as shown in subsection 5.3.3, the presence of biofouling causes the decrease in  $R_w$  and consequently  $R_T$  predicted using the newly proposed PPM is slightly higher than the one predicted using CFD. This can be seen in Figure 6.4, where the obtained  $\Delta P_E$  for KCS, KVLCC2 and BC are shown. The higher  $R_T$  leads to higher propeller load, which results in higher prediction of  $P_D$ . The increase in  $P_E$  for KCS range from 0% (PPM) and 0.48% (CFD) for R7 B up to 30.62% (PPM) and 25.76% (CFD) for R2 B, for KVLCC2 from 0% (PPM) and 0.01% (CFD) for R7 B up to 31.52% (PPM) and 27.95% (CFD) for R2 B and for BC from 0% (PPM) and 0.70% (CFD) for R7 B up to 29.51% (PPM) and 29.36% (CFD) for R2 B. The obtained  $\Delta n$  for KCS due to the presence of biofilm range from 0.17% (PPM) and 0.12% (CFD) for R7 B up to 6.43% (PPM) and 4.85% (CFD) for R2 B, for KVLCC2 from 0.02% (PPM) and 0.09% (CFD) for R7 B up to 7.38% (PPM) and 8.05% (CFD) for R2 B and for BC from 0.06% (PPM) and 0.41% (CFD) for R7 B up to 8.51% (PPM) and 7.57% (CFD) for R2 B. The highest discrepancies in the predicted  $\Delta n$  between PPM and CFD approach is obtained for KCS, which was expected as explained earlier.

The proposed method can adequately account for fouling effects on increases in  $T$  and  $Q$  as well, which can be seen from Figure 6.6. The obtained  $\Delta T$  for KCS due to the presence of

biofilm range from 0.06% (PPM) and 0.28% (CFD) for R7 B up to 30.66% (PPM) and 26.15% (CFD) for R2 B, for KVLCC2 from 1.88 % (PPM) for R5 B and 0.07% (CFD) for R7 B up to 31.53% (PPM) and 27.83% (CFD) for R2 B and for BC from 0.01% (PPM) for R5 B and 1.04 % (CFD) for R7 B up to 29.52% (PPM) and 28.87% (CFD) for R2 B. The obtained  $\Delta Q$  for KCS due to the presence of biofilm range from 0.72% (PPM) and 1.27% (CFD) for R7 B up to 34.78% (PPM) and 30.02% (CFD) for R2 B, for KVLCC2 from 0.44 % (PPM) and 0.27% (CFD) for R7 B up to 31.19% (PPM) and 29.92% (CFD) for R2 B and for BC from 0.06% (PPM) and 2.21% (CFD) for R7 B up to 31.59% (PPM) and 29.71% (CFD) for R2 B.

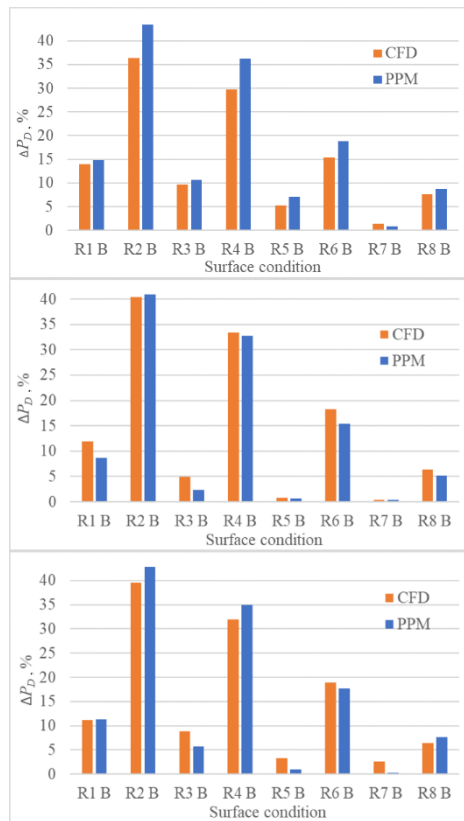


Figure 6.3 The obtained impact of biofilm on  $\Delta P_D$  for KCS (upper), KVLCC2 (middle) and BC (lower)

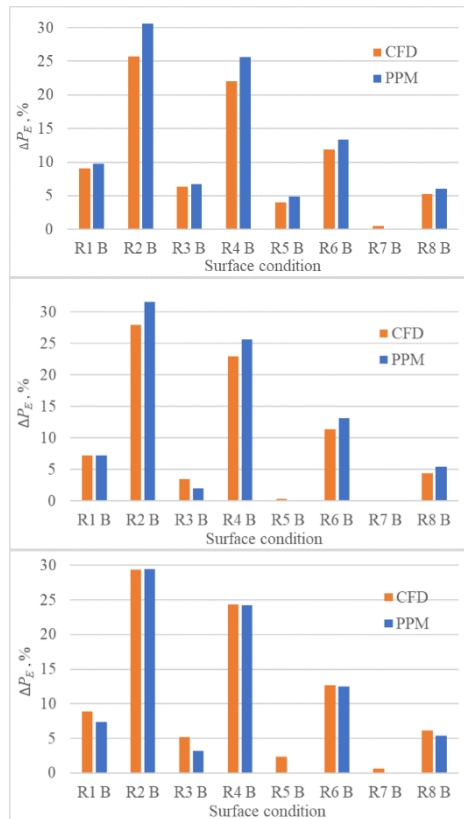


Figure 6.4 The obtained impact of biofilm on  $\Delta P_E$  for KCS (upper), KVLCC2 (middle) and BC (lower)

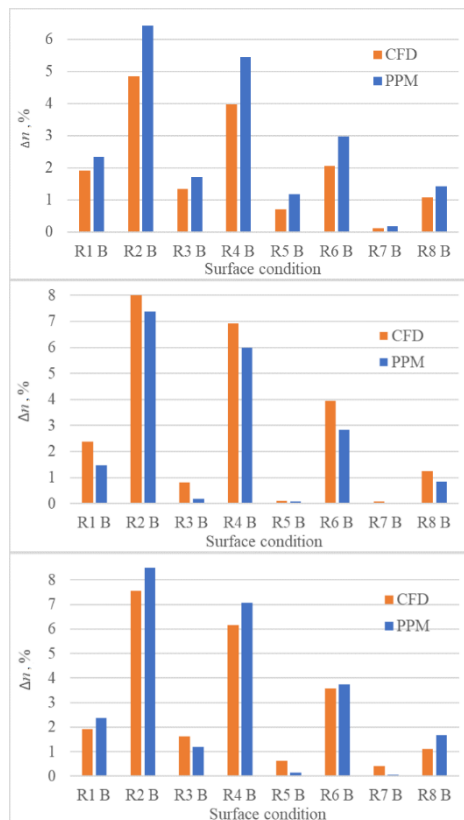


Figure 6.5 The obtained impact of biofilm on  $\Delta n$  for KCS (upper), KVLCC2 (middle) and BC (lower)

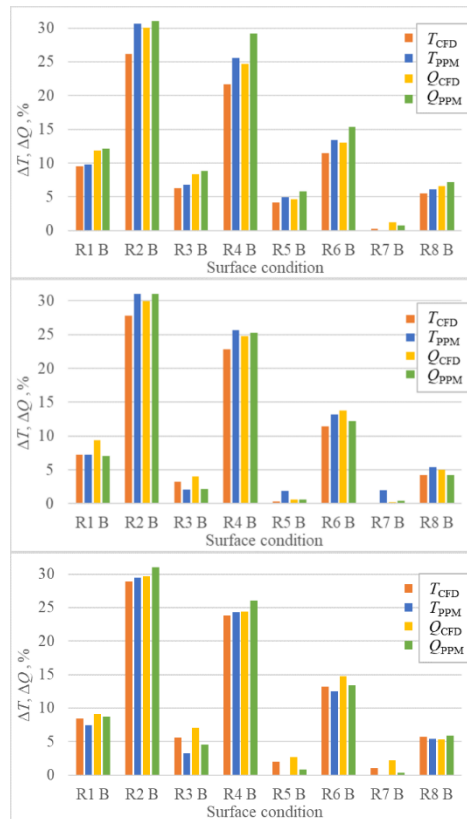


Figure 6.6 The obtained impact of biofilm on  $\Delta T$  and  $\Delta Q$  for KCS (upper), KVLCC2 (middle) and BC (lower)

The obtained open water characteristics for full-scale smooth propellers using CFD are used as one of the inputs for the assessment of the impact of biofouling on the propeller performance with the newly proposed PPM for fouled surfaces. The obtained results using this method are compared with the ones obtained using CFD approach, Table 6.7, Table 6.8 and Table 6.9. This impact is analysed for wide range of  $J$  (the same as for smooth propellers). However, due to large amount of data, this impact is only shown for one  $J$  value around  $J$  value for the self-propulsion point ( $J_{SP}$ ). The impact of biofilm on the propeller performance in open water conditions is assessed well using the proposed PPM in comparison with the CFD approach. Thus, the highest  $RD$  amongst the obtained  $K_{T, EX}$  and  $K_{T, CFD}$  for KP505 at  $J = 0.7$  is obtained for R2 B and it is equal to -1.001%, for KP458 at  $J = 0.5$  for R2 B and it is equal to 1.673%, while for WB at  $J = 0.56$  for R2 B as well and it is equal to -0.552%. The highest  $RD$  amongst the obtained  $10K_{Q, EX}$  and  $10K_{Q, CFD}$  for KP505 at  $J = 0.7$  is obtained for R2 B and is equal to 0.332%, for KP458 at  $J = 0.5$  for R2 B and it is equal to 1.299%, while for WB at  $J = 0.56$  for R2 B as well and it is equal to -0.405%. The highest  $RD$  amongst the obtained  $\eta_{o, EX}$  and  $\eta_{o, CFD}$  for KP505 at  $J = 0.7$  is obtained for R2 B and it is equal to -0.774%, for KP458 at  $J = 0.5$  for R2 B and it is equal to 0.389%, while for WB at  $J = 0.56$  for R2 B as well and it is equal to -0.257%. What is more, the obtained  $RD$  for  $K_T$  at all investigated  $J$  values below  $J$  value for which the curve  $\eta_o$  has its maximum are lower than 1.4% for KP505, 2% for KP458 and 1% for WB propeller. The obtained  $RD$  for  $10K_Q$  at all investigated  $J$  values below  $J$  value for which the curve  $\eta_o$  has its maximum are lower than 0.6% for KP505, 1.6%

for KP458 and 0.6% for WB propeller. Finally, the obtained  $RD$  for  $\eta_o$  at all investigated  $J$  values below  $J$  value for which the curve  $\eta_o$  has it maximum are lower than 0.8% for KP505, 1% for KP458 and 0.4% for WB propeller.

Table 6.7 The comparison between the obtained open water characteristics for KP505 propeller fouled with biofilm at  $J = 0.7$

Surface condition	$K_{T, CFD}$	$10K_{Q, CFD}$	$\eta_{o, CFD}$	$K_{T, EX}$ ( $RD, \%$ )	$10K_{Q, EX}$ ( $RD, \%$ )	$\eta_{o, EX}$ ( $RD, \%$ )
R1 B	0.1776	0.2986	0.6625	0.1767 (-0.482)	0.2976 (-0.325)	0.6614 (-0.157)
R2 B	0.1738	0.3035	0.6382	0.1721 (-1.001)	0.3027 (0.259)	0.6334 (-0.744)
R3 B	0.1782	0.2978	0.6668	0.1775 (-0.416)	0.2968 (-0.332)	0.6662 (-0.084)
R4 B	0.1748	0.3023	0.6440	0.1733 (-0.855)	0.3014 (0.305)	0.6405 (-0.552)
R5 B	0.1794	0.2959	0.6755	0.1789 (-0.269)	0.2952 (-0.225)	0.6752 (-0.044)
R6 B	0.1773	0.2987	0.6614	0.1765 (-0.464)	0.2979 (-0.279)	0.6602 (-0.185)
R7 B	0.1801	0.2946	0.6809	0.1798 (-0.129)	0.2942 (-0.154)	0.6810 (0.026)
R8 B	0.1790	0.2964	0.6727	0.1785 (-0.288)	0.2957 (-0.258)	0.6725 (-0.030)

Table 6.8 The comparison between the obtained open water characteristics for KP458 propeller fouled with biofilm at  $J = 0.5$

Surface condition	$K_{T, CFD}$	$10K_{Q, CFD}$	$\eta_{o, CFD}$	$K_{T, EX}$ ( $RD, \%$ )	$10K_{Q, EX}$ ( $RD, \%$ )	$\eta_{o, EX}$ ( $RD, \%$ )
R1 B	0.1311	0.1661	0.6282	0.1322 (0.809)	0.1669 (0.485)	0.6302 (0.323)
R2 B	0.1277	0.1675	0.6066	0.1299 (1.673)	0.1697 (1.299)	0.6089 (0.369)
R3 B	0.1317	0.1659	0.6319	0.1326 (0.637)	0.1665 (0.351)	0.6337 (0.285)
R4 B	0.1285	0.1672	0.6119	0.1305 (1.492)	0.1690 (1.098)	0.6143 (0.389)
R5 B	0.1329	0.1653	0.6402	0.1334 (0.337)	0.1655 (0.147)	0.6414 (0.190)
R6 B	0.1310	0.1661	0.6274	0.1321 (0.866)	0.1670 (0.539)	0.6295 (0.325)
R7 B	0.1337	0.1649	0.6453	0.1339 (0.154)	0.1649 (0.048)	0.6459 (0.107)
R8 B	0.1325	0.1654	0.6376	0.1331 (0.453)	0.1658 (0.228)	0.6390 (0.225)

Table 6.9 The comparison between the obtained open water characteristics for WB propeller fouled with biofilm at  $J = 0.56$

Surface condition	$K_{T, \text{CFD}}$	$10K_{Q, \text{CFD}}$	$\eta_{o, \text{CFD}}$	$K_{T, \text{EX}}$ (RD, %)	$10K_{Q, \text{EX}}$ (RD, %)	$\eta_{o, \text{EX}}$ (RD, %)
R1 B	0.1707	0.2427	0.6266	0.1702 (-0.314)	0.2418 (-0.382)	0.6273 (0.109)
R2 B	0.1679	0.2461	0.6077	0.1670 (-0.552)	0.2455 (-0.255)	0.6061 (-0.257)
R3 B	0.1711	0.2420	0.6300	0.1707 (-0.263)	0.2412 (-0.331)	0.6307 (0.108)
R4 B	0.1687	0.2456	0.6120	0.1678 (-0.534)	0.2446 (-0.405)	0.6115 (-0.090)
R5 B	0.1718	0.2406	0.6361	0.1716 (-0.095)	0.2401 (-0.178)	0.6369 (0.124)
R6 B	0.1705	0.2428	0.6255	0.1700 (-0.286)	0.2420 (-0.345)	0.6261 (0.100)
R7 B	0.1722	0.2398	0.6400	0.1722 (-0.031)	0.2395 (-0.121)	0.6409 (0.130)
R8 B	0.1715	0.2410	0.6341	0.1713 (-0.120)	0.2405 (-0.213)	0.6349 (0.133)

In Figure 6.7, Figure 6.8 and Figure 6.9 the impact of biofilm on  $K_T$ ,  $10K_Q$  and  $\eta_o$  is shown for one fouling condition, R2 B. The predicted impact of biofilm on  $K_T$ ,  $10K_Q$  and  $\eta_o$  using the newly proposed PPM and CFD is almost the same for KP505 and WB, while for KP458 this impact is slightly underpredicted for  $K_T$  and overpredicted for  $10K_Q$  at lower  $J$  values with PPM. However, it is important to notice that KP458 probably will not operate at lower  $J$  values, since  $\eta_o$  at those  $J$  values is low. In addition to, the impact of biofilm on  $\eta_o$  obtained using the newly proposed PPM and CFD approach is almost the same, except for the highest investigated  $J$ , where the impact of biofilm on  $\eta_o$  is slightly underpredicted using PPM. However, at this  $J$  value, KP458 will not operate, since this  $J$  is higher than  $J$  value for which the curve  $\eta_o$  has its maximum. Therefore, it can be concluded that the impact of biofilm on the propeller performance in open water conditions can be accurately assessed using PPM.

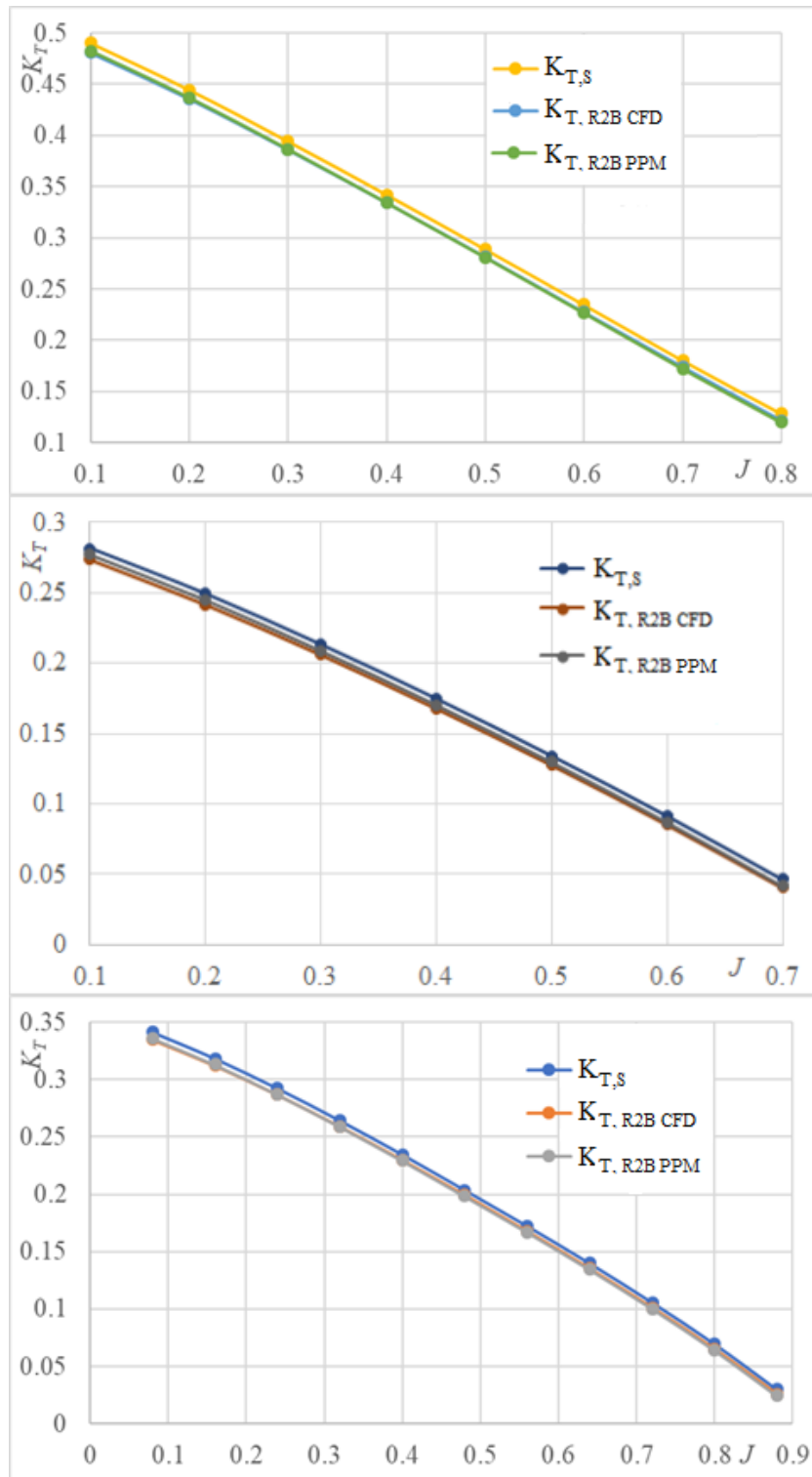


Figure 6.7 The obtained impact of biofilm on  $K_T$  for KP505 (upper), KP458 (middle) and WB (lower)



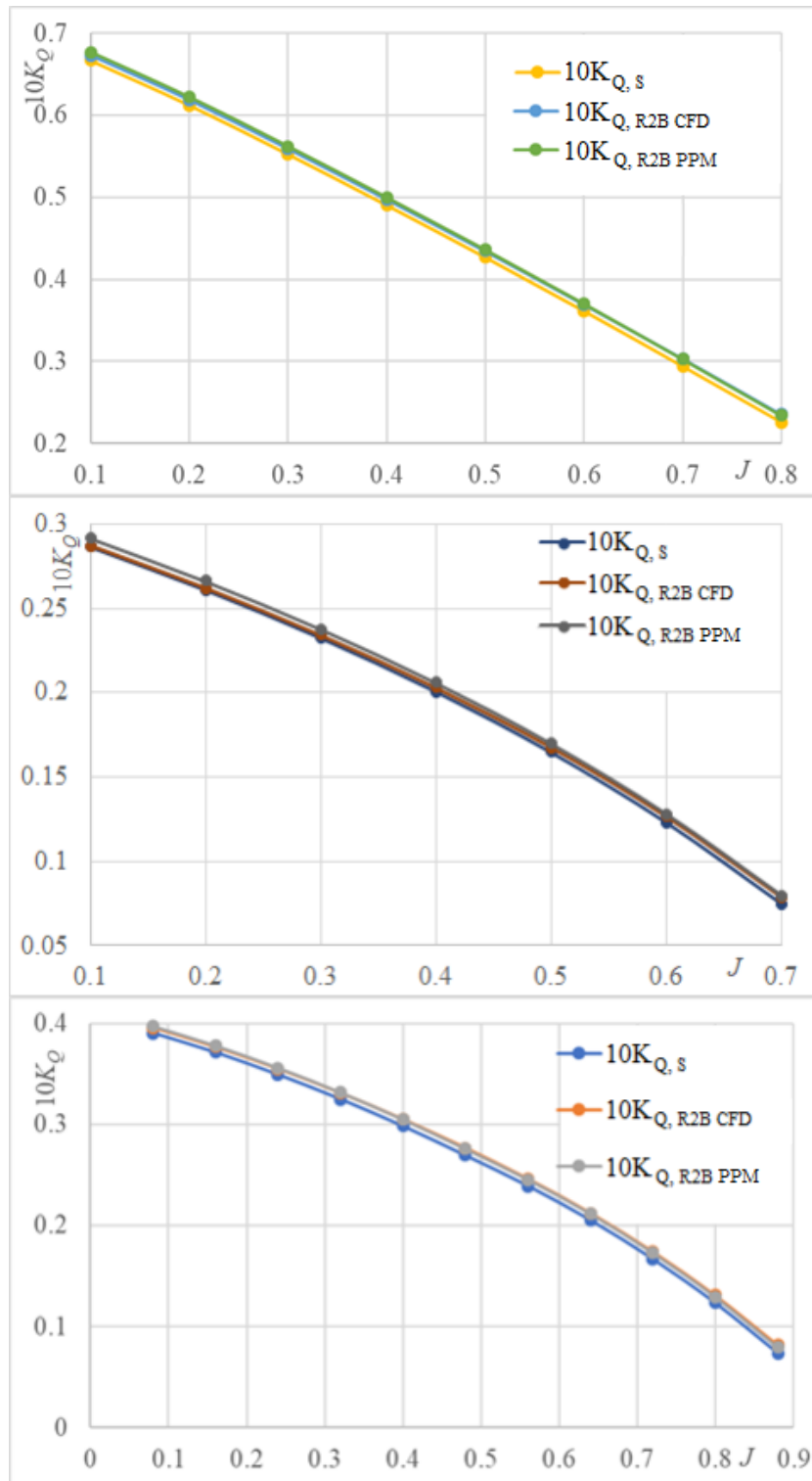


Figure 6.8 The obtained impact of biofilm on  $10K_Q$  for KP505 (upper), KP458 (middle) and WB (lower)

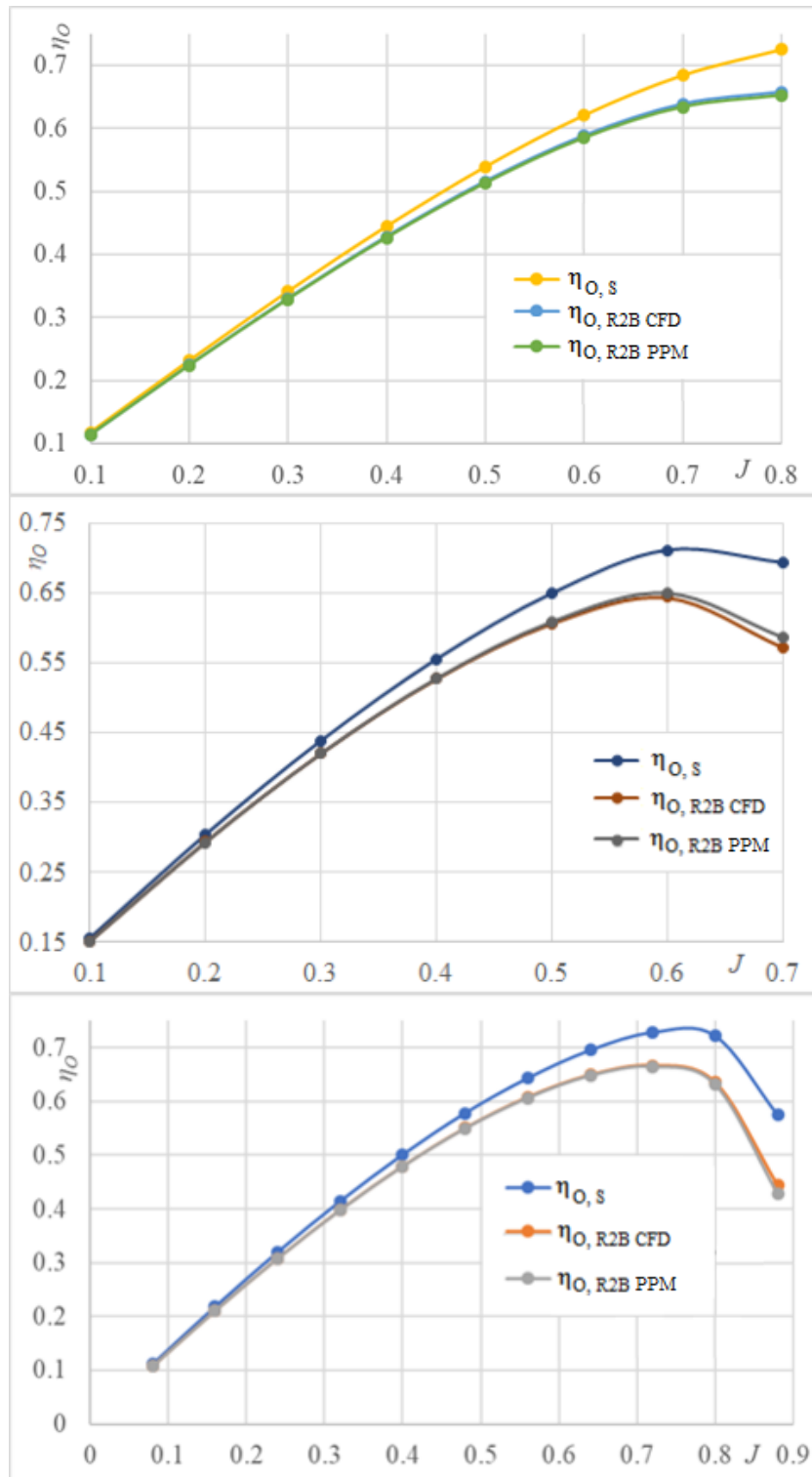


Figure 6.9 The obtained impact of biofilm on  $\eta_0$  for KP505 (upper), KP458 (middle) and WB (lower)

Once the applicability of the newly proposed PPM in the prediction of fouled propeller performance in the open water conditions is shown, the accuracy in the prediction of the impact of biofilm on the propulsion characteristics is studied. In Table 6.10, Table 6.11 and Table 6.12 the obtained propulsion characteristics using the newly proposed PPM are shown for three investigated ships and fouling conditions. Along with the obtained propulsion characteristics,

$RD$  from CFD results presented in Table 5.53, Table 5.54 and Table 5.55 are shown. The obtained propulsion characteristics using the newly proposed PPM have very low  $RD$  from the ones obtained using the CFD approach, which proves the applicability of the proposed method. The proposed method considers that  $t$  and  $\eta_r$  are the same for smooth and fouled condition, which was demonstrated in Section 5.5. Thus, the obtained  $RD$  between this two propulsion characteristics obtained using PPM and CFD are lower than 0.5% for all investigated fouling conditions and ships. The accurate prediction of the self-propulsion point for fouled surface condition depends on the accurate prediction of  $J$  for the self-propulsion point. As can be seen from Table 6.10, Table 6.11 and Table 6.12, the highest  $RD$  between  $J$  obtained using the newly proposed PPM and CFD for KCS is equal to 0.73%, for KVLCC2 to 1.1% and for BC to 1.77%. The obtained  $RD$  are lower than the numerical uncertainty in the prediction of  $J$  (Table 5.48) and therefore it can be concluded that the newly proposed PPM has successfully predicted  $J$  for the self-propulsion point of fouled ship and propeller. Regarding the prediction of  $1-w$  and  $\eta_H$ , it can be seen from Table 6.10, Table 6.11 and Table 6.12 that satisfactory agreement between the results obtained using the newly proposed PPM and CFD approach is obtained. Thus, the highest  $RD$  between  $1-w$  obtained using the newly proposed PPM and CFD for KCS is equal to 0.85%, for KVLCC2 to 1.97% and for BC to 1.92%, while the highest  $RD$  between  $\eta_H$  obtained using PPM and CFD for KCS is equal to 1%, for KVLCC2 to 1.97% and for BC to 1.49%. The prediction of  $\eta_O$  and  $\eta_B$  within PPM depends on the accurate prediction of propeller load defined with equation (6.10) and fouled propeller performance in open water conditions. Namely, once the propeller load has been calculated, the intersection with  $K_T = f(J)$  from open water test could be found. This intersection defines  $J$ ,  $K_T$  and  $K_Q$  for open water condition ( $K_{Q,OWT}$ ) values.

In order to represent the applicability of the newly proposed PPM in the prediction of the change of propulsion characteristics, within Figure 6.10 the obtained  $\Delta J$  using the newly proposed PPM and CFD approach are presented for all three investigated ships. It was decided to represent the impact of biofilm on  $\Delta J$ , as the accurate prediction of  $J$  signifies that the propeller load is accurately predicted. As can be seen from Figure 6.10, satisfactory agreement between the obtained  $\Delta J$  using PPM and CFD is achieved. The obtained  $\Delta J$  for KCS due to the presence of biofilm range from -0.17% (PPM) and -0.18% (CFD) for R7 B up to -8.71% (PPM) and -8.12% (CFD) for R2 B, for KVLCC2 varies from -0.02 % (PPM) and -0.10% (CFD) for R7 B up to -11.94% (PPM) and -11.05% (CFD) for R2 B and for BC varies from -0.06% (PPM) for R7 B and -1.23% (CFD) for R5 B up to -11.39% (PPM) and -11.58% (CFD) for R2 B. It is clear that the newly proposed PPM can accurately account for the impact of biofilm on the change in  $J$  for the self-propulsion point, i.e. the impact of biofilm on the propeller load.

Table 6.10 The obtained propulsion characteristics for KCS using PPM

Propulsion characteristic	R1 B	R2 B	R3 B	R4 B	R5 B	R6 B	R7 B	R8 B
$1-t$ RD, %	0.867 0.43%	0.867 -0.31%	0.867 0.12%	0.867 0.33%	0.867 -0.10%	0.867 0.35%	0.867 0.20%	0.867 -0.19%
$1-w$ RD, %	0.766 0.43%	0.751 0.85%	0.768 0.15%	0.754 0.68%	0.769 0.12%	0.763 0.45%	0.773 0.06%	0.768 0.15%
$\eta_H$ RD, %	1.132 0.00%	1.155 -0.53%	1.129 -0.28%	1.149 -1.00%	1.127 -0.02%	1.136 -0.80%	1.122 -0.25%	1.128 0.04%
$\eta_O$ RD, %	0.664 -0.12%	0.620 -0.96%	0.672 -0.35%	0.630 -1.25%	0.683 -0.85%	0.660 -0.98%	0.694 -0.12%	0.679 -0.43%
$\eta_B$ RD, %	0.665 0.05%	0.621 -0.73%	0.673 -0.11%	0.631 -1.07%	0.685 -0.70%	0.661 -0.80%	0.696 0.33%	0.681 -0.26%
$\eta_R$ RD, %	1.002 0.17%	1.002 0.23%	1.002 0.24%	1.002 0.19%	1.002 0.15%	1.002 0.18%	1.002 0.45%	1.002 0.17%
$\eta_D$ RD, %	0.753 0.05%	0.717 -1.26%	0.760 -0.39%	0.725 -2.05%	0.772 -0.72%	0.751 -1.59%	0.780 0.08%	0.768 -0.22%
$J$ RD, %	0.706 0.01%	0.666 -0.65%	0.713 -0.21%	0.675 -0.73%	0.718 -0.35%	0.699 -0.45%	0.728 0.01%	0.715 -0.21%
$K_T$ RD, %	0.173 -0.50%	0.191 0.52%	0.171 -0.18%	0.187 0.38%	0.169 -0.17%	0.177 -0.08%	0.165 -0.32%	0.170 -0.18%
$10K_Q$ RD, %	0.293 -0.54%	0.325 0.61%	0.288 -0.28%	0.318 0.71%	0.283 0.19%	0.298 0.26%	0.275 -0.65%	0.285 -0.12%

Table 6.11 The obtained propulsion characteristics for KVLCC2 using PPM

Propulsion characteristic	R1 B	R2 B	R3 B	R4 B	R5 B	R6 B	R7 B	R8 B
$1-t$ RD, %	0.820 0.04%	0.820 -0.10%	0.820 -0.17%	0.820 -0.04%	0.820 -0.02%	0.820 0.02%	0.819 0.05%	0.820 -0.16%
$1-w$ RD, %	0.660 -0.33%	0.632 -1.61%	0.666 0.29%	0.638 -1.97%	0.668 0.01%	0.653 -0.62%	0.668 0.01%	0.662 0.13%
$\eta_H$ RD, %	1.243 0.38%	1.298 1.54%	1.232 -0.46%	1.284 1.97%	1.227 -0.02%	1.256 0.65%	1.227 0.04%	1.239 -0.29%
$\eta_O$ RD, %	0.585 2.59%	0.530 0.87%	0.597 1.49%	0.543 0.72%	0.608 1.83%	0.575 3.70%	0.610 1.69%	0.596 1.89%
$\eta_B$ RD, %	0.584 2.77%	0.529 0.89%	0.596 1.70%	0.542 0.75%	0.607 1.62%	0.574 3.35%	0.609 1.85%	0.595 2.37%
$\eta_R$ RD, %	0.998 0.17%	0.998 0.01%	0.998 0.20%	0.998 0.03%	0.998 -0.20%	0.998 -0.34%	0.998 0.16%	0.998 0.47%
$\eta_D$ RD, %	0.726 3.16%	0.687 2.44%	0.734 1.23%	0.696 2.73%	0.745 1.60%	0.721 4.03%	0.747 1.90%	0.738 2.08%
$J$ RD, %	0.445 0.58%	0.403 -1.00%	0.455 0.94%	0.412 -1.10%	0.457 0.03%	0.435 0.44%	0.457 0.08%	0.449 0.53%
$K_T$ RD, %	0.155 1.87%	0.170 4.19%	0.151 0.19%	0.166 4.09%	0.151 1.58%	0.159 3.72%	0.152 2.09%	0.154 1.96%
$10K_Q$ RD, %	0.188 -0.30%	0.205 2.24%	0.184 -0.56%	0.201 2.19%	0.181 -0.01%	0.191 0.79%	0.181 0.31%	0.185 0.13%

Table 6.12 The obtained propulsion characteristics for BC using PPM

Propulsion characteristic	R1 B	R2 B	R3 B	R4 B	R5 B	R6 B	R7 B	R8 B
$1-t$ <i>RD, %</i>	0.764 -0.43%	0.764 -0.38%	0.764 0.38%	0.764 -0.45%	0.764 -0.38%	0.764 0.49%	0.764 -0.34%	0.764 -0.42%
$1-w$ <i>RD, %</i>	0.646 0.94%	0.628 1.09%	0.650 1.33%	0.632 1.05%	0.653 0.61%	0.642 1.92%	0.653 1.07%	0.648 0.42%
$\eta_H$ <i>RD, %</i>	1.182 -1.35%	1.218 -1.45%	1.176 -0.94%	1.209 -1.49%	1.171 -0.98%	1.190 -1.40%	1.171 -0.73%	1.179 -0.84%
$\eta_O$ <i>RD, %</i>	0.595 -0.59%	0.543 -0.65%	0.605 2.07%	0.555 -0.69%	0.616 0.90%	0.586 2.51%	0.620 2.33%	0.605 -1.28%
$\eta_B$ <i>RD, %</i>	0.595 -0.15%	0.543 -0.72%	0.605 1.91%	0.555 -0.83%	0.616 0.98%	0.586 2.34%	0.620 2.32%	0.605 -0.94%
$\eta_R$ <i>RD, %</i>	1.000 0.45%	1.000 -0.08%	1.000 -0.16%	1.000 -0.14%	1.000 0.08%	1.000 -0.16%	1.000 -0.01%	1.000 0.35%
$\eta_D$ <i>RD, %</i>	0.703 -1.50%	0.661 -2.16%	0.711 0.96%	0.671 -2.31%	0.722 -0.01%	0.697 0.91%	0.726 1.58%	0.714 -1.78%
$J$ <i>RD, %</i>	0.515 0.48%	0.472 0.21%	0.524 1.77%	0.482 0.18%	0.532 1.09%	0.505 1.77%	0.533 1.43%	0.520 -0.11%
$K_T$ <i>RD, %</i>	0.188 -1.84%	0.202 -1.23%	0.185 -1.39%	0.199 -1.38%	0.183 -0.98%	0.192 -0.89%	0.183 -0.30%	0.187 -1.32%
$10K_Q$ <i>RD, %</i>	0.259 -1.22%	0.279 -0.30%	0.255 -1.53%	0.274 -0.38%	0.251 -0.87%	0.263 -1.45%	0.250 -1.17%	0.256 -0.49%

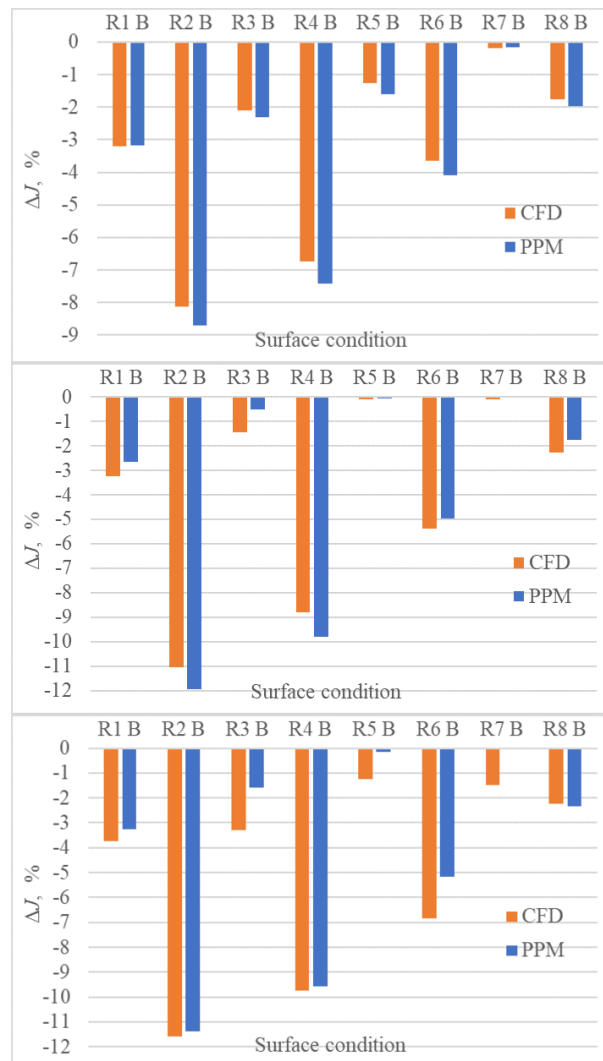


Figure 6.10 The obtained impact of biofilm on  $\Delta J$  for KCS (upper), KVLCC2 (middle) and BC (lower)

### 6.3. Discussion regarding the newly proposed PPM for fouled surfaces

For ship owners or ship operators it is crucial to determine the economic aspect of implementing certain operational measure once considering the improvement of ship energy efficiency. Since biofouling represents an important problem, which causes the increase in fuel consumption, or reduction of ship speed, it reduces the ship energy efficiency. The optimization of maintenance schedule represents an important operational measure over which ship owner or ship operator has a large degree of control and for successful implementation of such measure the assessment of the effects of biofouling on the ship performance are valuable. During the optimization of maintenance schedule economic aspect is crucial, i.e. ship owner or ship operator will clean ship and propeller if the costs of cleaning are economically justified. Since cleaning cannot be performed during a sail, but in port or in dry dock it is important to estimate whether is economically justified to clean a ship and/or propeller. Obviously, it is important to make such an assessment rapidly, since whenever ship does not operate, i.e. does not sail, its owner or operator is losing the money. In the investigation regarding the economic aspect of cleaning a lot of costs must be considered, as presented in [259]. The benefits of cleaning will be achieved through the reduction of fuel consumption, i.e. the fuel costs will be lower which is very

important since fuel costs represent 60–70% of the entire operational costs [45]. Therefore, the accurate assessment of the fuel savings related to hull and propeller cleaning enables the accurate assessment of economic aspects regarding the implementation of this operational measure. The CFD approach based on the implementation of  $\Delta U^+$  model within the wall function has imposed itself as the one of the most promising tools for this prediction. However, the important shortcomings of the CFD approach are that it requires significant amount of calculation time and that user must have certain experience in its application. The newly proposed PPM has enabled rapid and accurate assessment of resistance, open water and propulsion characteristics of fouled ship. This method can utilize as an input data either towing tank results of investigated ship, or full-scale CFD results for smooth ship. The applicability of the newly proposed method is demonstrated in subsections 6.2.1 and 6.2.2, depending on the input data. It should be noted that if towing tank measurements are used as an input data the role of the proposed method is twofold: scaling of the input data and estimating the fouling effects. Consequently, higher  $RD$  between the obtained resistance, open water and propulsion characteristics using the newly proposed PPM and CFD approach are obtained. More appropriate investigation regarding the accuracy of the proposed method in the prediction of fouling effects can be performed if full-scale CFD results are utilised as an input data. This was done for three ships and the obtained results are presented in subsection 6.2.2. The most important parameters in the prediction of fuel consumption are related to the propeller operating point, i.e.  $P_D$  and  $n$ . The obtained  $P_D$  and  $n$  using the newly proposed PPM and CFD approach for eight investigated fouling conditions and for three ships are presented in Table 6.13 and Table 6.14. It should be noted that the obtained  $RD$  are presented as well in Table 6.13 and Table 6.14.

Table 6.13 The obtained  $P_D$  using the newly proposed PPM and CFD approach

Ship	KCS		KVLCC2		BC	
	$P_{D, CFD}$ , MW	$P_{D, PPM}$ , MW $RD$ , %	$P_{D, CFD}$ , MW	$P_{D, PPM}$ , MW $RD$ , %	$P_{D, CFD}$ , MW	$P_{D, PPM}$ , MW $RD$ , %
R1 B	28.063	28.262 0.71%	19.988	19.390 -2.99%	7.476	7.487 0.15%
R2 B	33.569	35.321 5.22%	25.057	25.144 0.35%	9.383	9.602 2.34%
R3 B	27.030	27.248 0.81%	18.727	18.264 -2.48%	7.319	7.115 -2.78%
R4 B	31.932	33.552 5.07%	23.815	23.697 -0.50%	8.877	9.078 2.26%
R5 B	25.940	26.357 1.60%	17.988	17.974 -0.08%	6.950	6.792 -2.27%
R6 B	28.405	29.261 3.02%	21.106	20.607 -2.37%	7.995	7.914 -1.01%
R7 B	24.968	24.843 -0.50%	17.913	17.932 0.10%	6.902	6.750 -2.21%
R8 B	26.518	26.771 0.95%	18.975	18.769 -1.09%	7.160	7.240 1.12%

Table 6.14 The obtained  $n$  using the newly proposed PPM and CFD approach

Ship Surface condition	KCS		KVLCC2		BC	
	$n_{\text{CFD}}$ , rpm	$n_{\text{PPM}}$ , rpm $RD$ , %	$n_{\text{CFD}}$ , rpm	$n_{\text{PPM}}$ , rpm $RD$ , %	$n_{\text{CFD}}$ , rpm	$n_{\text{PPM}}$ , rpm $RD$ , %
R1 B	101.242	101.663 0.42%	72.550	71.890 -0.91%	101.436	101.905 0.46%
R2 B	104.159	105.727 1.51%	76.560	76.084 -0.62%	107.074	108.008 0.87%
R3 B	100.672	101.036 0.36%	71.440	70.978 -0.65%	101.144	100.713 -0.43%
R4 B	103.288	104.758 1.42%	75.762	75.092 -0.88%	105.662	106.588 0.88%
R5 B	100.035	100.505 0.47%	70.927	70.911 -0.02%	100.166	99.692 -0.47%
R6 B	101.374	102.293 0.91%	73.646	72.869 -1.05%	103.113	103.264 0.15%
R7 B	99.462	99.511 0.05%	70.919	70.869 -0.07%	99.950	99.598 -0.35%
R8 B	100.404	100.762 0.36%	71.741	71.449 -0.41%	100.655	101.193 0.53%

As can be seen from Table 6.13 the obtained  $P_D$  using the newly proposed PPM are in satisfactory agreement with the obtained  $P_D$  using the CFD approach. Thus, the highest  $RD$  between  $P_{D, \text{PPM}}$  and  $P_{D, \text{CFD}}$  for KCS is equal to 5.22%, for KVLCC2 to -2.99% and for BC to -2.78%. The obtained  $RD$  between  $n_{\text{EX}}$  and  $n_{\text{CFD}}$  are even lower and for KCS the highest  $RD$  is equal to 1.51%, for KVLCC2 to -0.91% and for BC to 0.88%. Therefore, it can be concluded that detrimental effects of biofilm on the ship performance can be accurately predicted using the proposed PPM. The important benefit of the proposed method is that it can be utilised for various ships, as well as for various fouling conditions defined with certain  $\Delta U^+$  model. Furthermore, the impact of cleaning solely the propeller or ship hull on the ship performance can be investigated as well. This represents an important benefit over the performance monitoring methods, which are usually used for the assessment of the impact of biofouling on the ship performance nowadays. Namely, as mentioned earlier, it is very difficult to separate the impact of biofouling on the hull and propeller once performance monitoring methods are used. However, it is important to note that this method is more suitable for the prediction of the fouling effects on the ship performance for fouling with lower fouling severity because of two reasons. The first reason is that within the newly proposed PPM it is assumed that  $R_w$  is the same for smooth and fouled ship. While the impact of fouling on  $R_w$  is moderate for fouling with lower fouling severity, this impact is significantly higher for fouling with higher fouling severity, such as hard fouling, as presented in subsection 5.3. Since it has been shown that the presence of fouling is causing the decrease in  $R_w$ , the newly proposed PPM will predict too high  $R_T$  in a case of fouling with higher fouling severity. Consequently, the propeller load will be too high and  $J$  for the self-propulsion point will not be adequately predicted. The impact of biofouling on  $R_w$  is more important for a ships which sail at higher  $Fn$ , i.e. for the with higher



portion of  $R_w$  in  $R_T$ . Because of this the highest  $RD$  between  $P_{D, PPM}$  and  $P_{D, CFD}$  is achieved for KCS for fouling conditions R2 B and R4 B, which represent conditions with the highest  $k_{eff}$ , Table 5.3. Therefore, it can be concluded that the proposed PPM is the most accurate for fouling conditions with lower fouling severity and ships with higher portion of  $R_v$  in  $R_T$ . Mentioned drawback can be overcome with the correction of  $C_w$  due to the presence of biofouling, i.e. roughness. In order to estimate this correction, several other studies regarding the impact of biofouling or roughness on  $R_w$  for various ship forms must be performed. Additional reason for the inaccurate prediction of the fouling effects on the ship performance in the case of higher fouling severity lies in the inaccurate prediction of  $C_{F0,R}$  using the Granville similarity law scaling method. Namely, as shown in subsection 5.2.2, higher  $RD$  between  $C_{F0,R}$  obtained using CFD approach and the Granville similarity law scaling method are obtained for hard fouling than biofilm. This can be attributed to the fact that only one value of  $k^+$  is assumed once the Granville method is used, which means that only one  $\Delta U^+$  value is used along the whole flat plate. For the proposed method the accurate prediction of  $C_{F0,R}$  is of utmost importance, since  $C_{F0,R}$  is utilised for the prediction of  $R_{TR}$ ,  $w_R$  and therefore the propeller load as well. Since the flat plate simulation requires relatively low computational effort, especially in comparison with full-scale self-propulsion tests, mentioned drawback can be overcome with those numerical simulations, i.e. that  $C_{F0,R}$  is obtained from the numerical simulations of flat plate. If so, the assessment of the effect of hard fouling on the performance of KVLCC2 using the newly proposed PPM would probably be more accurate, since the portion of  $R_w$  in  $R_T$  for KVLCC2 is negligible.

Therefore in order to investigate the applicability of the newly proposed PPM for different fouling type and ship, two aspects must be analysed. The first is that the portion of  $R_w$  in  $R_T$  for the investigated ship must be moderate and the second one is the accuracy of the Granville similarity law scaling method in the prediction of  $C_{F0,R}$ .

It is important to note that in case of higher fouling severity on the immersed surface, the ship owner or ship operator will have to clean ship or propeller, since the fouling penalties are too high, as presented in subsection 5.5.3. Therefore it is more important to determine a proper time to clean ship or propeller for fouling with lower fouling severity, i.e. before the occurrence of hard fouling, which will result in high fuel penalties. The newly proposed method can be valuable tool for the assessment of the impact of such fouling condition on the ship performance and in that way it can be used for economic analysis of the ship and propeller cleaning, which represents the most important barrier in the optimization of maintenance schedule.

## 7. Conclusions

The determination of the impact of biofouling on the ship performance is very important and can be considered as evenly valuable as the improvement of the ship energy efficiency through the application of new AF coatings, since it can point out the significance of hull and propeller cleaning. Consequently ship owners and ship operators require the development of a transparent and reliable standard for measuring hull and propeller performance. Within the optimization of the maintenance schedule, which represents an important operational measure for increasing ship energy efficiency, the speed loss or increase in the fuel consumption caused by the presence of biofouling must be considered in order to find the optimal balance between efficiency and costs. As a result, an accurate assessment of the impact of biofouling on the ship performance is of utmost importance. This was also recognized by ITTC, which has advised scientists to present new formulae or methods based on the experimental data to determine the impact of biofouling on ship resistance and propulsion characteristics.

The main objective of this thesis is the development of numerical procedure for the assessment of the impact of biofouling on the ship resistance and propulsion characteristics in calm water. This includes the effects on the ship resistance, wake and thrust deduction fractions, as well as the operating point of a propeller. This overall objective was accomplished through the fulfilment of several specific objectives and combining them with a goal to obtain one complete procedure. Firstly, a detail literature review was performed regarding the topics investigated in this thesis within Section 2. The roughness effects on the flow were presented, the concept of roughness function is defined, effects of biofouling on the resistance, open water and propulsion characteristics are revised and the gaps in the literature were reviewed. The methodology applied in this thesis was defined and presented in Section 3. Thus, an approach for the development of numerical procedure for the assessment of the effects of biofouling on the resistance, open water and self-propulsion characteristics was given. Also, the details regarding the numerical modelling were presented. Finally, the verification and validation studies were described. The developed numerical procedure is based on the wall similarity hypothesis and implementation of certain wall function within the CFD solver. Once the methodology has been defined, roughness function models used within this thesis were presented in Section 4. Two fouling types were analysed: biofilm, i.e. representative of soft fouling, and hard fouling. The investigation related to the impact of biofilm on the ship performance is of particular importance as the fouling with biofilm is almost inevitable regardless of the applied AF coating. This has also been recognized by ITTC, which have recommended researchers to include the effects of biofilm in the performance prediction method. Furthermore, ITTC has recommended that investigations related to paint performance must be widened to cover slime effect, which represents a hot issue in foul release coatings. Therefore, one of the objectives was to propose the roughness function model for biofilm based on the drag characterization studies available in the literature. This objective was fulfilled within Section 4, where three roughness function models were proposed for the analysis of the biofilm effects on the flow around immersed surface. For the assessment of the impact of hard fouling on the flow around immersed surfaces, the Grigson roughness function was utilised as recommended in the literature. After roughness function models for the investigated fouling types have been established, defined and presented, the following objective was to implement them within the wall function of the CFD solver. After the implementation, the validity and applicability of the CFD model for the simulation of

biofouling effects were shown. Thus, in subsections 4.1.4 and 4.2.4, the CFD model for simulation of biofilm and hard fouling effects on the flow were presented, discussed and validated. For this purpose, extensive verification and validation studies were performed. The simulation uncertainty was calculated and the obtained frictional resistance coefficients for fouled surfaces were validated with the experimental results from the literature. Also, the numerically and experimentally obtained roughness Reynolds values were compared and satisfactory agreement was achieved. It was demonstrated that the proposed CFD model can accurately predict the increase in frictional resistance coefficient due to the presence of biofouling even if surfaces have small differences in roughness length scales. This is of particular importance for fouling with biofilm, since it represents a fouling with low fouling severity. Finally, it can be concluded that the proposed CFD model and  $\Delta U^+$  models can be utilised for reliable assessment of the impact of biofilm and hard fouling on the flow around any immersed surface covered with those types of fouling. Afterwards, the numerical procedure was developed and proposed for the assessment of the impact of biofouling on resistance, open water and self-propulsion characteristics in Section 5. For that purpose, several types of numerical simulations were performed including flat plate, double body and free surface simulations. An extensive verification study was carried out in order to find sufficient grid size and time step and to estimate numerical uncertainties in the prediction of hydrodynamic characteristics. The obtained frictional resistance coefficients for fouled full-scale flat plates were compared with the ones obtained using the Granville similarity law scaling method. The advantages of the proposed numerical procedure over the Granville similarity law scaling method were discussed. Thereafter, the applicability of the proposed procedure for simulation of the effects of biofouling on 3D ship hulls and propellers was shown on the example of three merchant ships. Thus, CFD simulations of resistance, open water and self-propulsion tests were performed in full-scale. The obtained results for the smooth surface condition were validated with the extrapolated towing tank results. The proposed procedure has enabled the assessment of the effect of biofouling on the delivered power and propeller rotation rate, or the decrease in ship speed if the delivered power is kept constant as for the smooth surface condition. This is of particular importance, since these increases in the delivered power and propeller rotation rate can be related to an increase in the fuel consumption. In that way, the ship owner or ship operator can estimate more accurately the benefits of ship and propeller cleaning. What is more, a detail analysis of the obtained numerical results was performed and the impact of biofouling on the flow around fouled surfaces was detailly studied and discussed. Last objective in PhD thesis was to propose newly proposed performance prediction method for fouled surfaces, which would represent a robust and fast method for the estimation of fouling effects on the ship performance. The importance of such method is reflected during the optimization of maintenance schedule, where fast, robust and accurate assessment of the fouling effects on the ship performance is needed. Based on the obtained results related to the impact of biofouling on the ship performance presented in Section 5, a newly proposed performance prediction method for fouled surfaces was proposed in Section 6. This method combines the Granville similarity law scaling method and roughness function models for the determination of the impact of biofouling on the ship performance. It enables the assessment of the impact of biofouling on the propeller operating point, i.e. on the delivered power and propeller rotation rate. As an input, this method can utilise either towing tank results or full-scale CFD results. It should be noted that the method slightly differs depending on the input data. Namely, if towing tank results are used as an input data, those data must be extrapolated to full-scale and thereafter

extrapolated data can be used for the prediction of fouling effects. The applicability of the proposed method was demonstrated by comparison of the obtained results with CFD results. Satisfactory agreement between the obtained resistance, open water and self-propulsion characteristics using the proposed method and CFD approach was obtained. Finally, the advantages and disadvantages of the proposed method were discussed. The disadvantages of the proposed method currently restrict the applicability of this method to lower fouling severities or slower ships, however in future research this too can be overcome.

The performed research was based on the three hypotheses presented in subsection 1.4.2. If drag characterization study is performed, the roughness length scale can be expressed with easily measurable roughness parameters, such as fouling height and percentage of coverage and non-uniform surface roughness effects can be described with sufficient accuracy using roughness length scale and roughness function model, i.e.  $\Delta U^+ = f(k^+)$ . Throughout the thesis it was demonstrated that the CFD approach can be applied for the assessment of ship hydrodynamic characteristics for different fouling conditions on the immersed surfaces. The developed numerical procedure can be utilised for this assessment and the procedure describes the effect of biofouling on the ship performance more comprehensively than current methods, which are mostly based on the roughness allowance. The research was focused on the investigation of effects of predetermined fouling conditions on resistance, open water and self-propulsion characteristics in calm water. This was done, as biofouling is dependent on many different parameters and how long will AF coating successfully prevent fouling has remained elusive. The future studies related to biofouling problems are required for a more detailed insights related to time dependent biofouling growth of the ship hull and propeller surfaces. The most important assumption within this thesis was that the surface roughness affects the inner layer region of turbulent boundary layer, while the mean velocity and the turbulence intensity in the outer layer region were not affected by its presence. This hypothesis is known as the Townsend's wall similarity hypothesis and it claims that at sufficiently high  $Rn$ , the turbulent motions outside the roughness sublayer are independent of boundary condition at the wall, beside the fact that this boundary condition modifies the outer velocity and length scales. A detail discussion related to this hypothesis was given in subsection 2.2. Even though there is debate in the literature regarding its validity, there is general agreement that this hypothesis is valid for lower relative roughness and many authors in the literature have shown its validity for different ratios between roughness and turbulent boundary layer height. Within this thesis, all investigated fouling conditions were within the limit for which it was proven that this hypothesis holds. The proposed CFD model which can account for the effects of biofouling was validated by comparison of the obtained frictional resistance coefficients of flat plate with the experimental ones. Once this model was validated, it could be used for simulating the effects of biofouling on any arbitrary body. This enabled the investigation of the effects of biofouling on the ship performance. The further validation of the CFD model, which was used for the assessment of the impact of biofouling on resistance, open water and self-propulsion characteristics included a comparison of the obtained results with the experimentally measured ones. The first step regarding the validation of CFD model which employed roughness function within wall function was done recently in [197]. Within this thesis two types of fouling were analysed and even though the developed numerical procedure could be utilised for the prediction of the impact of other types of fouling on the ship performance, an extensive drag characterization study must be performed or the results of drag characterization study should

be found in the literature. Therefore, experimental data is still essential for the development of accurate CFD prediction methods.

Since within this thesis numerous numerical simulations were carried out, several exploratory studies were performed in order to estimate proper definition and location of domain boundaries, mesh refinements, time step, turbulence model, numerical setup etc. Some of these studies were presented in Appendix A and based on the results from this studies, computational setup was selected. Furthermore, based on the results of the verification study for each type of CFD simulation, sufficient grid spacing, and time step were selected. The proper implementation of roughness function models was checked with  $U^+ - y^+$  plots for smooth and fouled ships. Based on these plots it is clear that the presence of biofouling causes significant downward shift of the mean velocity profile in the log-law region of turbulent boundary layer. It was noticed that the implementation of roughness function within the wall function of the CFD solver did not cause any increase in required computational time when compared to numerical simulations for smooth surface. Within this thesis, self-propulsion tests were performed without discretized propeller, i.e. body force method was applied. However, it would be beneficial to perform future studies related to the impact of biofouling on the ship propulsion characteristics within self-propulsion tests with discretized propeller. The proposed performance prediction method for fouled surfaces was based on the several assumptions, which were presented in subsection 2.3.4 or confirmed in Section 5. However, it is important to notice that this method assumes that the impact of biofouling on the wave resistance is negligible, which may lead to certain errors. Because of this, the method is more suitable for slower ships, which have low portion of wave resistance in total resistance. As already noted, the future work will be focused on the exploratory studies related to the impact of biofouling on the wave resistance for several ship forms with an aim to develop a robust relation between fouling condition and ship wave resistance.

The main scientific contribution of this thesis was the development of numerical procedure which could be used for the assessment of the impact of biofouling on resistance, open water and self-propulsion characteristics. This procedure enabled the estimation of the operating point of propeller and consequently ship energy efficiency for different fouling conditions. This is of particular importance for the tools in the optimization of maintenance schedule, as this procedure enables the estimation of the increase in delivered power due to the presence of biofouling, rather than the increase in effective power. The procedure is based on the implementation of roughness functions within the CFD solver. Additional important scientific contribution is the development of newly proposed performance prediction method for the fouled surfaces. This method can be used as a practical tool during the optimization of maintenance schedule for the estimation of change in resistance, open water and self-propulsion characteristics for fouled ship. It is applicable to different ship and fouling types and enables a rapid assessment of fouling penalties to ship performance. Beside these two main scientific contributions, several other scientific contributions to the field were achieved. Thus, roughness function models for biofilm were proposed and implemented within the CFD solver. These models were proposed based on the experimentally determined roughness function values from the literature and the least squares method. After the implementation, a detailed verification and validation studies were performed and the prediction of the frictional resistance of the surfaces covered with biofilm, using solely roughness measurements, was enabled. The Grigson roughness function for hard fouling proposed in the literature was implemented in the wall function of the CFD solver. After the extensive verification and validation studies the

applicability in the prediction of frictional resistance of surface covered with hard fouling was demonstrated. Beside the impact of biofilm and hard fouling on the frictional resistance, a detail investigation related to the impact of biofilm and hard fouling on all other resistance characteristics was performed on the example of three merchant ships. Several interesting findings related to the impact of biofilm on the ship resistance characteristics and nominal wake were presented in subsection 5.3. Also, the impact of biofilm and hard fouling on the propeller performance in the open water conditions was studied and fouling penalties were calculated on the example of three propellers. Finally, the impact of biofilm and hard fouling on the self-propulsion characteristics was assessed. The quantification of numerical errors within the assessment of resistance characteristics was proposed. Simulation uncertainties in the prediction of resistance, open water and self-propulsion characteristics were calculated. It was shown that the presence of slime could have very detrimental effects on resistance, open water and self-propulsion characteristics and that slime should not be ignored, contrary to common opinion. Furthermore, the importance of determination of the effect of biofouling on the delivered power rather than on effective power was highlighted. The procedure for the assessment of speed reduction due to the presence of biofilm was presented and discussed. The detail analysis of the flow around fouled ship and propeller was performed and presented in Section 5. This represents an important benefit of the CFD model, as most of the impacts of biofouling on the resistance, open water and self-propulsion characteristics can be explained through the effect of biofouling on the flow. Finally, related to the newly proposed performance prediction method, an in-house code was developed in order to avoid potential numerical errors during the calculations and to enable more faster calculation.

## **7.1. Plans for future research**

The performed investigations within this thesis can be further extended in several directions. Thus, it would be beneficial to perform drag characterization study of other fouling types with a special attention to composite fouling. In that way a database of roughness function models would be extended and the impact of other types of biofouling on the ship performance could be investigated. Also, it would be beneficial to carry out drag characterization study for different AF coatings, including fouling release and biocidal coatings. The determination of roughness behaviour for various AF coatings could enable the comparison amongst them and using the developed numerical procedure, or performance prediction method, the selection of the most suitable AF coating would be enabled for a certain ship. However, this assessment can be made only for newly applied condition and therefore it would be valuable to study how long certain AF coating can prevent fouling occurrence. In that way, a proper selection of AF coating for a certain ship would be enabled, which would result in significant financial savings and improvement in ship energy efficiency. Also, in this thesis the fouling penalties were estimated through comparison with the smooth surface condition. If drag characterization study of AF coating is available, it would be possible to estimate fouling penalties using applied AF coating as a baseline condition. As environmental requirements regarding shipping industries are more and more strict, numerous measures for reducing GHG emissions have been proposed. One of the promising measure is the application of AF coatings with polymer injection, which enables significant savings in fuel consumption through reduction of frictional resistance. It would be therefore very interesting to perform drag characterization study of such coatings and by the application of developed numerical procedure to estimate potential savings in fuel consumption or GHG emissions. Regarding the numerical studies, it would be beneficial to perform CFD

simulations of heterogenous fouling condition, which is typically present on the hull surface. Within this thesis, the hull and propeller surfaces were treated as uniform rough surfaces. The impact of different percentage of fouling coverage was taken into account through different roughness length scale. However, it would be valuable to investigate the impact of roughness or biofouling on the ship performance with the roughness function applied only to certain areas on the immersed surfaces. These areas could be restricted to typical niche areas and in that way more realistic fouling condition would be investigated. What is more, in that way it would be possible to detect the region that is most critical for cleaning. In that way, if the ship owner or ship operator has limited funds for cleaning, on the basis of the results from this study it could be possible to estimate regions that are more important to clean. Also, investigations related to hull or propeller cleaning solely could be beneficial. In that way the cost effectiveness of partial cleaning would be investigated, which could be of particular importance for propeller cleaning, as it is known that propeller cleaning is more effective taken per unit area than the hull. As already noted, additional investigations related to the impact of biofouling on the wave resistance are necessary. These investigations must be performed systematically for various ship forms and based on the obtained results, some practical relation between fouling condition and wave resistance should be proposed. This would be beneficial for the proposed performance prediction method which could then be updated and more accurate. Also, investigations related to the impact of biofouling on the self-propulsion characteristics could be performed with discretized propeller and in that way more accurate results could be obtained. Based on the proposed numerical procedure or performance prediction method, future work will be focused on the estimation of the increase in fuel consumption and GHG emissions due to the presence of biofouling. In that way, economic benefits in terms of reducing fuel costs due to hull and propeller cleaning could be more easily determined. Finally, comprehensive tool for the optimization of the maintenance schedule, which would encompass all costs related to maintenance, could be developed using the performance prediction method for fouled surfaces proposed in this thesis. In that way significant savings in fuel consumption and reduction in GHG emissions would be enabled.

## References

- [1] United Nations Conference on Trade and Development. Review of Maritime Transport. Geneva: United Nations; 2019.
- [2] International Maritime Organisation. Third IMO Greenhouse Gas Study 2014. London: IMO; 2014.
- [3] Marine Environment Protection Committee 72/71/Add.1. Initial IMO Strategy on Reduction of GHG Emissions from Ships. London: IMO; 2018.
- [4] Balcombe P, Brierley J, Lewis C, Skatvedt L, Speirs J, Hawkes A, Staffell I. How to decarbonise international shipping: Options for fuels, technologies and policies. *Energy conversion and management*. 2019; 182: 72-88.
- [5] Bouman EA, Lindstad E, Riialand AI, Strømman, AH. State-of-the-art technologies, measures, and potential for reducing GHG emissions from shipping—a review. *Transportation Research Part D: Transport and Environment*. 2017; 52: 408-421.
- [6] Tillig F, Ringsberg JW, Mao W, Ramne B. A generic energy systems model for efficient ship design and operation. *Proceedings of the Institution of Mechanical Engineers, Part M: Journal of Engineering for the Maritime Environment*. 2017; 231(2): 649-666.
- [7] Rehmatulla N, Calleya J, Smith T. The implementation of technical energy efficiency and CO2 emission reduction measures in shipping. *Ocean engineering*. 2017; 139: 184-197.
- [8] Vogler F, Wursig G. Fuel cells in maritime applications challenges, chances and experiences. In: *The 4<sup>th</sup> International Conference on Hydrogen Safety (ICHS)*; San Francisco, USA, 12-14 September 2011. Sandia National Laboratories.
- [9] Rehmatulla N, Parker S, Smith T, Stulgis V. Wind technologies: Opportunities and barriers to a low carbon shipping industry. *Marine Policy*. 2017; 75: 217-226.
- [10] Mäkiharju SA, Perlin M, Ceccio SL. On the energy economics of air lubrication drag reduction. *International Journal of Naval Architecture and Ocean Engineering*. 2012; 4(4): 412-422.
- [11] Jensen S, Lützen M, Mikkelsen LL, Rasmussen HB, Pedersen PV, Schamby P. Energy-efficient operational training in a ship bridge simulator. *Journal of Cleaner Production*. 2018; 171: 175-183.
- [12] Corbett JJ, Wang H, Winebrake JJ. The effectiveness and costs of speed reductions on emissions from international shipping. *Transportation Research Part D: Transport and Environment*, 2009; 14(8): 593-598.
- [13] Martić I, Degiuli N, Farkas A. Impact of Slow Steaming on The Fuel Consumption of a Container Ship. In: *8<sup>th</sup> International Maritime Science Conference*; Budva, Montenegro, 11-12 April 2019. Faculty of Maritime Studies in Kotor, Faculty of Maritime Studies in Split.
- [14] Lee CY, Lee HL, Zhang J. The impact of slow ocean steaming on delivery reliability and fuel consumption. *Transportation Research Part E: Logistics and Transportation Review*. 2015; 76: 176-190.
- [15] Faber J, Wang H, Nelissen D, Russell B, Amand DS. Reduction of GHG emissions from ships: marginal abatement costs and cost effectiveness of energy-efficiency measures. London, UK: International Maritime Organization (IMO); 2011.



- [16] Cariou P. Is slow steaming a sustainable means of reducing CO<sub>2</sub> emissions from container shipping? *Transportation Research Part D: Transport and Environment*. 2011; 16(3): 260-264.
- [17] Rehmatulla N, Smith T. Barriers to energy efficient and low carbon shipping. *Ocean Engineering*. 2015; 110: 102-112.
- [18] Tezdogan T, Incecik A, Turan O, Kellett, P. Assessing the impact of a slow steaming approach on reducing the fuel consumption of a containership advancing in head seas. *Transportation Research Procedia*. 2016; 14, 1659-1668.
- [19] Adland R, Cariou P, Jia H, Wolff FC. The energy efficiency effects of periodic ship hull cleaning. *Journal of Cleaner Production*. 2018; 178: 1-13.
- [20] Farkas A, Degiuli N, Martić I. Impact of biofilm on the resistance characteristics and nominal wake. *Proceedings of the Institution of Mechanical Engineers, Part M: Journal of Engineering for the Maritime Environment*. 2020; 234(1): 59-75.
- [21] Demirel YK. *Modelling the Roughness Effects of Marine Coatings and Biofouling on Ship Frictional Resistance [PhD thesis]*. Glasgow: University of Strathclyde, Department of Naval Architecture, Ocean and Marine Engineering; 2015.
- [22] Nugroho B, Ganapathisubramani B, Utama IKAP, Suastika IK, Yusuf M, Tullberg M, Monty JP, Hutchins N. Managing international collaborative research between academics, industries, and policy makers in understanding the effects of biofouling in ship hull turbulent boundary layers. *International Journal of Maritime Engineering*. 2017;159(A3): 291-300.
- [23] Bixler GD, Bhushan B. Biofouling: lessons from nature. *Philosophical Transactions of the Royal Society A: Mathematical, Physical and Engineering Sciences*. 2012; 370(1967): 2381-2417.
- [24] Schultz MP, Bendick JA, Holm ER, Hertel WM. Economic impact of biofouling on a naval surface ship. *Biofouling*. 2011; 27(1): 87-98.
- [25] Davidson I, Scianni C, Hewitt C, Everett R, Holm E, Tamburri M, Ruiz G. Mini-review: Assessing the drivers of ship biofouling management—aligning industry and biosecurity goals. *Biofouling*. 2016; 32(4): 411-428.
- [26] Marine Environment Protection Committee 62/24/Add.1. *Guidelines for the Control and Management of Ships' Biofouling to Minimize the Transfer of Invasive Aquatic Species*. London: IMO; 2011.
- [27] Oliveira DR, Granhag L. Ship hull in-water cleaning and its effects on fouling-control coatings. *Biofouling*. 2020; 36(3): 332-350.
- [28] Nurioglu AG, Esteves ACC. Non-toxic, non-biocide-release antifouling coatings based on molecular structure design for marine applications. *Journal of Materials Chemistry B*. 2015; 3(32): 6547-6570.
- [29] Lehaitre M, Delauney L, Compère C. Biofouling and underwater measurements. Real-time observation systems for ecosystem dynamics and harmful algal blooms: Theory, instrumentation and modelling. *Oceanographic Methodology Series*. UNESCO, Paris, 2008, p. 463-493.
- [30] Van Mooy BA, Hmelo LR, Fredricks HF, Ossolinski JE, Pedler BE, Bogorff DJ, Smith PJ. Quantitative exploration of the contribution of settlement, growth, dispersal and grazing to the accumulation of natural marine biofilms on antifouling and fouling-release coatings. *Biofouling*. 2014; 30(2): 223-236.

- [31] Roberts D, Rittschof D, Holm E, Schmidt AR. Factors influencing initial larval settlement: temporal, spatial and surface molecular components. *Journal of Experimental Marine Biology and Ecology*. 1991; 150(2): 203-221.
- [32] Park JS, Lee JH. Sea-trial verification of ultrasonic antifouling control. *Biofouling*. 2018; 34(1): 98-110.
- [33] Menesses M, Belden J, Dickenson N, Bird J. Measuring a critical stress for continuous prevention of marine biofouling accumulation with aeration. *Biofouling*. 2017; 33(9): 703-711.
- [34] Mathiazhagan A, Joseph R. Nanotechnology-a New prospective in organic coating-review. *International Journal of Chemical Engineering and Applications*. 2011; 2(4): 225-237.
- [35] Zhang ZP, Song XF, Cui LY, Qi YH. Synthesis of polydimethylsiloxane-modified polyurethane and the structure and properties of its antifouling coatings. *Coatings*. 2018; 8(5), 157.
- [36] Ba M, Zhang Z, Qi Y. Fouling release coatings based on polydimethylsiloxane with the incorporation of phenylmethylsilicone oil. *Coatings*. 2018; 8(5): 153.
- [37] AMBIO, The Publishable Final Activity Report of the AMBIO Integrated Project (European Commission CORDIS Publications, 2010), [https://cordis.europa.eu/docs/results/11/11827/120142251-6\\_en.pdf](https://cordis.europa.eu/docs/results/11/11827/120142251-6_en.pdf) . [cited 30 September 2020];
- [38] Stojanović I, Farkas A, Alar V, Degiuli N. Evaluation of the Corrosion Protection of Two Underwater Coating Systems in a Simulated Marine Environment. *JOM*. 2019; 71(12): 4330-4338.
- [39] ABS. Ship Energy Efficiency Measures: Status and Guidance. [https://ww2.eagle.org/content/dam/eagle/advisories-and-debriefs/ABS\\_Energy\\_Efficiency\\_Advisory.pdf](https://ww2.eagle.org/content/dam/eagle/advisories-and-debriefs/ABS_Energy_Efficiency_Advisory.pdf) . [cited 30 September 2020];
- [40] Naval Ships' Technical Manual. Waterborne underwater hull cleaning of navy ships. S9086-CQ-STM-010/CH-081R5. Naval Sea Systems Command. 2002.
- [41] Poulsen RT, Johnson H. The logic of business vs. the logic of energy management practice: understanding the choices and effects of energy consumption monitoring systems in shipping companies. *Journal of Cleaner Production*. 2016; 112: 3785-3797.
- [42] Woods CM, Floerl O, Jones L. Biosecurity risks associated with in-water and shore-based marine vessel hull cleaning operations. *Marine pollution bulletin*. 2012; 64(7): 1392-1401.
- [43] Davidson IC, Brown CW, Sytsma MD, Ruiz GM. The role of containerships as transfer mechanisms of marine biofouling species. *Biofouling*. 2009; 25(7): 645-655.
- [44] Marine Environment Protection Committee 63/4-8. Air Pollution and Energy Efficiency: A Transparent and Reliable Hull and Propeller Performance Standard. London: IMO; 2011.
- [45] Park J, Kim B, Shim H, Ahn K, Park JH, Jeong D, Jeong S. Hull and Propeller Fouling Decomposition and Its Prediction based on Machine Learning Approach. In: Bertram V, editor. 3<sup>rd</sup> Hull Performance & Insight Conference -HullPIC'18; Redworth, UK, 12-14 March 2018.
- [46] van Ballegooijen E, Helsloot T. An Approach to Monitor the Propeller Separately from the Hull. In: Bertram V, editor. 4<sup>th</sup> Hull Performance & Insight Conference -HullPIC'19; Gubbio, Italy, 6-8 May 2019.

- [47] Holm E, Haslbeck E, Cusanelli, D. So, Your Ship is Not Operating Efficiently (Because of Biofouling) – Now What?. In: Bertram V, editor. 2<sup>nd</sup> Hull Performance & Insight Conference -HullPIC'17; Ulrichshusen, Germany, 27-29 March 2017.
- [48] Gundermann D, Dirksen T. A Statistical Study of Propulsion Performance of Ships and the Effect of Dry Dockings, Hull Cleanings and Propeller Polishes on Performance. In: Bertram V, editor. 1<sup>st</sup> Hull Performance & Insight Conference -HullPIC'16; Castello di Pavone, Italy, 13-15 April 2016.
- [49] Krapp A, Vranakis G. A Practical Way to Evaluate the In-Service Performance of Antifouling Coatings. SNAME meeting – Athens, Greece, December 2013.
- [50] Coraddu A, Oneto L, Baldi F, Cipollini F, Atlar M, Savio S. Data-driven ship digital twin for estimating the speed loss caused by the marine fouling. *Ocean Engineering*. 2019; 186: 106063.
- [51] Notti E, Figari M, Sala A, Martelli M. Experimental assessment of the fouling control coating effect on the fuel consumption rate. *Ocean Engineering*. 2019; 188, 106233.
- [52] van Ballegooijen E, Muntean T. Fuel Saving Potentials via Measuring Propeller Thrust and Hull Resistance at Full Scale: Experience with Ships in Service. In: Bertram V, editor. 1<sup>st</sup> Hull Performance & Insight Conference -HullPIC'16; Castello di Pavone, Italy, 13-15 April 2016.
- [53] Tarełko W. The effect of hull biofouling on parameters characterising ship propulsion system efficiency. *Polish Maritime Research*. 2015; 21(4): 27-34X.
- [54] Coraddu A, Lim S, Oneto L, Pazouki K, Norman R, Murphy AJ. A novelty detection approach to diagnosing hull and propeller fouling. *Ocean Engineering*. 2019; 176: 65-73.
- [55] Foteinos MI, Tzanos EI, Kyrtatos NP. Ship hull fouling estimation using shipboard measurements, models for resistance components, and shaft torque calculation using engine model. *Journal of Ship Research*. 2017; 61(2): 64-74.
- [56] International Organization for Standardization (ISO) ISO 19030-1:2016 Ships and Marine Technology-Measurement of Changes in Hull and Propeller Performance-Part 1: General Principles; 2016.
- [57] Solonen A. Experiences with ISO-19030 – and Beyond. In: Bertram V, editor. 1<sup>st</sup> Hull Performance & Insight Conference -HullPIC'16; Castello di Pavone, Italy, 13-15 April 2016.
- [58] Bertram V. Added Power in Waves – Time to Stop Lying (to Ourselves). In: Bertram V, editor. 1<sup>st</sup> Hull Performance & Insight Conference -HullPIC'16; Castello di Pavone, Italy, 13-15 April 2016.
- [59] Koboević Ž, Bebić D, Kurtela Ž. New approach to monitoring hull condition of ships as objective for selecting optimal docking period. *Ships and Offshore Structures*. 2019; 14(1): 95-103.
- [60] Tzamaloukas A, Glaros S, Bikli K. Different Approaches in Vessel Performance Monitoring, Balancing Accuracy, Effectiveness & Investment Aspects, from the Operator's Point of View. 3<sup>rd</sup> Hull Performance & Insight Conference -HullPIC'18; Redworth, UK, 12-14 March 2018.
- [61] Bertram V. Some Heretic Thoughts on ISO 19030. In: Bertram V, editor. 2<sup>nd</sup> Hull Performance & Insight Conference -HullPIC'17; Ulrichshusen, Germany, 27-29 March 2017.

- [62] Paereli S, Krapp A, Bertram V. Splitting Propeller Performance from Hull Performance – A Challenge. In: Bertram V, editor. 1<sup>st</sup> Hull Performance & Insight Conference - HullPIC'16; Castello di Pavone, Italy, 13-15 April 2016.
- [63] Oliveira DR. Roughest hour – approaches to ship hull fouling management [PhD thesis]. Gothenburg: Chalmers University of Technology, Department of Mechanics and Maritime Sciences; 2019.
- [64] Oliveira DR, Granhag L, Larsson L. A novel indicator for ship hull and propeller performance: Examples from two shipping segments. *Ocean Engineering*. 2020; 205: 107229.
- [65] Owen D, Demirel YK, Oguz E, Tezdogan T, Incecik A. Investigating the effect of biofouling on propeller characteristics using CFD. *Ocean Engineering*. 2018; 159: 505-516.
- [66] Song S, Demirel YK, Atlar M. An investigation into the effect of biofouling on full-scale propeller performance using CFD. In: International Conference on Offshore Mechanics and Arctic Engineering (Vol. 58776, p. V002T08A036). American Society of Mechanical Engineers; Glasgow, UK 9-14 June 2019.
- [67] Song S, Demirel YK, Atlar M. Propeller Performance Penalty of Biofouling: Computational Fluid Dynamics Prediction. *Journal of Offshore Mechanics and Arctic Engineering*. 2020; 142(6): 061901.
- [68] Song S, Demirel YK, Atlar M. Penalty of hull and propeller fouling on ship self-propulsion performance. *Applied Ocean Research*. 2020; 94: 102006.
- [69] Schultz MP. Effects of coating roughness and biofouling on ship resistance and powering. *Biofouling*. 2007; 23(5): 331-341.
- [70] Atlar M, Yeginbayeva IA, Turkmen S, Demirel YK, Carchen A, Marino A, Williams, D. (2018). A rational approach to predicting the effect of fouling control systems on "in-service" ship performance. *GMO Journal of Ship and Marine Technology*. 2018; 24(213): 5-36.
- [71] ITTC Specialist Committee on Surface Treatment. Final report and recommendation to the 26<sup>th</sup> ITTC. In: Proceedings of 26<sup>th</sup> ITTC – Volume II, Rio de Janeiro, Brazil, 2011.
- [72] ITTC – Recommended Procedures and Guidelines. 1978 ITTC Performance Prediction Method. 7.5-02-03-01.4. 2017.
- [73] Molland AF, Turnock SR, Hudson DA. Ship resistance and propulsion. 1<sup>st</sup> edition. New York: Cambridge university press; 2011.
- [74] Silva ER, Ferreira O, Ramalho PA, Azevedo NF, Bayón R, Igartua A, Bordado JC, Calhorda MJ. Eco-friendly non-biocide-release coatings for marine biofouling prevention. *Science of The Total Environment*. 2019; 650: 2499-2511.
- [75] Uzun D, Demirel YK, Coraddu A, Turan O. Time-dependent biofouling growth model for predicting the effects of biofouling on ship resistance and powering. *Ocean Engineering*. 2019; 191: 106432.
- [76] Kresic M, Haskell B. Effects of propeller design-point definition on the performance of a propeller/diesel engine system with regard to in-service roughness and weather conditions. *Transactions – The Society of Naval Architects and Marine Engineers*. 1983; 91: 195–224.
- [77] Schlichting H. *Boundary Layer Theory*. 4<sup>th</sup> edition. New York: McGraw-Hill Series in Mechanical Engineering; 1979.
- [78] Schultz MP, Swain GW. The influence of biofilms on skin friction drag. *Biofouling*. 2000; 15(1-3): 129-39.

- [79] Bradshaw P. Turbulence. 1<sup>st</sup> edition. Berlin: Springer-Verlag; 1976.
- [80] White F. Viscous fluid Flow. 3<sup>rd</sup> edition. Boston: McGraw Hill; 2006.
- [81] Devenport WJ, Sutton EP. Near-wall behaviour of separated and reattaching flows. *AIAA journal*. 1991;29(1): 25-31.
- [82] Ligrani PM. Structure of turbulent boundary layers. In: Cheremisinoff NP (ed). *Encyclopedia of Fluid Mechanics*. Gulf Publishing; 1989. pp 112-189
- [83] Tsuji Y, Nakamura I. Probability density function in the log-law region of low Reynolds number turbulent boundary layer. *Physics of Fluids*. 1999; 11(3) :647-58.
- [84] Marusic I, Monty JP, Hultmark M, Smits AJ. On the logarithmic region in wall turbulence. *Journal of Fluid Mechanics*. 2013; 716.
- [85] Lo TS, L'vov VS, Pomyalov A, Procaccia I. Estimating von Kármán's constant from homogeneous turbulence. *EPL (Europhysics Letters)*. 2005; 72(6): 943.
- [86] Leonardi S, Orlandi P, Antonia RA. Properties of d-and k-type roughness in a turbulent channel flow. *Physics of fluids*. 2007; 19(12): 125101.
- [87] Johnson RW. *Handbook of fluid dynamics*. 2<sup>nd</sup> edition. Boca Raton. Crc Press; 2016.
- [88] Schultz MP. The effect of biofilms on turbulent boundary layer structure [PhD thesis]. Melbourne, USA: Florida Institute of Technology; 1998.
- [89] Chung D, Chan L, MacDonald M, Hutchins N, Ooi A. A fast direct numerical simulation method for characterising hydraulic roughness. *Journal of Fluid Mechanics*. 2015; 773: 418-431.
- [90] Townsend AA. *The structure of turbulent shear flow*, 2<sup>nd</sup> edition. Cambridge, UK: Cambridge University Press; 1976.
- [91] Flack KA, Schultz MP. Roughness effects on wall-bounded turbulent flows. *Physics of Fluids*. 2014; 26(10): 101305.
- [92] Raupach MR, Antonia RA, Rajagopalan S. Rough-wall turbulent boundary layers. *Applied Mechanics Reviews*. 1991; 44: 1-25.
- [93] Flack KA, Schultz MP, Connelly JS. Examination of a critical roughness height for outer layer similarity. *Physics of Fluids*. 2007; 19(9): 095104.
- [94] Schultz MP, Flack KA. The rough-wall turbulent boundary layer from the hydraulically smooth to the fully rough regime. *Journal of Fluid Mechanics*, 2007; 580: 381.
- [95] Chan L, MacDonald M, Chung D, Hutchins N, Ooi A. A systematic investigation of roughness height and wavelength in turbulent pipe flow in the transitionally rough regime. *Journal of Fluid Mechanics*. 2015; 771: 743-777.
- [96] Saito N. Large-Eddy Simulations of Fully Developed Turbulent Channel and Pipe Flows with Smooth and Rough Walls [PhD thesis]. Pasadena, USA: California Institute of Technology; 2014.
- [97] Saito N, Pullin DI, Inoue M. Large eddy simulation of smooth-wall, transitional and fully rough-wall channel flow. *Physics of Fluids*. 2012; 24(7): 075103.
- [98] Flack KA, Schultz MP, Shapiro TA. Experimental support for Townsend's Reynolds number similarity hypothesis on rough walls. *Physics of Fluids*. 2005; 17(3): 035102.
- [99] Shockling MA, Allen JJ, Smits AJ. Roughness effects in turbulent pipe flow. *Journal of Fluid Mechanics*. 2006; 564: 267.
- [100] Squire DT, Hutchins N, Morrill-Winter C, Schultz MP, Klewicki JC, Marusic I. Applicability of Taylor's hypothesis in rough-and smooth-wall boundary layers. *Journal of Fluid Mechanics*. 2017; 812: 398-417.
- [101] Tsikata JM, Tachie MF. Adverse pressure gradient turbulent flows over rough walls. *International journal of heat and fluid flow*. 2013; 39: 127-145.

- [102] Jiménez J. Turbulent flows over rough walls. *Annual Review of Fluid Mechanics*. 2004; 36: 173-196.
- [103] Castro IP. Rough-wall boundary layers: mean flow universality. *Journal of Fluid Mechanics*. 2007; 585: 469-485.
- [104] Farkas A, Degiuli N, Martić I. Towards the prediction of the effect of biofilm on the ship resistance using CFD. *Ocean Engineering*. 2018; 167: 169-186.
- [105] Schultz MP. The relationship between frictional resistance and roughness for surfaces smoothed by sanding. *Journal of Fluids Engineering*. 2002; 124(2): 492-499.
- [106] Sucec J. A Relatively Simple Integral Method for Turbulent Flow Over Rough Surfaces. *Journal of Fluids Engineering*. 2017; 139(12).
- [107] Antonia RA, Krogstad PA. Effect of Different Surface Roughnesses on a Turbulent Boundary Layer. *Journal of the Brazilian Society of Mechanical Sciences*. 2000; 22(1): 1-15.
- [108] Yeginbayeva IA, Granhag L, Chernoray V. Review and historical overview of experimental facilities used in hull coating hydrodynamic tests. *Proceedings of the Institution of Mechanical Engineers, Part M: Journal of Engineering for the Maritime Environment*. 2019; 233(4): 1240-1259.
- [109] Schultz MP, Finlay JA, Callow ME, Callow, JA. Three models to relate detachment of low form fouling at laboratory and ship scale. *Biofouling*. 2003; 19(S1): 17-26.
- [110] Demirel YK, Khorasanchi M, Turan O, Incecik A, Schultz MP. A CFD model for the frictional resistance prediction of antifouling coatings. *Ocean Engineering*. 2014; 89: 21-31.
- [111] Monty JP, Dogan E, Hanson R, Scardino AJ, Ganapathisubramani B, Hutchins N. An assessment of the ship drag penalty arising from light calcareous tubeworm fouling. *Biofouling*. 2016; 32(4): 451-464.
- [112] Atencio BN, Chernoray V. A resolved RANS CFD approach for drag characterization of antifouling paints. *Ocean Engineering*. 2019; 171: 519-532.
- [113] Rushd S, Islam A, Sanders RS. CFD methodology to determine the hydrodynamic roughness of a surface with application to viscous oil coatings. *Journal of Hydraulic Engineering*. 2018; 144(2): 04017067.
- [114] Hakim ML, Nugroho B, Chin C, Putranto T, Suastika I, Utama I. Assessment of drag penalty resulting from the roughness of freshly cleaned and painted ship-hull using computational fluid dynamics. In 11<sup>th</sup> International Conference on Marine Technology (MARTEC), Kuala Lumpur, Malaysia; 2018.
- [115] Cui J, Patel VC, Lin CL. Large-eddy simulation of turbulent flow in a channel with rib roughness. *International Journal of Heat and Fluid Flow*. 2003; 24(3): 372-388.
- [116] Lu H, Zhang LZ. Large Eddy Simulation of Turbulent Channel Flows over Rough Walls with Stochastic Roughness Height Distributions. *Journal of Hydrodynamics*. 2020; 32: 570-581.
- [117] Sridhar A. Large-eddy Simulation of Turbulent Boundary Layers with Spatially Varying Roughness [PhD thesis]. Pasadena, USA: California Institute of Technology; 2018.
- [118] Forooghi P, Stroh A, Magagnato F, Jakirlić S, Frohnapfel B. Toward a universal roughness correlation. *Journal of Fluids Engineering*. 2017; 139(12): 121201.
- [119] Busse A, Lützner M, Sandham ND. Direct numerical simulation of turbulent flow over a rough surface based on a surface scan. *Computers & Fluids*. 2015; 116: 129-147.

- [120] Flack KA, Schultz MP. Review of hydraulic roughness scales in the fully rough regime. *Journal of Fluids Engineering*. 2010; 132(4): 041203.
- [121] Barros JM, Schultz MP, Flack KA. Measurements of skin-friction of systematically generated surface roughness. *International Journal of Heat and Fluid Flow*. 2018; 72: 1-7.
- [122] Howell D, Behrends B. A review of surface roughness in antifouling coatings illustrating the importance of cutoff length. *Biofouling*. 2006; 22(6): 401-410.
- [123] Schultz MP. Frictional resistance of antifouling coating systems. *Journal of Fluids Engineering*. 2004; 126(6): 1039-1047.
- [124] Flack KA, Schultz MP, Rose WB. The onset of roughness effects in the transitionally rough regime. *International journal of heat and fluid flow*. 2012; 35: 160-167.
- [125] Ünal UO, Ünal B, Atlar M. Turbulent boundary layer measurements over flat surfaces coated by nanostructured marine antifouling. *Experiments in fluids*, 2012; 52(6): 1431-1448.
- [126] Usta O, Korkut E. A study for the effect of surface roughness on resistance characteristics of flat plates. *Marine Coatings: London, UK*; 2013.
- [127] Ünal UO. Correlation of frictional drag and roughness length scale for transitionally and fully rough turbulent boundary layers. *Ocean Engineering*. 2015; 107: 283-298.
- [128] Yeginbayeva IA, Atlar M. An experimental investigation into the surface and hydrodynamic characteristics of marine coatings with mimicked hull roughness ranges. *Biofouling*. 2018; 34(9): 1001-1019.
- [129] Li C, Atlar M, Haroutunian M, Anderson C, Turkmen S. An experimental investigation into the effect of Cu<sub>2</sub>O particle size on antifouling roughness and hydrodynamic characteristics by using a turbulent flow channel. *Ocean Engineering*. 2018; 159: 481-495.
- [130] Aupoix B. Roughness corrections for the  $k-\omega$  shear stress transport model: status and proposals. *Journal of Fluid Engineering*. 2015; 137(2): 021202.
- [131] Erbas B. The turbulent boundary layer and frictional drag characteristics of new generation marine fouling control coatings. *Brodogradnja: Teorija i praksa brodogradnje i pomorske tehnike*. 2019; 70(4): 51-65.
- [132] Holm E, Schultz M, Haslbeck E, Talbott W, Field A. Evaluation of hydrodynamic drag on experimental fouling-release surfaces, using rotating disks. *Biofouling*. 2004;20(4-5): 219-226.
- [133] Schultz MP, Walker JM, Steppe CN, Flack KA. Impact of diatomaceous biofilms on the frictional drag of fouling-release coatings. *Biofouling*. 2015; 31(9-10): 759-773.
- [134] Li C, Atlar M, Haroutunian M, Norman R, Anderson C. An investigation into the effects of marine biofilm on the roughness and drag characteristics of surfaces coated with different sized cuprous oxide (Cu<sub>2</sub>O) particles. *Biofouling*. 2019; 35(1): 15-33.
- [135] Hartenberger J, Gose J, Ceccio S. Flow and drag measurement over soft biofilms. In: 32<sup>nd</sup> Symposium on Naval Hydrodynamics (SNH), Hamburg, Germany; 2018.
- [136] Yeginbayeva IA, Granhag L, Chernoray V. A multi-aspect study of commercial coatings under the effect of surface roughness and fouling. *Progress in Organic Coatings*. 2019; 135: 352-367.
- [137] Murphy EA, Barros JM, Schultz MP, Flack KA, Steppe CN, Reidenbach MA. Roughness effects of diatomaceous slime fouling on turbulent boundary layer hydrodynamics. *Biofouling*. 2018; 34(9): 976-988.

- [138] Turkmen S, Atlar M, Yeginbayeva I, Benson S, Finlay JA, Clare AS. Frictional drag measurements of large-scale plates in an enhanced plane channel flowcell. *Biofouling*. 2020; 36(2): 169-182.
- [139] Demirel YK, Uzun D, Zhang Y, Fang HC, Day AH, Turan O. Effect of barnacle fouling on ship resistance and powering. *Biofouling*. 2017; 33(10): 819-834.
- [140] Uzun D, Ozyurt R, Demirel YK, Turan O. Does the barnacle settlement pattern affect ship resistance and powering? *Applied Ocean Research*. 2020; 95: 102020.
- [141] Nikuradse J. (1950). *Laws of flow in rough pipes*. 2<sup>nd</sup> edition. Washington, USA: National Advisory Committee for Aeronautics; 1950.
- [142] Mckeon BJ, Li JD, Jiang W, Morrison JF, Smits AJ. Further observations on the mean velocity distribution in fully developed pipe flow. *Journal of Fluid Mechanics*. 2004; 501: 135-147.
- [143] Grigson CWB. Drag Losses of New Ships Caused by Hull Finish. *Journal of Ship Research*. 1992; 36: 182–196.
- [144] Hama FR. Boundary-layer characteristics for smooth and rough surfaces. *Transactions – The Society of Naval Architects and Marine Engineers*. 1954. 62: 333-351.
- [145] Granville PS. Three Indirect Methods for the Drag Characterization of Arbitrarily Rough Surfaces on Flat Plates. *Journal of Ship Research*. 1987; 31: 70–77.
- [146] Schultz MP, Myers A. Comparison of three roughness function determination methods. *Experiments in fluids*. 2003; 35(4): 372-379.
- [147] Schultz MP, Flack KA. Reynolds-number scaling of turbulent channel flow. *Physics of Fluids*. 2013; 25(2): 025104.
- [148] Zanon ES, Nagib H, Durst F. Refined cf relation for turbulent channels and consequences for high-Re experiments. *Fluid dynamics research*. 2009; 41(2): 021405.
- [149] Bertram V. *Practical ship hydrodynamics*. 2<sup>nd</sup> edition. Amsterdam, Netherland: Elsevier; 2011.
- [150] Seok J, Park JC. A fundamental study on measurement of hull roughness. *Brodogradnja: Teorija i praksa brodogradnje i pomorske tehnike*. 2020; 71(1): 59-69.
- [151] Farkas A, Degiuli N, Martić I. Assessment of hydrodynamic characteristics of a full-scale ship at different draughts. *Ocean Engineering*. 2018; 156: 135-152.
- [152] Pereira FS, Eça L, Vaz G. Verification and validation exercises for the flow around the KVLCC2 tanker at model and full-scale Reynolds numbers. *Ocean Engineering*. 2017; 129: 133-148.
- [153] Raven HC, van der Ploeg A, Starke AR, Eca L. Towards a CFD-based prediction of ship performance — progress in predicting full-scale resistance and scale effects. *Proceedings of RINA-CFD-2008*. In: RINA MARINE CFD Conference. London, UK; 2008.
- [154] Helma S. A scaling procedure for modern propeller designs. *Ocean Engineering*. 2016; 120: 165-174.
- [155] Lin TY, Kouh JS. On the scale effect of thrust deduction in a judicious self-propulsion procedure for a moderate-speed containership. *Journal of Marine Science and Technology*. 2015; 20(2): 373-391.
- [156] Woods Hole Oceanographic Institution, United States. Navy Department. Bureau of Ships. *Marine fouling and its prevention (No. 580)*. United States Naval Institute; 1952.
- [157] Towinsin, RL. The Ship Hull Fouling Penalty. *Biofouling*. 2003; 19(S1): 9-15.
- [158] ITTC – Recommended Procedures and Guidelines. 1978 ITTC Performance Prediction Method. 7.5-02-03-01.4. 2011.



- [159] ITTC Specialist Committee on Performance of Ships in Service. Final report and recommendation to the 28<sup>th</sup> ITTC. In: Proceedings of 28<sup>th</sup> ITTC – Volume II, Wuxi, China, 2017.
- [160] Townsin RL, Byrne D, Milne A, Svensen T. Speed, Power and Roughness: The Economics of Outer Bottom Maintenance. Transactions of RINA. 1980; 122.
- [161] Malone JA, Little DE, Allman M. Effects of Hull Foulants and Cleaning/Coating Practices on Ship Performance and Economics. Transactions – The Society of Naval Architects and Marine Engineers. 1980; 88.
- [162] Kan S, Shiba H, Tsuchida K, Yokoo K. Effect of fouling of a ship's hull and propeller upon propulsive performance. International Shipbuilding Progress. 1958; 5(41): 15-34.
- [163] ITTC Specialist Committee on Performance of Ships. In: Proceedings of 14<sup>th</sup> ITTC – Volume III, Ottawa, Canada, 1975.
- [164] Aucher M. Useful Points of View on the Section Drag on Propeller Characteristics. prepared for the International Towing Tank Conference, Performance Committee Meetings. Trondheim, Norway. 1973.
- [165] Lerbs H. On the Effects of Scale and Roughness on Free Running Propellers. Journal of the American Society of Naval Engineers. 1951; 1.
- [166] Townsin RL, Spencer DS, Mosaad M. Rough propeller penalties. Transactions – Society of Naval Architects and Marine Engineers. 1985; 93: 165-187.
- [167] Atlar M, Glover EJ, Candries M, Mutton R, Anderson CD. The effect of a Foul Release coating on propeller performance. Conference Proceedings Environmental Sustainability (ENSUS). University of Newcastle; 2002.
- [168] Candries M. Drag, boundary-layer and roughness characteristics of marine surfaces coated with antifouling [PhD thesis]. Newcastle, UK: University of Newcastle-upon Tyne; 2001.
- [169] Glover EJ. Propulsive devices for improved propulsive efficiency. Institute of Marine Engineers Transactions. 1987; 99: Paper 31.
- [170] Granville PS. 1958. The frictional resistance and turbulent boundary layer of rough surfaces. Journal of ship research. 1958; 2: 52-74.
- [171] Python Software Foundation. Python Language Reference, version 3.6. Available at <http://www.python.org>, accessed 1<sup>st</sup> February 2021.
- [172] Demirel YK, Song S, Turan O, Incecik A. Practical added resistance diagrams to predict fouling impact on ship performance. Ocean Engineering. 2019; 186: 106112.
- [173] Kiosidou, ED, Liarakapis DE, Tzabiras GD, Pantelis DI. Experimental investigation of roughness effect on ship resistance using flat plate and model towing tests. Journal of Ship Research. 2017; 61(2): 75-90.
- [174] Patel VC. Perspective: flow at high Reynolds number and over rough surfaces—Achilles heel of CFD. Journal of Fluids Engineering. 1998; 120: 434-444.
- [175] Eça L, Hoekstra M. Numerical aspects of including wall roughness effects in the SST  $k-\omega$  eddy-viscosity turbulence model. Computers & fluids. 2011; 40(1): 299-314.
- [176] Ohashi K. Numerical study of roughness model effect including low-Reynolds number model and wall function method at actual ship scale. Journal of Marine Science and Technology. 2020; 1-13.
- [177] Date JC, Turnock SR. A study into the techniques needed to accurately predict skin friction using RANS solvers with validation against Froude's historical flat plate experimental data. Report. 1999.

- [178] Leer-Andersen M, Larsson L. An Experimental/Numerical Approach for Evaluating Skin Friction on Full-Scale Ships With Surface Roughness. *Journal of Marine Science and Technology*. 2003; 8: 26–36.
- [179] Izaguirre-Alza P, Perez-Rojas L, Nunez-Basanez JF. Drag Reduction through Special Paints Coated on the Hull. In: *International Conference on Ship Drag Reduction SMOOTH-SHIPS*. Istanbul, Turkey, 20-21 May 2010.
- [180] Siemens. STAR-CCM+, version 2020.1.1. software package.
- [181] Khor YS, Xiao Q. CFD simulations of the effects of fouling and antifouling. *Ocean Engineering*. 2011; 38(10): 1065-1079.
- [182] Castro AM, Carrica PM, Stern F. Full scale self-propulsion computations using discretized propeller for the KRISO container ship KCS. *Computers & fluids*. 2011; 51(1): 35-47.
- [183] Vargas A, Shan H. A numerical approach for modelling roughness for marine applications. In: *Proceedings of the ASME 2016 Fluids Engineering Division Summer Meeting FEDSM2016*. Washington, USA, 10-14 July 2016.
- [184] Kidd B, Finnie AA, Chen H. Predicting the Impact of Fouling Control Coatings on Ship Powering Requirements and Operational Efficiency. In: Bertram V, editor. *1<sup>st</sup> Hull Performance & Insight Conference -HullPIC'16*; Castello di Pavone, Italy, 13-15 April 2016.
- [185] Goedicke T. Numerical Investigation on Hull Roughness Effects on Propulsion Performance. In: Bertram V, editor. *2<sup>nd</sup> Hull Performance & Insight Conference - HullPIC'17*; Ulrichshusen, Germany, 27-29 March 2017.
- [186] Seok J, Park JC. Numerical simulation of resistance performance according to surface roughness in container ships. *International Journal of Naval Architecture and Ocean Engineering*. 2020; 12: 11-19.
- [187] Karabulut UC, Özdemir YH, Barlas B. Numerical Study on the Hydrodynamic Performance of Antifouling Paints. *Journal of Marine Science and Application*. 2020; 19(1): 41-52.
- [188] Demirel YK, Turan O, Incecik A. Predicting the effect of biofouling on ship resistance using CFD. *Applied Ocean Research*. 2017; 62: 100-118.
- [189] Ostman A, Koushan K, Savio L. Study on Additional Ship Resistance due to Roughness using CFD. In: Bertram V, editor. *4<sup>th</sup> Hull Performance & Insight Conference - HullPIC'19*; Gubbio, Italy, 6-8 May 2019.
- [190] Vargas A, Shan H. Modeling of Ship Resistance as a Function of Biofouling Type, Coverage, and Spatial Variation. In: Bertram V, editor. *2<sup>nd</sup> Hull Performance & Insight Conference -HullPIC'17*; Ulrichshusen, Germany, 27-29 March 2017.
- [191] Vargas A, Shan H, Holm E. Using CFD to Predict Ship Resistance due to Biofouling, and Plan Hull Maintenance. In: Bertram V, editor. *4<sup>th</sup> Hull Performance & Insight Conference -HullPIC'19*; Gubbio, Italy, 6-8 May 2019.
- [192] Speranza N, Kidd B, Schultz MP, Viola IM. Modelling of hull roughness. *Ocean Engineering*, 2019; 174: 31-42.
- [193] Song S, Demirel YK, Atlar M. An investigation into the effect of biofouling on the ship hydrodynamic characteristics using CFD. *Ocean Engineering*. 2019; 175: 122-137.
- [194] Andersson J, Oliveira DR, Yeginbayeva I, Leer-Andersen M, Bensow RE. Review and comparison of methods to model ship hull roughness. *Applied Ocean Research*. 2020; 99: 102119.

- [195] Mikkelsen H, Walther JH. Effect of roughness in full-scale validation of a CFD model of self-propelled ships. *Applied Ocean Research*. 2020; 99: 102162.
- [196] García S, Trueba A, Boullosa-Falces D, Islam H, Soares CG. Predicting ship frictional resistance due to biofouling using Reynolds-averaged Navier-Stokes simulations. *Applied Ocean Research*. 2020; 101: 102203.
- [197] Song S, Demirel YK, Atlar M, Dai S, Day S, Turan O. Validation of the CFD approach for modelling roughness effect on ship resistance. *Ocean Engineering*. 2020; 200: 107029.
- [198] Ferziger JH, Perić M. *Computational Methods for Fluid Dynamics*. 3<sup>rd</sup> edition. Berlin; Heidelberg; New York; Barcelona; Hong Kong; London; Milan; Paris; Tokyo: Springer; 2002.
- [199] Tezdogan T, Demirel YK, Kellett P, Khorasanchi M, Incecik A, Turan O. Full-scale unsteady RANS CFD simulations of ship behaviour and performance in head seas due to slow steaming. *Ocean Engineering*. 2015; 97, 186-206.
- [200] Sezen S, Dogrul A, Delen C, Bal S. Investigation of self-propulsion of DARPA Suboff by RANS method. *Ocean Engineering*. 2018; 150: 258-271.
- [201] Hai-long S, Obwogi EO, Yu-min S. Scale effects for rudder bulb and rudder thrust fin on propulsive efficiency based on computational fluid dynamics. *Ocean Engineering*. 2016; 117: 199-209.
- [202] Bašić J, Degiuli N, Dejhalla R. Total resistance prediction of an intact and damaged tanker with flooded tanks in calm water. *Ocean engineering*. 2017; 130: 83-91.
- [203] Sigmund S, el Moctar O. Numerical and experimental investigation of propulsion in waves. *Ocean Engineering*. 2017; 144: 35-49.
- [204] Larsson L, Stern F, Visonneau M. *Numerical Ship Hydrodynamics: An assessment of the Gothenburg 2010 Workshop*. 1<sup>st</sup> edition. Dordrecht; Heidelberg; London; New York: Springer; 2014.
- [205] Siemens. *STAR-CCM+ User Guide*. 2020.
- [206] Farkas A, Degiuli N, Martić I. Numerical investigation into the interaction of resistance components for a series 60 catamaran. *Ocean engineering*. 2017; 146: 151-169.
- [207] Perić R, Abdel-Maksoud M. Reliable damping of free-surface waves in numerical simulations. *Ship Technology Research*. 2016; 63(1): 1-13.
- [208] Choi J, Yoon SB. Numerical simulations using momentum source wave-maker applied to RANS equation model. *Coastal Engineering*. 2009; 56(10): 1043-1060.
- [209] ITTC – Recommended Procedures and Guidelines. *Uncertainty Analysis in CFD Verification and Validation Methodology and Procedures*. 7.5-03-01-01. 2008.
- [210] ITTC – Recommended Procedures and Guidelines. *Practical Guidelines for Ship CFD Applications*. 7.5-03-02-03. 2011.
- [211] Terziev M, Tezdogan T, Incecik A. Application of eddy-viscosity turbulence models to problems in ship hydrodynamics. *Ships and Offshore Structures*. 2020; 15(5): 511-534.
- [212] Terziev M, Tezdogan T, Oguz E, Gourlay T, Demirel YK, Incecik A. Numerical investigation of the behaviour and performance of ships advancing through restricted shallow waters. *Journal of Fluids and Structures*. 2018; 76: 185-215.
- [213] Donlan RM. Biofilms: microbial life on surfaces. *Emerging infectious diseases*. 2002; 8(9): 881-890.
- [214] Stoodley P, DeBeer D, Lewandowski Z. Liquid flow in biofilm systems. *Applied and environmental microbiology*. 1994; 60(8): 2711-2716.

- [215] Molino PJ, Wetherbee R. The biology of biofouling diatoms and their role in the development of microbial slimes. *Biofouling*, 2008; 24(5): 365-379.
- [216] Hunsucker KZ, Vora GJ, Hunsucker JT, Gardner H, Leary DH, Kim S, Lin B, Swain G. (2018). Biofilm community structure and the associated drag penalties of a groomed fouling release ship hull coating. *Biofouling*. 2018; 34(2): 162-172.
- [217] Zargiel KA, Swain GW. Static vs dynamic settlement and adhesion of diatoms to ship hull coatings. *Biofouling*. 2014; 30(1): 115-129.
- [218] Hunsucker JT, Hunsucker KZ, Gardner H, Swain G. Influence of hydrodynamic stress on the frictional drag of biofouling communities. *Biofouling*. 2016; 32(10): 1209-1221.
- [219] Durst F, Fischer M, Jovanovic J, Kikura H. Methods to set up and investigate low Reynolds number, fully developed turbulent plane channel flows. *Journal of Fluids Engineering*. 1998; 120: 496-503.
- [220] Moffat RJ. Describing the uncertainties in experimental results. *Experimental Thermal and Fluid Science*. 1988; 1: 3-17.
- [221] Oliveira D, Granhag L. Matching forces applied in underwater hull cleaning with adhesion strength of marine organisms. *Journal of Marine Science and Engineering*. 2016; 4(4): 66.
- [222] ASTM D3623. Standard Test Method for Testing Antifouling Panels in Shallow Submergence. 1994; Vol. 6.02.
- [223] Kempf G. On the Effect of Roughness on the Resistance of Ships. *Transactions of the Institution of Naval Architects*. 1937; 79: 109-119.
- [224] Leer-Andersen M, Larsson L. An Experimental/Numerical Approach for Evaluating Skin Friction on Full-Scale Ships With Surface Roughness. *Journal of Marine Science and Technology*. 2003; 8: 26-36.
- [225] Bradshaw P. A Note on "Critical Roughness Height and Transitional Roughness. *Physics of Fluids*. 2000; 12: 1611-1614.
- [226] Kim WJ, Van SH, Kim DH. Measurement of flows around modern commercial ship models. *Experiments in fluids*. 2001; 31(5): 567-578.
- [227] Hino T. Proceedings of CFD workshop Tokyo 2005. Tokyo, Japan. National Maritime Research Institute. 2005.
- [228] Simonsen CD, Otzen JF, Joncquez S, Stern F. EFD and CFD for KCS heaving and pitching in regular head waves. *Journal of Marine Science and Technology*. 2013; 18(4): 435-459.
- [229] Bingjie G, Steen S. Added resistance of a VLCC in short waves. In: 29<sup>th</sup> International Conference on Ocean, Offshore and Arctic Engineering OMAE 2010; Shanghai, China, 6-11 June 2010.
- [230] Brodarski institute. 6389 report. Zagreb, Croatia. 2014.
- [231] SIMMAN 2008. <http://www.simman2008.dk/index.html> [accessed 30 September 2020].
- [232] U.S. Coast Guard Research and Development Center. Preliminary Investigations of Biofouling of Ships' Hulls: Non-Indigenous Species Investigations in the Columbia River. April 2006.
- [233] Pullin DI, Hutchins N, Chung D. Turbulent flow over a long flat plate with uniform roughness. *Physical Review Fluids*. 2017; 2(8): 082601.
- [234] Farkas A, Degiuli N, Martić I. An investigation into the effect of hard fouling on the ship resistance using CFD. *Applied Ocean Research*. 2020; 100: 102205.

- [235] van der Ploeg A, Raven HC, Windt J, Leroyer A, Queutey P, Deng GB, Visonneau M. Computations of free-surface viscous flows at model and full scale—a comparison of two different approaches. In: Proceedings of the 27<sup>th</sup> symposium on naval hydrodynamics. Seoul, South Korea, 5-10 October 2008.
- [236] Song S, Demirel YK, Muscat-Fenech CDM, Tezdogan T, Atlar M. Fouling effect on the resistance of different ship types. *Ocean Engineering*. 2020; 216: 107736.
- [237] Sun S, Chang X, Guo C, Zhang H, Wang C. Numerical investigation of scale effect of nominal wake of four-screw ship. *Ocean Engineering*. 2019; 183: 208-223.
- [238] Sadat-Hosseini H, Wu PC, Carrica PM, Kim H, Toda Y, Stern F. CFD verification and validation of added resistance and motions of KVLCC2 with fixed and free surge in short and long head waves. *Ocean Engineering*. 2013; 59: 240-273.
- [239] Watson DGM. *Practical Ship Design*. 1<sup>st</sup> edition. Oxford, UK: Elsevier. 1998.
- [240] Farkas A, Degiuli N, Martić I, Dejhalla R. Numerical and experimental assessment of nominal wake for a bulk carrier. *Journal of Marine Science and Technology*. 2019; 24(4): 1092-1104.
- [241] Hyun Shin J, Jin Song S. Pressure gradient effects on smooth and rough surface turbulent boundary layers—part I: Favorable pressure gradient. *Journal of Fluids Engineering*. 2015; 137(1): 011203-1.
- [242] Shin JH., Jin Song S. Pressure gradient effects on smooth-and rough-surface turbulent boundary layers—part II: Adverse pressure gradient. *Journal of Fluids Engineering*. 2015; 137(1): 011204-1.
- [243] Mosaad M. *Marine propeller roughness penalties [PhD Thesis]*. Newcastle: University of Newcastle upon Tyne; 1986.
- [244] ICCT. *Reducing Greenhouse Gas Emissions from Ships – Cost Effectiveness Available Options*. White Paper Number 11. 2011.
- [245] NMRI. Tokyo 2015 A Workshop on CFD in Ship Hydrodynamics. <http://www.t2015.nmri.go.jp/kcs.html> (2015, accessed 30 September 2020).
- [246] Farkas A, Degiuli N, Martić I, Ančić I. Performance prediction method for fouled surfaces. *Applied Ocean Research*. 2020; 99: 102151.
- [247] Farkas A, Song S, Degiuli N, Martić I, Demirel YK. Impact of biofilm on the ship propulsion characteristics and the speed reduction. *Ocean Engineering*. 2020; 199: 107033.
- [248] Atlar M, Glover EJ, Candries M, Mutton R, Anderson CD. The effect of a Foul Release coating on propeller performance. In: *Conference Proceedings Environmental Sustainability (ENSUS)*. University of Newcastle. 2002.
- [249] Farkas A, Degiuli N, Martić I, Dejhalla R. Impact of hard fouling on the ship performance of different ship forms. *Journal of Marine Science and Engineering*. 2020; 8(10): 748.
- [250] Huang TT, Groves NC. *Effective Wake: Theory and Experiment*. (No. DTNSRDC-81/033). DAVID W TAYLOR Naval Ship Research and Development Center, Bethesda MD. 1981.
- [251] Gokce MK, Kinaci OK, Alkan AD. Self-propulsion estimations for a bulk carrier. *Ships and Offshore Structures*. 2019; 14(7): 656-663.
- [252] Machado TAD. *Self-propulsion CFD calculations using the Continental Method [Master Thesis]*. Erasmus Mundus Master Course in Integrated Advanced Ship Design. EMSHIP; 2018.

- [253] Gaggero S, Villa D, Viviani M. An extensive analysis of numerical ship self-propulsion prediction via a coupled BEM/RANS approach. *Applied Ocean Research*. 2017; 66: 55-78.
- [254] Choi JE, Min KS, Kim JH, Lee SB, Seo HW. Resistance and propulsion characteristics of various commercial ships based on CFD results. *Ocean engineering*. 2010; 37(7): 549-566.
- [255] Carlton J. *Marine Propellers and Propulsion*. 2<sup>nd</sup> edition. Burlington USA: Butterworth-Heinemann; 2007.
- [256] MAN Energy Solutions. CEAS engine calculations. Available at <https://www.man-es.com/marine/products/planning-tools-and-downloads/ceas-engine-calculations>, accessed 1<sup>st</sup> February 2021.
- [257] ITTC – Recommended Procedures and Guidelines. Testing and Extrapolation Methods Propulsion, Performance Propulsion Test. 7.5-02-03-01.1. 2008.
- [258] Kauffeldt A, Hansen H. Enhanced Performance Analysis and Benchmarking with CFD Baselines. In: Bertram V, editor. 3<sup>rd</sup> Hull Performance & Insight Conference - HullPIC'18; Redworth, UK, 12-14 March 2018.
- [259] Belamarić B. Utjecaj hrapavljenja oplakane površine na eksploatacijska svojstva broda (in Croatian) [PhD thesis]. Zagreb: Faculty of Mechanical Engineering and Naval Architecture; 2008.
- [260] ITTC The Specialist Committee on Scaling of Wake Field. Final report and recommendation to the 26<sup>th</sup> ITTC. In: Proceedings of 26<sup>th</sup> ITTC – Volume II, Rio de Janeiro, Brazil, 2011.
- [261] Xing T, Stern F. Factors of safety for Richardson extrapolation. *Journal of Fluids Engineering*. 2010; 132(6): 061403.
- [262] Eça L, Saraiva G, Vaz G, Abreu, H. The pros and cons of wall functions. In: 34<sup>rd</sup> International Conference on Offshore Mechanics and Arctic Engineering. American Society of Mechanical Engineers. St John's, Canada. 1-6 June 2015.

## A Appendix

### The influence of the applied turbulence model on the numerically obtained hydrodynamic characteristics

In order to investigate the influence of applied turbulence model on the numerically obtained ship resistance, open water and self-propulsion characteristics, four different turbulence models were applied within numerical simulations of resistance, open water and self-propulsion tests [151] in full-scale. What is more, the influence of the applied turbulence model on the numerically obtained nominal wake was investigated in [240] using three different turbulence models.

The first study [151] included the application of two versions of  $k-\varepsilon$  turbulence models, standard (SKE) and realizable (RKE),  $k-\omega$  SST (SSTKO) as well as Reynolds Stress Model (RSM). As said before,  $k-\omega$  and  $k-\omega$  SST turbulence models represent the most frequently applied turbulence models in the field of numerical ship hydrodynamics, while RSM was chosen as a representation of anisotropic turbulence models. Numerical simulations of resistance, open water and self-propulsion tests were performed using RANS equations and VOF method for tracking and locating the free surface in simulations with free surface effects included. Numerical simulations of open water tests were carried out using MRF method, while numerical simulations of self-propulsion tests were performed using body force method. In order to simulate surface condition which is present at sea trial,  $\Delta U^+$  model proposed in [188] was implemented within the wall function of CFD solver and  $k$  is set to  $30 \mu\text{m}$ , as proposed in [69]. Even though, the study was performed for a handymax bulk carrier for three different loading conditions at two speeds, the influence of the application of various turbulence models was performed only for design loading condition at design speed. It should be noted that within this thesis, a handymax bulk carrier for design loading condition, analysed within [151], [240] is selected as one of the case studies.

Verification studies for grid size and time step were carried out for resistance test for design loading condition at design speed and numerical uncertainties were determined for all turbulence models. For that purpose, three meshes were generated: coarse mesh (around 2.5 million cells), medium mesh (around 5 million cells) and fine mesh (around 10 million cells). Three different time steps were investigated: coarse time step ( $0.01L/v$ ), medium time step ( $0.005L/v$ ) and fine time step ( $0.0025L/v$ ), where  $L$  is the ship length and  $v$  is the ship speed. According to the ITTC recommendations [210] time step should be  $\Delta t = (0.01 \div 0.005)L/v$ , and the limits of this range correspond to coarse and medium time step. The obtained temporal and grid uncertainties in the prediction of  $R_T$  were low for all four investigated turbulence models, i.e. below 0.2%. Verification study for grid size was carried out for self-propulsion test for design loading condition at design speed and numerical uncertainty was calculated for realizable  $k-\varepsilon$  turbulence model only. For that purpose, three meshes were generated: coarse mesh (around 1.9 million cells), medium mesh (around 4.1 million cells) and fine mesh (around 8.9 million cells). The obtained grid uncertainty for the prediction of  $n$  was low and it was equal to 1.2%, while for  $P_D$  was higher and it was equal to 6.8%.

The validation of the obtained numerical results was performed by comparison with the extrapolated towing tank results, obtained by Brodarski institute [230]. It should be noted that experimental results were extrapolated using five different extrapolation procedures in order to assess the differences among them. Thereafter, a detail analysis of the obtained results was presented, as well as the advantages and disadvantages of extrapolation methods. In general, the lowest  $RD$  between the numerically obtained results and extrapolated ones were obtained with the application of RSM turbulence model.

The numerically obtained  $R_T$  along with  $RD$  from the extrapolated  $R_T$  obtained using different PPM are presented within Table A.1. It can be seen that the numerically obtained  $R_T$  are lower than the extrapolated ones. The highest  $RD$  are obtained with ITTC 1957 PPM, which decompose  $C_T$  on  $C_F$ ,  $C_R$  and  $C_A$ . Thus within this PPM,  $C_R$  is assumed to be independent of the scale, what represents the shortcoming of this PPM. Since  $C_{vp}$  depends on  $Rn$  value it should be scaled. A part of this shortcoming is taken into account with  $C_A$ . However, within ITTC 1957 PPM it is not prescribed how to assess this value, i.e. several towing tank institutes have different methods for its assessment. ITTC 1978 and 1999 PPM, have the same procedure for the assessment of  $R_T$  and this procedure is described in subsections 2.3.1 and 2.3.2. The main difference between ITTC 1978 PPM and ITTC 2017 PPM in the assessment of  $R_T$  lies in the separation of  $C_A$  and  $\Delta C_F$  within ITTC 2017 PPM, as shown in subsection 2.3.1. Consequently, the obtained difference of  $R_T$  obtained using ITTC 1978 PPM and ITTC 2017 PPM is small and it is lower than 0.2%. The important deficiency of ITTC PPM is that form factor value is independent of scale. Lately, it has been shown by Pereira et al. [152] that this is not valid if ITTC 1957 model-ship correlation line is used. However, as shown by Raven et al. [153], that deficiency is overcome if Grigson friction line has been used in the extrapolation procedure. Grigson extrapolation procedure has two friction lines depending on  $Rn$ , i.e. one for model and one for full-scale. It can be seen from Table A.1 that the lowest  $RD$  are obtained using RSM turbulence model and the lowest  $RD$  is obtained for RSM turbulence model and Grigson extrapolation procedure, i.e. 4.1%. As already noted, Reynolds stress tensor within RSM turbulence model is obtained from six additional equations rather than being modelled. In this way, RSM considers the anisotropy of Reynolds stress tensor and predicts the vortices better. Because of this, the computational time of numerical simulation with RSM turbulence model was significantly larger when compared to eddy-viscosity models [151].

In the prediction of open water characteristics all turbulence models predicted relatively similar results, Table A.2. Within this table, open water characteristics for advance coefficients around self-propulsion point are shown ( $J$  for self-propulsion point is closest to  $J = 0.56$ ). The obtained  $RD$  are relatively low for all open water characteristics regardless of the applied turbulence model, with the highest  $|RD|$  obtained for  $K_T$  equal to 5.8%, for  $K_Q$  equal to 5.7% and for  $\eta_o$  equal to 0.7% at  $J = 0.56$ .



Table A.1 Validation of the obtained  $R_T$  for design loading condition at design speed (adapted from [151])

PPM	$R_{T,EX}$ , kN	RKE	SKE	SSTKO	RSM
$R_{T,CFD}$ , kN	/	611.35	622.61	596.60	625.26
		<i>RD</i> , %	<i>RD</i> , %	<i>RD</i> , %	<i>RD</i> , %
ITTC 1957	664.24	-7.96	-6.27	-10.18	-5.87
ITTC 1978	657.75	-7.05	-5.34	-9.30	-4.94
ITTC 1999	657.75	-7.05	-5.34	-9.30	-4.94
ITTC 2017	658.59	-7.17	-5.46	-9.41	-5.06
Grigson	652.06	-6.24	-4.52	-8.51	-4.11

Table A.2 Validation of the obtained numerical results in OWT (adapted from [151])

$J$		EX	RKE <i>RD</i> , %	SKE <i>RD</i> , %	SSTKO <i>RD</i> , %	RSM <i>RD</i> , %
0.48	$K_T$	0.2147	0.2026 -5.66	0.2021 -5.89	0.2025 -5.68	0.2025 -5.69
	$K_Q$	0.0292	0.0274 -6.46	0.0273 -6.48	0.0272 -6.81	0.0274 -6.39
	$\eta_o$	0.5610	0.5658 0.86	0.5643 0.59	0.5678 1.21	0.5652 0.75
0.56	$K_T$	0.1814	0.1712 -5.66	0.1709 -5.82	0.1711 -5.70	0.1710 -5.74
	$K_Q$	0.0257	0.0243 -5.30	0.0243 -5.16	0.0242 -5.73	0.0243 -5.30
	$\eta_o$	0.6299	0.6275 -0.38	0.6253 -0.73	0.6301 0.03	0.6269 -0.47
0.64	$K_T$	0.1478	0.1385 -6.30	0.1383 -6.42	0.1385 -6.29	0.1384 -6.39
	$K_Q$	0.0222	0.0209 -5.68	0.0210 -5.44	0.0208 -6.11	0.0209 -5.65
	$\eta_o$	0.7090	0.6749 -4.81	0.6721 -5.20	0.6781 -4.36	0.6740 -4.94

The obtained  $n$  and  $P_B$  using for different turbulence models are shown within Table A.3. It can be seen that the highest  $RD$  for  $n$  is not greater than 6.3% regardless of the applied turbulence model, while  $RD$  obtained for  $P_B$  are generally below 10%. It should be noted that the best agreement with the extrapolated values is obtained utilizing  $k-\omega$  SST turbulence model, for which the obtained  $RD$  for both  $n$  and  $P_B$  are below 5.1%.

Table A.3 Validation of the obtained results for  $n$  and  $P_B$  (adapted from [151])

PPM	$n_{SPP,EX}$ , rpm	RKE	SKE	SSTKO	RSM
$n_{SPP,CFD}$ , rpm	/	109.265	109.791	108.285	109.045
		$RD$ , %	$RD$ , %	$RD$ , %	$RD$ , %
ITTC 1957	103.300	+5.77	+6.28	+4.83	+5.56
ITTC 1978	103.512	+5.56	+6.07	+4.61	+5.35
ITTC 1999	103.110	+5.97	+6.48	+5.02	+5.76
ITTC 2017	103.418	+5.65	+6.16	+4.71	+5.44
	$P_{BSPP,EX}$ , kW	RKE	SKE	SSTKO	RSM
$P_{BSPP,CFD}$ , kW	/	8167.1	8318.9	7849.2	8256.9
		$RD$ , %	$RD$ , %	$RD$ , %	$RD$ , %
ITTC 1957	7575.0	+7.82	+9.82	+3.62	+9.00
ITTC 1978	7496.3	+8.95	+10.97	+4.71	+10.15
ITTC 1999	7464.9	+9.41	+11.44	+5.15	+10.61
ITTC 2017	7481.3	+9.17	+11.20	+4.92	+10.37

Validation of propulsion characteristics had shown that the obtained propulsion characteristics had the lowest  $RD$  using RSM turbulence model, Table A.4. As can be seen from Table A.4, satisfactory agreement was achieved for all propulsion characteristics and the obtained  $RD$  were below 5.1% regardless of the applied turbulence model or PPM for all propulsion characteristics except  $1-w$ , where higher  $RD$  were obtained, but still in line with the ones published in the literature [253], [254]. The obtained  $RD$  could be prescribed to various aspects, for example insufficiently precise assessment of the nominal wake or open water characteristics (since body force method was applied) and this could be directly related to the overestimated values of  $n$ , Table A.3. However, modelling error should be considered as well, as only effect of the propeller was modelled, i.e. the propeller was not discretized. Also, within numerical simulations of self-propulsion tests, the correction for induced velocity was not applied. Obviously, lower  $RD$  would be obtained if the rigid body simulation was performed, i.e. if the propeller was discretized. For example, Sezen et al. [200] have compared the obtained results using body force method and rigid body method and shown that body force method predicts lower  $\eta_D$  and consequently higher  $n$  than rigid body method. This can be attributed to the fact

that  $\eta_H$  was underestimated with body force method, which can be related to the inability of the method to assess accurately the interaction between ship hull and propeller. Sezen et al. [200] have not mentioned whether they have applied induced velocity correction within body force method. Numerical error was present as well, which could be reduced if a grid with higher number of cells was utilized. It should be noted that there are also aspects regarding PPM which will cause the increase in  $RD$  and this is mostly related to ITTC 1957 PPM, where  $1-w$  is not scaled, which is proven to be incorrect [152]. Therefore, it would be the best to compare the numerical results with the measured values in full-scale and in that way the errors introduced by PPM would be eliminated. Unfortunately, the data related to ship resistance and propulsion characteristics in full-scale is very rare and often confidential. Therefore, researchers compare numerically obtained results in full-scale with the extrapolated towing tank values [151].

The lowest  $RD$  in the prediction of  $\eta_p$  is obtained utilizing RSM turbulence model, which is expected since RSM is the most complex turbulence model.

The assessment of nominal wake is of crucial significance, as it directly influences  $J$  in self-propulsion test and therefore propeller performance as well. Recently, CFD simulations in full-scale have become relevant tool for the assessment of the nominal wake [260]. Namely, the boundary layer is relatively thicker in model than in full-scale due to lower  $Rn$ . What is more, the strength of bilge vortex is reduced in full-scale when compared to model scale, however the wake gradient is higher. Since, the measurements of full-scale nominal wake are extremely difficult, CFD simulations in full-scale are considered as very useful for the assessment of nominal wake. However, the nominal wake distribution is significantly influenced by the selection of turbulence model and consequently it is important to analyse the influence of turbulence model on the numerically obtained nominal wakes, beside the grid and time step sensitivity. Axial velocity contours, obtained using fine mesh within numerical simulations of resistance test for design loading condition at design speed with four turbulence models are shown in Figure A.1. As can be seen from Figure A.1, nominal wake distribution is characterized with significant reduction of axial velocity due to the presence of boundary layer at  $0^\circ$  above the hub, what is accurately predicted with all turbulence models. On the other hand, the obtained vortex near the hub is significantly narrower for RKE and SKE turbulence models than for SSTKO and RSM. The largest vortex is obtained with RSM turbulence model, which stands as the most accurate turbulence model for the assessment of nominal wake [253], [152]. The transversal velocity distribution obtained using fine mesh within numerical simulations of resistance test for design loading condition at design speed with four turbulence models is shown in Figure A.2. It can be seen from Figure A.2 that the largest hub vortex is obtained for RSM turbulence model.

Table A.4 Validation of the obtained propulsion characteristics for different turbulence models (adapted from [151])

PPM	$1-t_{EX}$	RKE	SKE	SSTKO	RSM
$1-t_{CFD}$	/	0.77473	0.78046	0.77887	0.77798
		<i>RD, %</i>	<i>RD, %</i>	<i>RD, %</i>	<i>RD, %</i>
ITTC 1957	0.78990	-1.92	-1.20	-1.40	-1.51
ITTC 1978	0.79387	-2.41	-1.69	-1.89	-2.00
ITTC 1999	0.79387	-2.41	-1.69	-1.89	-2.00
ITTC 2017	0.79211	-2.19	-1.47	-1.67	-1.78
	$1-w_{EX}$	RKE	SKE	SSTKO	RSM
$1-w_{CFD}$	/	0.79988	0.80236	0.79861	0.78612
		<i>RD, %</i>	<i>RD, %</i>	<i>RD, %</i>	<i>RD, %</i>
ITTC 1957	0.66433	+20.40	+20.78	+20.21	+18.33
ITTC 1978	0.70638	+13.24	+13.59	+13.06	+11.29
ITTC 1999	0.69793	+14.61	+14.96	+14.43	+12.64
ITTC 2017	0.70129	+14.06	+14.41	+13.88	+12.10
	$\eta_{R,EX}$	RKE	SKE	SSTKO	RSM
$\eta_{R,CFD}$	/	1.00273	1.00269	1.00263	1.00244
		<i>RD, %</i>	<i>RD, %</i>	<i>RD, %</i>	<i>RD, %</i>
ITTC 1957	1.04100	-3.68	-3.68	-3.69	-3.70
ITTC 1978	1.02959	-2.61	-2.61	-2.62	-2.64
ITTC 1999	1.02959	-2.61	-2.61	-2.62	-2.64
ITTC 2017	1.03486	-3.10	-3.11	-3.11	-3.13
	$\eta_{B,EX}$	RKE	SKE	SSTKO	RSM
$\eta_{B,CFD}$	/	0.65206	0.64918	0.65754	0.64560
		<i>RD, %</i>	<i>RD, %</i>	<i>RD, %</i>	<i>RD, %</i>
ITTC 1957	0.62560	+4.23	+3.77	+5.11	+3.20
ITTC 1978	0.64203	+1.56	+1.11	+2.42	+0.56
ITTC 1999	0.63701	+2.36	+1.91	+3.22	+1.35
ITTC 2017	0.64010	+1.87	+1.42	+2.72	+0.86

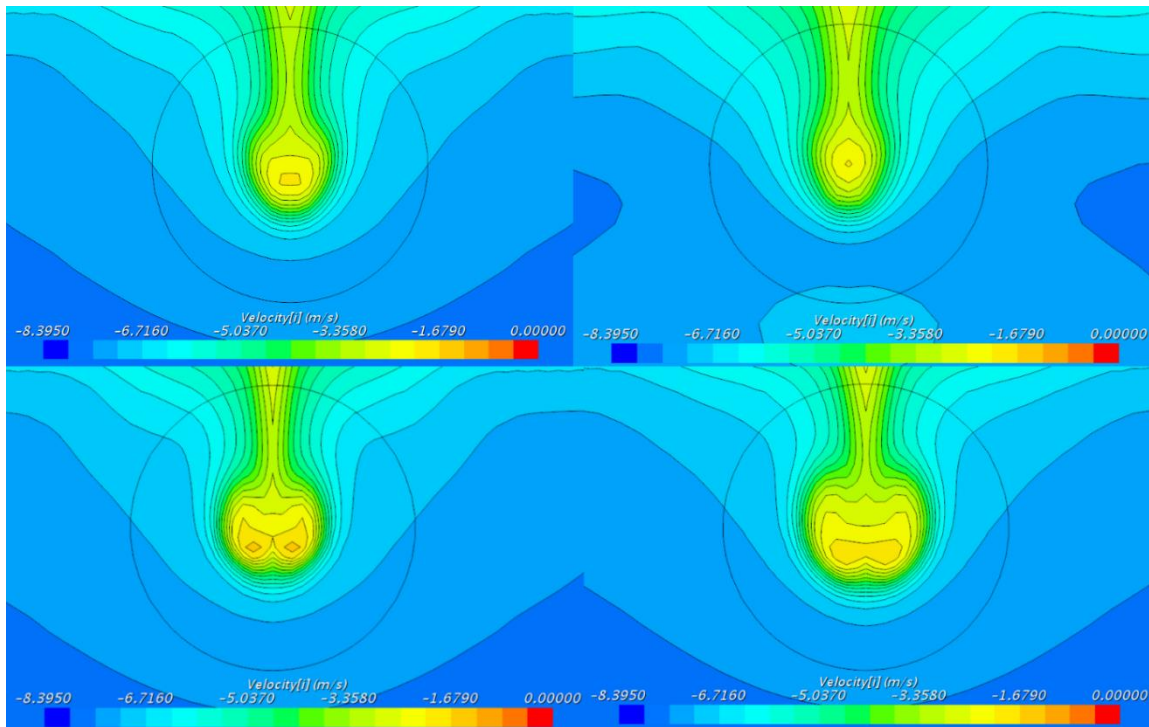


Figure A.1 Axial velocity contours obtained with: RKE (upper left), SKE (upper right), SSTKO (lower left) and RSM (lower right) turbulence models (adapted from [151])

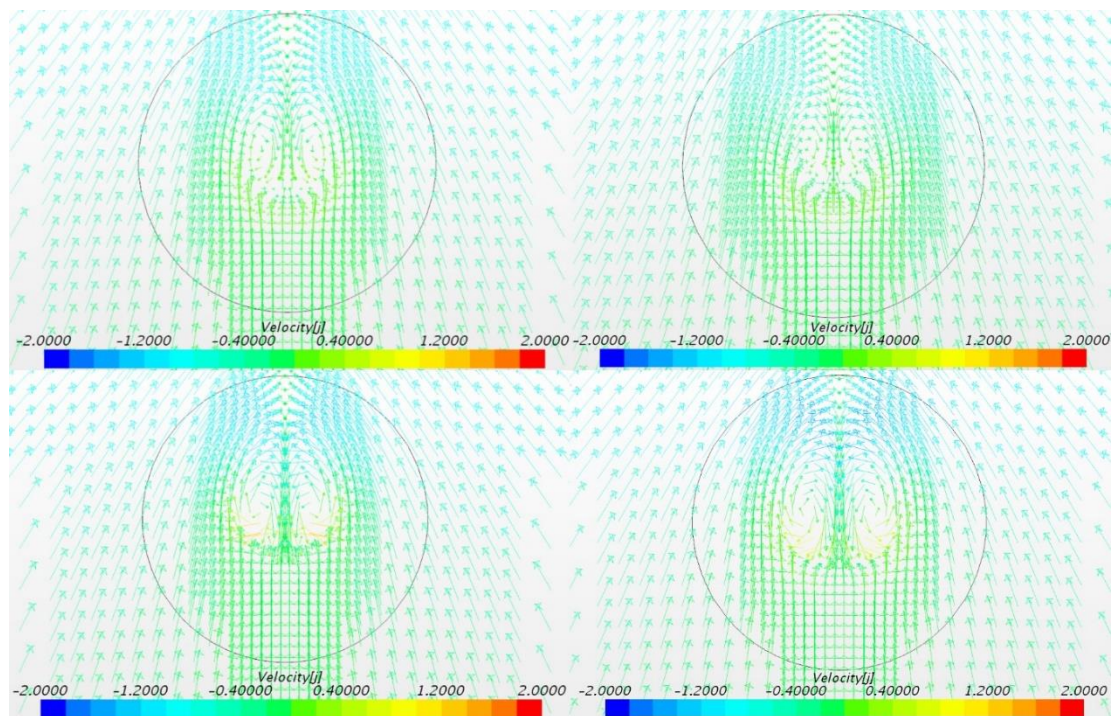


Figure A.2 The transversal velocity distribution obtained with: RKE (upper left), SKE (upper right), SSTKO (lower left) and RSM (lower right) (adapted from [151])

The obtained longitudinal wave cuts along the centreline of ship within resistance test for design loading condition at design speed using four different turbulence models are shown in Figure A.3. As can be seen from Figure A.3, no significant difference is obtained regardless of the applied turbulence model in longitudinal wave cuts along the centreline of ship. It should be

noted that within Figure A.3, the stern wave begins at the transom, while bow wave begins at fore perpendicular.

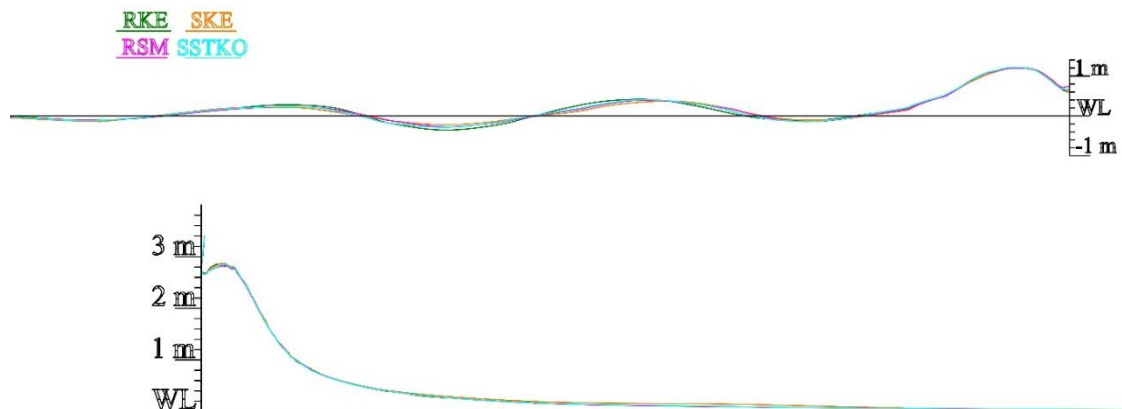


Figure A.3 The longitudinal wave cuts along the centreline of the ship: stern (upper), bow (lower) (adapted from [151])

Since the accurate assessment of the full-scale nominal wake is very important and it depends on the applied turbulence model [260], more detail investigation regarding the assessment of nominal wake in full-scale, as well as the influence of the applied turbulence model were performed [240]. Namely, within [240] nominal wake for a full-scale was obtained according to the procedure described in the ITTC recommendations [260]. Firstly, numerical simulations based on RANS equations were carried out for hydrodynamically smooth ship model. Thereafter, the obtained results were verified and validated by comparison against available towing tank results [230]. Nominal wake of a ship was validated by visual comparison, by comparison of circumferentially averaged nominal wake at certain radii and by comparison of integral values obtained numerically and experimentally. Furthermore, the influence of the choice of the turbulence model was investigated and the advantages and disadvantages of certain turbulence models were highlighted. The effect of near wall modelling, i.e. the solution obtained with and without application of wall functions, was analysed in model scale. Full-scale simulations were carried out using the same mesh type, discretization scheme and turbulence model as at model scale.

Thus, DBS of the flow around a handymax bulk carrier were performed using RANS equations, along with  $k-\varepsilon$  and  $k-\omega$  SST and RSM turbulence models. DBS are usually used for the assessment of nominal wake, as shown by many researchers [152], [253], [254], as DBS allow the significant reduction of computational time without compromising the accuracy.

Verification study was performed for the prediction of  $R_F$ ,  $R_{VP}$ ,  $R_V$  and integral value of nominal wake ( $w_N$ ) both in model and full-scale. Since DBS were performed as steady simulations, numerical uncertainty was consisted of grid uncertainty only, as iterative uncertainty was considered to be negligible as was done in [152]. Three different meshes were generated and DBS in model scale were performed with coarse mesh (around 2 million cells), medium mesh (around 4.5 million cells) and fine mesh (around 9.5 million cells) for simulations with and without the application of wall functions. DBS in full-scale were performed with coarse mesh (around 3.6 million cells), medium mesh (around 7.7 million cells) and fine mesh (around 15.6 million cells) with the application of the wall functions. Numerical uncertainties were estimated using the factor of safety approach [261]. The obtained numerical uncertainties

in the predictions of  $R_F$  and  $R_V$  were relatively low, and the highest obtained numerical uncertainty was obtained for RSM turbulence model in model scale. Thus, in the prediction of  $R_F$ , the highest numerical uncertainty was obtained with RSM turbulence model without the application of wall functions and it was equal to 4.2%, while in the prediction of  $R_V$ , the highest numerical uncertainty was obtained with RSM turbulence model with the application of wall functions and it was also equal to 4.2%. In the prediction of  $R_{VP}$ , significantly higher numerical uncertainties were obtained, especially in full-scale and the highest numerical uncertainty was obtained for  $k-\varepsilon$  turbulence model and it was equal to 18.5%. It should be noted that higher numerical uncertainties in the prediction of  $R_{VP}$  were also obtained within [152], where the authors have investigated the application of several turbulence models in the prediction of  $R_F$ ,  $R_{VP}$ ,  $R_V$ ,  $w_N$  and  $1+k$  for KVLCC2 using DBS without the application of wall functions. In the prediction of  $1-w_N$  relatively low numerical uncertainties were obtained for all applied turbulence models in model scale without wall functions and in full-scale [240]. Thus, the highest numerical uncertainty was obtained in model scale with  $k-\omega$  SST turbulence model and it was equal to 6.3%. However, numerical uncertainties in the prediction of  $1-w_N$  with the application of wall functions in model scale were significantly higher, with the highest numerical uncertainty equal to 21.6% obtained with RSM turbulence model. The higher numerical uncertainty obtained with the application of wall functions can be attributed to the fact that near wall grid had not enough resolution to capture the high gradients of the boundary layer, especially for the coarse mesh. Namely, meshes generated by commercial grid generators have cells which increase with the distance to the wall, i.e. prism layer cells [262]. However, in the region above the near wall cells, i.e. above prism layer cells grid can be too coarse, especially for coarse mesh. Since the solution obtained utilizing coarse mesh was taken into account in the verification study, the obtained numerical uncertainty was higher.

The obtained numerical results in model scale were validated by comparison with the obtained towing tank measurements with the five-hole Pitot tube in the towing tank of Brodarski institute [230]. A comparison between numerically and experimentally obtained circumferential averaged non-dimensional axial velocity distribution is shown in Figure A.4. In this figure circumferential averaged non-dimensional axial velocity distributions were obtained using three different turbulence models with and without the application of wall functions and fine mesh. In numerical simulations with and without the application of wall functions, the smallest  $RD$  between numerically and experimentally obtained results were obtained using RSM turbulence model, which allows solving the complex interactions in turbulent flow fields more reliable than eddy-viscosity turbulence models. Thus, in numerical simulations with the application of wall functions up to radius  $0.7R$ , the numerical values obtained with RSM were almost the same as the experimentally obtained ones. As can be seen from Figure A.4, the obtained circumferentially averaged non-dimensional axial velocity distributions using SSTKO turbulence model were quite satisfactory, even though this turbulence model is significantly simpler than RSM. The obtained  $RD$  for all turbulence models were in accordance with the results obtained in [253], [254].

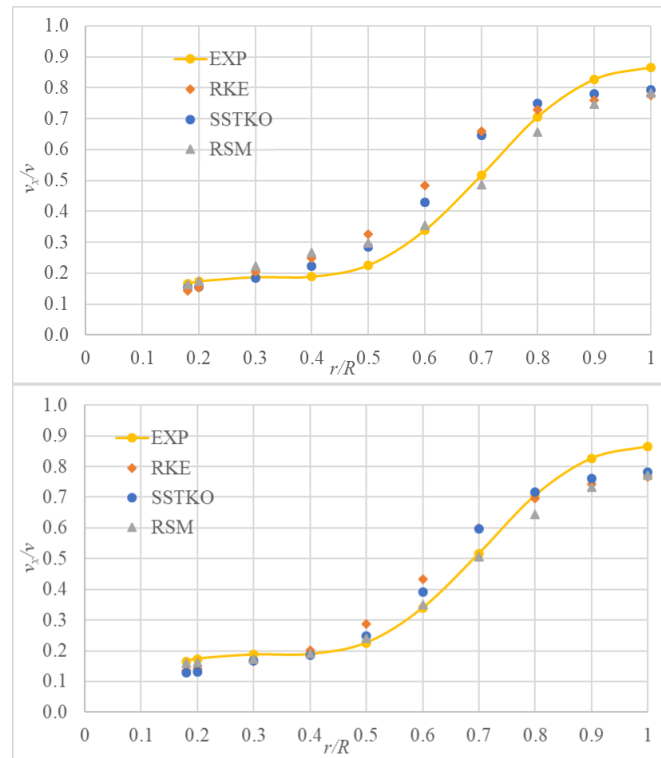


Figure A.4 The comparison between numerically and experimentally obtained circumferentially averaged non-dimensional axial velocity distribution without (upper) and with (lower) wall functions at model scale

After the comparison between numerically and experimentally obtained circumferentially averaged non-dimensional axial velocity distribution, visual comparison of the obtained nominal axial wake field was performed. In Figure A.5, nominal axial wake fields obtained using three turbulence models with the application of wall functions along with the experimentally obtained one are shown. The best agreement between numerically and experimentally obtained nominal axial wake field was achieved with the application of RSM. Nominal axial wake field of the investigated handymax bulk carrier in model scale was characterized with the strong velocity reduction at  $180^\circ$ , as well as around the hub. Numerically obtained nominal axial wake fields were characterized with a hook under the hub, which was probably caused by the implementation of the symmetry condition at the centre plane. RKE did not reliably represent the vortex positioned near the hub and it provided a weaker representation of velocity reduction at  $180^\circ$  than SSTKO and RSM. Velocity reduction around the hub was best predicted with RSM [240].

Finally, the integral values of  $1-w_N$  were compared and the obtained results are presented in Table A.5. The validation of the numerically obtained integral values of  $1-w_N$  was achieved at validation uncertainty ( $U_V$ ) level, except for solution obtained with RKE without the application of wall functions. It should be noted that  $U_V$  was consisted of experimental uncertainty ( $U_D$ ) (which is equal to 3%) and numerical uncertainty. The lowest  $RD$  between numerical and experimental results was achieved with RSM in numerical simulations without the application of wall functions and with RKE in numerical simulations with the application of wall functions.



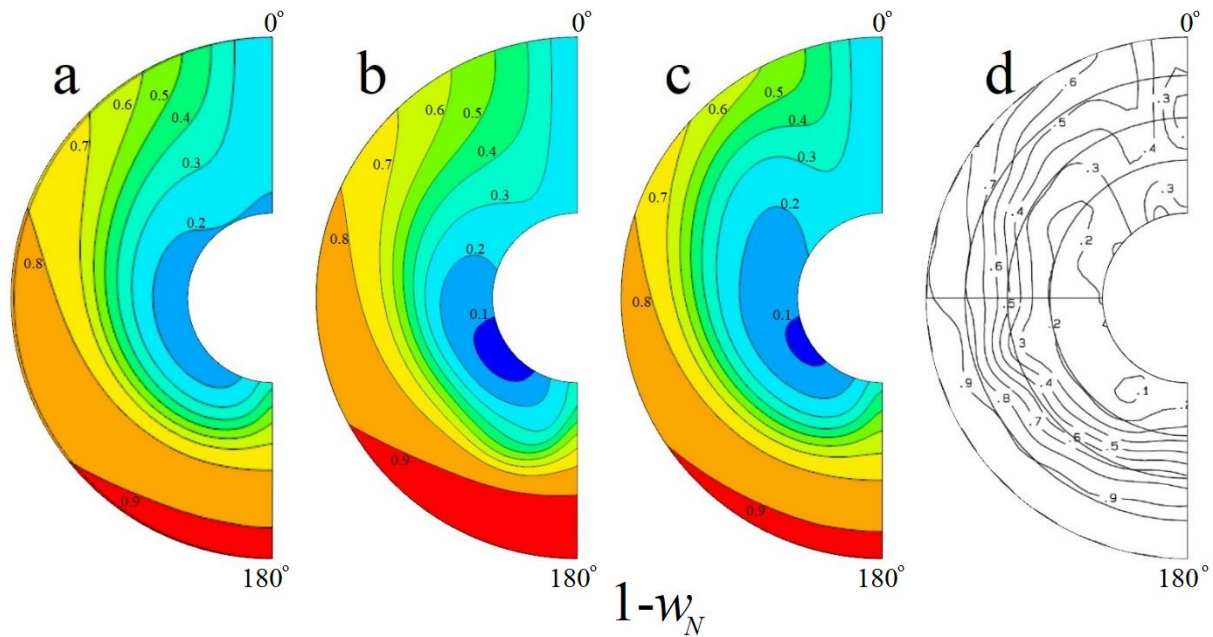


Figure A.5 Comparison between nominal axial wake field obtained utilizing RKE (a), SSTKO (b), RSM (c) and experimentally (d)

Table A.5 The comparison between numerically and experimentally obtained integral values of nominal wake

	Turbulence model	$(1 - w_N)_{CFD}$	$(1 - w_N)_{EXP}$	$RD, \%$
Model scale without wall functions	RKE	0.5672	0.5302	+6.9722
	SSTKO	0.5600		+5.6194
	RSM	0.5156		-2.7473
Model scale with wall functions	RKE	0.5273		-0.5432
	SSTKO	0.5266		-0.6814
	RSM	0.4916		-7.2835

After the validation of the obtained numerical results in model scale, the influence of the near wall modelling was investigated. The comparison between the obtained circumferentially averaged non-dimensional axial velocity distribution with and without the application of wall functions is shown in Figure A.6, while comparison between nominal axial wake field obtained with and without the application of wall functions is shown in Figure A.7. As can be seen from Table A.5 and in Figure A.6 and Figure A.7, the influence of near wall modelling on the obtained results was present. Thus, the differences between the obtained integral values of  $1 - w_N$  with and without the application of wall functions ranged from 7% for RKE to 4.6% for

RSM. The smallest differences in the obtained circumferentially averaged non-dimensional axial velocity distribution with and without the application of wall functions were obtained for RSM, Figure A.6. Thus, the obtained ratios between circumferentially averaged axial velocity and ship model speed ( $v_x / v$ ) with and without wall functions for RSM were almost same at all radii, except at  $r/R = 0.3, 0.4$  and  $0.5$ . The differences in the obtained circumferentially averaged non-dimensional axial velocity distribution with and without application of wall functions were smaller for SSTKO than for RKE. The differences in nominal axial wake field obtained with and without the application of wall functions were smaller for RSM and SSTKO than for RKE, Figure A.7.

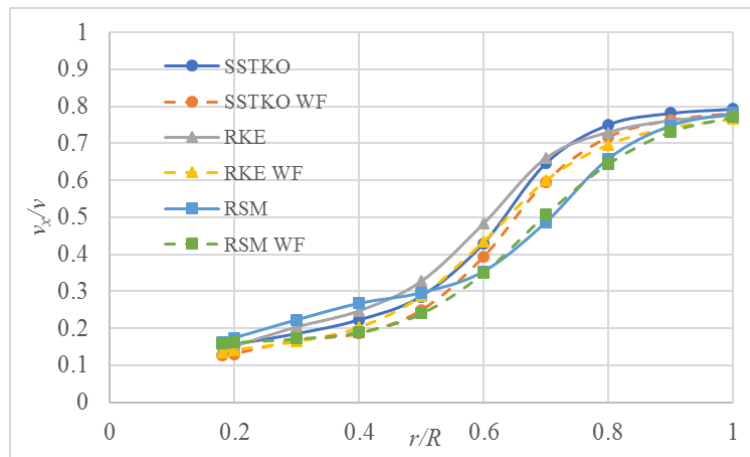


Figure A.6 Comparison between obtained circumferentially averaged non-dimensional axial velocity distribution with and without wall functions (adapted from [240])

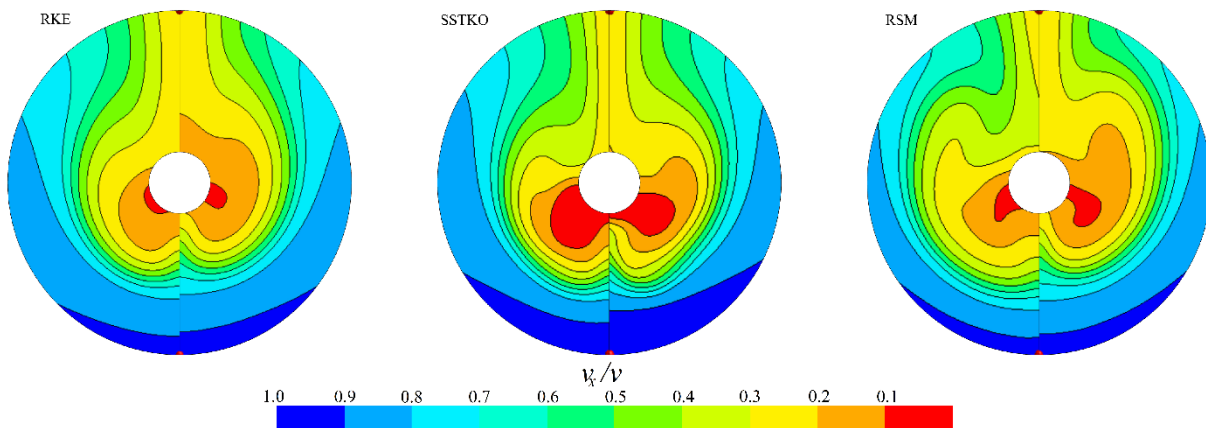


Figure A.7 Comparison between nominal axial wake field obtained without (left) and with (right) the application of wall functions

Even though, the nominal wake field was dependent on near wall modelling, it could be concluded that differences in the nominal wake field due to different near wall modelling were not significant. Furthermore, these differences were lower than the obtained differences due to the application of different turbulence models. Also, the number of cells in full-scale simulations would be significantly larger for simulations without the application of wall functions, because high aspect ratio of order  $10^3$  of prismatic cells near the wall is required in order to assure  $y^+ < 1$ . Consequently, the mesh near the wall must be refined causing

significantly greater number of cells [206]. Therefore, numerical simulations for full-scale were performed without the application of wall functions in order to avoid too large cell number.

The comparison of the numerically obtained circumferentially averaged non-dimensional axial velocity distribution using different turbulence models in full-scale is presented in Figure A.8, while contours of axial velocity in the propeller disc plane for model scale and full-scale are presented in Figure A.9. Regardless of the applied turbulence model in full-scale, the obtained  $v_x/v$  were almost the same for  $r/R \geq 0.6$ , Figure A.8. The lowest values of  $v_x/v$  were obtained for RSM, followed with SSTKO and RKE respectively. Generally, RSM is considered to be the best turbulence model for the assessment of the wake field for both model scale and full-scale [260]. Significant scale effects can be seen in contours of axial velocity in the propeller disc plane, Figure A.9. Thus, in model scale velocity is more reduced than in full-scale and the difference in this reduction can be particularly seen in the upper part of the propeller disc plane, i.e. in the range from  $135^\circ$  to  $180^\circ$ . This can be attributed to the relatively thicker boundary layer in model scale than in full-scale. As can be seen from Figure A.9, the obtained contours of axial velocity in the propeller disc plane for investigated turbulence models are more similar in full-scale than in model scale. The largest velocity reduction and the longitudinal vortex shed from the boundary layer is obtained using RSM both in model scale and full-scale. The numerically obtained  $1-w_N$  are compared with extrapolated  $1-w_N$  values obtained with towing tank measurements, Table A.6. For this purpose, experimentally obtained  $1-w_N$  values were extrapolated with ITTC 1978 PPM, i.e. equation (2.48), where  $\Delta C_F$  was equal to zero. As can be seen from Table A.6, the numerically obtained  $1-w_N$  in full-scale are more similar for different turbulence models than in model scale, i.e. the effect of the selection of certain turbulence model in full-scale is reduced in comparison with model scale. The lowest  $RD$  between numerical and extrapolated results is obtained for RSM turbulence model. Through comparison between numerical  $1-w_N$  both in model scale and full-scale as well as experimental  $1-w_N$  in model and extrapolated  $1-w_N$  in full-scale it can be concluded that numerical scale effects are more pronounced than the ones predicted with equation (2.48) [240].

Finally, it can be concluded that even though the obtained nominal wake field is dependent on the chosen turbulence model, the differences in the obtained nominal wake fields decrease in full-scale. Thus for larger radii, i.e.  $r/R \geq 0.6$ , the obtained circumferentially averaged non-dimensional axial velocity distributions are the same regardless of the applied turbulence model. RSM has predicted the largest velocity reduction in the propeller disc plane as well as the strongest longitudinal vortex shed from the boundary layer. This was expected since RSM turbulence model is the most complex amongst the investigated ones. In comparison between two eddy-viscosity models, the results obtained using SSTKO are in better agreement with experimental results. ITTC has advised to use SSTKO turbulence model for the efficient assessment of the wake field, while the application of RSM is advised in high resolution CFD simulations [260].

According to an extensive investigation of the influence of the applied turbulence model on the numerically obtained resistance, open water and propulsion characteristics [151], [240], within this thesis  $k-\omega$  SST turbulence model is chosen for the closure of set of equations (3.1) and (3.2).

Table A.6 The comparison between numerically and experimentally obtained integral values of nominal wake in full-scale

	Turbulence model	$(1 - w_N)_{CFD}$	$(1 - w_N)_{EX}$	$RD, \%$
Full-scale with wall functions	RKE	0.7142	0.6549	+9.3707
	SSTKO	0.7058		+8.8090
	RSM	0.6869		+5.3809

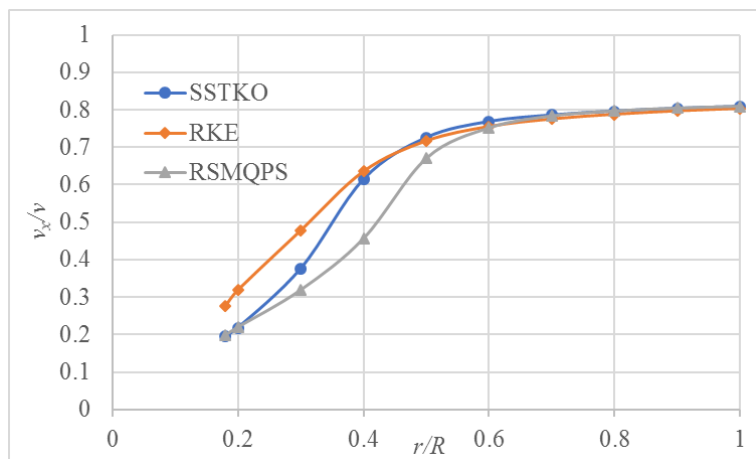


Figure A.8 Numerically obtained circumferentially averaged non-dimensional axial velocity distribution utilizing different turbulence models in full-scale (adapted from [240])

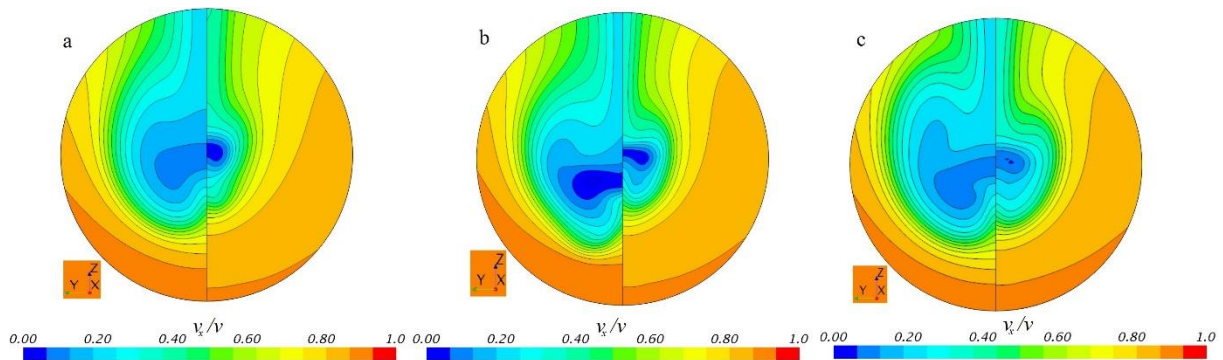


Figure A.9 Contours of axial velocity in the propeller disc plane for model scale (left) and full-scale (right) obtained utilizing RKE (a), SSTKO (b) and RSM (c) (adapted from [240])

## Curriculum vitae

Andrea Farkas was born on December 2<sup>nd</sup>, 1992 in Split. He finished primary and secondary school in Split and in academic year 2011/2012 enrolled Naval Architecture course at the Faculty of Mechanical Engineering and Naval Architecture, University of Zagreb. During his studies, he won several scholarship including state scholarship for excellent students, a scholarship from the University of Zagreb for excellence in studying and a scholarship from the Croatian Register of Ships. Also, he won two Davorin Bazjanac awards, two Medals of the Faculty of Mechanical Engineering and Naval Architecture, Dean's award, Bureau Veritas annual award for excellence in studying and he received the Rector's Award for individual scientific and artistic work. He graduated in Naval Architecture in 2016 and since October 2016, he has been employed as a teaching and research assistant at the Chair of Ship Hydromechanics, Department of Naval Architecture and Ocean Engineering. He enrolled postgraduate doctoral study in Naval Architecture and Ocean Engineering in academic year 2016/2017. He became a member of the Technical Committee TO 8, Shipbuilding at the Croatian Standards Institute in 2017. He is an Executive editor of journal *Brodogradnja*, indexed by Web of Sciences (WoS) Science Citation Index Expanded since 2008, for data transfer to a bibliographic database since 2017. He is Head of the Laboratory for Ship hydromechanics since 2018. He was awarded with the Annual award of the Society of university teachers, scholars and other scientists – Zagreb in 2018, AMAC UK award in 2019 as well as the award form Doctoral study for the best PhD student at the University of Zagreb, Faculty of Mechanical Engineering and Naval Architecture in the year 2018. He actively participates in teaching and is involved in other scientific and professional activities of the Chair of Ship Hydromechanics. So far, as an author or co-author, he has published 19 scientific papers in journals indexed in Web of Science Core Collection database, of which 16 papers are indexed in Current Contents database. He also published 14 papers in proceedings of conferences held in the country and abroad. He speaks and writes English.